UNIVERSITAT DE BARCELONA

Rational chemical design of Triarylmethyl-based devices and 2D materials

Isaac Alcón Rovira

Secció de Química Física

Departament de Ciència de Materials i Química Física

Facultat de Química

Universitat de Barcelona

Programa de doctorat de Química Teòrica i Modelització Computacional

Rational chemical design of Triarylmethyl-based devices and 2D materials

Memòria presentada per:

Isaac Alcón Rovira

per a optar al grau de Doctor per la Universitat de Barcelona

Dirigida per:

Dr. Stefan T. Bromley
(Universitat de Barcelona)

Dr. Francesc Illas i Riera
(Universitat de Barcelona)

Tutor:

Dr. Iberio De Pinho Ribeiro Moreira
(Universitat de Barcelona)

UNIVERSITAT DE BARCELONA

UNIVERSITAT DE BARCELONA

FACULTAD DE QUÍMICA

DEPARTAMENT DE CIÈNCIA DE MATERIALS I QUÍMICA FÍSICA

INTITUT DE QUÍMICA TEÒRICA I COMPUTACIONAL

Rational chemical design of Triarylmethyl-based devices and 2D materials

Isaac Alcón Rovira

Barcelona, 2018

UNIVERSITAT DE BARCELONA

Institut de Química Teòrica i Computacional
UNIVERSITAT DE BARCELONA

a l'Avi i la Iaia

The work presented in this doctoral thesis has been carried out at the Materials Science and Physical Chemistry Department of the Chemistry Faculty at the University of Barcelona (UB) and within the Institute of Theoretical and Computational Chemistry (IQTC-UB) and the Reference Network of Theoretical and Computational Chemistry of Catalunya (XRQTC).

This project has been possible in virtue of the financial support provided by the Spanish (MAT2012-30924 project) and the Catalan Government (2014SGR97 and XRQTC grants). Computer resources were partly provided by the Red Española de Supercomputación (RES) and the Centre de Supercomputació de Catalunya (CESCA).

Isaac Alcón Rovira is also grateful for the pre-doctoral grants from the Catalan (FI-DGR) and Spanish Government (FPU14/01470), as well as for the grant-in-aid that covered the research stay at Imperial College London given by the Spanish Government (FPU).

Agraïments

First of all I would like to thank Stefan Bromley, main supervisor of this PhD thesis, for his supervision and help during all these four years. I believe the success of this work has enormously relied on the intellectual freedom that Stefan gave me since the first day, promoting my own creativity and accepting new ideas, as well as being patient at the time of clarifying concepts and theories every time I needed. His accessibility has been of great value for me: I have had access to his time 80% of the occasions I pop up by his office, always open for discussion. I believe this is not that common within science. From a scientific perspective, I must recognise there are few more people with whom I connect more. That passion to seek for truth, even at the most fundamental level, is something I noticed even before starting this PhD thesis, and greatly appreciate. Again, unfortunately, this is a fundamental aptitude I fear is not that general in science today. All in all, I think we both have strongly believed in the work performed during time which, probably, is the result of the shared desire to do original, excellent and useful science. So... Thanks Stefan!!

També vull expressar el meu agraïment al Francesc Illas, co-director d'aquest treball. La seva actitud oberta i ganes de donar un cop de mà en el que fes falta han estat claus durant tot aquest temps, en molts aspectes. De nou, la accessibilitat al seu coneixement i consell és quelcom que em va sobtar des d'un començament: el seu despatx sempre ha estat obert per discutir de qualsevol qüestió laboral, científica o, fins i tot, d'actualitat política. La seva actitud pro-activa constant és una de les qualitats pel que li estic més agraït. Estic convençut que no hauria estat capaç de portar a terme els seminaris Interns del IQTC (conjuntament amb el Manel Mondelo) si no hagués estat pel suport i ànim que el Francesc em va donar amb aquesta qüestió des del mateix matí que va sorgir la idea discutint al cafè. Aquesta visió de voler provar noves iniciatives "bottop-up" la comparteixo totalment. I també li vull agrair els coffee-breaks del CMSL on he aprés més de com funciona el món científic que en uns quants congressos als que he assistit: de nou una mostra més de la gran accessibilitat que s'ofereix al grup del Francesc i el Stefan, on sembla que la única barrera personal entre estudiants i professors és la distancia que hi ha entre oficines. Un gust!

I per tancar el pack de direcció/tutoria, vull agrair al Iberio les seves classes particulars sobre mecànica quàntica i, en concret, els mètodes computacionals d'estructura electrònica. Al arribar a la UB el meu coneixement de tota aquesta branca de la ciència era completament nul·la, ha estat una sort per a mi poder nodrir-me del coneixement tan profund sobre els diferents models, aproximacions i "pegues" de cadascun d'ells que el Iberio m'ha aportat. Gràcies a ell tinc una idea aproximada (amb DFT... no podia ser d'un altre manera) del camp dels mètodes d'estructura electrònica la qual desitjo poder aprofundir en un futur amb més temps al meu abast.

En termes més generals, vull agrair a tots els membres del IQTC i de la Secció de Química Física de la UB tota l'ajuda rebuda i moments compartits durant aquest temps. En especial, moltes gràcies Jordi, Carme, Paniagua, Konstantin, Gabor, Federico, Ángel, Viñes, Rosendo i a tots els companys de oficines varies: Ilker, Sergey, Dani, Vera, Maria, Marçal, Alberto, Julia, Almu, Tommy, Andy, Toni, Lorena, Cristina, Raul, Sergi, Oriol (salvador de portades), Hèctor, Gerard, Manel, etc etc etc... Tot i que ha estat un període de treball força elevat, sempre us he tingut a un o a l'altre per xerrar una estona, fer una de *bolos*, o discutir sobre qualsevol tema, el qual m'ha ajudat enormement en aquesta difícil empresa que és el doctorat. Moltíssimes gràcies nanus/es! També vull agrair al Manel la co-organització dels Seminaris Interns del IQTC. Organitzar-los no ha estat

una empresa fàcil, però crec que finalment hem fet una feina prou ben feta amb, sembla, recorregut! Moltes gràcies també al Ramón, tècnic del Departament per la seva ajuda en repetides ocasions amb els varis pòsters que li he anat donant durant aquest temps. I abans de tancar el bloc IQTC/Departament no em puc oblidar dels Srs. Administradors de sistema; Jordi i Teresa. Ha estat un plaer poder resoldre els meus dubtes sobre el Linux i els ordinadors en general amb la vostra constant ajuda. Sempre que ho he necessitat, m'heu facilitat tot el temps necessari, sense la mínima mostra de cansament (i mira que he pujat vegades a la planta 7a eh...). Dóna gust aprendre coses tan interessants com la *command-line* amb gent tan disposada a ensenyar com vosaltres, així que moltíssimes gràcies companys!

Dedicaré una part d'aquests agraïments a la Dr. Marta Mas, ja no només per la qualitat com a persona i com d'agust es col·labora/treballa amb ella, si no també en particular per la vista que va tenir durant la meva tesis de Màster al proposar-me fer el doctorat dins la branca de la Química Computacional... Mai havia pensat en aquest camp, ni per descartar-lo. En canvi tu Marta vas veure que podia encaixar-hi i, 4 anys després, tinc clar que vull construir la meva carrera professional en aquesta direcció. Gràcies per veure en els teus estudiants quelcom més que eines per produir articles i preocupar-te pels seus camins personals, dins o fora de la teva línea de recerca. En el meu cas particular, ha estat clau.

En un terreny més personal vull agrair en general a tota la família per la paciència que han tingut durant aquests últims anys amb el escàs temps que he tingut per ells. Papa, Mama, Gerard, *sorry* per tots aquests no-possibles dinars, o dinars mirant el rellotge per temes de treball, i gràcies per comprendre-ho i adaptar-vos sense dir ni "mu". En la mateixa línea, gràcies Avi, Iaia, per entendre les meves visites cada cop més espaiades a mesura que ha anat avançant aquesta tesis doctoral.

M'agradaria també agrair al Víctor, company de converses durant tots aquests anys, per la teva saviesa i guia en moments difícils. Que important és poder rebre un bon consell de tant en tant. Ha estat fantàstic.

And *last but not least*, com se sol dir, et vull donar les gràcies, Jèssica, per ser-hi. El suport i estima que m'has donat tot aquest temps no es pot descriure en una frase o paràgraf. Simplement espero poder continuar el meu camí al teu costat per molts més anys.

Avi, Iaia, gràcies per ser casa meva.

Aquest treball va per vosaltres.

And nobody seems to like him
They can tell what he wants to do
And he never shows his feelings

But the fool on the hill
Sees the sun going down
And the eyes in his head
See the world spinning around

Oh, oh, oh, oh, oh, oh, oh
Round and round and round and round and round

And he never listens to them
He knows that they're the fools
They don't like him

The fool on the hill
Sees the sun going down
And the eyes in his head
See the world spinning around

John Lennon & Paul McCartney – *The Fool on the Hill*

Table of contents

Chapter 1
INTRODUCTION

As may be deduced from the title of this work, this PhD thesis has been mainly focused on the study, by means of first principles density functional theory (DFT) calculations, of triarylmethyl-based (TAM) devices and 2D materials. Some of the works in this thesis in collaboration with the experimental group of Prof Jaume Veciana and Dr Marta Mas-Torrent study different physic-chemical properties of TAMs that could be exploited within different type of devices for nano-electronics applications such as molecules wires, molecular switches and spintronic components. Hence, my contribution in those works has mainly been a support to the experimental findings where, by means of computational chemistry, I have been able to provide a more detailed insight into the studied TAM systems. Such a collaboration has proven to be very successful during these last four years, producing interesting works such as those presented in publications **#1**, **2**, **3** and **#7**. The proposition of TAM-based 2D covalent organic frameworks (TAM 2D-COFs) has arose using first principles DFT calculations as a tool to predict new molecular systems not experimentally realized yet (2nd part of this thesis). Despite the fact TAMs have been already used to construct different sorts of devices and materials, TAM 2D-COFs represent a class of materials which has not been experimentally realized yet. During this PhD project I have found such materials of primary interest, especially as future platforms for nano-electronics, and hence, by means of this work and key publications resulting from it, I propose such platforms to be applied in such direction in the future. The studies on different TAM 2D-COFs are described in publications **#5**, **#6** and **#8**. Contribution **#4** is a study of single-molecule TAMs that, later, lead to the design of TAM 2D-COFs and hence it may be considered as the starting point of such a research line.

Consistently, in this chapter I will first introduce TAM molecules and their role as building blocks to prepare different sorts of multi-functional materials and devices. In the second part I will briefly introduce the relatively new field of 2D covalent organic frameworks (2D-COFs) to provide a basic idea about the type of molecular arrays that are being generated in this branch of chemistry and a few studies highlighting their potential for future nano-electronics.

1.1 Triarylmethyls: A bit of history

1.1.1 The discovery

The start of the family of TAMs represents the start of organic radical chemistry, due to the fact the synthesis of the triphenylmethyl by Moses Gomberg in 1900 (see Fig. 1.1) is the first instance of a trivalent carbon atom;[1] i.e. an organic radical. Gomberg was trying to synthesize the tetra-phenyl methyl, but the resulting synthesized product showed to be an unsaturated hydrocarbon which easily reacted with both atmospheric oxygen or even in contact with diluted solution of iodine, not fitting with the expected behaviour for saturated hydrocarbons such as the pursued tetraphenylmethyl or the potential dimer, the hexaphenyl-ethyl. After a long number of experiments Gomberg concluded he was dealing with the first

instance of a trivalent carbon atom: i.e. the first instance of an organic radical, the triphenylmethyl[1] (Fig. 1b).

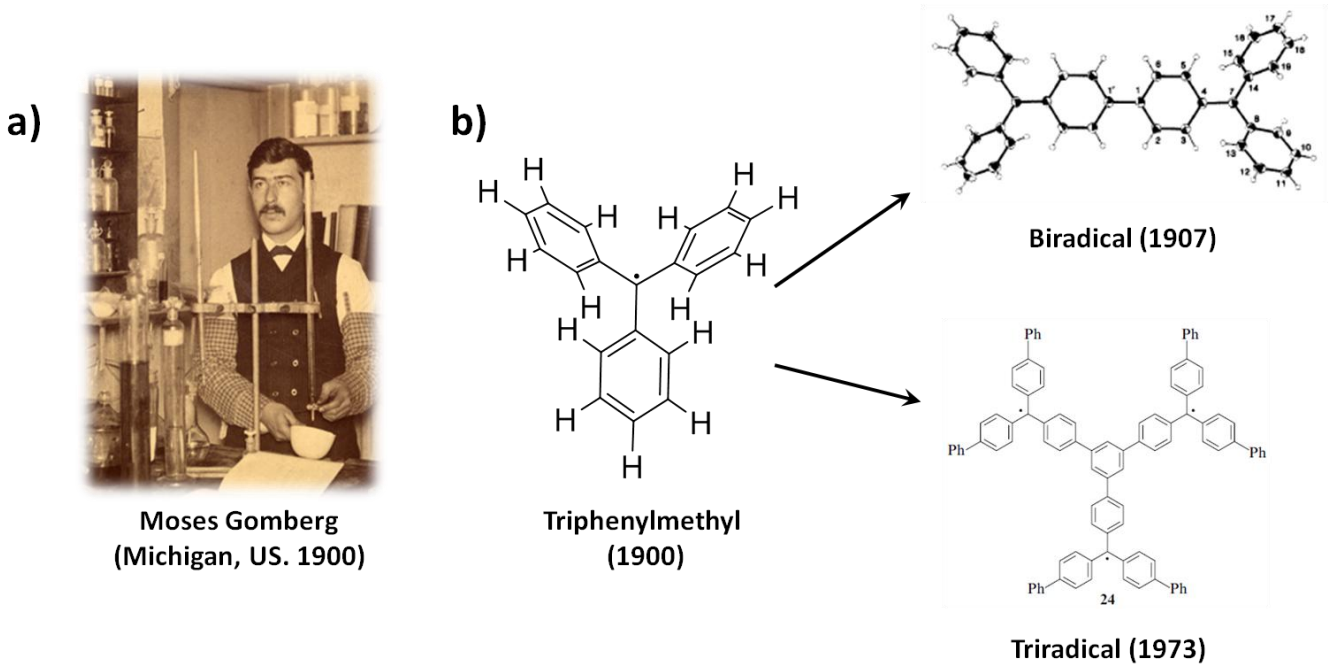

Fig. 1.1 a) Moses Gomberg working in his laboratory in Michigan. **b)** Chemical structure of the triphenylmethyl where the unpaired electron (dot) sits on the central methyl carbon atom.

As showed by Gomberg, the triphenylmethyl was not an isolated case, but actually just the first example of a new family of compounds bearing a trivalent carbon atom.[2] Indeed, his discovery opened the family of TAMs but, more importantly, the field of organic radicals. After his investigation, many more TAM compounds were synthesized during the 20th century. Moreover, some works showed that it was possible to have not only one trivalent carbon atom, but two,[3] three,[4] or multiple[5] radical centres in the same purely organic compound, which was the start of organic poly-radicals.[6,7] The importance of Gomberg's synthesis of the triphenylmethyl is also highlighted by the interest of important chemists who synthesized some triphenylmehyl derivatives, such as Wilhelm Schlenk,[8] or studied the optical properties of such a new family of compounds, such as Gilbert Newton Lewis.[9]

1.1.2 Towards chemical persistence: the PTM sub-family

Triphenylmethyl-derivatives are not persistent organic radicals (i.e. they last no longer than some days in solution[2]) and hence, besides being of great fundamental significance, their discovery lacks any applicability for any chemical technology. This dramatically changed in 1971 thanks to the work pioneered by an organic chemist from the University of Barcelona, Manuel Ballester, who started synthesizing a new family of TAMs where the three aryl rings were substituted with chlorine atoms.[10] These compounds were named perchlorotriarylmethyls or, in short, PTMs. As described by Ballester himself, PTMs showed a remarkable persistence not reacting with highly aggressive chemical species such as concentrated sulphuric and nitric acids, sodium hydroxide or halogens, not decomposing up to

300°C and having half-lives of decades in air.[10] As pointed out in that first contribution, the principal reason for the inertness of the PTM series of radicals relied on the sterical protection, or shielding effect, provided by Cl- atoms of aryl rings on the central radical carbon (see Fig. 1.2a).

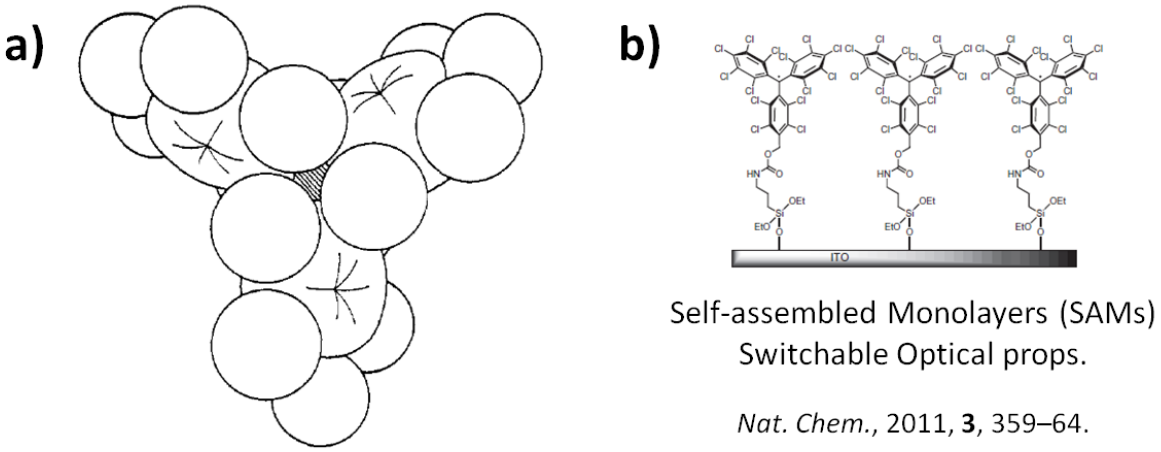

Fig. 1.2 a) PTM structure using Van-der-Waals radius to illustrate the important sterical shielding effect of chlorine atoms on the central radical carbon (dashed central point). **b)** PTM-based self-assembled monolayer exploited as a robust memory device.

With such outstanding chemical persistence, Ballester showed the chemical versatility of PTMs, where different chemical groups could be attached on the outer positions of the perchlorated aryl rings[12] or where hetero-aromatic rings (such as pyridine) could also substitute one of the aryl rings.[13]

1.1.3 Towards application

Again, as pioneered by Ballester, the outstanding chemical persistence of the new series of inert organic radicals made them very attractive for applications. Ballester exploited PTMs for the spin labelling of biomolecules (such as amino acids and peptides) which could be detected by EPR.[14] However, it was two of Ballester's followers, Profs Jaume Veciana and Concepció Rovira established at the Institute of Materials Science of Barcelona (ICMAB), who took the lead on the exploitation of PTMs for different applications mainly focused in materials science and electronics (see Fig. 1.2b).

It turns out that the unpaired electron in TAMs (and, consequently, in PTMs) gives rise to a series of interesting properties such as a spin moment, enhanced electrical conduction, absorption and emission of UV-vis. light (i.e. colour and fluorescence) and redox activity. Upon acquiring the chemical persistence provided by PTMs, all these characteristics become suddenly available, which obviously has made the use of PTMs very attractive as appealing molecular monomers to construct different multi-functional materials and devices. In the following section I will describe most important instances where TAMs (but mainly PTMs) have been exploited as building blocks in the field of materials science for applications in electronics and magnetism. It is worth remembering that some TAMs have been highly used in the field of oxygen detection,[15–19] spin labelling of bio-molecules[15,20–22] (as previously mentioned) and also as

dynamic nuclear polarization agents[23,24] (to improve NMR signal/noise ratio). However, given the focus of this thesis toward applications in the field of materials science and devices for electronics and spintronics, those different applications will not be explained with further detail in this work.

1.2 TAM-based applications

1.2.1 TAM-based polymer magnets

The first major applicability of TAMs in the field of materials science was, for obvious reasons, for the preparation of organic magnets. The basic rational was to covalently bond as many TAM units as possible so that the final oligomer or polymer could retain a magnetic moment by the interaction of all individual spin moments. Without going too much in details, the first stage in this research line was the synthesis of magnetic clusters where two TAM units, or more, were covalently bonded together in different ways and their magnetic properties assessed through electron paramagnetic resonance (EPR) measurements. A very instructive review was written by Nicolai M. Shishlov, where most of the synthesized TAM-based oligomers are reported.[7] There, it is also possible to see the use of PTMs to synthesize such magnetic clusters, as pioneered by Veciana's group. This race eventually culminated in a series of promising works,[5,25,26] by Suchada and Andrzej Rajca who in 2001 reported the synthesis of the first magnetic plastic based in a triphenylmethyl polymer[6] (Fig. 1.3).

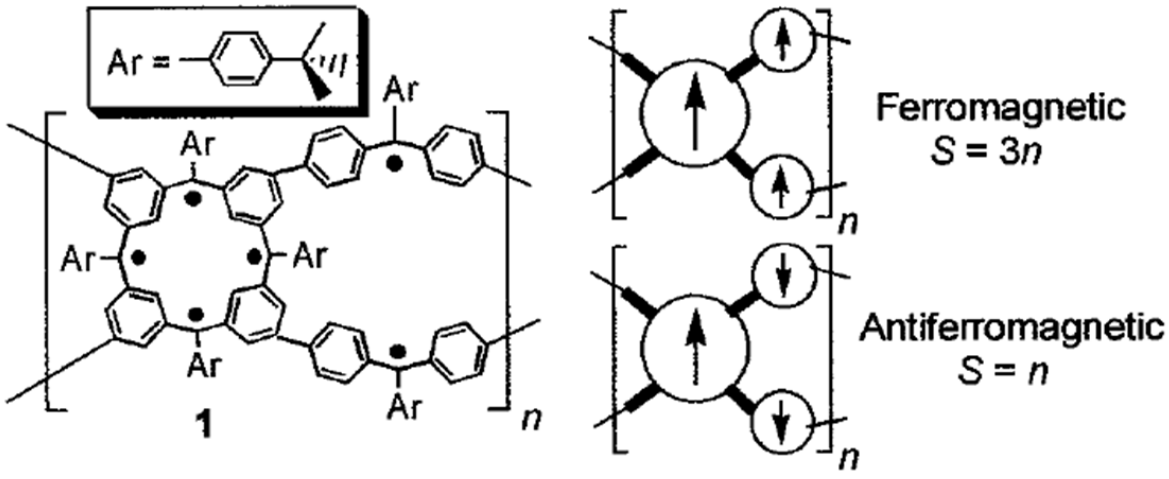

Fig. 1.3 Chemical structure of the highly cross-linked triphenylmethyl (or TPM) based polymer, where an effective magnetic moment corresponding to an average S equal to 5000 was measured at 10K by susceptibility SQUID measurements.

Rajca and co-workers were able to synthesize the magnetic plastic shown in Fig. 1.3 by previously preparing the polymer based on methoxy-triphenylmethyl (i.e. non-radical species) which upon de-protection of methoxy groups by Na/K reduction and following mild oxidation with I_2 generated the multi-radical disordered mesh. Such synthesis gave rise to the highest recorded spin moment for an organic polymer, with an average S equal to 5000 below 10 K, as found with susceptibility SQUID measurements.[6]

1.2.2 TAM-based supra-molecular frameworks

The important sterical hindrance provided by Cl atoms in PTMs prevented the successful synthesis of large PTM-based oligomers in a similar way as was done with the hydrogenated TAM (the triphenylmethyl).[7] Oligomers with three[27] or four[28] covalently bonded PTM units already exhibit very crowded and highly constrained structures, even influencing the resulting magnetic behaviour,[28] and hence those represent the furthest attempts of synthesizing PTM radical polymers. However, Veciana and co-workers found another very successful manner to generate PTM-based molecular frameworks through H-bonding. They found that PTM derivatives with carboxylate groups in *para*- positions bear an outstanding tendency to self-assemble.[29] Changing the number of carboxyl groups, PTMs self-assemble in 1D, 2D and 3D supra-molecular orderings, where the H-bonding between carboxyl groups of adjacent PTM molecules is the driving force defining the topology of the different frameworks.[29] As a culmination of such approach they reported a PTM-Cu(II) metal organic framework with large ordered pores (3 nm of diameter) with bulk magnetic ordering (see Fig. 1.4).[30]

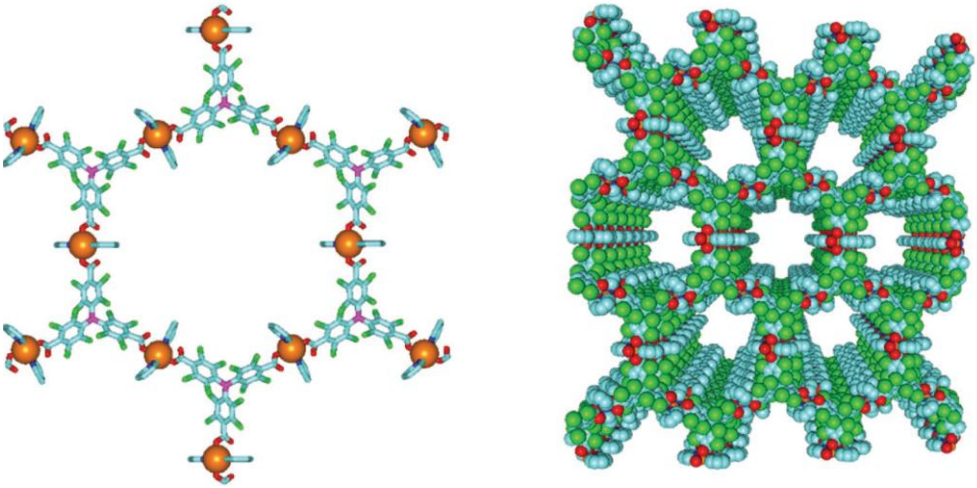

Fig. 1.4 Different structural representations of the metal-organic framework based on a tri-carboxylated PTM radical and Cu^{2+}.

As reported by Maspoch *et al.*,[30] the PTM-Cu-MOF showed the ability to change its pore size depending on the solvent that was absorbed while maintaining the main hexagonal porous skeleton. Such structural distortions lead to important changes in the magnetic interactions between radical PTM units within the material, which could be tracked by SQUID magnetometry observing different magnetic ordering depending on the swallowed solvent.[30] As mentioned in that contribution, these materials could be used as highly selective solvent sensors.

1.2.3 TAM-based data-memory devices

The spin moment in TAMs is not the only characteristic which makes them potential candidates for different applications in magnetism and electronics. Another appealing property of TAMs (and PTMs) is that they are easily reduced to the corresponding anion species; i.e. they are redox active.[31,32] Moreover, the radical and anion species present distinct optical and magnetic properties. For instance the anion is not

magnetically active, contrary to the neutral state due to the existence of the unpaired electron. Based on that and thanks to the persistence of PTMs on different substrates[33] Concepció Rovira and co-workers were able to prepare a PTM-based data memory device[34] (see Fig. 1.5).

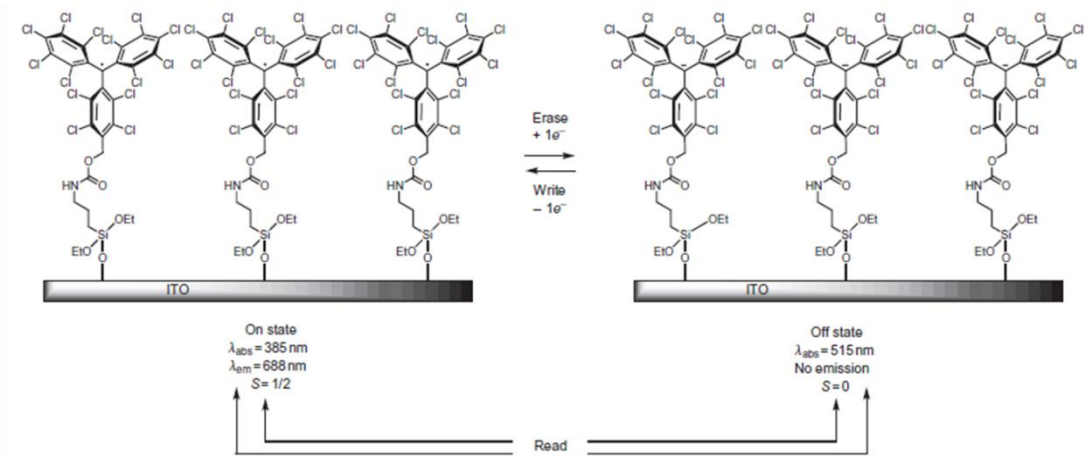

Fig. 1.5 Molecular switch based on a PTM self-assembled monolayer on ITO. As shown, the neutral and anion states of the PTM monolayer can be switched by means of positive and negative applied electrical bias. Both optical and magnetic properties of the monolayer change with the redox state, which then may be used as output signals of the device.

Hence, PTMs were chemically bonded on a transparent and conductive substrate (Indium-Tin oxide, or ITO) and, by applying a negative (positive) voltage on the substrate, it was possible to switch the PTM SAM from the neutral to the -1 redox state (and viceversa) in a highly reversible manner. Because of the different magnetic and optical properties of the molecular monolayer in each state Rovira and co-workers were able to track the state of the switch by EPR and by UV-vis. spectroscopies (see Fig. 1.5 for details). As reported, the device was switched more than 60 times without showing any signal loss.

1.2.4 TAM-based molecular wires

Having an unpaired electron which is π-conjugated through the entire molecular skeleton brings another interesting characteristic for molecular electronics and spintronics, which is the existence of a π-conjugated singly-unoccupied molecular orbital (SUMO) through which incoming unpaired electrons may flow. Again, Veciana's group took the lead in exploring such characteristic to build different types of electronic devices. One of the first demonstrations of such increased electrical conductivity was reported by the work of Nuria Crivillers et.al that compared the electrical conductivity of a radical PTM SAM and its hydrogenated version[35] (where the H atom is bonded to the central carbon atom, and hence the PTM molecule becomes closed-shell, i.e. with all electrons paired), as schematically shown in Fig 1.6.

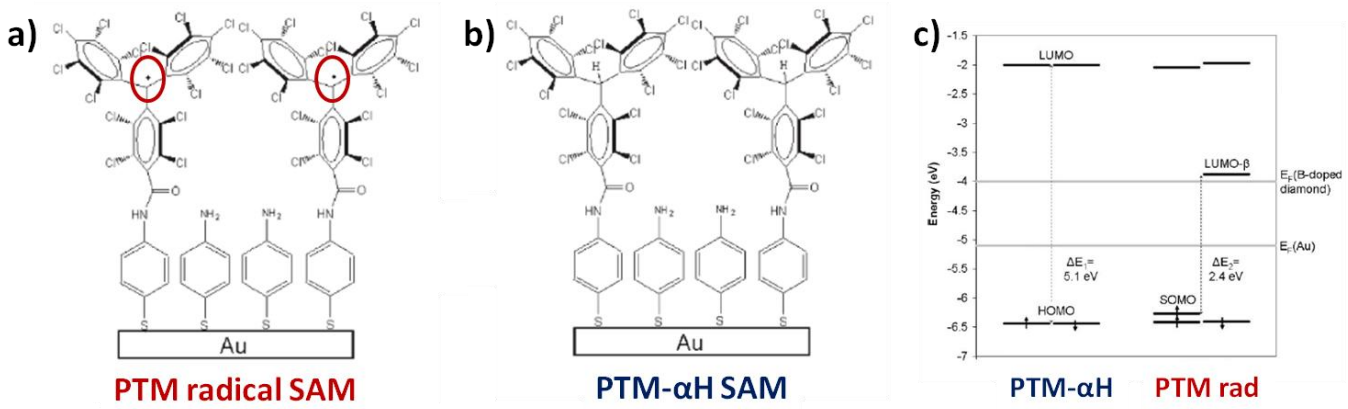

Fig. 1.6 a) Open-shell and **b)** closed-shell PTM-based SAMs on gold. **c)** Calculated orbital energies for each PTM monolayer compared with the Fermi energy levels of the utilized Au substrate and diamond tip (grey bars).

By means of STM measurements, Crivillers *et al.* found that the single-molecule electronic conductivity through the open-shell PTM monolayer was an order of magnitude larger than the corresponding hydrogenated closed-shell counterpart. As highlighted in that work,[35] such large differences in the conductivity could not be assigned to different molecular structures due to the fact both cases showed almost the same molecular conformation but, actually, an electronic effect due the π-conjugated SUMO in the radical PTM SAM in very close energy with the incoming electrons from the diamond tip (see Fig. 1.6c).[35] A more recent work comparing such two systems using a GaIn electrode has determined a difference of two orders of magnitude between the radical and the hydrogenated closed-shell PTM SAMs.[36]

1.2.5 TAMs as spintronic devices

Ultimately, the fact that, as demonstrated in the work presented above, electrical conduction takes place through the SUMO associated to the π-conjugated unpaired electron in TAMs, these organic radicals may present some potential for spintronics.[37] The field of spintronics relies on the fact that conductive electrons may feel a resistance upon moving through magnetic defects. A signature of such phenomena is the so-called Kondo effect,[38] which is translated in the appearance of the so-called Kondo peak in electrical current measurements through magnetic centres, such as radical centres. Such a peak was first reported for organic radical compounds for a physisorbed layer of a verdazyl radical derivative[39] by means of scanning tunnelling spectroscopy (STS) measurements. The great difficulties in measuring such phenomena is due the fact that it is highly sensitive to other phenomena such as temperature. Because of this, very low temperature experiments are required, which imposes the necessity of using state-of-the-art equipment capable of running such type of electrical measurements at temperatures as low as 1K or below. Such measurements were able to measure the electrical conduction in a two and three terminal solid-state devices having a single PTM radical molecule as the central component of the molecular break-junction,[40] as depicted in Fig. 1.7. Prof Bromley and myself participated in this work with specific DFT calculations (not included in this thesis).

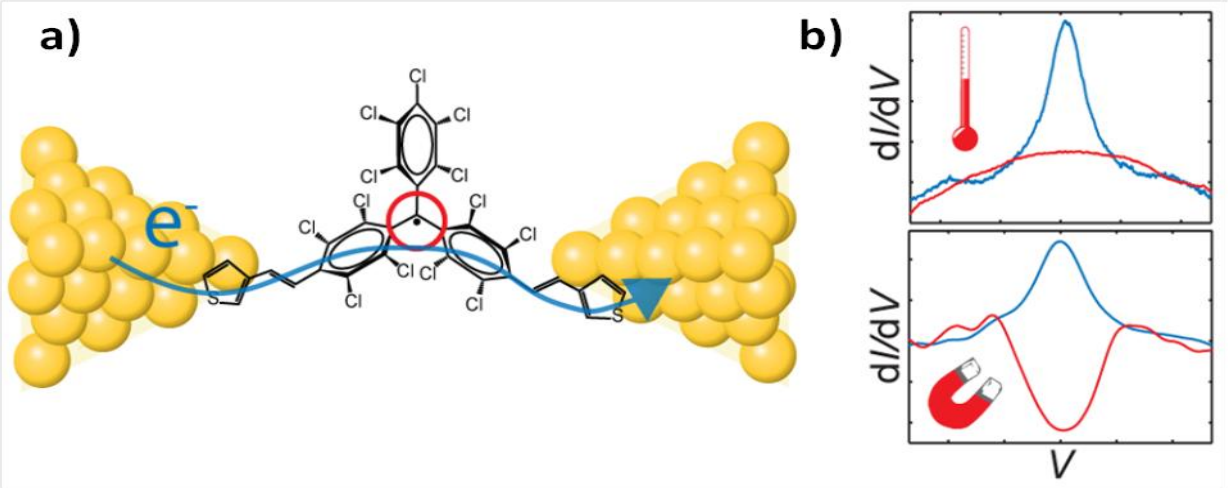

Fig. 1.7 a) Single-molecule break junction based on a specifically designed PTM organic radical. **b)** Detected Kondo peak in the corresponding dI/dV vs. V curves between both Au electrodes, indicative of the interaction between the unpaired electron in the radical centre and conductive electrons. The changes of the detected peak with an applied magnetic field demonstrate the magnetic nature of such feature.

Testing two- and three- terminal devices, dI/dV vs. V STS (Scanning Tunneling Spectroscopy) curves showed the appearance of a Kondo peak at 0V.[40] As it was reported, and shown in Fig. 1.7b, such a Kondo resonance was highly sensitive to temperature (already not detectable at 6K) and, very importantly, to the application of local magnetic fields (from 0 to 8T) where a Zeeman splitting may be observed (Fig. 1.7b). The latter demonstrates the paramagnetic nature of the Kondo resonance and, hence, its origin in the unpaired electron within the PTM core, demonstrating the potential of PTM (and TAMs) as organic spintronics components.

As explained in the beginning of this chapter, the predictive part of this PhD thesis has been focused on the design of a new class of as yet unexplored 2D materials: TAM-based 2D covalent organic frameworks (TAM 2D-COFs). At the following section I will briefly introduce 2D-COFs, their potential for nano-electronic applications and provide some relevant examples.

1.3 2D covalent organic frameworks (2D-COFs)

1.3.1 Preparation and structure of 2D-COFs

2D covalent organic frameworks are 2D materials made through a bottom-up approach[41,42]. Specifically designed discrete molecules are first deposited, normally by chemical vapour deposition (CVD), on a solid substrate (normally metals) at a certain temperature that allows the molecules to re-organize on the surface and form ordered physisorbed molecular arrays (see Fig. 1.8a). Application of higher temperatures leads to the 2D-COF formation, normally, as isolated islands over the substrate (see Fig. 1.8b and zoomed image in 1.8c).

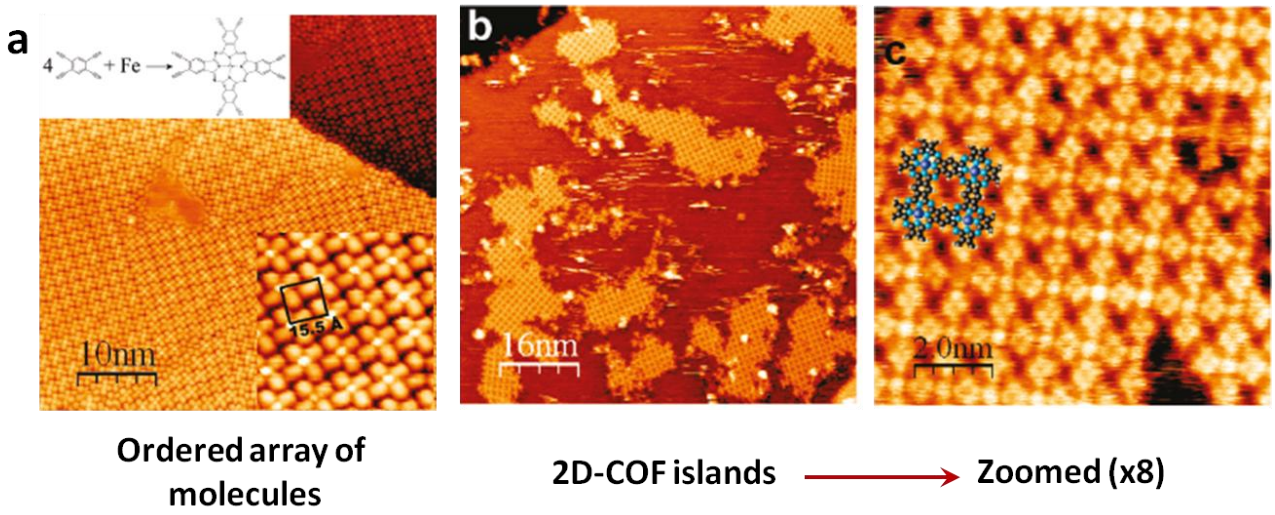

Fig. 1.8 STM images of **a)** an ordered array of Fe(II) phthalocyanine units and **b-c)** corresponding squared 2D covalent frameworks.

Normally metallic substrates are used for the preparation of 2D-COFs, because they may catalyze the chemical bonding between molecular units (i.e. like through Ullman coupling reaction[42–44]). However, there are other possible bonding types that do not require the metal catalytic intervention, such as amine condensation[41,45] or boronic acid-base coupling,[41] and so the corresponding 2D-COFs may be prepared on top of other substrates such as oxides[46] or salts,[47] which should allow exploiting the electronics of the 2D-COF without electronic interference from the substrate[46] (which is a difficult task when using metallic substrates).

A very appealing characteristic of 2D-COFs is their chemical and structural versatility,[41] only found in similar molecule-based network materials such as MOFs[48] or COFs.[49] Depending on the molecular building block, the supporting surface and the applied temperature, both the topology and physic-chemical properties of the resulting network may be tailored. Due to the great versatility of organic synthesis, many different molecular building blocks may be synthesized giving rise to 2D-COFs with very distinct topologies such as hexagonal[45,50–52] (Fig. 1.9a), squared[42,47] (1.9b), rectangular[53] (1.9c), linear[54,55] (1.9d) and rombohedral[56,57] (1.9e) among others.[58] Even more, using functional groups with different reacting temperatures (like I, Br or H), it is possible to step-wise control the nano-scale building process of the 2D-COF by application of different temperature profiles,[54] adding an extra level of tailorability.[59]

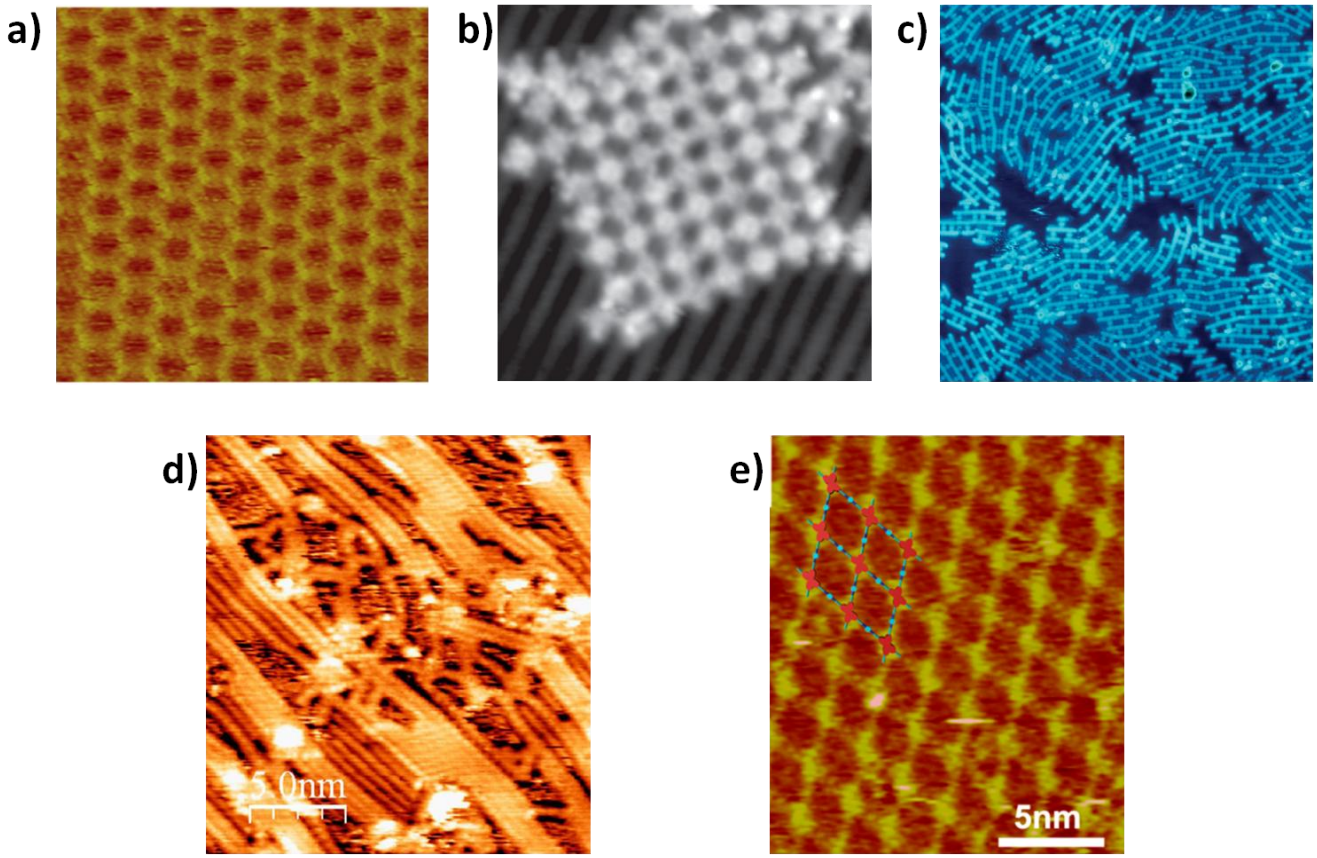

Fig. 1.9 STM images of hexagonal **(a)**, squared **(b)**, rectangular **(c)**, linear **(d)** and rombohedral **(e)** 2D-COFs on different substrates. The 2D-COF's topology depends on the utilized molecular building block to construct it. More information about each case may be found in refs 45, 59, 53, 54 and 56, respectively.

1.3.2 2D-COFs as platforms for future nano-electronics

2D-COFs, due to their robustness and highly tailorable structure at the nano-scale, possess inherent potential as future platforms for nano-electronics.[41,60] However, most present studies on 2D-COFs are focused on reporting their structural and chemical characteristics and preparation methods,[41,42] due to the very early stage of this new research field. Experimentally assessing how electrons behave in the on-surface prepared polymer materials is more common for 1D covalent chains,[46,55,61] where there is clear potential as molecular wires. For 2D-COFs, the assessment of the electronics is limited to measuring the band gap of the 2D network via scanning tunnelling spectroscopy (STS) measurements.[52] One type of 1D COF (or 2D-COFs depending on their width) which are actively studied as components for nano-electronics are graphene nano-ribbons (GNRs).[62] The interest in these materials for nano-electronics is a legacy[63] from their 2D predecessor, graphene.[64] However, during the last years GNRs with atomic precision are being prepared through the on-surface self-assembly of specifically designed building blocks on metal surfaces,[65] in the same spirit as 2D-COFs. In this line GNRs with atomically precise zig-zag edge topology[65,66] (Fig. 1.10a) and with boron[67] or nitrogen[68] doping (Fig. 1.10b), where dopants occupy specific predesigned positions within the network,[65] have been prepared.

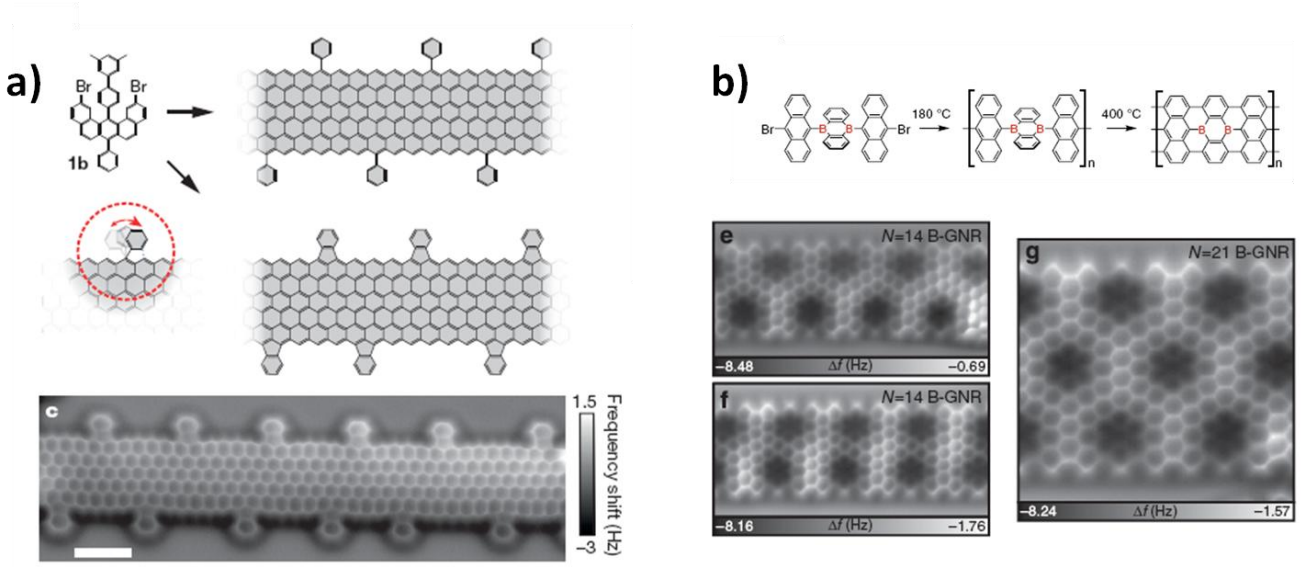

Fig. 1.10 Atomic force microscopy (AFM) images of bottom-up prepared GNRs with **(a)** zig-zag edge topology and **(b)** atomically-precise boron doping. For more information see refs 66 and 67, respectively.

Overall, the role of 2D-COFs for nano-electronics is still in its infancy, but certainly there is plenty of room at the bottom for these materials to be explored, and exploited, in this promising direction.

1.4 PhD thesis motivation and outline

This PhD thesis has had a two-fold objective: (1) To support the experimental study of PTM and H-PTM systems with potential as molecular devices. This part will be mainly focused on the preparation of PTM SAMs where the radical monolayer has been formed from a close-shell quinoidal precursor. In these studies, matching theoretical simulations with experimental measurements has required an important proportion of my work. (2) By means of accurate DFT calculations, to study ways to control the unpaired electron in TAM derivatives. As it will be shown, a unique control parameter was found at an early stage of this thesis which, hypothetically, should give rise to fine control over all properties of any TAM-based material or device. As a second step of part (2), we have moved forward for the search of a TAM-based platform where such controllability could be exploited, which led us to the design of TAM-based 2D-covalent organic frameworks (or TAM 2D-COFs). Becoming the most important intellectual contribution of this PhD work, as it will be shown, we have found TAM 2D-COFs present an electronic tunability far beyond any other material or device based on TAM building blocks.

Based on the above outline structure, the following chapters of this thesis are organized as follows:

2. **Methodology**: Here I will briefly introduce the different simulation methods used during this PhD project, mainly focused on force-field (FF) calculations and, to get insight into the electronics, first principles density functional theory simulations (DFT). Providing a simple, but clear, background on the

latter I will then briefly introduce particular tools and approaches within DFT with special relevance to this work, such as *ab initio* molecular dynamics (AIMD) simulations or periodic calculations.

3. **Modelling TAMs as potential devices**: Here I will present the works in collaboration with the experimental groups of Prof Jaume Veciana and Dr Marta Mas-Torrent on the study of PTMs for different sorts of devices. This chapter will be mainly focused in the preparation of a radical PTM SAM using a closed-shell quinoidal monomer. These studies will be complemented with another collaborative work where my calculations provided a possible structural explanation for the experimentally found kinetic blockage of a cis ↔ trans isomerisation of a H-PTM stilbene derivative.

4. **From aryl rings' twist to TAM 2D-COFs**: Here I will present purely computational works of this thesis. In the first work we show the existence of the spin-localization dependence on the twist angle of the three aryl rings in TAMs. In the second contribution we propose TAM 2D-COFs as the perfect platform to exploit such electronic-structural correlation for the preparation of 2D materials with externally controllable properties. Finally, in the third contribution we screen for a number of possible experimentally feasible TAM 2D-COFs where aryl ring twist angles could be externally manipulated as proposed in the previous publication.

5. ***para*-connected TAMs: Towards 2D semimetals**: With this chapter we will present the last contributions composing these PhD thesis. Complementing the TAM 2D-COFs designed in Chapter 4 that behave as electrical insulators, in this chapter I will present the work where we show TAM 2D-COFs behaving as a multi-state semi-metal. Here I will explain the correlation between such striking differences between both TAM 2D-COFs (those of publications **#5** and **#8**) and the way in which TAM units are covalently connected in each network. Moreover, in this chapter I will also present the last collaborative work with the experimental group at ICMAB where such influence of the connectivity is experimentally demonstrated in bi-PTM mixed-valence compounds. Again, in this collaborative work, our computational results provided a theoretical point of view not considered by the experimentalists at an early stage of the collaboration, highlighting the active role this thesis work has played in such collaborative contributions.

6. **Conclusions**: Here I will summarize most important results of this PhD thesis and give my personal point of view about the future potential of TAMs and, more specifically, TAM 2D-COFs, for nano-electronics.

7. **Contribution to publications**

8. **Resum en Català**

1.5 Bibliography

1 M. Gomberg, *J. Am. Chem. Soc.*, 1900, **22**, 757–771.

2 M. Gomberg, *J. Am. Chem. Soc.*, 1903, **25**, 1274–1277.

3 A. E. Tschitschibabin, *Berichte der Dtsch. Chem. Gesellschaft*, 1907, **40**, 1810–1819.

4 G. Kothe and H. Zimmermann, *Tetrahedron*, 1973, **29**, 2305–2313.

5 A. Rajca, K. Lu and S. Rajca, *J. Am. Chem. Soc.*, 1997, **119**, 10335–10345.

6 A. Rajca, J. Wongsriratanakul and S. Rajca, *Science*, 2001, **294**, 1503–1505.

7 N. M. Shishlov, *Russ. Chem. Rev.*, 2006, **75**, 863–884.

8 W. Schlenk, T. Weickel and A. Herzenstein, *Justus Liebig's Ann. der Chemie*, 1910, **372**, 1–20.

9 G. N. Lewis, D. Lipkin and T. T. Magel, *J. Am. Chem. Soc.*, 1944, **66**, 1579–1583.

10 M. Ballester and J. Riera-Figueras, *J. Am. Chem. Soc.*, 1971, **4254**, 2215–2225.

11 M. Gomberg, *J. Am. Chem. Soc.*, 1901, **23**, 496–502.

12 M. Ballester, J. Castañer, J. Riera, A. Ibáñez and J. Pujadas, *J. Org. Chem.*, 1982, **47**, 259–264.

13 L. Juliá, M. Ballester, J. Riera, J. Castañer, J. L. Ortin and C. Onrubia, *J. Org. Chem.*, 1988, **53**, 1267–1273.

14 M. Ballester, J. Riera, J. Castañer, C. Rovira, J. Veciana and C. Onrubia, *J. Org. Chem.*, 1983, **48**, 3716–3720.

15 B. Driesschaert, V. Marchand, P. Levêque, B. Gallez and J. Marchand-Brynaert, *Chem. Commun.*, 2012, **48**, 4049–51.

16 A. A. Bobko, I. Dhimitruka, D. A. Komarov and V. V Khramtsov, *Anal. Chem.*, 2012, **84**, 6054–60.

17 I. Dhimitruka, A. A. Bobko, T. D. Eubank, D. A. Komarov and V. V Khramtsov, *J. Am. Chem. Soc.*, 2013, **135**, 5904–10.

18 V. K. Kutala, N. L. Parinandi, R. P. Pandian and P. Kuppusamy, *Antioxid. Redox Signal.*, 2004, **6**, 597–603.

19 C. Rizzi, A. Samouilov, V. K. Kutala, N. L. Parinandi, J. L. Zweier and P. Kuppusamy, *Free Radic. Biol. Med.*, 2003, **35**, 1608–1618.

20 N. Bézière, C. Decroos, K. Mkhitaryan, E. Kish, F. Richard, S. Bigot-Marchand, S. Durand, F. Cloppet, C. Chauvet, M.-T. Corvol, F. Rannou, Y. Xu-Li, D. Mansuy, F. Peyrot and Y.-M. Frapart, *Mol. Imaging*, 2012, **11**, 220–8.

21 N. Chattergoon, F. Martínez-Santiesteban, W. B. Handler, J. H. Ardenkjaer-Larsen and T. J. Scholl, *Contrast Media Mol. Imaging*, 2013, **8**, 57–62.

22 T. J. Reddy, T. Iwama, H. J. Halpern and V. H. Rawal, *J. Org. Chem.*, 2002, **67**, 4635–4639.

23 D. Banerjee, J. C. Paniagua, V. Mugnaini, J. Veciana, A. Feintuch, M. Pons and D. Goldfarb, *Phys. Chem. Chem. Phys.*, 2011, **13**, 18626–18637.

24 C. Gabellieri, V. Mugnaini, J. C. Paniagua, N. Roques, M. Oliveros, M. Feliz, J. Veciana and M. Pons, *Angew. Chem. Int. Ed. Engl.*, 2010, **49**, 3360–2.

25 A. Rajca, S. Rajca and J. Wongsriratanakul, *J. Am. Chem. Soc.*, 1999, **121**, 6308–6309.

26 S. Rajca, A. Rajca, J. Wongsriratanakul, P. Butler and S. M. Choi, *J. Am. Chem. Soc.*, 2004, **126**, 6972–86.

27 J. Veciana, C. Rovira, N. Ventosa, M. I. Crespo and F. Palacio, *J. Am. Chem. Soc.*, 1993, **115**, 57–64.

28 D. Ruiz-Molina, J. Vidal-Gancedo, N. Ventosa, J. Campo, F. Palacio, C. Rovira and J. Veciana, *J. Phys. Chem. Solids*, 2004, **65**, 737–744.

29 V. Mugnaini, M. Mas-Torrent, I. Ratera, C. Rovira and J. Veciana, in *Supramolecular Soft Matter: Applications in Materials and Organic Electronics*, ed. T. Nakanishi, John Wiley & Sons, Inc., First Edit., 2011, pp. 193–215.

30 D. Maspoch, D. Ruiz-Molina, K. Wurst, N. Domingo, M. Cavallini, F. Biscarini, J. Tejada, C. Rovira and J. Veciana, *Nat. Mater.*, 2003, **2**, 190–5.

31 A. Datcu, N. Roques, V. Jubera, D. Maspoch, X. Fontrodona, K. Wurst, I. Imaz, G. Mouchaham, J. P. Sutter, C. Rovira and J. Veciana, *Chem. - A Eur. J.*, 2012, **18**, 152–162.

32 C. Franco, M. Mas-Torrent, A. Caballero, A. Espinosa, P. Molina, J. Veciana and C. Rovira, *Chem. - A Eur. J.*, 2015, **21**, 5504–5509.

33 M. Mas-Torrent, N. Crivillers, C. Rovira and J. Veciana, *Chem. Rev.*, 2012, **112**, 2506–27.

34 C. Simão, M. Mas-Torrent, N. Crivillers, V. Lloveras, J. M. Artés, P. Gorostiza, J. Veciana and C. Rovira, *Nat. Chem.*, 2011, **3**, 359–64.

35 N. Crivillers, C. Munuera, M. Mas-Torrent, C. Simão, S. T. Bromley, C. Ocal, C. Rovira and J. Veciana, *Adv. Mater.*, 2009, **21**, 1177–1181.

36 L. Yuan, C. Franco, N. Crivillers, M. Mas-Torrent, L. Cao, C. S. S. Sangeeth, C. Rovira, J. Veciana and C. A. Nijhuis, *Nat. Commun.*, 2016, **7**, 12066.

37 M. Mas-Torrent, N. Crivillers, V. Mugnaini, I. Ratera, C. Rovira and J. Veciana, *J. Mater. Chem.*, 2009, **19**, 1691.

38 L. Kouwenhoven and L. Glazman, *Phys. World*, 2001, **14**, 33–38.

39 J. Liu, H. Isshiki, K. Katoh, T. Morita, B. K. Breedlove, M. Yamashita and T. Komeda, *J. Am. Chem. Soc.*, 2013, **135**, 651–8.

40 R. Frisenda, R. Gaudenzi, C. Franco, M. Mas-Torrent, C. Rovira, J. Veciana, I. Alcon, S. T. Bromley, E. Burzurí and H. S. J. van der Zant, *Nano Lett.*, 2015, **15**, 3109–3114.

41 X. H. Liu, C. Z. Guan, D. Wang and L. J. Wan, *Adv. Mater.*, 2014, **26**, 6912–20.

42 Q. Fan, J. M. Gottfried and J. Zhu, *Acc. Chem. Res.*, 2015, **48**, 2484–2494.

43 Q. Fan, T. Wang, L. Liu, J. Zhao, J. Zhu and J. M. Gottfried, *J. Chem. Phys.*, 2015, **142**, 101906.

44 M. Bieri, M.-T. Nguyen, O. Groning, J. Cai, M. Treier, K. Aït-Mansour, P. Ruffieux, C. A. Pignedoli, D. Passerone, M. Kastler, K. Müllen and R. Fasel, *J. Am. Chem. Soc.*, 2010, **132**, 16669–16676.

45 X.-H. Liu, C.-Z. Guan, S.-Y. Ding, W. Wang, H.-J. Yan, D. Wang and L.-J. Wan, *J. Am. Chem. Soc.*, 2013, **135**, 10470–4.

46 G. Vasseur, M. Abadia, L. A. Miccio, J. Brede, A. Garcia-Lekue, D. G. de Oteyza, C. Rogero, J. Lobo-Checa and J. E. Ortega, *J. Am. Chem. Soc.*, 2016, **138**, 5685–5692.

47 M. Abel, S. Clair, O. Ourdjini, M. Mossoyan and L. Porte, *J. Am. Chem. Soc.*, 2011, **133**, 1203–1205.

48 A. Walsh, K. T. Butler and C. H. Hendon, *MRS Bull.*, 2016, **41**, 870–876.

49 N. Huang, P. Wang and D. Jiang, *Nat. Rev. Mater.*, 2016, **1**, 16068.

50 M. Bieri, M. Treier, J. Cai, K. Aït-Mansour, P. Ruffieux, O. Gröning, P. Gröning, M. Kastler, R. Rieger, X. Feng, K.

Müllen and R. Fasel, *Chem. Commun. (Camb).*, 2009, 6919–21.

51 X.-H. Liu, Y.-P. Mo, J.-Y. Yue, Q.-N. Zheng, H.-J. Yan, D. Wang and L.-J. Wan, *Small*, 2014, **10**, 4934–9.

52 C. Steiner, J. Gebhardt, M. Ammon, Z. Yang, A. Heidenreich, N. Hammer, A. Görling, M. Kivala and S. Maier, *Nat. Commun.*, 2017, **8**, 14765.

53 W. Liu, X. Luo, Y. Bao, Y. P. Liu, G.-H. Ning, I. Abdelwahab, L. Li, C. T. Nai, Z. G. Hu, D. Zhao, B. Liu, S. Y. Quek and K. P. Loh, *Nat. Chem.*, 2017, **9**, 563–570.

54 A. Basagni, F. Sedona, C. A. Pignedoli, M. Cattelan, L. Nicolas, M. Casarin and M. Sambi, *J. Am. Chem. Soc.*, 2015.

55 A. Basagni, G. Vasseur, C. A. Pignedoli, M. Vilas-Varela, D. Peña, L. Nicolas, L. Vitali, J. Lobo-Checa, D. G. de Oteyza, F. Sedona, M. Casarin, J. E. Ortega and M. Sambi, *ACS Nano*, 2016, **10**, 2644–2651.

56 W. Dong, L. Wang, H. Ding, L. Zhao, D. Wang, C. Wang and L.-J. Wan, *Langmuir*, 2015, **31**, 11755–11759.

57 Q. Sun, C. Zhang, L. Cai, L. Xie, Q. Tan and W. Xu, *Chem. Commun.*, 2015, **51**, 2836–2839.

58 G. Gu, N. Li, L. Liu, X. Zhang, Q. Wu, D. Nieckarz, P. Szabelski, L. Peng, B. K. Teo, S. Hou, Y. Wang, R. Bhosale, A. Mateo-Alonso, J. V. Barth, K. Wu and Y. F. Wang, *RSC Adv.*, 2016, **6**, 66548–66552.

59 L. Lafferentz, V. Eberhardt, C. Dri, C. Africh, G. Comelli, F. Esch, S. Hecht and L. Grill, *Nat. Chem.*, 2012, **4**, 215–20.

60 D. F. Perepichka and F. Rosei, *Science (80-.).*, 2009, **323**, 216–217.

61 C. Nacci, F. Ample, D. Bleger, S. Hecht, C. Joachim and L. Grill, *Nat. Commun.*, 2015, **6**, 7397.

62 J. P. Llinas, A. Fairbrother, G. Borin Barin, W. Shi, K. Lee, S. Wu, B. Yong Choi, R. Braganza, J. Lear, N. Kau, W. Choi, C. Chen, Z. Pedramrazi, T. Dumslaff, A. Narita, X. Feng, K. Müllen, F. Fischer, A. Zettl, P. Ruffieux, E. Yablonovitch, M. Crommie, R. Fasel and J. Bokor, *Nat. Commun.*, 2017, **8**, 633.

63 J. Baringhaus, M. Ruan, F. Edler, A. Tejeda, M. Sicot, A. Taleb-Ibrahimi, A.-P. Li, Z. Jiang, E. H. Conrad, C. Berger, C. Tegenkamp and W. A. de Heer, *Nature*, 2014, **506**, 349–354.

64 K. S. Novoselov, A. K. Geim, S. V. Morozov, D. Jiang, Y. Zhang, S. V. Dubonos, I. V. Grigorieva and A. A. Firsov, *Science (80-.).*, 2004, **306**, 666–669.

65 A. Narita, X.-Y. Wang, X. Feng and K. Müllen, *Chem. Soc. Rev.*, 2015, **44**, 6616–6643.

66 P. Ruffieux, S. Wang, B. Yang, C. Sanchez, J. Liu, T. Dienel, L. Talirz, P. Shinde, C. A. Pignedoli, D. Passerone, T. Dumslaff, X. Feng, K. Muellen and R. Fasel, *Nature*, 2015, **531**, 15.

67 S. Kawai, S. Saito, S. Osumi, S. Yamaguchi, A. S. Foster, P. Spijker and E. Meyer, *Nat. Commun.*, 2015, **6**, 8098.

68 C. Bronner, S. Stremlau, M. Gille, F. Brauße, A. Haase, S. Hecht and P. Tegeder, *Angew. Chemie Int. Ed.*, 2013, **52**, 4422–4425.

Chapter 2
Methodology

This PhD thesis has involved the computational modelling of different organic systems, mainly single-molecules, self-assembled monolayers on metal surfaces (i.e. hybrid systems) and 2D covalent networks constructed by specific molecular building blocks. Each system has required its particular computational methodology and specific models. Such particularities are explained in detail on the methodology section within each publication presented in this work. However, throughout this PhD thesis I have used two different types of computational based methods, namely, force-fields (FFs) and density functional theory (DFT). FFs have been mainly utilized to optimize the atomic structure of molecules or periodic molecule-based 2D networks. DFT calculations have been used to further refine the pre-optimized structures by FFs and to obtain reliable information about the electronic structure and related properties (something not accessible just with FFs). In this section, I will briefly introduce FFs and devote most of it to a general introduction to electronic-structure modelling, placing special attention to DFT. Specific modelling tools and schemes used in this work such as molecular dynamics and periodic calculations will also be briefly introduced at the end of this chapter.

2.1 Force field calculations

Force field (FF) calculations are the most computationally efficient way to optimize the atomic structure of molecules and materials. In such methods atoms are described as point masses interacting under classical potentials based on a number of structural parameters (like distances, angles, dihedrals) which determine the total energy of the system. The mathematical form of such classical potentials with respect to those structural parameters is often constructed by fitting analytical expressions to values from experimental data or higher-level theory calculations such as wave-function methods. The total energy of a molecular system can be separated as follows:

(1.1) $E_{total} = E_{bonded} + E_{non-bonded}$

where E_{total} is the total energy of the system, E_{bonded} includes interactions between covalently bonded atoms, such as those within a molecule, and $E_{non-bonded}$ includes those interactions that do not require a covalent bond to take place, such as electrostatic interactions, H-bonds, etc. E_{bonded} and $E_{non-bonded}$ can be further split into its different components:

(1.2) $E_{bonded} = E_{bond} + E_{angle} + E_{dihedral} = \sum_{bonds} K_r(r - r_{eq})^2 + \sum_{angles} K_\theta(\theta - \theta_{eq})^2 + \sum_{dihedrals} \sum_n V_n\left(1 + \cos\left(n\varphi - \varphi_{eq}\right)\right)$

(1.3) $E_{non-bonded} = E_{electrostatic} + E_{van-der-Waals} + E_{Pauli} = \sum_{i>j} \left(\left(\frac{q_i q_j}{R_{ij}}\right) - 2\varepsilon_{ij} \left(\frac{R_{ij}^{min}}{R_{ij}}\right)^6 + \varepsilon_{ij} \left(\frac{R_{ij}^{min}}{R_{ij}}\right)^{12} \right).$

In eq. 1.2 r_{eq}, θ_{eq} and φ_{eq} are equilibrium values for bond distances, bond angles and dihedral angles, respectively. E_{bond} represents the energy dependence on the distance between two bonded atoms, and E_{angle} the energy of the system upon varying the angle between two atoms bonded with the same connecting atom (i.e. bending). Both contributions are represented by simple harmonic potentials. $E_{dihedral}$ completes the E_{bonded} part and describes the energy associated to dihedral angles; i.e. those involving two molecular planes, such as the two phenyl rings twisting one respect each other in the bi-phenyl molecule. As it may be seen in eq. 1.2 $E_{dihedral}$ presents a periodic form based in a cosine function with respect to the dihedral angle ($n\varphi$), where n is a non-negative number indicating periodicity.

The $E_{non-bonded}$ term includes forces occurring between atoms which are non bonded. $E_{electrostatic}$ represents coulombic repulsion and attraction interactions between partial charges (q_i and q_j) associated to different atom types with separation R_{ij}, having the Coulombic $\left(\frac{q_i q_j}{R_{ij}}\right)$ form. This term will be positive (i.e. repulsive) or negative (i.e. attractive) depending on the sign of both involved charges. $E_{van-der-Waals}$ describes weakly attractive interactions between atoms such as dipole-dipole interactions, induced dipole-dipole interactions and dispersive interactions, all being collected in the $-2\varepsilon_{ij}\left(\frac{R_{ij}^{min}}{R_{ij}}\right)^6$ term in eq. 1.3. R_{ij}^{min} is the equilibrium distance between atoms i and j and ε_{ij} is a weighting parameter determining the energetic contribution of such interaction to E_{total}. Finally, the last term in $E_{non-bonded}$ (see eq. 1.3) comes due to the Pauli exclusion principle, which is accounted for with a repulsive (i.e. positive) $\varepsilon_{ij}\left(\frac{R_{ij}^{min}}{R_{ij}}\right)^{12}$ term which repels two atoms at short separation. These last two terms (i.e. $E_{van-der-Waals}$ and E_{Pauli}) compose the so-called Lennard-Jones potential,[1] describing the interaction between two atoms not taking into account coulombic interactions. Sometimes for some force-fields a Morse potential[2] of the form $D(1-e^{-a\rho})^2$, where $\rho = \frac{r-r_0}{r_0}$, is used instead of the Lennard-Jones potential.

All these different energy terms will allow us to compute the total energy of our system (E_{total} in eq. 1.1) in a particular conformation and to optimize the atomic structure by minimizing E_{total} through methods such as the conjugate gradient[3] or Newton-Raphson. Hence, the positions of all atoms will vary upon minimizing the total contribution of all terms in equations 1.2 and 1.3 and we will get the structural minima leading to the lowest value of E_{total}. These methods are the same used in electronic structure calculations to optimize the atomic structure of the system. However, in those cases the atoms will move through a potential energy surface defined by the electrons,[4] contrary to FFs where the energy is expressed through eq. 1.1 – 1.3.

Notice that from FF methods no electronic information is obtained at all. Through these calculations only an approximate atomic structure may be obtained and its accuracy will entirely rely on the particular FF utilized (determining all predesigned constant parameters appearing in equations 1.2 and 1.3). Hence, we may use FF calculations to get appropriate initial molecular structures which later we may use to obtain refined conformations and the associated electronic information by electronic structure methods, introduced in the following sections.

2.2 The Schrödinger equation

The non-relativistic time-independent Schrödinger equation is normally used to describe the electronic structure of molecular systems:

(2.1) $\widehat{H}|\Psi(\vec{R},\vec{r})\rangle = E|\Psi(\vec{R},\vec{r})\rangle$

Where $\Psi(\vec{R},\vec{r})$ is the wave function of a system described by the position of all nuclei ($\vec{R}$) and electrons ($\vec{r}$), $\widehat{H}$ is the Hamiltonian operator and E is the associated energy of the system. The Hamiltonian is thus the operator which, upon being applied to a certain wave function (fully describing our system of nucleus and electrons) provides the associated energy of that system. The Hamiltonian has the following form:

(2.2) $\widehat{H} = -\sum_{i=1}^{N}\frac{1}{2}\nabla_i^2 - \sum_{A=1}^{M}\frac{1}{2m_A}\nabla_A^2 - \sum_{i=1}^{N}\sum_{A=1}^{M}\frac{Z_A}{r_{iA}} + \sum_{i=1}^{N}\sum_{j>i}^{N}\frac{1}{r_{ij}} + \sum_{A=1}^{M}\sum_{B>A}^{M}\frac{Z_A Z_B}{R_{AB}}$.

Note that here we have made use of atomic units for simplification, where the electron mass and charge, the reduced Planck's constant and the Coulomb's constant are all unity by definition.[5] Therefore, in eq. 2.2 m_A is the mass of a nucleus A in multiples of the mass of an electron, Z_A is the atomic charge of nucleus A in multiples of the charge of an electron (in absolute value) and ∇_i^2 and ∇_A^2 are the Laplacian operators (where $\nabla_q^2 = \frac{\partial^2}{\partial x_q^2} + \frac{\partial^2}{\partial y_q^2} + \frac{\partial^2}{\partial z_q^2}$) applied to the spatial coordinates of the i-th electron and the A-th nucleus, respectively. r_{iA}, r_{ij} and R_{AB} are the distances between an electron i and a nucleus A ($r_{iA} = |\vec{r_i} - \vec{r_A}|$), between two electrons ($r_{ij} = |\vec{r_i} - \vec{r_j}|$) and between two nucleus ($R_{AB} = |\overrightarrow{R_A} - \overrightarrow{R_B}|$), respectively. The first two terms in eq. 2.2 define the kinetic energy for electrons and nucleus, respectively. The third, fourth and fifth terms define the electrostatic interaction energy between electrons and nucleus, between electrons with each other and between nucleus with each other, respectively.

Because of their smaller mass, electrons move much faster than nuclei. The Born-Oppenheimer approximation assumes that, because of this, one may separate both movements, and consider the nuclei at fixed positions and the electrons as moving particles in such a nuclei-fixed structure. In such a situation, the previous equation can be simplified as such:

(2.3) $\widehat{H} = \widehat{H}_{elec} + V_{NN}$

where

(2.4) $\hat{H}_{elec} = -\sum_{i=1}^{N}\frac{1}{2}\nabla_i^2 - \sum_{i=1}^{N}\sum_{A=1}^{M}\frac{Z_A}{r_{iA}} - \sum_{i=1}^{N}\sum_{j>i}^{N}\frac{1}{r_{ij}} = \hat{T} + \hat{V}_{Ne} + \hat{V}_{ee}$

and V_{NN} is the remaining Coulomb interaction term between nuclei ($\sum_{A=1}^{M}\sum_{B>A}^{M}\frac{Z_A Z_B}{R_{AB}}$). Hence, the total Hamiltonian, $\hat{H}$, is defined as the sum of a constant potential (V_{NN}) and the so-called electronic Hamiltonian that, as it may be seen in eq. 2.4, is only composed of those terms related to electrons: namely the electronic kinetic term ($\hat{T}$) and the electrostatic interaction of electrons with fixed nuclei ($\hat{V}_{Ne}$) and with themselves ($\hat{V}_{ee}$). Now, solving the Schrödinger equation using such electronic Hamiltonian:

(2.5) $\hat{H}_{elec}|\Psi_{elec}(\vec{r};\vec{R})\rangle = E_{elec}|\Psi_{elec}(\vec{r};\vec{R})\rangle$

we get the electronic wave function (Ψ_{elec}) which only depends on the electron coordinates, $\vec{r}$ (note that the atomic coordinates, $\vec{R}$, enter as parameters, not variables) and the electronic energy (E_{elec}). If now we include the repulsion between fixed nuclei we may define the total energy of the system as:

(2.6) $E_{tot} = E_{elec} + \sum_{A=1}^{M}\sum_{B>A}^{M}\frac{Z_A Z_B}{R_{AB}}$.

Therefore, with these equations one should be able to calculate both the electronic wave function ($\Psi_{elec}(\vec{r};\vec{R})$) and the total associated energy for any given system composed of N electrons moving in a potential generated by M fixed nuclei. From now on we will focus on the electronic Schrödinger equation (eq. 2.5) and, hence, the *elec* label (i.e. Ψ_{elec} , $\hat{H}_{elec}$, E_{elec}) will be dropped out. Also it will be assumed that the nuclei coordinates are used as parameters in Ψ without the necessity to specify it anymore (i.e. $\Psi(\vec{r};\vec{R}) \rightarrow \Psi(\vec{r})$).

2.2.1 The Variational Principle

The problem upon solving the eq. 2.5 is finding the wave function corresponding to the ground state of our system, Ψ_0, which, when introduced in eq. 2.5 will deliver the true ground state energy, E_0. It turns out that the exact form of $\Psi_0(\vec{r})$ is only available for the so-called hydrogen-like atoms, which are atoms with only one electron, like the hydrogen atom (i.e. H, He^+, Li^{2+}, Be^{3}+…). For those cases we may know the exact analytical form of $\Psi_0(\vec{r})$. However, for any more complex system, like any atom composed of more than one electron, there is no possible way of knowing the exact mathematical form of $\Psi_0(\vec{r})$. Fortunately, there is a method to approach $\Psi_0(\vec{r})$, and this is the variational principle, which states the following:

(2.7) $\langle\Psi_{trial}(\vec{r})|\hat{H}|\Psi_{trial}(\vec{r})\rangle = E_{trial} \geq E_0 = \langle\Psi_0(\vec{r})|\hat{H}|\Psi_0(\vec{r})\rangle$

in other words, any trial wave function ($\Psi_{trial}(\vec{r})$) introduced in the Hamilton operator will provide an associated trial energy E_{trial} which will always be an upper bound of the true ground state energy E_0 associated to the true ground state wave function $\Psi_0(\vec{r})$ of the system. Therefore, the obvious strategy is minimizing the $E[\Psi]$ functional (eq. 2.7) searching through all acceptable N-electron wave functions (i.e. wave functions which are continuous everywhere and quadratic integrable). Upon doing so, the function providing the lowest energy will be the true ground state wave function Ψ_0 and the associated energy the true ground state energy, E_0:

(2.8) $E_0 = \min_{\Psi\to N} E[\Psi] = \min_{\Psi\to N}\langle\Psi|T + V_{Ne} + V_{ee}|\Psi\rangle$.

Hence, through eq. 2.8 we have an strategy to find the true wave function Ψ_0 of the ground state of our system and its corresponding energy, E_0. As previously mentioned, for any relevant chemical system composed of several electrons and nuclei (like for instance, an organic compound) it is impossible to try all acceptable N-electron wave functions and test which one presents the lowest energy upon applying the electronic Hamiltonian through eq. 2.5. Because of this we need to use approximated ways to construct a subset of acceptable N-electron trial wave functions $\Psi_{trial}(\vec{r})$ which, upon minimization following eq. 2.8, will provide our best approximation to the true wave function and ground state energy. Below I will describe the most popular approximate methods which, ultimately, led to the most utilized of them all: density functional theory.

2.3 The Hartree-Fock Approximation

From basic quantum mechanics we know that the representation of the wave function describing our system of electrons (i.e. fermions) must be anti-symmetric. This means that upon interchanging the position of two electrons, the sign of the wave function must change. In the HF scheme we make an approximation to the N-electron wave function represented by an anti-symmetrised product of N one-electron wave functions $\chi_i(\vec{X}_1)$ in the form of the so-called Slater determinant:[6]

(3.1) $\Psi_0 \approx \Phi_{SD} = \frac{1}{\sqrt{N!}}\begin{bmatrix}\chi_1(\vec{X}_1) & \cdots & \chi_N(\vec{X}_1)\\ \vdots & \ddots & \vdots \\ \chi_1(\vec{X}_N) & \cdots & \chi_N(\vec{X}_N)\end{bmatrix}$.

The Slater determinant is composed of one-electron wave functions, $\chi_i(\vec{X}_j)$, which are called spin-orbitals, due to the fact they are composed of a spatial (orbital) part, $\Phi(\vec{r})$, and a spin function $\sigma(s)$, where s may be α or β (i.e. spin up or down):

(3.2) $\chi_i(\vec{X}_1) = \Phi(\vec{r}) \cdot \sigma(s)$.

Spin orbitals are orthonormal by construction (i.e. $\langle\alpha|\alpha\rangle = \langle\beta|\beta\rangle = 1$ and $\langle\alpha|\beta\rangle = \langle\beta|\alpha\rangle = 0$). For closed-shell systems, electrons will be paired in spatial orbitals, $\Phi(\vec{r})$, having opposite spin components, $\sigma(s)$. For open-shell systems (i.e. with unpaired electrons) other representations are considered, like un-restricted HF (see below), where α and β spin-orbitals do not share the same spatial part ($\Phi(\vec{r})$). For now we will consider only closed-shell systems for simplicity.

The Slater determinant accomplishes the anti-symmetry principle because interchanging the position of two electrons, which is equivalent to interchanging the position of two rows (each row in the Slater determinant is associated to one electron, $\vec{X}_i$) it may be easily demonstrated that this leads to a change of sign of the determinant.[6] Because of the anti-symmetry property, it may also be demonstrated that having two electrons occupying the same spin orbital (i.e. having two columns equal to each other) makes the Slater determinant equal to 0. In other words, two electrons cannot occupy the same spin orbital, which fulfils the Pauli exclusion principle, also arising from the anti-symmetry principle.

Developing the Slater determinant in terms of orbital products (so called Hartree products) and applying the Hamiltonian operator we get the energy functional of the system of electrons with the following form:

(3.3) $E_{HF} = \langle\phi_{SD}|\hat{H}|\phi_{SD}\rangle = \sum_i^N\langle i|\hat{h}|i\rangle + \frac{1}{2}\sum_i^N\sum_j^N\big((ii|jj) - (ij|ji)\big)$

where

(3.4) $\langle i|\hat{h}|i\rangle = \int \chi_i^*(\vec{x}_1)\left\{-\frac{1}{2}\nabla^2 - \sum_A^M \frac{Z_A}{r_{1A}}\right\}\chi_i(\vec{x}_1)d\vec{x}_1$

is the mono-electronic operator defining the kinetic energy of electron 1 and its attractive interaction energy with the nucleus, and

(3.5) $(ii|jj) = \int\int|\chi_i(\vec{x}_1)|^2\frac{1}{r_{12}}\left|\chi_j(\vec{x}_2)\right|^2 d\vec{x}_1 d\vec{x}_2$

(3.6) $(ij|ji) = \int\int\chi_i(\vec{x}_1)\chi_j^*(\vec{x}_1)\frac{1}{r_{12}}\chi_j(\vec{x}_2)\chi_i^*(\vec{x}_2)d\vec{x}_1 d\vec{x}_2$

define the energy terms related to the Coulomb and exchange interactions between two electrons (1 and 2). The first represents the electrostatic repulsive interaction between electrons (due to their negative charge) and the second, the exchange term, originates from quantum mechanics and only applies for electrons (i and j) of equal spin (i.e. α with α or β with β).

According to the variational principle (see section 2.2.1), the energy obtained from E_{HF} provided a trial ϕ_{SD} will always be an upper bound of the energy associated to the best possible wave function representation within the HF approximation of the system:

(3.7) $\mathrm{E}_{\mathrm{HF}}^{\mathrm{trial}} \geq \mathrm{E}_{\mathrm{HF}}^{0}$.

Hence, we must minimize E_{HF} (Eq. 3.3) to get the Slater determinant, Φ_{SD}, best representing our system:

(3.8) $\mathrm{E}_{\mathrm{HF}}^{0} = \min_{\Phi_{SD}\to N} E[\Phi_{SD}]$.

We must remember at this point that our set of spin orbitals $\{\chi_i\}$ are the only flexibility within the Slater determinant Φ_{SD}, and also in the expression of the E_{HF} (Eq. 3.3), because it is a functional of the $\{\chi_i\}$ set through equations 3.5 and 3.6. Therefore, the minimum value of E_{HF} should be found by finding the set of χ_i that, upon little variations $\partial\chi_i$, E_{HF} remained constant. Without going into further detail, we must know eq. 3.8 gives rise to the so-called Hartree-Fock equations which are a recipe to obtain the best set of spin orbitals, $\{\chi_i\}$; i.e. those χ_i giving rise to the lowest total energy $\mathrm{E}_{\mathrm{HF}}^{0}$ of the system. The Hartree-Fock equations present the general form:

(3.9) $\hat{f}\chi_i = \varepsilon_i\chi_i$

where $\hat{f}$ is the Fock operator and ε_i are the so-called *Lagrangian multipliers* and have the physical interpretation of being associated to the orbital energies of each χ_i. According to Koopman's theorem,[7] ε_i can be physically interpreted as the ionization energies upon removing an electron from that particular orbital χ_i. The Fock operator is an effective one-electron operator with the following form:

(3.10) $\hat{f}_i = -\frac{1}{2}\nabla_i^2 - \sum_{A=1}^{M}\frac{Z_A}{r_{iA}} - \sum_j^N\left(\int\left|\chi_j\left(\vec{X}_2\right)\right|^2\frac{1}{r_{i2}}d\vec{x}_2 - \int\chi_j^*\left(\vec{X}_2\right)\frac{1}{r_{i2}}\chi_i\left(\vec{X}_2\right)d\vec{x}_2\right)$.

In this equation we have, by order in the expression on the right hand side, the mono-electronic kinetic energy, the electrostatic interaction with nuclei and the coulombic and exchange interaction terms, respectively, with all the electrons (considered through the *j* iterator). The last two terms in eq. 3.10 depend on the spin orbitals which, in turn, are the solutions that we are looking for by applying the Fock operator through eq. 3.9. Hence, this is not a regular eigenvalue problem but a pseudo-eigenvalue problem (the operator is composed, partly, by the solution itself) and, thus, it must be solved iteratively. The utilized method for such a purpose is the so called self-consistent field (SCF) in which we use a set of initially guessed spin orbitals, which are used to calculate the form of our Fock operator, later utilized, through eq. 3.9, to calculate a new set of improved spin orbitals, which will later be utilized again to recalculate a new Fock operator, and so on. This process will be repeated until two sequential sets of spin orbitals differ by less than a predetermined threshold. At that point we will have obtained the best set of spin orbitals, $\{\chi_i\}$, constructing our best Slater determinant, Φ_{SD}, giving rise to the lowest possible energy within the HF approximation, $\mathrm{E}_{\mathrm{HF}}^{0}$.

2.3.1 Restricted and Unrestricted HF Models

At this point is worth introducing the $\hat{S}^2$ and $\hat{S}_z$ spin operators. These operators are applied to our wave function:

(3.11) $\hat{S}^2|\phi_{SD}\rangle = S(S+1)|\phi_{SD}\rangle$

(3.12) $\hat{S}_z|\phi_{SD}\rangle = M_S|\phi_{SD}\rangle$

providing the spin quantum numbers describing the total spin of our N-electron state, S, and its z component, M_S, respectively. As previously mentioned, up to now we have only considered systems where all electrons have been paired sharing the same spatial part, $\Phi(\vec{r})$, with opposite spin function, $\sigma(s)$ (see eq. 3.2). This is the situation, for instance, for methane, water, ethanol, hexane, amine, etc, and such molecules are called closed-shell systems. Using spin orbitals (i.e. χ_p and χ_q) that share the same spatial part Φ_p, but with opposite spin functions (α and β, respectively) is the so called restricted Hartree Fock (or RHF approach). However, for systems with unpaired electrons (so called open-shell systems), RHF does not provide a proper way to describe the electronic structure. In fact, such systems are not eigenfunctions of $\hat{S}^2$, unlike the closed-shell systems described by RHF, where the $\hat{S}^2$ operator provides a proper total spin quantum number equal to zero (i.e. $S = 0$). Hence, to improve the behaviour of RHF for such open-shell situations there are two possible approaches within the HF approximation: the restricted open-shell HF scheme (or ROHF) and the unrestricted HF (or UHF). In the former all orbitals are set as in the RHF method, except the orbitals bearing the unpaired electrons, where then χ_p and χ_q will not share the same spatial part and hence may present different spatial distributions and orbital energies (ε_i). In the UHF, differently, α and β do not share the spatial part (this applies to all electrons, both those paired and unpaired), and hence all α-orbitals and β-orbitals present different spatial distributions (Φ_p) and orbital energies (ε_i). UHF is represented by a single determinant wave function, which is then solved in a rather simplified manner. ROHF, conversely, is normally composed of a linear combination of different determinants with fixed coefficients (i.e. a configuration) to properly represent the spin state of the system (determined by $\hat{S}^2$ and $\hat{S}_z$) and the corresponding HF Hamiltonian is more complicated to be solved. UHF is the most common utilized methodology in the HF scheme, due to its electronic freedom and low cost. However, because of the high degree of electronic freedom (specially regarding the separation of α and β spin orbitals) it normally possesses so called spin contamination due to the mixing of the ground state with states with higher spin multiplicity. Because of that, UHF is no longer an eigenfunction of the spin operator $\hat{S}^2$ and the more the UHF solution deviates from the expectation value of the operator ($S(S+1)$), where S represents the total spin of the system, the more spin contaminated is said to be the calculated state.

2.3.2 Electron Correlation

The HF method is an *ab initio* approach, however, as it is an approximate method the best Slater determinant wave function, in a given basis set, will not coincide with the true wave function of our system. Consequently, according to the variational principle, the best HF wave function energy, E_{HF}, being the lowest possible energy within this scheme, will always be higher than the exact wave function energy (i.e. the true ground state energy; E_0). A generally accepted parameter to measure how good (or how bad) the obtained HF wave function is, as compared to the exact one, is the so called correlation energy,[8]

(3.13) $E_C^{HF} = E_0 - E_{HF}$.

Hence, E_C^{HF} is a measure about how bad (or how good) our HF representation is compared to the exact wave function.

One source of error in the HF approximation is the fact that the coulombic repulsion is treated as an average through eq. 3.10. This is the so called dynamical correlation because it is related with the fact that within HF the instantaneous repulsive interaction between electrons is not taken into account. Also, as we have seen before, there are systems where using one Slater determinant does not properly represent the electronic structure (such as in systems with one unpaired electron; i.e. a doublet). This is the so called static correlation. To improve the situation different approaches have been developed over the years to get energies closer and closer to the exact ground state energy, E_0; these are the so called post-HF methods, or correlated methods.

2.3.3 Post-HF methods

Wave function correlated methods[9] are those which, by addition of extra Slater determinants to improve the representation of the true wave function, deliver energies which are closer to the exact ground state energy E_0, as compared to the HF approach. Such methodologies normally involve a linear combination of Slater determinants which allow consideration of different electronic configurations which cannot be taken into account with a single determinant wave function (such as in HF). The great inconveniency of all these post-HF methodologies is the high computational cost associated to the corresponding calculations which restricts its application to systems where the number of atoms and electrons is small (i.e. small organic and inorganic molecules). For medium-large molecular systems and solids the resolution of the corresponding equations is intractable. The most common correlated methods are Configuration Interaction (CI; that adds a truncated number of Slater determinants each one representing a particular electronic excitation), Perturbation Theory[10] (which adds correlation as perturbation terms in the Hamiltonian), Coupled Cluster (CC) and multi-configurational procedures, such as CASPT2 which combines the multi-configurational approach with Moller-Plesset perturbations of second order.[11,12] All

these methods represent important tools in the quantum chemistry community, however, they have not been used in the work of this thesis and, hence, they will not be explained any further.

2.4 Density Functional Theory based methods

As an alternative to all these methods, density functional theory (DFT) has provided a computationally efficient, though accurate, way to study atomic systems ranging from small molecules to big systems such as polymers, bio-molecules (like DNA) or periodic systems (like inorganic solids). In the following section I will introduce the first attempts at using the electronic density as the only electronic variable in the electronic Hamiltonian to describe a system. After that I will present the Hohenberg-Kohn principles which demonstrated that using the electronic density as the unique variable of your system is physically justified. Then, I will describe the Kohn-Shan approach which provided a recipe to exploit the potential of DFT for actual chemical applications (i.e. simulations) paving the way for the tremendous success which today DFT bears, leading to a number of flavours with different characteristics, accuracies and computational efficiencies, as it will be briefly explained in the following section. I will briefly introduce the basis sets which are used to construct the Kohn-Shan one-electron orbitals as well as specific tools or approaches within DFT which have been used in this thesis, such as *ab initio* molecular dynamics simulations (AIMD) and periodic simulations.

2.4.1 The electron density

The electron density is a physical observable (i.e. a measurable) and is defined as follows:

(4.1) $\rho(\vec{r}) = N \int \dots \int |\Psi(\vec{x}_1, \vec{x}_2, \dots, \vec{x}_N)|^2 \, d\vec{x}_1 d\vec{x}_2 \dots d\vec{x}_N$

and determines the probability of finding any of the N electrons within the volume differential $d\vec{r}_1$. Strictly speaking, $\rho(\vec{r})$ is a probability density, but it is common practise to call it the electron density, since it describes an electron distribution. It vanishes upon moving to infinity out of our electronic system and, upon integrating it over all space, it sums up to the total number of electrons:

(4.2) $\rho(\vec{r} \to \infty) = 0$

(4.3) $\int \rho(\vec{r}) \, d\vec{r}_1 = N$.

Moreover, differently to the wave function, $\rho(\vec{r})$ is a measurable property: it may be measured by X-ray, scanning tunnelling microscopy (STM) or atomic-force microscopy (AFM), for instance.

2.4.2 First attempts: the Thomas-Fermi model

Could we replace the complicated N-electron wave function, depending on *(3+1)N* variables (where N is the total number of electrons), by a simpler quantity, such as the electron density (depending only on 3 spatial variables)? It turns out that from the electronic density one may calculate all parameters that determine the Hamiltonian operator for a specific system: namely the number of electrons (N), the position of the nuclei ($\vec{R}_A$) and their charges (Z_A). Hence, it makes sense that with the simple electron density function one should, in principle, be able to determine the Hamiltonian of the system (and hence the wave function, the energy, and all other properties).

The first attempt to use the electronic density as the central variable to determine the energy of our system dates back to 1927 and it was proposed by Thomas and Fermi,[13,14] who proposed the following expression to connect $\rho(\vec{r})$ with the ground state energy of the studied system:

(4.4) $$E_{TF}[\rho(\vec{r})] = \frac{3}{10}(3\pi^2)^{2/3}\int \rho^{5/3}(\vec{r})\,d\vec{r} - Z\int \frac{\rho(\vec{r})}{r}\,d\vec{r} + \frac{1}{2}\int\int \frac{\rho(\vec{r}_1)\rho(\vec{r}_2)}{r_{12}}\,d\vec{r}_1\,d\vec{r}_2$$

where the three terms of the right hand expression are, respectively, the kinetic energy (T_{TF}), the electron-nuclei electrostatic interaction and the electron-electron repulsive interaction, all expressed as functions of the density, $\rho(\vec{r})$. Therefore, this is, strictly speaking, the first reported density functional.

Later on, in 1951, Slater proposed a way to represent the complicated exchange energy term in HF in a much simpler way.[15] Simplifying the exchange functional based on the Fermi hole, Slater was able to arrive to this much simplier equation (compare it with eq. 3.6 where the exact HF exchange form is showed):

(4.5) $$E_{X\alpha}[\rho] = -\frac{9}{8}\left(\frac{3}{\pi}\right)^{2/3}\alpha\int \rho(\vec{r}_1)^{4/3}\,d\vec{r}_1 \ .$$

In fact, a work pioneered by Dirac[16] and Block[17] in 1930, arrived to the same dependence of the exchange energy with respect to the electronic density (with the same $^4/_3$ exponential factor), but from a completely different approach, based on the idea of the uniform electron gas. Combining eq. 4.4 with that expression for E_X derived by Dirac leads to the famous Thomas-Fermi-Dirac equation:

(4.6) $$E_{TFD}[\rho(\vec{r})] = \frac{3}{10}(3\pi^2)^{2/3}\int \rho^{5/3}(\vec{r})\,d\vec{r} - Z\int \frac{\rho(\vec{r})}{r}\,d\vec{r} + \frac{1}{2}\int\int \frac{\rho(\vec{r}_1)\rho(\vec{r}_2)}{r_{12}}\,d\vec{r}_1\,d\vec{r}_2 - C_X\int \rho(\vec{r}_1)^{4/3}\,d\vec{r}_1$$

where C_X is a different prefactor than that derived by Slater in 1951[15] (eq. 4.5). Now all terms considered in the electronic Hamiltonian are exclusively represented (including the exchange contribution to the electron-electron interactions missing in the Thomas-Fermi model; eq. 4.4) as functionals of the

electronic density. However, such model was not very successful for chemical applications, and hence it is mostly interesting from a historical point of view.

2.5 The Hohenberg-Kohn theorems

In 1964 Hohenberg and Kohn published a paper in the Physical Review that represents the landmark basis for modern density functional theory.[18] In a strikingly simple way, they demonstrated that the electronic density of a system $\rho(\vec{r})$ uniquely determines the corresponding Hamiltonian and, consequently, the wave function of the system, its ground state energy, and all other properties. In the same work they also proposed a way through which the ground state density (i.e. that determining the ground state wave function, ground state energy and so on) could be, hypothetically, obtained, based on the previously introduced variational principle.

2.5.1 First theorem: Proof of existence

Hohenberg and Kohn stated that '*the external potential* $V_{ext}(\vec{r})$ *is (to within a constant) a unique functional of* $\rho(\vec{r})$*; since, in turn* $V_{ext}(\vec{r})$ *fixes* $\hat{H}$ *we see that the full many particle ground state is a unique functional of* $\rho(\vec{r})$'. That demonstration was based on *reductio ad absurdum* and it took into account the fictitious hypothesis that two different external potentials, i.e. $V_{ext}(\vec{r})$ and $V'_{ext}(\vec{r})$, gave rise to the same ground-state electron density $\rho_0(\vec{r})$. In a more pictorial way this situation could be represented in the following way:

(5.1) $V_{ext} \Rightarrow \hat{H} \Rightarrow \Psi_0 \Rightarrow \rho_0 \Leftarrow \Psi'_0 \Leftarrow \hat{H}' \Leftarrow V'_{ext}$

If we now apply $\hat{H}$ to Ψ'_0 (i.e. the unprimed Hamiltonian to the primed wave function) we get, according to the variational principle:

(5.2) $E_0 < \langle \Psi' | \hat{H} | \Psi' \rangle = \langle \Psi' | \hat{H}' | \Psi' \rangle + \langle \Psi' | \hat{H} - \hat{H}' | \Psi' \rangle$

Due to the fact that the two Hamiltonians only differ by the external potential (i.e. the kinetic and electron-electron interaction energy terms are universal) we have:

(5.3) $E_0 < E'_0 + \langle \Psi' | \hat{T} + \hat{V}_{ee} + \hat{V}_{ext} - \hat{H} - \hat{V}_{ee} - \hat{V}'_{ext} | \Psi' \rangle$

Leading to:

(5.4) $E_0 < E'_0 + \int \rho(\vec{r}) \{ \hat{V}_{ext} - \hat{V}'_{ext} \} d\vec{r}$

As shown by Hohenberg and Kohn, applying now the primed Hamiltonian to the unprimed wave function (i.e. $\hat{H}'$ to Ψ_0), and following the same simple steps shown above we get:

(5.5) $E'_0 < E_0 - \int \rho(\vec{r}) \{ \hat{V}_{ext} - \hat{V}'_{ext} \} d\vec{r}$

Now, if we sum up equations 5.4 and 5.5 we get to the mathematical contradiction:

(5.6) $E_0 + E'_0 < E'_0 + E_0$ or $0 < 0$

This demonstrates that there cannot be two different external potentials (V_{ext} and V'_{ext}) giving rise to the same electronic density (ρ_0) or, in other words, that the ground-state-density uniquely determines the external potential and, consequently, the Hamiltonian of our system and, thus, the ground state wave function and energy and all related properties:

(5.7) $\rho_0 \Rightarrow V_{ext}\{N, Z_A, R_A\} \Rightarrow \hat{H} \Rightarrow \Psi_0 \Rightarrow E_0$.

Because the ground state energy is a functional of the electronic density, it is assumed that all its components must, also, be functionals of such simple variable, thus we end up with:

(5.8) $E_0[\rho_0] = T[\rho_0] + E_{ee}[\rho_0] + E_{Ne}[\rho_0]$

where the terms in the equation are the kinetic energy of the system, the electron-electron interaction (both coulombic and exchange included in $E_{ee}[\rho_0]$) and the electron-nuclei attraction term. Summarizing, the 1964 publication[18] by Hohenberg and Kohn provided a mathematical simple demonstration that it is physically sound to use the electronic density of your system as the only variable determining the ground state energy and all other properties, by virtue of determining the corresponding Hamiltonian. However, nothing was known as to what mathematical form the energy terms of eq. 5.8 had to present with respect to that density, or even the density itself.

2.5.2 Second theorem: The variational principle

In the 1964 contribution by Hohenberg and Kohn[18] they also proposed a simple recipe to get the ground state electronic density, ρ_0; i.e. the quantity which then leads to the ground state energy E_0 and all other properties. Taking into account that eq. 5.8 is equivalent to applying the Hamiltonian to the ground state wave function:

(5.9) $E_0[\rho_0] = \langle \Psi_0 | \hat{H} | \Psi_0 \rangle$

It should be possible to take advantage of the variational principle which, applied to the density functional shown in eq. 5.8, states that the ground-state energy (E_0) will be obtained if, and only if, the ground-state density (ρ_0) is input in the equation. This, as already explained in the wave-function case, means that for any given trial electronic density, $\tilde{\rho}$, the calculated corresponding energy given by eq. 5.8 will always be an upper bound to the true ground state energy. Mathematically:

(5.10) $E_0 \leq E[\tilde{\rho}] = T[\tilde{\rho}] + E_{ee}[\tilde{\rho}] + E_{Ne}[\tilde{\rho}]$

This, as previously done for the wave function, gives rise to a minimization process (Levy constrained-search[19]) of the type:

(5.11) $E_0 = \min_{\rho \to N}(T[\rho(\vec{r})] + J[\rho(\vec{r})] + E_{ncl}[\rho(\vec{r})] + \int \rho(\vec{r}) V_{Ne}\, d\vec{r})$

where the first term within the minimization is the kinetic energy, the second is the coulomb electronic repulsion term, the third includes all non-classical electronic interaction effects (such as exchange, correlation, etc) and the last term is the interaction with the external potential, i.e. electrostatic interaction of electrons with nuclei. The first three terms normally compose what is called the universal functional $F[\rho(\vec{r})]$, because they are system-independent, unlike the external potential that depends on the position and charge of the nuclei of our system. This method is called the constrained search because, as noted in the first minimization symbol ($\min_{\rho \to N}$), the input trial densities must integrate to the total number of N electrons, hence $\rho \to N$. Upon carrying out the minimization of eq. 5.11 we should obtain the ground state density (ρ_0) and ground state energy (E_0).

Of course, applying eq. 5.11 presents a fundamental problem which prevents any practical application of the constrained-search approach: we have not clue at all about the actual form of the first three terms within the minimization with respect to the density. However, this problem was, also, solved back in the 60s', just a year later after the Hohenberg-Kohn theorems when Kohn and Sham presented a method to circumvent the fact that the universal functional ($F[\rho(\vec{r})]$) exact form was unknown.[20] This would, finally, make density functional theory ready to work.

2.6 The Kohn-Sham approach

The Hohenberg-Kohn theorems represent the theoretical basis, fundamental demonstration that using the electronic density as the only variable to determine the total energy of our system was in fact a physically sound assumption. The variational principle also provided a hypothetical method through which it should be possible to find the ground state density (ρ_0) of our system and, hence, the ground state energy (E_0). However, from a practical perspective, such demonstrations were completely useless because they did not provide any clue about the form of the $T[\rho(\vec{r})]$ and $E_{ncl}[\rho(\vec{r})]$ components of the universal functional $F[\rho(\vec{r})]$:

(6.1) $F[\rho(\vec{r})] = T[\rho(\vec{r})] + J[\rho(\vec{r})] + E_{ncl}[\rho(\vec{r})]$.

As known from the Thomas-Fermi model[13,14,16] where all components of the energy were explicitly established as functional of the electronic density ρ, the major reason of total failure of this method to correctly describe realistic systems (e.g. according to calculations using this methodology, bond formation is not energetically favourable) is the over-simplified expression of the kinetic energy as

$\int \rho^{5/3}(\vec{r})\, d\vec{r}$. As the rest of the terms presented in equations 4.4 and 4.6, the kinetic energy of our system should be defined following a more complex equation with respect to the electronic density.

Going back to the HF method, we know that it uses an approximate representation of the true wave function; i.e. a Slater determinant. Also, we know that such representation is actually the true wave function of a system of N non-interacting electrons under the effect of an average effective potential. We know that the exact kinetic energy of such model is:

(6.2) $T_{HF} = -\frac{1}{2}\sum_{\mathrm{i}}^{\mathrm{N}} \langle \chi_i | \nabla^2 | \chi_i \rangle$

which, without being the exact kinetic energy of the true wave function, it is the exact kinetic energy of a system of N non-interacting fermions.

Kohn and Sham suggested[20] that instead of trying to find the exact functional connecting the kinetic energy and the electronic density (as done in the Thomas-Fermi model[13,14,16]) a better idea would be to compute a fraction of the kinetic energy exactly and to try to approximate the remaining part. The terms calculated exactly would be that of a reference system of non-interacting electrons under an external applied potential (i.e. that one calculated following equation 6.2, as in the HF model) whose associated electronic density would correspond to the true ground-state electronic density in the real interacting system, so:

(6.3) $\rho_S(\vec{r}) = \sum_i^N \sum_s |\varphi_i(\vec{r}, s)|^2 = \rho_0(\vec{r})$

where $\varphi_i(\vec{r}, s)$ are the spin-orbitals of our reference N-electron non-interacting system composing the Slater determinant and, following the analogy with the Hartree-Fock approximation, are determined by:

(6.4) $\hat{f}^{KS}\varphi_i = \varepsilon_i \varphi_i$.

Defining the one-electron Kohn-Shan operator as:

(6.5) $\hat{f}^{KS} = -\frac{1}{2}\nabla^2 + V_S(\vec{r})$

where the first term is the mono-electronic exact kinetic energy operator (remember that $\nabla^2 = \frac{\partial^2}{\partial x^2} + \frac{\partial^2}{\partial y^2} + \frac{\partial^2}{\partial z^2}$) and $V_S(\vec{r})$ is the mono-electronic local effective potential (recall HF equations in section 2.3). Now, we need to find those orbitals of the reference non-interacting system φ_i which upon integration according to eq. 6.3 will give rise to the true ground state density $\rho_0(\vec{r})$ of the real interacting sytem. Writing down the energy expression of the real interacting system of N-electrons, but now introducing the exact kinetic energy term of our reference non-interacting system we get:

(6.6)

$$E[\rho(\vec{r})] = T_S[\rho] + J[\rho] + E_{XC}[\rho] + E_{Ne}[\rho] =$$
$$-\frac{1}{2}\sum_i^N \langle\varphi_i|\nabla^2|\varphi_i\rangle + \frac{1}{2}\sum_i^N\sum_j^N \int\int |\varphi_i(\vec{r}_1)|^2 \frac{1}{r_{12}} \left|\varphi_j(\vec{r}_2)\right|^2 d\vec{r}_1 d\vec{r}_2 + E_{XC}[\rho(\vec{r})] - \sum_i^N \sum_A^M \int |\varphi_i(\vec{r}_1)|^2 \frac{Z_A}{r_{1A}} d\vec{r}_1$$

where $T_S[\rho]$ is the exact kinetic energy of our N-electrons non-interacting system, $J[\rho]$ is the exact coulomb energy and $E_{Ne}[\rho]$ represents the external potential due to nuclei. $E_{XC}[\rho]$ is the functional which contains all the unknown terms; i.e. the self-interaction error correction, exchange contribution and correlation effects and the residual part of kinetic energy which is not accounted by $T_S[\rho]$. Similarly as we did in the HF approximation, we may now apply the variational principle to eq. 6.6 and find the conditions that the orbitals φ_i must fulfil in order to minimize $E[\rho(\vec{r})]$ (remember that, through eq. 6.2 and 6.3 all terms, except the big unknown $E_{XC}[\rho]$, in eq. 6.6 may be expressed as functionals of φ_i). Upon doing so, as previously done for the HF approach, we now arrive to the Kohn-Sham mono-electronic equations which provide a means to get the spin-orbitals which will minimize the energy in eq. 6.6:

(6.7) $$-\frac{1}{2}\nabla^2 + \left[\int \frac{\rho(\vec{r}_2)}{r_{12}} d\vec{r}_2 + V_{XC}(\vec{r}_1) - \sum_{A=1}^M \frac{Z_A}{r_{1A}}\right]\varphi_i = \varepsilon_i \varphi_i \ .$$

Now, comparing this equation with the one-electron equations for our reference non-interacting N-electron system, as previously introduced in eq. 6.5, we easily see that the external potential $V_S(\vec{r})$ of our non-interacting N-electron system equals an effective potential composed by all energy terms within the brackets in eq. 6.7, i.e.:

(6.8) $$V_S(\vec{r}) \equiv V_{eff}(\vec{r}) = \int \frac{\rho(\vec{r}_2)}{r_{12}} d\vec{r}_2 + V_{XC}(\vec{r}_1) - \sum_{A=1}^M \frac{Z_A}{r_{1A}} \ .$$

Because of the fact that the electronic density appears in the definition of the effective local potential through the coulombic term ($\int \frac{\rho(\vec{r}_2)}{r_{12}} d\vec{r}_2$), as the Hartree-Fock method, we will have to solve eq. 6.7 iteratively through the self-consistent field, getting the mono-electronic KS orbitals φ_i that deliver the true ground state electronic density $\rho_0(\vec{r})$ of our real interacting system (through eq. 6.3) which, in turn, provides the associated ground state energy E_0 through eq. 6.6.

It is worth noting that, if we knew exactly the form of $V_{XC}(\vec{r}_1)$ in eq. 6.8, the big unknown, we would have access to the exact ground state energy of the system, E_0 (under the Born-Openheirmer approximation and neglecting relativistic effects). However, unfortunately, nor the Hohenberg-Kohn neither Kohn-Sham contributions give a clue about the exact form of $V_{XC}(\vec{r}_1)$. Giving, better and better approximate forms to such unknown functional is the holy grail of state-of-the-art density functional

theory and in the following section most common approaches developed since the late 80s up to the most popular ones today are reviewed.

2.7 Approximate exchange-correlation functionals

After the Kohn and Sham constribution[20] it was clear that the main goal in density functional theory was to come up with approximated explicit forms to $E_{XC}[\rho]$, i.e., the universal functional containing the exchange and correlation contributions about the inter-electronic interactions and the remaining kinetic energy not accounted within $T_S[\rho]$ (i.e. the exact kinetic energy of the non-interacting reference system; see section 2.6). Without entering into technical details, the different most popular approximations to $E_{XC}[\rho]$ and their main features and drawbacks are now described.

2.7.1 The Local Density Approximation (LDA)

The first approximation to $E_{XC}[\rho]$ was based on considering the system of electrons as a uniform electron gas; i.e. a cloud of electrons under the influence of a positive uniform background charge, resembling pretty well simple metals such as sodium. This scheme, already proposed in the 1965 contribution by Kohn and Sham[20], utilized as exchange density functional the one previously proposed by Dirac[16] and Block[17] in 1930 (included in the Thomas-Fermi-Dirac equation, eq. 4.6). In the local density approximation the universal functional presents the following form:

(7.1) $E_{XC}^{LDA}[\rho] = \int \rho(\vec{r})\varepsilon_{XC}(\rho(\vec{r}))\, d\vec{r}$

where $\varepsilon_{XC}\big(\rho(\vec{r})\big)$ is split in:

(7.2) $\varepsilon_{XC}\big(\rho(\vec{r})\big) = \varepsilon_X\big(\rho(\vec{r})\big) + \varepsilon_C\big(\rho(\vec{r})\big)$

The exchange part presents the same form as that proposed by Dirac[16] and Block[17] in the 20s':

(7.3) $\varepsilon_X\big(\rho(\vec{r})\big) = -\frac{3}{4}\sqrt[3]{\frac{3\rho(\vec{r})}{\pi}}$

Introducing eq. 7.3 into eq. 7.1 we get, again, the $^4/_3$ exponential factor, as derived by Slater within the HF scheme in 1951.[15] No explicit formula exists for the $\varepsilon_C\big(\rho(\vec{r})\big)$ term in eq. 7.2, but different authors have presented different analytical expressions for ε_C based on highly accurate numerical quatum Monte-Carlo simulations based on the homogeneous electron gas.[21]

Despite the fact that considering our system as a uniform electron gas with a constant electron density is quite a drastic approximation (most chemical systems present largely varying densities within their structures), it turns out that LDA (and its spin unrestricted version; i.e. that one which works with the α and β parts of the total density: $\rho(\vec{r}) = \rho_\alpha(\vec{r}) + \rho_\beta(\vec{r})$) provides results that are comparable to those

obtained within the Hartree-Fock approximation, or even better (comparing with experimental atomization energies from the G2 data set of molecules as reference, the average error of LDA is about 36 kcal/mol, whereas HF averages to 78 kcal/mol).[22] In this line, LDA provides good estimates of equilibrium structures, harmonic frequencies or dipole moments, however, it usually fails with respect to bonding energies, where it tends to provide too high binding energies (contrary to HF that underestimates them).

2.7.2 The Generalized Gradient Approximation (GGA)

Despite the fact LDA (and hence DFT) performed much better than expected and it was popular in some fields of solid-state physics, its accuracy for molecular systems was too poor to become popular among chemists, and hence DFT could not be considered for chemical applications yet. This situation started to change in the eighties were the first developments on top of LDA began to emerge. The first extension came up from the idea that, to improve LDA, one should not only consider the electronic density $\rho(\vec{r})$ at a given position in space but also its gradient; i.e. $\nabla\rho(\vec{r})$. This was done with the purpose of taking into account the non-homogeneity of the true electron density. The series of new functionals which appeared in this realm are collected to which is known as the generalized gradient approximation (or GGA) and present the following general form:

(7.4) $E_{XC}^{GGA}[\rho_\alpha, \rho_\beta] = \int f(\rho_\alpha, \rho_\beta, \nabla\rho_\alpha, \nabla\rho_\beta)\, d\vec{r}$

where, as previously done in the LDA scheme, the E_{XC}^{GGA} is normally separated in its two basic contributions:

(7.5) $E_{XC}^{GGA} = E_X^{GGA} + E_C^{GGA}$.

It is worth noting that the form of E_X^{GGA} and E_C^{GGA} is no longer determined by the physics behind the concept of the exchange and correlation effects described for wave function theory but just adjusted to provide the best results as compared to standard reference data sets. Therefore, it can be seen how in DFT a formal rigorous approach is substituted by a pragmatic necessity of constructing a method which, at an affordable computational cost, provides good enough accurate results. The E_X^{GGA} term usually takes the following form:

(7.6) $E_X^{GGA} = E_X^{LDA} - \sum_\sigma \int F(s_\sigma)\rho_\sigma^{4/3}(\vec{r})d\vec{r}$

where s_σ, the reduced density gradient is defined as:

(7.7) $s_\sigma(\vec{r}) = \frac{|\nabla\rho_\sigma(\vec{r})|}{\rho_\sigma^{4/3}(\vec{r})}$

where σ in eq. 7.6 is summed for both spin channels, i.e. α and β. There are different forms for $F(s_\sigma)$ in eq. 7.6 proposed over the years. A typical one is that proposed by Becke in 1988[23]:

(7.8) $F^B = \frac{\beta {s_\sigma}^2}{1+6\beta s_\sigma sinh^{-1} s_\sigma}$

but much more complex forms of the $F(s_\sigma)$ function with respect to s_σ exist such as that proposed by Perdew in 1986.[24] Regarding the correlation part E_C^{GGA} they present even more complicated analytical expressions which cannot be understood by any physical interpretation but, as previously stated, they are obtained by fitting the outcome results to established reference data sets.

Different GGA functionals have been proposed over the years, combining different forms of E_X^{GGA} and E_C^{GGA}. The most popular GGA functionals are PBE,[25] BLYP,[26,27] or BP86,[28] which have become the workhorses of current density functional theory for chemical applications (errors with respect to the G2 reference data go down to about 5-7 kcal/mol).

2.7.3 Hybrid functionals

As explained before, the Kohn-Sham scheme proposes to calculate the exact kinetic energy of a N-electron non-interacting system (i.e. represented by a Slater determinant, as in the HF scheme), T_S, and to approximate the remaining part to the exact kinetic energy of the real, interacting system, T. It was realized that the same could be done with the exchange contribution to E_{XC}. Within the Kohn-Sham approach, the N-electron non-interacting electron system, whose wave function is represented by a Slater determinant (just as the Hartree-Fock method), the exchange can be exactly calculated as follows:

(7.9) $E_X^{KS} = \frac{1}{2}\iint \frac{\rho_0 h_X^{KS}(\vec{r}_1;\vec{r}_2)}{r_{12}} d\vec{r}_1 d\vec{r}_2$

where $h_X^{KS}(\vec{r}_1;\vec{r}_2)$ is the exchange hole function determining the negative probability density of finding an electron at position $\vec{r}_2$ once we know another reference electron is sitting at position $\vec{r}_1$. Hence, as previously done for the kinetic energy in the Kohn-Sham approach, now we could calculate a part of our E_{XC}^{GGA} term exactly (for the non-interacting reference system) and another part approximately (for our real, interacting system). The simplest model based on such ideas was introduced by Becke in 1993 proposing the half-and-half combination[29]:

(7.10) $E_{XC}^{HH} = \frac{1}{2}E_{XC}^{\lambda=0} + \frac{1}{2}E_{XC}^{\lambda=1}$

where λ is a term that connects the non-interacting system (for λ=0; i.e. HF model) and the fully interacting real system (for λ=1). For the former we know, exactly, the exchange contribution to E_{XC}^{GGA}, but correlation effects are completely neglected, and for the second case both the exchange and correlation must be approximated, as done within the previously explained LDA and GGA flavours of

DFT. The functional in eq. 7.10 represents the simplest form of what are known as DFT/HF *hybrid* functionals. More elaborated versions have been presented over the years, where the different contributions of correlation and exchange are normally combined through parameters that have been calculated semi-empirically (i.e. optimizing them to get the best fit with reference data such as the G2 set). Of this type we have a second functional also proposed by Becke in 1993[30]:

(7.11) $E_{XC}^{B3} = E_{XC}^{LSD} + a\left(E_{XC}^{\lambda=0} - E_{X}^{LSD}\right) + bE_{X}^{B} + cE_{C}^{PW91}$.

Parameters a, b and c were fitted to optimize the resulting ionization energies and proton affinities with respect to the G2 data set, getting values of a = 0.20, b = 0.72 and c = 0.81. This semi-empirically formulated equation results in an average error of only 2-3 kcal/mol with respect to the G2 data set, representing the best approximate DFT models. Some of the most commonly used hybrid DFT functionals are B3LYP[31] and PBE0[32] (by Perdew, Burke and Ernzerhof) possessing 20% and 25% of exact exchange, respectively. PBE0 has been the main DFT functional utilized through this thesis, previously found to properly represent the electronic structure of π-conjugated radicals.[33] It is worth mentioning that over the last few years an effort has been made to continue with the improvement of hybrid functionals beyond the most commonly used B3LYP and PBE0. In this direction some new hybrid functionals have been developed including empirical dispersion terms, such as APFD[34] and X3LYP,[35] to improve long-range weak interactions such as London interactions, hydrogen bonds and polarizabilities. Another successful approach has been the range-corrected exchange-correlation functionals, such as the so-called HSE06 functional,[36] where the exact HF exchange varies with an adjustable distance parameter (ω). This approach has been especially helpful for using the hybrid scheme in inorganic solids.[37] Other proposed functionals are the LC-ωPBE[38] (improves the asymptotic limit) or the range separated corrected versions of the Minnesota functionals such as M11[39] or MN12-SX,[40] that improve the accuracy of the results but are heavily parameterized density functionals (22 and 80 parameters, respectively).

2.8 DFT at work: Introduction to basis sets

2.8.1 The Linear Combination of Atomic Orbitals (LCAO)

As in the HF approximation, in the core of KS approach we have to calculate the one electron KS equations:

(8.1) $\left(-\frac{1}{2}\nabla^2 + \left[\sum_j^N \int \frac{|\varphi_j(\vec{r}_2)|^2}{r_{12}} d\vec{r}_2 + V_{XC}(\vec{r}_1) - \sum_{A=1}^{M} \frac{Z_A}{r_{1A}}\right]\right)\varphi_i = \varepsilon_i \varphi_i$

having the more compact expression:

(8.2) $\hat{f}^{KS}\varphi_i = \varepsilon_i \varphi_i$.

Upon minimization of these equations we should get the set of one-electron orbitals φ_i which, if using the exact exchange-correlation functional V_{XC}, should provide the ground state density ρ_0 and the corresponding ground state energy E_0. These equations, though, are very complicated coupled integro-differential equations and numerical approaches are needed to solve them,[41] these being too expensive for common chemical applications where larger systems than just single atoms or small molecules are studied.[41] To circumvent this problem KS DFT applications make use of a scheme introduced by Roothaan in 1951[42] which defines each one-electron orbital as a linear combination of atomic orbitals (or LCAOs):

(8.3) $\varphi_i = \sum_{\mu=1}^{L} c_{\mu i}\eta_\mu$

where η_μ are specific simple functions of different forms (originally they were constructed mimicking the hydrogen atomic orbitals, hence the name) which, upon being added through the weight parameters $c_{\mu i}$ provide an estimation for the particular orbital φ_i. The larger the number of basis functions utilized (L) the better the representation of the particular orbital, φ_i; or, in other words, if L = ∞ the orbital φ_i could be represented exactly. Now, thanks to the orbital representation according to eq. 8.3, the complicated integro-differential KS equation (eq. 8.1) is transformed in a much more affordable linear problem, where $c_{\mu i}$ are the only variables to be calculated in our equations (remember $\{\eta_\mu\}$ is a pre-established fixed set of basis functions):

(8.4) $\hat{\mathrm{f}}^{\mathrm{KS}}(\vec{\mathrm{r}}_1)\sum_{\mu=1}^{\mathrm{L}} \mathrm{c}_{\mu\mathrm{i}}\eta_\mu(\vec{\mathrm{r}}_1) = \varepsilon_\mathrm{i}\sum_{\mu=1}^{\mathrm{L}} \mathrm{c}_{\mu\mathrm{i}}\eta_\mu(\vec{\mathrm{r}}_1)$

which is equivalent to:

(8.5) $\boldsymbol{F^{KS}\cdot C = S\cdot C\cdot \varepsilon}$

where $\boldsymbol{F^{KS}}$ is the so-called Kohn-Sham matrix (equivalent to the Fock matrix in the HF scheme), $\boldsymbol{S}$ is the overlap matrix, $\boldsymbol{C}$ is a matrix containing the coefficient values of each orbital mapped on all basis functions and $\boldsymbol{\varepsilon}$ is a matrix whose diagonal terms are the orbital energies. Hence, the complicated coupled integro-differential equations (eq. 8.1) has transformed into a standard linear algebra problem which may be resolved working with matrices. As expressed in eq. 8.1, the KS operator (or Fock operator if working within the HF approximation) must be split in its individual parts and, each of them, calculated using the LCAO. Without going into much detail, it is worth mentioning that normally the term which requires more computational time due to its relatively complex mathematical structure is the Coulomb electron-electron repulsion term:

(8.6) $\mathrm{J}_{\mu\nu} = \sum_{\lambda}^{\mathrm{L}}\sum_{\sigma}^{\mathrm{L}} \mathrm{P}_{\lambda\sigma}\int\int \eta_\mu(\vec{\mathrm{r}}_1)\,\eta_\nu(\vec{\mathrm{r}}_1)\frac{1}{\mathrm{r}_{12}}\eta_\lambda(\vec{\mathrm{r}}_2)\,\eta_\sigma(\vec{\mathrm{r}}_2)\mathrm{d}\vec{\mathrm{r}}_1\mathrm{d}\vec{\mathrm{r}}_2$

which is a four centre two electron integral. Hence, even after defining our set of orbitals φ_i as a linear combination of pre-established simple basis functions (eq. 8.3), the calculation of the Coulomb term (eq. 8.6) is the most computationally demanding one.

2.8.2 Types of basis sets

There are different basis sets which have been introduced since the early days of wave function methods (such as HF), each presenting its own advantages and disadvantages. One of the most utilized types are the so-called cartesian Gaussian-type orbitals (or GTOs), which have the following form:

(8.7) $\eta^{GTO} = N \cdot x^l y^m z^n \exp\left[-\alpha r^2\right]$

where N is the normalization factor and α determines how compact or diffuse the Gaussian function is. The additional l, m, and n terms determine whether the functions are of *s* type (l + n + m = 0), *p* type (l + n + m = 1), *d* type (l + n + m = 2), etc. GTO functions are the preferred basis sets because there are efficient ways to analytically calculate the complicated four-centre two-electron equations needed to calculate the coulomb contribution $J_{\mu\nu}$ in KS (eq. 8.6) or the coulomb and exchange terms in HF (eq. 3.5 and 3.6, respectively).

Another type of basis sets are the so-called Slater-type orbitals (or STOs). STOs are more physically sound due to the fact they ressemble very well the hydrogen atomic orbitals, with the following general form:

(8.8) $\eta^{STO} = N \cdot r^{n-1} \exp[-\xi r]\, Y_{lm}(\Theta, \phi)$.

Here n is the principal quantum number and $Y_{lm}(\Theta, \phi)$ are spherical harmonics describing the angular part of the function. However, there is no analytical treatment to solve the complex equations for the coulomb energy $J_{\mu\nu}$ in KS nor the exchange in HF when using STOs as the basis set, which then imply solving those equations using numerical methods (see below), which are more computationally demanding and present their own particular difficulties. For such reasons the use of STOs is not that popular as compared to GTOs.

As a way to have physically sensible basis sets while being computationally accessible, contracted Gaussian functions (CGF) were proposed.[43,44] CGFs are functions where several primitive GTOs are linearly combined to resemble more physically sound functions (such as STOs). CGFs present the following general form:

(8.9) $\eta_\tau^{CGF} = \sum_a^A d_{a\tau} \eta_a^{GTO}$

where we can see that a single CGF function (η_{τ}^{CGF}) is constructed by a number of GTO functions (η_{a}^{GTO}) and the corresponding contraction coefficients ($d_{a\tau}$) allowing to shape the η_{τ}^{CGF} in the desired way (e.g. resembling a STO function while being analytically solvable).

Another type of basis sets to describe periodic systems are plane waves.[45] Plane-waves are solutions of the Schrödinger equation for the free particle in a box, which imposes boundary conditions and, because of that, they represent periodical systems. Plane-waves present the following general form:

(8.10) $\eta^{PW} = \exp[i\vec{k}\vec{r}]$

Where $\vec{k}$ is the reciprocal space vector (see below) and it is related to the momentum of the wave and to the periodic boundary conditions. Because plane-waves are not centred on the atom it is difficult to model finite molecular systems using such type of basis sets and many plane-waves are required to induce such localized states.

Finally it is worth remembering that the basis set completeness is determined by the number of functions of the particular type per atomic orbital of the system. Hence, for instance, having one basis function per each orbital of our system up to valence orbitals is normally called the minimal set, because it is the most basic reasonable representation. Having two functions (or contracted functions) per orbital represents the next step in sophistication, and this are the so-called *double-zeta* sets. The so-called polarization functions, with higher angular momentum, are normally used to allow the atomic orbitals to distort in different ways depending on their molecular environment. Common basis sets presenting these characteristics are 6-31G or, including polarization functions resembling *d* and *p* orbitals, 6-31G(d,p)[46,47] or the SVP (split-valence polarization).[48] Examples of very high quality and expensive basis sets are those of the type of *quadruple* and *quintuple zeta* with polarized functions, such as cc-pVQZ and cc-pV5Z.[49]

2.8.3 Numerical basis sets and the exchange-correlation potential

While the coulomb repulsion electronic term $J_{\mu\nu}$ is calculated through eq. 8.6 which is a complex four-centre two-electron integral, the exchange-correlation term is calculated through the, apparently, simpler following equation:

(8.11) $V_{\mu\nu}^{XC} = \int \eta_{\mu}(\vec{r}_1)\, V_{XC}(\vec{r}_1)\eta_{\nu}(\vec{r}_1)\, d\vec{r}_1$.

However, as explained above, even the simplest form of DFT such as LDA presents quite a complex structure for the $V_{XC}(\vec{r}_1)$ term and, consequently, there do not exist analytical mathematical methods to solve the integral in eq. 8.11. Because of this, numerical methods are required, which are based on the construction of a grid of points which resemble the form of the orbitals or the basis sets composing them. The denser such grids, the more accurate results are obtained but also the more computationally

demanding they become. Hence a compromise must be reached between accuracy and efficiency, as happens with GTA and CGF basis sets as previously explained. Hence, after defining the number of points of our grid (P) and their positions ($\vec{r}_p$) the $V_{\mu\nu}^{XC}$ term will be calculated as the sum of its value on each of those grid points through something like:

(8.12) $V_{\mu\nu}^{XC} \approx \widetilde{V}_{\mu\nu}^{XC} = \sum_p^P \eta_\mu(\vec{r}_p)\, V_{XC}(\vec{r}_p) \eta_\nu(\vec{r}_p)\, W_p$

where W_p is a weighting factor determining the contribution of each product on the total summation. The actual form of currently used grids is atom-centred, where multiple grids are defined per atom centre and their superposition defines the total grid. Such atom-centred grids are defined in a way that their contribution (i.e. W_p) is maximum in the corresponding nucleus position and vanishes on the positions of any other nucleus. The actual form of such atom-centred grids (i.e. how W_p varies with the radial distance) was mainly defined by Becke in 1988[50] and is based in concentric spheres around each nucleus, mathematically represented by polar coordinates with radial and angular components: i.e. *r* and ϕ, Θ, respectively. Hence, the atom-centred grids are defined as a summation of points based on such polar coordinates with the form:

(8.13) $I_A \approx \sum_p^P W_p^{rad} \sum_q^Q W_q^{ang} F_A(r_p, \Theta_q, \phi_q)$

where the grid is defined as a number of concentric spheres at P distances from the nucleus with a particular weight defined by W_p^{rad} and, within each of them, a number of Q points defined by $F_A(r_p, \Theta_q, \phi_q)$ and weighted by W_q^{ang}. Despite the fact such methods normally carry associated numerical errors[51] (due to the fact we are dealing with finite grids, and hence, always approximated representations of our system) these are the only possibility to accurately calculate the exchange part $V_{\mu\nu}^{XC}$ within DFT. Moreover, the possibility of using quite dense grids thanks to the availability of supercomputing resources decreases such numerical errors to very small amounts which, for most applications, are negligible. The FHI-AIMS package, main computational code used in this PhD thesis, uses this type of basis sets.[52]

2.9 *Ab initio* DFT Molecular dynamics

As it will be later shown, in this thesis I have made an extensive use of *ab initio* molecular dynamics simulations (AIMD). This is because most of the applications considered in this work would, quite certainly, be applied at finite temperatures. Hence, basing our studies purely in fully optimized molecular structures at 0K represents an approximation. Here I will briefly introduce the basic ideas that underlay AIMD simulations. In particular, I will describe Born-Oppenheimer AIMD as used in this thesis (without touching other possible schemes such as the Car-Parrinello MD[53]).

The Born-Oppenheimer approximation considers that because of the fact atoms move much slower than electrons, they may be treated separately as classical particles within a potential energy surface imposed by the electrons and calculated via solving the electronic Hamiltonian using the atomic positions as bare parameters (i.e. not as actual variables). Such a potential energy surface defines the forces that the atoms will experience which, in turn, will determine their acceleration at a given time through Newton's second law:

(9.1) $\vec{\mathrm{F}} = \frac{\partial V(\vec{r})}{\partial \vec{r}} = m \cdot \frac{\partial^2 \vec{r}}{\partial t^2}$

where $\vec{\mathrm{F}}$ is the force acting on each nucleus, determined by the variation of $V(\vec{r})$ (the potential energy at a given position) with respect to $\vec{r}$ (the spatial position of that nucleus). Integrating eq. 9.1, which is normally done through numerical methods (i.e. not analytically), will give us the position of each nucleus (or particle) at each time; or, in other words, the motion of all particles with respect to time.

$V(\vec{r})$, as previously mentioned, is calculated through solving the electronic Schrödinger equation under the Born-Oppenheimer approximation. This may be done with any of the different computational methods explained above (i.e. HF or any of the DFT approaches). $V(\vec{r})$ will be obtained upon minimizing the electronic structure for a given arrangement of nucleus positions which will be introduced as fixed parameters to get $V(\vec{r})$. Then, upon using eq. 9.1, we will again get the forces acting to each nucleus and, for a predetermined time step (Δt), we will recalculate the new atomic positions, for which $V(\vec{r})$ will be calculated again at a particular level of theory (hybrid DFT in our case). The time step Δt must be chosen small enough to catch fast atomic vibrations. In this work we have used a time step equal to 0.5 fs ($1fs = 10^{-12}s$), which allows one to describe very rapid processes such as C-H bond vibrations, which are among the fastest molecular vibrations of all.

In an AIMD simulation we are modelling our system at a chosen temperature. Normally in this work we have modelled our atomic systems at room temperature ($\sim 300K$). Hence the calculation needs to provide energy to the system in order to maintain that chosen temperature. The temperature of the system is proportional to the average of the kinetic energy through the following equation:

(9.2) $\langle \mathrm{E}_{kin} \rangle = \frac{1}{2}(3N_{atoms} - N_{constraint})kT$.

The number of constrains ($N_{constraint}$) is normally three for periodic systems, corresponding to the conservation of linear momentum, and six for finite systems (such as molecules) where rotational freedom must also be constrained. There are different ensembles which may be used in an AIMD simulation which define the variables which are allowed to vary and those which are maintained constant. The NVE is the natural ensemble where the number of atoms (N), volume (V) and total energy (E) are

maintained constant. However, there are other ensembles such as the NVT or NPT where it is the temperature (T) which is maintained constant together with volume (V) or pressure (P), respectively. In these two later cases, our system will be connected to a *heat bath*, which gradually adds or removes kinetic energy to/from the system under a time constant, called *thermostat*, in our case the Bussi-Donadio-Parrinello thermostat.[54] Thermostats normally re-scale the kinetic energy of our system by multiplying the velocities of all particles by a factor α equal to:

(9.3) $$\alpha = \sqrt{\frac{\langle \bar{E}_{kin} \rangle}{\langle E_{kin} \rangle}}$$

where $\langle E_{kin} \rangle$ and $\langle \bar{E}_{kin} \rangle$ are the kinetic energies connected through eq. 9.2 with the actual and target temperatures, respectively, T and $\bar{T}$. Thus, by applying the scale factor to all velocities of all nucleus of our system, we may enforce the total kinetic energy of the system, $\langle E_{kin} \rangle$ (and its associated temperature, T) to equal the desired total kinetic energy and temperature: $\langle \bar{E}_{kin} \rangle$ and $\bar{T}$. Normally, this is done in repeated times during the equilibration time (initial period where the system adapts to the desired conditions defined by the NVT ensemble) or also during production time if the total kinetic energy varies too much from the target average value, $\langle \bar{E}_{kin} \rangle$. However, this method normally disturbs considerably the velocities of nucleus generating nuclear motions which deviate too much from physically-sensible trajectories. To avoid this, in the Bussi-Donadio-Parrinello scheme the kinetic-energy re-scaling is distributed over a number of time steps, hence ensuring a smother change of velocities in a more physically sound manner. For more details about this method see ref. 54.

2.10 Periodic calculations

As it will found in later chapters, the study of periodic solids conforms an important fraction of this thesis work. In this section I will briefly introduce how such extended systems are modelled using periodic boundary conditions and the basic principles to describe their electronic structure, focused in the production of band structures, as used in the published works presented in the latest chapters of this thesis.

2.10.1 Periodicity: the solution for solids' modelling

Solids are composed of a number of atoms proportional to the Avogradro's number (i.e. $6.0221409 \cdot 10^{+23}$), hence modelling such systems with atomic precision represents an impossible goal using any of the methods introduced in this chapter (both force-fields and post-wave function methods). To overcome this we may, however, make use of the periodicity defining the atomic interior structure of such materials. Making so we will be able to model the structure of the solid through by a periodic representation composed by a reduced and manageable number of atoms. Such reduced representation will be composed of a number of atoms in certain positions which, upon extension in one, two or three

dimensions, will construct an infinitely periodic solid (representation of our finite solid). Only periodic representations in 3D bear physical sense (we are in a 3D space), however, mathematically we may also construct 1D and 2D periodic systems. The parameter determining the dimensionality of our periodic model and its shape are the linearly independent vectors defining the periodic translation of the system. Fig. 2.1 shows three different examples of periodic representations in 1, 2 and 3 dimensions (i, ii and iii, respectively).

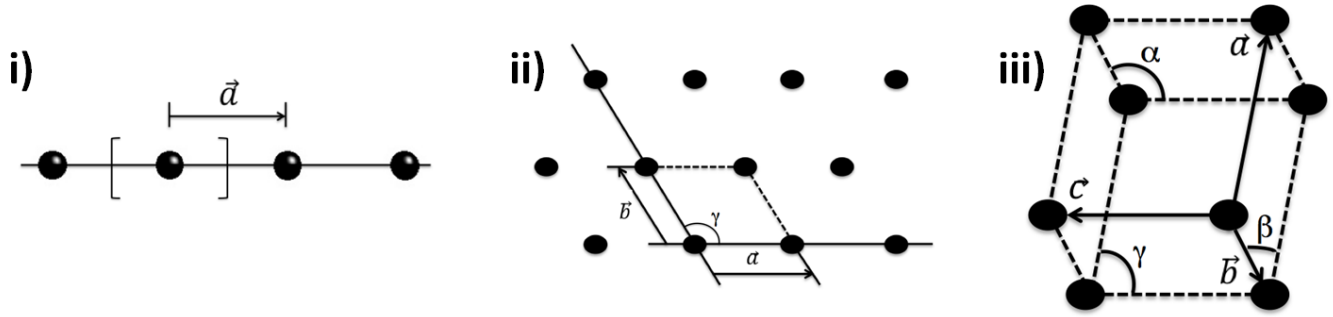

Fig. 2.1 Different unit cells representing periodic solids in 1, 2 and 3 dimensions (**i**, **ii** and **iii**, respectively), where the different linearly independent vectors defining the translational periodicity of the system are indicated ($\vec{a}$, $\vec{b}$ and $\vec{c}$). For the 2D and 3D cases, the angles between the different vectors (α, β and γ) may also be used to define the periodic unit cell.

Thus we may define an infinite chain of atoms using the simple one-atom unit cell shown in Fig 2.1-i defined by the $\vec{a}$ parameter. A 2D network of ordered atoms may be defined correspondingly with two linearly independent vectors $\vec{a}$ and $\vec{b}$ as shown in Fig 2.1-ii and a periodic 3D solid would require an extra perpendicular component ($\vec{c}$ vector in Fig 2.1-iii). Of course the systems represented in Fig. 2.1 are very simple mono-elementary systems (such as metals) represented by one-atom unit cells but more complex solids may be represented having unit cells composed of a certain number of atoms placed in certain positions which will be repeated in the different translation directions.

2.10.2 Electrons in periodic solids: Bloch's theorem

At the time of solving the Schrödinger equation for electrons within our periodic solid we must, again, make use of the periodic boundary conditions, due to the fact having to deal with all the electrons of our solid individually is not an affordable computational task today. This was first proposed by Felix Bloch in 1928[55] who utilized the translational symmetry to generate the crystal's wave function, composed of the so-called crystal orbitals or, also, electronic bands. Due to the periodic arrangements of nuclei, we must also have a periodic electronic potential which will possess the translational periodicity of the lattice:

(10.1) $V(\vec{r} + \vec{T}) \equiv V(\vec{r})$

where $V(\vec{r})$ is the electronic potential in a $\vec{r}$ position within the unit cell ($\vec{r}$ is a three dimensional vector) and $\vec{T}$ is a lattice vector (i.e. a multiple of the unit cell parameters $\vec{a}$, $\vec{b}$ and $\vec{c}$, see above) so that $V(\vec{r} + \vec{T})$

defines the electronic potential at the same position but within another equivalent unit cell (i.e. at $\vec{r} + \vec{T}$).[56] As a consequence of this electronic potential the wave functions associated to the electrons of such system also present translational periodicity in the following way:

(10.2) $\Psi(\vec{k}, \vec{r} + \vec{T}) = e^{i\vec{k}\vec{T}} \cdot \Psi(\vec{k}, \vec{r})$

where $\vec{k}$ is a vector defined in the reciprocal space (see below) which is associated to a particular symmetry of the periodic system. Hence, eq. 10.2 equals the value of the wave functions of our periodic solid at two points $\vec{r}$ and $\vec{r} + \vec{T}$ through a phase factor $e^{i\vec{k}\vec{T}}$ for a given propagation symmetry (or direction) defined by $\vec{k}$. Therefore, through eq. 10.2, by defining the wave function (or crystal orbital) at point $\vec{r}$ we may know its value for all equivalent $\vec{r} + \vec{T}$ positions for a particular translational symmetry by applying the phase factor $e^{i\vec{k}\vec{T}}$; in other words, eq. 10.2 defines the periodicity of our wave function. In the same way that the LCAO (linear combination of atomic orbitals) ansatz allows us to construct molecular orbitals by combination of atomic ones (or atomic orbitals by use of a basis set; see section 2.8) we may also construct our crystal orbital ($\Psi(\vec{k}, \vec{r})$) as follows:

(10.3) $\Psi(\vec{k}, \vec{r}) = \sum_j e^{i\vec{k}\vec{r}_j} \cdot \varphi_j$

where φ_j are each of the atomic orbitals that will be used to construct our periodic wave function (these will depend on the atoms composing our unit cell) and $e^{i\vec{k}\vec{r}_j}$ is a pre-factor determining their weight at the given position $\vec{r}$.[56] Therefore, through eq. 10.3 we have a way to construct our crystal orbitals using the atomic ones associated to the atoms composing our unit cell. However, before that, we need to understand the meaning of $\vec{k}$ and what are the values that we need to provide to this vector.

2.10.3 The reciprocal space and the Brillouin zone

The reciprocal space is a mathematical invention to facilitate the electronic study of periodical systems such as crystals. In the same way that we may define a vector $\vec{R}$ in the real space as a function of three vectors ($\vec{a}_1$, $\vec{a}_2$ and $\vec{a}_3$) linearly independent:

(10.4) $\vec{R} = n_1\vec{a}_1 + n_2\vec{a}_2 + n_3\vec{a}_3$

we may also define a vector, $\vec{K}$, in the reciprocal space with a base $\vec{g}_1$, $\vec{g}_2$ and $\vec{g}_3$ in the following way:

(10.5) $\vec{K} = m_1\vec{g}_1 + m_2\vec{g}_2 + m_3\vec{g}_3$.

Real-space and reciprocal space vectors must obey the following relation:

(10.6) $e^{i\vec{K}\vec{R}} = 1$

which implies:

(10.7-a) $g_1 = \frac{2\pi}{V}(\vec{a}_2 x \vec{a}_3)$

(10.7-b) $g_2 = \frac{2\pi}{V}(\vec{a}_3 x \vec{a}_1)$

(10.7-c) $g_3 = \frac{2\pi}{V}(\vec{a}_1 x \vec{a}_2)$

where V is the volume in the real space defined as $\vec{a}_1(\vec{a}_2 x \vec{a}_3)$. Hence, a particular lattice of points in the real space defined by periodical vectors $\vec{R}$ will be associated to a corresponding lattice in the reciprocal space whose translational vectors, $\vec{K}$, will obey equations 10.6 and 10.7.[56] For the electronic wave-function (or crystal orbitals) this is equivalent to apply the Fourier transformation to obtain the equivalent wave-function in the reciprocal lattice.

Recall $\vec{k}$ quantum number that defines our crystal orbitals in the real space, $\Psi(\vec{k}, \vec{r})$. $\vec{k}$ is a vector in the reciprocal space which, without going into details, may take the following values:

(10.8) $-\frac{\pi}{\vec{a}} \leq \vec{k} \leq \frac{\pi}{\vec{a}}$

Being $\vec{a}$ the vector defining the unit cell in the real space. These limited values of $\vec{k}$ define what is called the first Brillouin zone which may be understood as the unit cell in the reciprocal space. For instance, for the rectangular unit cell of a 2D arrangement of atoms defined by vectors $\vec{a}$ and $\vec{b}$ (see Fig. 2.2a) we will get the associated reciprocal vectors $\vec{a}^*$ and $\vec{b}^*$ (Fig. 2.2b).[57]

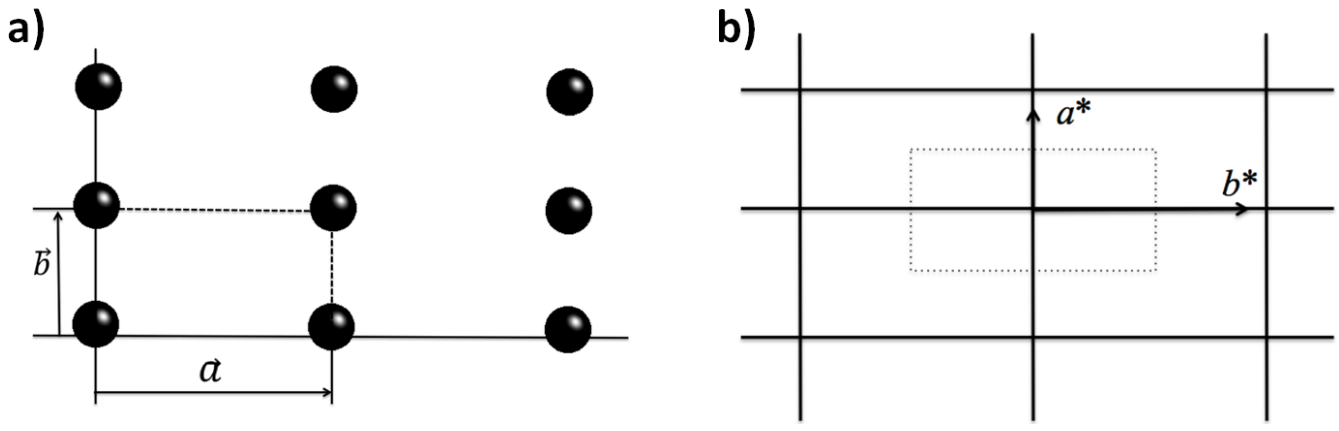

Fig. 2.2 a) Two dimensional unit cell of a 2D crystal defined with $\vec{a}$ and $\vec{b}$ vectors and **b)** associated reciprocal-space unit cell defined by reciprocal vectors $\vec{a}^*$ and $\vec{b}^*$.

The dotted squared area shown in Fig. 2.2 represents the first Brillouin zone defined by $\vec{k}$ through eq. 10.8. Of course, more complex solids presenting more complex unit cells in three dimensions will have

correspondingly more complex Brillouin zones. Fig. 2.3 shows one of such cases corresponding to the first Brillouin zone of the fcc Bravais lattice of bulk silicon indicating high-symmetry k-points (see below).

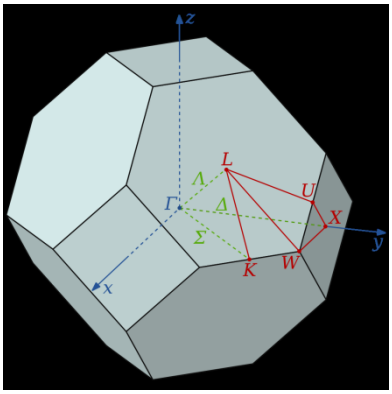

Fig. 2.3 first Brillouin zone of the fcc Bravais lattice of bulk silicon showing high-symmetry directions and points.

2.10.4 High symmetry points, band structure and density of states

The limited values of $\vec{k}$ in eq. 10.8 define the first Brillouin zone, as previously explained, $\vec{k}$ is used to define the crystal orbitals through equation 10.3 may take any value in the reciprocal space. Each particular $\vec{k}_i$ will define a particular wave propagation direction in the reciprocal space with its particular modulus ($|\vec{k}_i|$). Hence, for each $\vec{k}_i$ we will be able to construct a $\Psi(\vec{k},\vec{r})$ based in the atomic orbitals φ_j. Because there are infinite values of $\vec{k}$ in the reciprocal space (in the same way there are infinite $\vec{R}$ vectors in real space) we should strictly speaking calculate infinite $\Psi(\vec{k},\vec{r})$ values to properly represent the electronic structure of our solid. Likewise for each of these infinite crystal orbitals $\Psi(\vec{k},\vec{r})$ (each defined with a particular value of $\vec{k}$) we should apply the Hamiltonian for each of them (i.e. infinitely) to obtain the total energy of our solid. Of course, this is completely unfeasible and what is done in practise is representing the crystal orbitals of the system $\Psi(\vec{k},\vec{r})$ and calculating the corresponding energy at particular high-symmetry points in the reciprocal space within the first Brillouin zone that will capture the most important contribution of $\Psi(\vec{k},\vec{r})$ to the total energy. In Fig. 2.4 it may be seen the unit cell of the 2D hexagonal structure of graphene and the corresponding first Brillouin zone indicating the high-symmetry points.

Depending on the symmetry of the unit cell (Fig. 2.4a), the first Brillouin zone in the reciprocal space will present also a particular symmetry (Fig. 2.4b). The irreducible first Brillouin zone is that which by application of the symmetry operators of the particular symmetry group, may construct the entire first Brillouin zone. For graphene such irreducible first Brillouin zone is that defined by the high-symmetry points Γ, K and M.

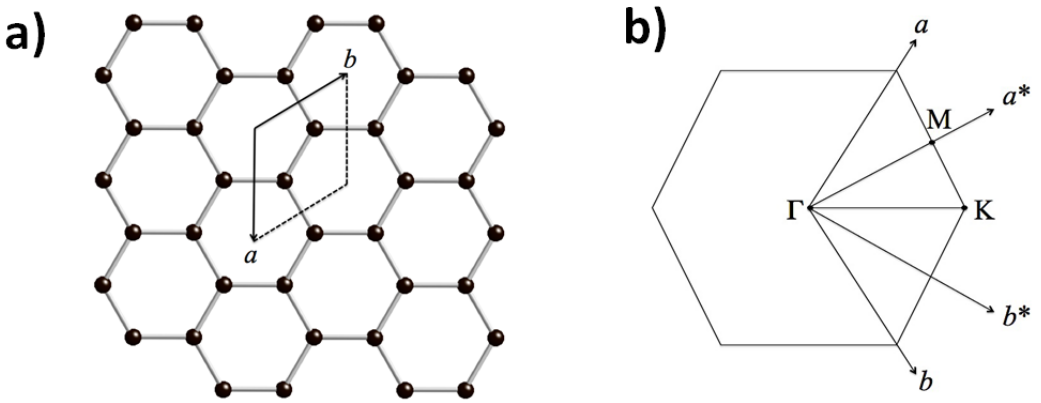

Fig. 2.4 a) 2D hexagonal structure of graphene where the unit cell constructed with $\vec{a}$ and $\vec{b}$ vectors and **b)** Brillouin zone defined with the reciprocal vectors $\vec{a}^*$ and $\vec{b}^*$ highlighting the high-symmetry points Γ, K and M.

Due to the fact these high-symmetry points, by symmetry operations, may construct the entire Brillouin zone, normally the vector $\vec{k}$ used to construct the crystal orbitals of the solid takes discrete values connecting those point. Hence, for graphene, $\vec{k}$ would take a finite set of values in the linear path from Γ to K, from K to M and from M to Γ. With these set of $\vec{k}$ values we would then construct our set of crystal orbitals through:

(10.9) $\Psi(\vec{k},\vec{r}) = \sum_j e^{i\vec{k}\vec{r}_j} \cdot \varphi_j$

and for each crystal orbital $\Psi(\vec{k},\vec{r})$ we could calculate the corresponding energy by applying the Hamiltonian:

(10.10) $E(k) = \langle \Psi(\vec{k},\vec{r}) | H | \Psi(\vec{k},\vec{r}) \rangle$.

As we may see the energy is expressed as a function of $\vec{k}$ which, in turn, will take discrete values (as many we may efficiently calculate) between the high-symmetry points in the reciprocal space as shown in Fig. 2.4 for graphene. In this way we will get the so-called band structure of our material where the energy of our set of crystal orbitals will be expressed as a function of $\vec{k}$. Fig. 2.5a shows the band structure for graphene where $\vec{k}$ takes values between high-symmetry points Γ, K and M.

As we may see in Fig. 2.5a upon doing so with graphene we get the very characteristic linear-dispersion crossing of bands at the Fermi level (dotted line) at the high-symmetry K point; the so-called Dirac cone. As it will be found in later chapters this electronic feature (i.e. the Dirac cone) plays a significant role in the latest works presented in this thesis. Normally, the band structure of any material is properly characterized plotting the crystal orbitals' energy versus $\vec{k}$, as shown in Fig. 2.5a for graphene. However, if required a more complete representation of the first Brillouin zone may also be obtained upon plotting

the variation of the energy of crystal orbitals $\Psi(\vec{k},\vec{r})$ against two reciprocal vectors $\vec{k}_x$ and $\vec{k}_y$, as shown also for graphene in Fig. 2.5b.

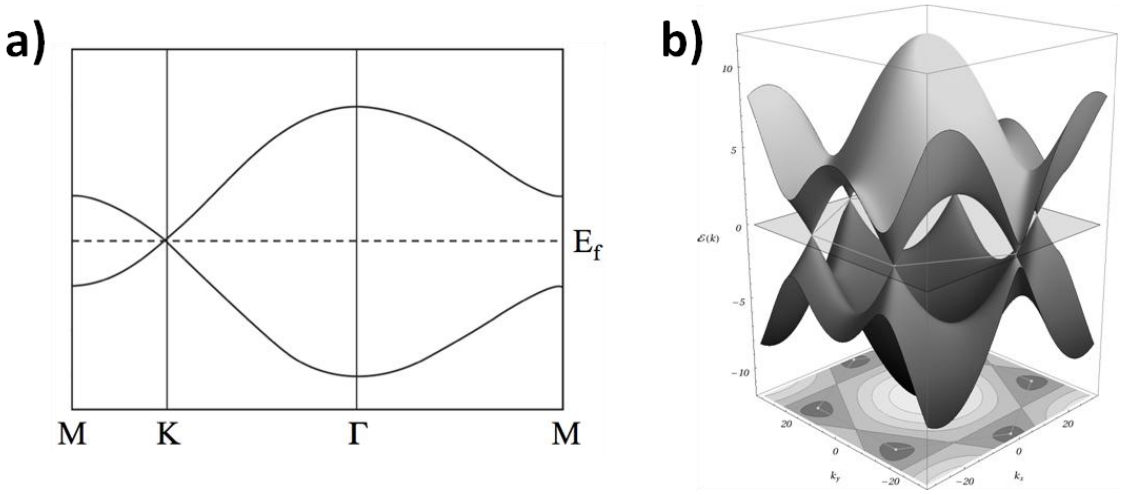

Fig. 2.5 a) Band structure of graphene versus $\vec{k}$ which takes the values between high-symmetry points Γ, K and M. **b)** Band structure of graphene versus $\vec{k}_x$ and $\vec{k}_y$ which allow to represent the crystal orbitals' energy in the entire first Brillouin zone.

Graphene unit cell is an example of a very simple unit cell (it is composed by two atoms) due to the high-symmetry that this 2D material presents. Accordingly, its band structure sampling the different high-symmetry points is rather simple (Fig. 2.5a). However, most of the times this is not the case, and very complex band structures may be obtained depending on the modelled solid and the chosen units cell in real space and associated Brillouin zone (in the reciprocal space). This is for instance the case for the fcc Bravais lattice of bulk silicon, as shown in Fig. 2.6.

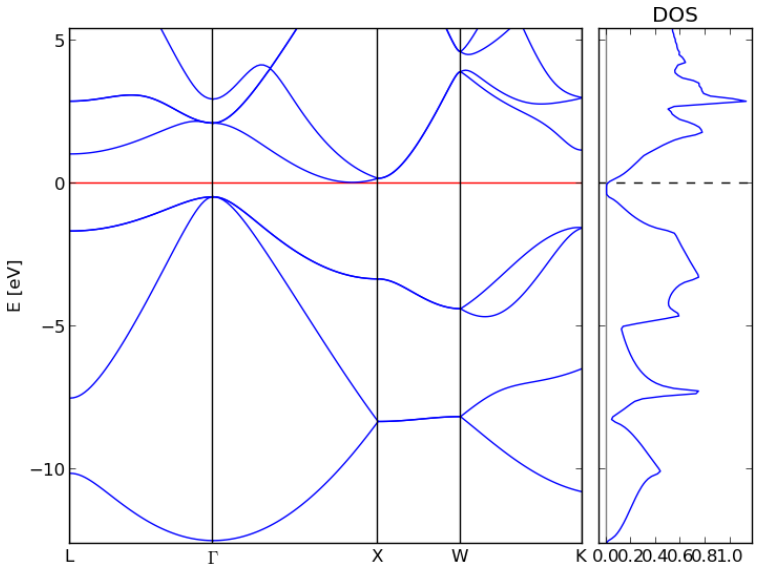

Fig. 2.6 Band structure of fcc Bravais lattice of bulk silicon through the high-symmetry points (see Fig. 2.3). The red horizontal line indicates the Fermi level energy.

In such cases it is convenient to calculate the so-called density of states (or DOS). The DOS, as the name indicates, provides a measure about the density of states at a particular energy, as shown in the right panel in Fig. 2.6. The DOS is inversely proportion to the slope (also called dispersion) of bands against $\vec{k}$.[58] Hence, the flatter a band (i.e. the more invariant its energy versus $\vec{k}$) the larger the DOS will be for in the corresponding energy values. Contrary, the higher the energy variation of a particular band (or crystal orbital) the lower the DOS for that range of energies will be. If a number of crystal orbitals appear at a given range of energies, the sum of their contributions will define the DOS in that energetic range. As it may be understood, DOS does not provide information about the symmetry of bands (there is no dependency with $\vec{k}$) but rather it is a simplified representation of the electronic structure of our solid facilitating important information like the energetic position of the valence and conduction bands of the material below and above the Fermi level, respectively.

2.11 Bibliography

1 J. E. Lennard-Jones, *Proc. R. Soc. Lond. A*, 1924, **106**, 463–477.

2 J. P. Dahl and M. Springborg, *J. Chem. Phys.*, 1988, **88**, 4535–4547.

3 T. A. Straeter, *NASA Tech. Reports Serv.*, 2011.

4 R. P. Feynman, *Phys. Rev.*, 1939, **56**, 340–343.

5 H. Shull and G. G. Hall, *Nature*, 1959, **184**, 1559–1560.

6 A. Szabo and N. S. Ostlund, *Modern quantum chemistry : introduction to advanced electronic structure theory*, Macmillan, 1982.

7 T. A. Koopmans, *Physica*, 1934, **1**, 104.

8 P. O. Löwdin, *Adv. Chem. Phys.*, 1959, **2**, 207.

9 R. J. Bartlett and J. F. Stanton, *Rev. Comput. Chem.*, 1995, **5**, 65.

10 C. Moller and M. S. Plesset, *Phys. Rev.*, 1934, **46**, 618.

11 K. Andemson, P.-A. Malmqvist, B. O. Roos, A. J. Sadlej and K. Wolinskit, *J. Chem. Phys.*, 1990, **94**, 5483.

12 K. Andersson, P.-A. Malmqvist and B. O. Roos, *J. Chem. Phys.*, 1992, **96**, 1218.

13 L. H. Thomas, *Proc. Camb. Phil. Soc.*, 1927, **23**, 542.

14 E. Fermi, *Rend. Accad. Lincei*, 1927, **6**, 602.

15 J. C. Slater, *Phys. Rev.*, 1951, **81**, 385.

16 P. A. M. Dirac, *Proc. Camb. Phil. Soc.*, 1930, **26**, 376.

17 F. Bloch, *Z. Phys.*, 1929, **57**, 545.

18 P. Hohenberg and W. Kohn, *Phys. Rev.*, 1964, **136**, B864.

19 M. Levy, *Proc. Natl. Acad. Sci.*, 1979, **76**, 6062.

20 W. Kohn and L. J. Sham, *Phys. Rev.*, 1965, **140**, A1133.

21 D. M. Ceperley and B. J. Alder, *Phys. Rev. Lett.*, 1980, **45**, 566.

22 W. Koch and M. C. Holthausen, *A Chemist's Guide to Density Functional Theory*, Wiley-VCH Verlag GmbH, 2001.

23 A. D. Becke, *Phys. Rev. A*, 1988, **38**, 3098.

24 J. P. Perdew, *Phys. Rev. B*, 1986, **33**, 8822.

25 J. P. Perdew, K. Burke and M. Ernzerhof, *Phys. Rev. Lett.*, 1996, **77**, 3865–3868.

26 C. Lee, W. Yang and R. G. Parr, *Phys. Rev. B*, 1988, **37**, 785–789.

27 A. D. Becke, *Phys. Rev. A*, 1988, **38**, 3098–3100.

28 A. D. Becke, *Phys. Rev. A*, 1988, **38**, 3098–3100.

29 A. D. Becke, *J. Chem. Phys.*, 1993, **98**, 1372.

30 A. D. Becke, *J Chem Phys*, 1993, **98**, 5648.

31 P. J. Stephens, J. F. Devlin, C. F. Chabalowski and M. J. Frisch, *J. Phys. Chem.*, 1994, **98**, 11623.

32 C. Adamo and V. Barone, *J. Chem. Phys.*, 1999, **110**, 6158.

33 R. Improta and V. Barone, *Chem. Rev.*, 2004, **104**, 1231–54.

34 A. Austin, G. A. Petersson, M. J. Frisch, F. J. Dobek, G. Scalmani and K. J. Throssell, *Chem. Theory Comput.*, 2012, **8**, 4989–5007.

35 X. Xu and W. A. Goddard III, *Proc. Natl. Acad. Sci.*, 2004, **101**, 2673–77.

36 J. Heyd, G. E. Scuseria and M. Ernzerhof, *J. Chem. Phys.*, 2003, **118**, 8207.

37 B. G. Janesko, T. M. Henderson and G. E. Scuseria, *Phys. Chem. Chem. Phys.*, 2009, **11**, 443–454.

38 O. A. Vydrov and G. E. Scuseria, *J. Chem. Phys.*, 2006, **125**, 234109.

39 R. Peverati and D. G. Truhlar, *J. Phys. Chem. Lett.*, 2011, **2**, 2810–2817.

40 R. Peverati and D. G. Truhlar, *Phys. Chem. Chem. Phys.*, 2012, **14**, 16187.

41 A. D. Becke, *Int. J. Quant. Chem. Symp.*, 1989, **23**, 599.

42 C. C. J. Roothaan, *Rev. Mod. Phys.*, 1951, **23**, 69.

43 D. Feller and E. R. Davidson, *Rev. Comput. Chem.*, 1990, **1**, 1.

44 T. Helgaker and P. R. Taylor, in *Modern Electronic Structure Theory, Part II*, ed. D. R. Yarkony, World Scientific Publishing, Singapore, 1995.

45 P. E. Blöchl, P. Margl and K. Schwarz, in *Chemical Applications of Density Functional Theory*, eds. B. B. Laird, R. B. Ross and T. Ziegler, American Chemical Society, Washington DC, 1996.

46 W. J. Hehre, R. Ditchfield and J. A. Pople, *J. Chem. Phys.*, 1972, **56**, 2257.

47 P. C. Hariharan and J. A. Pople, *Theor. Chim. Acta.*, 1973, **28**, 213.

48 A. Schäfer, H. Horn and R. Ahlrichs, *J. Chem. Phys.*, 1992, **97**, 2571.

49 T. H. Dunning, *J. Chem. Phys.*, 1989, **90**, 1007.

50 A. D. Becke, *J. Chem. Phys.*, 1988, **88**, 2547.

51 P. M. W. Gill, B. G. Johnson and J. A. Pople, *Chem. Phys. Lett.*, 1993, **209**, 506.

52 V. Blum, R. Gehrke, F. Hanke, P. Havu, V. Havu, X. Ren, K. Reuter and M. Scheffler, *Comp. Phys. Comm.*, 2009,

180, 2175–2196.

53 R. Car and M. Parrinello, *Phys. Rev. Lett.*, 1985, **55**, 2471.

54 G. Bussi, D. Donadio and M. Parrinello, *J. Chem. Phys.*, 2007, **126**, 14101.

55 F. Bloch, *Z. Phys.*, 1928, **52**, 555.

56 R. Dronskowski, *Computational Chemistry of Solid State Materials*, Wiley-VCH, 2005.

57 E. Canadell, M. L. Doublet and C. Iung, *Orbital Approach to the Electronic Structure of Solids*, Oxford University Press, 2012.

58 R. Hoffmann, *Solids and Surfaces: A Chemist's View of Bonding in Extended Structures*, VCH Publishers, Inc., 1988.

Chapter 3
Modelling TAMs as potential devices

This chapter is composed of two main parts, both involving work done in close collaboration with the experimental groups at the Institute of Materials Science of Barcelona (ICMAB) led by Profs Jaume Veciana and Concepció Rovira and Dr Marta Mas-Torrent, respectively. In the first section, the goal of the project was the preparation of radical (open-shell) self-assembled monolayers using closed-shell quinoidal TAM derivatives, following a theoretical prediction reported by Rissner et.al. in 2012. In the second part of this chapter, we study the irreversible E → Z isomerization process of a PTM-functionalized ethylene derivative, where the theoretical contribution was key for the interpretation of the experimental findings. Three works on these two studies are included in this chapter highlighting the relevance of the studied TAM systems for potential future molecular devices and demonstrating the capacity of this thesis work to provide meaningful fundamental insight into experimentally studied systems, hence improving their interpretation and applicability.

3.1. Introduction

3.1.1 Realization of an open-shell monolayer using closed-shell precursors

Rissner et.al. predicted in 2012 that the chemical adsorption (i.e. covalent bonding) of specifically designed quinoidal molecules bonded to metal substrates (such as Au) should lead to a π-conjugated cascade mechanism giving rise to the appearance of an unpaired electron as sketched in Fig. 3.1.[1]

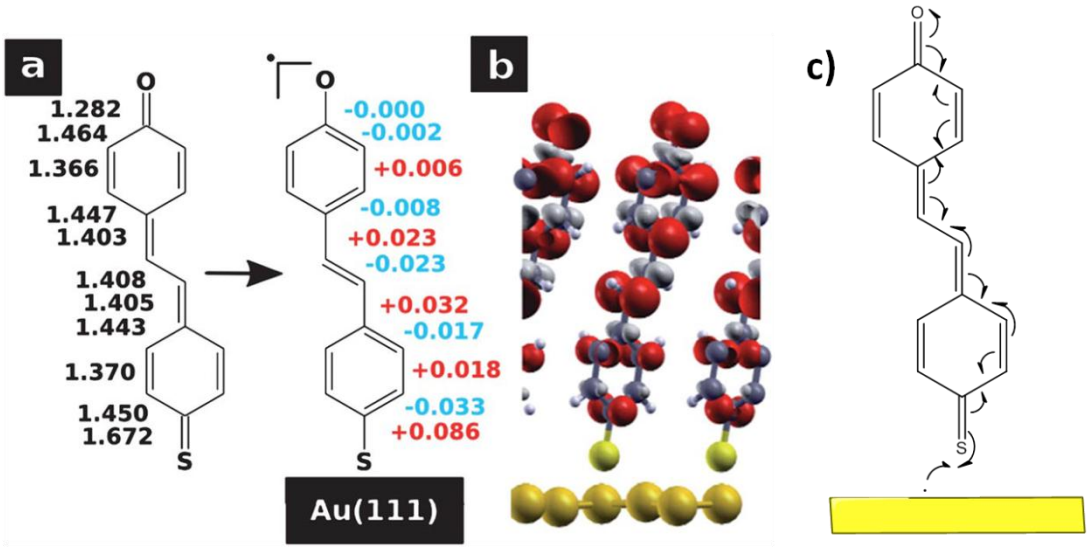

Fig. 3.1 a) Formation of an open-shell radical self-assembled monolayer using a specifically designed quinoidal molecule with a thio-docking anchoring group. **b)** Spin density iso-surface (α-spin in red; β-spin in grey) associated to the resulting unpaired electron. **c)** Electronic mechanism explaining the radical character of the molecular monolayer upon covalent bonding with the metallic surface.

Hence, in a very elegant manner, one may form a radical self-assembled monolayer (SAM) on Au using closed-shell quinoidal compounds. This would allow, in principle, avoiding the experimental difficulties of working with open-shell molecules (i.e. radicals, highly reactive species) and, at the same time,

obtaining a radical SAM on a solid substrate with all the benefits associated to such open-shell hybrid systems, as explained in Chapter 1 and highlighted in the literature.[2,3] The molecular systems proposed by Rissner et.al., though, are of limited experimental interest because both the quinoidal derivatives proposed and the resulting radical SAM would be far too reactive to be isolated and detectable under normal conditions. The reason for this is both the structural flexibility of the proposed molecular compounds and the accessibility to their generated unpaired π-conjugated electron which would cause its quick reaction with air (e.g. oxygen) or with the surface itself.

In collaboration with the experimental groups at ICMAB we aimed at demonstrating the experimental applicability of the predicted ideas of Rissner et.al. in the laboratory through a collaborative work combining on-surface experiments with state-of-the-art theoretical periodic calculations. Molecules depicted in Fig. 3.2 were initially proposed to carry out such study.

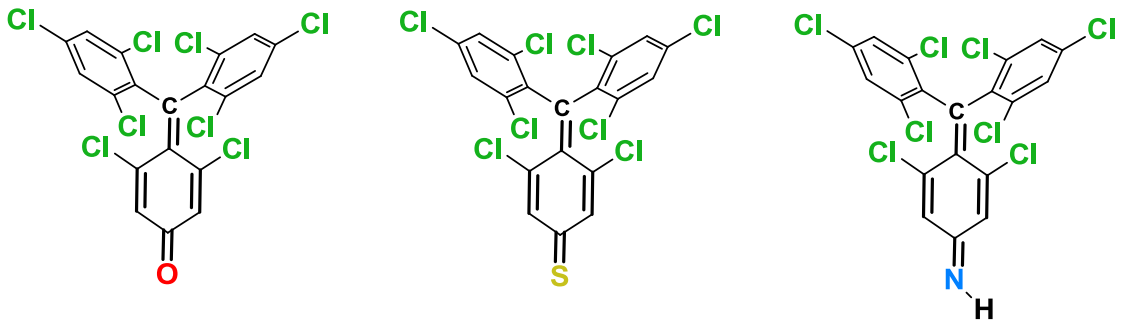

Fig. 3.2 Molecular candidates with oxo- (red), thio- (yellow) and nitro-carbonyl (blue) docking groups. Bulky chlorine atoms are in green and the quinoidal double-bond system is highlighted in bold in each derivative's skeleton.

As shown in Fig. 3.2 our molecular candidates are composed of a quinoidal skeleton (bold alternating double-bonds) in the lower ring connecting with particular docking groups (oxo-, thio- or nitro-carbonyl), which are the molecular fragment to be chemically bonded with the metallic substrate. The upper carbon atom in the quinoidal skeleton (bold central carbon in each structure in Fig. 3.2) is the position where the hypothetically generated unpaired electron would reside, and that position is bonded to two perchlororinated aryl rings which would sterically protect the generated radical centre (as it happens in the PTM family of organic radicals[4]). Hence, such compounds may be appropriate molecular candidates to experimentally demonstrate the ideas predicted by Rissner et.al. (Fig. 3.1).

Publication-draft #1 presented in this chapter is a preliminary draft summarizing the experimental efforts carried out to synthesize the molecular candidates shown in Fig. 3.2 and their use to generate the corresponding radical SAMs. Moreover, the theoretical modelling of each molecule-metallic hybrid system is also shown, explaining the efforts that have been needed to understand the experimental measurements and computational results in a single physico-chemical interpretation. Overall, I describe in **Publication-draft #1** how we have experimentally demonstrated the ideas predicted by Rissner et.al.

However, we also show that particular molecule-metal systems are necessary to realize the pursued radical monolayers; in other words, not all quinoidal molecules, nor all metal substrates, give rise to the electronic cascade mechanism depicted in Fig. 3.1c.

3.1.2 A structural explanation to chemical instability

As it will be shown in **Publication-draft #1** only the oxo-carbonyl TTM derivative (first molecule in Fig. 3.2) was stable enough to be experimentally isolated. Fig. 3.3 shows the structure of the TTM quinoidal oxo-carbonyl derivative optimized using the DFT hybrid PBE0 functional.[5]

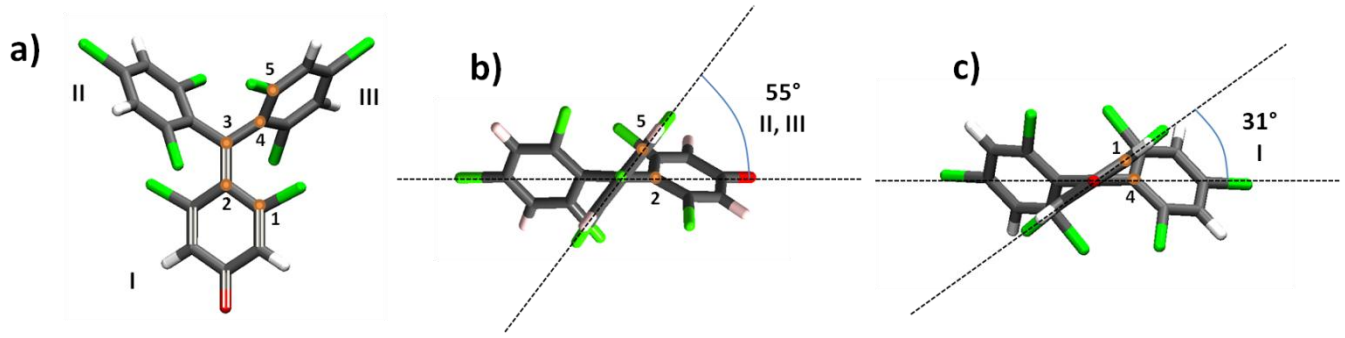

Fig. 3.3 Optimized TTM-quinoidal oxo-carbonyl derivative using the PBE0 functional within the FHI-AIMS code[6] both from the top **(a)** and side **(b-c)** views. Side views show the twist angle of the quinoidal ring **(b)** and the aromatic rings **(c)**.

As shown in Fig. 3.3b-c, the three aryl rings (included the quinoidal one) are highly twisted with respect to the molecular plane (dashed horizontal line). This is typical of the propeller-like conformation of PTM derivatives[7] where, due to the high steric hindrance associated with the bulky chlorine atoms in ortho-positions, the three aryl rings are twisted by around 56°. Taking a closer look at Fig. 3.3b we may see that aryl rings II and III (see labelling in 3.3a) are twisted by around 55° very much as in PTM radicals. Again, chlorine atoms in ortho-positions are the main factor determining such dihedral angle. Differently, the quinoidal ring with the oxo-carbonyl group (ring I in 3.3a) has a twist angle of only 31° (see Fig. 3.3c). This is caused by the quinoidal bonding pattern (double white bars in 3.3a) leading to a double bond between carbon atoms 2 and 3. This double-bond induces planarity of this aryl ring, opposing the sterical hindrance by chlorine atoms, leading to the more planar conformation shown in Fig. 3.3c.

The 31° twisted conformation shown in Fig. 3.3 is very constrained, both because of steric hindrance of chlorine atoms (pushing for higher twist angles) and the double-bond (pushing for lower twist angles). Hence one may guess the three quinoidal derivatives shown in Fig. 3.2 should tend to form the corresponding radical species (by dimerization, for instance, see next section) because in such open-shell form the double-bond between carbon atoms 2 and 3 shown in Fig. 3.3 would become a free-to-rotate single bond. Due to sterical hindrance by chlorine atoms that single bond would twist to more perpendicular conformations (55° - 56°) partially relaxing the structural constrain of the quinoidal form. This simple structural rationalization may explain the chemical instabilities of the three quinoidal

derivatives depicted in Fig. 3.2 and why the oxo-carbonyl derivative, with the greater stability of such double-bond group ($E_{C=O}$ = 745 KJ/mol; $E_{C=S}$ = $E_{C=N}$ = 615 KJ/mol) was the only isolated compound in the lab.

3.1.3 Direct covalent grafting of an organic radical core on gold and silver

Among other side reactions, the quinoidal thio-carbonyl functionalized TTM derivative dimerized leading to the corresponding bi-radical species (see Fig. 3.4). This reaction is highly favoured from an sterical point of view, as explained in the previous section, because the double-bond in the upper C-C position (bold bonds in left structure in Fig. 3.4) becomes a single bond in the bi-radical, which is free to twist, allowing the twist angle to be approximately 55° as in PTMs.[7]

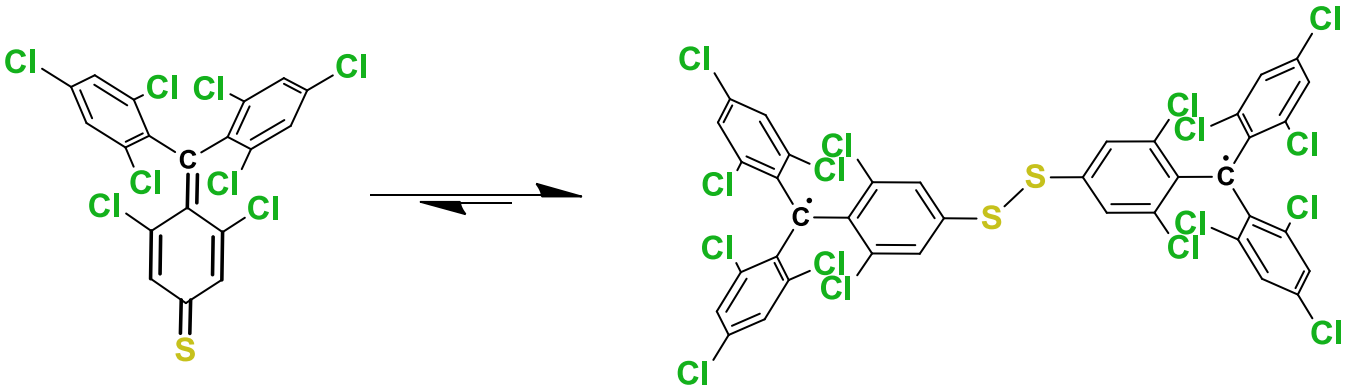

Fig. 3.4 Dimerization process of quionidal the thio-carbonyl TTM derivative in solution, leading to the corresponding bi-radical.

Such dithiol molecules may be used to form SAMs on gold due to the breakage of the S-S bond and the posterior formation of S-Au chemical bonds. Such a chemical route has been previously utilized to form similar PTM-based SAMs which behave as electro-active molecular switches.[8] Hence, the bi-radical product shown in Fig. 3.4 could be used to prepare the corresponding SAM on Au or Ag. Such SAM formation has the particularly interesting feature that the TTM core would be directly bonded to the surface. SAMs are normally formed using a linker (also called spacer) which usually is an alkyl or aromatic chain which physically separates the active unit of the compound (i.e. PTM core) from the metallic surface, hence avoiding any potential charge transfer phenomena or bonding (see Fig. 3.5).

Using the bi-radical shown in Fig. 3.4 we would be forming a SAM of the type shown in Fig. 3.5-right, where the TTM core is only separated from the metallic surface by the anchoring group (i.e. by a S atom in this case). In such a configuration, charge transfer phenomena may take place, which would then destroy the open-shell character of the SAM, or give rise to uncontrolled interface phenomena hampering any potential applicability of the hybrid system.

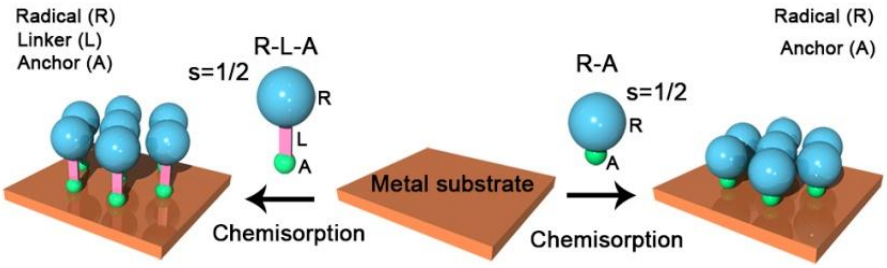

Fig. 3.5 *Left:* Usual self-assembly monolayers (SAMs) formation for PTMs. The radical head (blue) is spatially separated from the metallic surface through a linker (purple) which connects the radical core with the anchoring group (green) within the molecule. *Right:* As an alternative, the radical centre (blue) may directly bear the anchoring group (green), hence being directly bonded to the substrate upon SAM formation.

However, if the TTM core maintains its open-shell character, then the close proximity between the radical core and the metallic surface could give rise to interesting phenomena for spintronics applications,[2] such as magnetoresistance,[9] arising from the interaction between mobile electrons in the surface with the magnetic moment of the localized unpaired electrons in the radical SAM.

In **Publication #2** the bi-radical depicted in Fig. 3.4 was used to form the corresponding SAM in Ag and Au surfaces where the radical centres were directly chemically bonded to the surface by the closest distance reported to date. Our theoretical calculations supported the persistence of the unpaired electron directly bonded to the metallic surface, hence highlighting the potential of such systems for spintronics applications.

3.1.4 Study of the E-Z ethylene isomerisation in perchlorotriphenyl-methane (H-PTM) derivatives

Changing the nature of the target systems, in the second part of this chapter we focus on ethylene-based derivatives, such as stilbene, which may undergo the so-called trans-cis (or E↔Z) isomerisation, as depicted in Fig. 3.6.

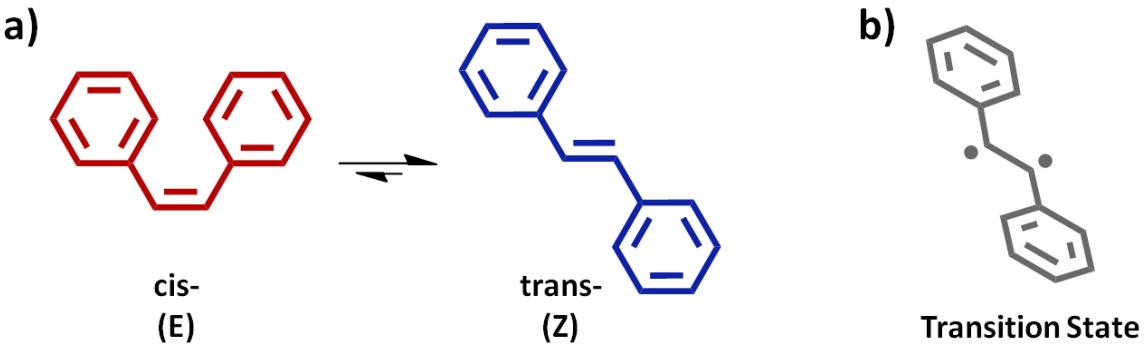

Fig. 3.6 a) Photo-isomerization equilibrium between the E and Z conformations in stilbene. **b)** Bi-radical transition state connecting both isomers at the maximum energy conformation where the dihedral angle in the ethylene unit is 90°.

Such an isomerisation process, as theoretically demonstrated,[10] must pass through an excited bi-radical triplet state (see Fig. 3.6b) where the ethylene unit is free to twist due to thermal fluctuations, jumping

from the E to the Z isomer, or vice versa. Because of the great stability of the ethylene double-bond, such triplet state lays around 2 eV above the closed-shell ground state and, hence, it cannot be reached purely by thermal energy (not by temperatures, for instance, between RT and 500°C). Because of this, the E ↔ Z isomerisation must be catalyzed by UV-vis. light or by chemical reagents,[11] such as iodine, oxygen or nitrogen oxide which will induce the formation of the bi-radical species shown in Fig. 3.6b, and then, allow for the ethylene unit to rotate via thermal fluctuations and switch between both conformations. Hence, under dark conditions and without specific chemical reagents, the equilibrium process shown in Fig. 3.6a will not take place and each isomer will simply remain in that particular conformation. Under light irradiation, though, each isomer is photo-activated and then the isomerisation takes place. The proportion of each conformer under such photo-activated conditions will be determined by thermodynamical aspects (i.e. relative total energy of each conformer with respect to the other). Despite the fact one may think that the equilibrium should be completely shifted to the trans- (E) isomer due to sterical reasons, under photo-activation the proportion of each conformer highly depends on the actual conditions of the system, such as the chemical functionalization of the stilbene unit, temperature, solvent or wavelength of irradiating light.[12]

Profs Veciana, Rovira and co-workers designed and synthesized two PTM-ethylene derivatives: one with a bromine atom in the *para*- position of the aryl ring bonded to the ethylene unit (shown in Fig. 3.7) and another one with an acetyl-thio group (S-Ac).

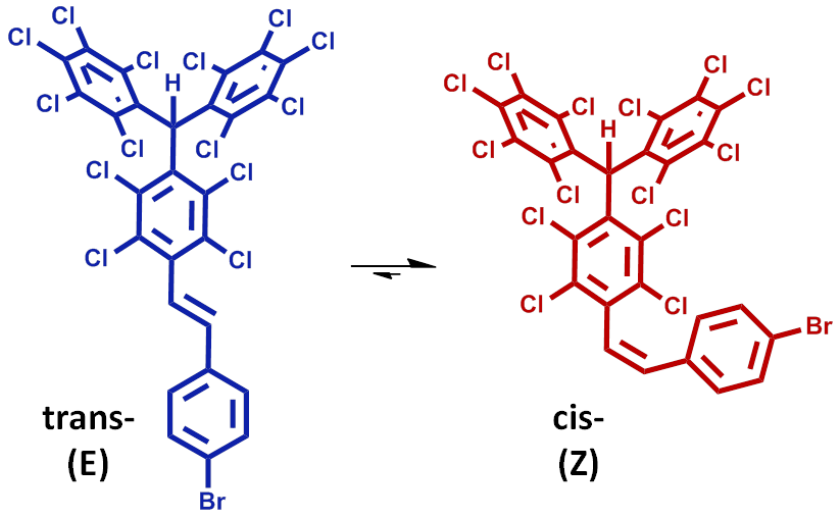

Fig. 3.7 E↔Z Photo-isomerization process for the PTM-ethylene derivative synthesized by Veciana and co-workers, where the equilibrium is shifted to the cis- (Z) isomer (right-hand structure).

Curiously, upon irradiating with UV-vis. light a solution of trans- (E) isomers (most stable conformer obtained as major product in the synthesis of each compound) the isomerisation to the cis- (Z) conformer takes place almost completely. Moreover, neither by photo-irradiation nor by chemical treatment (with I_2)

did the cis- (Z) conformers reverse back to the most thermodynamically stable trans- (E) isomers. This could not be explained by energetic reasons, due to the fact the trans- isomer is the most stable one.

In the experimental/theoretical collaborative **Publication #3** we aimed, by DFT calculations and molecular dynamics simulations, to understand the fundamental reasons why the E → Z process in both PTM-ethylene derivatives was completely shifted to the cis- isomer and irreversible (Fig. 3.7). Taking a close look at the dynamic fluctuations of both studied molecules in both conformations and comparing with the simplier stilbene case (Fig. 3.6) I came up with an original hypothesis to explain the unexpected experimental results. The core idea of my proposition is based on a sterical blockade of the torsion dynamics of the ethylene unit by the PTM bulky group.

3.2. Bibliography

1 F. Rissner, Z. Ma, O. T. Hofmann, C. Slugovc, Z. Shuai and E. Zojer, *J. Mater. Chem.*, 2012, **22**, 4269.

2 M. Mas-Torrent, N. Crivillers, V. Mugnaini, I. Ratera, C. Rovira and J. Veciana, *J. Mater. Chem.*, 2009, **19**, 1691.

3 M. Mas-Torrent, N. Crivillers, C. Rovira and J. Veciana, *Chem. Rev.*, 2012, **112**, 2506–27.

4 M. Ballester and J. Riera-Figueras, *J. Am. Chem. Soc.*, 1971, **4254**, 2215–2225.

5 C. Adamo and V. Barone, *J. Chem. Phys.*, 1999, **110**, 6158.

6 V. Blum, R. Gehrke, F. Hanke, P. Havu, V. Havu, X. Ren, K. Reuter and M. Scheffler, *Comp. Phys. Comm.*, 2009, **180**, 2175–2196.

7 J. Guasch, X. Fontrodona, I. Ratera, C. Rovira and J. Veciana, *Acta Crystallogr.*, 2013, **C69**, 255–7.

8 N. Crivillers, M. Mas-Torrent, J. Vidal-Gancedo, J. Veciana and C. Rovira, *J. Am. Chem. Soc.*, 2008, **130**, 5499–5506.

9 R. Frisenda, R. Gaudenzi, C. Franco, M. Mas-Torrent, C. Rovira, J. Veciana, I. Alcon, S. T. Bromley, E. Burzurí and H. S. J. van der Zant, *Nano Lett.*, 2015, **15**, 3109–3114.

10 W.-G. Han, T. Lovell, T. Liu and L. Noodleman, *ChemPhysChem*, 2002, **3**, 167–178.

11 C. Dugave and L. Demange, *Chem. Rev.*, 2003, **103**, 2475–2532.

12 D. Gegiou, K. A. Muszjat and E. Fischer, *J. Am. Chem. Soc.*, 1968, **90**, 3907–3918.

3.3. Results

Publication-draft #1

Realization of an open-shell self-assembled monolayer using closed-shell quinoidal molecular building blocks

In preparation

M. R. Ajayakumar, C. Moreno, I. Alcón, S. T. Bromley,* F. Illas, J. Veciana, A. Mugarza* and M. Mas-Torrent*

Realization of an open-shell self-assembled monolayer using closed-shell quinoidal molecular building blocks

M. R. Ajayakumar,[a] C. Moreno,[b] I. Alcón,[c] S. T. Bromley,[c,d] F. Illas,[c] J. Veciana,[a] A. Mugarza[b]* and M. Mas-Torrent[a,]**

[a]Institut de Ciència de Materials de Barcelona (ICMAB-CSIC) and CIBER-BBN, Campus UAB, 08193 Bellaterra, Spain.

[b]Institut Català de Nanociència i Nanotecnologia (ICN2), Campus UAB, 08193 Bellaterra, Spain.

[c]Departament de Ciència de Materials i Física Química & Institut de Química Teòrica i Computacional (IQTCUB), Universitat de Barcelona, E-08028 Barcelona, Spain

[d]Institució Catalana de Recerca i Estudis Avançats (ICREA), E-08010 Barcelona, Spain

Corresponding Authors

mmas@icmab.es, aitor.mugarza@icn2.cat, s.bromley@ub.edu

Abstract

In this work we have experimentally demonstrated that it is possible to use especially designed closed-shell quinoidal molecules to obtain an open-shell self-assembled monolayer (SAM) supported on metal substrates. The fundamental idea herein experimentally demonstrated was previously theoretically predicted, despite the fact the molecular candidates previously proposed could not be experimentally used because of the lack of persistence of the corresponding radical SAM. Here, by using specifically designed quinoidal trichloro-triaryl-methyl (TTM) derivatives whose corresponding open-shell analogues are persistent due to steric protection effects we have shown that such radical formation process takes place when chemically adsorbing such molecules on Ag(111), due to chemical bonding between the molecule and the surface. In addition, by combining on-surface XPS and ARUPS measurements with first principles DFT periodic calculations, we conclude that Ag is the only possible metal substrate presenting the appropriate features to generate the radical SAM. Au (and Cu) is too inert (reactive) leading to physisorved (highly dehalogenated) monolayers. Our results hence demonstrate that it is possible to use quinoidal closed-shell compounds to form radical SAMs on Ag with potential for organic electronics and spintronics.

Introduction

An important step towards taking full advantage of all potential of organic functional molecules for future applications is their integration on solid substrates such as metals and metal oxide surfaces,[1–4] with special relevance in fields such as organic electronics,[5–8] sensors[9,10] and biological arrays.[11–14] Specifically, in the field of molecular electronics, molecules grafted on surfaces are identified as one of the unique platforms for device miniaturization where, ultimately, the active unit would consist in a single molecule. In that respect, covalently bonded self-assembled monolayers (SAMs)[15–17] gained tremendous interest due to their ease of fabrication process and effectiveness to integrate organic molecules on inorganic (metallic) substrates. Organic radicals based SAMs[18] (r-SAMs) have emerged as potential

building units for spintronic materials, which could be applied for downscaling memory devices.[19,20] However, handling organic radicals is always an experimental challenge due to the inherent reactivity of radical centres. In that respect, Rissner et al. proposed in 2012 an electronic mechanism through which, by using closed-shell quinoidal compounds with specific docking groups, it would be possible to generate, upon chemical adsorption on Au, a radical SAM,[21] as sketched in Fig. 1.

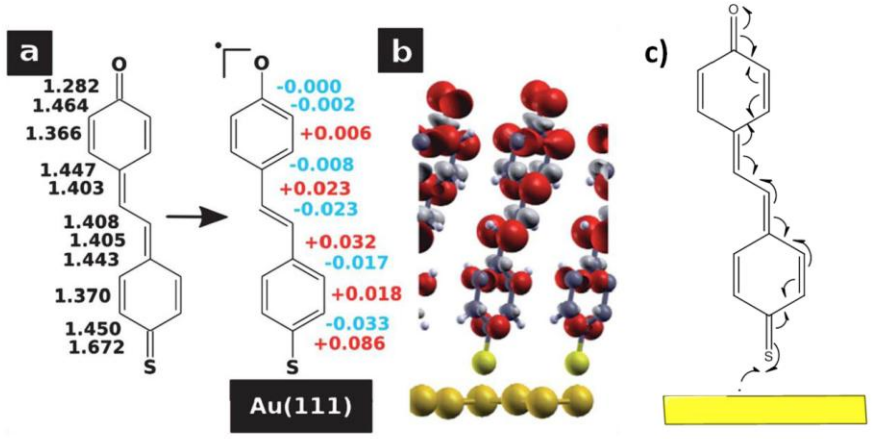

Fig. 1. a) Formation of a radical self-assembled monolayer using a specifically designed closed-shell quinoidal molecules with a thio-docking group used as anchoring group. b) Spin density iso-surface (α-spin in red; β-spin in grey) of the generated radical-SAM in the process depicted in (a). c) Electronic cascade mechanism through which an unpaired electron is generated in the molecular monolayer due to the formation of a single bond with the metallic surface.

As demonstrated in that work by means of periodic DFT calculations, upon chemically adsorbing a closed-shell quinoidal compound (Fig. 1a) on a Au surface, a radical like SAM is generated (see Fig. 1b). The electronic mechanism explaining such results is shown in Fig. 1c, where it is possible to understand the key role of the C=S docking group in the generation of the unpaired electron (and associated spin density) upon formation of the chemical bond with the metal surface.

An important weakness of the proposition by Rissner et.al. is the instability of the resulting radical-SAM under normal experimental conditions. π-conjugated organic radicals are normally very reactive species and, hence, to make them persistent normally steric protection by bulky groups is needed, as is the case for the perchlorotriarylmethyls (or PTMs) radicals.[22,23] Hence, the molecular systems (Fig. 1a) proposed by Rissner et.al.,[21] besides being very convenient as a computational proof of concept, they cannot be experimentally realized.

In this work we have experimentally demonstrated the fundamental principles of Rissner et.al. by using specifically designed quinoidal tris(2,4,6-trichloro-phenyl)methyl-based (TTM) compounds which, upon chemisorption on different tested metal substrates, generate a persistent open-shell monolayer (radical-SAM), as predicted theoretically.[21] Our molecular candidates have been designed in a way that in the resulting radical SAM the radical centre would have steric protection from its environment. This is a basic principle in the family of PTM radicals,[22,23] where the carbon bearing the unpaired electron is protected by the three perchlorated aryl rings.

By testing the radical SAM generation in three different metal substrates with increasing chemical reactivity (namely Au, Ag and Cu), our results demonstrate the on-surface formation of the radical SAM by surface science techniques such as X-ray photo-electron spectroscopy (XPS) and angle-resolved ultra-violet photo-electron spectroscopy (ARUPS). In the case of the Ag substrate, state-of-the-art DFT-based periodic theoretical calculations unveil the physical mechanisms leading to the surface radical species.

The present results indicate that the singly-occupied molecular orbital is only generated upon chemisorption on Ag and the theoretical calculations show that it appears at an energy value nicely coinciding with the measured peak with ARUPS. Hence, with this work, we demonstrate that the mechanism proposed by Rissner et.al. in 2012 may actually be experimentally used if the proper molecular units are utilized in particular metal substrates with a particular degree of chemical reactivity.

Methods

DFT modelling

We modelled the adsorption of the oxo-carbonyl TTM monomer on each of the three considered metal surfaces by periodic density functional theory (DFT) based calculations employing the PBE[24] generalised gradient approximation (GGA) functional with van der Waals corrections with the electron density expanded in a plane wave basis set with 500 eV energy cut-off and the effect of inner cores described through the PAW approach. Gamma point calculations were employed due to relatively large unit cell size (i.e. explicit k-points not necessary). Vacuum separated (25 Å) slabs of 3-5 atomic layers were used to represent the Ag(111) surface. Equivalent slab models with the TTM molecule in "vertical" (i.e. =*O* group towards surface) or "planar" (with respect to the three aryl rings) orientations relative to the surface were considered. All calculations were carried out with the VASP code[28] explicitly including spin polarization. Indeed, spin polarized solutions were obtained in full agreement with the experimental observations.

On-surface characterization

All samples were prepared in situ under UHV conditions by using (111) terminated surfaces of Au, Ag and Cu single crystals. Clean metal surfaces were obtained by cycles of sputtering by Ar^+ bombardment (< 1 keV) at room temperature and annealing at 400-450ºC for 10 min in ultra-high vacuum. Surface cleanliness was confirmed with x-ray photoelectron spectroscopy (XPS) prior molecules deposition. In order to deposit organic molecules we sublimated them in UHV from a home-made Knudsen-cell type evaporator with an alumina crucible. The sublimation temperature was accurately controlled by a thermo-couple in contact with the crucible. Before deposition, the molecules were outgased for several hours at temperatures around 120ºC. The sublimation temperature of the molecules was close to 185ºC. The pressure deposition of molecules was about 1×10^{-8} mbar with a base pressure around 1×10^{-9} mbar. XPS measurements were carried out using a Specs Phoibos 150 hemispherical energy analyser using a monochromatic X-ray source (Al K line with an energy of 1486.6 eV and 400 W) and energy referenced to the Fermi level. UPS experiments were performed with incident light from the He I emission at 21.2 eV. The fits have been performed with Voigt functions (Lorentzian-Gaussian curves), with a Gaussian-Lorentzian ratio of 0.3. Fitting was performed using XPST macro for IGOR (Dr. Martin Schmid, Philipps University Marburg) using the minimum number of peaks required to minimize the R-factor.

Results

Synthesis of quinoidal TTM derivatives

Three different molecular candidates utilized in this work are the tris(2,4,6-trichloro-phenyl)methyl (TTM) functionalized with oxygen (TTM-O), sulfur (TTM-N) and nitrogen (TTM-N), as shown in Scheme 1a. The three cases should, in principle, give rise to a covalent single bond between the adsorbate and the metal substrate leading to a radical SAM formation (see Scheme 1b).

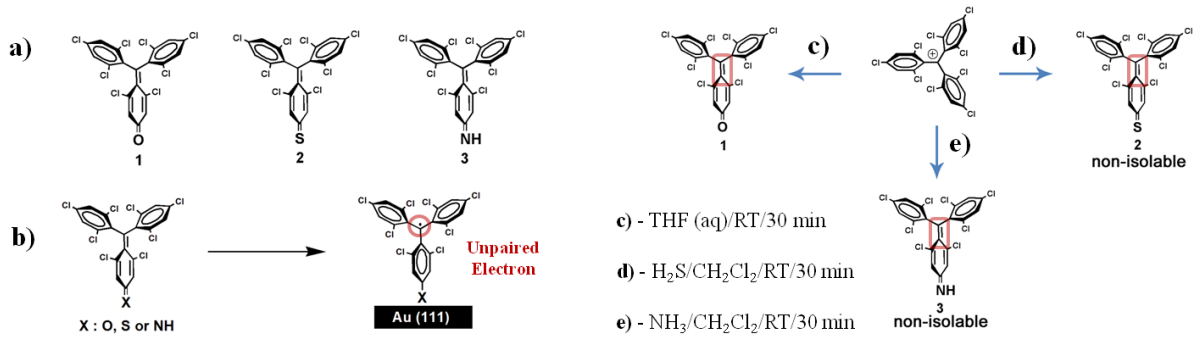

Scheme 1. a) Molecular candidates initially proposed to give rise to an open-shell radical SAM, through the process shown in b). Synthesis routes for the oxo- (c), nitro- (d) and thio-carbonyl (d) quinoidal TTM derivatives.

The three molecular candidates shown in Scheme 1a were synthesized following different synthesis routes as sketched in Scheme 1c-e (right panel in Scheme 1). TTM-O was produced by generating the TTM cation in a $THF_{(aq)}$ media (Scheme 1c) and stirring the solution at room temperature for 30 minutes. TTM-S was synthesized generating the TTM cation in a H_2S solution (Scheme 1d) in dichloromethane also stirring the solution at room temperature for 30 minutes. TTM-N was synthesized in the same way (i.e. through the TTM cation) in a NH_3 solution in dichloromethane (Scheme 1e). TTM-S and TTM-N probed to be very unstable compounds in solution with an important tendency to decompose or react with atmospheric oxygen and humidity, and hence it was not possible to isolate them. Most probable reason for such instability is the high twist angle of the quinoidal aryl ring with respect to the upper sp^2 carbon atom (red rectangle in Scheme 1c-e). Such important twisting is caused by Cl atoms in ortho- positions in each aryl ring. Such Cl atoms are necessary to stabilize the radical centre generated upon forming the radical SAM (Scheme 1b) but, at the same time, unstabilize the double bond (red rectangle in Scheme 1c-e) within the initially utilized quinoidal compounds (Scheme 1a). Because of such instability caused by the important twist angle of that bond, the entire quinoidal structure presents an important tendency to react and form the corresponding radical (and aromatic ring) hence liberating the huge sterical hindrance caused by the presence of the double-bond. S=C and H-N=C double bonds are not strong enough to maintain such sterical tension, which leads to their easy reactivity in solution (see above). However, the O=C bond in TTM-O is strong enough to maintain the quionidization of the molecule, and hence proved to be a fairly stable compound under ambient conditions easily isolable. Consequently TTM-O was our final molecular candidate to form the radical SAM.

On-surface deposition of TTM-O on Au, Ag and Cu

TTM-O was sublimated in ultra-high vacuum over the (111) surfaces of Au, Ag and Cu. We investigated the surface chemistry and electronic properties by means of X-ray (XPS) and angle-resolved ultraviolet photoemission spectroscopy (ARUPS).

XPS results

Cl 2p

The chemical state of chlorine was examined using the Cl 2p XPS emission (Fig.2a). The spectra were fitted with $2p_{3/2}$–$2p_{1/2}$ spin–orbit doublets separated by 1.6 eV with the intensity ratio of 2:1. In Au(111), the spectrum shows a single doublet with the Cl $2p_{3/2}$ peak at 200.2 eV. In the case of Ag(111) and

Cu(111), an additional chlorine contribution appear at ~2 eV lower binding energy. This second component is small in Ag, but dominates the Cl spectra in Cu(111). The table below summarizes the energy position and relative intensity for each component, obtained as the position of the $2p_{3/2}$ level and the area of the doublet respectively.

Surface	$2p_{3/2}$ level of I	$2p_{3/2}$ level of II	Relative intensity of I	Relative intensity of II
Au(111)	200.2		100%	0%
Ag(111)	200.3	197.7	77.7%	22.3%
Cu(111)	199.8	198.1	41.4%	58.6%

The high binding energy component (I) can be attributed in the three cases to the covalent Cl-C bond of the Chlorine at the molecule.[29–31] The lower binding energy contribution (II) on the other hand is most likely related to dissociated Cl adatoms bonded to the metallic surface.[29,30,32–34] That would mean that Cl atoms undergo partial dissociation, with the ratio increasing gradually with the reactivity of the substrate, from 0% in Au, to 22.3% in Ag, and to 58.6% in Cu.

Surface-induced dehalogenation of organic molecules has been widely observed in the synthesis of graphene nanoribbons via Ullman polymerization of PAHs, Br, I and Cl showing a similar reactivity trend.[35–37] Brominated precursors such as di-bromo-bi-anthracene, for instance, undergo full dehalogenation between 200-300ºC on Au(111), 150-175ºC on Ag(111), and at -30ºC on Cu(111).[38,39] In the case of chloro-substituted perylene-3,4,9,10-tetracarboxylic acid bisimides (PBIs) polymeric chains have been also created on gold at around 200ºC.[40] Other organic molecules as the CF_3CCl_3 on Pg(1111) dehalogenates at -110ºC.[30] In some cases the resulting C radicals are passivated by bonding to surface metal atoms but, in particular in Au and Ag, polymers are easily formed either by direct intermolecular C-C bonds or mediated by metal adatom coordination. These results are in perfect agreement with the increasing dehalogenation scenario proposed for TTM-O with the increasing reactivity of the surface (i.e. Au - Ag - Cu).

Previously, similar Cl 2p core level shifts where attributed to the interaction with the underying metal in a "flat" adsorption configuration of the molecule.[41,42] However, the many experiments done with halogenated PAH in the past years indicate that the interaction with the metal does not lead to any sizeable shift of the halogen 2p peaks.[38,43,44] When brominated molecules are deposited intact in a noble metal, the energy position of the 2p Br-C contribution is very similar to that in the gas-phase (variations below 0.2 eV).[45] Thus we temptatively revisit these results within the scenario of dehalogenation, which are further supported by the observation of adatom mediated formation of linear chains of tri-para-carboxylic polychlorotriphenylmethyl radical (PTMTC) on Cu modified gold surface and no chains formation on clean gold surface.[46,47]

A final origin of the shifted component could be the presence of ionic Cl, with very similar energies as the Cl-metal component[48], however it is difficult to find an origin for such ionization of Cl. We can exclude the formation of the radical as a source of charge accumulation in Cl, since the Cl 2p level of the PTMTC radical on Au is at the neutral Cl-C position, consistent with the negligible localization of the radical electron at Cl atoms in this molecule.[41] As derived from the negligible peak shifts described

above, the interaction with the metal is not also expected to lead to sizeable charge transfer to a C-bonded halogen.

In conclusion, we believe the most plausible scenario for observed trends in the Cl 2p core level analysis is that of dehalogenation.

C 1s

The C 1s spectrum of Au(111) (Fig.2b) can be decomposed into four constituents corresponding to C-C, C-H, C-Cl and C-O and centred at 284.6, 285.2, 286.0 and 286.7 eV.[31,49,50] The large number of peaks and their energetic proximity makes the fitting with all free parameters unreliable, therefore we reduced the degrees of freedom of the fit by assuming the pristine molecular stoichiometry (C-C:C-H:C-Cl:C-O=19:8:6:1) to fix the relative peak intensities in the fit of the peak obtaining a good fit.

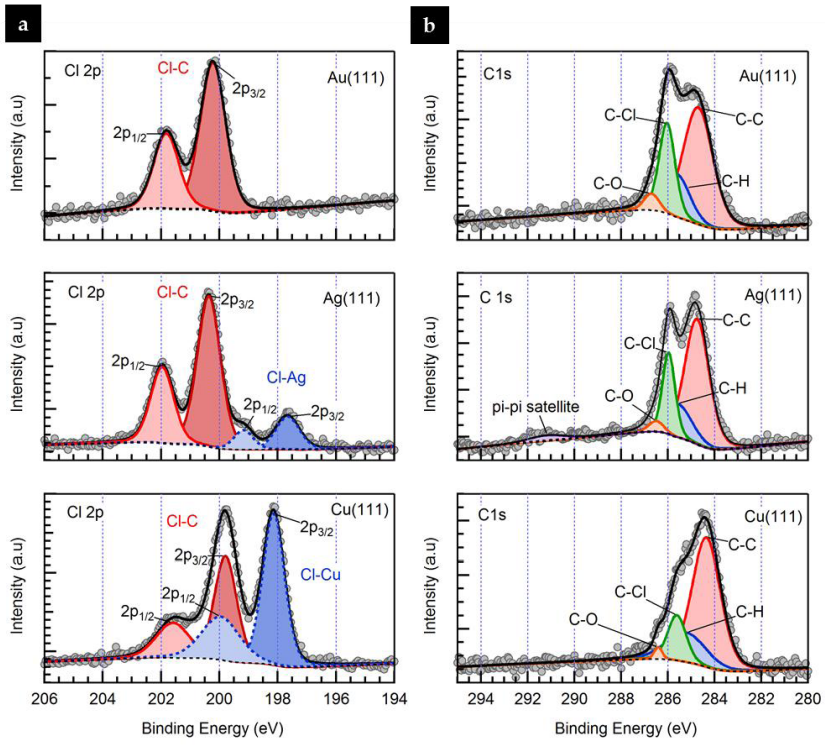

Fig. 2. Adsorption of TTM derivative molecules on (111) surfaces of Au, Ag and Cu. Cl2p (a) and C1s (b) core level spectra and their decomposed components. Raw data is displayed by grey dots and the fitting results and subcomponents by solid lines.

A rough inspection of the C 1s spectrum for Ag and Cu evidences a gradual decrease of the C-Cl component in line with the gradual reduction of the Cl-C contribution found in the Cl 2p spectra. For the Ag and Cu spectra, the C1s peak was decomposed into four components, but here the stoichiometry was corrected assuming the dissociation scenario, where the relative loss of Cl on the molecule obtained from the Cl 2p spectra is represented by a corresponding shift of intensity from the C-Cl to the C-C contribution. In Fig. 2b it is possible to observe how the fit precisely match with the experimental data under these constraints. The increase in the C-C contribution suggests that polymerization takes place between the dehalogenated molecules.

The analysis of the C 1s spectra is therefore in agreement with the scenario where the adsorbed molecules remain intact on Au and undergo partial dissociation with increasing intensity on Ag and Cu.

O 1s

Inspection of the O1*s* core-level region shows the presence of oxygen in all three cases (Fig. 3). Molecules in all three surfaces exhibit a peak at the 530-531 eV range, characteristic of the carbonyl C=O bond.[51] The preservation of the double C=O bond indicates that these molecules are not chemically attached to the metal via the Oxygen. Whereas this is the only O 1s contribution in Au and Cu, the Ag spectrum shows an additional, more intense peak at 533 eV. This contribution could be related to the Ag-O covalent bond formation predicted by DFT calculations in the "vertical" adsorption configuration. The Ag-O-C to C=O ratio of 68/32 is comparable but slightly higher than the uncleaved Cl-C/Cl-Ag ratio of 77.7/22.3, which can be explained by assuming that only some of the Cl in the "flat" configuration dissociate, whereas the "vertical" molecules remain essentially intact. Within this assumption we obtain the number of 5 dissociated Cl per "flat" molecule, which is in close coincidence with the 4 Cl atoms that are in contact in the "flat" adsorption configuration obtained by DFT. We note that, if we consider that all molecules are in the "flat" adsorption configuration, we obtain the same amount of 4-5 dissociated Cl per molecule.

Alternatively, the peak at 533 eV could be assigned to C-O-C bonds,[51] which could be a signature of polymerization via intermolecular C-O cross coupling. This, together with the results on C 1s, where the C-Cl component was replaced by an increase in the C-C component, would suggest that polymerization in Ag involves both C-C and C-O cross coupling, whereas on Cu only C-C coupling takes place. We note that we do not detect any C-O component in the C 1s spectra, though its contribution could be below the sensitivity of our fit.

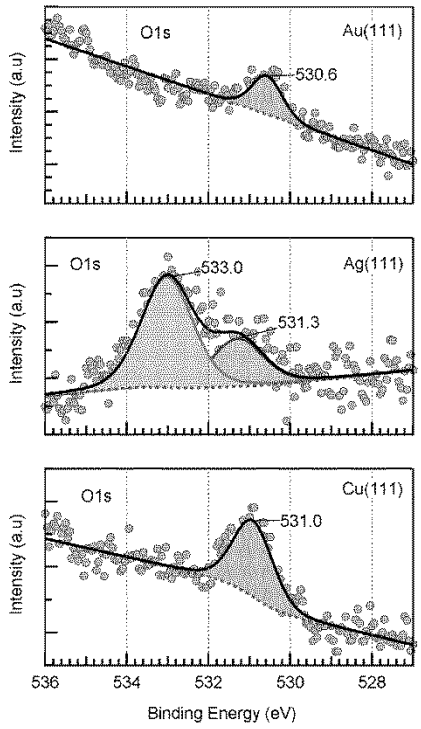

Fig. 3. O1s core level spectra for (111) surfaces of Au, Ag and Cu with one deposited monoloyer coverage.

The fact that DFT calculations predict radical formation only for the "vertical" configuration (see below), together with the presence of a molecular orbital that can be attributed to the SOMO in the ARUPS spectra (see below), points towards the first scenario, where the 533 eV peak is related to the Ag-O bond formation. That would mean that TTM adsorbs in a "vertical" configuration only in Ag(111).

ARUPS results

Fig. 4 shows the ARUPS spectra (angle-resolved ultraviolet photoemission spectroscopy) of the clean and one monolayer covered metal surfaces. Close to the Fermi energy (EF), the Shockley-type surface states (SS) with parabolic dispersion are clearly visible in the three cases (Figs 4 a-c, g-i). Due to their strong localization at the surface, Shockley states represent a sensitive probe for surface modifications, adsorption processes, and interactions between adsorbate and substrate.[52] The surface state parabola in clean Au(111) (Fig. 4a,g), has the band bottom at ~0.4 eV below the EF. The state remains at the same energy within the experimental resolution after the

deposition of 1ML of TTM (the intensity loss is due to the attenuation of the molecular layer). In clean Ag(111), the parabolic dispersion of the surface state is hardly discernible due to its proximity to the Fermi level (the band bottom is at less than 0.1eV below the EF) (Fig. 4b,h). Similarly to the case of Au, no appreciable shift is observed upon deposition of the molecular layer. In contrast, the surface state in Cu(111) vanishes when molecules are deposited (Fig. 4c,i) evidencing a strong interaction of the TTM-O with the Cu surface. These results indicate that molecules are physisorbed on Au and Ag (or weakly chemisorbed in Ag, considering there is a Ag-O bond), and strongly chemisorbed on Cu, in line with the gradual increase of reactivity for dehalogenation found by XPS.

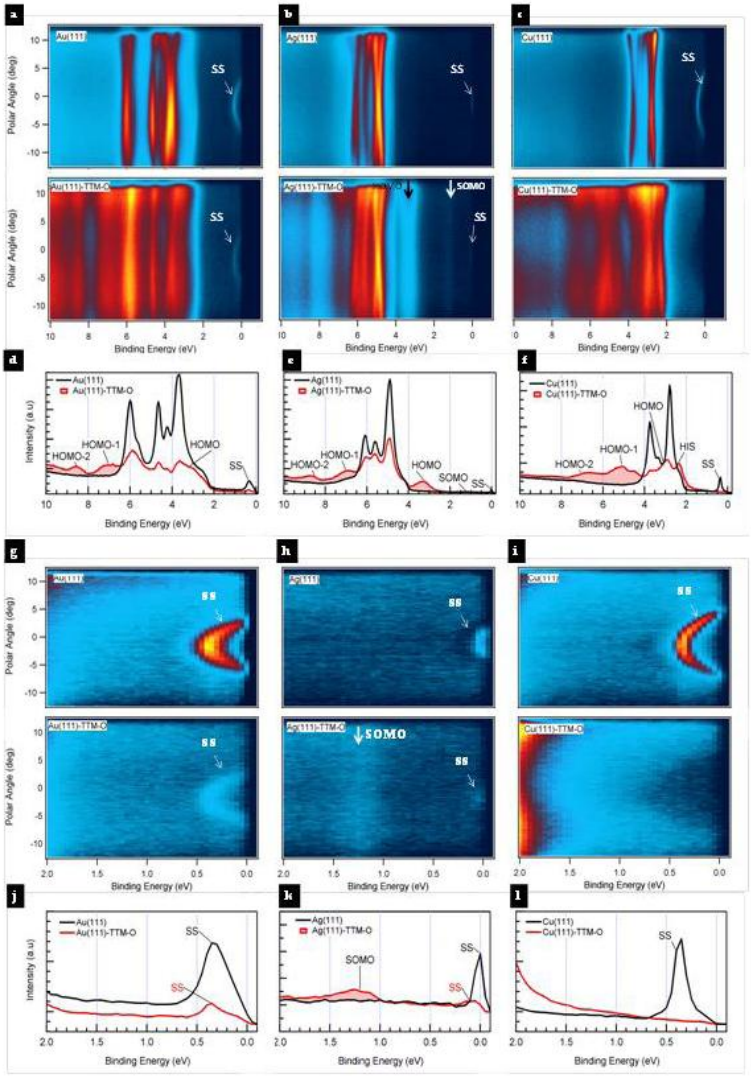

Fig. 4. ARUPS on clean Au, Ag and Cu surfaces (a, b and c top panels, respectively) and with one monolayer of TTM-O molecules (a, b and c bottom panels, respectively). (d)-(f) Integrated profiles along the spectra. (g)-(l) are short energy range zooms of (a)-(f).

The states related to occupied molecular orbitals also appear as non-dispersing features in the spectra (Figs 4d-f). On the unperturbed molecules on Au, the lowest binding energy molecular feature appears at ~3.1 eV, overlapping with Au 3d bands, which we label as HOMO. The HOMO-1 and HOMO-2 appear at 7.0 and 8.5 eV respectively. In the Ag(111) spectra none of these features overlap with the metallic 3d band, and thus they can be clearly identified at the energies of 3.3, 7.0 and 8.7 eV. More interestingly, we can also identify a new peak at around 1.2 eV, the same energy regime where the SOMO has been found for PTMTC radicals on Au and Ag[41] and TTM-S on Ag.[42] This can be best appreciated in the zoomed colour plot of Fig.4h and the integrated spectrum of Fig.4k. Finally, the molecular features in the Cu spectrum appear at quite different energies as compared to Au and Ag. The lowest binding energy peak is at ~2.3 eV, close to the 3d band onset. We believe this is related to hybrid interface states that arise in chemisorbed systems rather than an unperturbed molecular SOMO that appears shifted in energy with respect to that found in Ag. Yet, the presence of a SOMO cannot be discarded, since similar energy shifts of ~0.5 eV have also been found in the filling of PTCDA orbitals in Ag(111) and Cu(111).[53] However, the partially dehalogenated "flat" configuration derived from XPS analysis is not very likely to lead to radical formation. In this sample we

were able to study the spectra as a function of subsequent depositions up to the multilayer regime. A series of spectra are shown in Fig. 5, where we can see how a hybrid-interface state (HIS) arising from the interaction with the substrate evolves into the intrinsic molecular orbitals that appear at the same energies as for Au and Ag.

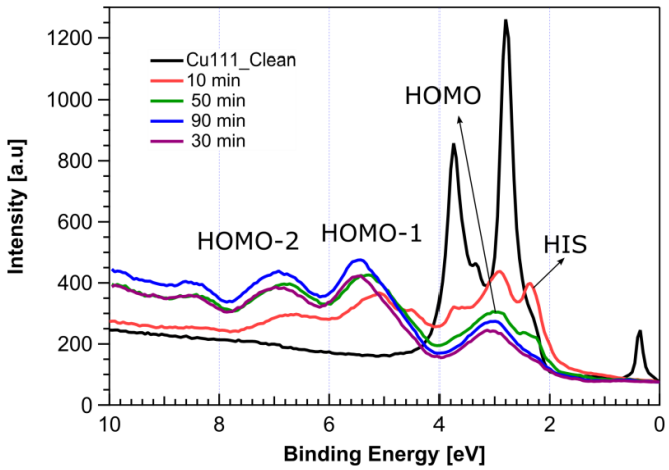

Fig. 5. ARUPS spectra of TTM-O on Cu(111) for increasing deposition times. The hybrid interface state (HIS) appearing at submonolayer deposition (red curve) disappears in multilayers where a shift of molecular HOMO, HOMO-1, and HOMO-2 towards the energies found for Au and Ag

In conclusion, the evolution of the surface states in the ARUPS data provides complementary evidence of the gradually increasing interaction in Au-Ag-Cu. In Au and Ag molecules are physisorbed and hence molecular orbitals are not expected to be significantly distorted. In contrast, the quenching of the surface state in Cu indicates strong chemisorption and hence interfacial hybridization.

Consistently, the molecular layer on Au does not show any signature of radical formation, whereas the presence of a new state on Ag(111) at the same energy of parent radicals is a clear indication of radical formation in this surface. The scenario in Cu(111) is not so clear, although XPS data suggest a configuration that hardly leads to the radical formation.

The main conclusion that we derive from the combined XPS/ARUPS analysis is that: i) in Au(111) the TTM molecules adsorb intact, without forming any O-metal bond and remain neutral; ii) in Ag(111) ~70% of the molecules bond to the surface via O-Ag bonds, with halogens intact, thus a "vertical" configuration is expected. Clear radical related signatures are found, which we assign to this "vertical", O-bonded molecules; iii) in Cu(111) all molecules adsorb "flat" and lose approximately five chlorine atoms. Radical formation cannot be discarded from the ARUPS, but the adsorption configuration points more towards the formation of strongly hybridized interfacial states.

DFT modelling of the TTM-O/metal systems

To gain some fundamental insight about the electronics of the TTM-O SAM on the different studied substrates we carried out first principles periodic DFT based calculations, as described in the Methodology section (see above). First we optimized separately the TTM-O molecule confirming its closed-shell nature by the lack of spin density. We also optimized 3-atom thick metal slabs of 6x6 atom lateral size from the corresponding bulk structures. Next, the optimized TTM-O molecule was placed on top of each slab in two conformations: horizontal and vertical with respect to the surface, respectively. The three hybrid TTM-O/metal systems were optimized (also optimizing *a* and *b* cell parameters while maintaining a constant vacuum level through the *c* parameter), for both studied conformations in each case. The resulting structures are shown in Fig. 6, where binding energies for each case are shown, as

well as magnetic moments on the central radical carbon atom in the adsorbed molecules, indicative of radical formation.

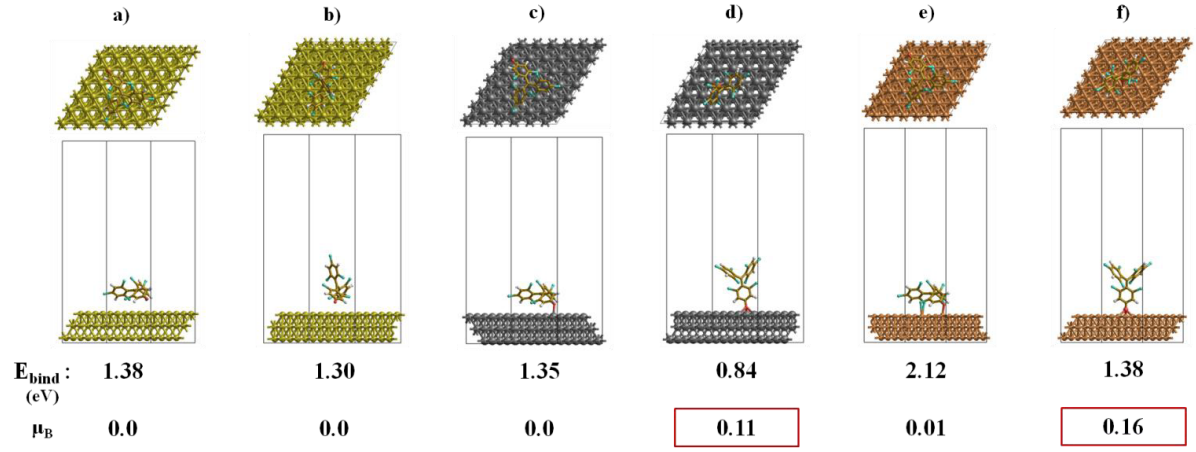

Fig. 6. Optimized periodic structures of the TTM-O molecule adsorbed on Au (a-b), Ag (c-d) and Cu (e-f) surfaces. Both horizontal and vertical conformations are shown in a,c,e and b,d,f, respectively, with the corresponding binding energies and magnetization values (in Bohr magnetons) below each periodic cell.

As it may be seen in Fig. 6, the TTM-O molecule exhibits large enough interaction energy to claim that it adsorbs on each metallic substrate in both horizontal and vertical conformations with respect to the substrate's plane. Moreover we found that the chemisorbed conformations that lead to a spin-polarized solution for the SAM (see red squared μ_B values in Fig. 6) are not as stable as the corresponding flat physisorbed conformations (6a, 6c and 6e), which may explain why the detected SOMO for the Ag case presents such a low intensity in the ARUPS measurements (see Fig. 4). Taking a look at the spin population generated in the molecule upon adsorption, we confirm that only for the vertically oriented TTM-O on Ag and Cu there is the appearance of an important spin polarization. In such a conformation, the docking oxo- group is pointing towards the surface with the oxygen atom close to the surface (1.32 and 1.51A for Cu and Ag, respectively, as compared to the 2.50A in Au), in full agreement with the bonding mechanism predicted by Rissner et.al.[21] which should give rise to the appearance of the spin-polarized unpaired electron.

For comparison with the UPS data we extracted the density of states (DOS) from our calculations. For the model in Fig. 6d (vertically oriented TTM-O on Ag) a single covalent bonding between the Ag(111) and the TTM molecule occurred giving rise to a singly occupied molecular orbital (SOMO) localised on the central carbon atom of the TTM molecule (radical αC in PTMs[54]). Note that a similar result was found for analogous calculations on Cu(111) but not for Au(111), qualitatively in line with the UPS data. In Fig. 7 representative TTM-O/metal projected DOS plots are shown (7b) from corresponding calculations as compared to UPS data for the Ag case, where the appearance of the peak associated to the SOMO may be seen (7a).

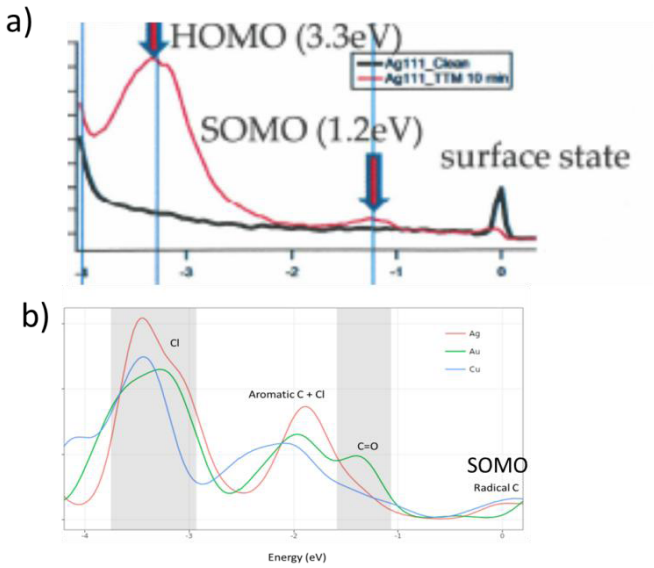

Fig. 7. a) Experimental UPS data of the TTM molecule when deposited on Ag(111). b) Representative TTM-projected DOS from DFT calculations of the TTM molecule on the three considered surfaces. Labels indicate the molecular origin of the peaks in the calculations. The "Radical C" peaks for Ag and Cu are due to a SOMO state. The grey areas show the experimental energies tentatively assigned to the HOMO (peak centred at ~-3.3 eV) and SOMO (peak centred at ~-1.2 eV) from UPS data.

The distinguishing feature of the UPS data for the TTM-Ag(111) system is the presence of a small peak around -1.2 eV – which is attributed to the covalent-bonding-induced SOMO. This feature is not observed in the TTM-Au(111) UPS data and its presence is unclear in the TTM-Cu(111) case (see Fig. 4). The calculated DOS shows that in all three TTM-metal combinations there is a peak at or in the vicinity of -1.2 eV. However, it is the TTM-Au(111) system (not the TTM-Ag(111) system) that has the most pronounced DFT-DOS magnitude at this energy, contrary to experiment. This feature for TTM-Au(111) is due to the C=O bond which has not reacted with the Au(111) surface (i.e. it is not a SOMO). In the cases of Ag(111) and Cu(111) where a reaction occurs with the TTM molecule (as demonstrated with the appearance of spin density for up-right vertical conformations, see Fig. 6) the SOMO appears close to 0 eV and the peak at ~-1.8-2.0 eV is due to the aromatic C-Cl system of the TTM-O molecule. For even lower energies the DFT-DOS of all three TTM-surface systems is very similar not indicating any distinguishing features for the Ag(111) system. Thus, although the DFT and UPS spectra look apparently very similar, the chemical/physical basis of their comparable features would be very different.

Level alignment at molecule-metal interfaces:

Based on the above there would appear to be little direct correspondence between the DFT-DOS and the experimental UPS data. The best qualitative link between the two is that both show the presence of a (SOMO) peak for the TTM-Ag(111) system and its absence in the TTM-Au(111) one. However, the SOMO peak in the calculated DOS is very close to the Fermi level where it overlaps with the surface state of the metal (taken to be 0 eV), whereas in experiment the peak assigned to the SOMO is at -1.2 eV. In previous work (see ref [41]) on PTM radicals (perchorotriarylmethyl radicals) on Ag(111) and Au(111) a similar qualitative comparison between calculated DOS and experimental spectroscopic data was used to support the persistence of a SOMO state in Au(111)-physisorbed PTM molecules (see Fig 3).

From detailed theoretical studies of molecule-metal interfaces it is clear that DFT has serious deficiencies in treating such systems quantitatively. Nevertheless, once the causes of the deficiencies in the DFT calculations are identified, it is possible to correct for them with varying degrees of accuracy in order to

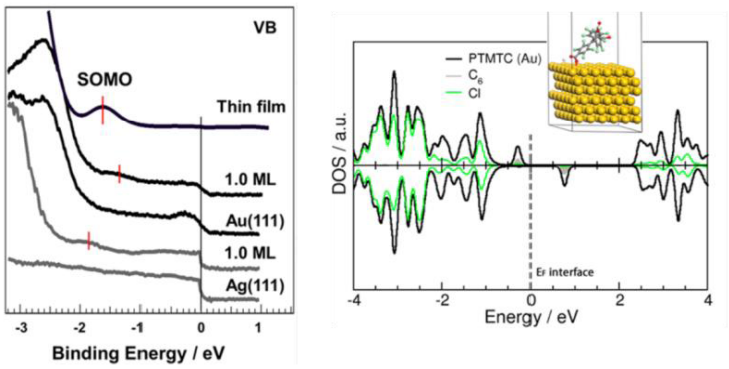

Fig. 3. Left: Experimental data indicating a SOMO of a radical molecule physisorbed on Au(111) with a energy of between -1.4 eV and -1.6 eV. Right: Periodic DFT calculated DOS using a GGA functional with a SOMO at approximately -0.3 eV (from ref. 41).

improve the interpretation of bare periodic DFT results. The main problems that affect periodic DFT calculations of molecule-metal interfaces are:

1. *Deficiencies of the functional (typically of GGA type as in our calculations) in recovering the electronic structure of the adsorbed molecule.* GGA functionals are typically good at describing the electronic structure of bulk metals. In particular the work function of Au(111), Ag(111) and Cu(111) – which is a measure of the shift of the highest energy DOS peaks with the vacuum - is predicted with typical upper error bounds of ±0.15 eV. Specifically, for Ag(111) PBE calculations give a work function of 4.49 eV which compares with 4.53 ± 0.07 eV from experiment indicating an error of approximately ±0.1 eV.[55] Conversely, the orbital energies provided by GGA-DFT calculations for organic molecules are generally not a good direct measure of their true electronic structure (i.e. one should be careful comparing molecular orbital energies with UPS peaks). We have estimated the error of our periodic GGA-DFT calculations with respect to the molecule by performing hybrid-functional (PBE0[56,57]) DFT to calculate the ionisation potential (IP) of the isolated TTM molecule attached to a single Ag atom. For molecules PBE0 is known to be very accurate with respect to experiment (i.e. mean absolute error of 0.15 eV[56]). Comparing the calculated energy of the SOMO of the isolated Ag-terminated molecule (i.e. TTM-O bonded to a single Ag atom through the oxo- group) using PBE to the IP calculated using PBE0 and a total energy difference approach, gives us an error estimate of +1.75 eV (i.e. the orbital energy of the isolated molecular SOMO is approximately 1.75 eV too high). Note: Computationally expensive periodic DFT calculations using screened hybrid functionals (e.g. HSE) generally do not significantly help to reduce the GGA error. Our HSE calculations on test systems lead to a relative down-shift of the SOMO of approx. 0.25 eV.

2. *Deficiencies of DFT in recovering screening due to the metal support.* Going beyond the framework of one electron picture of electronic structure, dynamical polarization effects renormalize molecular states resulting in a reduction in the gap between the molecule's occupied and unoccupied molecular orbitals.[58] This effect is not captured by DFT in general, regardless of the type of functional used. The extent of this effect is dependent on the degree of coupling between the metal and the molecule and the nature of the metal and molecule in question. Computationally expensive Green's function based many body calculations on organic molecules physisorbed on metal surfaces which go beyond the one electron picture have shown that this effect is of the order 1 eV (see ref. [58]). Less reliable but much simpler semi-classical screening corrections has also been used in order to provide an estimate of this effect for a similar class of systems also giving a typical effect of ~1.5 eV (see ref. [59]). It has also been theoretically predicted that this HOMO-LUMO gap narrowing could be enhanced in some chemisorbed molecule-metal systems (see Fig. 4 and ref. [60]). We note that this correction is of the opposite sign to that

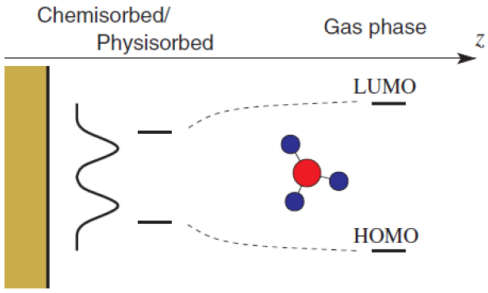

Fig. 4. Schematic illustration of metal-induced renormalisation of frontier orbital energies (from ref 59).

in point 1 and is of a similar order of magnitude. This cancellation of errors can sometimes lead to bare PBE-DFT calculations being in very good "agreement" with UPS data. In our case the large correction needed in point 1 is unlikely to be totally cancelled by this renormalisation correction.

A rough estimate of the magnitude of the effect in our case can be obtained by using the semi-classical image-charge correction ($1/4(d-z_0)$), where d is the surface-molecule separation and z_0 is the DFT-corrected image-charge plane displacement (see ref. [59] for details). Taking d in our case to be the distance between the surface and the SUMO-carrying tri-bonded C atom and z_0 to be 0.9 Å (value used for Au(111) in ref [59]) we get a rough estimate of 0.55 eV for the destabilisation of the SOMO. We note that the main reason for the relatively small magnitude of this correction is the relatively large value of d in our case (approx. 7 Å) as compared to approximately half this distance for most physisorbed molecules.[59]

3. *Change in orbital energies due to charge transfer with the surface through reactive chemisorption.* In our system, we have a covalent bond formation (i.e. formed with one electron from the molecule and one electron from the surface) rather than a charge transfer from or to the surface (i.e. one electron from the surface jumping to the molecule, or vice versa). This is confirmed by comparing the spin distribution pattern obtained for the TTM-O/Ag-surface system (calculated with the PBE functional) with the TTM-O-Ag-atom non-periodic system calculated with PBE and PBE0 functionals (see comparison in point 1). Due to the fact the same spin distribution is obtained by both systems and even similar spin populations are obtained in the PBE calculations, we may conclude that indeed a classical covalent bond is formed between the molecule and the surface, being the only cause for the formation of the SOMO. In such situation charge transfer phenomena is not likely to take place, as already demonstrated with previous PTM SAMs where the monolayer maintains its electronic structure intact.[61–64]

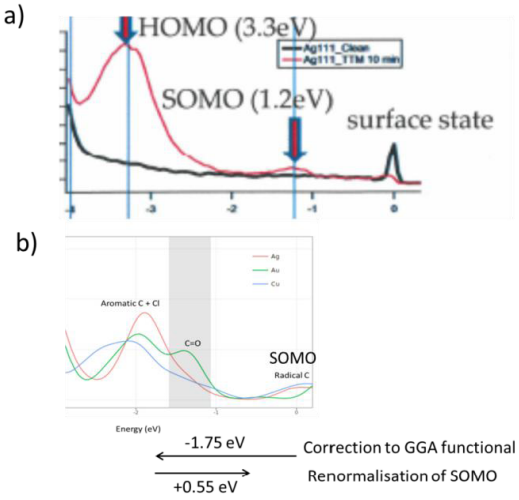

Fig. 5 Comparison between: a) experimental UPS data, and b) corrected DFT data for the TTM-O/Ag system.

Applying these corrections to shift the DFT-DOS we arrive at an improved match with the experimental UPS data (compare red lines in Fig. 5a-b). Although the match is undoubtedly fortuitously good considering the approximations and known errors involved, the magnitude of the two most important corrections (those of points 1 and 2 above) is likely to be reasonable and can help explain how the UPS data and the DFT calculations can be compared and thus provide a consistent interpretation.

Concluding our computational assessment, the apparent good match between the DFT-derived DOS with the UPS data leads to two differing interpretations of the peaks.

DFT-DOS peaks of molecules on metals are susceptible to two main errors (see points 1 and 2 above) which act to shift the DOS up and down respectively. These errors are of a similar magnitude and cancel to varying degrees depending on the system. In the important case of TTM-Ag(111) we have made a good estimate of the first error (points 1 and 3) and a reasonable estimate of the second one (point 2) leading us to a correction which would shift the DFT-DOS down in energy by approximately 1.2 eV. Although this derived value is subject to some error due to the approximations made in its derivation, we feel that its magnitude is likely to be solid. With this correction match between the SOMO peaks and the HOMO peaks in both the experimental UPS and the DFT calculations is significantly improved.

Conclusions

In conclusion, in this work we have experimentally realized the theoretical prediction by Rissner et.al. where it was predicted that it should be possible to form radical SAMs by using closed-shell quinoidal monomers through a covalent bonding mechanism with metallic surfaces. As explained in the introduction of this work, it is important to pick up molecular candidates where, upon radical formation, the resulting unpaired electron will be persistent. Hence we chose TTM molecules where the resulting unpaired electron is protected by six ortho chlorine atoms of the three aryl rings bonded to the radical centre, as it happens in the PTM family of organic radicals. However, as shown above, not all TTM quinoidal derivatives are stable, due to the important steric hindrance acting on the double-bonding pattern due to chlorine atoms in ortho-positions of aryl rings, which impose an important twisting of such rings. Because of this, we could only use TTM-O, which was persistent enough to be isolated. Our on-surface experimental results show that not all metallic substrates are good candidates to form the radical SAM. As shown by XPS and ARUPS measurements, in Au the TTM-O molecules are simply physisorbed and do not form a bond with the surface and in Ag and Cu there is chemical bond formation. In the latter two cases on-surface measurements detect different degrees of de-chlorination, as previously reported.[35–37] While on Cu the reaction of TTM-O seems to be very important, even leading to dehalogenated TTM-O oligomers of uncertain structure, for Ag such process seems to be less severe. More importantly, in Ag a peak in ARUPS at -1.2 eV is detected and may be assigned to a singly occupied molecular orbital associated to the appearance of an unpaired electron on the organic units. By means of accurate DFT calculations, the radical character of the SAM is confirmed, by the appearance of spin density on our periodic calculations. Correspondingly, a SOMO appears in the DOS of such systems. Despite the fact such electronic peaks do not appear at the measured position by the experimental ARUPS characterization, after applying some well established corrections associated to the used theoretical model (GGA and DFT) we obtain a corrected position of the SOMO, quite surprisingly, at -1.2 eV with respect to the metallic surface states, nicely coinciding with the experimental measurements. Despite the fact the predicted corrected SOMO energy bears a certain associated error, the applied corrections are sensible, and hence the approximated position of such molecular orbital should be trustable. Hence, based on the agreement of our theoretical DFT calculations and the on-surface measurements we may safely conclude that our TTM-O derivative adsorbed on Ag generates a radical SAM, becoming the first example on the use of close-shell molecules to form an open-shell SAM, as previously theoretically predicted.

Bibliography

1 F. P. Netzer and M. G. Ramsey, *Crit. Rev. Solid State*, 1992, **17**, 397–475.

2 H. Ishii, K. Sugiyama, E. Ito and K. Seki, *Adv. Mater.*, 1999, **11**, 605–625.

3 S. Braun, W. R. Salaneck and M. Fahlman, *Adv. Mater.*, 2009, **21**, 1450–1472.

4 M. Franke, F. Marchini, H. P. Steinrück, O. Lytken and F. J. Williams, *J. Phys. Chem. Lett.*, 2015, **6**, 4845–4849.

5 C. Joachim, J. K. Gimzewski and A. Aviram, *Nature*, 2000, **408**, 541–548.

6 M. Halik and A. Hirsch, *Adv. Mater.*, 2011, **23**, 2689–2695.

7 G. Heimel, L. Romaner, E. Zojer and J. L. Bredas, *Acc. Chem. Res.*, 2008, **41**, 721–729.

8 A. Nitzan and M. A. Ratner, *Science (80-.).*, 2003, **300**, 1384–1389.

9 L. Basabe-Desmonts, J. Beld, R. S. Zimmerman, J. Hernando, P. Mela, M. F. G. Parajó, N. F. van Hulst, A. van den Berg, D. N. Reinhoudt and M. Crego-Calama, *J. Am. Chem. Soc.*, 2004, **126**, 7293–7299.

10 G. De Ruiter, T. Gupta and M. E. van der Boom, *J. Am. Chem. Soc.*, 2008, **130**, 2744–2745.

11 B. A. Bejjani and L. G. Shaffer, *J. Mol. Diagn.*, 2006, **8**, 528–533.

12 J. Lamartine, *Mater. Sci., Eng. C*, 2006, **26**, 354–359.

13 M. J. Heller, *Annu. Rev. Biomed. Eng.*, 2002, **4**, 129–53.

14 T. M. Herne and M. J. Tarlov, *J. Am. Chem. Soc.*, 1997, **119**, 8916– 8920.

15 J. C. Love, L. A. Estroff, J. K. Kriebel, R. G. Nuzzo and G. M. Whitesides, *Chem. Rev.*, 2005, **105**, 1103–1170.

16 A. Ulman, *Chem. Rev.*, 1996, **96**, 1533–1554.

17 F. Chen, J. Hihath, Z. Huang, X. Li and N. J. Tao, *Annu. Rev. Phys. Chem.*, 2007, **58**, 535–564.

18 M. Mas-Torrent, N. Crivillers, C. Rovira and J. Veciana, *Chem. Rev.*, 2012, **112**, 2506–2527.

19 M. Mas-Torrent, N. Crivillers, V. Mugnaini, I. Ratera, C. Rovira and J. Veciana, *J. Mater. Chem.*, 2009, **19**, 1691–1695.

20 N. Crivillers, M. Mas-Torrent, C. Rovira and J. Veciana, *J. Mater. Chem.*, 2012, **22**, 13883–13890.

21 F. Rissner, Z. Ma, O. T. Hofmann, C. Slugovc, Z. Shuai and E. Zojer, *J. Mater. Chem.*, 2012, **22**, 4269.

22 J. Guasch, X. Fontrodona, I. Ratera, C. Rovira and J. Veciana, *Acta Crystallogr.*, 2013, **C69**, 255–7.

23 M. Ballester and J. Riera-Figueras, *J. Am. Chem. Soc.*, 1971, **4254**, 2215–2225.

24 J. P. Perdew, K. Burke and M. Ernzerhof, *Phys. Rev. Lett.*, 1996, **77**, 3865–3868.

25 I. Y. Zhang, X. Ren, P. Rinke, V. Blum and M. Scheffler, *New J. Phys.*, 2013, **15**, 123033.

26 V. Havu, V. Blum, P. Havu and M. Scheffler, *J. Comput. Phys.*, 2009, **228**, 8367–8379.

27 V. Blum, R. Gehrke, F. Hanke, P. Havu, V. Havu, X. Ren, K. Reuter and M. Scheffler, *Comp. Phys. Comm.*, 2009, **180**, 2175–2196.

28 G. Kresse and J. Furthmüller, *Comput. Mater. Sci.*, 1996, **6**, 15–50.

29 X. Zhang, *Adv. Funct. Mater.*, 2015, **25**, 4163–4169.

30 B. Immaraporn, P. Ye and A. J. Gellman, *J. Catal.*, 2004, **223**, 98–105.

31 Y. Z. Tan, *Nat. Commun.*, 2013, **4**, 1–7.

32 W. Sesselmann and T. J. Chuang, *Surf. Sci.*, 1986, **176**, 32–66.

33 H. Piao, K. Adib and M. A. Barteau, *Surf. Sci.*, 2004, **557**, 13–20.

34 I. Pelech, *J. Nanomater.*, 2013, **2013**, 9.

35 L. Grill, *Nat. Nanotechnol.*, 2007, **2**, 687–691.

36 J. Cai, *Nature*, 2010, **466**, 470–3.

37 P. H. Jacobse, A. van den Hoogenband, M. E. Moret, R. J. M. Klein Gebbink and I. Swart, *Angew. Chemie - Int. Ed.*, 2016, **55**, 13052–13055.

38 K. Simonov, *ACS Nano*, 2015, **9**, 8997–9011.

39 C. Moreno, *to_be_published.*

40 H. Zhang, *Small*, 2014, **10**, 1361–1368.

41 V. Mugnaini, A. Calzolari, R. Ovsyannikov, A. Vollmer, M. Gonidec, I. Alcon, J. Veciana and M. Pedio, *J. Phys. Chem. Lett.*, 2015, **6**, 2101–2106.

42 M. R. Ajayakumar, I. Alcón, S. T. Bromley, J. Veciana, C. Rovira and M. Mas-Torrent, *RSC Adv.*, 2017, **7**, 20076–20083.

43 K. A. Simonov, *J. Phys. Chem. C*, 2014, **118**, 12532–12540.

44 D. G. De Oteyza, *ACS Nano*, 2016, **10**, 9000–9008.

45 R. P. Vasquez, *Surf. Sci. Spectra*, 1998, **5**, 262–266.

46 F. Grillo, H. Früchtl, S. M. Francis, V. Mugnaini, M. Oliveros, J. Veciana and N. V. Richardson, *Nanoscale*, 2012, **4**, 6718.

47 F. Grillo, V. Mugnaini, M. Oliveros, S. M. Francis, D. J. Choi, M. V. Rastei, L. Limot, C. Cepek, M. Pedio, S. T. Bromley, N. V. Richardson, J. P. Bucher and J. Veciana, *J. Phys. Chem. Lett.*, 2012, **3**, 1559–1564.

48 C. D. Wanger, W. M. Riggs, L. E. Davis, J. F. Moulder and G. E. Muilenberg, *Handbook of X-ray Photoelectron Spectroscopy*, Muilenberg Perkin-Elmer Corp., Eden Prairie, Minnesota, USA, Physical E., 1981.

49 H. L. Poh, P. Šimek, Z. Sofer and M. Pumera, *Chem. - A Eur. J.*, 2013, **19**, 2655–2662.

50 S. A. Savu, *RSC Adv.*, 2012, **2**, 5112–5118.

51 D. R. T. Zahn, G. N. Gavrila and G. Salvan, *Chem. Rev.*, 2007, **107**, 1161–1232.

52 F. Forster, A. Bendounan, J. Ziroff and F. Reinert, *Phys. Rev. B*, 2008, **78**, 161408.

53 S. Duhm, A. Gerlach, I. Salzmann, B. Bröker, R. L. Johnson, F. Schreiber and N. Koch, *Org. Electron.*, 2008, **9**, 111–118.

54 I. Alcón and S. T. Bromley, *RSC Adv.*, 2015, **5**, 98593–98599.

55 A. Patra, J. E. Bates, J. Sun and J. P. Perdew, *Proc. Natl. Acad. Sci. U. S. A.*, 2017, **114**, E9188–E9196.

56 C. Adamo and V. Barone, *J. Chem. Phys.*, 1999, **110**, 6158.

57 R. Improta and V. Barone, *Chem. Rev.*, 2004, **104**, 1231–54.

58 J. B. Neaton, M. S. Hybertsen and S. G. Louie, *Phys. Rev. Lett.*, 2006, **97**, 216405.

59 D. A. Egger, Z.-F. Liu, J. B. Neaton and L. Kronik, *Nano Lett.*, 2015, **15**, 2448.

60 K. S. Thygesen and A. Rubio, *Phys. Rev. Lett.*, 2009, **102**, 46802.

61 N. Crivillers, M. Paradinas, M. Mas-Torrent, S. T. Bromley, C. Rovira, C. Ocal and J. Veciana, *Chem. Commun.*, 2011, **47**, 4664–6.

62 N. Crivillers, M. Mas-Torrent, J. Vidal-Gancedo, J. Veciana and C. Rovira, *J. Am. Chem. Soc.*, 2008, **130**, 5499–5506.

63 C. Simão, M. Mas-torrent, J. Veciana and C. Rovira, *Nano Lett.*, 2011, **11**, 4382–4385.

64 C. Simão, M. Mas-Torrent, N. Crivillers, V. Lloveras, J. M. Artés, P. Gorostiza, J. Veciana and C. Rovira, *Nat. Chem.*, 2011, **3**, 359–64.

Publication #2

Direct covalent grafting of an organic radical core on gold and silver

RSC Adv., 2017,**7**, 20076-20083

M. R. Ajayakumar, I. Alcón, S. T. Bromley, J. Veciana*, C. Rovira and M. Mas-Torrent*

RSC Advances

PAPER

View Article Online
View Journal | View Issue

Cite this: *RSC Adv.*, 2017, 7, 20076

Direct covalent grafting of an organic radical core on gold and silver†

M. R. Ajayakumar,[a] I. Alcón,[b] S. T. Bromley,[bc] J. Veciana,*[a] C. Rovira[a] and M. Mas-Torrent*[a]

The functionalisation of surfaces with organic radicals, such as perchlorotriphenylmethyl (PTM) radicals or tris(2,4,6-trichloro-phenyl)methyl (TTM) radicals, is appealing for the development of molecular spintronic devices. Conventionally, organic radicals are chemisorbed to metal substrates by using long alkyl or aromatic spacers resulting in a weak spin–electron coupling between the radical and the substrate. To circumvent this problem, here we have employed a new design strategy for the fabrication of radical self-assembled monolayers (r-SAMs). This newly designed radical–anchor (R–A) molecule, a TTM based radical disulfide (**1**), can be easily synthesized and it was here characterized by electron spin resonance (ESR), cyclic voltammetry (CV) and superconducting quantum interference device magnetometry (SQUID). We have succeeded in fabricating TTM based r-SAMs by using thiolate bonds (Au–S and Ag–S) where the TTM cores are only one-atom distance from the metal surface for the first time. The resultant robust **1**/Au and **1**/Ag r-SAMs were well characterized, and the electrochemical and the magnetic properties were unambiguously confirmed, proving the persistence of the molecular spin.

Received 9th February 2017
Accepted 24th March 2017

DOI: 10.1039/c7ra01686g

rsc.li/rsc-advances

Introduction

Metal and metal oxide surfaces decorated with organic functional molecules[1–4] have widespread applications in fields such as organic electronics,[5–8] sensors[9,10] and biological arrays,[11–14] among others. Specifically, in the field of molecular electronics, molecules grafted on surfaces are identified as one of the unique building blocks for device miniaturization since ultimately the active unit would consist of a single molecule. The question that arises then is if the molecules at the surface, which experience a very different environment compared to those in the bulk, preserve the same properties. It is noteworthy that the extent of the electronic coupling between the π-molecule and a metallic surface depends on the structure and electronic nature of the π-molecule and the Fermi level of the metal.[15] Importantly, the π-conjugated molecule has to be positioned close to the metal surface to establish electronic interaction although its properties can be then altered.

Amongst these materials, covalently self-assembled monolayers (SAMs)[16–19] gained tremendous interest due to their ease of fabrication process and effectiveness to integrate organic molecules on inorganic (metallic) substrates. Importantly, organic radicals based SAMs[20] (r-SAMs) have emerged as potential building units for spintronic materials, which could be applied for downscaling the memory devices.[21,22] The general strategy for achieving r-SAMs comprises the utilization of chemisorption for anchoring rationally designed functional organic radicals, *i.e.* radical–linker–anchor (R–L–A) molecules, on metal or metal oxide substrates (Scheme 1). In this regard, our group has fabricated several r-SAMs[23–26] based on perchlorotriphenylmethyl radical (PTM, Scheme 2), a highly persistent class of organic radicals, on ITO and Au. Although these r-SAMs are promising building blocks for bottom-up spintronics, the synthesis of appropriate PTM precursor is often challenging due to the complex multi-step synthetic protocols[27,28] for integrating the PTM and the linker–anchor (L–A) functionality. In addition, the alkyl or aromatic linker can drastically reduce the spin–electron coupling between the radical entity and the metallic substrate,

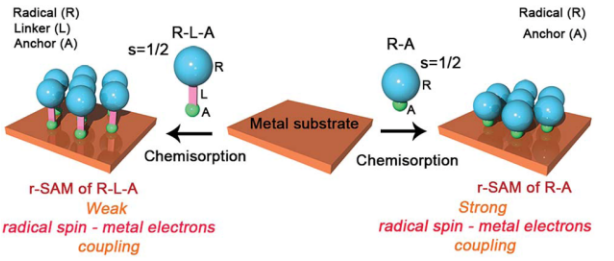

Scheme 1 Radical–linker–anchor (R–L–A) and radical–anchor (R–A) based molecules and their chemisorption processes on a metal substrate.

[a]*Institut de Ciència de Materials de Barcelona (ICMAB-CSIC), CIBER-BBN, Campus UAB, 08193 Bellaterra, Spain. E-mail: vecianaj@icmab.es; mmas@icmab.es*
[b]*Departament de Ciència de Materials i Física Química, Institut de Química Teòrica i Computacional (IQTCUB), Universitat de Barcelona, E-08028 Barcelona, Spain*
[c]*Institució Catalana de Recerca i Estudis Avançats (ICREA), E-08010 Barcelona, Spain*

† Electronic supplementary information (ESI) available. See DOI: 10.1039/c7ra01686g

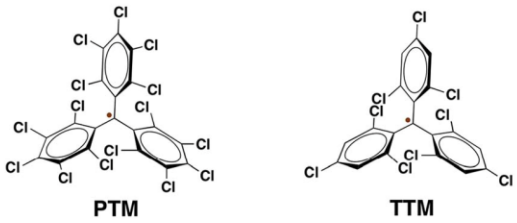

Scheme 2 Molecular structures of PTM and TTM radicals.

which is not acceptable for certain vital phenomenon such as Kondo resonance.[29–32] Moreover, the integration of long linkers can cause conformational variations that may end up in several molecular self-assembly anomalies. Therefore, the utilization of a radical–anchor (R–A) type molecule (*i.e.*, without a linker L unit) to be chemically bonded to a metal surface has fundamental importance as a model compound for the novel generation of r-SAMs (Scheme 1), even though, to the best of our knowledge, there are no examples of such kind. Additionally, the radical character persistence of a covalently grafted PTM or similar radicals at one-atom distance from the metal surface remains an open question.

Herein, we describe a simple one-pot reaction strategy for the synthesis of a novel tris(2,4,6-trichloro-phenyl)methyl (TTM,[33] Scheme 2) radical derivative (**1**), a PTM analogue, of R–A type. The diradical nature of **1** was evaluated by means of electron spin resonance (ESR), cyclic voltammetry (CV) and superconducting quantum interference device magnetometry (SQUID). The r-SAMs of **1** were generated on Au and Ag by solution based chemisorption reactions. The S atoms acted as the anchors that covalently graft the radical units to Au and Ag by forming Au–S and Ag–S bonds, respectively. The yielded robust r-SAMs were well characterized with X-ray photoelectron spectroscopy (XPS), UV photoelectron spectroscopy (UPS), CV, and ESR. Remarkably, it was clearly elucidated that the radical character of the molecules is persistent even when they are closely chemically bonded to a metal surface.

Results and discussion

Among organic radicals, the PTMs are potential candidates for the fabrication of r-SAMs due to their synthetic tailorability to attach suitable L–A functionalities.[21,23,25,34] However, for this proposed R–A chemisorption pathway, we excluded PTM derivatives due to the steric hindrance of the meta-Cl atoms upon the r-SAM formation. Hence, we have chosen TTM as an ideal scaffold for establishing this strategy. We decided to utilize Au and Ag substrates since their promising applicability due to their compatibility with the well-established lithographic techniques. In addition, Au–S and Ag–S are the most widely utilized chemical bonds for SAM generation.[35]

To pursue R–A pathway of r-SAM generation on Au and Ag, we synthesized a novel molecule **1** by replacing a Cl with S (Scheme 3). To achieve this molecule, we carried out a simple one-pot reaction employing 3,5-dichloro-4-[bis-(2,4,6-trichlorophenyl)methylen] cyclohexa-2,5-dien-1-one (**2**)[36] as precursor. Compound **2** in dry

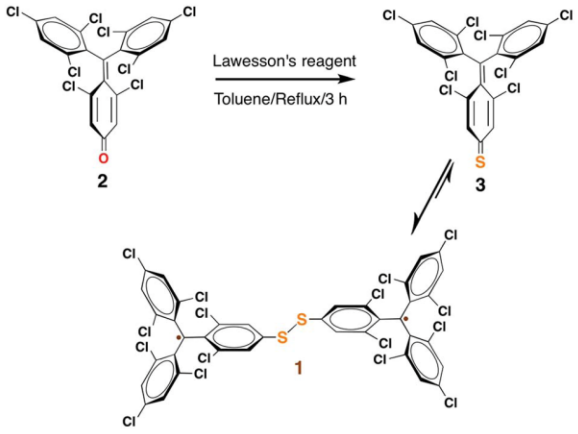

Scheme 3 One-pot reaction strategy for the synthesis of **1**.

toluene was refluxed with Lawesson's reagent for 3 h under argon and light exclusion to incorporate the S anchor to the phenyl moiety. The obtained **3** readily turned to stable diradical **1** which was isolated as a dark-brown solid by column chromatography in neutral alumina in 18% yield (see ESI†). PTM and TTM radicals are typically synthesized *via* the precursor analogue with the central carbon atom hydrogenated. On the contrary, in this reaction, we could avoid the usual, but difficult, deprotonation (using base such as tetrabutylammonium hydroxide) and oxidation (with oxidizing agents such as *p*-chloranil or $AgNO_3$) steps that are involved in the conventional PTM/TTM radical formation from the respective hydrogenated precursor. Hence reaction–purification processes were significantly simplified.

The formation of **1** was unequivocally confirmed by mass and infrared (IR) spectroscopy (Fig. S1 and S2 in the ESI†). Moreover, XPS (Fig. S3†) were employed for understanding the elemental composition of **1**. UV-vis spectra of **1** (1.3×10^{-5} M) in CH_2Cl_2 showed the characteristic PTM/TTM radical bands at 375 ($\varepsilon = 43\,700$ M^{-1} cm^{-1}), 394 (29 420 M^{-1} cm^{-1}), 540 (2020 M^{-1} cm^{-1}) and 572 (2030 M^{-1} cm^{-1}) nm, which are slightly red shifted compared to the model compound TTM (Fig. S4a†). Moreover, **1** shows very strong fluorescence and the λ_{max} (615 nm) is 49 nm bathochromically shifted compared to that of TTM radical (Fig. S4b†).

To get a detailed insight of the paramagnetic nature, the diradical **1** was examined by X-band EPR spectroscopy. The powder sample of **1** displayed EPR signal with no definite fine-structure with a *g* value of 2.0032 and a linewidth of 6.1 G at 300 K (Fig. S5†). Temperature dependent EPR measurements were conducted for **1** (5×10^{-4} M) in CH_2Cl_2/toluene (1 : 1 v/v). At 300 K, **1** showed a signal at *g* value of 2.0037 with a hyperfine splitting due to the coupling of the unpaired electron with ^1H and ^{13}C (Fig. S6†). All these spectra are consistent with that typically obtained for TTM derivatives.[23,34] On cooling to 220 K, two superimposed signals are observed. A broad band and a narrower line with well-defined hyperfine structure of 7 lines corresponding to the coupling of 6 meta-^{1}Hs together with satellite lines arising from the coupling of ^{13}Cs are found (Fig. S6†). The simulation of this latter signal give hyperfine

coupling constants values of $a_H = 1.2$ G, and $a_C = 13.2$ G and 11.0 G, which are typical values for monoradical derivatives.[37] Thus, it is assumed that the broad band comes from the diradical species **1**, but some monoradical impurity coexists in the sample. In frozen CH_2Cl_2/toluene (1 : 1 v/v) solution, the line corresponding to the monoradical impurity appears as a central broad signal, and large changes are observed in the diradical band due to strong electron–electron dipolar interactions (Fig. 1a). This band can be simulated giving a zero-field splitting parameter D of 34 G. Under these conditions also a weak peak ($|\Delta m_S| = 2$, forbidden transition) is observed at the half-field region attributed to the thermally accessible triplet state (Fig. 1a), which confirms the diradical nature of **1**.[38,39]

Furthermore, the magnetic character of **1** was monitored by using SQUID magnetometer at the temperature range of 2–300 K. Plots of the product of molar magnetic susceptibility (χ_m) and temperature (T) *versus* T in the warming and cooling modes at set magnetic field (H) of 5 kOe confirm the paramagnetic behaviour of **1** (Fig. 1b). $\chi_m T$ at 300 K gave 0.61 emu K mol^{-1}, which is lower than the value expected for a diradical with isolated or non-interacting spins ($\chi_m T = 0.75$ emu K mol^{-1}), and hence is in agreement with the presence of some monoradical impurity. From 300 K to ~100 K, the $\chi_m T$ values slowly decrease and fall off steeply on cooling down in agreement with the antiferromagnetic behaviour of **1** due to the intramolecular exchange coupling. The electrochemical properties of **1** were investigated by CV using 0.1 M of tetrabutylammonium hexafluorophosphate (n-Bu_4NPF_6) as supporting electrolyte in toluene/MeCN (1 : 1 v/v). The CV revealed two reversible redox processes with half-wave potentials ($E_{1/2}$ *vs.* Ag/AgCl) at −0.39 and −0.60 V, which were attributed to distinct single and sequential electron transfer process of each TTM unit (Fig. 1c). This is indicative of the strong electron–electron interaction existing between the two TTM moieties.

We assume that the monoradical impurity might be the thiol derivative, which could be formed during the synthesis of the compound **1** (Fig. S7†). This would be in agreement with the CV and SQUID results. Unfortunately, the monoradical impurity was not possible to separate by the chromatographic technique due to their identical polarity to **1**. However, the presence of such monoradical was not considered crucial or detrimental to proceed with the surface functionalisation since it would lead to identical SAMs.

The preparation of r-SAM on Au and Ag were conducted under similar experimental conditions. Freshly cleaned Au or template-striped Ag (Ag^{TS})[40–42] substrates were immersed in a 0.5 mM solution of **1** in dry toluene under Ar at 50 °C with the exclusion of light (Scheme 4). After 12 h, the temperature of the set-up was gradually brought to room temperature and the substrates were left in the solution for 36 h more. Afterwards, the substrates were thoroughly rinsed with fresh toluene to remove the physisorbed molecules and dried under nitrogen stream.

The obtained r-SAMs were well characterized with the aid of XPS, UPS, EPR and CV. XPS measurements provided an in-depth chemical and structural information of r-SAMs.[35] Firstly, to understand the elemental composition of surface, XPS survey scans (Fig. S8†) were collected for both **1**/Au and **1**/Ag and peaks corresponding to Au, Ag, S, Cl and C were identified, confirming thus the presence of TTM moiety of **1** on Ag and Au. The r-SAM formation was demonstrated by the high-resolution XPS of S 2p, Cl 2p and C 1s (Fig. 2). In detail, for S 2p data of **1**/Au, the best fit could be generated with three doublets by using 2 : 1 peak area ratio and a 1.2 eV splitting, and hence indicated the presence of three S species (Fig. 2a). The main doublet (56%) at 162.2 and 163.5 eV was assigned to S $2p_{3/2}$ and S $2p_{1/2}$, respectively, of typical Au–S bonds.[35] We also observed another component of S 2p doublet (28%) at 161.3 and 162.6 eV as the S $2p_{3/2}$ and S $2p_{1/2}$, respectively, and could be attributed to the self-assembly constraints or due to the *in situ* generated atomic S *via* C–S scission while the X-ray irradiation.[43–45] Additionally, a small

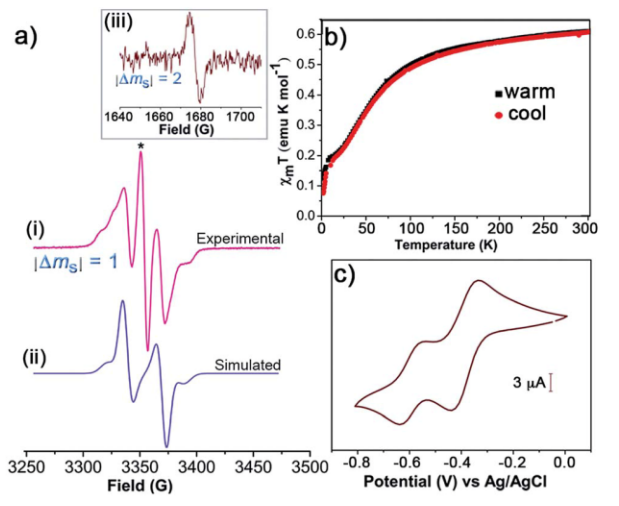

Fig. 1 (a) The experimental (i) and simulated (ii) EPR spectra of **1** (5×10^{-4} M) in frozen CH_2Cl_2/toluene (1 : 1 v/v) at 120 K. The line marked with the symbol * corresponds to the monoradical impurity. (iii) EPR signal corresponding to the half-field transition ($|\Delta m_S| = 2$). (b) Plots of temperature-dependent $\chi_m T$ for **1** (solid) at 5 kOe from 2 to 300 K for the warming and cooling modes. (c) CV of **1** (5×10^{-4} M) in toluene/MeCN (1 : 1 v/v) with 0.1 M n-Bu_4NPF_6 (*vs.* Ag/AgCl) at 100 mV s^{-1} using Pt wires as working and counter electrodes.

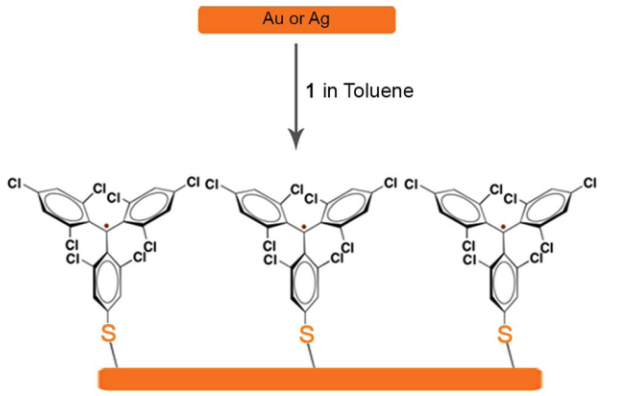

Scheme 4 r-SAM formation of **1** on Au or Ag.

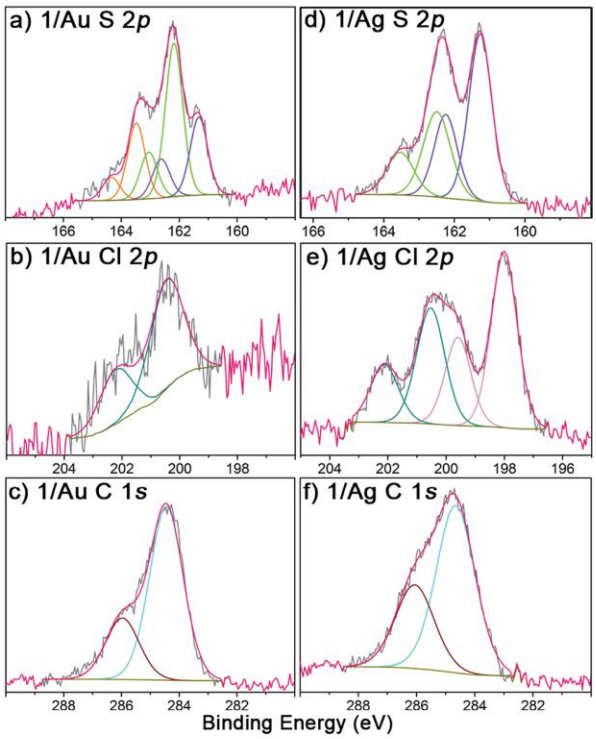

Fig. 2 High-resolution XPS of S 2p, Cl 2p and C 1s regions (grey) of **1**/Au (a–c) and **1**/Ag (d–f).

fraction of physisorbed **1** (16%) is also found over the substrate by observing a doublet at 163.1 and 164.4 eV. Similarly, **1**/Ag also gave S 2p emission corresponding to Ag–S bonds and notably no unreacted/physisorbed molecules of **1** were observed (Fig. 2d) suggesting a more densely packed r-SAM. The Cl 2p region of both **1**/Au and **1**/Ag showed a doublet at 200.4 and 202.2 eV, which corresponds to Cl $2p_{3/2}$ and Cl $2p_{1/2}$, respectively, of C–Cl bonds (Fig. 2b and e). Interestingly, Ag has a tendency to interact with Cl and caused a Cl 2p doublet at 198.0 and 199.6 eV.[46] The best fit of the C 1s spectra gave two peaks for both **1**/Au and **1**/Ag, which are consistent with the previously reported r-SAMs of PTM formed by physisorption (Fig. 2c and f).[46] The peak around 284.5 eV is attributed to the C 1s of C–H and C–S bonds, whereas ~286.0 eV peak arose from C 1s of C–Cl bonds. It is worth mentioning that the reaction of **1** on Ag is notably more favoured, compared to that on Au under similar experimental conditions, and that is reflected by the high emission counts and the excellent signal-to-noise ratio in the XPS measurements. This observation is justified by the higher surface energy of Ag which facilitates the disulfide cleavage required for the r-SAM formation.

The paramagnetic nature of **1**/Au and **1**/Ag were further analyzed with UPS and EPR spectroscopy. The UPS features confirmed its open shell behaviour by observing the respective single occupied molecular orbitals (SOMO), *i.e.*, ~1.5 and ~1.7 eV for **1**/Au (Fig. S9†) and **1**/Ag, respectively (Fig. 3a).[46,47] As expected, EPR spectroscopy revealed signals at $g = 2.0038$ for **1**/Au (Fig. S10†) with a linewidth of 4.9 G and 2.0041 for **1**/Ag with

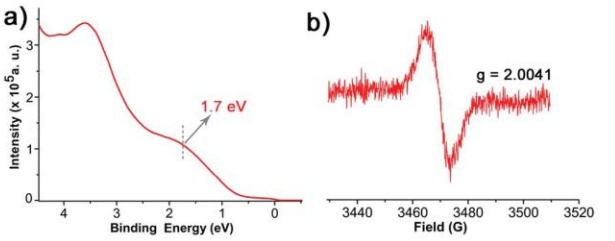

Fig. 3 (a) UPS of **1**/Ag. (b) EPR of **1**/Ag at 300 K under ambient condition.

a linewidth of 8.3 G under ambient conditions and, therefore, successfully confirmed that the immobilized TTM units maintain their radical nature after the chemisorptions (Fig. 3b).[23,25] This result contrasts with the previous findings on physisorbed PTM radical derivatives on Ag surface where an electron charge transfer from the metal to the radical was observed.[46]

Considering these results, the electrochemical characteristics of the r-SAM **1**/Ag were also investigated. The CV was performed using a three-electrode cell assembly in 0.1 M *n*-Bu_4NPF_6 in degassed dry MeCN under Ar at room temperature between −0.6 and 0.1 V. A custom-built electrochemical cell was equipped with **1**/Ag as the working electrode, a Ag wire as pseudo-reference electrode and a Pt wire as counter electrode. The CV displayed one quasi-reversible redox wave at −0.24 V corresponding to the one electron reduction of the TTM unit (Fig. 4a).[23] Unlike the reported PTM based r-SAMs, the difference between the oxidation and reduction waves ($\Delta E \sim 110$ mV for scan rate of 100 mV) is significantly higher and could be rationalized by the presence of strong TTM–metal and (or) TTM–TTM interactions in **1**/Ag.[48] It was also observed that the anodic peak current linearly increased with scan rate and that further confirmed the surface confinement of the TTM units (Fig. 4a and b). From the integration of the anodic wave at scan rate of 100 mV s^{-1}, we have estimated the surface coverage (Γ) of **1**/Ag to be 1.5×10^{-10} mol cm^{-2}, which is of the same order as that reported for other PTM SAMs with longer linkers. We have carried out 20 consecutive redox cycles with a scan rate of 20 mV s^{-1} without any noticeable current intensity decrease and

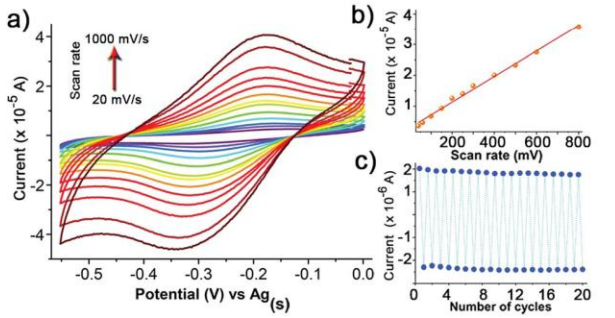

Fig. 4 (a) CV of **1**/Ag in MeCN, with 0.1 M *n*-Bu_4NPF_6 (*vs.* Ag(s)) at different scan rates (20–1000 mV s^{-1}). Plots of the current intensity (b) *vs.* scan rate and (c) *vs.* the number of cycles of the redox wave of **1**/Ag.

View Article Online
RSC Advances Paper

thereby proved the robustness and stability of the r-SAM (Fig. 4c).

Periodic density functional theory calculations, as implemented in the FHI-AIMS simulation package,[49,50] were employed to study the interaction between the adsorbed **1** r-SAM and the Ag surface. All calculations were performed using the PBE functional[51] and a light/tier 1 atom-centered numerical basis set, with van der Waals interactions taken into account using the Tkatchenko–Scheffler method.[52] The Ag substrate was represented by a three-layered Ag(111) slab cut from a fully optimized Ag crystal. A periodic cell size of $a = b = 17.7$ Å; $c = 40$ Å; $\alpha_{ab} = 60°$; $\alpha_{ac} = \alpha_{bc} = 90°$ was used, where the large c parameter was used to provide a vacuum space sufficient to avoid spurious interactions between repeated images. In the calculations the two top layers of the Ag slab were allowed to relax, with the bottom Ag layer and the cell parameters kept fixed to mimic the bulk rigidity of the substrate. Separately, a half fragment of **1** (breaking the molecule at the S–S bond, see Scheme 4) was fully optimized. This optimized molecule was placed with the S atom at a distance of 3.5 Å from the Ag surface with the S–C bond perpendicular to the plane of the Ag(111) support (Fig. 5). The substrate–molecule system was then optimized (fixing only the cell parameters and lower Ag layer). After optimization, the adsorbed molecules remain stable in a "vertical" conformation, which should facilitate the maintenance of the open-shell nature of the **1** r-SAM. More planar or inclined conformations might lead to charge transfer effects,[15,46] which may destroy completely or partially the open-shell character of the monolayer. From the calculated spin densities in Fig. 5b, it can be observed that the open-shell character of the **1** r-SAM is maintained after surface chemisorption. Moreover, there appears a partial beta-spin polarization in the Ag surface atoms below the adsorbed molecular unit which is likely due to the proximity of the radical centre **1** with the metal surface.

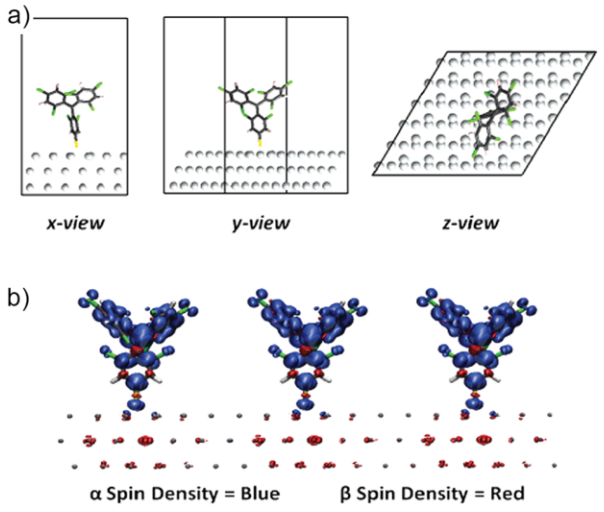

Fig. 5 (a) *x*, *y* and *z* views of the fully optimized periodic structure of the adsorbed **1** radical SAM onto the 3-layered Ag slab. Atom colour-key: C – dark-grey, Cl – green, S – yellow, Ag – light-grey, H – white. (b) Spin density (alpha = blue, beta = red).

Conclusions

In summary, we have synthesized a stable disulfide diradical by utilizing a single-pot reaction. Unlike the conventional PTM based r-SAM, these r-SAMs are fabricated without incorporating the linker unit for the first time. By using this strategy, we could avoid the conventional methodology that involves the utilization of aromatic or alkyl linkers and hence the associated synthetic difficulties. The obtained robust r-SAMs were fully characterized and, importantly, it was proved that the radical character is preserved despite the short distance with the metal and in contrast with previous works on physisorbed PTM radicals on Ag.[46] Therefore, we succeed in preparing free r-SAMs with the spin-bearing cores directly and covalently grafted to a metal surface, ensuring excellent spin–spin and spin–electron interactions, as supported by *ab initio* density functional calculations. This design strategy and easy synthetic protocol make these r-SAMs promising building blocks for the futuristic preparation of spintronic materials and devices.

Experimental

1. General procedure

NMR spectra were recorded on a Bruker Avance 400 MHz. EPR spectra were recorded in a Bruker ELEXYS E500 X-band spectrometer. The simulation of the EPR spectra was realised with software Simfonia. Electrochemical experiments were performed with a potentiostat/galvanostat Autolab/PGSTAT204 from Metrohm Autolab B.V. in a standard three-electrode cell, by using a platinum wire as working and counter electrode and Ag/AgCl as reference electrode. Tetrabutylammonium hexafluorophosphate (Fluka, 99%) was used as the supporting electrolyte. UV-vis spectra were recorded on a Varian Carey 5000 in double-beam mode. Mass spectra were recorded with a Bruker Ultraflex LDI-TOF mass spectrometer. The IR spectra were recorded with an ATR-IR Perkin Elmer Spectrum One. The synthesis and manipulation of the radicals in solution was performed under red light.

2. Synthesis and characterization of 1

Compound **2** was synthesised by following previously reported method.[36] **2** (2.16 g, 4.05 mmol) and 2,4-bis(4-methoxyphenyl)-2,4-dithioxo-1,3,2,4-dithiadiphosphetane (Lawesson's reagent; 2.02 g, 4.99 mmol) were transferred to a 50 mL R.B. flask, and 60 mL of dry toluene was added under Ar atmosphere and under light exclusion. The reaction mixture was heated at 95 °C for 2.5 h on a magnetic stirrer with gentle stirring and cooled to RT. After drying under vacuum, the crude product was purified by column chromatography over activated neutral Al_2O_3 where *n*-hexane was used as eluent.

Yield: 18%. $R_f = 0.39$ (SiO_2 TLC, hexane as eluent). Melting point: 264 °C. MS (MALDI-TOF, positive mode): calculated for $C_{38}H_{12}Cl_{16}S_{22}^{\cdot}$ (m/z) 1099.83, found 1100.2 $[M]^+$, 1068.9 $[M - Cl]^+$, 1029.9 $[M - 2Cl]^+$, 996.1 $[M - 3Cl]^+$, 959.2 $[M - 4Cl]^+$, and 925.1 $[M - 5Cl]^+$. IR (ATR, ν cm^{-1}) = 3082, 2921, 1729, 1550, 1524, 1364, 1183, 1137, 857. UV-vis (CH_2Cl_2): λ_{max} (ε) = 375 nm

(43 700 M^{-1} cm^{-1}), 394 nm (29 420 M^{-1} cm^{-1}), 540 nm (2020 M^{-1} cm^{-1}) and 572 nm (2030 M^{-1} cm^{-1}).

3. Magnetic susceptibility measurements

Variable temperature magnetic susceptibility measurements of **1** (55.9 mg) were carried out in a Quantum Design MPMS-5S SQUID magnetometer down to 2 K. The molar magnetic susceptibility (χ_m) values were corrected for the temperature-independent diamagnetic contribution of the atoms/bonds by means of Pascal's tables and the magnetic contribution of the sample holder (35.9 mg).

4. Preparation of the SAMs on Au and Ag^{TS}

All the glassware employed for the SAM preparation were immersed in Hellmanex II solution (2% v/v) in distilled water for overnight, thoroughly washed with MilliQ water, and dried in an oven at 80 °C. The solvents used in the surface chemistry experiments were of HPLC grade from ROMIL-SpS (Super Purity Solvent).

We have used Ag wire (1.5 mm diameter) with purity of 99.99% obtained from Kurt J. Lesker Company, Spain. Si/SiO_x (200 nm SiO_x, sourced from Si-mat, Germany) with a thickness of 525 ± 25 μm with one side polished. This was first cleaned by blowing nitrogen and then by reactive ion etching (RIE). An O_2 flux of 20 standard cubic centimeters per minute for 1 min under 100 W power and 100 mTorr pressure were used for RIE (RIE 2000 CE, South Bay Technology). For the 300 nm Ag evaporation, BOC Edwards Auto 306 electron beam evaporation systems was used at a base pressure of ~2×10^{-6} bar. The rate of the deposition was at 0.1–0.2 Å s^{-1} for the first 50 nm and the rate increased gradually to 1 Å s^{-1} for the remaining 250 nm. Glass (2.6×1 cm^2) or quartz (0.5×1.6 cm^2) slides (1 mm thick) were immersed in piranha solution (concentrated H_2SO_4 and 30% H_2O_2 (aq) in 3 : 1 ratio. Warning: piranha solution should be handled with caution: it has been reported to detonate unexpectedly). These slides were washed thoroughly with high purity water (MilliQ, 18.2 MΩ cm at 25 °C) and isopropanol (HPLC). After drying under a nitrogen stream, the slides were further cleaned by UV ozone chamber for 25 min. Then the slides were glued onto the Ag layer with a thermally-curable epoxy adhesive (Epo-tek 353-ND) and kept at 80 °C for 15 h for curing. The glass (or quartz)/glue/Ag substrate was stripped off from the Si/SiO_x wafer-template to obtain Ag^{TS} by using a sharp razor blade and immediately transferred to Ar filled reaction vessel. Au substrates (300 nm, on mica) were purchased from Georg Albert PVD-Beschichtungen. Au/mica (0.8×2.6 cm) were rinsed with CH_2Cl_2, acetone and isopropanol, respectively, and dried under nitrogen stream. These substrates were placed in UV ozone chamber for 20 minutes and thereafter immediately transferred to isopropanol. After 30 min, the substrates were rinsed with pure isopropanol, blown dry with a stream of N_2 and transferred to Ar filled reaction vessel.

To the freshly prepared substrates (Au and Ag), 0.5 mM solution of **1** in dry toluene was slowly added under Ar and kept at 50 °C for 24 h. Then, the temperature was gradually decreased to RT and left the reaction vessel undisturbed for another 24 h. Then, the substrates were removed from the solution and washed with abundant toluene, followed by drying in a stream of N_2.

5. X-ray photoelectron and UV photoelectron spectroscopy (XPS and UPS)

XPS and UPS measurements were performed with a Phoibos 150 analyzer (SPECS GmbH, Germany) instrument with monochromatic AlKα X-ray (1486.74 eV) and HeI UV (21.2 eV) sources under ultra-high vacuum conditions (base pressure 3×10^{-10} mbar). The X-ray radiation is at an angle of 55° to the sample with a spot size of 3.5×0.5 mm in ellipsoidal arrangement. A pass energy of 50 eV, a dwell time of 500 ms, and an energy step size of 1 eV were employed for the general scan. For specific element scanning, pass energy of 20 eV and step size of 0.05 eV were used. The binding energies were calibrated with respect to Au $4f_{7/2}$ at 84.0 eV for Au/SAMs and Ag $3d_{5/2}$ at 368.27 eV for Ag/SAMs. The sample for UPS was held at an angle of 55° with respect to the UV radiation and the spot size was 0.5 mm diameter. The overall resolution for XPS, as measured by the full width at half-maximum intensity (FWHM) of the Ag $3d_{5/2}$ peak for a sputtered silver foil, is 0.57 eV and for UPS as measured by FWHM of Fermi level is 0.12 eV.

A 1 mM solution of **1** in CH_2Cl_2 was drop casted on a Au substrate and dried instantly by blowing a gentile stream of nitrogen, and the resultant **1** multilayers were examined by XPS. The spectra gave peaks corresponding to one kind of S (163.7 and 164.9 eV for $2p_{3/2}$ and $2p_{1/2}$, respectively) attributed to the disulfide group and one kind of Cl (200.3 and 201.9 eV for $2p_{3/2}$ and $2p_{1/2}$, respectively) attributed to C–Cl groups. In addition, the C 1s peaks at 284.9 and 286.0 eV indicated the existence of C–H and C–Cl bonds. However, C of methyl–C and C–S were overwhelmed by C–Cl and C–H, and could not be resolved. Along with these elements, Au from substrate and trace amount of ubiquitous O were also detected.

Acknowledgements

This work was funded by ERC StG 2012-306826 e-GAMES. The authors also thank ITN iSwitch 642196 project, the Networking Research Center on Bioengineering, Biomaterials and Nanomedicine (CIBER-BBN), DGI (Spain) BE-WELL CTQ2013-40480-R and FANCY CTQ2016-80030-R, and Generalitat de Catalunya 2014-SGR-17. The authors also acknowledge the Spanish Ministry of Economy and Competitiveness, through the "Severo Ochoa" Programme for Centres of Excellence in R&D (SEV-2015-0496). We thank Dr V. Lloveras for ESR spectroscopy characterization, Mr A. Bernabé for MALDI-TOF measurements and Dr G. Sauthier from ICN2 for XPS and UPS measurements. We also thank Dr N. Crivillers for useful discussions. S. T. B. and I. A. acknowledge support from the Spanish MINECO grant CTQ2015-64618-R grant and, in part, by Generalitat de Catalunya grants 2014SGR97 and XRQTC. IA acknowledges the Spanish Ministerio de Educación Cultura y Deporte for a FPU PhD scholarship. Access to supercomputer resources as

provided through grants from the Red Española de Supercomputación is also acknowledged.

Notes and references

1 F. P. Netzer and M. G. Ramsey, *Crit. Rev. Solid State Mater. Sci.*, 1992, **17**, 397.
2 H. Ishii, K. Sugiyama, E. Ito and K. Seki, *Adv. Mater.*, 1999, **11**, 605.
3 S. Braun, W. R. Salaneck and M. Fahlman, *Adv. Mater.*, 2009, **21**, 1450.
4 M. Franke, F. Marchini, H. P. Steinrück, O. Lytken and F. J. Williams, *J. Phys. Chem. Lett.*, 2015, **6**, 4845.
5 C. Joachim, J. K. Gimzewski and A. Aviram, *Nature*, 2000, **408**, 541.
6 M. Halik and A. Hirsch, *Adv. Mater.*, 2011, **23**, 2689.
7 G. Heimel, L. Romaner, E. Zojer and J. L. Bredas, *Acc. Chem. Res.*, 2008, **41**, 721.
8 A. Nitzan and M. A. Ratner, *Science*, 2003, **300**, 1384.
9 L. Basabe-Desmonts, J. Beld, R. S. Zimmerman, J. Hernando, P. Mela, M. F. G. Parajó, N. F. van Hulst, A. van den Berg, D. N. Reinhoudt and M. A. Crego-Calama, *J. Am. Chem. Soc.*, 2004, **126**, 7293.
10 G. De Ruiter, T. Gupta and M. E. van der Boom, *J. Am. Chem. Soc.*, 2008, **130**, 2744.
11 B. A. Bejjani and L. G. Shaffer, *J. Mol. Diagn.*, 2006, **8**, 528.
12 J. Lamartine, *Mater. Sci. Eng., C*, 2006, **26**, 354.
13 M. J. Heller, *Annu. Rev. Biomed. Eng.*, 2002, **4**, 129.
14 T. M. Herne and M. J. Tarlov, *J. Am. Chem. Soc.*, 1997, **119**, 8916.
15 G. Heimel, S. Duhm, I. Salzmann, A. Gerlach, A. Strozecka, J. Niederhausen, C. Bürker, T. Hosokai, I. Fernandez-Torrente, G. Schulze, S. Winkler, A. Wilke, R. Schlesinger, J. Frisch, B. Bröker, A. Vollmer, B. Detlefs, J. Pflaum, S. Kera, K. J. Franke, N. Ueno, J. I. Pascual, F. Schreiber and N. Koch, *Nat. Chem.*, 2013, **5**, 187.
16 J. C. Love, L. A. Estroff, J. K. Kriebel, R. G. Nuzzo and G. M. Whitesides, *Chem. Rev.*, 2005, **105**, 1103.
17 A. Ulman, *Chem. Rev.*, 1996, **96**, 1533.
18 H. Hamoudi, K. Uosaki, K. Arigaa and V. A. Esaulov, *RSC Adv.*, 2014, **4**, 39657.
19 E. Marchante, M. S. Maglione, N. Crivillers, C. Rovira and M. Mas-Torrent, *RSC Adv.*, 2017, **7**, 5636.
20 M. Mas-Torrent, N. Crivillers, C. Rovira and J. Veciana, *Chem. Rev.*, 2012, **112**, 2506.
21 M. Mas-Torrent, N. Crivillers, V. Mugnaini, I. Ratera, C. Rovira and J. Veciana, *J. Mater. Chem.*, 2009, **19**, 1691.
22 N. Crivillers, M. Mas-Torrent, C. Rovira and J. Veciana, *J. Mater. Chem.*, 2012, **22**, 13883.
23 N. Crivillers, M. Mas-Torrent, J. Vidal-Gancedo, J. Veciana and C. Rovira, *J. Am. Chem. Soc.*, 2008, **130**, 5499.
24 N. Crivillers, C. Munuera, M. Mas-Torrent, C. Simão, S. T. Bromley, C. Ocal, C. Rovira and J. Veciana, *Adv. Mater.*, 2009, **21**, 1177.
25 C. Simão, M. Mas-Torrent, N. Crivillers, V. Lloveras, J. Artés, P. Gorostiza, J. Veciana and C. Rovira, *Nat. Chem.*, 2011, **3**, 359.
26 C. Simão, M. Mas-Torrent, J. Veciana and C. Rovira, *Nano Lett.*, 2011, **11**, 4382.
27 N. Crivillers, M. Mas-Torrent, S. Perruchas, N. Roques, J. Vidal-Gancedo, J. Veciana, C. Rovira, L. Basabe-Desmonts, B. Ravoo, M. Crego-Calama and D. N. Reinhoudt, *Angew. Chem., Int. Ed.*, 2007, **46**, 2215.
28 O. Shekhah, N. Roques, V. Mugnaini, C. Munuera, C. Ocal, J. Veciana and C. Wöll, *Langmuir*, 2008, **24**, 6640.
29 R. Frisenda, R. Gaudenzi, C. Franco, M. Mas-Torrent, C. Rovira, J. Veciana, I. Alcon, S. T. Bromley, E. Burzurí and H. S. J. van der Zant, *Nano Lett.*, 2015, **15**, 3109.
30 J. Liu, H. Isshiki, K. Katoh, T. Morita, B. K. Breedlove, M. Yamashita and T. Komeda, *J. Am. Chem. Soc.*, 2013, **135**, 651.
31 Y.-h. Zhang, S. Kahle, T. Herden, C. Stroh, M. Mayor, U. Schlickum, M. Ternes, P. Wahl and K. Kern, *Nat. Commun.*, 2013, **4**, 2110.
32 S. Müllegger, M. Rashidi, M. Fattinger and R. Koch, *J. Phys. Chem. C*, 2013, **117**, 5718.
33 O. Armet, J. Veciana, C. Rovira, J. Riera, J. Castaner, E. Molins, J. Rius, C. Miravitlles, S. Olivella and J. Brichfeus, *J. Phys. Chem.*, 1987, **91**, 5608.
34 N. Crivillers, M. Paradinas, M. Mas-Torrent, S. T. Bromley, C. Rovira, C. Ocal and J. Veciana, *Chem. Commun.*, 2011, **47**, 4664.
35 D. G. Castner, K. Hinds and D. W. Grainger, *Langmuir*, 1996, **12**, 5083.
36 J. Carilla, L. Fajari, L. Julia, J. Riera and L. Viadel, *Tetrahedron Lett.*, 1994, **35**, 6529.
37 J. Veciana, C. Rovira, M. I. Crespo, O. Armet, V. M. Domingo and F. Palacio, *J. Am. Chem. Soc.*, 1991, **113**, 2552.
38 A. Rajca, K. Shiraishi, M. Vale, H. Han and S. Rajca, *J. Am. Chem. Soc.*, 2005, **127**, 9014.
39 V. Lloveras, E. Badetti, K. Wurst, V. Chechik, J. Veciana and J. Vidal-Gancedo, *Chem.–Eur. J.*, 2016, **22**, 1805.
40 E. A. Weiss, R. C. Chiechi, G. K. Kaufman, J. K. Kriebel, Z. Li, M. Duati, M. A. Rampi and G. M. Whitesides, *J. Am. Chem. Soc.*, 2007, **129**, 4336.
41 R. C. Chiechi, E. A. Weiss, M. D. Dickey and G. M. Whitesides, *Angew. Chem., Int. Ed.*, 2008, **47**, 142.
42 N. Nerngchamnong, L. Yuan, D.-C. Qi, J. Li, D. Thompson and C. A. Nijhuis, *Nat. Nanotechnol.*, 2013, **8**, 113.
43 O. Cavalleri, G. Gonella, S. Terreni, M. Vignolo, P. Pelori, L. Floreano, A. Morgante, M. Canepa and R. Rolandi, *J. Phys.: Condens. Matter*, 2004, **16**, S2477.
44 V. Lloveras, E. Badetti, J. Veciana and J. Vidal-Gancedo, *Nanoscale*, 2016, **8**, 5049.
45 J. Jia, A. Giglia, M. Flores, O. Grizzi, L. Pasquali and V. A. Esaulov, *J. Phys. Chem. C*, 2014, **118**, 26866.
46 V. Mugnaini, A. Calzolari, R. Ovsyannikov, A. Vollmer, M. Gonidec, I. Alcon, J. Veciana and M. Pedio, *J. Phys. Chem. Lett.*, 2015, **6**, 2101.
47 F. Grillo, V. Mugnaini, M. Oliveros, S. M. Francis, D.-J. Choi, M. V. Rastei, L. Limot, C. Cepek, M. Pedio, S. T. Bromley, N. V. Richardson, J.-P. Bucher and J. Veciana, *J. Phys. Chem. Lett.*, 2012, **3**, 1559.

48 N. Nerngchamnong, D. Thompson, L. Cao, L. Yuan, L. Jiang, M. Roemer and C. A. Nijhuis, *J. Phys. Chem. C*, 2015, **119**, 21978.
49 V. Blum, R. Gehrke, F. Hanke, P. Havu, V. Havu, X. Ren, K. Reuter and M. Scheffler, *Comput. Phys. Commun.*, 2009, **180**, 2175.
50 V. Havu, V. Blum, P. Havu and M. Scheffler, *J. Comput. Phys.*, 2009, **228**, 8367.
51 J. P. Perdew, K. Burke and M. Ernzerhof, *Phys. Rev. Lett.*, 1996, **77**, 3865.
52 A. Tkatchenko and M. Scheffler, *Phys. Rev. Lett.*, 2009, **102**, 073005(1).

Publication #3

Study of the *E*–*Z* stilbene isomerisation in perchlorotriphenyl-methane (PTM) derivatives

RSC Adv., 2017,7, 15278-15283

F. Bejarano, I. Alcón, N. Crivillers, M. Mas-Torrent*, S. T. Bromley, J. Veciana*, C. Rovira*

RSC Advances

PAPER

View Article Online
View Journal | View Issue

Cite this: RSC Adv., 2017, 7, 15278

Received 23rd December 2016
Accepted 24th February 2017

DOI: 10.1039/c6ra28618f

rsc.li/rsc-advances

Study of the *E*–*Z* stilbene isomerisation in perchlorotriphenyl-methane (PTM) derivatives†

F. Bejarano,‡[a] I. Alcon,‡[b] N. Crivillers,[a] M. Mas-Torrent,*[a] S. T. Bromley,[bc] J. Veciana[a] and C. Rovira*[a]

The *E*–*Z* isomerisation of two perchlorotriphenylmethane derivatives containing stilbene units has been investigated, both thermally and photochemically. The irreversibility of the *E* → *Z* isomerisation in both compounds is experimentally demonstrated and supported by density functional calculations.

The photoinduced *E*–*Z* isomerization phenomenon has been a longstanding interesting topic in organic and inorganic chemistry as well as in biology. The change in the functional properties depending on the molecular structure of the different meta-stable isomers has been exploited for many applications in biochemistry, pharmacology and supramolecular chemistry.[1] The most representative isomeric switchable systems are azobenzenes[2] and stilbenes.[3] Both, upon illumination with a specific wavelength, can undergo a reversible photoisomerisation between the *trans* and *cis* conformation. They have been extensively investigated as molecular switches[4] and also have led to many different applications such as molecular motors[5] or solar-thermal fuels.[6] In the latter, solar energy is stored in the chemical bonds by photoconversion and, upon activation, the stored energy is released in the form of heat. Here we study, both photochemically and thermally, the *E*–*Z* isomerisation of perchlorotriphenylmethane (PTM) derivatives containing a stilbene unit with one of their phenylene rings substituted with four chlorine atoms and a perchlorodiphenylmethyl group at the *para* position. This phenomenon is presented herein with the study of two differently substituted stilbene derivatives (Scheme 1). This family of molecules is very appealing since it has been demonstrated that, with a proper design, they can be excellent building blocks to form functional supramolecular nano- and micro-structures driven by Cl···Cl and Cl···phenyl interactions. Indeed, very recently, it was demonstrated that PTM moieties substituted with *p*-vinylphenylene groups functionalised with long alkyl chains can be employed to prepare molecular micro-scale objects with unprecedented shapes (*i.e.*, flowers, cones, fibres, *etc.*) following the so-called "hydrophobic–amphiphilic" approach.[7] Moreover, by chemical modification of the phenyl substitution pattern, robust micro-capsules that could encapsulate hydrophilic contents were prepared. Interestingly, such hydrophilic contents were neatly released upon UV irradiation due to photochemical decomposition leading to a phenanthrene derivative.[8] Further, chemically bonded self-assembled monolayers (SAMs) on gold were previously prepared using the *E* isomer of compound **1** (Scheme 1).[9] In this case, the SAMs were employed as precursors to form the organic free radical derivative which has been shown to constitute an excellent platform for the fabrication of robust molecular memories due to its electroactive character.[10] In view of the interesting properties of the functional materials prepared employing the PTM derivatives as building blocks, we were interested in studying the isomerisation processes that these systems can undergo when they are irradiated or heated.

Compounds **1** and **2** were obtained through a Wittig and a Horner–Wadsworth–Emmons reaction, respectively. In the case of **1**, the reaction was carried out between the PTM phosphonium bromide salt and the 4-(acetylthio)benzaldehyde (see details on the synthesis in ref. 11). Molecule **2** was prepared through the coupling of PTM phosphonate and

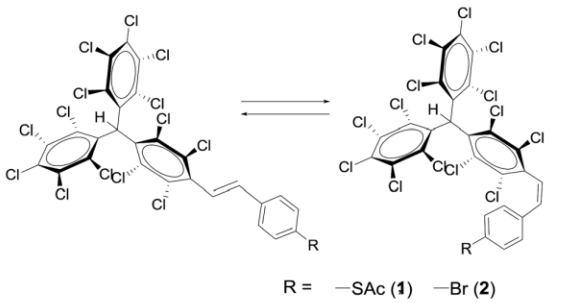

Scheme 1 Isomerisation of PTM–SAc (**1**) and PTM–Br (**2**); *E*-**1**/**2** to *Z*-**1**/**2**.

[a]*Institut de Ciència de Materials de Barcelona (ICMAB-CSIC), Networking Research Center on Bioengineering, Biomaterials and Nanomedicine (CIBER-BBN), Campus de la UAB, 08193 Bellaterra, Spain. E-mail: cun@icmab.es; mmas@icmab.es*

[b]*Departament de Ciència de Materials I Química Física, Institut de Química Teórica i Computacional, Universitat de Barcelona (IQTCUB), E-08028 Barcelona, Spain*

[c]*Institució Catalana de Recerca i Estudis Avançats (ICREA), 08010 Barcelona, Spain*

† Electronic supplementary information (ESI) available. See DOI: 10.1039/c6ra28618f

‡ Equally contributed.

4-bromobenzaldehyde (synthesis adapted from ref. 12). It is known that the ^{1}H-NMR chemical shift of the hydrogen atoms of C=C groups, as well as their coupling constant J, allows for the identification of the two possible isomers that can be obtained from these synthetic routes. For the compounds presented here, the J value of the E isomers is around 17 Hz, while for the Z isomers it is around 12 Hz. It was determined that the E isomer was the major component of the reaction mixtures, with a ratio of *ca.* 92% and 99% for E-**1** and E-**2**, respectively (determined by ^{1}H-NMR signal integration).

In order to follow and quantify the E/Z isomerisation processes for compounds **1** and **2**, High Performance Liquid Chromatography (HPLC) was employed using reversed-phase conditions, at room temperature and under an isocratic regime. Mixtures of acetonitrile/tetrahydrofuran (9 : 1) and acetonitrile/chloroform (8 : 2) were found as optimal conditions for an adequate separation of the corresponding isomers for **1** and **2**, respectively.

After reaching a good separation of the two isomers, we proceeded to study the photo-isomerisation conversion from the E to the Z form of **1** and **2**. The samples were irradiated with a Hg(Xe) lamp 300 W placed at around 30 cm from the sample. In the case of **1**, a 0.07 mM solution in a THF/ACN (1 : 1) mixture was used for this experiment. To follow the evolution of the isomerisation process, several aliquots were taken during the irradiation time and analysed by HPLC. Fig. 1 shows the corresponding chromatograms and the retention times. The relative peak areas (in %) are depicted for each analysed aliquot in Table 1. See ESI† for the monitoring performed for **2**.

As expected, the Z/E ratio increases in both cases during the irradiation time until the photostationary state is reached. The ^{1}H-NMR (see ESI†) of the sample after irradiation confirmed that the peak at a retention time of 12 minutes corresponds to the expected Z-**1** compound. The same analysis was performed for compound **2**.

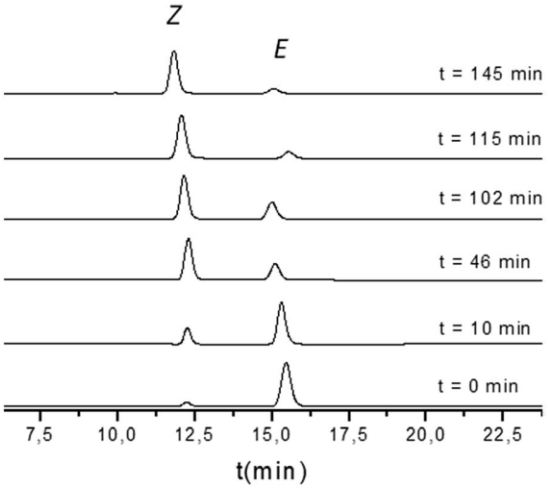

Fig. 1 Evolution of the HPLC chromatograms obtained upon irradiation of E-**1** in a solvent mixture of THF/ACN (1 : 1). Experimental conditions: 25 °C, mobile phase THF/ACN (10/90), stationary phase ODS, UV detector with a fixed wavelength of 230 nm and a flow of 1 mL min^{-1}.

Table 1 Time evolution of the relative area of the HPLC chromatogram peaks at retention times of *ca.* 12 and 15 min for compound **1** during sample irradiation

Time (min)	% Area (Z-**1**)	% Area (E-**1**)	(Z/E) Peak areas ratio
0	7.5	92.5	0.08
10	23.0	77.0	0.30
46	67.7	31.3	2.16
102	75.5	24.5	3.08
115	87.9	12.1	7.26
145	88.8	11.2	7.93

The characterization by ultraviolet-visible (UV-vis) spectroscopy shows that there is an overlap of the absorption spectra of both isomers (see ESI†). In addition, the Z isomer absorbs white light more poorly than the E isomer. For these two reasons the back $Z \rightarrow E$ phoisomerization could not be carried out.

Since the most thermodynamically favoured isomer for stilbenoid compounds is usually the E isomer, we proceeded with the study of the thermally induced conversion of the Z form back to the E. To do that, the photostationary state mixture obtained by irradiation was refluxed in different solvents: chloroform, tetrahydrofuran, cyclohexane, toluene and *o*-dichlorobenzene for, at least 3 hours. These solvents do not only allow access to different heating temperatures, but also they provide different polarities of the media, as well as interactions between the solvent and the PTM derivatives through their ability to form π–π and Cl–Cl interactions. Again, the solution evolution was followed by HPLC. In this case, the thermal back conversion was not observed for either compound **1** or **2**. This result is in agreement with previous studies which determined an activation barrier for the $Z \rightarrow E$ isomerisation for stilbenoid compounds of the order of 1.9 eV (43.8 kcal mol^{-1}), which makes the thermal back reaction unlikely.[13]

We attempted to carry out the PTM $Z \rightarrow E$ isomerisation process using catalytic amounts of iodine. This is an established methodology to convert isomeric mixtures to the E derivative.[14] The obtained photostationary state mixture of **2** was dissolved in toluene (0.022 M) with iodine (0.03 eq.) and the solution was refluxed for 5 hours. The evolution of the mixture was followed by HPLC and no back isomerisation was observed by HPLC monitoring. Then, 0.03 more equivalents of I_2 were added and the solution was refluxed 19 additional hours. After such a long period of time at high temperature many products of decomposition appeared (see Fig. S5 in ESI†) but no isomer E formation was observed. Therefore, this suggests that back isomerisation, in the best case, is less favoured than several decomposition pathways.

Density functional theory (DFT) calculations were carried out to better understand the irreversible isomerisation process $Z \rightarrow E$ observed for both PTM derivatives **1** and **2**. It is known that, unlike azobenzene derivatives, in ethylene derivatives photo-activated twisting of the C=C bond is the main mechanism for E–Z isomerisation[15] as represented with the red arrow

View Article Online
RSC Advances Paper

on the stilbene structure in Fig. 2a. To obtain the ground state energy profile associated with such a twisting process in compounds **1** and **2**, we systematically varied the corresponding C=C dihedral angle and performed constrained optimisations of the molecular structure for each conformation. In all cases, the *E* conformer ($\varphi = 0°$, 360°) is slightly more stable than the *Z* conformer ($\varphi = 180°$), with the perpendicular conformation (*i.e.* $\varphi = 90°$, 270°) being the most energetically unstable by 1.9 eV (*i.e.* the $E \leftrightarrow Z$ energetic barrier height, see ESI†). These results are fully in accordance with previous studies.[13,14] Time dependent DFT (TD-DFT) calculations were then used to obtain approximate absorption spectra for *E* and *Z* conformers for both derivatives **1** and **2**. For the *E* conformers we found the most intense peak at 340 and 345 nm (for **1** and **2**, respectively). In the corresponding *Z* conformers, these peaks slightly shift towards higher energies (315 and 317 nm for **1** and **2**, respectively) and decreases in intensity by ~60%. These calculations coincide with our experimental UV-vis spectroscopy measurements (see ESI Fig. S1†), where the peak at ~310 nm for the *E* conformer decreases in intensity upon photo-generating the *Z* conformer and shifts towards higher energy wavelengths. This UV-vis band variation has been observed for other stilbene derivatives, where such optical absorptions were associated with the photo-activation of the C=C moiety.[16]

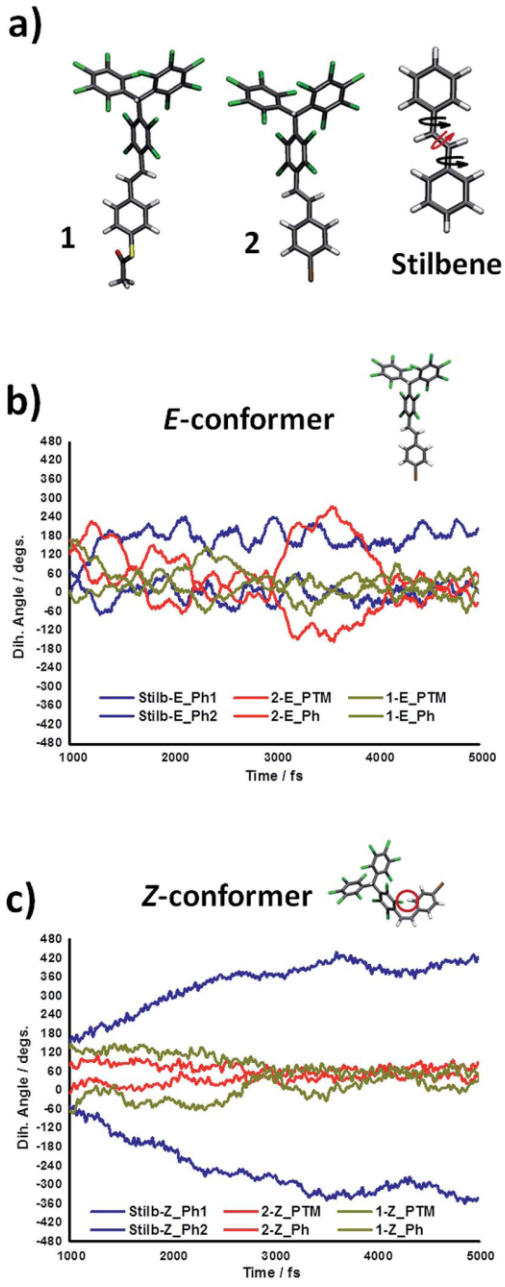

Fig. 2 (a) Fully optimized structures of the *E*-isomers of PTM derivatives **1** and **2**, and stilbene. The coloured arrows on the structure of stilbene highlight the important twist angles (red: main C=C axis, black: twist angles of the aryl groups bonded to the ethylene unit). (b) and (c) Evolution of the twist angles of the aryl groups bonded to the ethylene unit for each molecule (see legends) during 4 ps of an AIMD run at 450 K for the *E* and *Z* conformers respectively.

The higher absorbance of the *E* conformer might explain the high production of the *Z* conformer upon light absorption. However, the thermal irreversibility of the photo-isomerisation of *Z* towards the *E* isomer (even under I_2 catalyzed conditions) suggests that the different UV-vis absorption characteristics of the two conformers may not fully explain the experimental findings.[16] In the C=C twisting process assessed by constrained DFT optimizations (see ESI†) we found that, for both **1** and **2**, the aryl ring groups bonded to the ethylene unit had to be twisted to specifically chosen angles (black arrows on stilbene structure in Fig. 2a) in order to prevent steric interactions and hence allow the rotation around the C=C bond axis (red arrow on stilbene structure in Fig. 2a). The key role of such aryl ring twist angles for the $E \leftrightarrow Z$ photo-isomerisation has been demonstrated both theoretically[17] and experimentally,[18] and proven to be more relevant for the $Z \rightarrow E$ process[19] than for the $E \rightarrow Z$ one.[20] Based on this, we performed *ab initio* molecular dynamics (AIMD) simulations at 450 K (see computational details below) to compare the thermal fluctuations of such aryl ring twist angles in compounds **1** and **2** and stilbene (where the $E \leftrightarrow Z$ isomerisation is completely reversible) in each conformation.

Extracting the twist angle of the central ethylene unit (red arrow in Fig. 2a) we could find that, for all cases, the C=C bond hardly rotates (see ESI†). This is in full accordance with its associated high twisting energy and corroborates the need for light irradiation to induce the $E \leftrightarrow Z$ transition, even at high temperatures (see ESI†). In contrast, by following the variation in the twist angles of the aryl rings with respect to the ethylene unit (black arrows in Fig. 2a), it is possible to observe significant differences between the *E* and *Z* conformer profiles (Fig. 2b and c).

For both PTM derivatives and stilbene in the *E* conformation such aryl ring twist angles fluctuate significantly over time (Fig. 2b) which is consistent with the little steric interaction between the two aryl ring groups bonded to the C=C unit. For stilbene in the *Z* conformation the two aryl rings tend to keep rotating in opposite directions leading to a gradual increase in the magnitude of the associated twist angle (see blue lines in

Fig. 2c). Although in this case the two rings are close to each other, by counter rotating in this manner they are able to avoid significant steric hindrance. In the *Z* conformers of derivatives **1** and **2**, however, the aryl ring twist angles quickly converge to fixed values of about 60°. The lack of rotation in these cases comes from two different factors. From one side, the bulky PTM group possesses relatively high inertia to move which impedes the rotation of that bulky group attached to the ethylene unit. Also, the close proximity of the *ortho*-chlorine atoms within the PTM unit with the opposite aryl ring (see the *Z*-**1** structure in Fig. 2c) gives rise to large steric constraints which prevent the free rotation of the brominated aryl ring. Hence, overall, the rotational freedom of both groups bonded to the ethylene unit in the *Z* conformation of **1** and **2** is significantly suppressed.

As noted above, when calculating the twisting of derivatives **1** and **2** about the C=C bond specific twist angles of the aryl ring groups are needed to avoid significant steric interactions and allow the isomerisation to occur. In the *E* conformer such specific aryl ring twist angles should be easily accessible due to the freely rotating behaviour in such conformation for **1**, **2** and stilbene (see Fig. 2b). However, in the *Z* conformation, aryl rings in compounds **1** and **2** do not rotate due to steric interactions between the two aryl ring groups and the larger inertia of the PTM unit. Such an effect does not occur for stilbene (blue curve in Fig. 2c), where the $E \leftrightarrow Z$ isomerisation is completely reversible.[16] These results suggest that the complete and irreversible formation of *Z* isomers under light irradiation (Fig. 1) for PTM derivatives **1** and **2** could be at least partially explained by the lack of free rotation of their aryl rings in the *Z* conformation, causing a kinetic blockage. This suggestion may also help explain why even when using a chemical catalyst (I_2) the $Z \rightarrow E$ process does not seem to occur and also the uniqueness of these observations as compared to less hindered stilbene derivatives reported in previous studies.[16] Therefore, as represented schematically in Fig. 3a, in stilbene the *E* and *Z* conformations stay in an equilibrium under conditions of light irradiation and high temperature, due to the high conformational flexibility of the molecule. Contrary, as sketched in Fig. 3b, in PTM derivatives **1** and **2** the *E* conformation is kinetically blocked, even when the ethylene unit is electronically excited with light, which impedes the $Z \rightarrow E$ process and, consequently, shifts the isomerisation equilibrium towards the less stable *Z* isomer.

In summary, we have studied the photo-induced isomerisation of *E*-*p*-vinylphenylene functionalised perchlorotriphenylmethane derivatives to the *Z* isomer. The isomerisation process has been monitored by HPLC which reveal an almost complete isomerisation. The higher absorption ability of the *E* isomer as compared to the *Z* isomer at the same wavelengths prevents the back $Z \rightarrow E$ isomerisation. No thermal back isomerisation takes place although the *E* isomer is the most thermodynamically favoured. Theoretical calculations point to the steric hindrance within the *Z* conformers leading to a possible kinetic blocking of the $Z \rightarrow E$ transition as the effect contributing to the thermal irreversibility of the $E \rightarrow Z$ process.

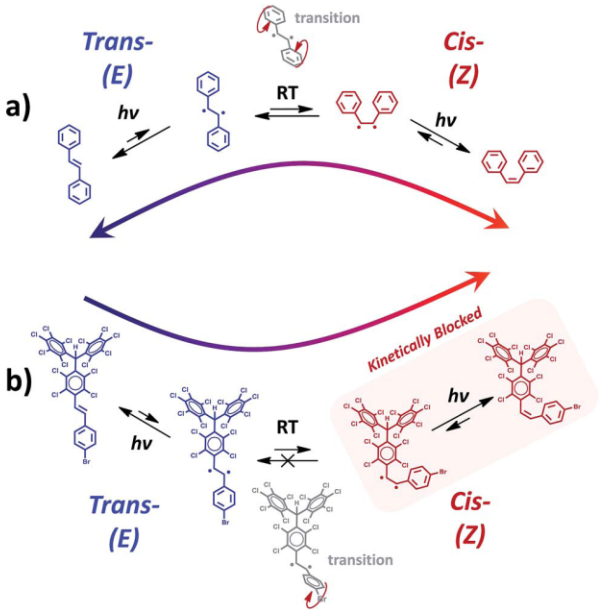

Fig. 3 (a) Mechanistic scheme of the isomerisation process taking place in stilbene (a) and the PTM derivative **1** (b), under the effect of light irradiation and temperature. In both cases light opens the central double-bond, which allows the free rotation of the ethylene unit due to thermal fluctuations (RT). Contrary to stilbene, PTM derivatives **1** and **2** get kinetically blocked in the *Z* conformation, shifting the equilibrium towards such conformation.

Experimental details

Synthesis of **1** was carried out as previously reported.[11]

Characterization of *E*-1

UV-vis: λ_{max} (THF)/nm 222 (ε/dm^3 mol^{-1} cm^{-1} 168 894), 297 (15 709). FT-IR (KBr): $\nu_{max.}$/cm^{-1} 3032, 1712 (CO), 1636, 1532, 1493, 1406, 1368, 1351, 1338, 1297, 1240, 1139, 1118, 1115, 1088, 969, 943, 871, 718, 688, 668, 648, 613, 536, 528, 507, 484. ^{1}H-NMR: δ_H(500 MHz; $CDCl_3$; Me_4Si) 7.60 (2H, d, J = 8.5 Hz, ArH), 7.48 (2H, d, J = 8.5 Hz, ArH), 7.13 (1H, d, J = 17 Hz), 7.09 (1H, d, J = 17 Hz, –(C_6Cl_4)–CH=CH–), 7.06 (1H, s, –(C_6Cl_4)–CH=CH–), 2.48 ppm (3H, s, –CH_3). ^{13}C-NMR: δ_C(101 MHz; $CDCl_3$; Me_4Si) 137.22, 136.88, 136.82, 136.24, 135.97, 134.82, 134.75, 134.58, 134.53, 133.68, 133.65, 133.37, 133.2, 133.14, 132.21, 132.18, 132.03, 128.19, 127.28, 124.11, 56.34 (α), 30.00 (–CH_3). MALDI-ToF (negative mode) ($C_{29}Cl_{14}H_{10}SO$, M = 902.8) m/z (M − 902.08); (M − 43 859.08), (M − 70 832.08).

Characterization of *Z*-1

UV-vis: λ_{max} (THF)/nm 222 (ε/dm^3 mol^{-1} cm^{-1} 104 222), 254 (35 917), 285 (14 087). ATR-IR $\nu_{max.}$/cm^{-1} 3125, 1711 (CO), 1534, 1493, 1462, 1358, 1338, 1296, 1262, 1239, 1207, 1188, 1133, 1115, 1090, 1015, 946, 871, 835, 808, 764, 719, 709, 687, 678, 661, 646, 630, 611, 573, 550, 541. ^{1}H-NMR: δ_H(600 MHz; CD_2Cl_2; Me_4Si) 7.30 (2H, d, J = 8.5 Hz, ArH), 7.02 (2H, m, ArH and 1H αH-PTM), 6.9 (1H, d, J = 12 Hz, –(C_6Cl_4)–CH=CH–), 6.6 (1H, d, J

= 12 Hz, -{C_6Cl_4}-CH=CH-), 2.38 (3H, s, CH_3) ppm. ^{13}C-NMR: δ_H(101 MHz; CD_2Cl_2; Me_4Si): δ = 193.87 (CO), 138.32, 137.52, 136.98, 136.96, 135.43, 135.31, 134.84, 134.52, 134.37, 134.30, 134.05, 134.01, 133.93, 133.73, 132.92, 132.68, 129.08, 128.66, 127.88, 125.95, 57.01 (α), 30.48 (-CH_3). MS (negative mode) ($C_{29}Cl_{14}H_{10}SO$, M = 902.8) *m/z* (M + 4906.4).

Synthesis of **2** (adapted from ref. 12): potassium *tert*-butoxide (95 mg, 0.87 mmol) was added to a solution of diethyl 4-[bis(2,3,4,5,6-pentachlorophenyl)methyl]-2,3,5,6-tetrachlorobenzyl phosphonate (500 mg, 0.57 mmol) in dry tetrahydrofuran (10 mL) at −90 °C, in a N_2/acetone bath. The resulting yellow-orange ylide solution was stirred for 30 minutes. Then, *p*-bromobenzaldehyde (188 mg, 1.04 mmol) dissolved in 4 mL of dry THF was added drop-wise. The solution was allowed to stir for 24 hours without changing the N_2/acetone bath, which reached room temperature along the reaction. The reaction was monitored by thin-layer chromatography (silica-gel). Once the reaction finished, one drop of concentrated HCl was added to the resulting dark purple solution, which turned on a yellow suspension. The reaction mixture was extracted with water (10 mL) and dichloromethane (10 mL). The phases were separated and the aqueous phase was washed with further dichloromethane (2 × 10 mL). The combined organic layers were dried over anhydrous sodium sulfate, filtered and concentrated under vacuum. Almost pure *E*-**2** isomer (97%) (473 mg, 92%) was obtained through purification by chromatography (silica gel with hexane as eluent).

Characterization of *E*-2

UV-vis: λ_{max} (C_6H_{12})/nm 222 (ε/dm^3 mol^{-1} cm^{-1} 107 000), 304 (29 000). FT-IR (KBr): ν_{max}/cm^{-1} 3015, 1635, 1590, 1535, 1490, 1405, 1365, 1340, 1295, 1240, 1140, 1075, 1010, 965, 940, 870, 805, 790, 715, 645, 532, 495. ^{1}H-NMR: δ_H(400 MHz; CD_2Cl_2; Me4Si) 7.59 (2H, m, ArH), 7.48 (2H, m, ArH), 7.12 (1H, d, J = 16.6 Hz, -{C_6Cl_4}-CH=CH-), 7.07 (1H, s, αH-PTM) 7.06 ppm (1H, d, J = 16.6 Hz, -{C_6Cl_4}-CH=CH-). ^{13}C-NMR: δ_C(101 MHz, CD_2Cl_2) δ = 137.70, 137.58, 137.05, 137.04, 136.63, 135.55, 135.48, 135.46, 135.26, 134.47, 134.37, 134.00, 133.98, 133.94, 133.91, 133.84, 132.89, 132.72, 132.37, 128.85, 124.22, 123.17, 57.09 (α). MS ($C_{27}Cl_{14}H_7Br$, M = 907.6) (negative mode) (*m/z*) (M − 1906.4). UV-Vis (C_6H_{12}) $\lambda(\varepsilon)$ [nm (M^{-1} cm^{-1})] 304 (29 000); 222 (107 000).

The *Z*-**2** isomer was obtained after irradiating a 3.7 mM solution in THF of the as synthesized **2** for 300 min. Then the solvent was evaporated to characterize the solid.

Characterization of *Z*-2

UV-vis: λ_{max}(THF)/nm 221 (ε/dm^3 mol^{-1} cm^{-1} 116 098), 284 (12 337). FT-IR ν_{max}/cm^{-1} 3015, 1725, 1585, 1485, 1370, 1335, 1295, 1240, 1130, 1070, 1010, 830, 805, 760, 710, 680, 655, 640, 550, 530, 460, 425. ^{1}H-RMN: δ_H(400 MHz; CD_2Cl_2; Me_4Si) 7.39 (2H, m, ArH), 7.00 (1H, s, αH-PTM), 6.91 (2H, d, J = 7.52 Hz, ArH), 6.83 (1H, d, J = 12.01 Hz, -{C_6Cl_4}-CH=CH-), 6.57 ppm (1H, d, J = 12.01 Hz, -{C_6Cl_4}-CH=CH-).^{13}C-RMN: δ_H(101 MHz; CD_2Cl_2; Me_4Si) 138.25, 136.97, 136.95, 135.56, 135.39, 135.29, 134.52, 134.34, 134.30, 134.07, 134.03, 133.95, 133.71, 133.57, 132.94, 132.65, 132.02, 130.04, 125.48, 122.58, 108.39, 57.01 (α). MS (negative mode) ($C_{27}Cl_{14}H_7Br$, M = 907.6) (*m/z*) (M − 1906.4).

DFT calculations

For assessing the isomerisation energy profile we twisted the molecular skeleton about the ethylene double-bond axis from 0 to 360 degrees. At each point the molecular structure was optimized while freezing the twist angle of the C=C bond. These constrained optimizations were done using the hybrid PBE0 functional[21,22] and a 6-311-G++ basis set as implemented in the Gaussian09 code [Gaussian 09, Revision E.01, D. J. Fox, Gaussian, Inc., Wallingford CT, 2009]. Within the same code, the time-dependent DFT method[23–29] was used to calculate absorption spectra. *Ab initio* molecular dynamics (AIMD) simulations at 450 K were run for 5 ps (1 ps of equilibrations plus 4 ps of production) using the Bussi–Donadio–Parrinello thermostat.[30] For these calculations the PBE0 functional and a "light" numerical basis set was used as implemented in the FHI-AIMS code.[31,32]

Acknowledgements

We thank Carlos Franco for his help with the HPLC analysis and Amable Bernabé CTQ2016-80030-R for the MALDI-ToF characterizations. We thank the Networking Research Center on Bioengineering, Biomaterials and Nanomedicine (CIBER-BBN); DGI (Spain) with projects BE-WELL CTQ2013-40480-R and MAT2012-30924, and Generalitat de Catalunya (grant 2009SGR00516, 2014SGR97 and XRQTC). We also thank the EU projects ERC StG 2012-306826 e-GAMES, ITN iSwitch (GA no. 642196), ACMOL (GA no. 618082) and CIG-ELECTROMAGIC (PCIG10-GA-2011-303989). Spanish Ministry of Economy and Competitiveness, through the 'Severo Ochoa' Programme for Centres of Excellence in R&D (SEV-2015-0496). N. C. thanks the RyC contract. F. B. acknowledges the FPU fellowship. F. B. is enrolled in the Materials Science PhD program of UAB.

References

1 B. G. Levine and T. J. Martínez, *Annu. Rev. Phys. Chem.*, 2007, **58**, 613–634.
2 H. M. D. Bandara and S. C. Burdette, *Chem. Soc. Rev.*, 2012, **41**, 1809–1825.
3 D. H. Waldeck, *J. Mol. Liq.*, 1993, **57**, 127–148.
4 E. Merino and M. Ribagorda, *Beilstein J. Org. Chem.*, 2012, **8**, 1071–1090.
5 C. A. Stanier, S. J. Alderman, T. D. W. Claridge and H. L. Anderson, *Angew. Chem., Int. Ed.*, 2002, **41**, 1769–1772.
6 E. Durgun and J. C. Grossman, *J. Phys. Chem. Lett.*, 2013, **4**, 854–860.
7 F. Vera, M. Mas-Torrent, J. Esquena, C. Rovira, Y. Shen, T. Nakanishi and J. Veciana, *Chem. Sci.*, 2012, **3**, 1958–1962.
8 F. Vera, M. Mas-Torrent, C. Avci, J. Arbiol, J. Esquena, C. Rovira and J. Veciana, *Chem. Commun.*, 2013, **49**, 7827–7829.

9 N. Crivillers, M. Mas-Torrent, J. Vidal-Gancedo, J. Veciana and C. Rovira, *J. Am. Chem. Soc.*, 2008, **130**, 5499–5506.
10 C. Simao, M. Mas-Torrent, N. Crivillers, V. Lloveras, J. Artés, P. Gorostiza, J. Veciana and C. Rovira, *Nat. Chem.*, 2011, **3**, 359–364.
11 S. Furukawa, N. Crivillers, A. Minoia, A. Ver Heyen, M. Mas-Torrent, C. Sporer, M. Linares, A. Volodin, C. Van Haesendonck, M. Van Der Auweraer, R. Lazzaroni, S. De Feyter, J. Veciana and C. Rovira, *J. Am. Chem. Soc.*, 2009, **131**, 6246–6252.
12 C. Rovira, D. Ruiz-Molina, O. Elsner, J. Vidal-Gancedo, J. Bonvoisin, J. P. Launay and J. Veciana, *Chemistry*, 2001, **7**, 240–250.
13 F. Leyssner, S. Hagen, L. Óvári, J. Dokić, P. Saalfrank, M. V. Peters, S. Hecht, T. Klamroth and P. Tegeder, *J. Phys. Chem. C*, 2010, **114**, 1231–1239.
14 V. Lloveras, J. Vidal-Gancedo, T. M. Figueira-Duarte, J. F. Nierengarten, J. J. Novoa, F. Mota, N. Ventosa, C. Rovira and J. Veciana, *J. Am. Chem. Soc.*, 2011, **133**, 5818–5833.
15 H. Meier, *Angew. Chem., Int. Ed.*, 1992, **31**, 1399–1420.
16 D. Gegiou, K. A. Muszjat and E. Fischer, *J. Am. Chem. Soc.*, 1968, **90**, 3907–3918.
17 W.-G. Han, T. Lowell, T. Liu and L. Noodleman, *ChemPhysChem*, 2002, **3**, 167–178.
18 D. H. Waldeck, *Chem. Rev.*, 1991, **91**, 415–436.
19 H. Petek, K. Yoshihara, Y. Fujiwara, Z. Lin, J. H. Penn and J. H. Frederick, *J. Phys. Chem.*, 1990, **94**, 7539–7543.
20 M. Lee, a. J. Bain, P. J. McCarthy, C. H. Han, J. N. Haseltine, a. B. Smith Iii and R. M. Hochstrasser, *J. Chem. Phys.*, 1986, **85**, 4341–4347.
21 C. Adamo and V. Barone, *J. Chem. Phys.*, 1999, **110**, 6158.
22 R. Improta and V. Barone, *Chem. Rev.*, 2004, **104**, 1231–1253.
23 R. Bauernschmitt and R. Ahlrichs, *Chem. Phys. Lett.*, 1996, **256**, 454–464.
24 M. E. Casida, C. Jamorski, K. C. Casida and D. R. Salahub, *J. Chem. Phys.*, 1998, **108**, 4439.
25 R. E. Stratmann, G. E. Scuseria and M. J. Frisch, *J. Chem. Phys.*, 1998, **109**, 8218–8224.
26 C. Van Caillie and R. D. Amos, *Chem. Phys. Lett.*, 1999, **308**, 249–255.
27 C. Van Caillie and R. D. Amos, *Chem. Phys. Lett.*, 2000, **317**, 159–164.
28 F. Furche and R. Ahlrichs, *J. Chem. Phys.*, 2002, **117**, 7433–7447.
29 G. Scalmani, M. J. Frisch, B. Mennucci, J. Tomasi, R. Cammi and V. Barone, *J. Chem. Phys.*, 2006, **124**, 094107.
30 G. Bussi, D. Donadio and M. Parrinello, *J. Chem. Phys.*, 2007, **126**, 014101.
31 V. Blum, R. Gehrke, F. Hanke, P. Havu, V. Havu, X. Ren, K. Reuter and M. Scheffler, *Comput. Phys. Commun.*, 2009, **180**, 2175–2196.
32 V. Havu, V. Blum, P. Havu and M. Scheffler, *J. Comput. Phys.*, 2009, **228**, 8367–8379.

Supporting Information of Publication #3

Study of the *E*–*Z* stilbene isomerisation in perchlorotriphenyl-methane (PTM) derivatives

RSC Adv., 2017,7, 15278-15283

F. Bejarano, I. Alcón, N. Crivillers, M. Mas-Torrent*, S. T. Bromley, J. Veciana*, C. Rovira*

Electronic Supplementary Material (ESI) for RSC Advances.

Supporting Information

Study of the *E-Z* stilbene isomerisation in perchlorotriphenyl-methane (PTM) derivatives

Francesc Bejarano,[#a] Isaac Alcon, [#b] Núria Crivillers,[a] Marta Mas-Torrent,[*a] Stefan T. Bromley,[b] Jaume Veciana[a] and Concepció Rovira[*a]

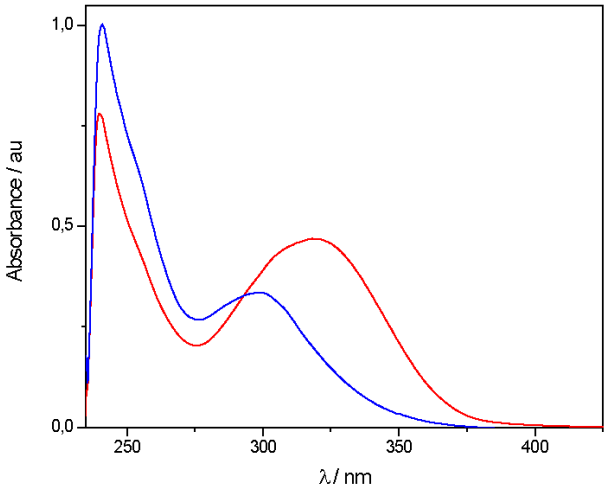

Figure S1. UV-vis spectrum in THF of *E*-**2**, in red, and of a *Z*-**2**/*E*-**2** mixture (99:1) in blue.

[a] *Dr. N. Crivillers, F. Bejarano, Dr. M. Mas-Torrent, Prof. J. Veciana and Prof. C. Rovira*
Corresponding Authors: M. Mas-Torrent and C. Rovira
Institute of Materials Science of Barcelona (ICMAB-CSIC) and Networking Research Center on Bioengineering, Biomaterials and Nanomedicine(CIBER-BBN) Campus de la UAB, 08193, Bellaterra ,Spain
E-mail: mmas@icmab.es; cun@icmab.es
[b] *Prof. S. T. Bromley*
Departament de Química Física & Institut de Química Teòrica i Computacional (IQTCUB), Universitat de Barcelona, 08028, Barcelona, Spain and Institució Catalana de Recerca i Estudis Avançats (ICREA), 08010 Barcelona, Spain.
[#] These authors contributed equally

Supporting information for this article is available on the WWW under http://dx.doi.org/10.1002/open.20xxxxxx.

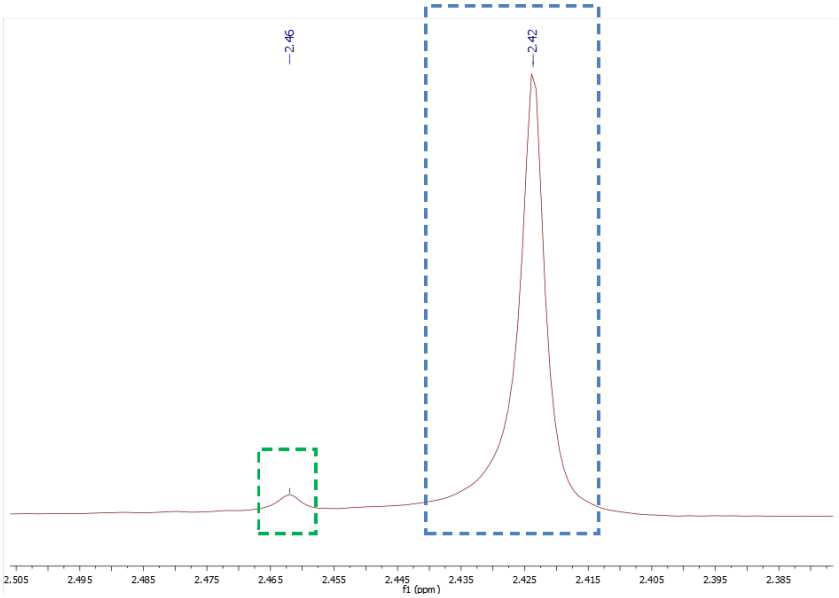

Figure S6. ^{1}H-NMR (400MHz) of the *Z*-**1** in CD_2Cl_2 after irradiation during 145 minutes. *Z*-isomer signals are squared in blue, whereas the non-converted *E*-isomer signals are squared in green.

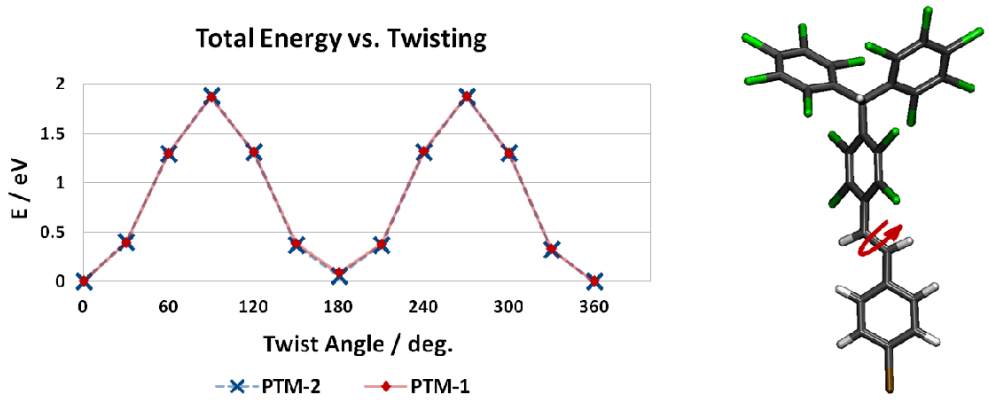

Figure S7. Manual twisting of the C=C bond (see red arrow on **2** structure) by means of DFT constrained optimizations using the PBE0 hybrid functional and a 6-311-G++ basis set as implemented in the Gaussian09 code. The plotted energies are referenced to the most stable conformation for each compound (i.e. *E*-**1** and *E*-**2**, respectively).

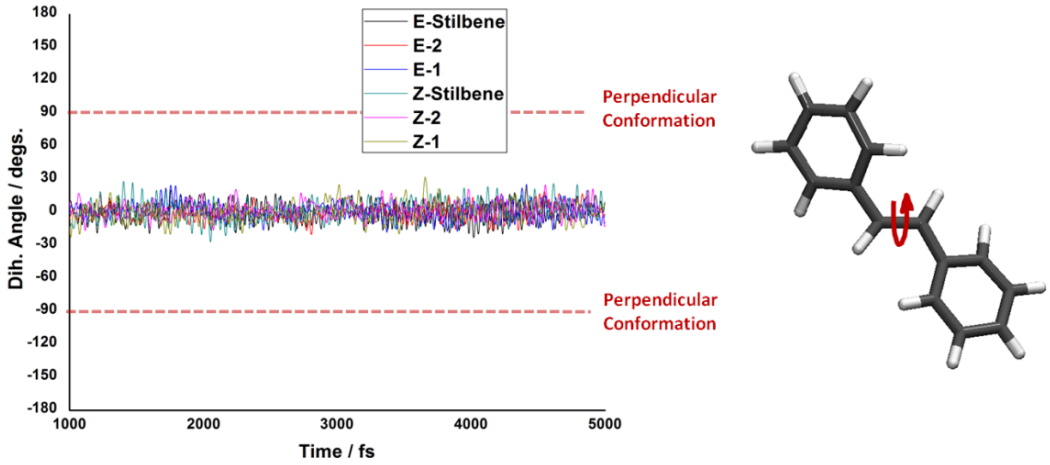

Figure S8. Variation of the dihedral angle of the central vinylene unit (C=C bond, see red arrow on stilbene structure) during 4 ps of a molecular dynamics simulation at 450K for our three studied compounds (**1**, **2** and stilbene) in each conformation (*E* and *Z*). Such calculations were performed using the PBE0 hybrid functional, the Bussi-Donadio-Parrinello thermostat and a light numerical basis set as implemented in the FHI-AIMS code. Red dashed lines point to the hypothetical perpendicular conformations for comparison.

3.4. Overview

Rissner et.al. theoretically proposed in 2012 some specifically designed quinoidal derivatives that, upon chemical adsorption on a metal substrate, such as Au, would generate a radical self-assembled monolayer (SAM) through a cascade electronic mechanism emerging from the covalent bonding with the surface and leading to an unpaired electron. Such ideas were backed up with periodic DFT calculations, supporting the fundamental prediction. However, from an experimental point of view the molecules proposed could not be used because they were not chemically persistent and, similarly, the resulting radical SAM would be very reactive under normal conditions. In **Publication-draft #1** presented in this thesis we have circumvented such problems by using a type of quinoidal compound which, upon generation of the unpaired electron, would lead to a sterically protected radical centre. Such steric protection is based on three aryl rings with six chlorine atoms in ortho- positions, and it is already known to be a very effective manner to ensure chemical persistence of organic radicals, such as in the family of PTM radicals. The compounds initially proposed were based on a quinoidal tris(2,4,6-trichloro-phenyl)methyl core (TTM) using an oxo-, nitro- and sulfo-carbonyl groups as anchoring units of the molecule, respectively. Only the oxo-carbonyl based TTM derivative (TTM-O) was stable enough and it was the chosen molecular candidate. TTM-O was deposited in Au, Ag and Cu under ultra-high vacuum and the deposited monolayer was studied by on-surface techniques such as X-ray photo-electron spectroscopy (XPS) and angle-resolved ultraviolet photoemission spectroscopy (ARUPS). In parallel we performed DFT-based periodic calculations to model the chemical adsorption of the chosen molecular building block on each metallic surface. On-surface measurements demonstrated the formation of singly occupied molecular orbitals at particular binding energies for the Ag based system. Our computational simulations showed that vertical adsorptions of the molecule on Ag and Cu led to spin-polarized states, in agreement with the theoretical studies by Rissner et.al. For Cu we observed a greater interaction with the substrate, especially with chlorine atoms of the molecule, which was also in agreement with the experimental observations in Cu where an important degree of dehalogenation and posterior polimerization (with no SOMO detection) was measured. Summarizing, the main contribution of **Publication-draft #1** is the experimental demonstration of the theoretical prediction by Rissner et.al. However, we also show that not all quinoidal candidates ensuring sterical protection of the later generated radical centre (via chlorine functionality) are stable enough due to the greatly twisted conformation of the upper quinoidal double-bond. In our case, only the TTM-O was stable enough to be used. Additionally, we also show that not all metallic substrates may be used to induce the radical formation: a very particular level of reactivity is needed which, in our particular case, has been proven to exist only in Ag (i.e. Au is too inert and Cu too reactive).

TTM-S (i.e. TTM with a sulfo-carbonyl group as anchoring unit) in solution generates the corresponding dithiol bi-radical (see **Publication #2** for details). As previously shown, such dithiol compounds may be used to form SAMs of the monomeric units on metals. Hence, after characterizing the TTM-S-S-TTM bi-

radical with electron paramagnetic resonance (EPR) and cyclic voltametry, Au and Ag substrates were functionalized with the compound via in-solution SAM formation procedures (see **Publication #2** for details). The functionalized surfaces were characterized by XPS where peaks corresponding to C, Cl and S were detected. Moreover, EPR measurements showed a peak corresponding to the unpaired electrons in the TTM-S monolayer. The corresponding singly occupied molecular orbital (SOMO) was also detected by UV-vis. photo-electron spectroscopy (UPS). Cyclic voltammetry measurements (CV) were also done where typical reduction peaks of PTMs were detected, confirming the electro-activity of the monolayer. Our periodic DFT calculations using the PBE functional confirmed the presence of spin polarized states centred on the TTM core for the upstanding conformation (i.e. vertical) of the chemically adsorbed molecule. Our DFT results also showed a small, but non negligible, spin polarization on the metallic surface. Overall, **Publication #2** confirmed the possibility of preparing TTM-S SAMs from the corresponding bi-radical directly bonding the radical core to the surface (i.e. without use of linker chains of any sort) while maintaining the unpaired electron localized in the TTM core (i.e. no charge transfer phenomena between the monolayer and the substrate).

With regard to **Publication #3**, both PTM ethylene derivatives shown in the associated paper were synthesized through a Wittig and Horner–Wadsworth–Emmons reactions, respectively. These molecules were composed of the hydrogenated (closed-shell) PTM unit bonded to an ethylene unit (C=C) functionalized with a phenyl ring. The phenyl ring was then functionalized in the *para-* position either with a thio-acetate group (compound 1) or a Br atom (compound 2). Due to sterical reasons, the E isomer (trans-) was obtained as major product for compounds 1 and 2 with 92% and 99% purity, respectively. E-isomers were separated from the corresponding Z ones. The photo-isomerization was performed using a Hg(Xe) 300 W lamp placed at 30 cm from a 0.07 mM solution of each (E) compound in a mixture of THF/ACN (1:1). To follow the E → Z conversion consecutive aliquots from the reaction solution were taken during the irradiation process and analyzed by High Performance Liquid Chromatography (HPLC). As shown in **Publication #3**, the E → Z conversion takes place almost completely, reaching a 90% of Z conformer fraction. Quite surprisingly, the Z → E isomerisation was not taking place by light irradiation, despite the fact the E isomer is the thermodynamically most stable conformer. Z solutions were heated up under reflux conditions in different solvents with different polarities and reflux temperatures, however, the conversion back to the E isomer did not take place. As a final experimental trial, in the Z solutions a catalytic amount of iodine was added, due to the fact it is a common methodology to convert isomeric mixtures to the E isomer (see *J. Am. Chem. Soc.*, 2011, 133 (15), pp 5818–5833). Even then, either compound 1 nor 2 were converted to the E isomer. UV-vis. spectra show both conformers (Z and E) absorb light at close wave-lengths and the E conformer shows a significantly higher absorbance. This could explain why under light irradiation the Z isomer is produced with higher yield; i.e. the E isomer is more photo-excited (higher absorption coefficient) and hence the equilibrium is displaced towards the Z

conformer. However, the impossibility of forming the E isomer with the treatment of iodine, which is an established method to catalyze the Z→E process, cannot be explained due to the different light absorbance and points to the possibility that another physico-chemical phenomenon is the cause of such particular results.

DFT calculations were done to model the behaviour of stilbene (reference compound) and compounds 1 and 2. Differently to azo-benzenes (N=N), where the E ↔ Z conversion may take place through different structural mechanisms, for ethylenes (C=C) there is mainly one mechanism, and it is the twisting of the C-C bond once the π double-bond is broken (be it by light irradiation or chemical treatment). Firstly, we modelled such twisting of the ethylene unit, where we found an energetic barrier for such a twisting process (going from E to Z and from Z to E conformers) of around 1.9 eV, coinciding with previous reports (see ref 10). More interestingly we found out that only certain conformations of the PTM unit and the functionalized phenyl ring with respect to the ethylene unit allowed for the twisting process of the ethylene unit. In other words, there were certain conformations of both the PTM and the phenyl ring that did not allow for the twisting of the ethylene unit because during such process both groups would physically find each other blocking any further twist. To assess the conformational behaviour of such systems we performed AIMD simulations of compounds 1 and 2 and stilbene at 300K. We found that in the trans- isomers for stilbene and compounds 1 and 2 both PTM and phenyl units had the freedom to rotate, hence accessing into all possible conformations allowing the twisting of the ethylene unit (see **Publication #3** for details). However, in the Z isomer, compounds 1 and 2 showed a constrained conformation where the PTM and phenyl units were close to each other and, due to the bulky chlorine atoms in the PTM unit, both groups bonded to the ethylene unit could not freely twist. This did not happen for the less sterically constrained stilbene. Such a conformational constraint, in turn, based on the constrained 0K calculations previously done (results shown in the ESI of **Publication #3**), was blocking the photo-activated twist of the ethylene unit, due to the fact that the PTM and phenyl rings would find each other in the twisting process. This relatively complex structural scenario explains the particular behaviour of the PTM-based ethylene derivatives studied in **Publication #3** and the difficulties of interconverting the photo-induced Z conformer back to the most thermodynamically stable E conformer, by light, temperature, or chemical treatment.

Chapter 4
From aryl rings' twist to TAM 2D-COFs

4.1 Introduction

4.1.1 What "controls" the unpaired electron in TAMs?

As explained in the introduction of this PhD thesis, the use of TAMs in materials science and electronics has greatly increased during the last decades.[1] Indeed, TAMs have been used to prepare different sorts of materials and devices such as metal-organic frameworks with solvent sensitive magnetic behaviour (Fig. 4.1a),[2] self-assembled monolayers with redox switchable optical and magnetic properties (Fig. 4.1b),[3] single-molecule devices with magnetoresistance phenomena[4] (Fig. 4.1c) and magnetic plastics[5] (Fig. 4.1d).

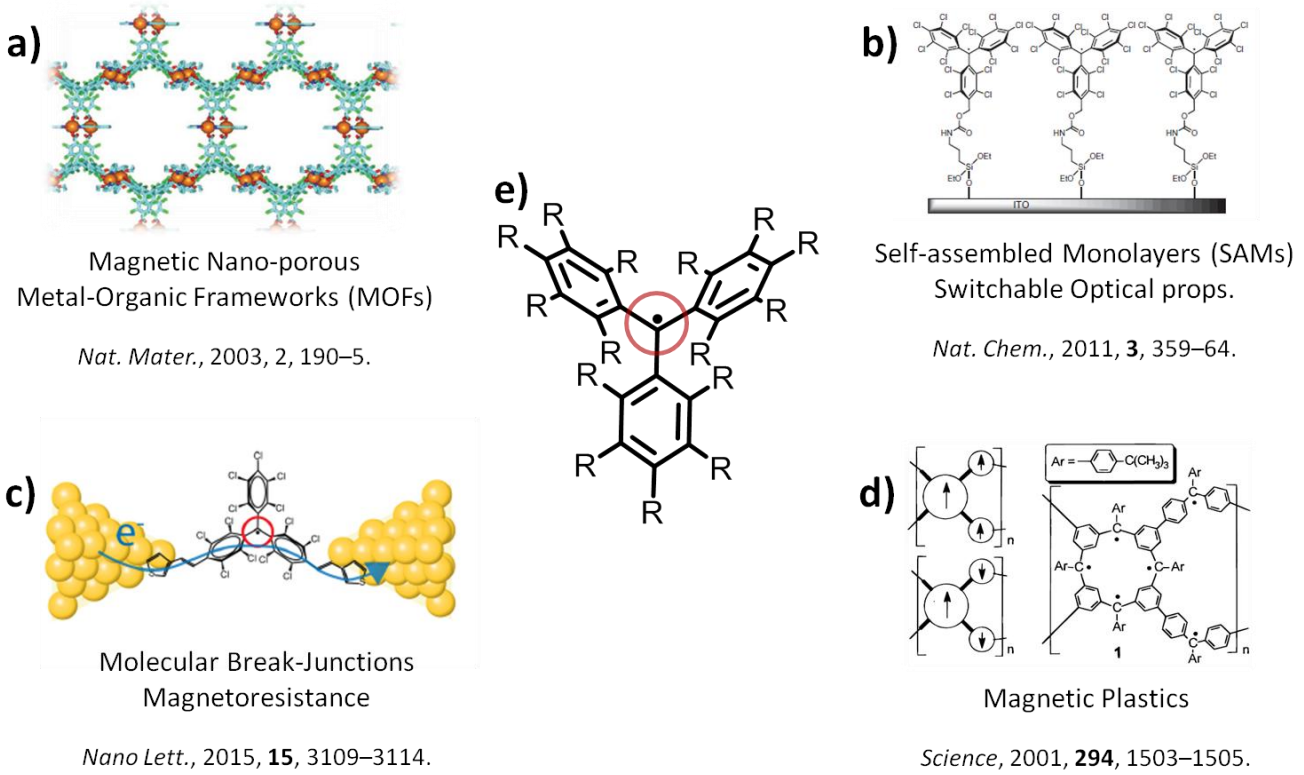

Fig. 4.1 Utilization of TAMs to prepare different sorts of materials and devices such as magnetic MOFs **(a)**, redox-switchable SAMs **(b)**, magnetoresistance single-molecule junctions **(c)** and magnetic plastics **(d)**. **e)** In TAMs, the unpaired electron giving rise to all these interesting characteristics resides on the central carbon atom but it is spread over the entire π-conjugated system.

It is very interesting to realize that, for all such cases, the main target properties in each case are directly related with the existence of the unpaired electron in these open-shell molecules. For instance, magnetism (in Fig. 4.1a,d) is related with the spin moment of unpaired electrons, the colour and fluorescence (Fig. 4.1b) are associated with electronic transitions involving the electronic levels of the unpaired electron (i.e. the singly occupied/unoccupied molecular orbitals; SOMO/SUMO), the redox activity of TAMs (being easily reduced to the anion) is also because of the existence of the unpaired electron and, finally, the enhanced electrical conduction through TAMs (Fig. 4.1c) takes place through the SUMO, as demonstrated in ref 4. Therefore, at the start of this PhD thesis it was a primary objective for us to

understand the nature of the unpaired electron in TAMs and, more importantly, if there was any chemical or structural way to control its spatial distribution and energy. If there was a simple manner to manipulate such unpaired electrons, this would lead to fine control over all the above mentioned properties for materials science applications.

As shown in Fig. 4.2a, optimizing the structure of the simplest TAM within the DFT scheme (using the PBE functional[6] in Gaussian09[7]), the triphenylmethyl (or TPM, where all aryl rings are hydrogenated), one may take a look at the α-spin distribution (in green, associated to the unpaired electron) which permits one to see how the unpaired electron in TAMs is distributed. Here it can be seen that the unpaired electron is not completely localized on the central carbon atom (herein called αC) but it is actually spread over the entire molecule through the π-conjugated system. This is because the SOMO (and SUMO) associated to the unpaired electron are *p* orbitals, and hence are π-conjugated through the three aromatic aryl rings directly bonded to αC.

Lewis resonance forms of π-conjugated electrons in organic systems normally provide a reasonable estimation about how these electrons behave. If we write down the different resonance forms that the unpaired electron (black dot in Fig. 4.2b) may follow through a particular aryl ring, we may see that besides being in the upper carbon atom, it may also reside in the *ortho*- and *para*- positions of a particular aryl ring. Very clearly, this is confirmed upon looking at the computed α-spin density in Fig. 4.2a (in green), where we may see it distributes only through those three positions, i.e. in αC and in *ortho*- and *para*- positions of each aryl ring. This π-conjugation of the unpaired electron is responsible for most of the interesting properties previously mentioned: electrical conduction through TAMs[4] takes advantage of the fully delocalized SUMO orbital (i.e. a delocalized open channel for electrons to conduct); magnetism in TAM-based framework materials[2,5] is also promoted through delocalized spin distributions enhancing magnetic interactions; the peculiar optical properties of TAMs, such as the reported non-linear optical response,[8] are also found to arise due to the π-conjugated unpaired electron.

If we take a closer look at the Lewis resonance forms in Fig. 4.2b, we may realize that those where the unpaired electron (black dot) resides in a position in the aryl ring require the formation of a double-bond between such an aryl ring and the upper carbon atom (red rectangles in Fig. 4.2b). Double-bonds are formed through overlap of *p* orbitals (perpendicular to the bonding direction) of the involved carbon atoms. Due to the fact that the overlap between those *p* orbitals forming the double bond depends on the twist angle between them (the less coplanar, the lower the overlap), it turns out that the degree of delocalization of the unpaired electron depending on the formation of such double-bond (see Fig. 4.2b) will entirely depend on the twist angle between the sp^2 αC plane and the aryl ring plane (Fig. 4.2c). Different theoretical works from the 50s' and 60s', comparing their results with hyperfine coupling constants extracted from EPR measurements, pointed out that the spin delocalization and twist angle

follow a $cos^2\varphi$ correlation,[9–12] where φ is the twist angle between both planes as represented in Fig. 4.2c.

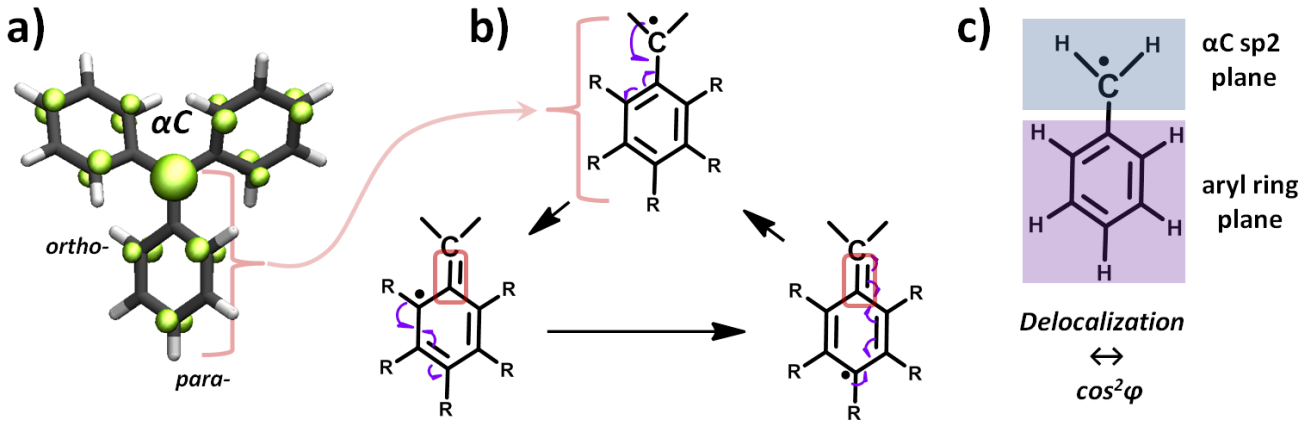

Fig. 4.2 a) Structure of the triphenylmethyl (or TPM), the simplest TAM, with the α-spin density associated to the unpaired electron, in green. **b)** Lewis resonance forms explaining the delocalization mechanism of the unpaired electron through each aryl rings bonded to αC. **c)** Molecular planes defining the twist angle that determines the localization/delocalization of the unpaired electron in the simplified phenyl-methyl radical (so-called benzyl radical).

Having such a simple structural parameter to control the localization/delocalization of the unpaired electron in TAMs would represent a powerful tool to tune all related characteristics with potential for materials science applications (see above). However, in TAMs there are three aryl rings bonded to αC and no study has evaluated whether the chemical functionalization of these aryl rings also influences the spatial distribution of the unpaired electron.

In **Publication #4** presented in this chapter our core goal was to clarify the actual correlation between the localization of the unpaired electron in TAMs (represented by the corresponding spin localization) and the three aryl ring twist angles. Moreover we also assess the effect of different chemical functional groups of aryl rings with different electro-negativities and test the effect of finite temperatures on the electronic-structural correlation, where both bond vibrations and aryl ring rotations take place. Overall, as it is explained in detail in this contribution and later summarized, in **Publication #4** we have been able to unambiguously demonstrate for the first time that in TAMs the spin localization (and hence the unpaired electron) is fully determined by the three aryl ring twist angles, following a linear correlation with the average of the cosines squared of the three dihedrals ($\langle cos^2\varphi_i \rangle$). We also show that the chemical functionalization of aryl rings only affects the spin localization as much as it determines each of the three φ_i values via steric hindrance, and also demonstrate that such electronic-structural correlation is robust at finite temperatures. Consequently, our results show that if it was possible to manipulate aryl ring twist angles in a TAM-based material or device, the localization/delocalization of the unpaired electrons of the system could be controlled and, with it, any related property such as light-absorption bands,[3] electrical conduction[4] or magnetic interactions.[2]

4.1.2 Towards external manipulation of aryl ring twist angles

Aryl ring twist angles, as shown in **Publication #4** (and previously demonstrated for TAMs by Lewis[13]) are determined by the particular chemical functionalization of aryl rings, mainly due to steric hindrance effects. Such a correlation was utilized by Venkataraman and co-workers[14] to tune the twist angle in bi-phenyl single-molecule break junctions to demonstrate that the electrical conduction through such single-molecule device entirely depends on this conformational parameter, also following a cos^2 correlation (see Fig. 4.3).

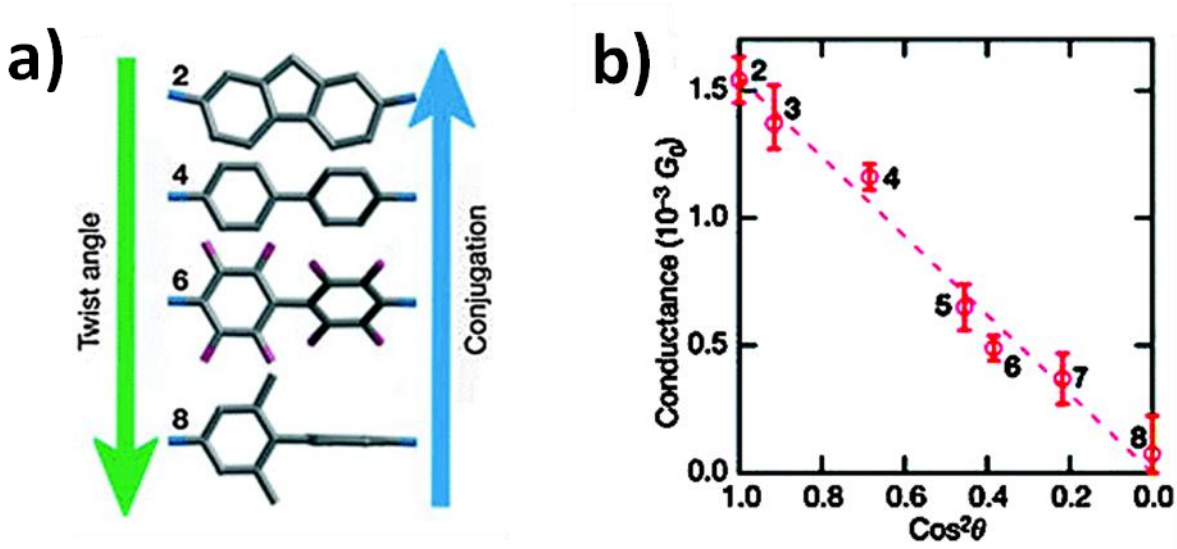

Fig. 4.3 a) Bi-phenyl series of compounds studied by Venkataraman and coworkers in 2006 as molecular wires in single-molecule break junctions. The different aryl ring functionalizations force different dihedral angles between the two rings (green arrow) and, correspondingly, different degrees of electronic π-conjugation (blue arrow). **b)** Measured electrical conductivity versus $cos^2\theta$, where θ is the dihedral angle between both phenyl rings in each single-molecule break junction.

Hence, chemical functionalization is a powerful manner to tailor aryl ring twist angles and, in turn, determine certain properties of our molecular material or device such as electrical conductance[14] or spin localization (**Publication #4**). However, chemical functionalization does not allow for externally manipulating aryl ring twist angles; in other words, given a chemical design of our molecules, the twist angle becomes a fixed parameter of our system. Hence, we need another way to manipulate aryl ring twist angles in order to design multi-functional TAM-based materials with externally controllable properties.

As it will be explained in **Publication #5**, it turns out that there are no experimentally realized TAM-based materials that accomplish all structural requirements in order to allow for an efficient external manipulation of aryl ring twist angles of TAM monomers. We find that most appropriate type of materials are 2D-covalent organic frameworks (2D-COFs; for more information about this type of novel materials see Section 1.2 in the Introduction of this thesis – Chapter 1). Having such periodically ordered networks composed of TAM units covalently bonded with each other would permit one to apply strong enough external forces to overcome steric hindrance (which determines aryl ring twist angles) without breaking

the basic skeleton of the 2D material. Moreover, the ordered structure of the material should ensure a homogeneous structural response to any external stimulus, hence facilitating the interpretation of the electronic outcome and its reproducibility. As explained in **Publication #5**, we found that stretching our designed TAM 2D-COFs in one direction parallel to the materials' plane is an efficient manner to externally manipulate aryl ring twist angles of all TAM units composing it. Studying the effect of such mechanical distortion on the electronic structure of the material, we demonstrate the success of our approach to design TAM-based materials with externally controllable properties. Additionally, we also assess how the chemical functionalization of the network affects such external controllability and what is the effect of finite temperatures.

4.1.3 Searching for structural flexibility and chemical persistence

As previously stated, perchlorotriarylmethyls (or PTMs) are the most persistent (i.e. chemically stable) class of TAMs because chlorine atoms provide a steric shielding effect on the central carbon atom (i.e. αC) where the unpaired electron mainly resides. The triphenylmethyl, or TPM, (i.e. fully hydrogenated TAM) only lasts in solution for few days[15] due to its reaction with atmospheric O_2.[16,17] Conversely, PTMs are expected to last for tens of years under normal conditions,[18,19] which highlights the tremendous steric protection effect of chlorine atoms on the αC central position. As a consequence, PTMs are by far the most utilized type of TAM building blocks for materials science and electronics,[1] as explained in detail in Chapter 1.

As demonstrated in **Publication #5**, chemical functionalization of aryl rings in TAM units within the 2D-COF (see Fig. 4.4) determine the ease by which aryl rings may be externally twisted by uniaxial strain. For the TPM-based 2D-COF (Fig. 4.4a), due to the small sterical hindrance imposed by H- atoms, a significant twisting of aryl rings is caused upon strain application, which then leads to a detectable variation of the properties of the 2D material. However, for the most experimentally relevant PTM 2D-COF (Fig. 4.4b), the huge steric hindrance of bulky Cl- atoms prevents an effective manipulation of the aryl ring twist angles. Consequenly, as showed in **Publication #5** by running AIMD simulations at 300K, even upon stretching the PTM 2D-COF by a 20% of its length, no detectable changes of the material's electronic properties take place at room temperature.

This raises the problem that bulky perchlorated aryl rings needed for chemical persistence prevent the structural flexibility required to design multi-functional TAM 2D-COFs with externally controllable properties. To resolve such a dilemma in **Publication #6** we made use of force-field calculations (using the universal force-field, UFF[20]) to screen over a number of different chemical functionalizations of TAM monomers composing the 2D material, focusing on the halogen series of atoms and studying different degrees and distributions of halogenation.

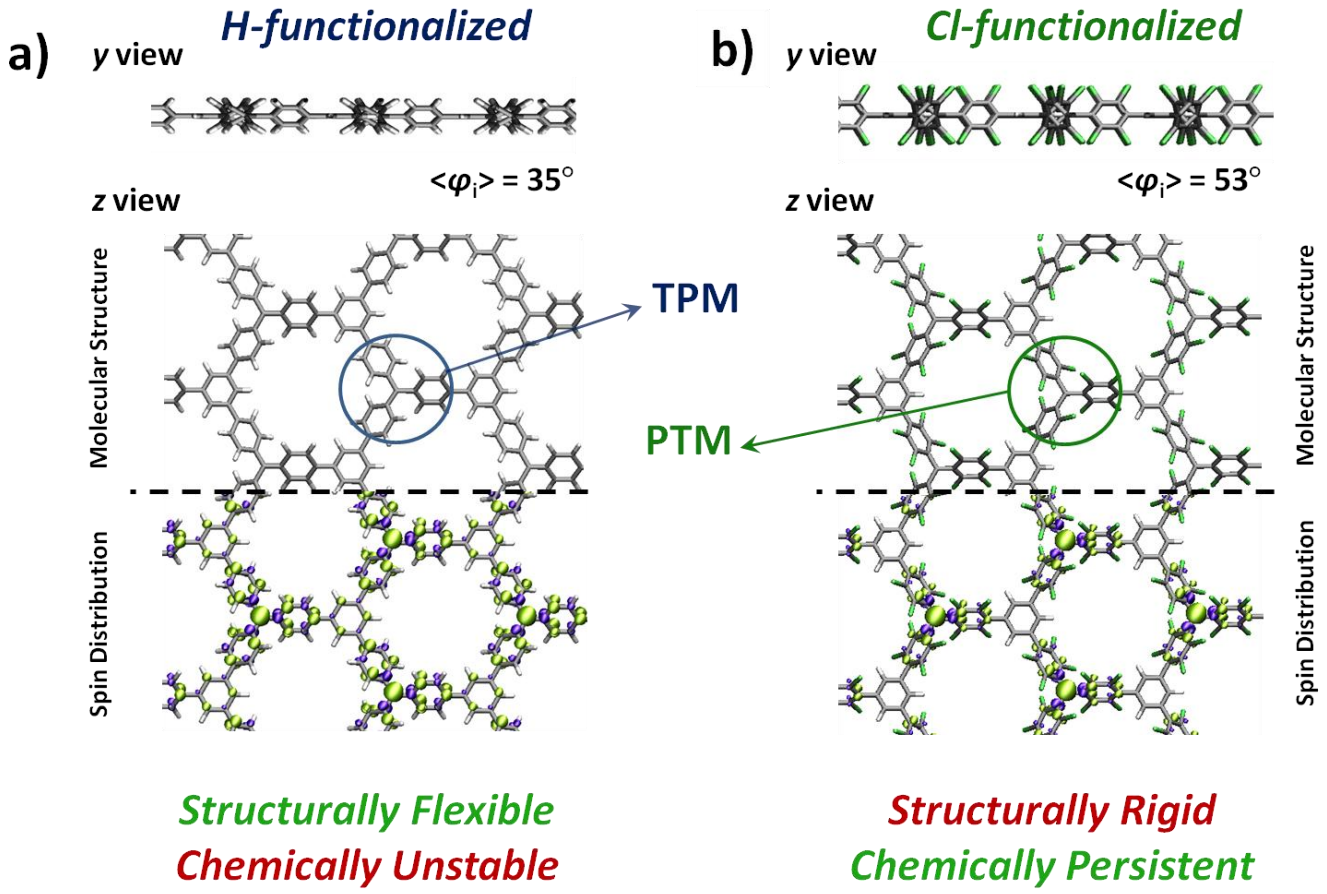

Fig. 4.4 TPM **(a)** and PTM **(b)** based 2D-COFs from the *y* and *z*-views, also plotting the associated spin density in the bottom panels (green: α spin; purple: β spin).

For each designed TAM 2D-COF based on a particularly functionalized TAM monomer, we smoothly stretch its structure uniaxially as done in **Publication #5** and measure the resulting aryl ring twisting by calculating the average twist angle within the unit cell $\langle \varphi_i \rangle$ at each stretching point. As shown in **Publication #6**, considering 50 different TAM 2D-COFs each composed of a distinct TAM monomer and performing over 1700 FF calculations to obtain the stretching profile for each of them, we conclude that there are experimentally available TAM monomers which could be used to construct TAM 2D-COFs where chemical persistence and structural flexibility would co-exist.

4.2 Bibliography

1 J. Veciana and I. Ratera, in *Stable Radicals: Fundamentals and Applied Aspects of Odd-Electron Compounds*, ed. R. G. Hicks, John Wiley & Sons, Inc., 2010, pp. 33–80.

2 D. Maspoch, D. Ruiz-Molina, K. Wurst, N. Domingo, M. Cavallini, F. Biscarini, J. Tejada, C. Rovira and J. Veciana, *Nat. Mater.*, 2003, **2**, 190–5.

3 C. Simão, M. Mas-Torrent, N. Crivillers, V. Lloveras, J. M. Artés, P. Gorostiza, J. Veciana and C. Rovira, *Nat. Chem.*, 2011, **3**, 359–64.

4 R. Frisenda, R. Gaudenzi, C. Franco, M. Mas-Torrent, C. Rovira, J. Veciana, I. Alcon, S. T. Bromley, E. Burzurí and

H. S. J. van der Zant, *Nano Lett.*, 2015, **15**, 3109–3114.

5 A. Rajca, J. Wongsriratanakul and S. Rajca, *Science*, 2001, **294**, 1503–1505.

6 J. P. Perdew, K. Burke and M. Ernzerhof, *Phys. Rev. Lett.*, 1996, **77**, 3865–3868.

7 M. J. Frisch, G. W. Trucks, H. B. Schlegel, G. E. Scuseria, M. A. Robb, J. R. Cheeseman, G. Scalmani, V. Barone, B. Mennucci, G. A. Petersson, H. Nakatsuji, M. Caricato, X. Li, H. P. Hratchian, A. F. Izmaylov, J. Bloino, G. Zheng, J. L. Sonnenberg, M. Had and D. J. Fox, 2009.

8 I. Ratera, D. Ruiz-Molina, C. Sporer, S. Marcen, S. Montant, J.-F. Létard, E. Freysz, C. Rovira and J. Veciana, *Polyhedron*, 2003, **22**, 1851–1856.

9 F. C. Adam and S. I. Weissman, *J. Am. Chem. Soc.*, 1958, **80**, 2057–2059.

10 M. Karplus and G. K. Fraenkel, *J. Chem. Phys.*, 1961, **35**, 1312–1323.

11 J. A. Pople and D. L. Beveridge, *J.Chem.Phys.*, 1968, **49**, 4725–4726.

12 M. J. S. Dewar, *J. Am. Chem. Soc.*, 1952, **74**, 3345–3350.

13 G. N. Lewis, D. Lipkin and T. T. Magel, *J. Am. Chem. Soc.*, 1944, **66**, 1579–1583.

14 L. Venkataraman, J. E. Klare, C. Nuckolls, M. S. Hybertsen and M. L. Steigerwald, *Nature*, 2006, **442**, 904–907.

15 M. Gomberg, *J. Am. Chem. Soc.*, 1903, **25**, 1274–1277.

16 M. Gomberg, *J. Am. Chem. Soc.*, 1900, **22**, 757–771.

17 M. Gomberg, *J. Am. Chem. Soc.*, 1901, **23**, 496–502.

18 M. Ballester, J. Riera, J. Castañer, C. Badía and J. M. Monsó, *J. Am. Chem. Soc.*, 1971, **93**, 2215–2225.

19 J. Guasch, X. Fontrodona, I. Ratera, C. Rovira and J. Veciana, *Acta Crystallogr.*, 2013, **C69**, 255–7.

20 A. K. Rappe, C. J. Casewit, K. S. Colwell, W. A. Goddard III and W. M. Skiff, *J. Am. Chem. Soc.*, 1992, **114**, 10024–10035.

21 X. H. Liu, C. Z. Guan, D. Wang and L. J. Wan, *Adv. Mater.*, 2014, **26**, 6912–20.

22 Q. Fan, J. M. Gottfried and J. Zhu, *Acc. Chem. Res.*, 2015, **48**, 2484–2494.

4.3 Results

Publication #4

Structural control over spin localization in triarylmethyls

RSC Adv., 2015, 5, 98593-98599

Isaac Alcon and Stefan T. Bromley*

RSC Advances

PAPER

View Article Online
View Journal | View Issue

Cite this: *RSC Adv.*, 2015, **5**, 98593

Structural control over spin localization in triarylmethyls†

Isaac Alcón[a] and Stefan T. Bromley*[ab]

Triarylmethyls (TAMs) are a class of long-lived purely organic radicals discovered at the beginning of the twentieth century. The chemical versatility and high stability of TAMs have lead to their application in many fields of science and technology. All compounds of this class are composed of three aryl rings bonded to a central carbon atom, where their unpaired electron mainly resides. Due to the π-conjugated electronic nature of this molecular structure, the possibility arises of controlling the unpaired electron localization (*i.e.* spin localization) by the torsion angles of the three aryl rings. By using density functional theory calculations (DFT) we have carefully investigated this phenomenon for a wide range of TAMs and probed how it is influenced by other important parameters such as chemical functionalization and temperature. Our results demonstrate that a single general spin *versus* structure relation is followed for all of our studied TAMs confirming that having a predictable structure-dependent spin localisation is an intrinsic feature of these radicals. Considering that spin localisation in TAMs is linked to many other important properties (*e.g.* magnetic interactions, optical absorption bands, magnetoresistance phenomena), the fact that manipulation of aryl ring twist angles could lead to molecular level control over such features presents enormous potential for future scientific and technological applications.

Received 15th September 2015
Accepted 3rd November 2015

DOI: 10.1039/c5ra19008h

www.rsc.org/advances

Introduction

Over 100 years ago Moses Gomberg prepared the first persistent radical; the triphenylmethyl.[1] This discovery launched the field of radical chemistry at the beginning of the twentieth century and, since then, more than hundred triarylmethyl (TAM) derivatives have been synthesized.[2–20] All molecules in this class possess a main skeleton composed of three aryl rings bonded to a central carbon atom, where their unpaired electron mainly resides (Fig. 1). Such is the chemical versatility[13] and high stability[21,22] of this class of aromatic organic radicals, they have been widely promoted for many applications such as Electron Spin Resonance (EPR) imaging,[23–29] oxygen detection and pH monitoring,[25,30–37] Dynamic Nuclear Polarization (DNP),[38–42] donor–acceptor systems,[12,43–46] spin labelling of biomolecules,[3,29] discotic liquid crystals,[47] organic light emitting diodes,[14,48] molecular magnetic materials[21,49–55] and molecular spintronics,[45,56–60] among others.[12,14,61–63]

In TAMs, the most interesting physic-chemical properties such as magnetic interactions,[50] optical absorption bands,[64] electrical conductivities[59] or magnetoresistance phenomena[65] are closely linked to their unpaired electron. For this reason, it would be enormously useful for any TAM-based application to fully understand what factors mainly influence their unpaired electron distribution (*i.e.* spin distribution).

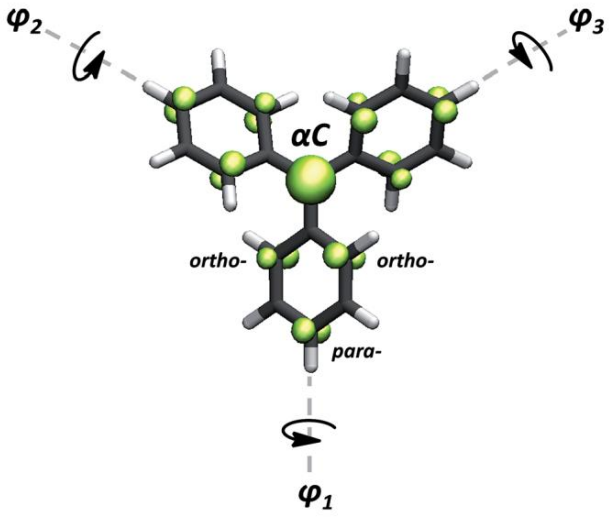

Fig. 1 Generic TAM structure. Their unpaired electron (*green*) mainly resides on the central methyl carbon atom (αC) but, due to the π-conjugated nature of these molecules, it partially delocalizes to the *ortho*- and *para*-positions of each aryl ring.

In 1944 Gilbert N. Lewis suggested that TAM radicals are not completely planar but, instead, their three aryl rings are

[a]*Department de Química Física & Institut de Química Teòrica i Computacional, Universitat de Barcelona, C/Martí i Franquès 1, E-08028 Barcelona, Spain. E-mail: s.bromley@ub.edu*

[b]*Institució Catalana de Recerca i Estudis Avançats (ICREA), E-08010 Barcelona, Spain*

† Electronic supplementary information (ESI) available. See DOI: 10.1039/c5ra19008h

twisted with respect to the sp^2 plane of the central methyl carbon atom (Fig. 1).[66] Later, this was confirmed by the measured magnetic properties of certain TAMs whereby it was found to be necessary to consider the non-planarity of the aryl rings in order to properly interpret the observations.[67–70] As suggested at the time, the link between non-planarity and magnetism is due to the influence of dihedral angles on the spin delocalization in magnetic aromatic systems.[67–71] With some simplifying assumptions (*e.g.* fixing all structural degrees of freedom apart from the torsion angle) one can employ π-orbital overlap arguments to estimate that the spin delocalization through a certain aryl ring is proportional to the cosine squared of its dihedral angle with respect to the sp^2 plane of the radical centre (*i.e.* $\cos^2\theta$).[67,68,70,72] Later, experimental works on some specific TAMs also effectively showed that the spin distribution is influenced by the torsion angles of the aryl rings.[16,18,20,73] However, despite these important early studies, as far as we know, there exists no detailed systematic study of the spin-localization *versus* structure relation covering a wide range of TAMs. Moreover, the influence of chemical functionalisation and temperature on this relation is currently unclear. The existence of a general and robust spin *versus* structure relationship for all TAMs would be extremely useful for the tailored design of TAM-based applications, and could open the possibility of preparing molecular materials with controllable magnetic, optical and electrical properties.

Herein, we have used *ab initio* density functional theory (DFT) calculations to accurately study the dependence of spin localization in TAMs on their chemical and structural characteristics. We consider the first order assumption that the spin localisation should entirely depend on the average of the cosine squared of each dihedral angle of the three aryl rings ($\langle\cos^2\varphi_i\rangle$). We test this proposal for a wide range of dihedral angle combinations and different chemical functionalisations. More generally, we also study whether this spin localisation *versus* structure relationship holds at finite temperatures. Our results also thus provide detailed insights into important and subtle dynamic factors that influence the degree of spin localization under more realistic conditions. We expect our results will be of interest and use for experimental chemists in order to optimize TAMs for future applications.

Methodology

The optimised structures of all TAM derivatives reported herein (see ESI† for chemical structures) were obtained using DFT calculations employing the PBE0 hybrid functional[74] and a 6-311++g(d,p) basis set as implemented in the GAUSSIAN-09 code.[75] The PBE0 functional has been demonstrated to provide a very good account of the geometry, electronic structure and spin polarisation in organic radicals.[74] Calculated spin densities were atomically partitioned using the Hirshfeld scheme.[76] For independently benchmarking our computational methodology we have also tested its capacity to reproduce reported EPR experimental data on a range of TAM derivatives.[16] The good match between our calculated spin dipolar coupling constants and the experimental data further validates the level of theory utilised herein. A discussion of this comparison and the corresponding results can be found in the ESI.†

For assessing the validity of our proposal at higher temperatures, canonical *ab initio* molecular dynamics (AIMD) calculations of 10 picoseconds (5 ps of equilibration followed by 5 ps of production) at a temperature of 300 K were also performed employing a 0.5 femtosecond time step and the Bussi–Donadio–Parrinello thermostat.[77] The AIMD runs were calculated using the FHI-AIMS code[78] employing the PBE0 functional and a light basis set for all atoms.

Results and discussion

As suggested by Lewis[66] and later corroborated by experimental work,[16,20] the dihedral angle of each aryl ring in TAMs mainly depends on the particular chemical functionalization of the molecule. Thus, for assessing the spin localization dependence on the three aryl rings twists, we first studied the structural and electronic properties of a set of 27 previously reported TAMs with a wide range of chemical and structural properties. Besides studying some triphenylmethyl derivatives, we also included some perchloro- and perfluoro-TAMs with different functionalizations.[16,79] Among them, phenyl-,[69,80] terbutyl-,[81] hydroxo-,[81] methoxy-,[20,82] carboxyl-,[31,41,54,83,84] amine-,[85] thioether[41,42,84] and nitro-functional[86] groups have been considered for our study. Some TAMs with direct aryl–aryl bonding that present constrained structures and more extreme angle values were also included.[17,20] Further, we also designed two TAMs (see ESI† for structural atomic coordinates) where the three aryl rings are forced by inter-ring linkages to be in perpendicular orientations with respect to the central sp^2 methyl plane, giving rise to configurations that have not yet been reported for any synthesized TAM. The chemical structures of TAMs **1**–**27** can be found in the ESI.†

Additionally, a series of constrained dihedral angle calculations were performed with the triphenylmethyl[1] (herein TAM**4**) and the perchloro-triarylmethyl[2,22,62] (TAM**12**). Here, the dihedral angles of the three aryl rings were constrained with equal (*i.e.* $\varphi_1 = \varphi_2 = \varphi_3$) or different (*i.e.* $\varphi_1 \neq \varphi_2 \neq \varphi_3$) values between 20–90°, while fully optimizing the rest of the molecular structure. In this way we could extract the intrinsic effect of aryl ring twisting on the spin distribution without the additional influence of chemical substitution (*e.g.* electro-withdrawing/donating nature of substituents). These calculations also mimic the hypothetical manipulation of the aryl ring twists by external stimulus, testing the spin-localization/structural relation for out-of-equilibrium configurations. For all cases the spin population on the central carbon atom (αC; see Fig. 1) was used as an indicator of the spin localization/delocalization, since this position is always that with the highest spin population in TAMs.

As a first order assumption, we consider that the spin delocalisation through a particular aryl ring only depends on the corresponding dihedral angle, regardless of its chemical

functionalization. In this scenario, based on π-overlapping ideas,[67,68,70,72] the spin delocalization should be essentially captured by $\cos^2\varphi_i$, where φ_i is the dihedral angle of the considered aryl ring with the central sp^2 carbon atom plane. Secondly, we consider that the effect of twisting any one aryl ring on the spin localization to be independent of the other two rings torsions. This simplifies the complex TAM case to three independent methyl-aryl units and, as a consequence, the average of the three $\cos^2\varphi_i$ (*i.e.* $\langle\cos^2\varphi_i\rangle = (\cos^2\varphi_1 + \cos^2\varphi_2 + \cos^2\varphi_3)/3$) should become a first order spin localization descriptor for TAMs. In Fig. 2 we plot the αC spin population against $\langle\cos^2\varphi_i\rangle$ for our set of more than 40 TAM structures.

As it can be seen in Fig. 2a, $\langle\cos^2\varphi_i\rangle$ is a good spin localization descriptor for the optimised TAM derivative structures (*i.e.* TAM**1–27**, Fig. 2b) where there is little scatter away from the ideal assumed behaviour (*dashed line*). The fact that the differently functionalized TAMs (*black diamonds*) nicely follow the main trend means that chemical functionalisation (see Fig. 2b) determines the spin localization by determining the three dihedral angles but other possible effects, such as the electro-donating/withdrawing nature of substituents, clearly play a secondary role. Therefore, for 0 K structures, the dihedral angles of the three aryl rings with αC almost entirely determine the spin localization in TAMs. As a consequence, by means of a proper chemical design, we can have a completely spin delocalized picture induced by a planar structure (TAM**1**, Fig. 2a-*down*) or, conversely, a configuration where most of the spin population resides on αC (TAM**27**) due to a perpendicular orientation of the three aryl rings (Fig. 2a-*up*).

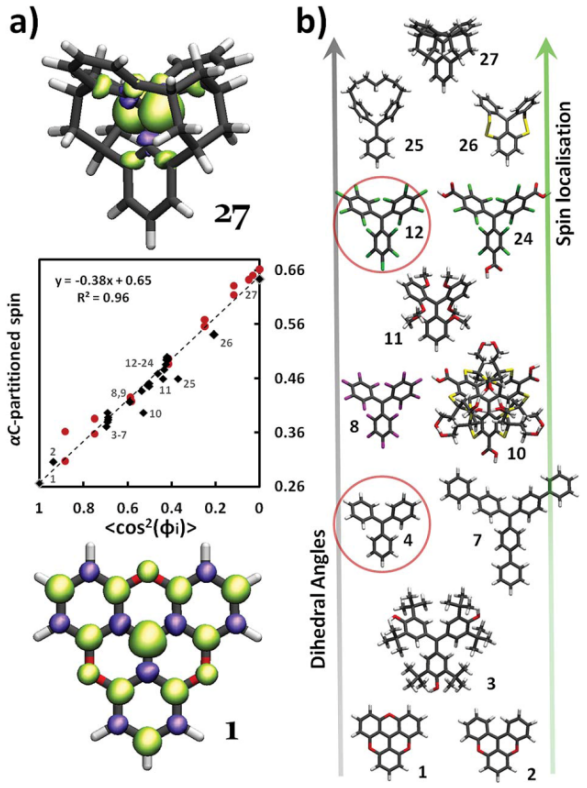

Fig. 2 (a) *Middle*; partitioned spin population on αC against $\langle\cos^2\varphi_i\rangle$, where $\langle\cos^2\varphi_i\rangle = (\cos^2\varphi_1 + \cos^2\varphi_2 + \cos^2\varphi_3)/3$, for each case. *Black diamonds* represent the fully optimized TAM**1–27** (numbers, X, refer to the TAMX, see ESI†) and *red spheres* correspond to the constrained optimisations of TAM**4** and TAM**12**. Values of φ lower than 20° were not possible in the constrained optimisations due to too large sterical hindrances between the three aryl rings. *Upper*/*lower*; spin population iso-surfaces (*green* = α; *violet* = β) for TAM**27** (*upper*) and TAM**1** (*lower*), exhibiting the most perpendicular and most planar aryl ring configurations, respectively. (b) Fully optimized structures of representative TAMs from our study, highlighting the broad range of studied structures. TAM**4** (triphenylmethyl) and TAM**12** (PTM), used for the constrained optimizations (red spheres in a), are circled. TAM**26** and TAM**27** have been specially designed for this study (see ESI† for atomic coordinates). Atom colour key: C – grey, H – white, O – red, S – yellow, Cl – green, F – violet.

The αC spin population for the structurally constrained versions of TAM**4** and TAM**12** structures (circled in Fig. 2b) also linearly varies with $\langle\cos^2\varphi_i\rangle$ (*red spheres* in Fig. 2a). This shows that the spin-localization structural relation is also maintained for out-of-equilibrium configurations. In effect, this set of calculations confirm the potential use of this relation for TAM-based materials and devices where the TAM structure could be externally controlled (*e.g.* by crystal packing, applied pressure) to affect physicochemical properties such as optical absorption bands, magnetic interactions, or electrical conductivities.

However, for real world applications temperature is a critical parameter that must also be taken into account. Thus, for testing the robustness of the spin-localization/structure relation at realistic conditions, we further performed AIMD simulations for radicals TAM**1**, TAM**4**, TAM**12** and TAM**27** at a temperature of 300 K (see computational details in the Methodology section). Fig. 3 shows the time evolution of the three dihedral angles (φ_{1-3}) for the four studied TAMs at 300 K. By comparing the structural oscillations of radicals TAM**1**, TAM**12** and TAM**27** (Fig. 3a) with that of radical TAM**4** (Fig. 3b) we notice important differences due to the correspondingly different chemical functionalisations. Direct aryl–aryl bonding in TAM**1** and TAM**27** clearly prevents rotation of the three aryl rings and this is shown by the quite constant values of the corresponding dihedral angles over time (*red* and *purple curves* in Fig. 3a, respectively). In the case of the fully chlorinated TAM**12** it is the strong sterical hindrance between chlorine atoms that inhibits free rotation of the aryl rings, giving rise to similarly dynamically restricted structural behaviour to that of radicals TAM**1** and TAM**27** (*green curves* in Fig. 3a). The triphenylmethyl (TAM**4**) though, presents a completely different scenario (Fig. 3b). Due to the lack of inter-ring bonding plus a low sterical hindrance between each phenyl ring, rotation is not prevented. This greater rotational freedom leads to the oscillations of each separate dihedral angle for TAM**4** (*blue curves* in Fig. 3b) to be much higher than those in Fig. 3a. Therefore, chemical functionality does not only determine the most stable 0 K configuration of each aryl ring, but also their associated rotational freedom and thus their finite temperature dynamic structural

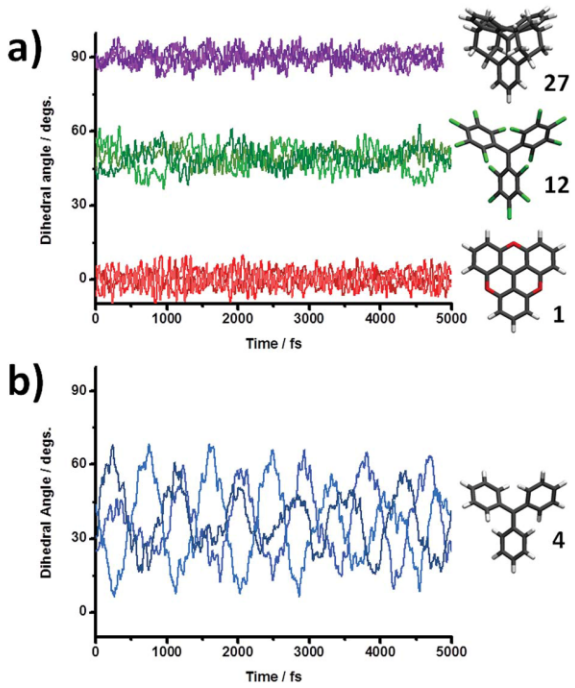

Fig. 3 Time dependence of φ_{1-3} during the 5 ps AIMD calculations at 300 K for radicals TAM1, TAM12 and TAM27 (*red*, green and *purple*, respectively) in (a) and radical TAM4 in (b) (*blue*). The chemical structures of the radicals are provided to the right of the corresponding plots.

behaviour. This also suggests that the ease with which dihedral angles could be manipulated by external means in TAM-based systems will depend on their individual chemical functionalization. Clearly, in addition to such molecular scale considerations, many other environmental factors can affect the degree to which the structure of a TAM can be tailored (*e.g.* type of solvent, crystal packing, applied external forces).

To test whether the structural dependence of the spin-localization is maintained at finite temperatures during these structural fluctuations, we compared the computed αC spin population over time with that *predicted* by the relation derived in Fig. 2a. Specifically, by using the fit equation in the plot of Fig. 2a, we extracted from the dihedral angle fluctuations (Fig. 3) a $\langle\cos^2\varphi_i\rangle$ – *predicted* αC spin population over time. In Fig. 4 we compare the actual calculated αC spin population (*coloured lines*), provided by DFT, with the $\langle\cos^2\varphi_i\rangle$ – *predicted* αC spin population (*black line*) for the four studied radicals.

In Fig. 4a, the αC spin population is evaluated every 0.5 fs. Even for such a small sampling time the predictions by $\langle\cos^2\varphi_i\rangle$ (*black lines*) is approximately followed (with ~10% variance) by the calculated spin localization (*coloured lines*) for each studied TAM over time. This consistent correlation confirms that the spin localization is also dynamically determined by the three aryl rings twists at finite temperatures and, thus, opens up the potential applicability of this dependence under realistic conditions. The computed αC spin populations (*coloured curves* in 4a) present a fast but fairly small oscillation over time that does not exist in the prediction (*black curves* in 4a). As already noted by M. Karplus in the 60 s',[72] this faster oscillation is likely to be associated with bond vibrations which are not accounted for by $\langle\cos^2\varphi_i\rangle$. To verify this hypothesis the average distance of the three central αC-aryl bonds were monitored over time together with the spin population on αC. In the zoomed inset to Fig. 4a it can be seen that, at the femtosecond time scale the rapid αC spin population variation (*blue*) perfectly correlates with the average of the bond length oscillation of those three bonds (*grey*), corroborating Karplus' suggestion. Therefore, based on the same π–π overlap ideas, thermal vibrations influence the spin localization by stretching/shortening the C–C bonds of the three aryl rings with αC. However, by looking at the plots in Fig. 4a it seems that their effect on the αC spin population is to simply add small random deviations away from the ideal behaviour predicted by $\langle\cos^2\varphi_i\rangle$. To test this idea we use the Savitzky–Golay filtering procedure[87,88] for removing the high frequency oscillations due to bond vibrations. As it can be seen in Fig. 4b, we then recover a slower αC-spin population variation over time (*coloured lines*) that matches almost perfectly with the predicted one by $\langle\cos^2\varphi_i\rangle$ (*black lines*). This demonstrates that, at sufficiently long times (*i.e.* hundreds of femto-seconds or higher) the effect of bond vibrations is averaged out and the spin localization is essentially entirely determined by the three dihedral angle values (collected by $\langle\cos^2\varphi_i\rangle$).

Finally, since most of laboratory experiments do not measure the physic-chemical properties at the time-scales of femto- or pico-seconds, but from the nano-second time-scale upwards, we wanted to probe the applicability of $\langle\cos^2\varphi_i\rangle$ as a spin localization predictor at such typically measured time-scales. For this we calculated the average value of $\langle\cos^2\varphi_i\rangle$ from the dihedral angle oscillations shown in Fig. 3 over the entire AIMD simulation (5 picoseconds). Then, by using the fit equation of Fig. 2a, we extract the predicted αC spin population for each TAM radical. In Fig. 4c we compare this predicted value with the computed αC spin population mean value during the entire AIMD. As it can be seen, once again, the matches for all four radicals are excellent.

Overall, our AIMD results confirm the robustness of $\langle\cos^2\varphi_i\rangle$ as a spin localization descriptor for TAMs even at finite temperatures. Over short time scales bond vibrations also affect spin localization, but their effect simply adds a small random deviation over the value predicted by $\langle\cos^2\varphi_i\rangle$.[72] For relatively long times (hundreds of femtoseconds or more) the effect of bond vibrations is averaged out and, then, the spin localization is essentially entirely determined by the dihedral angles of the three aryl rings. Therefore, at finite temperatures dihedral angles are shown to be effective spin localization descriptors in TAMs, opening the possibility of using them for tailoring this important electronic property and all related-characteristics under realistic conditions.

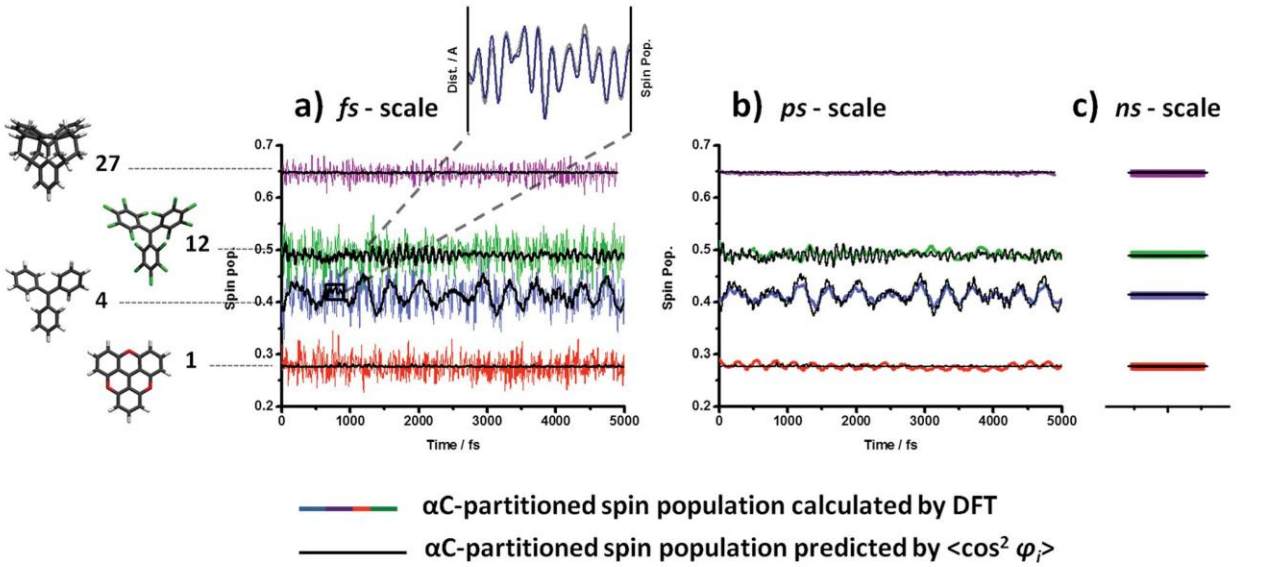

Fig. 4 (a) Computed (*coloured*) and predicted (*black*) by $\langle\cos^2\varphi_i\rangle$ (where $\langle\cos^2\varphi_i\rangle = (\cos^2\varphi_1 + \cos^2\varphi_2 + \cos^2\varphi_3)/3$) αC-partitioned spin population over 5 ps of the AIMD calculations at 300 K for radicals TAM1, TAM**4**, TAM**12** and TAM**27** (*red*, *blue*, *green* and *purple*, respectively). Inset: αC-partitioned spin population (*blue*) plotted together with the average distance of the three αC-aryl bonds (*grey*) over 0.2 ps for TAM**4**. (b) Smoothed αC-partitioned spin population (*coloured*; using the Savizky–Golay methodology) plotted together with the predicted one (*black*) over the same period of time. (c) Average of the computed αC-partitioned spin population (*coloured*) over the entire 5 ps AIMD simulation compared with the predicted one by using the average $\langle\cos^2\varphi_i\rangle$ value (*black*). The corresponding chemical structures of each TAM are also provided.

Conclusions

In summary, by using DFT calculations and by examining different TAMs with a range of chemical structures and at finite temperatures we have confirmed that, very generally, the average αC spin localization is well determined by $\langle\cos^2\varphi_i\rangle$ (where $\langle\cos^2\varphi_i\rangle = (\cos^2\varphi_1 + \cos^2\varphi_2 + \cos^2\varphi_3)/3$ and φ_i are the dihedral angles of each aryl ring with respect to the central sp^2 carbon atom plane). Chemical functionality determines the spin distribution as long as it determines the three dihedral angles but other chemical effects such as the electro-donating/withdrawing nature of substituents play a secondary role. By performing AIMD simulations at 300 K, the predictive power of $\langle\cos^2\varphi_i\rangle$ at finite temperatures has been probed. Bond vibrations also affect the spin localization at the femto-second time scale but their effect simply adds a rapid and small random deviation over the predicted value by $\langle\cos^2\varphi_i\rangle$. Moreover, at relatively long time-scales (hundreds of femto-seconds or higher) their effect is averaged out and the spin localization is essentially entirely determined by the three dihedrals. In TAMs, the existence of the unpaired electron gives rise to their most interesting properties.[50,59,64,65] Therefore, this general and robust spin-localization/structure relationship also represents a powerful tool for controlling other important characteristics such as magnetic interactions, optical absorption bands, magnetoresistance phenomena or electrical conductivities. Besides the possibility of tunning dihedral angles by chemical design,[89–91] some theoretical studies have pointed out the possibility of manipulating this structural feature by external means such as electrical fields,[92] mechanical strain[93] or optical excitations.[94,95] Hence, dihedral angles might be finely tuned by external stimulus in properly designed future materials and devices. In that scenario, we strongly believe that TAMs and their spin-localization *versus* structure dependence could become a key tool for the design and preparation of novel materials and devices with controllable magnetic, optical and electrical properties.

Acknowledgements

We acknowledge financial support from Spanish Government grant MAT2012-30924 and Generalitat de Catalunya grants (2014SGR97 and XRQTC). I. A. acknowledges the Generalitat de Catalunya for an FI-DGR PhD scholarship. We also acknowledge the Red Española de Supercomputacion (RES) for computing time. We also would like to thank Prof. Jaume Veciana and Prof. Juan-Carlos Paniagua for helpful discussions.

Notes and references

1 M. Gomberg, *J. Am. Chem. Soc.*, 1900, **22**, 757–771.
2 M. Ballester, J. Riera, J. Castañer, C. Badía and J. M. Monsó, *J. Am. Chem. Soc.*, 1971, **93**, 2215–2225.
3 M. Ballester, J. Riera, J. Castañer, C. Rovira, J. Veciana and C. Onrubia, *J. Org. Chem.*, 1983, **48**, 3716–3720.
4 L. Juliá, M. Ballester, J. Riera, J. Castañer, J. L. Ortin and C. Onrubia, *J. Org. Chem.*, 1988, **53**, 1267–1273.

5 M. K. Bowman, C. Mailer and H. J. Halpern, *J. Magn. Reson.*, 2005, **172**, 254–267.
6 S. López, J. Carilla, L. Fajarí, L. Juliá, E. Brillas and A. Labarta, *Tetrahedron*, 1995, **51**, 7301–7312.
7 V. M. Domingo, J. Castañer, J. Riera and A. Labarta, *J. Org. Chem.*, 1994, **59**, 2604–2607.
8 O. Elsner, D. Ruiz-Molina, J. Vidal-Gancedo, C. Rovira and J. Veciana, *Nano Lett.*, 2001, **1**, 117–120.
9 J. Guasch, X. Fontrodona, I. Ratera, C. Rovira and J. Veciana, *Acta Crystallogr., Sect. C: Cryst. Struct. Commun.*, 2013, **69**, 255–257.
10 Y. Hattori, T. Kusamoto and H. Nishihara, *Angew. Chem., Int. Ed. Engl.*, 2014, **53**, 11845–11848.
11 M. Ballester, J. Castañer, J. Riera and J. Pujadas, *J. Org. Chem.*, 1984, **49**, 2884–2887.
12 M. Souto, J. Guasch, V. Lloveras, P. Mayorga, J. T. López Navarrete, J. Casado, I. Ratera, C. Rovira, A. Painelli and J. Veciana, *J. Phys. Chem. Lett.*, 2013, **4**, 2721–2726.
13 T. T. Tidwell, in *Stable Radicals: Fundamentals and Applied Aspects of Odd-Electron Compounds*, ed. R. G. Hicks, John Wiley & Sons, Ltd, Chichester, UK., Ontario, 2010, pp. 1–31.
14 D. Velasco, S. Castellanos, M. López, F. López-Calahorra, E. Brillas and L. Juliá, *J. Org. Chem.*, 2007, **72**, 7523–7532.
15 O. Neunhoeffer and H. Haase, *Chem. Ber.*, 1958, **91**, 1801–1805.
16 O. Armet, J. Veciana, C. Rovira, J. Riera, J. Castañer, E. Molins, J. Rius, C. Miravitlles, S. Olivella and J. Brichfeus, *J. Phys. Chem.*, 1987, **91**, 5608–5616.
17 H. A. Staab, C. Kuo-chen and A. Ruland, *Chem. Ber.*, 1982, **115**, 1765–1774.
18 M. Stein and A. Rieker, *Tetrahedron Lett.*, 1975, **25**, 2123–2126.
19 Y. Tian, K. Uchida, H. Kurata, Y. Hirao, T. Nishiuchi and T. Kubo, *J. Am. Chem. Soc.*, 2014, **136**, 12784–12793.
20 M. J. Sabacky, C. S. Johnson, R. G. Smith, H. S. Gutowsky and J. C. Martin, *J. Am. Chem. Soc.*, 1967, **89**, 2054–2058.
21 N. M. Shishlov, *Russ. Chem. Rev.*, 2006, **75**, 863–884.
22 I. Ratera and J. Veciana, *Chem. Soc. Rev.*, 2012, **41**, 303–349.
23 N. Bézière, C. Decroos, K. Mkhitaryan, E. Kish, F. Richard, S. Bigot-Marchand, S. Durand, F. Cloppet, C. Chauvet, M.-T. Corvol, F. Rannou, Y. Xu-Li, D. Mansuy, F. Peyrot and Y.-M. Frapart, *Mol. Imaging*, 2012, **11**, 220–228.
24 N. Chattergoon, F. Martínez-Santiesteban, W. B. Handler, J. H. Ardenkjaer-Larsen and T. J. Scholl, *Contrast Media Mol. Imaging*, 2013, **8**, 57–62.
25 B. Driesschaert, V. Marchand, P. Levêque, B. Gallez and J. Marchand-Brynaert, *Chem. Commun.*, 2012, **48**, 4049–4051.
26 B. Driesschaert, P. Levêque, B. Gallez and J. Marchand-Brynaert, *Tetrahedron Lett.*, 2013, **54**, 5924–5926.
27 M. C. Krishna, S. Matsumoto, H. Yasui, K. Saito, N. Devasahayam, S. Subramanian and J. B. Mitchell, *Radiat. Res.*, 2012, **177**, 376–386.
28 T. J. Reddy, T. Iwama, H. J. Halpern and V. H. Rawal, *J. Org. Chem.*, 2002, **67**, 4635–4639.
29 G. Y. Shevelev, O. A. Krumkacheva, A. A. Lomzov, A. A. Kuzhelev, O. Y. Rogozhnikova, D. V. Trukhin, T. I. Troitskaya, V. M. Tormyshev, M. V. Fedin, D. V. Pyshnyi and E. G. Bagryanskaya, *J. Am. Chem. Soc.*, 2014, **136**, 9874–9877.
30 A. A. Bobko, I. Dhimitruka, D. A. Komarov and V. V. Khramtsov, *Anal. Chem.*, 2012, **84**, 6054–6060.
31 I. Dhimitruka, A. A. Bobko, T. D. Eubank, D. A. Komarov and V. V. Khramtsov, *J. Am. Chem. Soc.*, 2013, **135**, 5904–5910.
32 A. A. Bobko, I. Dhimitruka, T. D. Eubank, C. B. Marsh, J. L. Zweier and V. V. Khramtsov, *Free Radicals Biol. Med.*, 2009, **47**, 654–658.
33 V. K. Kutala, N. L. Parinandi, R. P. Pandian and P. Kuppusamy, *Antioxid. Redox Signal.*, 2004, **6**, 597–603.
34 Y. Liu, F. A. Villamena, J. Sun, T. Wang and J. L. Zweier, *Free Radicals Biol. Med.*, 2009, **46**, 876–883.
35 C. Rizzi, A. Samouilov, V. K. Kutala, N. L. Parinandi, J. L. Zweier and P. Kuppusamy, *Free Radicals Biol. Med.*, 2003, **35**, 1608–1618.
36 S. Xia, F. A. Villamena, C. M. Hadad, P. Kuppusamy, Y. Li, H. Zhu and J. L. Zweier, *J. Org. Chem.*, 2006, **71**, 7268–7279.
37 G. Meenakshisundaram, E. Eteshola, A. Blank, S. C. Lee and P. Kuppusamy, *Biosens. Bioelectron.*, 2010, **25**, 2283–2289.
38 K. Münnemann, C. Bauer, J. Schmiedeskamp, H. W. Spiess, W. G. Schreiber and D. Hinderberger, *Appl. Magn. Reson.*, 2008, **34**, 321–330.
39 R. A. Wind and J. H. Ardenkjaer-Larsen, *J. Magn. Reson.*, 1999, **141**, 347–354.
40 J.-L. Muñoz-Gómez, I. Marín-Montesinos, V. Lloveras, M. Pons, J. Vidal-Gancedo and J. Veciana, *Org. Lett.*, 2014, **16**, 5402–5405.
41 C. Gabellieri, V. Mugnaini, J. C. Paniagua, N. Roques, M. Oliveros, M. Feliz, J. Veciana and M. Pons, *Angew. Chem., Int. Ed. Engl.*, 2010, **49**, 3360–3362.
42 D. Banerjee, J. C. Paniagua, V. Mugnaini, J. Veciana, A. Feintuch, M. Pons and D. Goldfarb, *Phys. Chem. Chem. Phys.*, 2011, **13**, 18626–18637.
43 G. D'Avino, L. Grisanti, J. Guasch, I. Ratera, J. Veciana and A. Painelli, *J. Am. Chem. Soc.*, 2008, **130**, 12064–12072.
44 L. Grisanti, G. D'Avino, A. Painelli, J. Guasch, I. Ratera and J. Veciana, *J. Phys. Chem. B*, 2009, **113**, 4718–4725.
45 J. Guasch, L. Grisanti, M. Souto, V. Lloveras, J. Vidal-Gancedo, I. Ratera, A. Painelli, C. Rovira and J. Veciana, *J. Am. Chem. Soc.*, 2013, **135**, 6958–6967.
46 V. Lloveras, J. Vidal-Gancedo, T. M. Figueira-Duarte, J. F. Nierengarten, J. J. Novoa, F. Mota, N. Ventosa, C. Rovira and J. Veciana, *J. Am. Chem. Soc.*, 2011, **133**, 5818–5833.
47 S. Castellanos, F. López-Calahorra, E. Brillas, L. Juliá and D. Velasco, *Angew. Chem.*, 2009, **48**, 6515–6519.
48 Q. Peng, A. Obolda, M. Zhang and F. Li, *Angew. Chem., Int. Ed.*, 2015, **54**, 7091–7095.
49 A. Rajca, S. Rajca and J. Wongsriratanakul, *J. Am. Chem. Soc.*, 1999, **121**, 6308–6309.
50 A. Rajca, J. Wongsriratanakul and S. Rajca, *Science*, 2001, **294**, 1503–1505.
51 S. Rajca, A. Rajca, J. Wongsriratanakul, P. Butler and S. M. Choi, *J. Am. Chem. Soc.*, 2004, **126**, 6972–6986.
52 A. Rajca, K. Lu and S. Rajca, *J. Am. Chem. Soc.*, 1997, **119**, 10335–10345.

53 D. Maspoch, D. Ruiz-Molina and J. Veciana, *J. Mater. Chem.*, 2004, **14**, 2713–2723.
54 D. Maspoch, D. Ruiz-Molina, K. Wurst, N. Domingo, M. Cavallini, F. Biscarini, J. Tejada, C. Rovira and J. Veciana, *Nat. Mater.*, 2003, **2**, 190–195.
55 N. Roques, D. Maspoch, A. Datcu, K. Wurst, D. Ruiz-Molina, C. Rovira and J. Veciana, *Polyhedron*, 2007, **26**, 1934–1948.
56 N. Crivillers, M. Mas-Torrent, J. Vidal-Gancedo, J. Veciana and C. Rovira, *J. Am. Chem. Soc.*, 2008, **130**, 5499–5506.
57 N. Crivillers, M. Mas-Torrent, C. Rovira and J. Veciana, *J. Mater. Chem.*, 2012, **22**, 13883–13890.
58 N. Crivillers, M. Paradinas, M. Mas-Torrent, S. T. Bromley, C. Rovira, C. Ocal and J. Veciana, *Chem. Commun.*, 2011, **47**, 4664–4666.
59 N. Crivillers, C. Munuera, M. Mas-Torrent, C. Simão, S. T. Bromley, C. Ocal, C. Rovira and J. Veciana, *Adv. Mater.*, 2009, **21**, 1177–1181.
60 M. Mas-Torrent, N. Crivillers, C. Rovira and J. Veciana, *Chem. Rev.*, 2012, **112**, 2506–2527.
61 F. Vera, M. Mas-Torrent, J. Esquena, C. Rovira, Y. Shen, T. Nakanishi and J. Veciana, *Chem. Sci.*, 2012, **3**, 1958–1962.
62 J. Veciana and I. Ratera, in *Stable Radicals: Fundamentals and Applied Aspects of Odd-Electron Compounds*, ed. R. G. Hicks, John Wiley & Sons, Inc., 2010, pp. 33–80.
63 J. Guasch, L. Grisanti, S. Jung, D. Morales, G. D'Avino, M. Souto, X. Fontrodona, A. Painelli, F. Renz, I. Ratera and J. Veciana, *Chem. Mater.*, 2013, **25**, 808–814.
64 C. Simão, M. Mas-Torrent, N. Crivillers, V. Lloveras, J. M. Artés, P. Gorostiza, J. Veciana and C. Rovira, *Nat. Chem.*, 2011, **3**, 359–364.
65 R. Frisenda, R. Gaudenzi, C. Franco, M. Mas-Torrent, C. Rovira, J. Veciana, I. Alcon, S. T. Bromley, E. Burzurí and H. S. J. van der Zant, *Nano Lett.*, 2015, **15**, 3109–3114.
66 G. N. Lewis, D. Lipkin and T. T. Magel, *J. Am. Chem. Soc.*, 1944, **66**, 1579–1583.
67 M. J. S. Dewar, *J. Am. Chem. Soc.*, 1952, **74**, 3345–3350.
68 F. C. Adam and S. I. Weissman, *J. Am. Chem. Soc.*, 1958, **80**, 2057–2059.
69 A. H. Maki, R. D. Allendoerfer, J. C. Danner and R. T. Keys, *J. Am. Chem. Soc.*, 1968, **90**, 4225–4231.
70 M. Karplus and G. K. Fraenkel, *J. Chem. Phys.*, 1961, **35**, 1312–1323.
71 J. A. Pople and D. L. Beveridge, *J. Chem. Phys.*, 1968, **49**, 4725–4726.
72 M. Karplus, *J. Am. Chem. Soc.*, 1963, **85**, 2870–2871.
73 K. Schreiner, A. Berndt and F. Baer, *Mol. Phys.*, 1973, **26**, 929–939.
74 R. Improta and V. Barone, *Chem. Rev.*, 2004, **104**, 1231–1253.
75 M. J. Frisch, G. W. Trucks, H. B. Schlegel, G. E. Scuseria, M. A. Robb, J. R. Cheeseman, G. Scalmani, V. Barone, B. Mennucci, G. A. Petersson, H. Nakatsuji, M. Caricato, X. Li, H. P. Hratchian, A. F. Izmaylov, J. Bloino, G. Zheng, J. L. Sonnenberg, M. Had and D. J. Fox, *Gaussian-09. Revision-D.01*, 2009.
76 F. L. Hirshfeld, *Theor. Chem. Acc.*, 1977, **44**, 129–138.
77 G. Bussi, D. Donadio and M. Parrinello, *J. Chem. Phys.*, 2007, **126**, 014101.
78 V. Blum, R. Gehrke, F. Hanke, P. Havu, V. Havu, X. Ren, K. Reuter and M. Scheffler, *Comput. Phys. Commun.*, 2009, **180**, 2175–2196.
79 C. Trapp, C. S. Wang and R. Filler, *J. Chem. Phys.*, 1966, **45**, 3472.
80 W. Schlenk, T. Weickel and A. Herzenstein, *Justus Liebigs Ann. Chem.*, 1910, **372**, 1–20.
81 B. Kirste, W. Harrer and H. Kurreck, *J. Am. Chem. Soc.*, 1985, **107**, 20–28.
82 S.-H. Jang, P. Gopalan, J. E. Jackson and B. Kahr, *Angew. Chem., Int. Ed. Engl.*, 1994, **33**, 775–777.
83 D. Maspoch, L. Catala, P. Gerbier, D. Ruiz-Molina, J. Vidal-Gancedo, K. Wurst, C. Rovira and J. Veciana, *Chem.–A Eur. J.*, 2002, **8**, 3635–3645.
84 A. A. Kuzhelev, D. V. Trukhin, O. A. Krumkacheva, R. K. Strizhakov, O. Y. Rogozhnikova, T. I. Troitskaya, M. V. Fedin, V. M. Tormyshev and E. G. Bagryanskaya, *J. Phys. Chem. B*, 2015, **119**, 13630–13640.
85 L. Teruel, L. Viadel, J. Carilla, L. Fajarí, E. Brillas, J. Sañé, J. Rius and L. Juliá, *J. Org. Chem.*, 1996, **61**, 6063–6066.
86 R. Filler, A. E. Fiebig and B. K. Mandal, *J. Fluorine Chem.*, 2000, **102**, 185–188.
87 A. Savitzky and M. J. E. Golay, *Anal. Chem.*, 1964, **36**, 1627–1639.
88 J. Steinier, Y. Termonia and J. Deltour, *Anal. Chem.*, 1972, **44**, 1906–1909.
89 L. Venkataraman, J. E. Klare, C. Nuckolls, M. S. Hybertsen and M. L. Steigerwald, *Nature*, 2006, **442**, 904–907.
90 M.-H. Jung, K. H. Song, K. C. Ko, J. Y. Lee and H. Lee, *J. Mater. Chem.*, 2010, **20**, 8016–8020.
91 D. Vonlanthen, A. Rudnev, A. Mishchenko, A. Käslin, J. Rotzler, M. Neuburger, T. Wandlowski and M. Mayor, *Chem.–Eur. J.*, 2011, **17**, 7236–7250.
92 M. G. Vergniory, J. M. Granadino-Roldan, A. Garcia-Lekue and L.-W. Wang, *Appl. Phys. Lett.*, 2010, **97**, 262114.
93 T. B. Martins, A. Fazzio and A. J. R. da Silva, *Phys. Rev. B: Condens. Matter Mater. Phys.*, 2009, **79**, 115413.
94 K. M. Tibbetts, T. Bohinski, K. Munkerup, M. Tarazkar and R. Levis, *J. Phys. Chem. A*, 2014, **118**, 8170–8176.
95 T. Bohinski, K. M. Tibbetts, K. Munkerup, M. Tarazkar, D. A. Romanov, S. Matsika and R. J. Levis, *Chem. Phys.*, 2014, **442**, 81–85.

Supporting Information of Publication #4

Structural control over spin localization in triarylmethyls

RSC Adv., 2015, 5, 98593-98599

Isaac Alcon and Stefan T. Bromley*

Electronic Supplementary Material (ESI) for RSC Advances.

Supplementary Information:

Structural Control over Spin Localization in Triarylmethyls

Isaac Alcón and Stefan T. Bromley

EPR line-widths and calculated dipole-dipole couplings

In ref.[16], the TAM radicals 1-9 (numbers correspond to the labeling used in ref.[16], in our manuscript they are labeled as TAM13-21, correspondingly - see chemical structures below) are in dilute solutions and interactions between molecules are relatively rare and weak and their effect on the unpaired electron state can be neglected for calculation of spin dipolar (i.e. anisotropic dipole-dipole) couplings. This situation justifies our use of isolated molecule calculations. Although anisotropic dipole-dipole interactions are often not observed in solution where there is no a specific molecular orientation, it is known that for slow molecular tumbling rates (like in measurements done at low temperatures and/or with high viscosity solvents) EPR line-widths are proportional to the modulation of the dipole-dipole interactions through molecular tumbling (ref [16]). Since the EPR measurements in ref.[16] were done at low temperature (163K) in $CFCl_3$, except for Rad8 and Rad9 (notation of ref.[16]) which were measured at room temperature in tetrahydrofuran, the line-widths can be reasonably assumed to depend on the dipole-dipole interactions.

Specifically, we use the 3ZZ-RR components of the tensor of only the anisotropic dipole-dipole couplings (i.e. without the isotropic part). The Z component is taken as it is parallel to the p_z orbitals which form the conjugated pi system of TAM molecules, which provides the means for the delocalisation of the unpaired electron.

In Fig. 1 we plot the experimental line-widths (black circles) together with our calculated mean dipole-dipole couplings (red rhombuses) for the radical series of Ref. [16] (note that the mean dipole-dipole couplings are obtained by taking the average of the 3ZZ-RR components over all the atoms of each radical). The excellent agreement between the trends in both data sets, suggest that our calculations are able to capture very small variations of the EPR line-widths, confirms the accuracy of our computational approach. This match, additionally, appears to confirm the existence of a causal link between line-widths and dipole-dipole interactions.

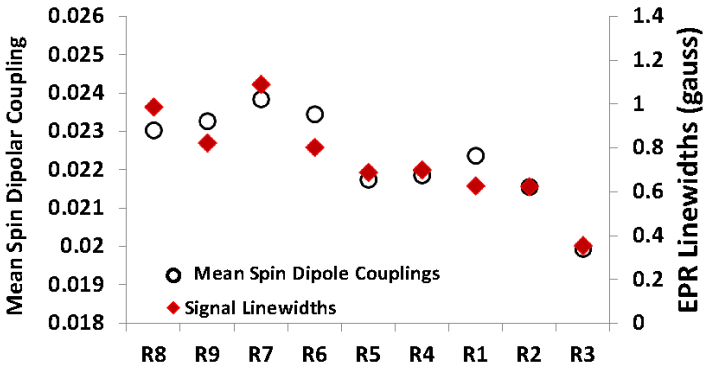

Figure 1. Experimental ESR line-widths (*black circles*) and calculated mean dipole-dipole couplings (*red*) provided by Gaussian09 for all reported radicals in ref.[16].

Chemical Structures of TAMs 1-25

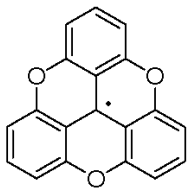

Figure 2. TAM1 chemical structure.

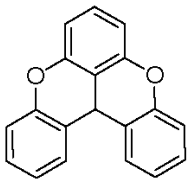

Figure 3. TAM2 chemical structure.

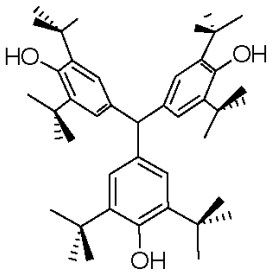

Figure 4. TAM3 chemical structure.

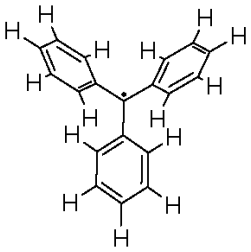

Figure 5. TAM4 chemical structure. This is the triphenylmethyl. First TAM (and organic radical) ever synthesized.

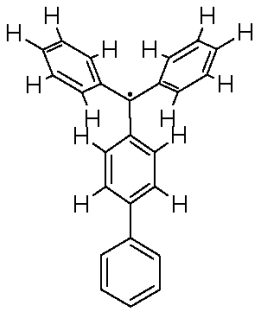

Figure 6. TAM5 chemical structure.

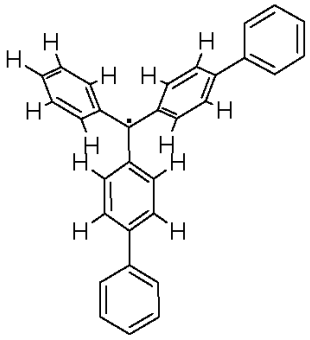

Figure 7. TAM6 chemical structure.

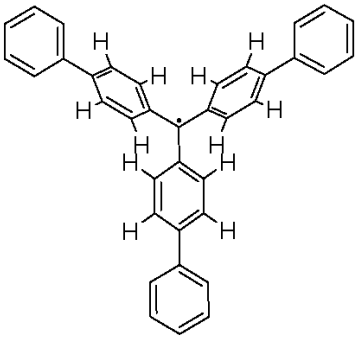

Figure 8. TAM7 chemical structure.

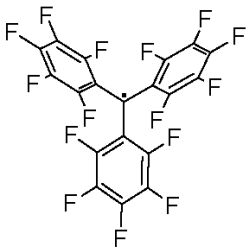

Figure 9. TAM8 chemical structure.

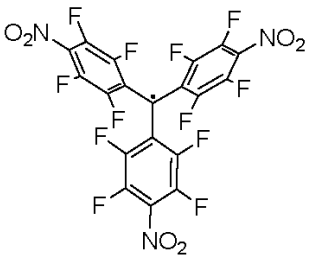

Figure 10. TAM9 chemical structure.

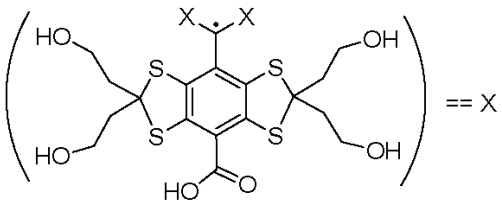

Figure 11. TAM10 chemical structure. This is the so-called OX63, a commercial TAM commonly used in DNP, oxygen detection or spin labeling.

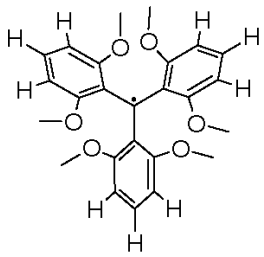

Figure 12. TAM11 chemical structure.

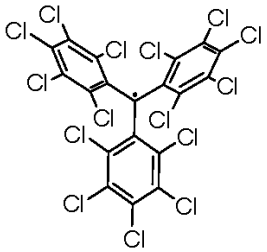

Figure 13. TAM12 chemical structure. This is the polychlorotriphenylmethyl, commonly abbreviated as PTM. Also Rad1 in ref. [16].

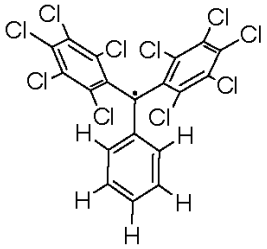

Figure 14. TAM13 chemical structure. Also Rad2 in ref. [16].

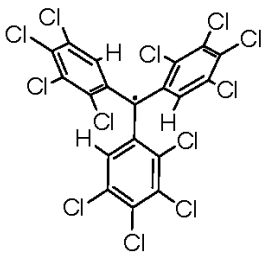

Figure 15. TAM14 chemical structure. Also Rad3 in ref. [16].

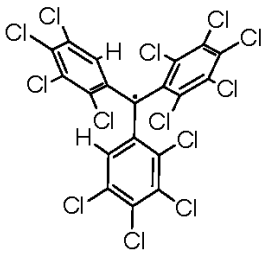

Figure 16. TAM15 chemical structure. Also Rad4 in ref. [16].

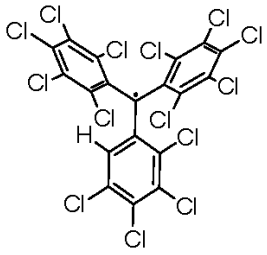

Figure 17. TAM16 chemical structure. Also Rad5 in ref. [16].

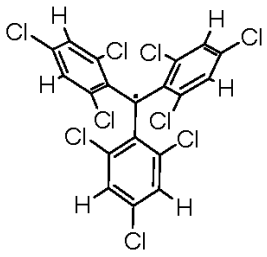

Figure 18. TAM17 chemical structure. Also Rad6 in ref. [16]

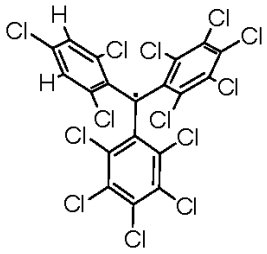

Figure 19. TAM18 chemical structure. Also Rad7 in ref. [16]

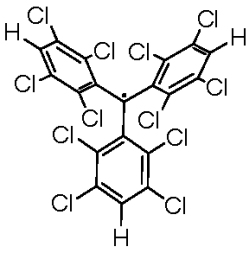

Figure 20. TAM19 chemical structure. Also Rad8 in ref. [16].

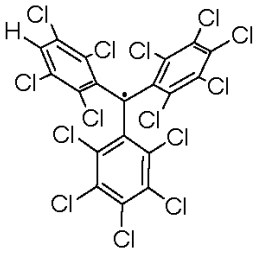

Figure 21. TAM20 chemical structure. Also Rad9 in ref. [16]

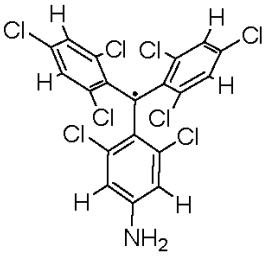

Figure 22. TAM21 chemical structure.

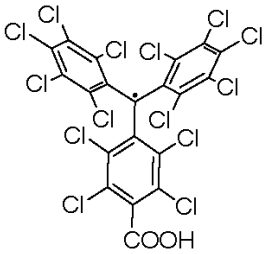

Figure 23. TAM22 chemical structure.

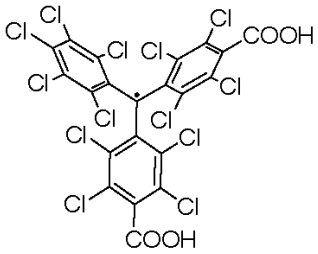

Figure 24. TAM23 chemical structure.

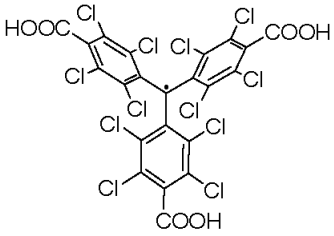

Figure 25. TAM24 chemical structure.

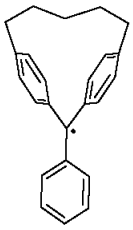

Figure 26. TAM25 chemical structure.

The structural atomic coordinates of our designed radicals TAM**26** and TAM**27,** having highly perpendicular aryl ring configurations, are given below.

Publication #5

Design of multi-functional 2D open-shell organic networks with mechanically controllable properties

Chem. Sci., 2017,**8**, 1027-1039

Isaac Alcón, Daniel Reta, Iberio de P. R. Moreira and Stefan T. Bromley*

Chemical Science

EDGE ARTICLE

View Article Online
View Journal | View Issue

Cite this: *Chem. Sci.*, 2017, **8**, 1027

Design of multi-functional 2D open-shell organic networks with mechanically controllable properties†

Isaac Alcón,[a] Daniel Reta,[a] Iberio de P. R. Moreira[a] and Stefan T. Bromley*[ab]

Received 30th March 2016
Accepted 30th August 2016

DOI: 10.1039/c6sc01412g

www.rsc.org/chemicalscience

Triarylmethyls (TAMs) are prominent highly attractive open shell organic molecular building blocks for materials science, having been used in breakthrough syntheses of organic magnetic polymers and metal organic frameworks. With their radical π-conjugated nature and a proven capacity to possess high stability *via* suitable chemical design, TAMs display a variety of desirable characteristics which can be exploited for a wide range of applications. Due to their particular molecular and electronic structure, the spin localization in TAMs almost entirely depends on the dihedral angles of their three aryl rings with respect to the central methyl carbon atom plane, which opens up the possibility of controlling their fundamental properties by twisting the three aryl rings. Aryl ring twist angles can be tuned to a single value by specific chemical functionalisation but controlling them by external means in organic materials or devices represents a challenging task which has not yet been experimentally achieved. Herein, through rational chemical design we propose two 2D covalent organic frameworks (2D-COFs) based on specific TAM building blocks. By employing *ab initio* computational modeling we demonstrate that it is possible to externally manipulate the aryl ring twist angles in these 2D-linked TAM frameworks by external mechanical means. Furthermore, we show this structural manipulation allows for finely tuning the most important characteristics of these materials such as spin localization, optical electronic transitions and magnetic interactions. Due to the enormous technological potential offered by this new class of material and the fact that our work is guided by real advances in organic materials synthesis, we believe that our predictions will inspire the experimental realization of radical-2D-COFs with externally controllable characteristics.

Introduction

Since their discovery by Moses Gomberg in 1900,[1] triarylmethyls (TAMs) have become one of the most prominent classes of molecules in the field of organic radical chemistry.[2,3] All TAMs are composed of three aryl rings bonded to a central methyl carbon atom (αC) where their unpaired electron mainly resides (Fig. 1). Due to the steric protection provided by the three aryl rings, TAMs display high radical stability which has allowed chemists to synthesize more than hundred TAM derivatives that have been used for different applications and as building blocks for multi-functional materials and devices.[4,5] The radical

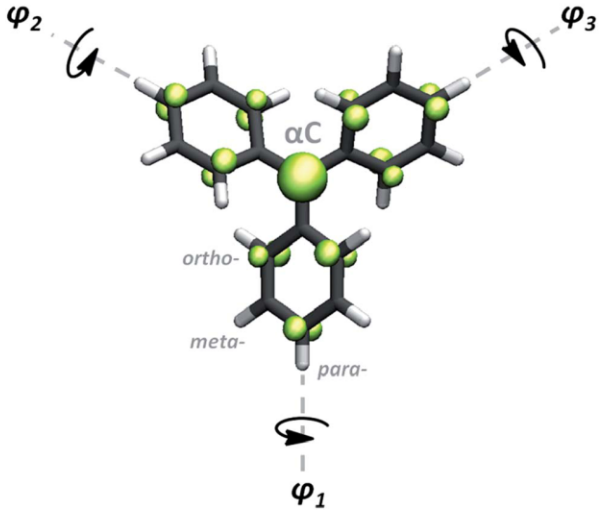

Fig. 1 Generic molecular structure of TAMs. φ_1, φ_2 and φ_3 represent the aryl ring twist angles mainly determining the spin density distribution associated with the unpaired electron (green) in TAMs.[11]

[a]*Institut de Química Teòrica i Computacional de la Universitat de Barcelona (IQTC-UB), Departament de Ciència de Materiales i Química Física de la Universitat de Barcelona, C/Martí I Franqués 1, 08028 Barcelona, Spain. E-mail: s.bromley@ub.edu*

[b]*Institució Catalana de Recerca i Estudis Avançats (ICREA), 08010 Barcelona, Spain*

† Electronic supplementary information (ESI) available: (1) plot of twist angle *vs.* energy profiles for TPM and PTM molecules, (2) plot of bi-axial *vs.* uni-axial strain, (3) plots of structure and spin density for PTM 2D-COF upon strain, (4) plots of band structure of PTM 2D-COF upon strain, (5) plot of SOMO–SUMO energy difference for TPM and PTM molecules, (6) full details of magnetic coupling calculations. See DOI: 10.1039/c6sc01412g

π-conjugation in TAMs is responsible for many of their key characteristics such as fluorescence,[6] enhanced electrical conductivities,[7] redox-activity[8,9] and magnetoresistance phenomena.[10] As a consequence, TAMs have been utilized for the preparation of organic magnets,[12–14] non-volatile memory devices,[8] molecular wires,[10,15] switchable surfaces,[9] dynamic-nuclear polarization components,[16] organic light emitting diodes[17] and nano-porous magnetic sensors,[18] among others.[19]

Recently, we used *ab initio* computational modelling to show that, due to the π-conjugated nature of the unpaired electron in TAMs, the degree of spin delocalization in this type of molecule almost entirely depends on the dihedral angle of each aryl ring with respect to the central methyl carbon atom plane (φ_1, φ_2, φ_3 in Fig. 1).[11] Based on π-overlap arguments,[20–23] we found that a linear relationship exists between the spin density on αC and the average of the cosine squared of the three dihedrals ($\langle\cos^2\varphi\rangle = (\cos^2\varphi_1 + \cos^2\varphi_2 + \cos^2\varphi_3)/3$). Moreover, we found that this relationship is independent of both the chemical functionalization of the considered TAM derivative and the system's temperature. In TAMs, the presence of the unpaired electron is responsible for their most interesting properties. Hence, due to the spin-localization structural relationship in these radicals, the manipulation of aryl ring twist angles represents a potentially powerful tool for controlling these properties in a precise manner.

Aryl ring twist angles in π-conjugated molecules are mainly determined by their chemical functionalisation through the correspondingly induced steric hindrance.[24,25] Some works studying bi-phenyl molecular junctions have pointed to the possibility of using electric fields[26] or electro-chemical potentials[27] to externally manipulate dihedral angles within molecular devices. However, chemical design is, by far, the most utilized approach to finely tune this structural parameter to a certain value in order to determine the associated electrical,[24,28] magnetic,[29] optical[30] and electro-chemical properties.[25] The challenging task of externally tuning aryl ring twist angles in single-molecule devices comes from the extreme difficulties associated with: (i) controlling the orientation of the molecular units within the device[15] and, (ii) the need to direct the external stimulus uniquely to twist aryl rings without causing other physico-chemical phenomena which may also interfere with the output characteristics of the system.[10]

Recently, it has been experimentally demonstrated that applying a uniaxial strain onto graphene mono- and multi-layers greatly influences the electrical properties of the 2D material due to the perturbation of its honey-comb like structure.[31–37] In a very similar way, externally applied strain onto a suitably designed TAM-based material could induce an aryl ring twist within every TAM unit composing the material's skeleton which, in turn, should open the possibility of externally controlling its most fundamental characteristics.[11] External manipulation of aryl ring twist angles in π-conjugated materials though, as far as we know, has not yet been experimentally achieved, highlighting the challenging task that it represents. To accomplish this objective there are some important criteria regarding the structural characteristics of the TAM-based material to be designed:

(1) The main skeleton of the material must be composed of TAM building blocks in such a way that an external perturbation of the material's structure will induce a significant change of the conformation of the TAM building units composing it.

(2) The bonding that sustains the basic structure of the material must be strong enough to withstand the mechanical loads required to overcome the sterical hindrance between aryl rings within TAM units.

(3) The material's skeleton should be ordered as to ensure a homogeneous structural response when applying the external mechanical stimulus, leading to correspondingly smooth, sensitive and reproducible observable physico-chemical changes.

Among the different TAM-based functional materials reported to date there are two examples that come close to fulfilling our three criteria. The first is the organic polymer magnet based on a triphenylmethyl derivative (*i.e.* fully hydrogenated TAMs herein abbreviated as TPMs) reported by Rajca *et al.* in 2001 (Fig. 2a).[13] In this case, the material's skeleton is composed of TPM units which are covalently bonded (criteria 1 and 2) but, as being a 1D organic polymer prepared in solution, its structure consists of a disordered organic network. As a consequence, the application of any type of external mechanical load would tend to generate different types of uncontrolled inelastic structural changes, preventing thus the use of aryl ring twist angles to uniquely determine the characteristics of the stretched material. The second interesting example is a metal–organic framework (MOF) based on a perchloro-triarylmethyl (*i.e.* fully chlorinated TAMs, herein abbreviated as PTMs) reported by Maspoch *et al.* in 2003 (Fig. 2b).[18] In this case the PTM units also make up the main structure of the material which, in turn, possesses crystalline ordering (criteria 1 and 3). However, the bonding interactions between building blocks are of a weak electrostatic nature and, thus, the strain release would probably change the relative positions of PTM units within the framework before perturbing their inner molecular conformation (*i.e.* aryl ring twist angles), thus also precluding the use of this interesting material for our goal.

Over the last few years a new type of organic material which could realize the proposed three requirements has emerged: so called 2D-covalent organic frameworks[38–41] (or 2D-COFs). 2D-COFs are organic bi-dimensional layers where initially discrete molecular building blocks occupy ordered positions within a covalent framework (Fig. 2c). The final properties of 2D-COFs entirely depend on the constituent molecular units, their connectivity (*i.e.* how building blocks are covalently bonded) and the utilized methodology to prepare them (preparation can be performed either in solution[42,43] or on surface[44,45]). 2D-COFs may be understood as a class of material which bridges between organic polymers and MOFs (2a and b), and which possesses the appropriate characteristics for our purpose: *i.e.* covalent bonding and crystalline ordering. A few computational studies have demonstrated the unique characteristics of polyradical 2D-COFs[46–52] but, due to the inherent instability of open shell molecules, as far as we know, no 2D-COF whose structure is composed of radical building blocks has yet been experimentally reported. However, the demonstrated chemical persistence of TAMs both in solution[53] and on surfaces[54,55] (Fig. 2d), the use of

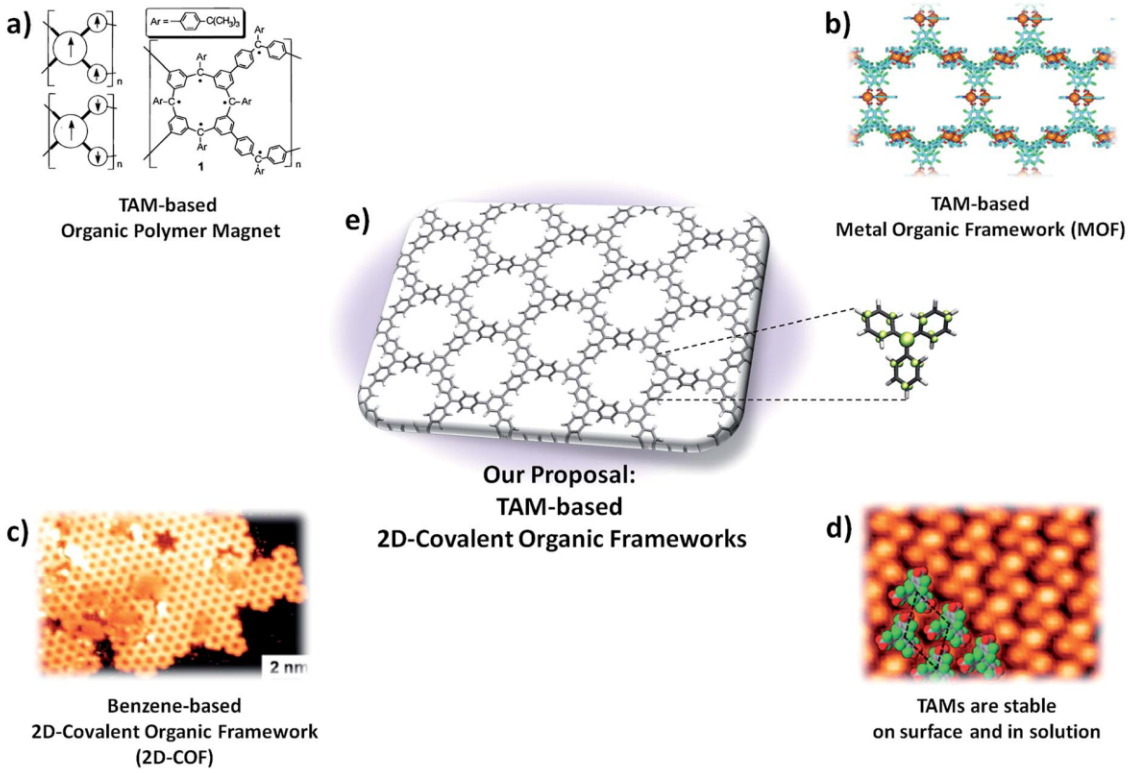

Fig. 2 (a) Organic polymer magnet based on the triphenylmethyl (TPM) reported in 2001.[13] (b) Metal–organic framework based on a perchloro-triarylmethyl (PTM) reported on 2003.[18] (c) STM image of a 2D-covalent organic framework (2D-COF) formed by the on surface self-reaction of 1,3,5-tri-iodo-benzene.[77] (d) STM image of a tri-carboxylic PTM monolayer on copper.[89] (e) TAM-based 2D-covalent organic framework proposed in this study.

TAMs as building blocks for other types of materials[13,18] (Fig. 2a and b) and the impressive recent developments in the field of 2D-COFs[40,56] represent strong support in favour of the possible preparation of TAM-based 2D-COFs in the near future (Fig. 2e).

In this study we have rationally designed two different 2D-COFs based on the triphenylmethyl (TPM 2D-COF) and the perchloro-triarylmethyl (PTM 2D-COF), which represent the most important families of TAM derivatives for materials science to date. By means of density functional theory (DFT) calculations we have optimized the corresponding 2D periodic model structures and studied their resulting physico-chemical characteristics. Our results show that both proposed 2D-COFs are stable planar nanoporous materials consisting of ordered arrays of linked open-shell centres. Application of a uniaxial strain to both networks gives rise to a smooth perturbation of the molecular structure within every TAM unit composing the material. In agreement with our previous study on single molecule TAMs,[11] the strain-induced aryl ring twist gives rise to a monotonic and homogeneous change in the spin localization within every radical centre. Accordingly, the electronic and magnetic properties of the materials are also found to change, demonstrating the validity of our approach to design 2D multi-functional materials with externally controllable characteristics. Further, we have carried out *ab initio* molecular dynamics (AIMD) simulations to test the effect of finite temperatures on the studied properties of the 2D networks. Here we observe a random small deviation in the studied variables produced by thermally activated bond vibrations. However, as we observed for isolated TAM monomers, the average value of each variable over time is clearly determined by the corresponding aryl ring twist angles. By comparing the different behaviours at finite temperatures of the differently functionalized 2D-COFs (TPM and PTM based) we also demonstrate the essential role of chemical functionality in determining the controllability of the material's properties by external manipulation of aryl ring twist angles.

Methodology

All the 2D model structures of the 2D-COFs considered in this work were constructed using periodic boundary conditions and fully optimized using an efficient cascade methodology. The universal force field (UFF)[57a] was first used within the General Utility Lattice Program (GULP)[57b] to obtain pre-optimized structures (atomic positions and cell-parameters). This was followed by a second full optimization of both structure and cell parameters with DFT using the PBE functional[58] and a light numerical basis set. Another full DFT optimization was performed using the hybrid PBE0 functional[59] and light numerical basis set. Finally, single point calculations using PBE0 hybrid

functional and tight numerical basis set were performed to obtain the electronic structure and properties of the system. Due to the large cell size ($a = b = 21.6$ Å with $c = 40$ Å to provide a large vacuum separation between repeated sheets in the c-direction) all periodic DFT calculations were performed at the gamma point in reciprocal space.

To mimic the application of a uniaxial strain on our 2D materials, we performed a series of restricted optimizations (following the cascade methodology indicated above), systematically increasing one of the in-plane cell parameters (by 0–5 Å) allowing the other in-plane cell parameter and internal atomic positions to relax. We note that due to the symmetry of the considered 2D-COF, increasing either the a or b cell parameter is equivalent. Biaxial isotropic strain was also investigated by applying the same degree of distortion to both a and b cell parameters simultaneously and optimizing all the internal independent coordinates. This kind of isotropic distortion was found to directly affect the sigma-bonded skeleton and the energy variation was significantly larger than the separate a (or b) uniaxial strain, even for small distortions. Results for biaxial strain are given in the ESI.† Herein we will focus our study on the uniaxial distorted structures.

The thermally-activated response of the materials was modelled *via ab initio* molecular dynamics (AIMD) simulations. Calculations were run for 5 ps (1 ps of equilibration plus 4 ps of production) at 300 K with fixed lattice parameters using the Bussi–Donadio–Parrinello[60] thermostat and the hybrid PBE0 functional.

All the above described DFT-based calculations were performed using the FHI-AIMS code,[61,62] employing the ferromagnetic solution of the system. All reported atomically partitioned spin populations were calculated using the Hirshfeld method.[63]

For the calculation of the relevant (*i.e.*: non zero) magnetic coupling constants, we used the CRYSTAL09 code[64,65] and the B3LYP[66] hybrid density functional based method with a standard 6-21G* basis set for all atoms.[67,68] ITOL values have been fixed to 7,7,7,7,14 to force stringent numerical convergence of energy and gradients and a shrinking factor of 6 within the Monkhorst–Pack scheme to define the reciprocal space mesh in the 2D irreducible Brillouin zone leading to a set of 20 k-points.

The description of the magnetic properties of a system of interacting localised magnetic moments is based on the Heisenberg–Dirac–Van Vleck (HDVV) spin Hamiltonian[69]

$$\hat{H}^{\mathrm{HDVV}} = -\sum_{\langle i,j \rangle} J_{ij} \hat{\mathbf{S}}_i \cdot \hat{\mathbf{S}}_j \qquad (1)$$

where J_{ij} is the exchange coupling constant between the $\hat{\mathbf{S}}_i$ and $\hat{\mathbf{S}}_j$ localized spin moments and the $\langle i,j \rangle$ symbol indicates that the sum is over nearest neighbours only. A positive value of the exchange coupling constant J_{ij} corresponds to ferromagnetic (FM) interactions, while negative values describe an antiferromagnetic (AFM) interaction (parallel and antiparallel spins respectively). The number, sign and magnitude of the most relevant J_{ij} determine the low-energy spectrum of the system and, consequently, the magnetic structure of the system. The extraction of the different J_{ij} values is based on the mapping approach described elsewhere.[70] In this approach, the extraction of the relevant magnetic coupling constants of the system is based on the use of broken symmetry solutions to represent different magnetic solutions of the Ising spin Hamiltonian[69]

$$\hat{H}^{\mathrm{Ising}} = -\sum_{\langle i,j \rangle} J_{ij} \hat{S}_i^{\,z} \hat{S}_j^{\,z} \qquad (2)$$

where J_{ij} are the exchange coupling constants and the $\hat{S}_i^{\,z}$ and $\hat{S}_j^{\,z}$ are the z components of the corresponding $\hat{\mathbf{S}}_i$ and $\hat{\mathbf{S}}_j$ localized spin moments. The Ising Hamiltonian corresponds to the diagonal terms of the HDVV Hamiltonian. It has been shown that a mapping procedure between the energy values of different broken symmetry solutions and the corresponding expectation values of the HDVV Hamiltonian can be related by using the Ising energy expectation values. A detailed description of this procedure can be found in ref. 71 and a general discussion of the mapping approach to extract J values from BS solutions in related systems can be found in.[70,72,73] In the ESI† we provide the relevant broken symmetry solutions and the particular relations to extract the non-zero magnetic coupling constants described below.

Results and discussion

The most important parameters that determine spin localization in TAMs are the twist angles of the three aryl rings with respect to the bonding plane of the central carbon atom (see Fig. 1).[11] In this respect, the role of chemical functionalization seems to be limited to determining the aryl ring twist angles due to steric hindrance, but other effects such as the electro-donating/withdrawing nature of substituents play a secondary role. The same steric repulsion, as determined by chemical functionality, also determines the rotational freedom of the three aryl rings and thus the ease with which their twist angles may be externally manipulated. Therefore, to explore the role of chemical functionality on the controllability of the material's properties following our approach we carried out our study on two differently functionalized 2D-COFs constructed separately with the TPM and PTM TAM derivatives. These two TAM derivatives present different degrees of aryl ring steric hindrance, due to the different functionalization with H (low) and Cl atoms (high), respectively. PTMs, in particular, have outstanding radical stability[53] due to the "shielding" effect provided by chlorine atoms but, in turn, manipulation of its aryl rings twist should be much more difficult in comparison with the fully hydrogenated TPM, due to the associated higher steric constrain (see the twisting energy profiles for each molecule in the ESI†).

Material design

In the design process our first objective was to ensure that the 2D networks maintained both their planarity and a multi-radical character. To avoid electron pairing (*i.e.* preservation of multi-radical character) based on topological considerations of molecular orbital principles,[74–76] the radical centres should be connected *via meta*-positions with respect to each other (*i.e.* in a non-Kekulé fashion). However, due to the propeller-like

View Article Online
Edge Article Chemical Science

structure of TAMs, connections through the *meta*-positions of aryl rings could lead to non-planar or highly constrained networks. Thus, to ensure planarity, the 2D networks should be propagated through the *para*-positions of TAMs' aryl rings (see Fig. 1 for position labelling). To overcome such contradictory requirements we introduced the use of benzene rings (commonly utilized building blocks composing many reported 2D-COFs[77]) that would connect three TAM units in *meta*-to-*meta* fashion one respect each other while being covalently bonded through the *para*-positions of the TAM aryl rings. Thus, in our resulting proposed periodic structure depicted in Fig. 3a (composed of three TAM units – shaded red, and three connecting benzene rings – shaded purple) both the multi-radical character of the networks and their planarity should be guaranteed.

Based on our designed structure (3a) we constructed two different networks with R = H (TPM 2D-COF) and R = Cl (PTM 2D-COF) whose atom coordinates and cell parameters were fully optimized (see Methodology section). We note that both our networks were constructed with all TAM units having the same helicity of their propeller-like structure; *i.e.* with all aryl rings within the unit cell twisted in the same direction. Experimentally, it is possible that networks may be obtained with some TAM centres possessing different helicities (*i.e.* plus and minus). However, for the properties studied in this work we do not expect this small conformal variability to significantly affect our predictions. As shown in Fig. 3b and c, after optimization, both the TPM and PTM 2D-COFs become, effectively, planar networks with stable radical centres placed in ordered positions within the 2D nano-porous array (pore radius: 0.7 nm). Benzene rings and αC radical centres (purple and red coloured in Fig. 3a, respectively) lay parallel to the network plane, whereas the corresponding aryl rings are partially twisted by 35° and 53° for the TPM and PTM 2D-COFs, respectively (see *y* view in Fig. 3b and c top). These angle values are slightly higher than those ones for the corresponding single molecules (34° and 49°, respectively), which may be attributed to the slightly higher steric congestion within the 2D materials (especially for the PTM case).

Examining the spin distribution (see Fig. 3b and c bottom), it can be seen that all TAM units within both 2D-COFs present spin density (alpha = green, beta = purple) which is mainly located on every αC with very little, or no spin population on the connecting benzene rings. Moreover, the TAM units are, in both cases, ferromagnetically coupled (*i.e.* all unpaired electrons present the same spin alignment). These two features are characteristic of non-Kekulé structures which, besides avoiding electron–electron pairing (*i.e.* quinoidization), induce FM spin alignments.[78] The FM solutions lay 16.2 and 1.6 meV (per unit cell) below the first excited AFM solutions for the TPM and PTM 2D-COFs, respectively. The lower FM stability for the PTM 2D-COF may be associated with a weaker interaction between its unpaired electrons due to the much more pronounced twisted conformation of its aryl rings ($\langle\varphi_i\rangle = 53°$) and the subsequent suppression of spin density on the connecting benzene units. We also note that the closed-shell solutions for the TPM and PTM 2D-COFs are 1.5 and 2.2 eV higher (per unit cell) than the corresponding open shell FM solutions.

The obtained bandgap values of 2.17 and 2.86 eV for the TPM and PTM 2D-COFs, respectively, are indicative of a localization of the electronic states near the Fermi energy level. This suggests that unpaired electrons are not delocalized through

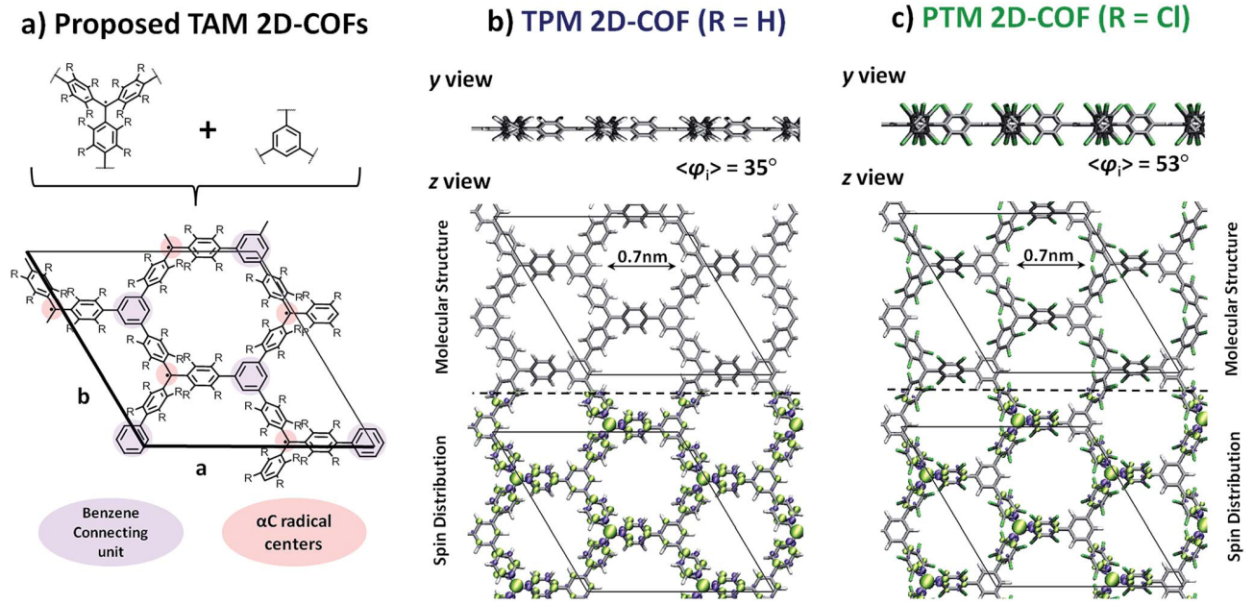

Fig. 3 (a) TAM and benzene building blocks (up) utilized to construct the TAM 2D-COF periodic structure proposed in this work (down). The indicated *a* and *b* in-plane cell parameters are equivalent. Optimized structures of the TPM (b) and PTM (c) 2D-COFs. The spin densities are also shown in the bottom area (alpha = green, beta = purple) of the *z*-view. Lateral *y*-view is provided (top) for facilitating the comparison between the different aryl ring twists within each network. Atom colour key: C – grey, H – white, Cl – green.

the whole π-conjugated electronic system, but rather confined within each corresponding TAM unit. Therefore, our designed TPM and PTM 2D-COFs are not in-plane electrical conductors as other 2D covalent π-conjugated organic materials (such as graphene, where a local perturbation has an effect on the whole π electronic system) but, more likely, covalent frameworks composed of electronically isolated TAM radical centres. However, due to the electro-active nature of TAMs already experimentally exploited for the preparation of non-volatile memory devices,[8] these TAM-based 2D-COFs may be potentially used as flexible data storage materials where every TAM centre within the ordered array may behave as a logic bit with two or more redox states and different output signals.

Structure response to strain

The application of a uniaxial strain onto mono- and multi-layered graphene has been experimentally proven to be a very effective way to tune the electrical properties of 2D materials.[31–37] Although several theoretical works have demonstrated the potential of applying a bi-axial strain to tune fundamental characteristics of many 2D extended systems[79–81] (including graphene[82] and certain 2D-COFs[83]) in experiments monolayered materials are often uniaxially stretched between two electrodes.[32] As mentioned above, we focus on uniaxial strain by increasing the *a* (or, equivalently, *b*) cell parameter of our 2D-COFs as it was found to be the energetically most facile way of distorting the material and was that which induced a high degree of aryl ring twisting, which is the principal objective of our work. We compare this situation with that for bi-axial strain in the ESI.†

Fig. 4 Fig. 4 shows the *z* and *y* views of the relaxed structures (top) and most stretched (+22%) structures (bottom) for the TPM (4a) and PTM (4b) 2D-COFs. As it can be observed, uniaxially stretching the networks effectively generates a twist on some of the aryl rings of the constituent TAMs. Specifically, for both cases, two of the three aryl rings within each TAM unit twist towards more orthogonal positions (1 and 2 in 4a and b) with respect to the 2D network's plane, whereas the third one becomes more flattened respectively (3 in 4a and b, see twist angle values below each conformer). This twisting effect arises from the compression of the structure of the material in the in-plane direction perpendicular to the applied strain and the subsequent increase in steric hindrance between adjacent aryl rings. In Fig. 4c it can be seen that the energetic cost associated with uniaxially stretching the 2D-COFs by more than +20% of their initial size is rather modest (*ca.* 0.1 eV per atom). Graphene monolayers, for comparison, suffer irreversible ruptures when being uniaxially stretched by +3%.[32,34,37] Moreover, our calculated Young's modulus for both networks (58 and 55 GPa for TPM and PTM 2D-COFs, respectively, as calculated for in-plane strains covering 0–15%) is around 20 times smaller than that of graphene (1024 GPa),[84] which corroborates the relatively high elasticity of our designed covalent networks. This property may be understood by their nanoporous structure which offers a number of mechanical relaxation modes (*i.e.* aryl ring bending, twisting, bond lengthening, *etc.*) upon stretching as compared to the perfectly flat and densely tessellated graphene.

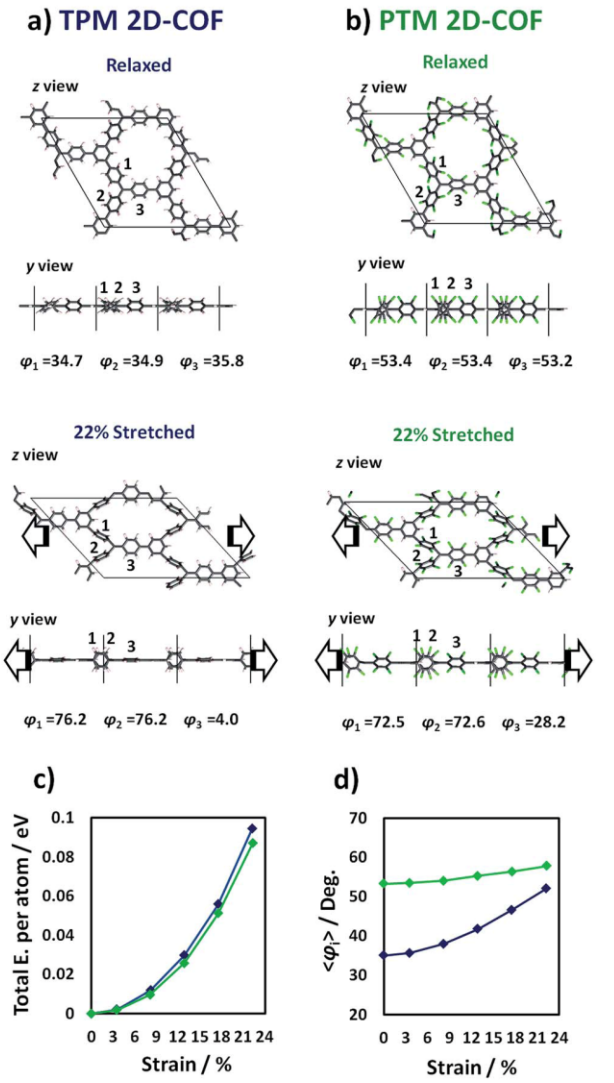

Fig. 4 Out-of-plane (*z* view) and in-plane (*y* view) perspectives of the relaxed (up) and 22% stretched (down) TPM (a) and PTM (b) 2D-COFs. Both nets were stretched from 0 to 5 Å in the *x* direction parallel to the network plane (see arrows) while allowing the periodic cell to relax in the other in-plane direction (*y*). The twist angles of the indicated aryl rings (1, 2 and 3) are provided below each structure. (c) Total energy variation per atom (relative to the relaxed structure) *vs.* applied strain for the TPM (blue) and PTM 2D-COFs (green). (d) Variation of $\langle\varphi_i\rangle$ (where $\langle\varphi_i\rangle = (\sum\varphi_i)/9$ and φ_i are the aryl ring twist angles with respect to the corresponding αC plane) *vs.* applied strain for the TPM (blue) and PTM 2D-COFs (green).

We also note that, with uniaxial strain, the nanopores of the 2D-COFs become elongated parallel to the stretched direction (1 nm) and narrower with respect to the perpendicular direction (0.3 nm), as compared to the more radially symmetric pores (0.7 nm diameter) of the unstrained structures.

In Fig. 4d we plot the average twist angle of all aryl rings within the unit cell with respect to the corresponding central αC plane ($\langle\varphi_i\rangle$) against uniaxial strain. Here it can be seen that, although not all aryl rings rotate in the same direction (see

View Article Online
Edge Article
Chemical Science

angle values in 4a and b), their average twist angle smoothly increases during the stretching process for both networks. Moreover, as already expected, the TPM 2D-COF, with a lower steric hindrance imposed by its phenyl rings, presents a wider variation of $\langle\varphi_i\rangle$ (blue curve in 4d) as compared to the more sterically hindered PTM 2D-COF (green curve in 4d).

Spin localization response to strain

The change in $\langle\varphi_i\rangle$ produced by the strain application (Fig. 4d) should give rise to a net change in spin localization within every radical centre within the networks as found for single TAM molecules.[11] By examining the spin density distribution for the relaxed (Fig. 5a) and most stretched (Fig. 5b) TPM 2D-COF structures we can see how, upon stretching, the spin distribution becomes localized on every αC and on the flattened aryl rings (similar changes are obtained for the PTM 2D-COF, see ESI†). For single molecule TAMs we found that the spin localization, as represented by the αC-partitioned spin population, linearly varies with the average cosine squared of the twist angles of the three aryl rings with respect to the αC plane (*i.e.* $\langle\cos^2\varphi_i\rangle = (\cos^2\varphi_1 + \cos^2\varphi_2 + \cos^2\varphi_3)/3$).[11] To test this relationship in our uniaxially stretched 2D networks we calculated the averaged αC-partitioned spin population for every conformation and the corresponding $\langle\cos^2\varphi_i\rangle$ value (where $\langle\cos^2\varphi_i\rangle = (\sum\cos^2\varphi_i)/9$ and φ_i is the twist angle of each aryl ring with respect to the corresponding αC plane). Fig. 5c shows the variation of the average αC-partitioned spin population against $\langle\cos^2\varphi_i\rangle$ for the differently stretched TPM and PTM 2D-COFs (blue and green, respectively).

As it can be seen in Fig. 5c, within both 2D-COFs the average αC partitioned spin population is linearly dependent on $\langle\cos^2\varphi_i\rangle$ for the differently stretched structures. Hence, the spin-localization structural dependence for single molecule TAMs is applicable to our mechanically stretched TAM-based 2D-COFs, confirming the power of aryl ring twist angles to control the localization of unpaired electrons within our designed materials. It is also worth noting the different responses of the two differently functionalized networks. The TPM 2D-COF, which can accommodate wider twisting angles (see Fig. 4d) presents an accordingly larger spin localization variation (blue points in 5c) as compared to the more structurally constrained chlorinated PTM 2D-COF (green points in 5c).

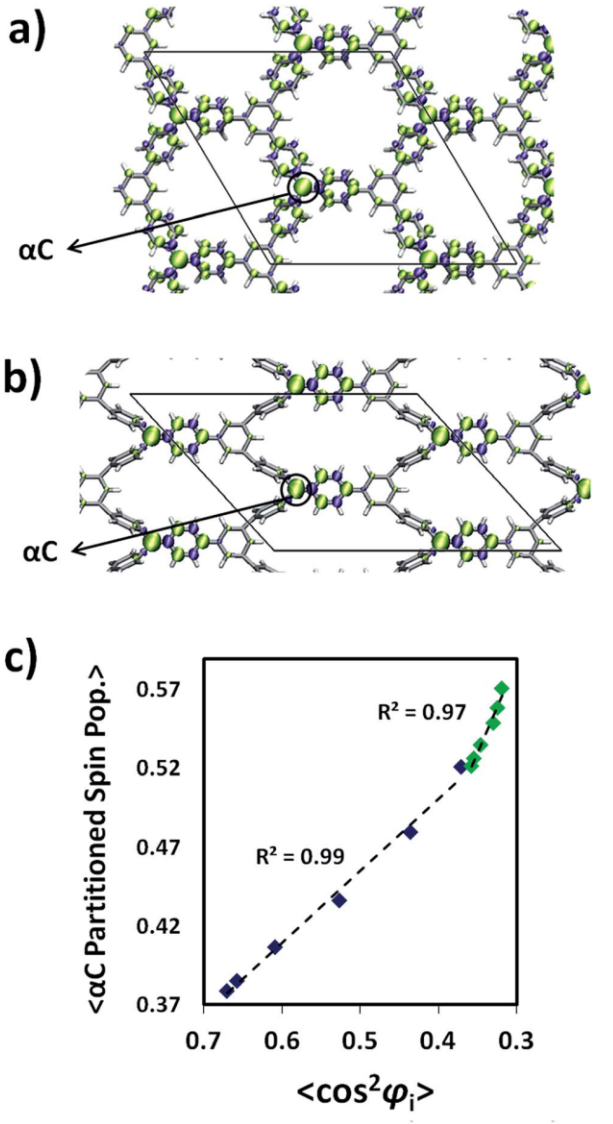

Fig. 5 Relaxed (a) and 22% stretched (b) TPM 2D-COF structures with the corresponding represented spin density (alpha = green, beta = purple). (c) Average αC-partitioned spin population against $\langle\cos^2\varphi_i\rangle$ (where $\langle\cos^2\varphi_i\rangle = (\sum\cos^2\varphi_i)/9$ and φ_i are the aryl ring twist angles with respect to the corresponding αC plane) for the differently stretched conformations for the TPM (blue) and PTM (green) 2D-COFs.

Electronic response to strain

The results of Fig. 5 demonstrate that it is possible to localize all unpaired electrons within our designed networks by applying uniaxial strain. As reported for bi-phenyl compounds, localizing electrons in π-conjugated systems dramatically influences their associated energies and, hence, the corresponding optical absorption bands.[30] Therefore, the mechanically induced spin localization shown in Fig. 5 should be accompanied by significant variations in the electronic band structure of both materials and the related physico-chemical properties. In Fig. 6 the band structure for the relaxed and mostly stretched conformations of the TPM 2D-COF are shown (blue lines = alpha spin, red lines = beta spin). For the PTM 2D-COF we obtained very similar band structure characteristics (see ESI†).

As it can be seen in Fig. 6a, in the relaxed conformation the π-conjugated double-bond system (πO) lays at low energies as a set of bands with non-negligible electronic dispersion, which is in accordance with its intrinsically delocalized nature. Above them and energetically well separated, the singly occupied levels (SO) corresponding to the three unpaired electrons within the unit cell appear as flat electronic bands, suggesting the lack of significant delocalization of these states. The singly unoccupied counterparts (SU) appear at higher energies showing,

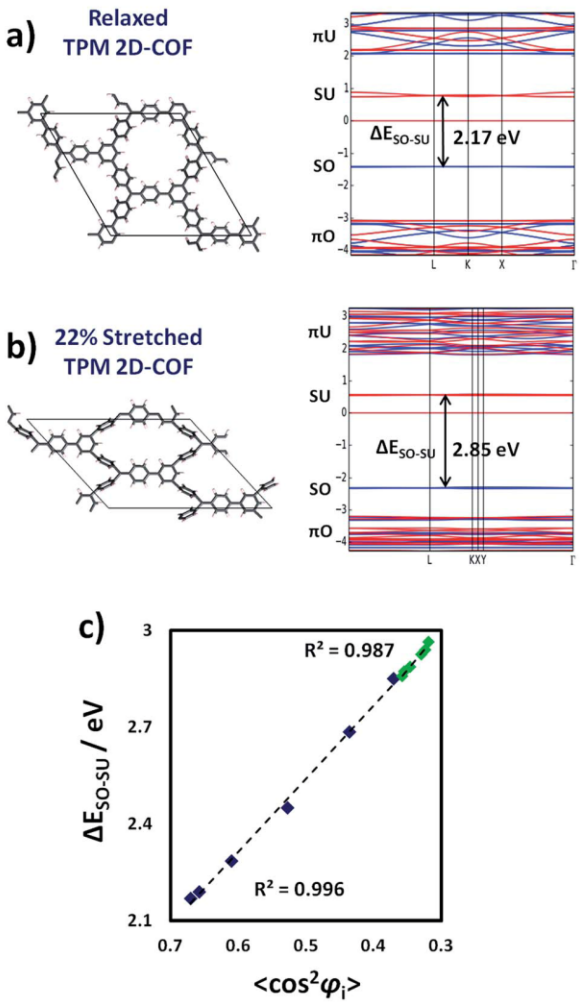

Fig. 6 Band structure for the relaxed (a) and 22% stretched (b) TPM 2D-COF. πO/πU and SO/SU correspond to π-double-bond occupied/unoccupied and singly-occupied/unoccupied electronic levels, respectively. (c) ΔE_{SO-SU} against $\langle\cos^2\varphi_i\rangle$ (where $\langle\cos^2\varphi_i\rangle = (\sum\cos^2\varphi_i)/9$ and φ_i are the aryl ring twist angles with respect to the corresponding αC plane) for each stretched conformation for the TPM (blue) and PTM (green) 2D-COFs.

again, little band dispersion. The flattening of the SO and SU levels are in full accordance with the mostly localized unpaired electrons on αC positions within our networks, as measured by the corresponding spin density distribution (Fig. 5). Above the SO and SU levels, the anti-bonding unoccupied bands of the π-conjugated double-bond system (πU) appear with significant dispersion.

Upon stretching (Fig. 6b), the π-conjugated double-bond bands (πO and πU) become substantially flattened, which indicates that aryl ring twisting cuts the delocalization of the π-conjugated double bond electrons. This effect is in agreement with the experimentally demonstrated electrical conductivity dependence on twist angles in π-conjugated single-molecule devices.[24] The singly occupied/unoccupied levels (SO and SU) do not present large changes with respect to the shape of their bands, but their relative energy difference (ΔE_{SO-SU}) increases upon stretching, as indicated by black arrows (Fig. 6a and b). Such type of energy gap variation has also been observed in differently functionalized bi-phenyl compounds where a linear correlation was obtained with the $\cos^2$ of the corresponding twist angles based, also, on the π-conjugation dependence on the structural parameter.[30] Therefore, due to the effective localization of unpaired electrons by twisting aryl rings (Fig. 5), we should expect a similar correlation between ΔE_{SO-SU} and the average of aryl ring twist angles ($\langle\cos^2\varphi_i\rangle$) during the uniaxial strain application. In Fig. 6c we plot ΔE_{SO-SU} against $\langle\cos^2\varphi_i\rangle$ (where $\langle\cos^2\varphi_i\rangle = (\sum\cos^2\varphi_i)/9$ and φ_i is the twist angle of each aryl ring with respect to the corresponding αC plane) for the differently stretched conformations for both the TPM and PTM 2D-COFs (blue and green, respectively).

As it can be seen in Fig. 6c there exists an excellent correlation between ΔE_{SO-SU} and $\langle\cos^2\varphi_i\rangle$ for the differently stretched TPM (blue) and PTM (green) 2D-COFs. In this case the link between the two parameters seems to be independent on the chemical functionalization of the networks, since for both 2D-COFs ΔE_{SO-SU} follows the same correlation line with $\langle\cos^2\varphi_i\rangle$. We found the same phenomenon when systematically twisting aryl rings in single TAM molecules by constrained optimizations (see ESI†), confirming the generality of this powerful structural–electronic relationship for TAM-based systems. Therefore, the intimate link between the delocalization of electrons and their energies[30] allows tuning of the electronic band structure of the material by manipulation of aryl ring twist angles (see Fig. 6a and b). In this way, it is possible for instance, to elastically tune ΔE_{SO-SU} by up to 0.7 eV within the TPM 2D-COF by simply stretching the network by a 22% of its initial size (blue points in Fig. 6c). We note that these singly occupied/unoccupied levels (SO and SU) participate in a number of important phenomena in TAM-based materials, such as colour absorption bands,[8] fluorescence[6] or enhanced single molecule electrical conductivities.[7] Therefore, the results of Fig. 6 demonstrate that it would be possible to finely tune optical and electrical (*e.g.* sheet to substrate) properties of the material by stretching it in one direction.

Magnetic response to strain

As previously mentioned, both the TPM and PTM 2D-COFs present ferromagnetic ordering in their ground state. We calculated the *J* coupling parameters (see Methodology section for computational details and employed equations) between first and second nearest neighbouring radical units (J_1 and J_2 in Fig. 7a). Thus we found that magnetic interactions within second nearest neighbours (J_2 = 0.00074 meV) are negligibly small compared to first neighbours interactions (J_1 = 0.68 meV), which is in concordance with previous studies in organic poly-radicals.[78,85] Fig. 7b depicts a particular pair of first TAM neighbours (1 and 2) whose corresponding unpaired electrons interact with each other on the connecting ring b. The magnitude of the magnetic interaction depends on the degree of delocalization of both unpaired electrons on ring b and, hence,

View Article Online
Edge Article Chemical Science

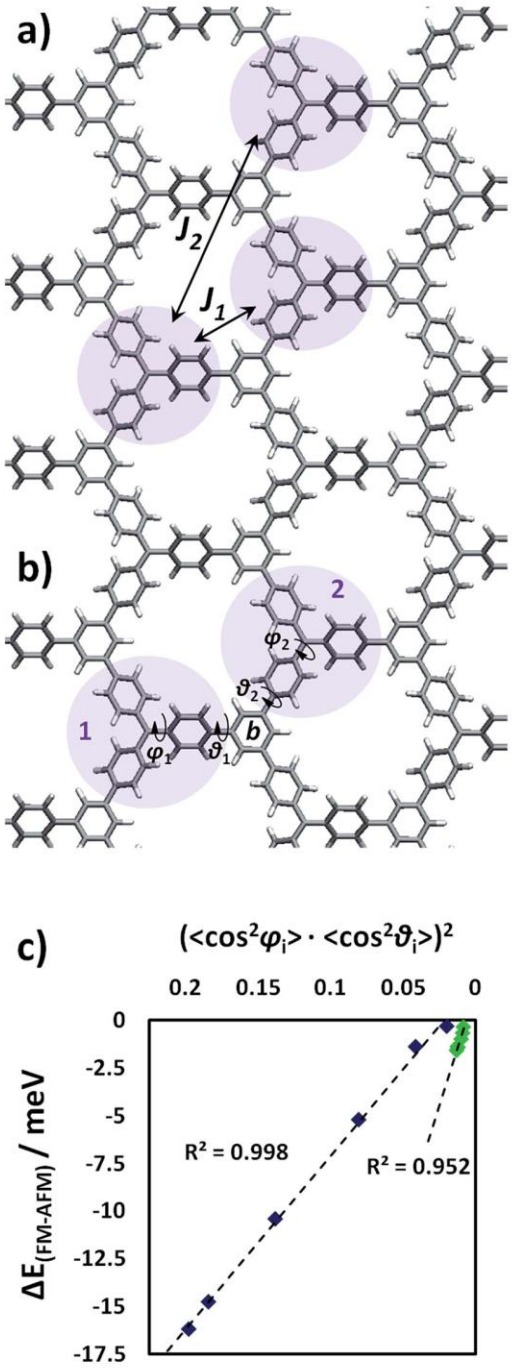

Fig. 7 (a) Calculated magnetic coupling constants between first (J_1) and second (J_2) nearest neighbouring TAM centers. Details on the calculation of J coupling constants can be found in the Methodology section. (b) Representation of the involved aryl ring twist angles. (c) Energetic difference (meV) between the ground state ferromagnetic solution and the first excited antiferromagnetic one (ΔE_{FM-AFM}) against $(\langle\cos^2\varphi_i\rangle \cdot \langle\cos^2\theta_i\rangle)^2$ (where φ_i and θ_i are the twist angles of aryl rings with respect to the corresponding αC and benzene ring planes, respectively) for the differently stretched TPM (blue) and PTM (green) 2D-COFs.

based on pi-overlapping arguments, the magnetic interaction strength between TAM units 1 and 2 can be well estimated by:

$$(\cos^2\varphi_1 \cdot \cos^2\theta_1) \times (\cos^2\varphi_2 \cdot \cos^2\theta_2) \quad (3)$$

where each term of the product is associated to the degree of delocalisation of each unpaired electron towards ring b (see Fig. 7b for labels). Due to the homogeneous structural response to the applied strain within both 2D-COFs, instead of treating every magnetic interaction individually, we could embrace the global magnetic response of the material by utilizing the average of the involved aryl ring twist angles. Hence,

$$(\langle\cos^2\varphi_i\rangle \cdot \langle\cos^2\theta_i\rangle)^2 \quad (4)$$

should correlate with the ferromagnetic stability of both TAM 2D-COFs, where φ_i and θ_i refer to the twist angles of the ith aryl ring with the corresponding αC and benzene ring planes, respectively. Note the overall square in eqn (4), arising from the fact that two unpaired electrons have to be considered in order to properly assess magnetic interactions. For every stretched conformation we extracted the energy difference between the ground state ferromagnetic solution and the first excited antiferromagnetic one (ΔE_{FM-AFM}).

In Fig. 7c we plot ΔE_{FM-AFM} against $(\langle\cos^2\varphi_i\rangle \cdot \langle\cos^2\theta_i\rangle)^2$ for the uniaxially stretched TPM and PTM 2D-COFs (blue and green points, respectively). As we can see, ΔE_{FM-AFM} linearly varies with $(\langle\cos^2\varphi_i\rangle \cdot \langle\cos^2\theta_i\rangle)^2$ for both TAM 2D-COFs due to the fundamental link between the aryl ring twist angles and the localization of unpaired electrons (Fig. 5). More specifically, as it can be seen in the ESI,† the magnetic coupling constants between first neighbours (J_1) split into two different new magnetic coupling constants upon stretching (J_{1b} and J_{1c}). This is a direct consequence of the uniaxial applied strain and the associated reduction in the symmetry of the triangle relating the three nearest radical centres (see ESI†), which goes from equilateral (relaxed) to isosceles (22% stretched).

More generally, as shown in Fig. 7c, for the most stretched conformations (22% strained) of both materials the ferro- and anti-ferromagnetic solutions become nearly degenerate. This corresponds to a situation that has been mechanically induced where unpaired electrons do not have any energetically preferred spin alignment. Thus the ground ferromagnetic state of both TAM 2D-COFs can be tailored by applying increasing strains, due to the corresponding twisting of aryl rings. Reports of a synthesized tri-TPM derivative, which may be understood as the analogue oligomer of our designed TPM 2D-COF (see ESI† for molecular structure), showed this derivative presents a quartet state (*i.e.* ferromagnetic interactions) at 93 K. Due to the very small obtained J coupling constants for both materials though, any spin alignment would be expected only below 10 K (as previously reported for TAM-based magnetic polymers[13]) This would thus limit the potential of our currently proposed materials as organic ferromagnets. However, our results demonstrate the existence of a general, simple and powerful way to externally tune magnetic interactions in multi-radical π-conjugated 2D systems and, hence, we believe these ideas may

be applied to other organic ferromagnets, or may inspire the rational design and preparation of similar organic materials with mechanically switchable magnetic properties.

Effect of finite temperature and the role of chemical functionalization

As we have seen above, despite the fact that both networks show similar physico-chemical tendencies upon stretching, the range of variation for the TPM 2D-COF characteristics always appears to be much larger than that for the PTM 2D-COF. These differences arise from the correspondingly different rotational freedom of aryl rings, due to the different steric hindrances within each material, as previously explained. Despite being much smaller, the variations in PTM 2D-COF characteristics upon stretching are still detectable, as it can be seen in Fig. 5–7 (green points). However, these results are obtained in the gas phase at 0 K and the effect of finite temperatures, which introduces random variations in the material's properties due to bond vibrations,[11] might hinder the detection of such mechanically induced physico-chemical changes at realistic conditions. Hence, we probed the behaviour of our designed TAM 2D-COFs under finite temperatures by performing AIMD simulations at 300 K for the relaxed and totally stretched (+22%) conformations of both the TPM and PTM 2D-COFs (see Methodology section for details). Fig. 8 shows the thermal fluctuation of most relevant properties during the simulated 4 ps at 300 K for the relaxed (thin lines) and most stretched (thick lines) conformations of the TPM (a) and PTM (b) 2D-COFs.

In the top panels of both Fig. 8a (TPM 2D-COF) and 8b (PTM 2D-COF) we can see how the average aryl ring twist angle (*i.e.* $\langle\varphi_i\rangle$) vary *versus* time at 300 K. Dashed lines represent the corresponding values at 0 K. Thus, it can be seen that the effect of finite temperatures does not importantly vary the average aryl ring twist angle from the corresponding value at 0 K, but rather introduces a random oscillation around the most stable conformation. Moving to the spin localization (Fig. 8a and b, middle panels) and ΔE_{SO-SU} variations (Fig. 8a and b bottom panel) *versus* time we can see that very similar results are obtained. For both quantities the predicted values at 0 K (dashed lines) are well maintained at 300 K and thermal energy simply introduces fast random fluctuations due to thermal vibrations. By comparing the three graphs within each network we can see how the rotational oscillations of aryl rings are approximately followed by the spin localization and the ΔE_{SO-SU} fluctuations. This demonstrates that the intimate link between the structural parameter and the physico-chemical properties within both 2D-COFs is well maintained at room temperature. This behaviour was also observed for single molecule TAMs.[11]

However, the most relevant conclusions from Fig. 8 are extracted by comparing the results from the two differently functionalized networks. In the TPM 2D-COF (Fig. 8a) thermal vibrations do not prevent distinguishing the different signals from the relaxed and most stretched conformations, as the perturbation produced by the uniaxial strain is substantially higher than the thermal noise for all studied properties. For the PTM 2D-COF (Fig. 8b) though, the mechanically induced changes on both the spin localization and ΔE_{SO-SU} are so small that they are similar in magnitude to the background noise produced by thermal fluctuations (Fig. 8b), hence making their detection over time much more difficult or even not possible. Thus, these results unambiguously demonstrate the key role of chemical functionalization in order to exploit the power of aryl ring twist angles to externally control fundamental characteristics of the materials. On the basis of these results (Fig. 8), the TPM 2D-COF appears to be a better candidate for such a purpose. However, as previously explained, it is more feasible to prepare a PTM 2D-COF in the lab due to the higher stability of

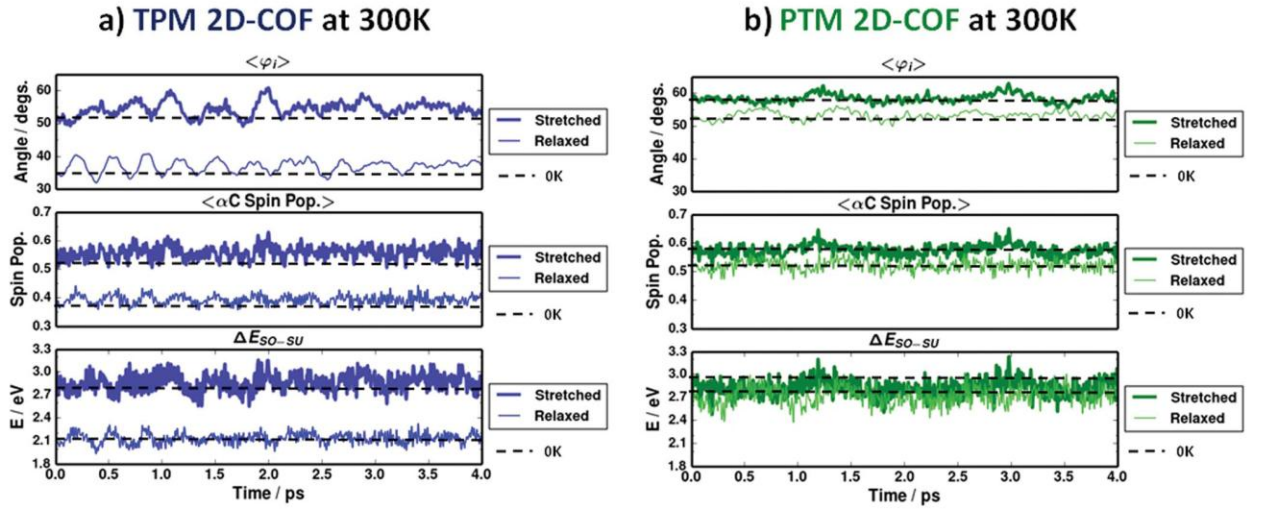

Fig. 8 Averaged aryl ring twist angle (up), αC-partitioned spin population (middle) and ΔE_{SO-SU} (down; SO and SU are the singly occupied/unoccupied levels corresponding to unpaired electrons) variations during 4 ps of an *ab initio* molecular dynamics simulation (AIMD) at 300 K for 5 ps of time (1 ps of equilibration plus 4 ps of production) for the TPM (a) and PTM (b) 2D-COFs. Dashed black lines represent the corresponding values at 0 K.

View Article Online
Edge Article Chemical Science

the fully chlorinated TAM derivatives. Therefore, an optimal candidate to design a TAM-based 2D-COF in the lab with externally controllable characteristics would be an intermediate derivative (between the TPM and PTM) with the most appropriate balance between chemical stability and structural flexibility. Such TAMs may be found by use of appropriately substituted PTM derivatives[86,87] or, more generally, in the extensive library of synthesized TAM derivatives.[2]

Conclusions and outlook

The main objective of this work was to demonstrate that the spin-localization *versus* structural dependence in single-molecule TAMs[41] could be exploited for the design of multi-functional materials with externally controllable characteristics. The principal barrier for achieving this aim was finding the most appropriate platform to manipulate the aryl ring twist angles by external means; a challenge that, although theoretically proposed,[88] as far as we are aware has not yet been experimentally achieved for any material. We found 2D-COFs to be the most appropriate platform for such a purpose, due to them realizing a set of three criteria that we believe to be crucial for our proposal. We thus designed two 2D-COFs based on the triphenylmethyl (TPM) and the perchloro-triarylmethyl (PTM), respectively. After 0 K structure optimization using DFT methods, the materials have shown to be stable planar multi-radical nanoporous networks which possess ferromagnetically coupled open-shell centres and moderately large bandgaps.

By mechanically stretching the networks in one of the in-plane directions, we show that most important properties of the designed materials can be finely and elastically tuned. Properties such as spin localization, ferromagnetic interactions and electronic energy levels can all be smoothly controlled by applying a uniaxial strain. This behaviour relies on the manipulation of TAM's aryl rings twist angles upon stretching the organic networks, which is confirmed by the linear dependence that all the studied properties show *versus* the averaged cosines squared of the corresponding dihedral angles.

By performing AIMD simulations at 300 K for the relaxed and most stretched conformations of the two 2D networks, we show that steric hindrance, determined by the chemical functionalization of the networks, plays a crucial role in determining the ease by which aryl rings can be twisted, and thus the external control of materials' properties. PTMs are the most promising building blocks to be used for preparing a TAM-based 2D-COF. However, for better control of properties *via* strain-induced aryl ring twist angles, a TPM-based material would be preferential. To avoid the technical difficulties of preparing a stable material based on TPM derivatives, a specifically designed TAM derivative presenting radical stability and aryl ring structural freedom (*i.e.* between PTM and TPM) would probably be the optimal practical building block for realizing TAM-based 2D-COFs with controllable characteristics by mechanical means. Fortunately, the wide range of existing and ever increasing experimentally synthesised TAM derivatives greatly facilitates finding such a molecular candidate.

In summary, we believe that this work represents the first instance where a material has been specifically and rationally designed to enable control of its most fundamental properties by external manipulation of its aryl ring twist angles. The power of this structural parameter in π-conjugated single molecule systems has been theoretical and experimentally demonstrated.[24,25,28–30] Our work shows how this fundamental molecular level link between structure and properties can be entirely transferred to extended materials, opening thus its potential use which may give rise to unprecedented technological applications. We hope this work becomes the starting line for the exploration of a new class of functional materials where aryl ring twist angles can be internally tuned (*e.g.* by chemical design) or externally varied (*e.g.* by mechanical strain, electric/magnetic fields, light irradiation) to yield molecular scale control of material's properties. Although of a predictive nature, our work is strongly grounded in the reported synthetic chemistry of both persistent radicals and 2D-COFs. As such we strongly believe in the chemical feasibility of our presented proposal which may inspire the experimental realization of similar extended 2D systems in the close future.

Acknowledgements

This research was supported by the Spanish MINECO grant CTQ2015-64618-R and, in part, by Generalitat de Catalunya grants 2014SGR97 and XRQTC. D. R. acknowledges funds from Spanish MINECO through research grants PRI-PIBIN-2011-1028. We acknowledge access to supercomputer resources as provided through grants from the Red Española de Supercomputación. I. A. also acknowledges the Spanish Ministerio de Educación Cultura y Deporte for a FPU PhD scholarship.

Notes and references

1 M. Gomberg, *J. Am. Chem. Soc.*, 1900, **22**, 757–771.
2 T. T. Tidwell, in *Stable Radicals: Fundamentals and Applied Aspects of Odd-Electron Compounds*, ed. R. G. Hicks, John Wiley & Sons, Ltd, Chichester, UK., Ontario, 2010, pp. 1–31.
3 I. Ratera and J. Veciana, *Chem. Soc. Rev.*, 2012, **41**, 303–349.
4 J. Veciana and I. Ratera, in *Stable Radicals: Fundamentals and Applied Aspects of Odd-Electron Compounds*, ed. R. G. Hicks, John Wiley & Sons, Inc., 2010, pp. 33–80.
5 M. Mas-Torrent, N. Crivillers, V. Mugnaini, I. Ratera, C. Rovira and J. Veciana, *J. Mater. Chem.*, 2009, **19**, 1691.
6 A. Datcu, N. Roques, V. Jubera, D. Maspoch, X. Fontrodona, K. Wurst, I. Imaz, G. Mouchaham, J. P. Sutter, C. Rovira and J. Veciana, *Chem.–Eur. J.*, 2012, **18**, 152–162.
7 N. Crivillers, C. Munuera, M. Mas-Torrent, C. Simão, S. T. Bromley, C. Ocal, C. Rovira and J. Veciana, *Adv. Mater.*, 2009, **21**, 1177–1181.
8 C. Simão, M. Mas-Torrent, N. Crivillers, V. Lloveras, J. M. Artés, P. Gorostiza, J. Veciana and C. Rovira, *Nat. Chem.*, 2011, **3**, 359–364.
9 C. Simão, M. Mas-torrent, J. Veciana and C. Rovira, *Nano Lett.*, 2011, **11**, 4382–4385.
10 R. Frisenda, R. Gaudenzi, C. Franco, M. Mas-Torrent, C. Rovira, J. Veciana, I. Alcon, S. T. Bromley, E. Burzurí and H. S. J. van der Zant, *Nano Lett.*, 2015, **15**, 3109–3114.

11 I. Alcon and S. T. Bromley, *RSC Adv.*, 2015, **5**, 98593–98599.
12 G. Kothe and H. Zimmermann, *Tetrahedron*, 1973, **29**, 2305–2313.
13 A. Rajca, J. Wongsriratanakul and S. Rajca, *Science*, 2001, **294**, 1503–1505.
14 N. M. Shishlov, *Russ. Chem. Rev.*, 2006, **75**, 863–884.
15 R. Gaudenzi, E. Burzurí, D. Reta, I. d. P. R. Moreira, S. T. Bromley, C. Rovira, J. Veciana and H. S. J. van der Zant, *Nano Lett.*, 2016, 1–17.
16 C. Gabellieri, V. Mugnaini, J. C. Paniagua, N. Roques, M. Oliveros, M. Feliz, J. Veciana and M. Pons, *Angew. Chem., Int. Ed.*, 2010, **49**, 3360–3362.
17 Q. Peng, A. Obolda, M. Zhang and F. Li, *Angew. Chem., Int. Ed.*, 2015, **54**, 7091–7095.
18 D. Maspoch, D. Ruiz-Molina, K. Wurst, N. Domingo, M. Cavallini, F. Biscarini, J. Tejada, C. Rovira and J. Veciana, *Nat. Mater.*, 2003, **2**, 190–195.
19 V. Mugnaini, M. Mas-Torrent, I. Ratera, C. Rovira and J. Veciana, in *Supramolecular Soft Matter: Applications in Materials and Organic Electronics*, ed. T. Nakanishi, John Wiley & Sons, Inc., 1st edn, 2011, pp. 193–215.
20 G. N. Lewis, D. Lipkin and T. T. Magel, *J. Am. Chem. Soc.*, 1944, **66**, 1579–1583.
21 F. C. Adam and S. I. Weissman, *J. Am. Chem. Soc.*, 1958, **80**, 2057–2059.
22 M. Karplus and G. K. Fraenkel, *J. Chem. Phys.*, 1961, **35**, 1312–1323.
23 A. H. Maki, R. D. Allendoerfer, J. C. Danner and R. T. Keys, *J. Am. Chem. Soc.*, 1968, **90**, 4225–4231.
24 L. Venkataraman, J. E. Klare, C. Nuckolls, M. S. Hybertsen and M. L. Steigerwald, *Nature*, 2006, **442**, 904–907.
25 D.-D. Kong, L.-S. Xue, R. Jang, B. Liu, X.-G. Meng, S. Jin, Y.-P. Ou, X. Hao and S.-H. Liu, *Chem.–Eur. J.*, 2015, **21**, 9895–9904.
26 M. G. Vergniory, J. M. Granadino-Roldan, A. Garcia-Lekue and L.-W. Wang, *Appl. Phys. Lett.*, 2010, **97**, 262114.
27 L. Cui, B. Liu, D. Vonlanthen, M. Mayor, Y. Fu, J. F. Li and T. Wandlowski, *J. Am. Chem. Soc.*, 2011, **133**, 7332–7335.
28 A. C. Benniston and A. Harriman, *Chem. Soc. Rev.*, 2006, **35**, 169–179.
29 T. B. Faust, F. Tuna, G. A. Timco, M. Affronte, V. Bellini, W. Wernsdorfer and R. E. P. Winpenny, *Dalton Trans.*, 2012, **41**, 13626.
30 D. Vonlanthen, A. Rudnev, A. Mishchenko, A. Käslin, J. Rotzler, M. Neuburger, T. Wandlowski and M. Mayor, *Chem.–Eur. J.*, 2011, **17**, 7236–7250.
31 N. Ferralis, *J. Mater. Sci.*, 2010, **45**, 5135–5149.
32 X. W. Fu, Z. M. Liao, J. X. Zhou, Y. B. Zhou, H. C. Wu, R. Zhang, G. Jing, J. Xu, X. Wu, W. Guo and D. Yu, *Appl. Phys. Lett.*, 2011, **99**, 213107.
33 L. Gong, R. J. Young, I. A. Kinloch, S. J. Haigh, J. H. Warner, J. A. Hinks, Z. Xu, L. Li, F. Ding, I. Riaz, R. Jalil and K. S. Novoselov, *ACS Nano*, 2013, **7**, 7287–7294.
34 M. Huang, T. A. Pascal, H. Kim, W. A. Goddard III and J. R. Greer, *Nano Lett.*, 2011, **11**, 1241–1246.
35 Z. H. Ni, T. Yu, Y. H. Lu, Y. Y. Wang, Y. P. Feng and Z. X. Shen, *ACS Nano*, 2008, **2**, 2301–2305.
36 H. H. Pérez Garza, E. W. Kievit, G. F. Schneider and U. Staufer, *Nano Lett.*, 2014, **14**, 4107–4113.
37 J. Zhao, G. Wang, R. Yang, X. Lu, M. Cheng, C. He, G. Xie, J. Meng, D. Shi and G. Zhang, *ACS Nano*, 2015, **9**, 1622–1629.
38 Z. Xiang, D. Cao and L. Dai, *Polym. Chem.*, 2015, **6**, 1896–1911.
39 P. J. Waller, F. Gándara and O. M. Yaghi, *Acc. Chem. Res.*, 2015, **48**, 3053–3063.
40 J. W. Colson and W. R. Dichtel, *Nat. Chem.*, 2013, **5**, 453–465.
41 J. Zhou and Q. Sun, *J. Am. Chem. Soc.*, 2011, **133**, 15113–15119.
42 J. Han, X. Fan, Z.-Z. Zhuang, W.-C. Song, Z. Chang, Y.-H. Zhang and X.-H. Bu, *RSC Adv.*, 2015, **5**, 15350–15353.
43 K. V. Rao, S. Mohapatra, T. K. Maji and S. J. George, *Chem.–Eur. J.*, 2012, **18**, 4505–4509.
44 X. H. Liu, C. Z. Guan, D. Wang and L. J. Wan, *Adv. Mater.*, 2014, **26**, 6912–6920.
45 A. Basagni, F. Sedona, C. A. Pignedoli, M. Cattelan, L. Nicolas, M. Casarin and M. Sambi, *J. Am. Chem. Soc.*, 2015, **137**, 1802–1808.
46 J.-J. Adjizian, P. Briddon, B. Humbert, J.-L. Duvail, P. Wagner, C. Adda and C. Ewels, *Nat. Commun.*, 2014, **5**, 5842.
47 E. C. Lee, Y. C. Choi, W. Y. Kim, N. J. Singh, S. Lee, J. H. Shim and K. S. Kim, *Chem.–Eur. J.*, 2010, **16**, 12141–12146.
48 X. Liu, J. Tan, A. Wang, X. Zhang and M. Zhao, *Phys. Chem. Chem. Phys.*, 2014, **16**, 23286–23291.
49 X. Li and Q. Wang, *Phys. Chem. Chem. Phys.*, 2012, **14**, 2065–2069.
50 X. Li, Q. Wang and P. Jena, *J. Phys. Chem. C*, 2011, **115**, 19621–19625.
51 X. Li, J. Zhou, Q. Wang, Y. Kawazoe and P. Jena, *J. Phys. Chem. Lett.*, 2013, **4**, 259–263.
52 J. Zhou, Q. Wang, Q. Sun and P. Jena, *Phys. Rev. B: Condens. Matter Mater. Phys.*, 2011, **84**, 081402.
53 M. Ballester, J. Riera, J. Castañer, C. Badía and J. M. Monsó, *J. Am. Chem. Soc.*, 1971, **93**, 2215–2225.
54 V. Mugnaini, A. Calzolari, R. Ovsyannikov, A. Vollmer, M. Gonidec, I. Alcon, J. Veciana and M. Pedio, *J. Phys. Chem. Lett.*, 2015, **6**, 2101–2106.
55 N. Crivillers, S. Furukawa, A. Minoia, A. Ver Heyen, M. Mas-Torrent, C. Sporer, M. Linares, A. Volodin, C. Van Haesendonck, M. Van Der Auweraer, R. Lazzaroni, S. De Feyter, J. Veciana and C. Rovira, *J. Am. Chem. Soc.*, 2009, **131**, 6246–6252.
56 E. L. Spitler and W. R. Dichtel, *Nat. Chem.*, 2010, **2**, 672–677.
57 (*a*) A. K. Rappe, C. J. Casewit, K. S. Colwell, W. A. Goddard III and W. M. Skiff, *J. Am. Chem. Soc.*, 1992, **114**, 10024–10035; (*b*) J. D. Gale and A. L. Rohl, *Mol. Simul.*, 2003, **29**, 291–341.
58 J. P. Perdew, K. Burke and M. Ernzerhof, *Phys. Rev. Lett.*, 1996, **77**, 3865–3868.
59 C. Adamo and V. Barone, *J. Chem. Phys.*, 1999, **110**, 6158.
60 G. Bussi, D. Donadio and M. Parrinello, *J. Chem. Phys.*, 2007, **126**, 014101.
61 V. Havu, V. Blum, P. Havu and M. Scheffler, *J. Comput. Phys.*, 2009, **228**, 8367–8379.
62 V. Blum, R. Gehrke, F. Hanke, P. Havu, V. Havu, X. Ren, K. Reuter and M. Scheffler, *Comput. Phys. Commun.*, 2009, **180**, 2175–2196.

63 F. L. Hirshfeld, *Theor. Chim. Acta*, 1977, **44**, 129–138.
64 R. Dovesi, R. Orlando and B. Civalleri, *Zeitschrift für Kristallographie*, 2005, **220**, 571–573.
65 R. Dovesi, V. R. Saunders, C. Roetti, R. Orlando, C. M. Zicovich-Wilson, F. Pascale, B. Civalleri, K. Doll, N. M. Harrison, I. J. Bush, P. D'Arco and M. Llunell, *CRYSTAL09 User's Manual*, Univ. Torino, 2009.
66 A. D. Becke, *J. Chem. Phys.*, 1993, **103**, 361–363.
67 P. C. Hariharan and J. A. Pople, *Theor. Chim. Acta*, 1973, **28**, 213–222.
68 M. M. Francl, W. J. Pietro, W. J. Hehre, J. S. Binkley, M. S. Gordon, D. J. DeFrees and J. A. Pople, *J. Chem. Phys.*, 1982, **77**, 3654.
69 E. Ising, *Z. Phys.*, 1925, **31**, 253–258.
70 I. d. P. R. Moreira and F. Illas, *Phys. Chem. Chem. Phys.*, 2006, **8**, 1645–1659.
71 P. Rivero, I. D. P. Moreira and F. Illas, *J. Phys.: Conf. Ser.*, 2008, **117**, 012025.
72 D. R. Mañeru, I. d. P. R. Moreira and F. Illas, *J. Am. Chem. Soc.*, 2016, **138**, 5271–5275.
73 J. P. Malrieu, R. Caballol, C. J. Calzado, C. De Graaf and N. Guihéry, *Chem. Rev.*, 2014, **114**, 429–492.
74 H. C. Longuet-Higgins, *J. Chem. Phys.*, 1950, **18**, 265.
75 W. T. Borden and E. R. Davidson, *J. Am. Chem. Soc.*, 1977, **99**, 4587–4594.
76 A. A. Ovchinnikov, *Theor. Chim. Acta*, 1978, **47**, 297–304.
77 Q. Fan, J. M. Gottfried and J. Zhu, *Acc. Chem. Res.*, 2015, **48**, 2484–2494.
78 N. M. Gallagher, A. Olankitwanit and A. Rajca, *J. Org. Chem.*, 2015, **80**, 1291–1298.
79 R.-N. Wang, X.-R. Zhang, S.-F. Wang, G.-S. Fu and J.-L. Wang, *Phys. Chem. Chem. Phys.*, 2016, **18**, 1258–1264.
80 Z. Ji, R. Zhou, L. C. Lew Yan Voon and Y. Zhuang, *J. Electron. Mater.*, 2016, 1–8.
81 J.-A. Yan, S.-P. Gao, R. Stein and G. Coard, *Phys. Rev. B: Condens. Matter Mater. Phys.*, 2015, **91**, 245403.
82 S.-H. Lee, S. Kim and K. Kim, *Phys. Rev. B: Condens. Matter Mater. Phys.*, 2012, **86**, 155436.
83 J. Zhou, Q. Wang, Q. Sun, Y. Kawazoe and P. Jena, *J. Phys. Chem. Lett.*, 2012, **3**, 3109–3114.
84 Z. G. Fthenakis and N. N. Lathiotakis, *Phys. Chem. Chem. Phys.*, 2015, **17**, 16418–16427.
85 K. Yoshizawa and R. Hoffmann, *Chem.–Eur. J.*, 1995, **1**, 403–413.
86 M. Ballester, J. Castañer, J. Riera, A. Ibáñez and J. Pujadas, *J. Org. Chem.*, 1982, **47**, 259–264.
87 O. Armet, J. Veciana, C. Rovira, J. Riera, J. Castañer, E. Molins, J. Rius, C. Miravitlles, S. Olivella and J. Brichfeus, *J. Phys. Chem.*, 1987, **91**, 5608–5616.
88 D. Miguel, I. R. Marquez, L. Álvarez de Cienfuegos, N. Fuentes, S. Rodríguez-Bolívar, D. J. Cardenas, A. J. Mota, F. Gómez-Campos and J. M. Cuerva, *Phys. Chem. Chem. Phys.*, 2015, **17**, 31902–31910.
89 F. Grillo, V. Mugnaini, M. Oliveros, S. M. Francis, D. J. Choi, M. V. Rastei, L. Limot, C. Cepek, M. Pedio, S. T. Bromley, N. V. Richardson, J. P. Bucher and J. Veciana, *J. Phys. Chem. Lett.*, 2012, **3**, 1559–1564.

Supporting Information of Publication #5

Design of multi-functional 2D open-shell organic networks with mechanically controllable properties

Chem. Sci., 2017,**8**, 1027-1039

Isaac Alcón, Daniel Reta, Iberio de P. R. Moreira and Stefan T. Bromley*

Electronic Supporting Information:

Design of Multi-functional 2D Open-Shell Organic Networks with Mechanically Controllable Properties

Isaac Alcón[1], Daniel Reta[1], Iberio de P. R. Moreira[1] and Stefan T. Bromley[1,2]*

1 Institut de Química Teòrica i Computacional de la Universitat de Barcelona (IQTC-UB). Departament de Química Física de la Universitat de Barcelona. C/ Martí I Franqués 1, 08028 Barcelona (Spain)

2 Institució Catalana de Recerca i Estudis Avançats (ICREA), 08010 Barcelona, Spain

1. Total energy variation vs. twisting aryl rings in TPM and PTM molecules

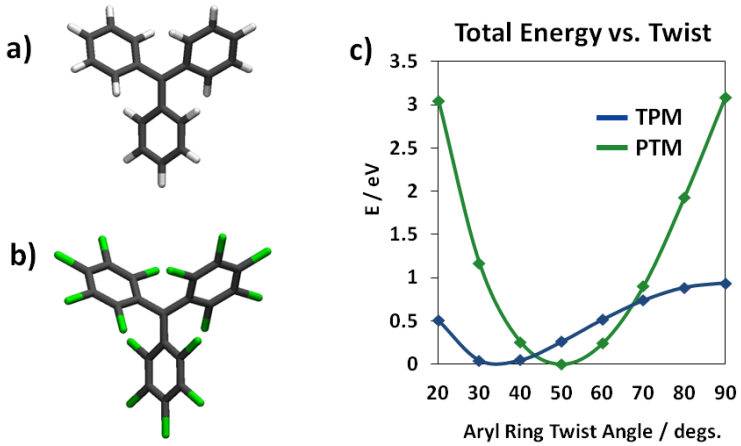

Fig. 1 The three aryl rings of the triphenylmethyl (TPM), (**a**) and perchloro-triarylmethyl (PTM), (**b**) TAM derivatives were systematically twisted from 20 to 90 degrees while relaxing the rest of the molecular structure by constrained optimizations. These calculations were done using the PBE0 hybrid functional[1] and the 6-311++g(d,p) basis set as implemented in the GAUSSIAN09[2] code. c) Resulting total relative energy (with respect to the most stable conformation) variation of the TPM (blue) and PTM (green) molecules against the corresponding $\langle\phi_i\rangle$ value (where $\langle\phi_i\rangle = (\phi_1 + \phi_2 + \phi_3)/3$) during the constrained optimizations.

2. Bi-axial vs. Uni-axial Strain

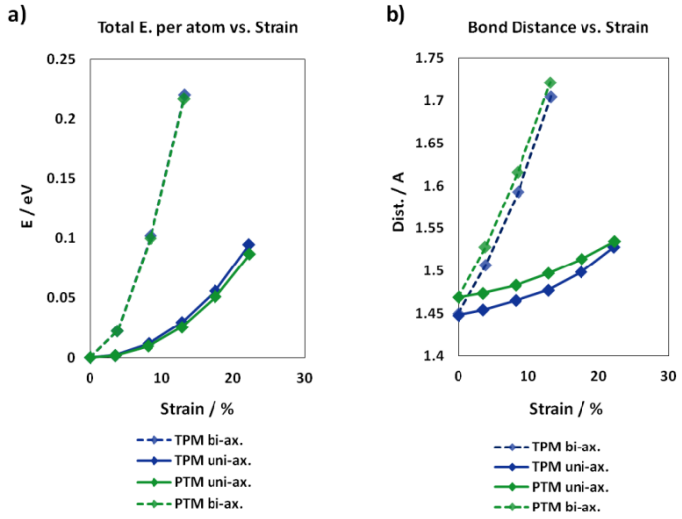

Fig. 2 Total energy per atom (relative to the most stable conformation), (a) and average αC bond distance (b) versus applied strain for both the uni-axial (continuous lines) and bi-axial (dotted lines) stretched TPM (blue) and PTM (green) 2D-COFs.

3. Structure and spin density for PTM 2D-COF

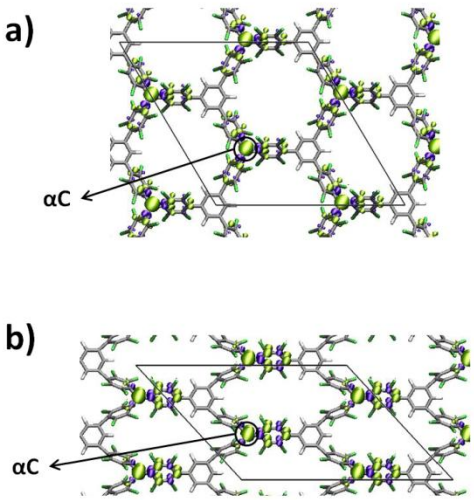

Fig. 3 Relaxed (a) and 22% stretched (b) PTM 2D-COF structures with the corresponding associated spin density (alpha = green, beta = purple). Both the atomic and electronic structures were optimized using the PBE0 hybrid functional[1] within the FHI-AIMS code.[3]

4. Band structures of PTM 2D-COF

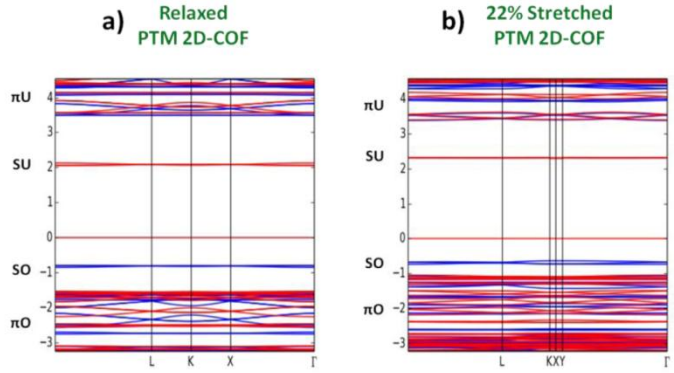

Fig. 4 Band structure for the relaxed (a) and 22% stretched (b) TPM 2D-COF structures. πO, πU, SO and SU correspond to π-double-bond occupied, π-double-bond unoccupied, singly-occupied and singly-unoccupied electronic levels, respectively. Results obtained by using the PBE0 hybrid functional[1] within the FHI-AIMS code.[3]

5. SOMO-SUMO energy difference for PTM and TPM molecules

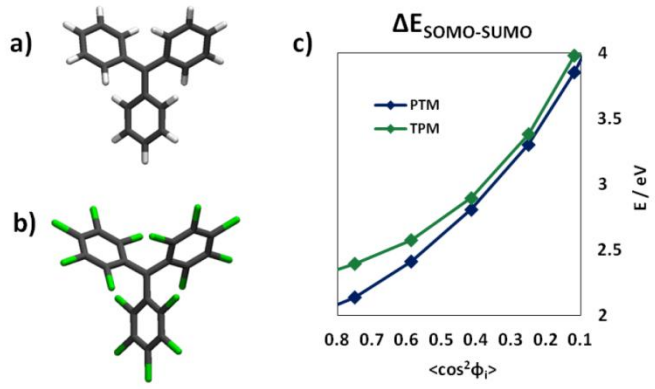

Fig. 5 The three aryl rings of the triphenylmethyl (TPM), (**a**) and perchloro-triarylmethyl (PTM), (**b**) TAM derivatives were systematically twisted from 20 to 90 degrees while relaxing the rest of the molecular structure by constrained optimizations. These calculations were done using the PBE0 hybrid functional[1] and the 6-31++g(d,p) basis set as implemented in the GAUSSIAN09[2] code. **c)** Resulting energy difference between the singly occupied (SOMO) and singly unoccupied (SUMO) molecular orbitals of the TPM (blue) and PTM (green) molecules against the corresponding $\langle\cos^2\phi_i\rangle$ value (where $\langle\cos^2\phi_i\rangle = (\cos^2\phi_1 + \cos^2\phi_2 + \cos^2\phi_3)/3$) during the constrained optimizations.

6. Magnetic coupling calculations

The description of the magnetic properties is based on the Ising spin Hamiltonian[5]

$$\hat{H}^{Ising} = -\sum_{\langle i,j \rangle} J_{ij} \hat{S}_i^z \hat{S}_j^z \qquad (1)$$

	2D-TPM		
	relaxed	Semi-distorted	distorted
	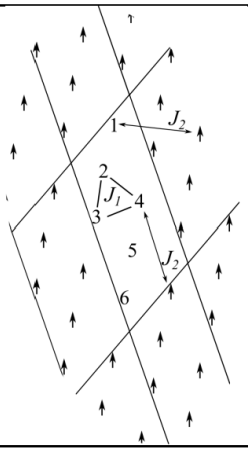	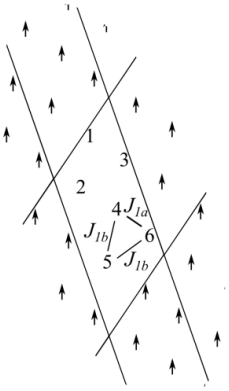	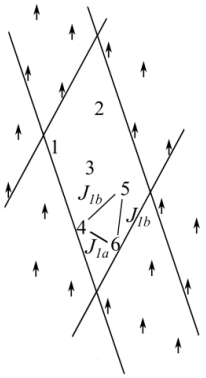
solution	$FM = 123456$ $AFM_1 = 1\bar{2}3456$ $AFM_2 = 1\bar{2}34\bar{5}6$	$FM = 123456$ $AFM_1 = 12345\bar{6}$ $AFM_2 = 1\bar{2}3\bar{4}5\bar{6}$	$FM = 123456$ $AFM_1 = 1234\bar{5}6$ $AFM_2 = 1\bar{2}\bar{3}4\bar{5}6$

	Energy expressions					
	E	ΔE_{FM-AFM}	E	ΔE_{FM-AFM}	E	ΔE_{FM-AFM}
FM	$-\frac{9}{2}(J_1 + J_2)$		$-\frac{1}{2}(3J_{1a} + 6J_{1b})$		$-\frac{1}{2}(3J_{1a} + 6J_{1b})$	
AFM_1	$-\frac{1}{2}(3J_1 + 5J_2)$	$-3J_1 - 2J_2$	$-\frac{1}{2}(J_{1a} + 2J_{1b})$	$-J_{1a} - 2J_{1b}$	$-\frac{1}{2}(J_{1a} + 2J_{1b})$	$-J_{1a} - 2J_{1b}$
AFM_2	$\frac{1}{2}(3J_1 - 9J_2)$	$-6J_1$	$\frac{1}{2}(-3J_{1a} + 6J_{1b})$	$-6J_{1b}$	$\frac{1}{4}(2J_{1a} + 5J_{1b})$	$-\frac{1}{4}(8J_{1a} + 17J_{1b})$

	Calculated energy differences per magnetic centre (cm^{-1})		
ΔE_{FM-AFM_1}	−16.0	−4.8	−0.1
ΔE_{FM-AFM_2}	−32.1	−14.0	−0.3

	Coupling constant values per magnetic centre (cm^{-1})		
J_{1a}	5.5	0.18	0.001
J_{1b}	5.5	2.33	0.06
J_2	-0.006	-	-

Table 1 Schematic representation of the magnetic solutions used to extract the relevant coupling constants in each geometry of the 2D-TPM system, corresponding energy expressions as predicted by the Ising spin Hamiltonian, calculated energy differences and associated coupling constants values.

In order to extract all relevant magnetic interactions, it was necessary to define a magnetic cell which is double in one direction the unit cell. Thus, the magnetic cell shows six different radical centres which provide enough linearly independent equations to extract the coupling constants. The different magnetic

solutions used are denoted FM, AFM1 and AFM2, as depicted in Table 1. With the energy expressions for each of the magnetic states obtained with Ising spin Hamiltonian, and the calculated energy differences associated with these states, based on the mapping approach[6] one can extract all relevant magnetic interactions.

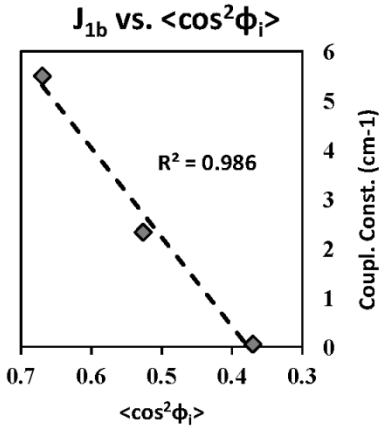

Fig. 6 Linear correlation between coupling constant values (cm^{-1}) against $\langle\cos^2\phi_i\rangle$ for the different geometries (relaxed, semi-stretched, totally stretched) of the TPM 2D-COF. All values are calculated using the B3LYP[7] functional as implemented in the Crystal09 program.[8,9]

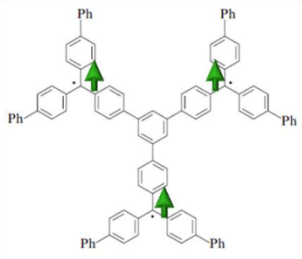

Fig. 7 Molecular structure of a tris-triphenylmethyl derivative experimentally synthesized and measured to present a quartet state at 93K° in solution.[4]

References

(1) Improta, R.; Barone, V. *Chem. Rev.* **2004**, *104* (3), 1231.

(2) Frisch, M. J.; Trucks, G. W.; Schlegel, H. B.; Scuseria, G. E.; Robb, M. A.; Cheeseman, J. R.; Scalmani, G.; Barone, V.; Mennucci, B.; Petersson, G. A.; Nakatsuji, H.; Caricato, M.; Li, X.; Hratchian, H. P.; Izmaylov, A. F.; Bloino, J.; Zheng, G.; Sonnenberg, J. L.; Had, M.; Fox, D. J. Gaussian, Inc.: Wallingford CT 2009,.

(3) Blum, V.; Gehrke, R.; Hanke, F.; Havu, P.; Havu, V.; Ren, X.; Reuter, K.; Scheffler, M. *Comp. Phys. Comm.* **2009**, *180* (11), 2175.

(4) Kothe, G.; Zimmermann, H. *Tetrahedron* **1973**, *29* (15), 2305.

(5) Ising, E. *Zeitschrift für Phys.* **1925**, *31* (1), 253–258.

(6) Moreira, I. de P. R.; Illas, F. *Phys. Chem. Chem. Phys.* **2006**, *8* (14), 1645–1659.

(7) Becke, a D. *J Chem Phys* **1993**, *103* (3-4), 361–363.

(8) Dovesi, R.; Orlando, R.; Civalleri, B. *Z. Krist.* **2005**, *220*, 571–573.

(9) Dovesi, R.; Saunders, V. R.; Roetti, C.; Orlando, R.; Zicovich-Wilson, C. M.; Pascale, F.; Civalleri, B.; Doll, K.; Harrison, N. M.; Bush, I. J.; D'Arco, P.; Llunell, M. *University of Torino*. Torino 2009.

Publication #6

Triarylmethyl-based 2D covalent networks: virtual screening of chemical functionalisation for optimising strain-induced property control

Phys. Chem. Chem. Phys., 2018, Advance Article

Isaac Alcón and Stefan T. Bromley*

PCCP

PAPER

View Article Online
View Journal

Cite this: DOI: 10.1039/c7cp08076j

Triarylmethyl-based 2D covalent networks: virtual screening of chemical functionalisation for optimising strain-induced property control†

I. Alcón [a] and S. T. Bromley *[ab]

Received 1st December 2017,
Accepted 18th January 2018

DOI: 10.1039/c7cp08076j

rsc.li/pccp

Two-dimensional covalent networks based on triarylmethyl (TAM) radical monomers have been proposed as versatile materials whose unpaired electrons may be externally localised/delocalised through the application of external uniaxial strain. This phenomenon arises through the strain-induced variance of the dihedral twist angles of the aryl rings within the network, and allows the control of important physico-chemical properties (*e.g.* magnetic interactions, electronic band gap). In order to experimentally realise such materials, one must find a compromise between the kinetic stability of the TAM monomers (through sterically protecting the radical centre with the appropriate aryl ring functionalisation) and the structural flexibility of the resulting material (provided by low intra-ring steric hindrance). In this work, through an efficient search procedure based on force field-based screening, employing ~1750 calculations, followed by selected accurate electronic structure calculations, we provide support for the experimental viability of TAM-based 2D networks with highly controllable properties.

1 Introduction

Triarylmethyls (TAMs) form an important family of persistent organic radicals in which an unpaired electron mainly resides on a central carbon atom that is partially protected by three surrounding aryl rings (see Fig. 1). The first discovered TAM, synthesised in 1900 by Moses Gomberg,[1] has H-functionalised aryl rings and is only kinetically stable for days under ambient conditions. However, by functionalizing the aryl rings with bulky groups, such as chlorine atoms, the radical centre becomes sterically protected leading to kinetic stabilities of tens of years.[2] Such stable open-shell organic species have great potential for device applications[3,4] and have already been used to prepare many different materials such as organic polymer magnets,[5,6] non-volatile memory devices,[7] molecular wires,[8,9] switchable surfaces,[10] dynamic-nuclear polarization components,[11] organic light emitting diodes[12] and nano-porous magnetic sensors,[13] among others.[14] In a recent study[15] we demonstrated that in TAMs there exists an intrinsic relationship between the average twist angle of the three aryl rings, $\langle\varphi_i\rangle$, and the degree of spin localization of the unpaired electron on the central carbon atom (see Fig. 1). The unpaired electron is linked to many physical characteristics of TAMs such as light absorption bands,[16] magnetoresistance phenomena[8] and enhanced electrical conductivities.[17] This suggests that varying electron localization/delocalization in TAMs could lead to an associated control over

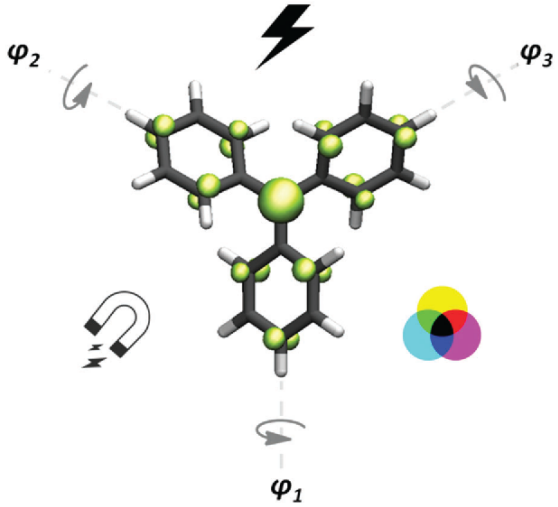

Fig. 1 Generic molecular structure of TAMs. φ_1, φ_2 and φ_3 represent the aryl ring twist angles mainly determining the spin density distribution associated with the unpaired electron (green) in TAMs. The unpaired electron and its degree of delocalization are strongly linked to the electrical, optical and magnetic properties of TAMs.

[a] Department de Ciència de Materials i Química Física & Institut de Química Teòrica i Computacional, Universitat de Barcelona, C/Martí i Franquès 1, E-08028 Barcelona, Spain. E-mail: s.bromley@ub.edu
[b] Institució Catalana de Recerca i Estudis Avançats (ICREA), E-08010 Barcelona, Spain

† Electronic supplementary information (ESI) available. See DOI: 10.1039/c7cp08076j

these characteristics. To take advantage of this inherent potential, we have designed semiconducting TAM-based 2D covalent networks whereby the aryl ring twist angles can be manipulated by externally applied in-plane strain.[18] As predicted for TAM molecules, this mechanically induced aryl ring twist, in turn, gives rise to fine control over the material's characteristics such as spin localization, electronic band gap and magnetic interactions.[18] Moreover, changing the manner by which the TAM monomers are interconnected within the 2D network can give rise to semiconductor materials which can exhibit graphene-like semimetallic states, potentially opening the door to strain-tailorable conduction.[19]

In a previous work[18] we studied the strain response of networks constructed from two differently functionalised TAMs: (1) fully hydrogenated (*i.e.* the triphenylmethyl, or TPM) and (2) fully chlorinated (*i.e.* the perchlorotriarylmethyl, or PTM). Upon the application of strain, the aryl rings in the network based on fully hydrogenated TAMs are easily twisted, leading to a highly responsive control over the properties of the 2D material. However, for the fully chlorinated network, the same corresponding range of applied strain gives rise to much less rotation of the aryl rings, thus restricting the extent to which the material's properties can be externally tailored. The difference in the relative strain response is explained by the higher steric hindrance associated with Cl atoms in the latter network, as compared to relatively low steric hindrance of H atoms. This difference highlights the fact that the necessary steric hindrance to ensure kinetic stability of TAM monomers (and the corresponding 2D networks) also tends to inhibit the degree to which their aryl ring twist angles, and thus their properties, can be tailored by the applied strain. Thus, for planning realistic syntheses of TAM-based materials with controllable characteristics, ideally a functionalisation which provides a compromise between responsiveness (*i.e.* ease of aryl ring twisting) and stability (*i.e.* sufficient steric shielding) should be sought.

In this work we have computationally screened a large set of TAM-based 2D covalent networks with different functionalisations of their aryl rings to assess their corresponding response to strain. We have focussed our study on the networks made from halogen-functionalised TAMs, due to the experimental feasibility of synthesising the corresponding monomeric units.[2,20–22] In particular, we consider both experimentally synthesised and computationally designed TAMs. We note that many of these TAMs possess mixed-halogen substitutions, with various combinations of H atoms and halogens atoms. This wide range of chemical variability is expected to give rise to a much finer tailoring of strain-induced response in the resulting networks. For each designed network, we uniaxially strained the material and monitored the induced change of aryl ring twist angles to assess the degree of the strain-induced structural response. In order to efficiently perform our screening we employed computationally inexpensive classical force field calculations. This procedure was found to be sufficiently reliable to rapidly evaluate the structural responsiveness of a wide range of networks. Subsequently, from this set we selected specific interesting networks where the explicit strain-induced response of the material's properties (*e.g.* band gap, spin distribution) was calculated using electronic structure calculations. Finally, following the known difficulty in experimentally preparing TAMs with a single chirality, we also assess the effect of having TAM units with different aryl ring helicities within the same 2D covalent network.

Via our extensive virtual screening (1750 optimizations performed) we confirm that TAM functionalisation could be tailored to provide 2D networks with a wide range of responsiveness with respect to strain. In particular, we are able to identify a number of TAMs that we predict should lead to materials that are both strain-responsive and experimentally viable.

2 Methodology

As a suitable test case for our study we considered 2D TAM-based networks having the same topology as that described in ref. 18 (see Fig. 2a). We study 50 such networks each composed of a single type of TAM with a distinct functionalisation. Specifically, taking the network based on fully hydrogenated TAMs as a reference, we consider networks based on fully-halogenated TAMs, and on a wide range of TAMs having variable degrees of functionalisation by using Cl and/or F atoms. Chemical

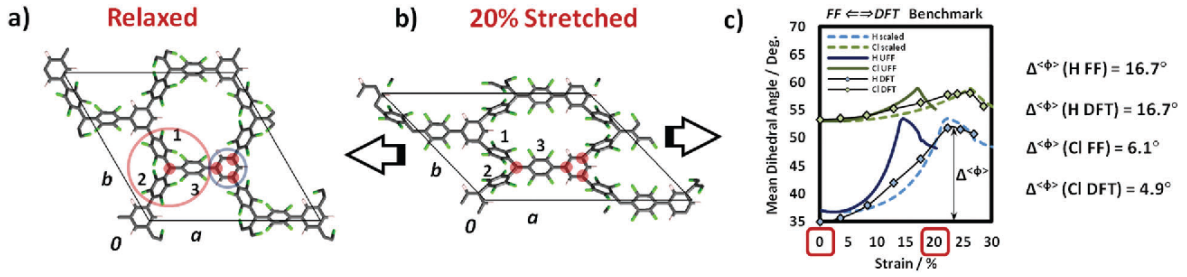

Fig. 2 z-View for the (a) relaxed and (b) 20% stretched conformations of the fully chlorinated TAM 2D-network. The in-plane cell parameters are indicated (a and b) as well as the stretching direction (arrows). 1, 2 and 3 indicate the three aryl rings within each TAM unit (red circle) being twisted during the stretching process. One of the benzene rings connecting the three TAM units is circled in blue. Red dots indicate the atoms with a frozen c-component during UFF optimizations. Atom colouring: C – dark grey, Cl – green, H – white. (c) Comparison of the mean aryl ring twist angle, $\langle\varphi_i\rangle$, variation for the fully H- and Cl-functionalized TAM 2D-networks with respect to strain from 0 to 20% of their initial size as calculated *via* FF and DFT methods. The network's responsiveness (*i.e.* $\Delta^{\langle\varphi\rangle} = \langle\varphi_i\rangle_{max} - \langle\varphi_i\rangle_{relax}$) is also provided per network and computational method.

structures of all considered TAMs used to construct the networks can be found in the ESI.† Previously, in this type of network, we found that the most effective way to induce a significant aryl ring twisting and a concomitant change in electronic properties is by application of a uniaxial strain in the *a* cell direction (equivalent to stretching in the *b* cell direction). Stretching the networks in both *a* and *b* directions at the same time did not cause a net aryl ring twisting but, rather, a direct stretching of the sigma covalent skeleton within the network. Compared to strains which induce ring twisting, this requires significantly larger forces to change the material's electronic properties, which vary in a more abrupt and less controllable manner. Therefore, in this study we focus on the response of the considered networks on *a*-directed strain, following our previous study.[18]

All screening calculations of the TAM-based 2D networks were performed using the universal force field (UFF)[23] as implemented in the general utility lattice program (GULP).[24] For each network modelled using UFF we sampled 35 strained conformations (including totally relaxed structures) which allowed us to smoothly track the resulting structural response. The combination of 50 differently functionalised TAM 2D covalent networks considered in 35 distinct conformations needed a total of 1750 periodic optimizations. This clearly shows the necessity of using computationally efficient UFF computations for the screening procedure. Specific networks from the UFF-based screening were selected in order to study their electronic properties using density functional theory (DFT) based calculations. For these networks, we also considered the effect of inverting the chirality (*i.e.* helicity of the three aryl rings) of one of the TAMs within the corresponding unit cell (composed of three TAM units). For all these chosen networks, the relaxed and five strained conformations were optimized at the DFT level of theory.

The DFT based calculations employed the hybrid PBE0[25] functional with a light/tier 1 numerical atom-centred basis set and used the Tkatchenko–Scheffler method to assess van der Waals interactions,[26] as implemented within the FHI-AIMS code.[27,28] All reported atomically partitioned spin populations are calculated using the Hirshfeld method.[29]

In both UFF and DFT calculations for the relaxed network conformations both in-plane cell parameters were optimised together with the internal atomic coordinates. For the strained conformations, the *a* cell parameter was fixed at progressively larger values with respect to the relaxed conformations, while optimising the other in-plane cell parameter (*b*) and atomic coordinates. In all cases the vacuum separation between repeated networks in the *c* direction was set to 30 Å. It was found that strained networks modelled using UFF were susceptible to out-of-plane distortions in the *c* direction which were not observed in the corresponding DFT calculations. In order to eliminate these unrealistic distortions, the *c*-components of carbon atoms defining the materials' plane (red shaded in Fig. 2a and b) were fixed during the UFF optimizations. We note that this constraint does not affect the structural response capacity of the networks with respect to the strain in the *a*–*b* plane.

In order to validate the use of UFF calculations as an adequate screening tool we compared UFF and DFT calculations of the strain-induced structural response for the fully hydrogenated and fully chlorinated networks (see Fig. 2c). As can be seen in Fig. 2c, the variation of the average twist angle of all aryl rings within the networks (*i.e.* $\langle\varphi_i\rangle$ in degrees) with respect to applied strain (in %) follows a similar tendency for both DFT (rhombohedral points) and UFF (coloured lines) calculations. We note that the strain at which the maximum $\langle\varphi_i\rangle$ value is reached for a particular network is predicted to be slightly lower using UFF as compared to DFT. Although we can largely correct for this difference by a scaling factor of 1.54 (see H/Cl scaled dashed lines in Fig. 2c), the main use of UFF screening is for rapidly assessing the magnitude of the structure *versus* strain responsiveness of a network. We estimate this property through the calculated maximum magnitude of $\langle\varphi_i\rangle$ relative to its initial relaxed value:

$$\Delta^{\langle\varphi\rangle} = \langle\varphi_i\rangle_{\max} - \langle\varphi_i\rangle_{\text{relax}},$$

which is similarly reproduced by both DFT and UFF (see $\Delta^{\langle\varphi\rangle}$ values in Fig. 2c for each network).

3 Results and discussion

The first set of networks we considered in the UFF screening calculations consisted of TAMs with all 12 aryl-ring substitutional sites being functionalised by a single halogen type (*e.g.* the perchlorinated network shown in Fig. 2a and b). Note that the functionalization of benzene rings connecting TAMs in the network (blue circle in Fig. 2a) is not changed over the screening procedure, being always H-atoms. Thus, in addition to the H- and Cl-functionalised networks[18] we also considered F-, Br- and I-functionalised systems. In Fig. 2 we show the structures of the relaxed (Fig. 2a) and 20% strained (Fig. 2b) conformations of the fully Cl-functionalised network as calculated with UFF. As can be seen, upon stretching the 2D covalent material, some of the aryl rings within each TAM unit twist out of the *a*–*b* plane (*e.g.* rings 1 and 2 in Fig. 2a and b) due to increased inter-ring steric repulsion, whereas other aryl rings (*e.g.* ring 3 in Fig. 2a and b) become flatter respectively.

To assess the responsiveness of the aryl ring twists with respect to applied strain for the differently halogenated networks, we extracted $\langle\varphi_i\rangle$ (*i.e.* the average twist angle of all aryl rings within the unit cell) for each of the 35 optimised conformations sampled during the stretching process. Fig. 3a shows the UFF-calculated variation of $\langle\varphi_i\rangle$ against strain (ε) for the H-, F-, Cl-, Br- and I-fully substituted 2D networks. For all these networks $\langle\varphi_i\rangle$ monotonically increases until a maximum value (typically at ε = 15–17%) and thereafter starts to slowly decrease. Thus the most strained conformations do not possess the most twisted aryl rings. Although all these networks have similar strain-structure response relations, the actual values of $\langle\varphi_i\rangle_{\text{relax}}$, $\langle\varphi_i\rangle_{\max}$ and $\Delta^{\langle\varphi\rangle}$ (*i.e.* $\langle\varphi_i\rangle_{\max} - \langle\varphi_i\rangle_{\text{relax}}$) vary considerably through the series. To help understand these similarities and differences we examine the structural chemistry involved in each case.

Compared to halogen substitutions, the fully H-functionalised 2D-network (dark blue curve in Fig. 3a) possesses a relatively flatter structure in its relaxed conformation (*i.e.* a low $\langle\varphi_i\rangle_{\text{relax}}$

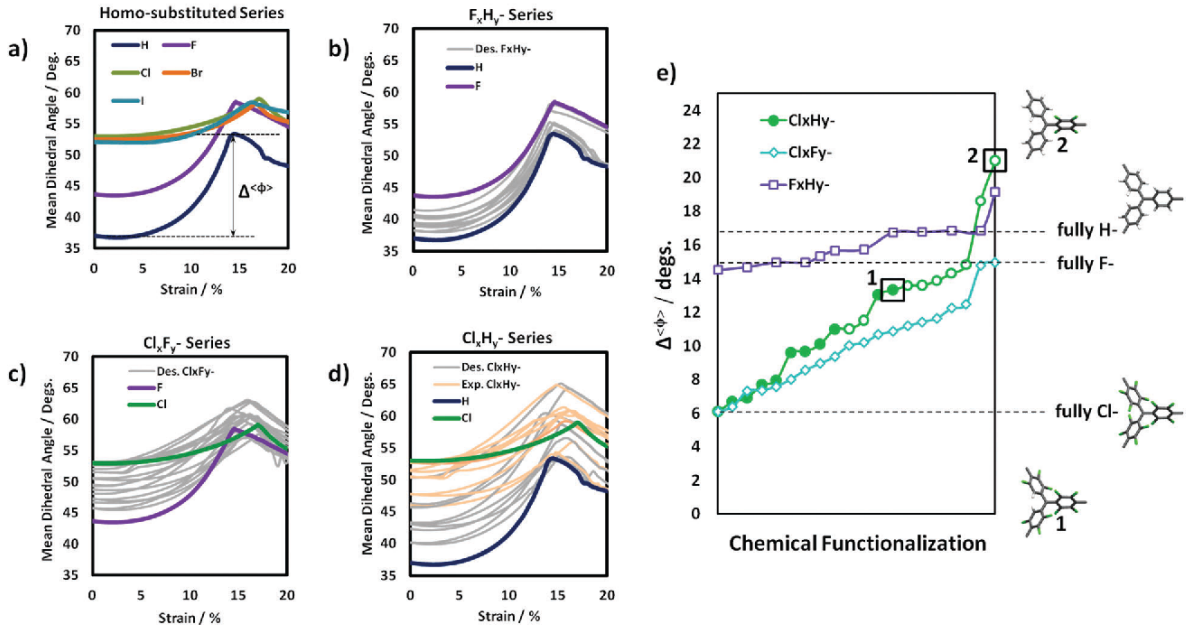

Fig. 3 Mean aryl ring twist angle, $\langle\varphi_i\rangle$, variation for the differently functionalized TAM 2D-networks during their strain from 0 to 20% of their initial size as calculated using UFF. The homo-substituted set (a) and the F_xH_y- (b), Cl_xF_y- (c) and Cl_xH_y- (d) sets are shown separately. In the latter, orange lines are associated with networks constructed using experimentally reported TAMs. (e) Network's responsiveness (*i.e.* $\Delta^{\langle\varphi\rangle} = \langle\varphi_i\rangle_{max} - \langle\varphi_i\rangle_{relax}$) for the networks within the different sets where those designed using experimentally reported monomers in the Cl_xH_y-set are associated with filled green circles.

value of 37°) due the relatively low inter-aryl ring H···H steric repulsion. Applying strain in the *a* direction induces an in-plane contraction of the network in the *b* direction which tends to bring the aryl rings of type 1 and type 2 closer together (see Fig. 2b). The resulting increased H···H steric repulsion between these aryl rings causes them to rigidly twist out of the *a*–*b* plane. At the same time the twist angles of the rings of type 3 remain relatively unchanged due to H···H steric repulsion with the adjacent benzene linker (see type 3 aryl ring and the right-hand connected benzene ring in Fig. 2b). Overall, this leads to an initial monotonic increase in $\langle\varphi_i\rangle$ (blue curve in Fig. 3a). At a certain point the type 1 and 2 rings are twisted to such an extent that they are completely perpendicular to the *a*–*b* plane and cannot twist any more. At this point $\langle\varphi_i\rangle$ is at its maximum and further strain acts to mainly elongate the bonds of the network. Increasing the length of the bonds between the type 3 rings and the benzene linker helps to reduce the H···H steric repulsion between them (see type 3 aryl ring in Fig. 2b), which then leads to a relaxation of the type 3 rings to more planar conformations with respect to the *a*–*b* plane and a resulting decrease in $\langle\varphi_i\rangle$ (see blue curve in Fig. 3a).

The F-functionalised network (purple curve in Fig. 3a) exhibits similar structural *versus* strain behaviour to that of the H-functionalised network, but with all the $\langle\varphi_i\rangle$ values higher due to the higher F···F steric repulsion. This is most evident in the higher twist angles of the aryl rings in the relaxed network leading to a higher $\langle\varphi_i\rangle_{relax}$ value of 44°. The value of $\langle\varphi_i\rangle_{max}$ for the F-functionalised network is also somewhat higher than that in the H-functionalised network. This is due to the type 3 rings in the F-functionalised network always being slightly twisted even for high strains, thus always increasing $\langle\varphi_i\rangle$. Overall, the responsiveness of the F-functionalised network (*i.e.* $\Delta^{\langle\varphi\rangle} = \langle\varphi_i\rangle_{max} - \langle\varphi_i\rangle_{relax}$) is similar to that of the H-functionalised one (compare blue and purple curves in Fig. 3a). As for the triphenylmethyl molecule, however, the fully F-functionalised TAMs are also not very chemically stable, and so the corresponding 2D networks are likely not to be experimentally feasible.

The Cl-, Br- and I-functionalised networks all show high $\langle\varphi_i\rangle_{relax}$ values (~53°) due to the associated high steric hindrances. Upon stretching, however, the strain responsiveness ($\Delta^{\langle\varphi\rangle}$) is much lower than those for the H- and F-functionalised networks. This dependence of $\Delta^{\langle\varphi\rangle}$ on functionalisation is in full accordance with our previous findings[15,18] and confirms the role of steric hindrance as the main parameter determining the ease by which aryl rings can be externally manipulated. Moreover, the very similar structural *versus* strain profiles for Cl-, Br- and I-functionalised networks (Fig. 3a) and their very similar $\langle\varphi_i\rangle_{relax}$ and $\langle\varphi_i\rangle_{max}$ values suggest that an upper bound on the effect of steric repulsion has been reached with the Cl-based network (green curve in Fig. 3a). As for the F-substituted network, the $\langle\varphi_i\rangle_{max}$ values for the Cl-, Br- and I-functionalised networks corresponds to a configuration in which the type 3 rings are twisted. This twist is partially due to steric repulsion with the bonded benzene linker (see structure in Fig. 2b). Furthermore, in these networks, the type 3 rings are partially buckled due to steric repulsion between them and the other two aryl rings in the same TAM unit. This latter interaction, in turn, prevents the

View Article Online
PCCP Paper

type 1 and 2 aryl rings in the TAM unit from becoming perfectly perpendicular with respect to the *a*–*b* plane. Overall, in these networks the low responsiveness (*i.e.* $\Delta^{\langle\varphi\rangle}$) can be explained both by the already large value of $\langle\varphi_i\rangle_{\mathrm{relax}}$ ($\sim 53^\circ$) and the high steric hindrance within these networks. As mentioned above, this hinders the use of these networks for applications (*e.g.* mechanical sensors) despite the fact that they are the most experimentally feasible (due to the stability of the corresponding sterically protected TAM monomers).

Experimentally, fully H-, F-, and Cl-functionalised TAM monomers have been synthesised.[2,20–22] However, fully chlorinated ones (*i.e.* PTMs) are, by far, the most widely used TAM building blocks for preparing functional materials[4,30] due to their associated outstanding chemical stability.[2] TAM derivatives with different degrees and distributions of Cl- and H-substitutions have also been experimentally prepared with varying degrees of kinetic stability.[31] The synthetic viability of TAMs with mixed substitutions may open the door to preparing TAM-based 2D networks possessing high structure *versus* strain responsiveness and reasonable kinetic stability. To assess the effect of combining atom substitutions on network responsiveness, we designed three sets of networks composed of TAM units possessing different distributions of: (i) F- and H-atoms (the F_xH_y-set), (ii) F- and Cl-atoms (the F_xCl_y-set) and (iii) Cl- and H-atoms (the Cl_xH_y-set). Chemical structures of all the considered TAMs can be found in the ESI.† In the Cl_xH_y-group we included networks based on experimentally reported TAM derivatives.[31] In Fig. 3b–d the variation of $\langle\varphi_i\rangle$ against applied strain (ε) is shown for each set of studied structures and in Fig. 3e we show how $\Delta^{\langle\varphi\rangle}$ varies within each of these sets.

In the F_xH_y-set, the $\langle\varphi_i\rangle$ *versus* ε curves tend to have the same shape and mainly fall inside the upper and lower limits defined by the fully H-functionalised and the fully F-functionalised networks, respectively (see Fig. 3b). The higher the degree of F-substitution of the respective TAMs in the network the closer the $\langle\varphi_i\rangle_{\mathrm{max}}$ and $\langle\varphi_i\rangle_{\mathrm{relax}}$ values are to those found for the fully F-functionalised network, and *vice versa*. As shown in Fig. 3e (purple squares), all F_xH_y-networks are found to be similarly responsive. Because of the low steric hindrance associated with H- and F-atoms, all F_xH_y-networks present relatively high $\Delta^{\langle\varphi\rangle}$ values ranging from 14.5–19.1° (as compared, for instance, with the fully Cl-functionalised network where $\Delta^{\langle\varphi\rangle} = 6.1^\circ$). Although understanding the structural behaviour of the F_xH_y-set of structures is technically interesting, it is important to keep in mind they are all unlikely candidates for realistic applications, due to the chemical instability of the corresponding TAM monomers.

For the Cl_xH_y-/F_xCl_y-sets (Fig. 3c and d), although all networks have $\langle\varphi_i\rangle_{\mathrm{relax}}$ values which lie between those of the fully chlorinated and fully hydrogenated/fluorinated networks respectively, the situation with applied strain is quite different. Here the $\langle\varphi_i\rangle$ variation strongly changes from case to case, and is often outside the limits of the corresponding extreme monofunctionalised cases. Although a few Cl_xH_y-networks exhibit $\langle\varphi_i\rangle$ values between those of the fully substituted Cl- and H-networks throughout the stretching process, most networks have $\langle\varphi_i\rangle_{\mathrm{max}}$ values that surpass those of both the fully hydrogenated and fully chlorinated networks (see Fig. 3d), many of them based on experimentally realised TAM monomers (orange curves in Fig. 3d). Higher $\langle\varphi_i\rangle_{\mathrm{max}}$ values than that for the fully chlorinated network can be achieved by using TAMs which have substitutions which do not strongly sterically hinder rings of type 1 and 2 to twist out of plane (*e.g.* H- or F-functionalisation), while maintaining sufficient steric hindrance on the type 3 rings (*e.g.* Cl-functionalisation) to prevent them twisting into a more planar configuration.

Examining the responsiveness for both Cl_xH_y-/F_xCl_y-sets (green and blue curves in Fig. 3e, respectively) we may clearly see that substitutions which combine atoms with extremely different steric hindrances (*e.g.* H- and Cl-) give rise to a broad spectrum of $\Delta^{\langle\varphi\rangle}$ values within the set. Interestingly, in the Cl_xH_y-set, we see that all considered networks composed of experimentally reported TAM monomers are more responsive ($\Delta\langle\varphi_i\rangle = 10^\circ$–$13.3^\circ$) than the fully chlorinated network ($\Delta\langle\varphi_i\rangle = 6.1^\circ$). As proposed above, this confirms that kinetically stable TAM monomers with mixed functionalisations could provide a basis for synthetically practicable TAM-based 2D networks that would perform better than the PTM-based network (*e.g.* as mechanical sensors). We finally note that two networks in the Cl_xH_y-set and one in the F_xH_y-set exhibit even higher $\Delta^{\langle\varphi\rangle}$ values than the fully hydrogenated network (*e.g.* highlighted network 2 in Fig. 3e). This further confirms that the appropriate mixed functionalisations with atoms of very different steric hindrances allows for tailoring the responsiveness of the resulting networks beyond homogeneously substituted networks.

To confirm that the structural responsiveness of our designed networks leads to a corresponding degree of strain-induced controllability of their electronic properties we selected two networks to study *via* DFT-based calculations. First, we chose the most responsive Cl_xH_y-network based on experimentally synthesised TAM units (*i.e.* the highlighted network 1 in Fig. 3e). Secondly, we selected the most responsive Cl_xH_y-network of all those tested (*i.e.* the virtual highlighted network 2 in Fig. 3e). Following our previous work, we used the fully H-functionalised and Cl-functionalised networks for benchmark comparisons. For all four networks we optimised a set of five conformations using DFT employing the corresponding UFF-optimised structures covering the entire range of applied strain. For each network and each conformation we calculated the average partitioned spin population on the central tri-bonded carbon atoms (αC; see Fig. 1) of each TAM unit within the periodic cell. We have found that this spin population measure is able to capture the degree of spin localization/delocalization in isolated TAMs.[15] As we previously demonstrated for TAM-based 2D covalent networks, this spin localization should be well correlated with the average cosine squared of the dihedral twist angles of all aryl rings with respect to the corresponding αC plane (*i.e.* $\langle\cos^2\varphi_i\rangle = (\sum\cos^2\varphi_i)/9$).[18] Moreover, due to the link between the localization of π-conjugated electrons and their associated energies,[32] the band gap of the material is also correlated with this structural parameter during the network stretching process.[18] To corroborate this for our newly designed networks in Fig. 4 we plot: (a) the average spin

population on αC atoms within the network, and (b) the electronic band gap of the 2D material against the corresponding $\langle \cos^2 \varphi_i \rangle$ value for the different stretched conformations.

As it may be seen in Fig. 3e, following the predictions from the UFF screening with respect to $\Delta\langle \varphi_i \rangle$ values, the ranges over which the band gaps and spin localisation are found to vary in networks 1 and 2 (red and cyan lines in Fig. 4, respectively) are significantly greater than in the case of the fully Cl-functionalised network (green lines in Fig. 4). These results clearly demonstrate the validity of our structural *versus* strain screening procedure to find networks which have a greater tailorability of their electronic properties while being more experimentally feasible as compared to the fully H-network.

Finally, we assessed how the variable helicity (*i.e.* chirality linked to the angular orientation of the aryl rings within a TAM unit) of compositionally identical TAMs within a 2D network may affect the materials' structural planarity (and hence, experimental feasibility) and its response to strain. Experimentally it has been demonstrated that chlorinated TAMs can be obtained with two distinct helicities and that these can give rise to different supramolecular arrangements on surfaces.[33] To assess the effect of having mixed helicities in a TAM-based 2D covalent network we changed the helicity of one TAM in the unit cell of each of our four selected networks and optimised the resulting structures for a range of strained conformations. We find that the structural response of these materials to strain (*i.e.* $\langle \varphi_i \rangle$ *vs.* ε curves) are very similar to that in the corresponding single-helicity networks, with significant differences only emerging at very high strains

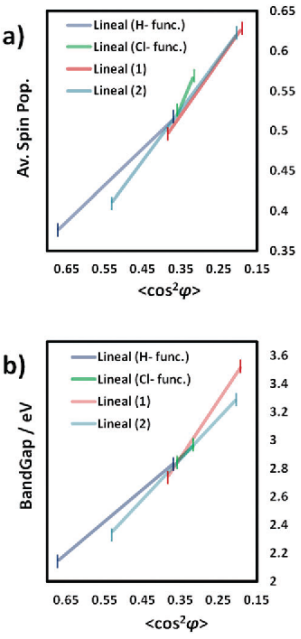

Fig. 4 Linear fit lines of the average αC-partitioned spin population data (a) and band gap (b) against $\langle \cos^2 \varphi_i \rangle$ (where $\langle \cos^2 \varphi_i \rangle = (\sum \cos^2 \varphi_i)/9$ and φ_i are the twist angles of each aryl ring with the corresponding αC plane) from the monotonically stretched conformations for the differently functionalised TAM 2D-networks.

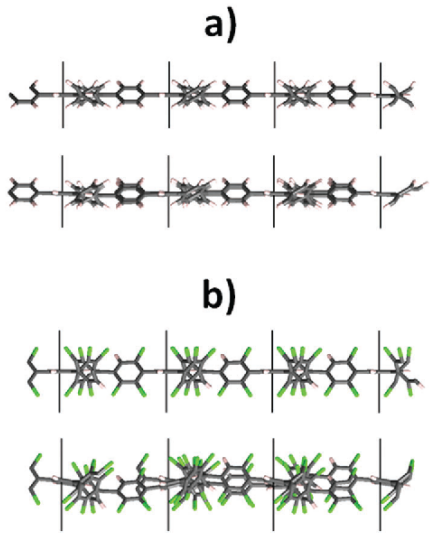

Fig. 5 x-View of the optimised structures for (a) the fully hydrogenated network and (b) a partially chlorinated network. In the upper structures in both (a and b) all TAM units present the same helicity of their aryl rings. In the bottom structures in (a) and (b) the three aryl rings within one of the TAM monomers within the unit cell have been twisted by 180 degrees, thus having the same twist angle of their aryl rings but in the opposing direction with respect to the other two TAM monomers in the unit cell.

(see ESI†). The corresponding variation of the spin localization and band gap are also found to be similar in both network types. Structurally, however, some mixed-helicity networks are found to exhibit out-of-plane distortions of their αC atoms. For low sterical hindrance conditions (*e.g.* the fully H-functionalised network) changing the helicity of one of the TAM units does not lead to any distortion and the material remains planar (see Fig. 5a).

However, for highly chlorinated networks, changing the helicity of one of the TAM units results in a clear distortion of the structure which leads to the loss of the material's planarity (see Fig. 5b). A similar distortion is also observed for other mixed-helicity Cl_xH_y-networks. This suggests that when the steric hindrance within the TAM network is high the effect of changing the helicity of one of the TAM units significantly disturbs the main skeletal structure of the 2D material, and *vice versa*. This result highlights the key role of chirality and molecular ordering with respect to structural stability for planar 2D TAM-based networks.

4 Conclusions

In this work we have screened the structure *versus* strain response of over 50 differently halogen-functionalised TAM-based 2D networks by means of reliable classical force-field calculations. Specifically, we have stretched the structures of these 2D covalent materials in one of the in-plane directions to probe how the aryl ring twist angles depends on the chemical functionalisation of the TAM units composing them. In this way we have confirmed the key role of steric hindrance in dictating the structural

response of such networks. By the appropriate choices of functionalisation of the individual TAMs with multiple substituents (*e.g.* H- and Cl-atoms) we show that the structural responsiveness of these materials can be tailored to a degree beyond that obtainable *via* TAMs functionalised by only one substituent (homo-series). We note that some of these TAMs with mixed functionalisations have been already synthesised. Moreover, as found by subsequent DFT calculations, we show that the structural response of these mixed-functionalised networks gives rise to an enhanced range of variation in both the spin localization and band gap with respect to networks based on TAMs with one type of substitution.

Finally, we also show the effect of having TAM units with a different helicity within the material's framework. These calculations are of particular relevance to the crucial role of molecular ordering and chirality for preparing these materials. On-surface synthesis methods could provide a means to ensure a high degree of ordering of the initial monomeric units for synthesis of our predicted networks. Fully chlorinated TAMs, for example, have been deposited on metal surfaces, and, depending on experimental conditions, monolayers with all TAMs having the same helicity or monolayers where the TAM neighbours present opposite helicities in a periodical way can be obtained.[33]

In summary, our virtual screening of TAM-based 2D networks shows that these materials are highly tuneable by a combination of chemical design and applied mechanical strain. As many of our proposed mixed-functionalisation TAMs and ordered self-assembled monolayers of TAMs have been experimentally prepared, we believe these versatile systems have real promise to be experimentally synthesized for use in future organic electronic/spintronic devices and sensors.

Conflicts of interest

There are no conflicts of interest to declare.

Acknowledgements

This research was supported by the Spanish MINECO grant CTQ2015-64618-R grant and, in part, by Generalitat de Catalunya grants 2014SGR97, XRQTC and the NOMAD Center of Excellence project, which received funding from the European Union's Horizon 2020 research and innovation programme under grant agreement No. 676580. We acknowledge access to supercomputer resources as provided through grants from the Red Española de Supercomputación. I. A. acknowledges the Spanish Ministerio de Educación Cultura y Deporte for a FPU PhD scholarship.

Notes and references

1 M. Gomberg, *J. Am. Chem. Soc.*, 1900, **22**, 757–771.
2 J. Guasch, X. Fontrodona, I. Ratera, C. Rovira and J. Veciana, *Acta Crystallogr.*, 2013, **C69**, 255–257.
3 T. T. Tidwell, in *Stable Radicals: Fundamentals and Applied Aspects of Odd-Electron Compounds*, ed. R. G. Hicks, John Wiley & Sons, Ltd, Chichester, UK, Ontario, 2010, pp. 1–31.
4 I. Ratera and J. Veciana, *Chem. Soc. Rev.*, 2012, **41**, 303–349.
5 A. Rajca, J. Wongsriratanakul and S. Rajca, *Science*, 2001, **294**, 1503–1505.
6 N. M. Shishlov, *Russ. Chem. Rev.*, 2006, **75**, 863–884.
7 C. Simão, M. Mas-Torrent, N. Crivillers, V. Lloveras, J. M. Artés, P. Gorostiza, J. Veciana and C. Rovira, *Nat. Chem.*, 2011, **3**, 359–364.
8 R. Frisenda, R. Gaudenzi, C. Franco, M. Mas-Torrent, C. Rovira, J. Veciana, I. Alcon, S. T. Bromley, E. Burzurí and H. S. J. van der Zant, *Nano Lett.*, 2015, **15**, 3109–3114.
9 R. Gaudenzi, E. Burzurí, D. Reta, I. de, P. R. Moreira, S. T. Bromley, C. Rovira, J. Veciana and H. S. J. van der Zant, *Nano Lett.*, 2016, **16**, 2066–2071.
10 C. Simão, M. Mas-torrent, J. Veciana and C. Rovira, *Nano Lett.*, 2011, **11**, 4382–4385.
11 C. Gabellieri, V. Mugnaini, J. C. Paniagua, N. Roques, M. Oliveros, M. Feliz, J. Veciana and M. Pons, *Angew. Chem., Int. Ed. Engl.*, 2010, **49**, 3360–3362.
12 Q. Peng, A. Obolda, M. Zhang and F. Li, *Angew. Chem., Int. Ed.*, 2015, **54**, 7091–7095.
13 D. Maspoch, D. Ruiz-Molina, K. Wurst, N. Domingo, M. Cavallini, F. Biscarini, J. Tejada, C. Rovira and J. Veciana, *Nat. Mater.*, 2003, **2**, 190–195.
14 V. Mugnaini, M. Mas-Torrent, I. Ratera, C. Rovira and J. Veciana, in *Supramolecular Soft Matter: Applications in Materials and Organic Electronics*, ed. T. Nakanishi, John Wiley & Sons, Inc., 1st edn, 2011, pp. 191–213.
15 I. Alcón and S. T. Bromley, *RSC Adv.*, 2015, **5**, 98593–98599.
16 A. Datcu, N. Roques, V. Jubera, D. Maspoch, X. Fontrodona, K. Wurst, I. Imaz, G. Mouchaham, J. P. Sutter, C. Rovira and J. Veciana, *Chem. – Eur. J.*, 2012, **18**, 152–162.
17 N. Crivillers, C. Munuera, M. Mas-Torrent, C. Simão, S. T. Bromley, C. Ocal, C. Rovira and J. Veciana, *Adv. Mater.*, 2009, **21**, 1177–1181.
18 I. Alcón, D. Reta, I. de P. R. Moreira and S. T. Bromley, *Chem. Sci.*, 2017, **8**, 1027–1039.
19 I. Alcón, F. Viñes, I. de P. R. Moreira and S. T. Bromley, *Nat. Commun.*, 2017, **8**, 1957.
20 R. Filler, A. E. Fiebig and B. K. Mandal, *J. Fluorine. Chem.*, 2000, **102**, 185–188.
21 C. Trapp, C. S. Wang and R. Filler, *J. Chem. Phys.*, 1966, **45**, 3472.
22 M. Ballester, J. Castañer, J. Riera, a. Ibáñez and J. Pujadas, *J. Org. Chem.*, 1982, **47**, 259–264.
23 A. K. Rappe, C. J. Casewit, K. S. Colwell, W. A. Goddard III and W. M. Skiff, *J. Am. Chem. Soc.*, 1992, **114**, 10024–10035.
24 J. D. Gale and A. L. Rohl, *Mol. Simul.*, 2003, **29**, 291–341.
25 C. Adamo and V. Barone, *J. Chem. Phys.*, 1999, **110**, 6158.
26 A. Tkatchenko and M. Scheffler, *Phys. Rev. Lett.*, 2009, **102**, 73005.
27 V. Havu, V. Blum, P. Havu and M. Scheffler, *J. Comput. Phys.*, 2009, **228**, 8367–8379.
28 V. Blum, R. Gehrke, F. Hanke, P. Havu, V. Havu, X. Ren, K. Reuter and M. Scheffler, *Comput. Phys. Commun.*, 2009, **180**, 2175–2196.

29 F. L. Hirshfeld, *Theor. Chem. Acc.*, 1977, **44**, 129–138.
30 J. Veciana and I. Ratera, in *Stable Radicals: Fundamentals and Applied Aspects of Odd-Electron Compounds*, ed R. G. Hicks, John Wiley & Sons, Inc., 2010, pp. 33–80.
31 O. Armet, J. Veciana, C. Rovira, J. Riera, J. Castañer, E. Molins, J. Rius, C. Miravitlles, S. Olivella and J. Brichfeus, *J. Phys. Chem.*, 1987, **91**, 5608–5616.
32 D. Vonlanthen, A. Rudnev, A. Mishchenko, A. Käslin, J. Rotzler, M. Neuburger, T. Wandlowski and M. Mayor, *Chem. – Eur. J.*, 2011, **17**, 7236–7250.
33 F. Grillo, V. Mugnaini, M. Oliveros, S. M. Francis, D. J. Choi, M. V. Rastei, L. Limot, C. Cepek, M. Pedio, S. T. Bromley, N. V. Richardson, J. P. Bucher and J. Veciana, *J. Phys. Chem. Lett.*, 2012, **3**, 1559–1564.

Supporting Information of Publication #6

Triarylmethyl-based 2D covalent networks: virtual screening of chemical functionalisation for optimising strain-induced property control

Phys. Chem. Chem. Phys., 2018, Advance Article

Isaac Alcón and Stefan T. Bromley*

Electronic Supplementary Material (ESI) for Physical Chemistry Chemical Physics.

Supplementary Information:
Triarylmethyl-based 2D covalent networks: virtual screening of chemical functionalisation for optimising strain-induced property control

Isaac Alcón and Stefan T. Bromley

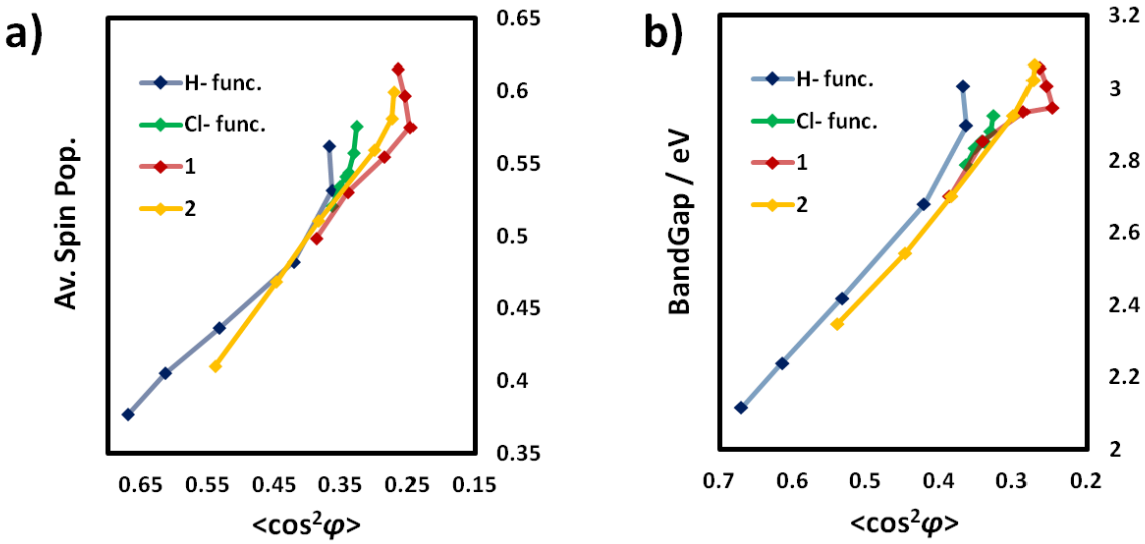

Figure S1. Average αC-partitioned spin population (**a**) and band gap (**b**) against $\langle\cos^2\varphi_i\rangle$ (where $\langle\cos^2\varphi_i\rangle = (\sum\cos^2\varphi_i)/9$ and φ_i are the twist angles of each aryl ring with respect to the corresponding αC plane) from the monotonically stretched conformations for four differently functionalized TAM 2D-networks where the three aryl rings within one of the TAM units in the unit cell have been set to the opposite helicity as compared to the rest of TAM units. Network labels correspond to those explained in the main text of the paper.

Chemical structures of considered TAMs

Below in figure S2-S8 we show the chemical structures of TAMs in the Cl_xH_y- set. TAM number 0 in the set is the fully chlorinated TAM, the so-called PTM. TAMs 0, 1-8 and 11-12 have all been experimentally synthesized (see *J. Phys. Chem.*, 1987, 91 (22), pp 5608–5616). Chemical structures of considered TAMs within the Cl_xF_y- set may be obtained upon substituting H atoms by F atoms in the TAMs shown below. Chemical structures of TAMs in the F_xH_y- set may be obtained by substituting Cl atoms by F atoms in TAMs 9, 10 and 13-19 below.

The chemical structures of all the shown TAMs have the same orientation as the red circled TAM unit in the PTM 2D-COF structure shown in Fig. 2a in the main text (i.e. the most planar aryl ring in the structures below points in a direction parallel to the direction of applied strain). Asterisks (*) indicate links with other identical TAMs within the 2D networks.

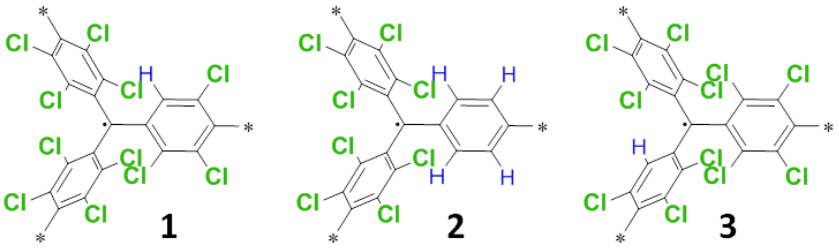

Figure S2. TAMs **1**, **2** and **3**.

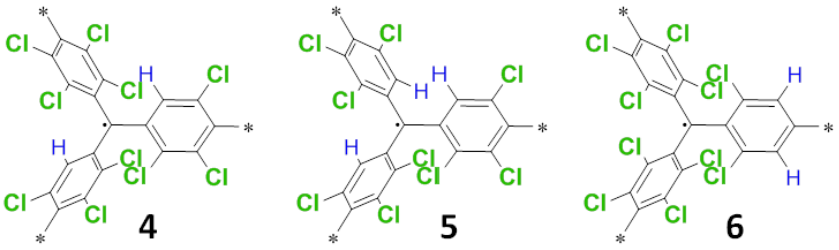

Figure S3. TAMs **4**, **5** and **6**.

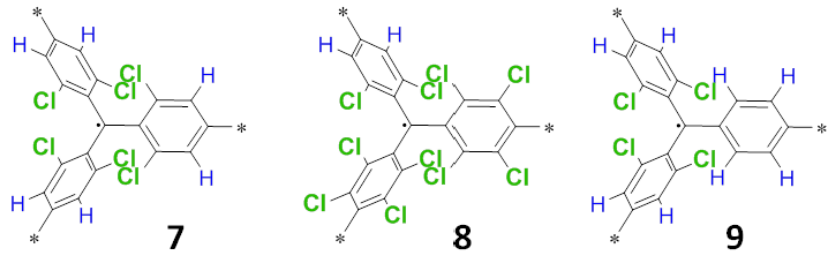

Figure S4. TAMs **7**, **8** and **9**.

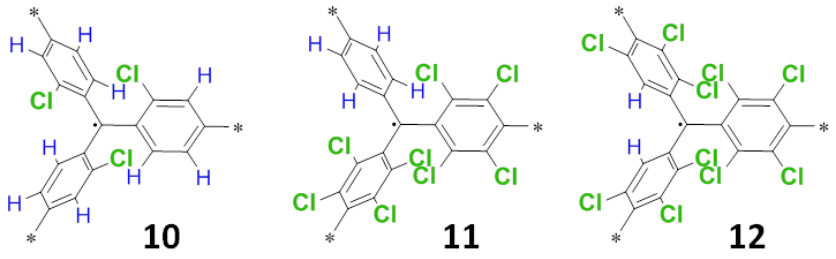

Figure S5. TAMs **10**, **11** and **12**.

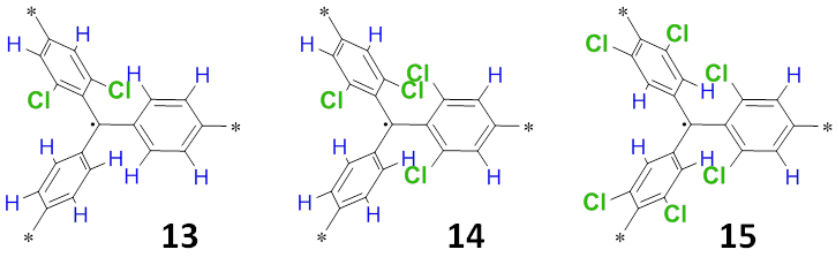

Figure S6. TAMs **13**, **14** and **15**.

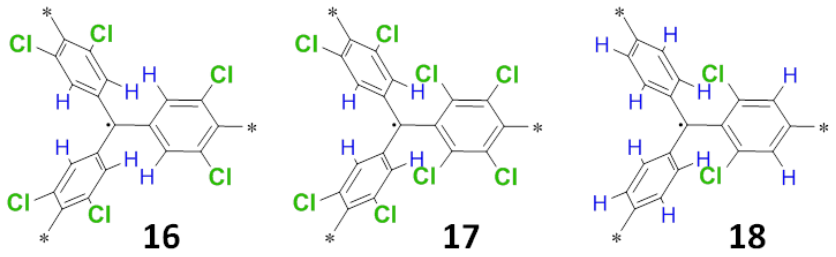

Figure S7. TAMs **16**, **17** and **18**.

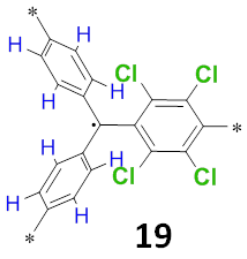

Figure S8. TAM **19**.

4.4 Overview

As explained in the introduction to this chapter, our preliminary objective was to understand what mainly determines the energy and spatial distribution of the unpaired electron in TAMs. The motivation for that is simply the fact that the unpaired electron in this family of compounds determines all associated properties with particular interest for applications in materials science such as absorption and fluorescence bands in the visible spectra,[3,8] magnetic interactions,[2,5] redox activity[3] and enhanced electrical conductivity through the molecular backbone.[4] Such objective was achieved in **Publication #4** presented in this chapter where we demonstrate the existence of a linear correlation between the spin localization on αC (and hence the associated unpaired electron localization) with $\langle cos^2\varphi_i\rangle$, where φ_i is the twist angle of each of the three aryl rings with respect to the sp^2 αC atom plane. As we showed in **Publication #4**, such a linear correlation is independent of the particular chemical functionalization of aryl rings in the TAM, which signifies that electro-donating/withdrawing considerations play a secondary role with regard to the localization of the π-conjugated unpaired electron in these organic radicals. Hence, chemical functionalization is mainly relevant in this regard as much as it determines the values of φ_1, φ_2 and φ_3 due to steric hindrance. Finally, in this first predictive contribution, we also show, by means of *ab initio* molecular dynamics simulations (AIMD), that the correlation between spin localization and $\langle cos^2\varphi_i\rangle$ is robust under the effect of finite temperatures (i.e. 300K). In other words, the spin localization fluctuations follow the thermal rotations of aryl rings as predicted with the $\langle cos^2\varphi_i\rangle$ correlation factor.

Publication #4 demonstrates the power of aryl ring twist angles to determine the localization of unpaired electrons in TAMs and, consequently, all related properties with interest for applications. Searching at the literature we found that an electronic-structural correlation has not been exploited in any experimentally prepared TAM-based material or device. In **Publication #5** we explain in detail that this is the case because none of TAM-based experimentally prepared materials or devices actually comprises the structural characteristics that are necessary to externally manipulate aryl ring twist angles. However, as we show in **Publication #5**, a 2D covalent organic framework[21,22] (2D-COF, see Section 1.2 in Chapter 1) composed of TAM units covalently bonded in an ordered fashion would allow for such manipulation in an efficient and reproducible manner. Hence, in **Publication #5** we go on with the design of such 2D materials (abbreviated TAM 2D-COFs), comparing those composed of flexible (but unstable) triphenylmethyl units (TPM 2D-COF) and stable, but rigid, perchlorotriarylmethyl units (PTM 2D-COF). Following, we present the properties of these materials (both are ordered arrays of weakly ferromagnetically coupled unpaired electrons and electrical insulators) and show that by applying an uniaxial strain the aryl rings of all TAM units composing the material smoothly twist. Consequently, important electronic properties of the 2D networks are also modified; namely spin localization, band gap and ferromagnetic interactions are shown to linearly vary with $\langle cos^2\varphi_i\rangle$ (i.e. the average $cos^2\varphi_i$ value for

all aryl rings within the unit cell), in full agreement with our previous study for single TAMs (**Publication #4**). Such variations are, for the TPM 2D-COF, very significant: e.g. the band gap is varied by 1 eV, which should dramatically change the optical properties of the TPM-based 2D network.

A final point raised in **Publication #5**, of key importance, is the fact that for the network composed of chemically persistent radicals (i.e. the PTM 2D-COF) it turns out that the structural modification caused by the uniaxial strain (i.e. variation of $\langle cos^2\varphi_i \rangle$) is not high enough to generate detectable changes in the studied electronic properties under the effect of finite temperatures (we show this by performing periodic AIMD simulations at 300K). In other words, the PTM 2D-COF is too rigid due to the huge steric hindrance of perchlorated aryl rings. To solve this issue, in **Publication #6** we performed a virtual screening of TAM 2D-COFs composed of TAM monomers with different chemical functionalizations and uniaxially stretched each of them (as done in **Publication #5**) assessing the variation of $\langle \varphi_i \rangle$ in each case. We focused on TAMs with halogen functionalization, due to the fact that most chemically stable TAMs are functionalized with halogen atoms,[18] studying both mono-functionalized TAMs (i.e. with all aryl ring positions equally functionalized) and also partially functionalized (i.e. combining two atom functionalizations such as H- and Cl- or Cl- and F-). Studying 50 different considered TAM 2D-COFs each optimized through 35 different stretching conformations, from 0 strain to 25% strain, requested 1750 periodic optimizations. Because of this we had to perform such a study using computationally efficient force field calculations (using the UFF force-field[20]). Benchmarking our FF-based methodology with DFT calculations we show in **Publication #6** that there are a number of TAM 2D-COFs based on experimentally realized, and persistent, TAMs with significant variations of $\langle \varphi_i \rangle$ through the applied strain with some cases, even, overcoming the $\langle \varphi_i \rangle$ variation values of the TPM 2D-COF. Hence, the final conclusion of this work is, in short, that there are available experimentally reported TAM monomers that should provide both chemical persistence and structural flexibility, hence allowing one to prepare in the laboratory TAM-based 2D networks with externally highly tunable characteristics.

Chapter 5
para-connected TAMs: Towards 2D semimetals

5.1 Introduction

5.1.1 Connecting π-conjugated organic radicals: *meta-* vs. *para-*

From the basic chemistry of π-conjugated organic systems, we know that multiple π-conjugated carbon radical centres may be connected to each other in essentially two ways: in *meta-* or in *para-*.[1–3] These two different connections are sketched in Fig. 5.1a-b.

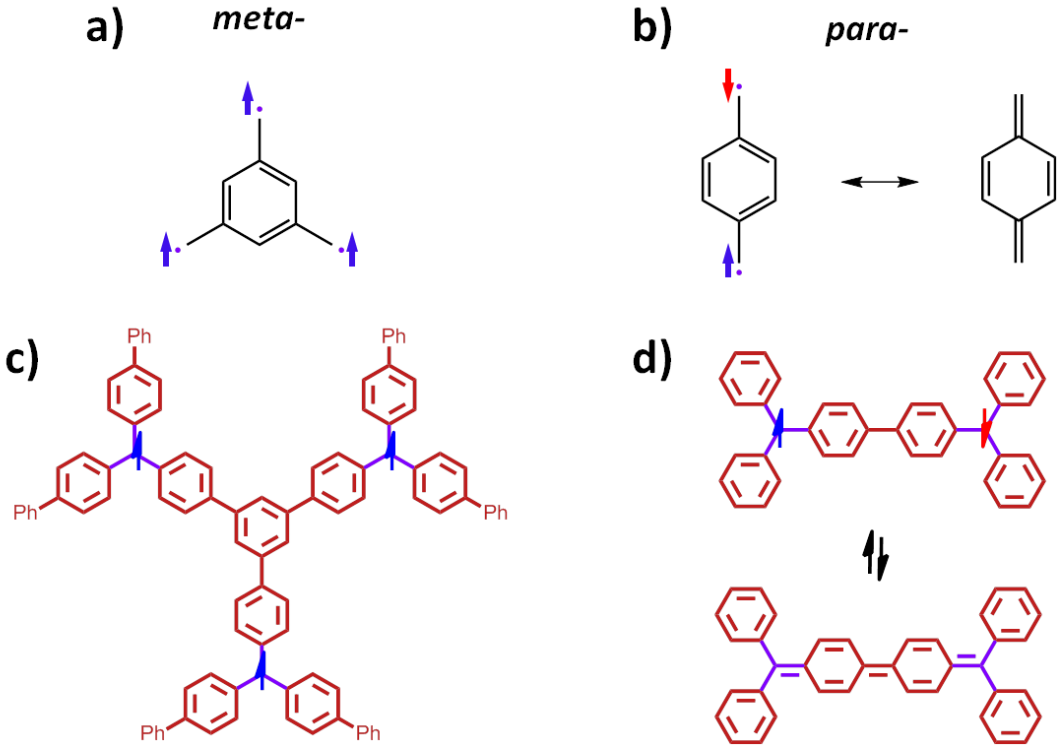

Fig. 5.1 *meta-* **(a)** and *para-* **(b)** connections between carbon-based radical centres (purple dots) in organic π-conjugated systems. **c)** and **d)** show the structure of experimentally synthesized TAM-based tri- and bi-radicals with *meta-* and *para-* connections of radical centres, respectively. For the *para-* case (right column) two Lewis resonance forms are possible.

As sketched in Fig. 5.1, each way of connecting the radical centres leads to a different electronic and magnetic ground state. As experimentally shown, radical centres connected in *meta-* present localized unpaired electrons with a tendency to be ferromagnetically coupled[3,4] (Fig. 5.1a,c). Despite the fact such magnetic interactions are not very strong (singlet-triplet energy difference around 10 kcal/mol)[3] *meta-* connected π-conjugated organic radicals have attracted much interest for designing organic magnets.[2,5] *para-* connected π-conjugated carbon radical centres tend to be anti-ferromagnetically coupled[3] (Fig. 5.1b,d) and, importantly, may give rise to so-called quinoidal electronic configurations,[6–8] where all electrons are paired (i.e. closed-shell state). This type of electronic structure has been experimentally demonstrated for Chichibabin's hydrocarbon[9] (shown in Fig. 5.1d) but also for other *para-* π-conjugated organic compounds such as nitroxo bi-radicals.[7]

5.1.2 Mixed-valence compounds: towards organic electronics

During the 80s' and 90s' multi-radical π-conjugated organic molecules attracted a lot of scientific interest among organic chemists in the field of organic magnetism,[2] finding them perfect candidates to construct magnetic plastics.[5,10,11] This research line culminated with the synthesis of the first magnetic plastic in 2001 composed of triphenylmethyl units.[5] During last 20 years such π-conjugated bi-/tri-radical compounds have gained more interest for molecular electronics. For instance, if one takes the bi-radical shown in Fig. 5.1d and adds an extra electron to one of the radical centres (i.e. reducing it to the -1 anion state), the resulting negative charge has the ability to "jump" between both π-conjugated moieties (see Fig. 5.2a).[12–14] This type of species is called a mixed-valence compound (see Fig. 5.2) because two moieties with a different number of valence electrons are connected through a molecular π-conjugated bridge and charge transfer phenomena between both centres may take place.[15] Triarylamines also play an important role in this field.[15–18]

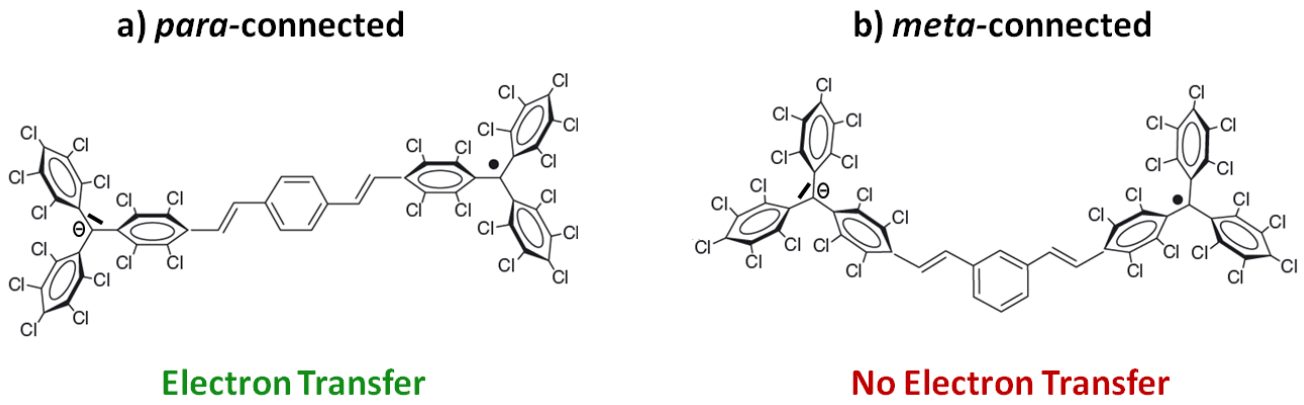

Fig. 5.2 a) *para*- and **b)** *meta*-connected PTM-based mixed-valence compounds, where one of the PTM units possesses an unpaired electron and the other a pair of electrons (negative charge).

As I explained above, depending on the way π-conjugated radical centres are covalently connected with respect to each other (i.e. in *meta*- or in *para*-) their electronic and magnetic interaction changes (see Fig. 5.1). Interestingly, such different connections also determine how TAM-based mixed-valence compounds behave. It was experimentally demonstrated that electron transfer takes place between two PTM units connected in *para*- in the mixed-valence compound depicted in Fig. 5.2a upon reducing one of the radical centres.[12,13] This is normally shown by means of variable-temperature electron paramagnetic resonance (EPR) measurements and spectro-electrochemistry experiments where the initial bi-radical compound is slowly chemically reduced to the anion state while measuring the UV-vis. spectra of the solution.[14] Without going into details, the number of peaks detected in EPR and their relative intensities depend on whether the unpaired electron (and thus the negative charge) is localized in one radical centre or fully delocalized between both extremes of the compound. UV-vis. spectroscopy in turn shows the appearance of a band at low frequencies (around 1400 nm)[13] associated to the charge transfer phenomena. As

reported in the same work, upon chemical reduction of the *meta*-connected mixed-valence analogous compound (Fig. 5.2b) no electron transfer was detected by EPR or UV-vis. spectroscopy.[12,13] Hence, the way TAM units are covalently connected through π-conjugated wires does not only determine their magnetic coupling (Fig. 5.1) but, most significantly for electronics, the ability (or inability) of added negative charges to conduct from one TAM unit to the other through the π-conjugated wire. For obvious reasons such structural features could be utilized as a powerful tool to tune electronic currents at the molecular scale in TAM-based systems.

5.1.3 About the charge transfer mechanism

The outstanding stability of PTM radicals has launched their role in the study of charge transfer phenomena at the molecular level in the corresponding mixed-valence species.[16,17,19,20] Recently, two main possible mechanisms were proposed to explain such charge-transfer phenomena taking place in *para*-connected bi-PTM mixed-valence compounds.[14] These are charge hopping and electron tunnelling, as schematically represented in Fig. 5.3 (image taken from ref. 14).

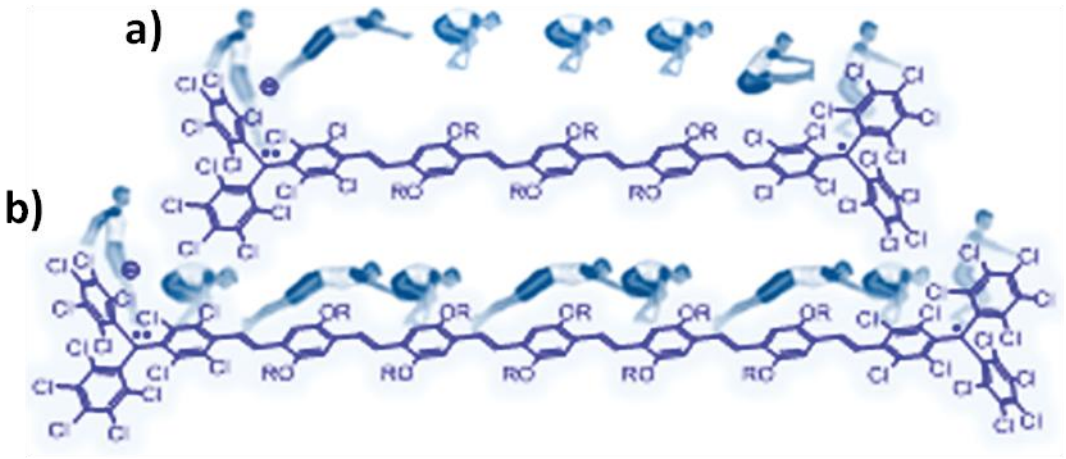

Fig. 5.3 a) In the tunnelling mechanism the extra electron tunnels directly from one PTM extreme to the other, with no intervention of the bridge. **b)** In the hopping mechanism the charge travels by sequential jumps through the bridge, hence leading to a much slower charge transfer process where the charge may actually be measured trapped in the bridge (the so-called polaron states). See ref. 14 for details.

As schematically shown in Fig. 5.3a, in the tunnelling regime the negative charge is expected to tunnel between one PTM extreme to the other, where the π-conjugated bridge does not play any significant role, besides determining the distance between both PTM units. Conversely, on the charge hopping mechanism (Fig. 5.3b), the extra electron is supposed to conduct by means of sequential jumps through the different π-conjugated units of the bridge. In such a scenario the charge transfer process takes place over longer times and the travelling charge (be it positive or negative) may be found localized in the bridge (the so-called polaron state[21]). As experimentally proposed by Lloveras et.al.[14] for short length bridges the tunnelling regime dominates in the studied bi-PTM mixed-valence compounds (Fig. 5.3), whereas for

long bridges a charge hopping mechanism is measured. This study was based on UV-vis. and NIR (near infra-red) optical spectroscopies, variable temperature EPR measurements and first principles DFT calculations.

In this PhD thesis I participated in the study of bi-PTM mixed-valence compounds using thiophene-vinylene (TV) wires of different lengths connecting the two PTM units (**Publication #7**). In this contribution, variable temperature EPR, UV-vis. and Raman spectroscopies have been utilized to assess the charge transfer mechanism of the studied compounds. As previously proposed,[14] for bi-PTM with long TV bridges experimental evidences point to a hopping mechanism where the negative extra electron would be transferred through the motion of positive charges (so-called polarons) through the electro-donating TV bridge (purple mechanism in Fig. 5.4).

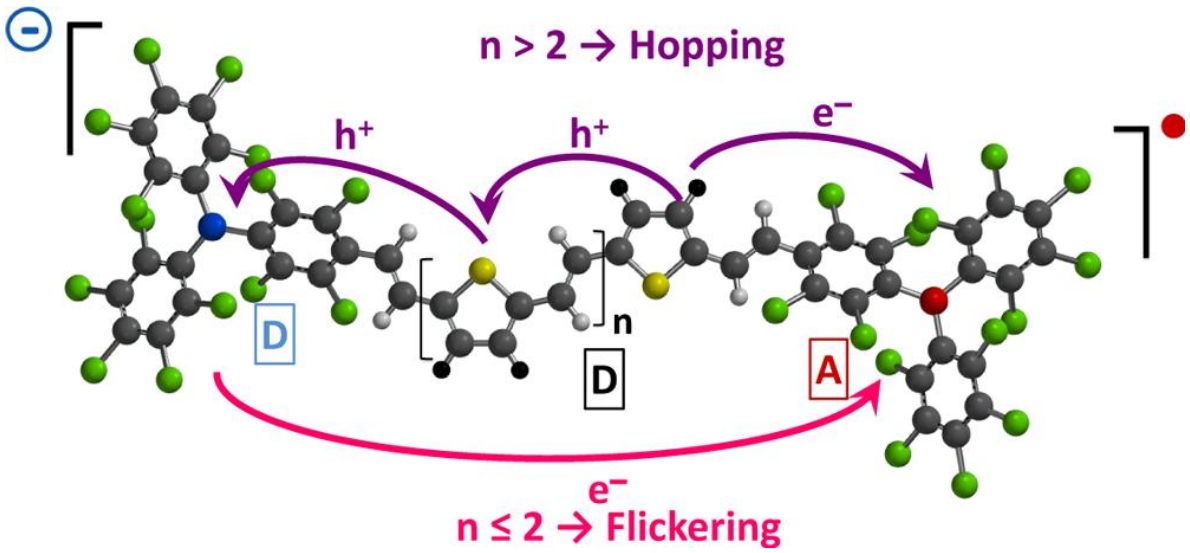

Fig. 5.4 Studied bi-PTM mixed-valence compounds with thiophene-vinylene (TV) bridges of increasing length. In this study, our first principles DFT calculations and AIMD simulations pointed out to a different mechanism for the shortest compounds of the studied series as that previously proposed in ref 14 (quatum tunnelling).

However, for the short TV bridged bi-PTM derivatives, our DFT calculations and AIMD simulations at 300K using hybrid DFT functionals (i.e. containing a proportion of HF-like exchange) as previously recommended for such systems,[22,23] pointed out to a new electronic mechanism explaining charge transfer phenomena: the so-called flickering resonance (FR). FR has been recently proposed for this type of organic electro-active systems[24] and it considers the delocalization of the negative charge through the π-conjugated states of the bridge as the main electronic mechanism allowing it to travel between both PTM extremes. In such a model thermal fluctuations significantly affect such delocalization path, and so certain thermally activated conformations may localize the charge or allow it to become delocalized through the entire π-conjugated system. The FR model may also be used to explain ballistic transport in graphene.[24]

5.1.4 Towards post-graphene organic Dirac 2D materials

What are the implications of *meta*- and *para*- topologies in 2 dimensions? Based on the experimental observations comparing *meta*- and *para*-connected bi-PTM mixed-valence compounds[12,13] there should be an appreciable difference in the electronic nature of *meta*-connected TAM 2D-COFs and *para*-connected ones. Recalling the studied TAM 2D-COFs presented in **Publication #5** in Chapter 4, we may see as shown in Fig. 5.5a, that within those networks TAM units are covalently bonded in *meta*- one respect each other through the connecting benzene ring (black circle in Fig. 5.5a).

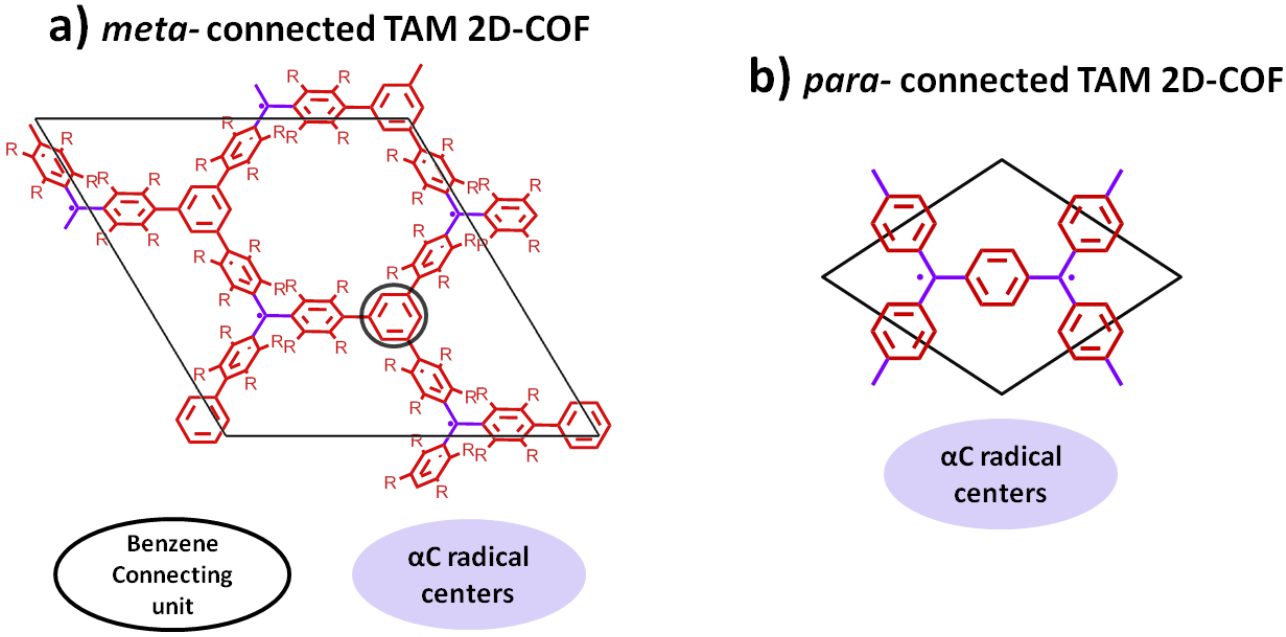

Fig. 5.5 a) Chemical structure of the *meta*-connected TAM 2D-COF presented in **Publication #5** in Chapter 4. **b)** *para*-connected TAM 2D-COF studied in **Publication #8** presented in this chapter.

As we found in **Publication #5**, *meta*-connected TAM 2D-COFs present a moderately stable ferromagnetic ordering of spin centres in the network (purple centres in Fig. 5.5a). However, most importantly, band structure calculations of such networks indicate they are electrical insulators, due to flat bands associated to the unpaired electrons in the material (purple centres in Fig. 5.5a). Such flat bands indicate that unpaired electrons in the *meta*-connected TAM 2D-COFs are essentially localized in each TAM unit and do not delocalize to neighbouring centres. This entirely coincides with previous experimental observations that indicate no charge-transfer phenomena for the *meta*-connected bi-PTM mixed valence compounds,[12,13] as sketched in Fig. 5.2.

What would be the scenario for a *para*-connected TAM 2D-COF, such as that shown in Fig. 5.5b? It turns out that, as reported by Adjizian et.al.[25,26] such a network behaves as a semimetal, presenting a linear crossing of electronic bands right at the Fermi level (see Fig. 5.6); what it is known as a Dirac cone. Such a feature has drawn a tremendous attention, especially since the discovery of graphene,[27] where the Dirac

cone appearing in its band structure[28] leads to ballistic transport (i.e. electrons moving as massless particles), as experimentally demonstrated.[29,30]

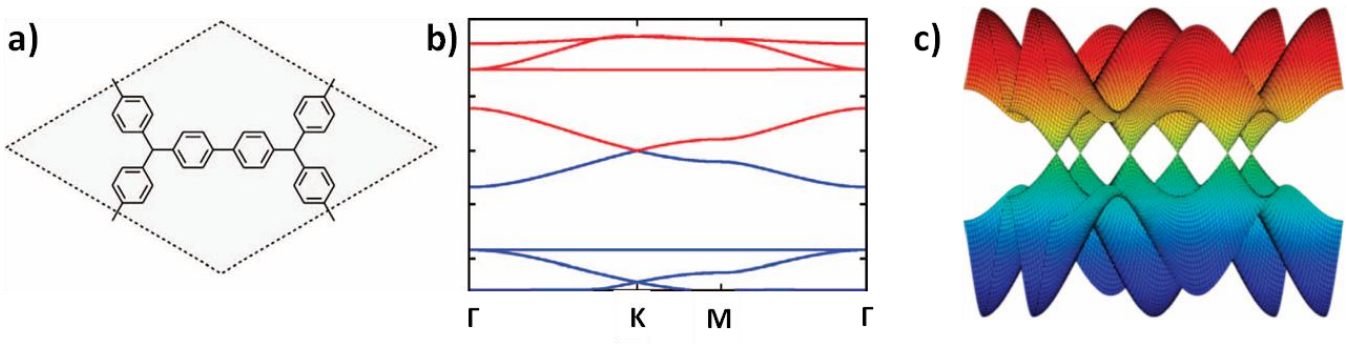

Fig. 5.6 a) Periodic structure of a *para*-connected TAM 2D-COF proposed by Adjizian et.al. in ref 25. **b)** Band structure of such 2D covalent framework showing the presence of a linear crossing of bands at the Fermi level (i.e. a Dirac cone). **c)** 3D plotting of such Dirac crossings at the Fermi level for this type of organic 2D materials.

Hence, we may see that, contrary to the *meta*-connected TAM 2D-COFs studied in **Publication #5**, in *para*-connected TAM 2D-COFs added negative charges may have the ability to conduct throughout the 2D material,[25,26] such as in graphene.[29,30] This is also in full agreement with the experimental observations in *para*-connected bi-PTM mixed-valence compounds where charge transfer takes place following different possible mechanisms (see ref 14 or **Publication #7**).

5.1.5 A *radical* approach to post-graphene organic Dirac 2D materials

Revisiting the introduction to this chapter, we may remember that for bi-radical systems with *para*-connected TAM units, as experimentally reported,[6–9] two resonance forms coexist: the open-shell anti-ferromagnetic (AFM) one and the closed-shell quinoidal (see Fig. 5.1d). However, for previously proposed *para*-connected TAM 2D-COFs,[25,26] such localized electronic solutions have not been reported (i.e. the open-shell AFM one and the closed-shell quinoidal), despite the fact they have been extensively studied both experimentally[6,31] and theoretically[8] for the analogous molecular systems.

In the very last contribution of this PhD thesis, **Publication #8**, we have looked for such localized solutions in *para*-connected TAM 2D-COFs presented in Figs. 5.5 and 5.6. I realized that a number of post-graphene organic Dirac materials (PGODs) sharing the same covalent skeleton of radical sp^2 carbon centres (see Fig. 5.7) should also present such localized solutions (i.e. the open-shell AFM one and the closed-shell quinoidal). Some of such considered PGODs are highly theoretically studied 2D materials such as graphynes and graphdiynes (Fig. 5.7).

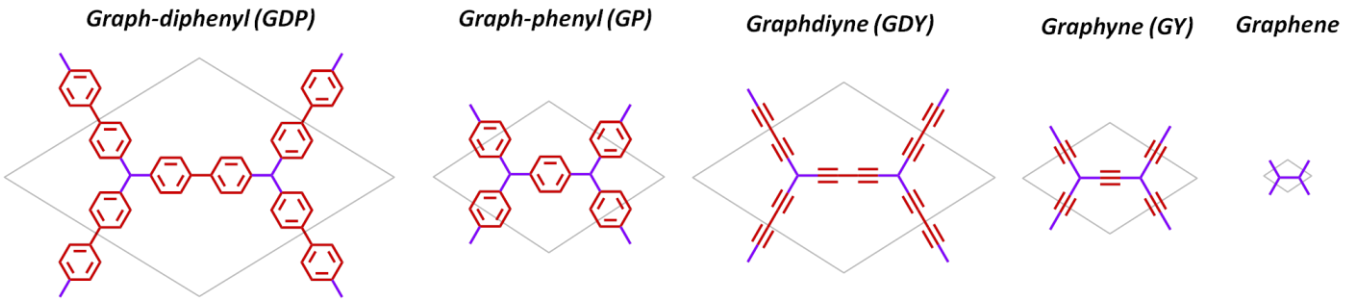

Fig. 5.7 Series of PGOD 2D materials studied in **Publication #8** in this chapter. All these materials present a Dirac cone in their band structures, which indicates their nature as semimetals, as graphene.

Hence, with this last contribution, we have been able to connect two important fields of materials science: that of bi-radicals[6,8,31] and mixed-valence compounds,[12,14,15,17,20] explored by chemists, and the world of graphene and post-graphene materials,[32–36] mainly studied by physicists. In this contribution we demonstrate the common nature of the systems studied in both fields, highlighting the higher necessity of a proper communication between both disciplines to push further the field of π-conjugated organic 2D materials for future nano-electronic applications.

5.2 Bibliography

1 K. Yoshizawa and R. Hoffmann, *Chem. - A Eur. J.*, 1995, **1**, 403–413.

2 N. M. Shishlov, *Russ. Chem. Rev.*, 2006, **75**, 863–884.

3 N. M. Gallagher, A. Olankitwanit and A. Rajca, *J. Org. Chem.*, 2015, **80**, 1291–8.

4 G. Kothe and H. Zimmermann, *Tetrahedron*, 1973, **29**, 2305–2313.

5 A. Rajca, J. Wongsriratanakul and S. Rajca, *Science*, 2001, **294**, 1503–1505.

6 Z. Zeng, X. Shi, C. Chi, J. T. López Navarrete, J. Casado and J. Wu, *Chem. Soc. Rev.*, 2015, **44**, 6578–6596.

7 P. Ravat and M. Baumgarten, *Phys. Chem. Chem. Phys.*, 2015, **17**, 983–991.

8 G. Trinquier and J.-P. Malrieu, *Chem. - A Eur. J.*, 2015, **21**, 814–28.

9 L. K. Montgomery, J. C. Huffman, E. A. Jurczak and M. P. Grendze, *J. Am. Chem. Soc.*, 1986, **108**, 6004–6011.

10 A. Rajca, K. Lu and S. Rajca, *J. Am. Chem. Soc.*, 1997, **119**, 10335–10345.

11 A. Rajca, S. Rajca and J. Wongsriratanakul, *J. Am. Chem. Soc.*, 1999, **121**, 6308–6309.

12 C. Rovira, D. Ruiz-Molina, O. Elsner, J. Vidal-Gancedo, J. Bonvoisin, J.-P. Launay and J. Veciana, *Chemistry (Easton).*, 2001, **7**, 240–250.

13 V. Lloveras, J. Vidal-Gancedo, D. Ruiz-Molina, T. M. Figueira-Duarte, J.-F. Nierengarten, J. Veciana and C. Rovira,

Faraday Discuss., 2006, **131**, 291.

14 V. Lloveras, J. Vidal-Gancedo, T. M. Figueira-Duarte, J. F. Nierengarten, J. J. Novoa, F. Mota, N. Ventosa, C. Rovira and J. Veciana, *J. Am. Chem. Soc.*, 2011, **133**, 5818–33.

15 M. Kaupp, M. Renz, M. Parthey, M. Stolte, F. Würthner and C. Lambert, *Phys. Chem. Chem. Phys.*, 2011, **13**, 16973–16986.

16 A. Heckmann, S. Dümmler, J. Pauli, M. Margraf, J. Köhler, D. Stich, C. Lambert, I. Fischer and U. Resch-Genger, *J. Phys. Chem. C*, 2009, **113**, 20958–20966.

17 A. Heckmann and C. Lambert, *J. Am. Chem. Soc.*, 2007, **129**, 5515–5527.

18 P. M. Burrezo, N.-T. Lin, K. Nakabayashi, S. Ohkoshi, E. M. Calzado, P. G. Boj, M. A. Díaz García, C. Franco, C. Rovira, J. Veciana, M. Moos, C. Lambert, J. T. López Navarrete, H. Tsuji, E. Nakamura and J. Casado, *Angew. Chemie Int. Ed.*, 2017.

19 J. Sedo, D. Ruiz, J. Vidal-Gancedo, C. Rovira, J. Bonvoisin, J.-P. Launay and J. Veciana, *Adv. Mater.*, 1996, **8**, 748–752.

20 J. Wu, X. Wu, J. O. Kim, S. Medina, F. J. Ramírez, P. M. Burrezo, S. Wu, Z. L. Lim, C. Lambert, J. Casado and D. Kim, *Chem. - A Eur. J.*, 2017.

21 P. M. Burrezo, N.-T. Lin, K. Nakabayashi, S. Ohkoshi, E. M. Calzado, P. G. Boj, M. A. Díaz García, C. Franco, C. Rovira, J. Veciana, M. Moos, C. Lambert, J. T. López Navarrete, H. Tsuji, E. Nakamura and J. Casado, *Angew. Chemie Int. Ed.*, 2017, **56**, 2898–2902.

22 A. Kubas, F. Gajdos, A. Heck, H. Oberhofer, M. Elstner and J. Blumberger, *Phys. Chem. Chem. Phys.*, 2015, **17**, 14342–14354.

23 M. Renz, K. Theilacker, C. Lambert and M. Kaupp, *J. Am. Chem. Soc.*, 2009, **131**, 16292–16302.

24 J. Blumberger, *Chem. Rev.*, 2015, **115**, 11191–11238.

25 J.-J. Adjizian, P. Briddon, B. Humbert, J.-L. Duvail, P. Wagner, C. Adda and C. Ewels, *Nat. Commun.*, 2014, **5**, 5842.

26 J.-J. Adjizian, A. Lherbier, S. M.-M. Dubois, A. R. Botello-Méndez and J.-C. Charlier, *Nanoscale*, 2016, **8**, 1642–1651.

27 K. S. Novoselov, A. K. Geim, S. V. Morozov, D. Jiang, Y. Zhang, S. V. Dubonos, I. V. Grigorieva and A. A. Firsov, *Science (80-.).*, 2004, **306**, 666–669.

28 D. A. Abanin, S. V. Morozov, L. A. Ponomarenko, R. V. Gorbachev, A. S. Mayorov, M. I. Katsnelson, K. Watanabe, T. Taniguchi, K. S. Novoselov, L. S. Levitov and A. K. Geim, *Science (80-.).*, 2011, **332**.

29 V. E. Calado, S.-E. Zhu, S. Goswami, Q. Xu, K. Watanabe, T. Taniguchi, G. C. A. M. Janssen and L. M. K. Vandersypen, *Appl. Phys. Lett.*, 2014, **104**, 23103.

30 J. Baringhaus, M. Ruan, F. Edler, A. Tejeda, M. Sicot, A. Taleb-Ibrahimi, A.-P. Li, Z. Jiang, E. H. Conrad, C. Berger, C. Tegenkamp and W. A. de Heer, *Nature*, 2014, **506**, 349–354.

31 P. Mayorga Burrezo, J. L. Zafra, J. T. López Navarrete and J. Casado, *Angew. Chemie*, 2017, **56**, 2250 –2259.

32 Z. Li, M. Smeu, A. Rives, V. Maraval, R. Chauvin, M. A. Ratner and E. Borguet, *Nat. Commun.*, 2015, **6**, 6321.

33 D. Malko, C. Neiss, F. Viñes and A. Görling, *Phys. Rev. Lett.*, 2012, **108**, 86804.

34 Q. Yue, S. Chang, J. Kang, J. Tan, S. Qin and J. Li, *J. Chem. Phys.*, 2012, **136**, 244702.

35 J. Chen, J. Xi, D. Wang and Z. Shuai, *J. Phys. Chem. Lett.*, 2013, **4**, 1443–1448.

36 Y. Li, L. Xu, H. Liu and Y. Li, *Chem. Soc. Rev.*, 2014, **43**, 2572–2586.

5.3 Results

Publication #7

Operative Mechanism of Hole-Assisted Negative Charge Motion in Ground States of Radical-Anion Molecular Wires.

J. Am. Chem. Soc. 2017, *139*, 686–692

C. Franco, P. M. Burrezo, V. Lloveras, R. Caballero, I. Alcón, S. T. Bromley*, M. Mas-Torrent, F. Langa, J. T. López Navarrete, C. Rovira*, J. Casado* and J. Veciana*

JACS
JOURNAL OF THE AMERICAN CHEMICAL SOCIETY
Article
pubs.acs.org/JACS

Operative Mechanism of Hole-Assisted Negative Charge Motion in Ground States of Radical-Anion Molecular Wires

Carlos Franco,[†] Paula Mayorga Burrezo,[‡] Vega Lloveras,[†] Rubén Caballero,[§] Isaac Alcón,[∥] Stefan T. Bromley,[*,∥,⊥] Marta Mas-Torrent,[†] Fernando Langa,[§] Juan T. López Navarrete,[‡] Concepciò Rovira,[*,†] Juan Casado,[*,‡] and Jaume Veciana[*,†]

[†]Department of Molecular Nanoscience and Organic Materials, Institut de Ciència de Materials de Barcelona (ICMAB-CSIC)/CIBER-BBN, Campus Universitari de Bellaterra, Cerdanyola, E-08193 Barcelona, Spain

[‡]Department of Physical Chemistry, University of Malaga, Campus de Teatinos s/n, 29071 Malaga, Spain

[§]Instituto de Nanociencia, Nanotecnología y Materiales Moleculares (INAMOL), University of Castilla-La Mancha, Campus de la Fábrica de Armas, 45071 Toledo, Spain

[∥]Department of Materials Science and Physical Chemistry, Faculty of Chemistry, University of Barcelona, Avenida Diagonal, 647, 08028 Barcelona, Spain

[⊥]Catalan Institution of Research and Advanced Studies (ICREA), 08010 Barcelona, Spain

Supporting Information

ABSTRACT: Charge transfer/transport in molecular wires over varying distances is a subject of great interest. The feasible transport mechanisms have been generally accounted for on the basis of tunneling or superexchange charge transfer operating over small distances which progressively gives way to hopping transport over larger distances. The underlying molecular sequential steps that likely take place during hopping and the operative mechanism occurring at intermediate distances have received much less attention given the difficulty in assessing detailed molecular-level information. We describe here the operating mechanisms for unimolecular electron transfer/transport in the ground state of radical-anion mixed-valence derivatives occurring between their terminal perchlorotriphenylmethyl/ide groups through thiophene−vinylene oligomers that act as conjugated wires of increasing length up to 53 Å. The unique finding here is that the net transport of the electron in the larger molecular wires is initiated by an electron−hole dissociation intermediated by hole delocalization (conformationally assisted and thermally dependent) forming transient mobile polaronic states in the bridge that terminate by an electron−hole recombination at the other wire extreme. On the contrary, for the shorter radical-anions our results suggest that a flickering resonance mechanism which is intermediate between hopping and superexchange is the operative one. We support these mechanistic interpretations by applying the pertinent biased kinetic models of the charge/spin exchange rates determined by electron paramagnetic resonance and by molecular structural level information obtained from UV−vis and Raman spectroscopies and by quantum chemical modeling.

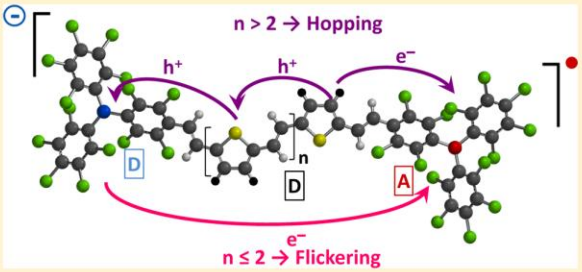

■ INTRODUCTION

The main mechanisms used to describe charge transfer/transport processes across a chain of ionizable molecular subunits are charge hopping (CH), flickering resonance (FR), and superexchange (SE).[1] CH is a thermally activated incoherent process where a localized charge excess is assumed to hop between consecutive sites on the bridge where relaxation takes place previous to each hop. In this model "real" wire states (i.e., excited, conformational, charged, hot vibrational, etc.) take an active part in the charge transport, and for this reason, this mechanism is operative even for long bridges. On the contrary, the SE mechanism occurs owing to the energy alignment of the levels of the two terminal subunits (resonance) which causes the charge to tunnel from one extreme of the wire to another without residence on the bridge. Thereby this mechanism is operative only for the shorter wires. Finally, the recently proposed FR[1] mechanism can be thought of as a compromise between CH and SE where the energy levels of the two terminal subunits and those of the bridge subunits become all in resonance due to thermal fluctuations. Then, the charge moves ballistically, without nuclear relaxation, through the energy-aligned states to become trapped at the end of the wire. Given the inherent nature of charge transfer/transport, it combines and competes with many other molecular processes, thus giving rise to a panoply of scenarios. In order to understand such complex phenomena, which are particularly relevant in molecular electronics and biological

Received: August 18, 2016
Published: December 20, 2016

DOI: 10.1021/jacs.6b08649
J. Am. Chem. Soc. 2017, 139, 686−692

systems, detailed knowledge from a range of experimental and theoretical probes is of vital importance.

The most commonly employed protocol for mechanistic studies of charge transport is the measurement of electrical currents through molecular junctions.[2−9] However, complementary *in situ* spectroscopic studies are difficult given the nanometer resolution often required. For analogous studies in solution, molecular charge transport in donor−bridge−acceptor compounds is usually evaluated by photoexcitation on the donor forming a adiabatic charge transfer state which relaxes in an energetically downhill movement of the charge through the wire, whereby its dynamics can be studied by time-resolved spectroscopies.[10] Unfortunately, these photoactivated transient methods also contain coupling terms among the excited states, thus potentially "masking" the intrinsic charge transport characteristics in the ground state.[11,12] It turns out that "clean" insights into the intrinsic conduction mechanisms are obtained in the unperturbed ground electronic state for which mixed-valence (MV) systems are very good choices. Among these, radical MV systems are ideal candidates for this purpose since they can be studied by means of electron paramagnetic resonance (EPR) in solution[13] which, in addition, facilitates the use of complementary *in situ* spectroscopic techniques, like UV−vis−NIR and Raman, providing further rich molecular level cross-information.

Perchlorotriphenylmethyl radicals (PTM) are persistent and stable open-shell derivatives with good electron accepting properties and have been successfully used as redox centers in MV radical-anion systems, allowing the study of electron transfer/transport through different bridges.[14−16] Bridges based on thiophene-vinylene oligomers (***n*TV**) have been recently demonstrated to perform as one of the most efficient π−conjugated extended molecular wires.[17−19] Given their electron-rich donor nature, these ***n*TV** bridges are typically considered as hole (positive charge) transmitters.[17−19] Conversely, ***n*TV** bridges have never been used to promote charge transfer/transport between negatively charged terminal groups.

In this work, a series of six electron-donor ***n*TV** oligomers,[17] substituted at their terminal sites with two PTM radical groups, **$^{\bullet}$PTM-*n*TV-PTM$^{\bullet}$** (Scheme 1), properly reduced to radical-anion MV species are studied. The excess charge conduction behavior in the resulting mixed-valence **[PTM-*n*TV-PTM]$^{\bullet-}$** species is studied by variable-temperature EPR complemented by *in situ* UV−vis−NIR and resonant Raman spectroscopies and supported by electronic structure calculations. This multifold information on the spin/charge exchange rate in the ground electronic states serves for the longer oligomers (***n*TV**; n = 4−7) to propose a biased bidirectional symmetrical charge-hopping mechanism through the ***n*TV** bridge, imparted by two reflecting PTM sites at opposite ends. The initial step of the mechanism is the thermally activated intramolecular oxidation of the donor wire by the acceptor "neutral" **PTM$^{\bullet}$** subunit forming a symmetric charge-separated state with a mobile positive polaron in the bridge flanked by two **PTM^{-}** anions. After the formation of this transitory positive polaronic species, the charge may hop among the TV units and finally decays by an electron−hole annihilation that restores the neutrality of the ***n*TV** bridge in the radical anion. This finding is rather unusual since charge transport of negative charge (**PTM$^{\bullet-}$** → **PTM$^{\bullet}$**) through hole transmitter bridges (***n*TV**) mostly occurs through empty "conduction" states able to accommodate an excess of charge rather than mediated by positive charges. On the contrary, in the shorter radical-anions (***n*TV**; n = 2, 3) the operative mechanism for the spin/charge exchange seems to be the FR mechanism favored by the higher rigidity (or quinoidization) of their bridges.

Scheme 1

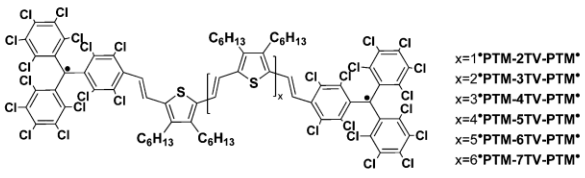

RESULTS AND DISCUSSION

Synthesis and Characterizations. The synthesis of diradicals **$^{\bullet}$PTM-*n*TV-PTM$^{\bullet}$** (n = 2−7) starts with the preparation of the corresponding hydrogenated derivatives, **(*α*H,*α*′H)-PTM-*n*TV-PTM**, through a Wittig Horner olefination between the polychlorotriphenylmethane phosponate derivative[20] and the suitable ***n*TV** dialdehydes (see Supporting Information). Treatment with an excess of base gives the corresponding biscarbanions **[PTM-*n*TV-PTM]$^{-2}$** that are subsequently oxidized to **$^{\bullet}$PTM-*n*TV-PTM$^{\bullet}$**. Diradicals **$^{\bullet}$PTM-*n*TV-PTM$^{\bullet}$** were completely characterized with usual spectroscopic techniques, like IR, UV−vis (Table S1), Raman, and MALDI-TOF MS (see Supporting Information). Cyclic voltammetries of diradicals **$^{\bullet}$PTM-*n*TV-PTM$^{\bullet}$** show well-resolved two-electron reduction peaks and reversible oxidations resulting in amphoteric redox behaviors of **$^{\bullet}$PTM-*n*TV-PTM$^{\bullet}$** (Table S2). Solution EPR spectra of diradicals **$^{\bullet}$PTM-*n*TV-PTM$^{\bullet}$** (Table S3) consist of four overlapped main lines from which two isotropic hyperfine coupling constants, a_i, that are half of those observed for the segmental model monoradical **PTM-2TV** (see Supporting Information). Such results indicate the existence of a magnetic interaction between the two unpaired electrons through the diamagnetic bridge, which are additionally confirmed by frozen solution EPR spectra of **$^{\bullet}$PTM-2TV-PTM$^{\bullet}$** and **$^{\bullet}$PTM-3TV-PTM$^{\bullet}$** (Figure 1a) that show ΔM_s = 2 half-field forbidden transitions due to thermally accessible triplet states (Figures S65−S70). Generation of radical-anions **[PTM-*n*TV-PTM]$^{\bullet-}$** was achieved by a stepwise chemical or electrochemical reduction of diradicals **$^{\bullet}$PTM-*n*TV-PTM$^{\bullet}$**.

***In Situ* Spectroscopic Studies.** Intramolecular spin/charge transfer in radical-anions **[PTM-*n*TV-PTM]$^{\bullet-}$** was examined by variable-temperature EPR measurements. In all these radical-anions, the EPR profiles changed with the temperature going from four to three overlapped lines when the temperature is increased (in the range 200−300 K), indicating a passage from the slow to fast exchange regime at the EPR time-scale. The first-order rate constants (k) for spin/charge exchange between the two PTM sites in each compound were determined by simulation of the experimental EPR spectra using the ESR-EXN software[21] (Figures 1a and S2−S7). The comparison at a given temperature for all radical anions demonstrates that k decreases with the increasing of the ***n*TV** bridge length (Figure 1b). For a given compound, k also exhibits a net dependence with the temperature (Figure 1b) disclosing that a thermally activated intramolecular dynamic spin/charge exchange occurs between the two terminal PTM sites for all radical-anions. From the

DOI: 10.1021/jacs.6b08649
J. Am. Chem. Soc. 2017, 139, 686−692

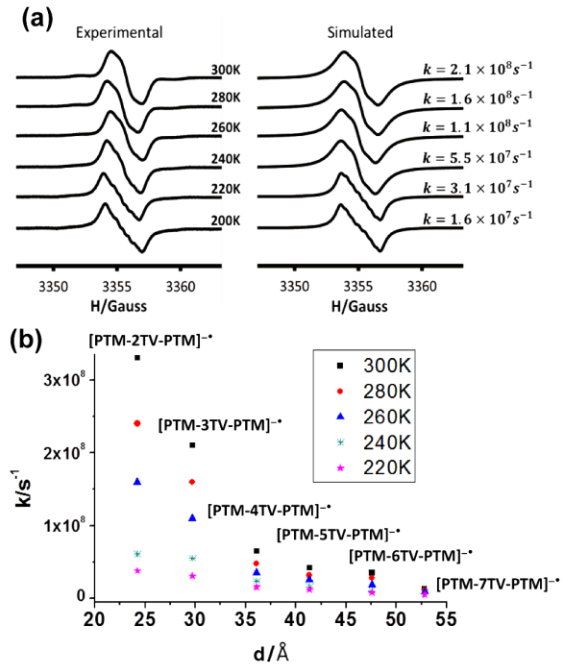

Figure 1. (a) Temperature-dependent changes in the EPR spectrum of [**PTM-3TV-PTM**]$^{\bullet-}$**NBu**$_4^+$ solution in CH_2Cl_2 (left), obtained by chemical reduction with $NBu_4^+OH^-$, and simulated spectra (right) with different spin/charge exchange rates. (b) Distance dependences of spin/charge exchange rates, *k*, of radical-anions [**PTM-*n*TV-PTM**]$^{\bullet-}$ in the temperature range 220–300 K.

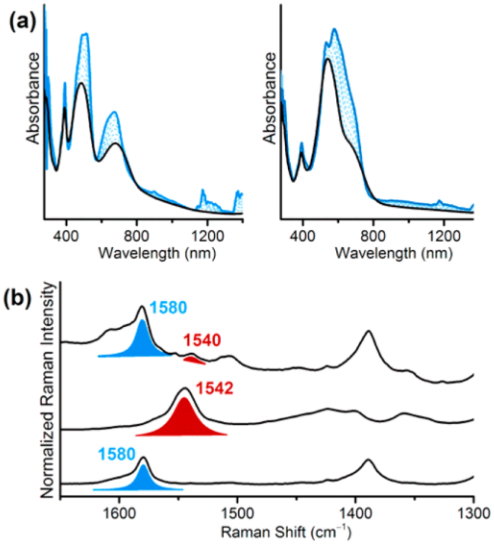

Figure 2. (a) Evolution of UV–vis–NIR spectra of the [**PTM-2TV-PTM**]$^{\bullet-}$**NBu**$_4^+$ (left) and [**PTM-5TV-PTM**]$^{\bullet-}$**NBu**$_4^+$ (right) as a function of the temperature, obtained by chemical reduction with $NBu_4^+OH^-$. Solid black line corresponds to UV–vis–NIR at room temperature and solid blue line at 77K. (b) Comparison of 633 nm Raman spectra in DCM of [**PTM-4TV-PTM**]$^{\bullet-}$**NBu**$_4^+$ (top), [**PTM-4TV-PTM**]$^{\bullet+}$**Cl**$^-$ (medium) and **$^\bullet$PTM-4TV-PTM$^\bullet$** (bottom).

thermal dependence of *k* values we deduced that for the shorter compounds the operating mechanism is strongly dependent on the temperature as well as on the length of the bridge, whereas for the longer ones both thermal and size variations are considerably smaller. Such different behaviors between shorter (***n*TV**; n= 2, 3) and longer (***n*TV**; *n* = 4–7) bridges point to the presence of two different mechanisms. The question about the particular electron transfer/transport mechanism which operates in these MV radical-anions is therefore pertinent.

Variable-temperature UV–vis–NIR electron absorption spectroscopy under the same conditions as the EPR measurements, were performed for all radical-anions. Spectra at room temperature (Figures 2a and S8) show three well-distinguished kinds of bands: a band at around 390 nm, characteristic of a **PTM$^\bullet$** radical chromophore, another set of very intense bands at 485–573 nm (***n*TV** centered bands), due to the conjugated ***n*TV** bridges, and finally absorption bands with medium intensity at 678–720 nm, assigned to the negatively charged **PTM$^-$** partially spreading out in the bridge (i.e., forming the PTM&***n*TV** segment). Worth noticing is the intervalence charge transfer (IVT) band exhibited by [**PTM-2TV-PTM**]$^{\bullet-}$ at 1372 nm (Figure S1 inset) which is not detected for the rest of radical-anions. This result is consistent with the typical exponential decay of the intensity (accompanied by a blue-shift) of IVT bands with increasing molecular lengths that makes the IVT band to be hidden by the PTM anion and ***n*TV** bands.

Interestingly, the ***n*TV** centered bands of radical-anions clearly show a red-shift with the enlargement of the bridge from 485 to 573 nm, while the PTM&***n*TV** absorption is less altered with the size (i.e., from 678 nm for [**PTM-2TV-PTM**]$^{\bullet-}$ to 720 nm in [**PTM-7TV-PTM**]$^{\bullet-}$). Furthermore, the ***n*TV** bands are broad and ill-resolved at room temperature but evolving into a clear vibronic structure at 77K which are more pronounced in the larger compounds (Figure 2a and S8). Conversely, the rest of the bands (from PTM chromophores and PTM&***n*TV** segments) are minimally affected by cooling. The detection of vibrational resolution in the absorption spectra on cooling might reveal the existence of an ample distribution of molecular conformers at room temperature formed by distortions among the repeating units around the thiophene vinylene C–C bonds. By removing the thermal energy the population of the most planar, rigid, and energetically stable conformer is increased providing the vibronic components. Furthermore, this indicates the flatness or flexibility of the ground electronic state potential energy curve against conformational distortions in the larger MV radical-anions, an aspect of relevance for the further discussion.

Resonant Raman spectra of radical-anions [**PTM-*n*TV-PTM**]$^{\bullet-}$ at room temperature (Figures 2b, top, and S9) taken with the excitation laser at 633 nm, in resonance with one of the absorption bands of the radical anion, provide their unique vibrational fingerprints. In comparison with the Raman spectra of the neutral diradicals (Figures 2b, bottom, and S10), radical-anions (Figures 2b, top, and S9) exhibit resonant Raman bands emerging from their different domains: (i) The bands at >1600 cm^{-1} are due to PTM-***n*TV** fragments mostly supporting the excess of negative charge. (ii) The bands at 1580–1590 cm^{-1} corresponding to the molecular fraction of the bridge without an excess of negative charge, as previously reported.[22] Nevertheless, the most significant finding in these resonant Raman spectra is the detection of bands with medium-low intensities around 1540 cm^{-1}, together with several other weaker bands in the region of 1390–1460 cm^{-1}. In Figure 2b, the spectrum of the radical cation [**PTM-4TV-PTM**]$^{\bullet+}$

DOI: 10.1021/jacs.6b08649
J. Am. Chem. Soc. 2017, 139, 686–692

(generated from •**PTM-4TV-PTM**• by addition of one equivalent of a $FeCl_3$ solution) is also shown which presents the most prominent band at 1540 cm^{-1} accompanied be weaker features in the same interval of 1390−1460 cm^{-1}, such as that in [**PTM-4TV-PTM**]•−. In the [**PTM-4TV-PTM**]•+, the charge is confined in the middle of the ***n*TV** moiety (the electro-deficient **PTM**• at each extreme repels the positive charge), and the thiophenes get quinoidal. However, the vinylenes are correspondingly strained, overall planarizing the bridge. Indeed, the resemblance between the 1540/1390−1460 cm^{-1} bands in [**PTM-4TV-PTM**]•+ and [**PTM-4TV-PTM**]•− reveals common structural features.

Mechanistic Analysis. To elucidate the mechanism of electron transfer, one often refers to the interpretation of the k values within the framework of the classical Marcus theory which includes the role of the temperature in connection with microscopic parameters of relevance such as reorganization energies, electronic couplings and driving forces. We propose that the mechanism of the spin/charge exchange, at least in the larger radical-anions [**PTM-*n*TV-PTM**]•−(n = 4−7), proceeds as shown in Scheme 2 (see also Scheme S5) where a hole is

Scheme 2

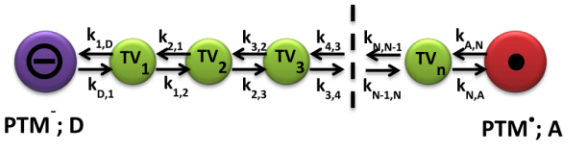

stepwise transported by a hopping mechanism along the ***n*TV** molecular wire. The election of this sequential mechanism is first justified since it takes into account the electron acceptor capability of PTM radical unit and the donor ability of ***n*TV** bridges as revealed by their amphoteric redox behavior. This redox property supports the simultaneous presence of the negative and positive charges (charge separated state) in the molecule. Assuming a hole in the ***n*TV** bridge, this simplified kinetic scheme can be described as a biased symmetrical bidirectional hopping of the positive charge process with two reflecting sites at the opposite molecular ends where the rates of site-to-site hopping inside the ***n*TV** toward ($k_1 = k_{2,1}$) and away ($k_2 = k_{1,2}$) from the terminal PTM units are different but identical to those rates of the other wire extreme ($k_1 = k_{2,1} = k_{N-1,N}$ and $k_2 = k_{1,2} = k_{N,N-1}$) as required by the molecular symmetry (see Supporting Information for more details). In particular, we assume that $k_1 > k_2$[23] because the rate of a hole moving toward a nearby negatively charged PTM site must be larger than that in the opposite direction due to electrostatic attraction. In addition, we assume that the hopping rates backward and forward inside the wire are similar ($k_{N-1,N-2} = k_{N-2,N-1} = k_3$; $\forall\ N \geq 4$) because the hopping hole is far from the charged termini. According to the classical Marcus theory and previous considerations on related systems,[24,25] the apparent spin/charge exchange rate k_{ET} is given by (see Supporting Information):

$$k_{ET} \simeq \frac{\pi}{\hbar}\frac{|V_{D1}|^2}{\sqrt{4\pi\lambda_D k_B T}}\, e^{-(\Delta E_{BD}+\lambda_{D1})^2/4\lambda_{D1}k_B T}\, e^{-\beta(R-R_0-2r)} \quad (1)$$

where ΔE_{BD} is the energy change corresponding to an electron injection from the TV bridge site nearest to PTM• radical to the latter site (transition TV1→ PTM•), λ_{D1} (= λ_{AN}) is the reorganization energy of such a transition, $|V_{D1}|$ (= $|V_{AN}|$) denotes the coupling of the PTM• to the corresponding terminal unit of the bridge, k_B the Boltzman's constant, T the absolute temperature, R (in Å) is the overall distance over which the spin/charge is transferred, R_0 corresponds to the distance between the PTM units separated by a single-bridging TV unit (17.9 Å), r is the distance between two neighboring TV units (4.6 $Å^{-1}$), and β ($Å^{-1}$) is the decay factor. R and R_0 values for all radical anions were determined as the distances between the central carbon atoms of the PTM units, obtained by quantum chemical calculations from the optimized geometries. The solution of eq 1 is linked to the underlying mechanism by means of ΔE_{BD} which is therefore inserted in the equation as a phenomenological parameter characteristic of the proposed mechanism. In our case, ΔE_{BD} represents the energy cost for the formation of a transient intermediate species which should contain a positive polaron in the middle of the ***n*TV** structure and therefore flanked by two PTMs each one with a negative charge. Assuming this, the barrier is accounted by the free energy required to form the dianion−cation charge separated state which is provided by the Weller formalism.[26] This formalism considers the cathodic and anodic redox potentials for the independent formation of a radical cation and a radical-anion and are directly taken from the CV data (see Supporting Information) in accordance with the donor character of the ***n*TV** bridges (Table S2)[17,27] and the acceptor nature of PTM radical units.[28] This approximation gave ΔE_{BD} values from +1.13 eV for the shorter (n = 2) to +0.83 eV for the larger (n = 7) radical anion (see Supporting Information). Finally, fitting the experimental k data of [**PTM-*n*TV-PTM**]•− (n = 4−7) to eq 1 using the latter ΔE_{BD} values gave the following parameters: $\lambda_{D1} = \lambda_{AN} \approx 0.5$ eV, $|V_{D1}| = |V_{AN}| \approx 0.07$ eV, and a decay factor β of 0.25 $Å^{-1}$. These values are fully consistent with our experimental observations: (i) Since $\lambda_{1A} > |V_{1A}|$, therefore all radical-anion systems can be classified as class II MV systems. (ii) The moderate decay factor value is in consonance with the capacity of the wire of transmitting the charge through large distances between the redox centers by means of a hopping mechanism. It must be highlighted that this mechanism conciliates the amphoteric redox behavior, and the detection in the Raman spectrum of the anion radical species of a weak feature which is due to the radical cation at the bridge (or dianion−cation species) and the rigidity at low temperatures of the bridge because of the contributions of the thienoquinoidal polarons.

Theoretical Modeling. To provide more insight into the underlying charge transfer phenomena, density functional theory (DFT) calculations were performed on [**PTM-2TV-PTM**]•− where the spectator C_6H_{13} side chains of the TV units were replaced by methyl groups to reduce computational cost. For improved agreement with experiment, previous studies of molecular MV systems have recommended using functionals 50% of Hartree−Fock-like exchange (HFLE)[29] or 35% HFLE together with a continuum treatment of solvation and a 6-311G ++ basis set.[30] We found that both approaches yielded stable charge localized states and here, unless otherwise stated, we report results obtained using the PBE functional[31] with 50% HFLE (referred to as PBE-50) employing the Gaussian 09 code.[32] Unfortunately, similar calculations on larger radical-anions were untractable due to the large sizes of molecules. The optimized structure of [**PTM-*n*TV-PTM**]•− (Figure 3a)

DOI: 10.1021/jacs.6b08649
J. Am. Chem. Soc. 2017, 139, 686−692

displays the 2TV bridge with a planar conformation and each PTM twisted by 40° with respect to the 2TV plane.

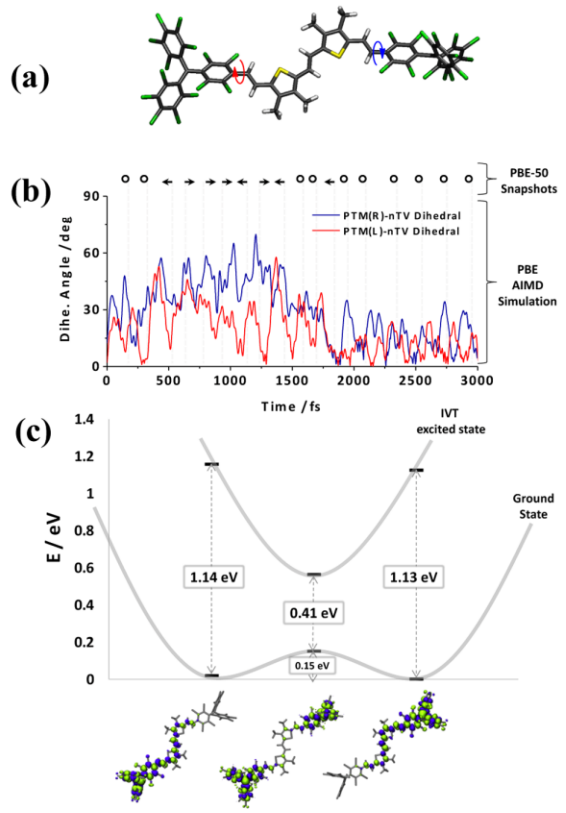

Figure 3. (a) Optimized structure of [**PTM-2TV-PTM**]$^{\bullet-}$. The helical arrows indicate the dihedral angles (φ) between each PTM unit and the 2TV wire. (b) Variation of the indicated dihedral angles in (a) during 3 ps of an AIMD simulation of [**PTM-2TV-PTM**]$^{\bullet-}$ at 300 K using the PBE functional. The left/right arrows and circles indicate left/right localization or delocalization of spin density respectively for particular tested snapshots with the PBE-50 functional. (c) Relative energies for each studied electronic configuration (left − localized, middle − delocalized, right − localized) in the corresponding relaxed conformations as obtained by PBE-50 optimizations. The calculated energies of the optical IVT (represented by the β-HOMO/β-SUMO gap) for each case are also provided. The structures of each configuration with the corresponding highlighted spin densities are provided below the x axis of panel c.

To assess the electron transfer/transport of [**PTM-2TV-PTM**]$^{\bullet-}$ at finite temperatures, we performed an *ab initio* molecular dynamics simulation (AIMD) at 300 K during 4 ps (1 ps of equilibration plus 3 ps of production) using the PBE functional, the Bussi−Donadio−Parrinello thermostat[33] and a light numerical basis set as implemented in the FHI-AIMS code.[34] From 18 sample "snapshots" of thermally activated conformations taken over a 3 ps period from these runs, we calculated the spin distribution using the PBE-50 method described above. As indicated in Figure 3b (top), during the thermal motion at 300 K the spin distribution fluctuates between being either localized on one of the two PTM units (← or →) or fully delocalized over the entire molecule (○). Figure 3b also plots the variation of the dihedral twist angle (φ) between each PTM unit and the 2TV wire. During the first 1.5 ps, φ presents large values, typical of highly twisted structures, and the spin distribution in [**PTM-2TV-PTM**]$^{\bullet-}$ tends to be localized on either one PTM unit (← or →). Conversely, for the latter 1.5 ps, φ values are much smaller (i.e., flatter conformation), and the spin distribution tends to delocalize over the entire molecular skeleton. Therefore, it seems that the spin density (and thus the negatively charged density) follows the thermally activated rotational fluctuations of [**PTM-2TV-PTM**]$^{\bullet-}$, in accordance with previous studies on single PTMs.[35] To investigate the 0 K potential energy landscape underlying the thermally perturbed conformers, we fully optimized the structures of the 18 snapshots using the PBE-50 method resulting in localized solutions in all cases. This suggests that the thermally excited structures with delocalized electronic states correspond to transitional conformations. The 0 K delocalized solution obtained from a highly symmetric structure is found 0.15 eV above all obtained localized solutions, providing a thermally accessible energy barrier between the localized electronic configurations (Figure 3c). Moreover, we have found that the β-HOMO/β-SUMO gap which we take as a reasonable approximation to the optical IVT energy depends on the degree of localization/delocalization of the ground electronic state. Specifically, we find that this gap ranges from 1.1 eV for the localized solutions to 0.4 eV for the transitional delocalized states, reproducing quite well the observed band appearing at 0.7 eV (i.e., 1372 nm). We further note that the experimental IVT value is also consistent with typical β-HOMO/β-SUMO gap values found for the 18 thermally activated snapshots.

According to the DFT results, the charge transfer mechanism for the shortest radical anion [**PTM-2TV-PTM**]$^{\bullet-}$ appears not to involve a net bridge polaron state but a transition state dependent on a resonance between the two PTM units, a situation more reconcilable with a SE mechanism. In pure SE, however, the bridge only plays a virtual role in the charge transfer, but in the case here our analysis reveals that the degree of coupling between the PTM units and the bridge (via the dihedral angles, φ) plays an essential role. Thus, a pure SE interpretation does not fully capture our theoretical findings. Between SE and hopping, the FR model aims to reconcile bridge participation without the presence of localized polarons on the bridge. We feel that for [**PTM-2TV-PTM**]$^{\bullet-}$ the FR mechanism is a reasonable alternative while for longer molecules the bridge will increasingly have more conformational freedom potentially allowing for charge/structure localization (i.e., polaron formation). In turn, this allows polaronic hopping to become increasingly prominent with respect to FR for bridges of $n \geq 3$ in [**PTM-*n*TV-PTM**]$^{\bullet-}$.

■ CONCLUSIONS

The use of a multitechnique approach, based on variable-temperature EPR, UV−vis−NIR, resonant Raman spectroscopies, and theoretical calculations, allowed us to thoroughly investigate the charge transfer mechanisms in the ground state of a series of six radical-anions [**PTM-*n*TV-PTM**]$^{\bullet-}$ (n = 2−7) of distinct lengths. For the shortest 2TV-bridged molecule we propose that charge transfer occurs through a flickering resonance type mechanism. On the contrary for molecules with bridges with 4 or more TV units, we propose that the exchange of the negative spin/charge occurs through a thermally activated incoherent biased bidirectional symmetrical charge hopping mechanism of positive charge. In this latter

DOI: 10.1021/jacs.6b08649
J. Am. Chem. Soc. 2017, 139, 686−692

mechanism, the transient polaron formation inside the bridge and the hopping of holes among the bridging TV units participate in the spin/charge exchange between the two terminal PTM units. The reported results show that a bridge with an electron-rich donor nature typically considered as an efficient hole transmitter can also be used to promote charge transfer/transport between neutral negatively charged terminal groups of molecular wires in their ground states.

■ ASSOCIATED CONTENT

Supporting Information

The Supporting Information is available free of charge on the ACS Publications website at DOI: 10.1021/jacs.6b08649.

Synthesis of dialdehyde *n*TV bridges; general procedure for the synthesis of **(αH,α′H)-PTM-*n*TV-PTM**, the segmental model **(αH)-PTM-2TV**, radical **2TV-PTM•**, and diradicals **•PTM-*n*TV-PTM•** (n = 2−7); EPR and CV data of radical **2TV-PTM•** and diradicals **•PTM-*n*TV-PTM•** (n = 2−7); CV of representative **(αH,α′H)-PTM-*n*TV-PTM**; vis−NIR of cations of diradical **•PTM-4TV-PTM•** and the model bridge; procedure for the generation of radical-anions **[PTM-*n*TV-PTM]$^{\bullet-}$** (n = 2−7) and VT-EPR, UV−vis−NIR, and Raman spectra; kinetic model and rate data of spin/charge exchange process of radical-anions **[PTM-*n*TV-PTM]$^{\bullet-}$**(n = 2−7); ^{1}H NMR, ^{13}C NMR, FT-IR, MALDI-MS and EPR spectra of all new compounds (PDF)

■ AUTHOR INFORMATION

Corresponding Authors

*E-mail: s.bromley@ub.edu.
*E-mail: cun@icmab.es.
*E-mail: casado@uma.es.
*E-mail: vecianaj@icmab.es.

ORCID

Fernando Langa: 0000-0002-7694-7722
Jaume Veciana: 0000-0003-1023-9923

Notes

The authors declare no competing financial interest.

■ ACKNOWLEDGMENTS

We acknowledge the financial support from the Spanish MINECO/FEDER (grants CTQ2013-40480-R, CTQ2016-7989-R, and CTQ2015-64618-R), Spanish Ministry of Economy and Competitiveness, through the "Severo Ochoa" Programme for Centres of Excellence in R&D (grant SEV-2015-0496), the Generalitat de Catalunya (grants 2014SGR-17, 2014SGR-97, and XRQTC). We also acknowledge supercomputing resources provided by the Red Española de Supercomputacion and the Networking Research Center of Bioengineering, Biomaterials and Nanomedicine (CIBER-BBN). The work carried out at the University of Malaga was supported by MINECO/FEDER through the reference projects CTQ2012-33733 andCTQ2015-69391-P. The "Servicios Centrales de Apoyo a la Investigación" of the University of Malaga are also acknowledged by generous access to its facilities. I.A. acknowledges the Spanish Ministerio de Educación Cultura y Deporte for a FPU PhD scholarship.

■ REFERENCES

(1) Blumberger, J. *Chem. Rev.* **2015**, *115*, 11191.
(2) Nitzan, A.; Ratner, M. A. *Science* **2003**, *300*, 1384.
(3) Choi, S. H.; Kim, B.; Frisbie, C. D. *Science* **2008**, *320*, 1482.
(4) Lu, Q.; Liu, K.; Zhang, H.; Du, Z.; Wang, X.; Wang, F. *ACS Nano* **2009**, *3*, 3861.
(5) Moreno-García, P.; Gulcur, M.; Manrique, D. Z.; Pope, T.; Hong, W.; Kaliginedi, V.; Huang, C.; Batsanov, A. S.; Bryce, M. R.; Lambert, C.; Wandlowski, T. *J. Am. Chem. Soc.* **2013**, *135*, 12228.
(6) Kaliginedi, V.; Moreno-García, P.; Valkenier, H.; Hong, W.; García-Suárez, V. M.; Buiter, P.; Otten, J. L. H.; Hummelen, J. C.; Lambert, C. J.; Wandlowski, T. *J. Am. Chem. Soc.* **2012**, *134*, 5262.
(7) Luo, L.; Choi, S. H.; Frisbie, C. D. *Chem. Mater.* **2011**, *23*, 631.
(8) Choi, S. H.; Risko, C.; Ruiz-Delgado, M. C.; Kim, B.; Brédas, J. L.; Frisbie, C. D. *J. Am. Chem. Soc.* **2010**, *132*, 4358.
(9) Hines, T.; Diez-Perez, I.; Hihath, J.; Liu, H.; Wang, Z. S.; Zhao, J.; Zhou, G.; Müllen, K.; Tao, N. *J. Am. Chem. Soc.* **2010**, *132*, 11658.
(10) Sukegawa, J.; Schubert, C.; Zhu, X.; Tsuji, H.; Guldi, D. M.; Nakamura, E. *Nat. Chem.* **2014**, *6*, 899.
(11) Ricks, A. B.; Brown, K. E.; Wenninger, M.; Karlen, S. D.; Berlin, Y. A.; Co, D. T.; Wasielewski, M. R. *J. Am. Chem. Soc.* **2012**, *134*, 4581.
(12) Gilbert, M.; Albinsson, B. *Chem. Soc. Rev.* **2015**, *44*, 845.
(13) Heckmann, A.; Lambert, C. *Angew. Chem., Int. Ed.* **2012**, *51*, 326.
(14) Sedó, J.; Ruiz, D.; Vidal-Gancedo, J.; Rovira, C.; Bonvoisin, J.; Launay, J. P.; Veciana, J. *Adv. Mater.* **1996**, *8*, 748.
(15) Elsner, O.; Ruiz-Molina, D.; Vidal-Gancedo, J.; Rovira, C.; Veciana, J. *Nano Lett.* **2001**, *1*, 117.
(16) Lloveras, V.; Vidal-Gancedo, J.; Figueira-Duarte, T. M.; Nierengarten, J.-F.; Novoa, J. J.; Mota, F.; Ventosa, N.; Rovira, C.; Veciana, J. *J. Am. Chem. Soc.* **2011**, *133*, 5818.
(17) Jestin, I.; Frère, P.; Blanchard, P.; Roncali, J. *Angew. Chem., Int. Ed.* **1998**, *37*, 942.
(18) Oswald, F.; Shafiqul Islam, D.-M.; El-Khouly, M. E.; Araki, Y.; Caballero, R.; de la Cruz, P.; Ito, O.; Langa, F. *Phys. Chem. Chem. Phys.* **2014**, *16*, 2443.
(19) Rodríguez-González, S.; Ruiz-Delgado, M. C.; Caballero, R.; de la Cruz, P.; Langa, F.; López-Navarrete, J. T.; Casado, J. *J. Am. Chem. Soc.* **2012**, *134*, 5675.
(20) Rovira, C.; Ruiz-Molina, D.; Elsner, O.; Vidal-Gancedo, J.; Bonvoisin, J.; Launay, J.-P.; Veciana, J. *Chem. - Eur. J.* **2001**, *7*, 240.
(21) Heinzer, J. *Mol. Phys.* **1971**, *22*, 167. *Quantum Chemistry Program Exchange*; 1972, no. 209. We thank Prof. A. Lund for a copy of this program.
(22) Rodríguez González, S.; Nieto-Ortega, B.; González Cano, R. C.; Lloveras, V.; Novoa, J. J.; Mota, F.; Vidal-Gancedo, J.; Rovira, C.; Veciana, J.; del Corro, E.; Taravillo, M.; Baonza, V. G.; López Navarrete, J. T.; Casado, J. *J. Chem. Phys.* **2014**, *140*, 164903.
(23) Ricks, A. B.; Brown, K. E.; Wenninger, M.; Karlen, S. D.; Berlin, Y. A.; Co, D. T.; Wasielewski, M. R. *J. Am. Chem. Soc.* **2012**, *134*, 4581.
(24) Berlin, Y. A.; Ratner, M. A. *Radiat. Phys. Chem.* **2005**, *74*, 124.
(25) Petrov, E. G.; Shevchenko, Y. V.; May, V. *Chem. Phys.* **2003**, *288*, 269.
(26) Weller, A. *Z. Phys. Chem.* **1982**, *133*, 93.
(27) Apperloo, J. J.; Raimundo, J.-M.; Frère, P.; Roncali, J.; Janssen, R. A. J. *Chem. - Eur. J.* **2000**, *6*, 1698.
(28) Ratera, I.; Veciana, J. *Chem. Soc. Rev.* **2012**, *41*, 303.
(29) Kubas, A.; Gajdos, F.; Heck, A.; Oberhofer, H.; Elstner, M.; Blumberger, J. *Phys. Chem. Chem. Phys.* **2015**, *17*, 14342.
(30) Renz, M.; Theilacker, K.; Lambert, C.; Kaupp, M. *J. Am. Chem. Soc.* **2009**, *131*, 16292.
(31) Perdew, J. P.; Burke, K.; Ernzerhof, M. *Phys. Rev. Lett.* **1996**, *77*, 3865.
(32) Frisch, M. J.; Trucks, G. W.; Schlegel, H. B.; Scuseria, G. E.; Robb, M. A.; Cheeseman, J. R.; Scalmani, G.; Barone, V.; Mennucci, B.; Petersson, G. A.; Nakatsuji, H.; Caricato, M.; Li, X.; Hratchian, H. P.; Izmaylov, A. F.; Bloino, J.; Zheng, G.; Sonnenberg, J. L.; Hada, M.; Ehara, M.; Toyota, K.; Fukuda, R.; Hasegawa, J.; Ishida, M.; Nakajima, T.; Honda, Y.; Kitao, O.; Nakai, H.; Vreven, T.; Montgomery, J. A., Jr.; Peralta, J. E.; Ogliaro, F.; Bearpark, M.; Heyd, J. J.; Brothers, E.; Kudin, K. N.; Staroverov, V. N.; Kobayashi, R.; Normand, J.; Raghavachari, K.;

DOI: 10.1021/jacs.6b08649
J. Am. Chem. Soc. 2017, 139, 686−692

Rendell, A.; Burant, J. C.; Iyengar, S. S.; Tomasi, J.; Cossi, M.; Rega, N.; Millam, J. M.; Klene, M.; Knox, J. E.; Cross, J. B.; Bakken, V.; Adamo, C.; Jaramillo, J.; Gomperts, R.; Stratmann, R. E.; Yazyev, O.; Austin, A. J.; Cammi, R.; Pomelli, C.; Ochterski, J. W.; Martin, R. L.; Morokuma, K.; Zakrzewski, V. G.; Voth, G. A.; Salvador, P.; Dannenberg, J. J.; Dapprich, S.; Daniels, A. D.; Farkas, O.; Foresman, J. B.; Ortiz, J. V.; Cioslowski, J.; Fox, D. J. *Gaussian 09*, revision A.08; Gaussian, Inc.: Wallingford, CT, 2009.

(33) Bussi, G.; Donadio, D.; Parrinello, M. *J. Chem. Phys.* **2007**, *126*, 014101.

(34) Blum, V.; Gehrke, R.; Hanke, F.; Havu, P.; Havu, V.; Ren, X.; Reuter, K.; Scheffler, M. *Comput. Phys. Commun.* **2009**, *180*, 2175.

(35) Alcón, I.; Bromley, S. T. *RSC Adv.* **2015**, *5*, 98593.

DOI: 10.1021/jacs.6b08649
J. Am. Chem. Soc. 2017, 139, 686−692

Publication #8

Existence of multi-radical and closed-shell semiconducting states in post-graphene organic Dirac materials.

Nat. Comm. 2017, *8*, 1957.

I. Alcón*, F. Viñes, I. de P.R. Moreira and S. T. Bromley*

nature COMMUNICATIONS

ARTICLE

DOI: 10.1038/s41467-017-01977-4 OPEN

Existence of multi-radical and closed-shell semiconducting states in post-graphene organic Dirac materials

Isaac Alcón [1], Francesc Viñes[1], Iberio de P.R. Moreira [1] & Stefan T. Bromley [1,2]

Post-graphene organic Dirac (PGOD) materials are ordered two-dimensional networks of triply bonded sp^2 carbon nodes spaced by π-conjugated linkers. PGOD materials are natural chemical extensions of graphene that promise to have an enhanced range of properties and applications. Experimentally realised molecules based on two PGOD nodes exhibit a bi-stable closed-shell/multi-radical character that can be understood through competing Lewis resonance forms. Here, following the same rationale, we predict that similar states should be accessible in PGOD materials, which we confirm using accurate density functional theory calculations. Although for graphene the semimetallic state is always dominant, for PGOD materials this state becomes marginally meta-stable relative to open-shell multi-radical and/or closed-shell states that are stabilised through symmetry breaking, in line with analogous molecular systems. These latter states are semiconducting, increasing the potential use of PGOD materials as highly tuneable platforms for future organic nano-electronics and spintronics.

[1] Departament de Ciència de Materials i Química Física & Institut de Química Teòrica i Computacional (IQTCUB), Universitat de Barcelona, Carrer Martí i Franquès 1, 08028 Barcelona, Spain. [2] Institució Catalana de Recerca i Estudis Avançats (ICREA), 08010 Barcelona, Spain. Correspondence and requests for materials should be addressed to I.Aón. (email: ialcon@ub.edu) or to S.T.B. (email: s.bromley@ub.edu)

The triply bonded sp^2 hybridised form of carbon has become crucially significant in both applied and fundamental solid state research[1] due to its intrinsic role as a building block of some of world's most widely studied materials (e.g. carbon nanotubes[2], fullerenes[3] and graphene[4]). Organic nanosystems based on sp^2 carbon networks are seen by many as an essential basis for many future technologies[1], arguably provoking a paradigm shift in materials science. Graphene, the simplest two-dimensional (2D) hexagonal network of sp^2 hybridised carbon, plays an especially prominent role in this respect[5]. Since its isolation[4], researchers have become fascinated with its many exceptional properties, which are progressively being more fully understood and exploited in many fields of science and technology. One particularly appealing characteristic of graphene is the existence of Dirac cones in its electronic band structure[5]. This feature, due to specific bands crossing at the Fermi level, E_F, gives rise to semimetallicity and ultra-high electron mobilities, and has promoted graphene as a potential candidate to replace silicon in the next generation of nanoelectronic devices[5]. However, the intrinsic connection of these features with the extended high symmetry of its electronic state limits its use in applications requiring nanostructuring (e.g., nano-electronics[6]).

The discovery of graphene has triggered a global search for other 2D materials with similar characteristics, but with higher electronic tunability and greater resilience to nanostructuring. In this direction, ab initio computational modelling has predicted that Dirac cones should be in the band structures of a number of non-carbon-based[7–9] and carbon-based[10, 11] 2D materials (the latter often referred to as post-graphene organic Dirac materials (PGOD)). An important class of PGOD materials are the so-called graphynes[12, 13] and graphdiynes[13], which present sp^2 carbon atoms linked via alkyne groups in a variety of ways[14]. Although some graphdiynes have been synthesised[15], those predicted to be Dirac materials are still awaiting experimental realisation. Recently, a series of 2D conjugated networks were predicted to present Dirac cones in their bandstructures[10]. These networks present a common basic skeleton: a hexagonal array of triply bonded sp^2 carbon atoms (or nodes of the hexagonal network) connected by π-conjugated linkers (see Fig. 1a). Replacing the trigonal sp^2 carbon nodes by other elements or aromatic groups opens up a finite band gap around E_F, highlighting the key role of these sp^2 carbon centres. In ref. [6]. one proposed material was formed from sp^2 carbon atoms connected with biphenyl linkers (graphdiphenyl–GDP). Herein, we further propose graphphenyl (GP), obtained when using phenyl ring as linker (see first two structures in Fig. 1b). Fitting this general scheme, α-graphyne and α-graphdiyne can be thought of as hexagonal networks of sp^2 carbon nodes connected by ethyn-1,2-diyl (-C≡C-) or buta-1,3-diyn-1,4-diyl (-C≡C-C≡C-) alkyne linkers, respectively. Finally, graphene is the densest hexagonal array of sp^2 carbon nodes directly linked by bonding based on π–π orbital overlap. This family of 2D materials is summarised in Fig. 1b.

Focusing on GDP (first structure in Fig. 1b), we note that its basic structure coincides with that of Tschitschibabin's hydrocarbon (see Fig. 1c)[16], one of the oldest bi-radical compounds ever synthesised. The triply bonded methyl radical carbon atoms in Tschitschibabin's hydrocarbon bear the two unpaired electrons of the bi-radical molecule. Due to the connectivity linking these two radical sites, the molecule possesses two possible Lewis resonance forms: 1) the open-shell anti-ferromagnetic (AFM) one with two unpaired localised electrons (Fig. 1c, left) and 2) the closed-shell one with paired π-conjugated electrons forming a quinoidal-like structure (Fig. 1c, right). Experimentally, the molecule presents a mixture of both extreme resonance forms in its electronic ground state, displaying a partial open-shell bi-radical character mixed with structural quinoidal characteristics[17]. Thus, seen as a 2D extended version of Tschitschibabin's bi-radical, and considering periodically extended Lewis resonance forms of the type shown in Fig. 1c, GDP may also be expected to display analogous electronic states (i.e. AFM and quinoidal).

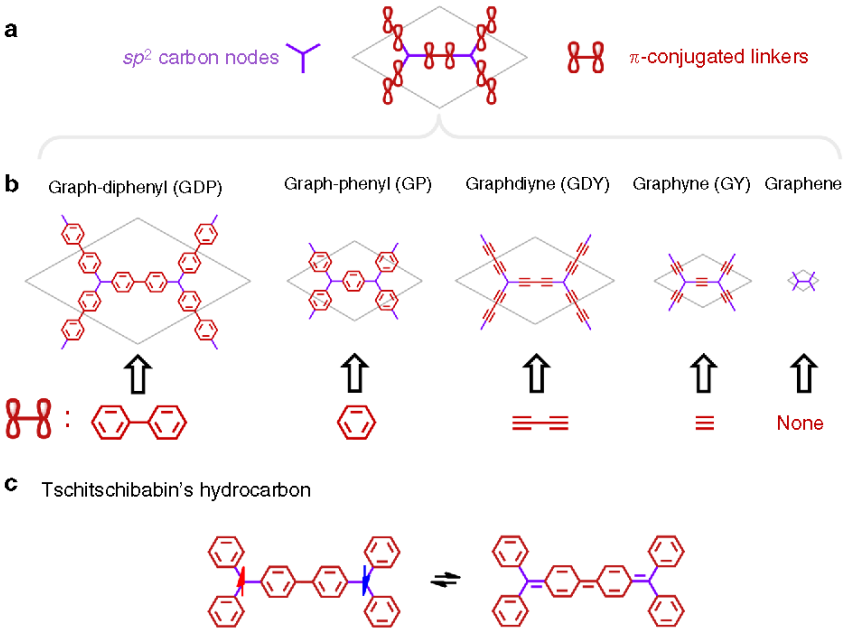

Fig. 1 PGOD chemical structures. **a** Basic covalent skeleton composed of triply bonded sp^2 carbon atoms (purple) and π-conjugated linkers (red). **b** Series of graphene and four PGOD materials with different π-conjugated linkers. **c** Schematic representation of the bi-radical (left) and quinoidal (right) Lewis resonance forms stabilized by spin polarisation and structural distortion, respectively, in the Tschitschibabin's hydrocarbon. Note: Hydrogen atoms in phenyl rings are omitted for clarity

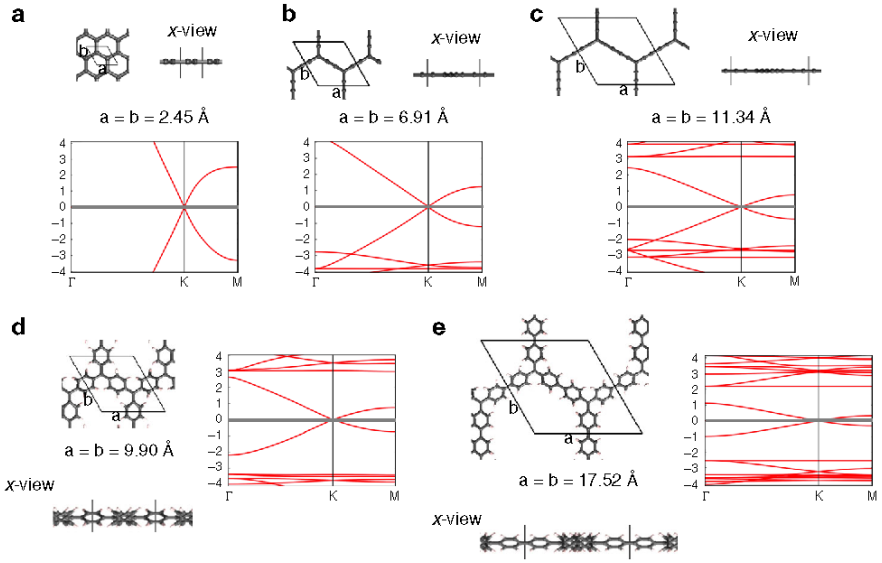

Fig. 2 Semimetallic state. Fully optimised structures of: **a** graphene, **b** GY, **c** GDY as obtained from spin-unrestricted calculations using the PBE0 hybrid functional. The results for GP (**d**) and GDP (**e**) were obtained from single point PBE0 calculations using fully symmetrised structures. The unit cell used in each case is highlighted from both *z* and *x* views, indicating the optimised cell parameters. The corresponding electronic band structures are also provided, setting E_F to zero energy in each case. Band structure energies are in eV. The broken symmetry structures for GP and GDP and their associated band structures are shown in Supplementary Fig. 4

Moreover, due to the common basic structure shared by all materials depicted in Fig. 1b (i.e. hexagonal lattice of sp^2 carbon nodes connected by π-conjugated linkers), it is chemically reasonable to expect that these extended resonance forms should lead to the accessibility of similar electronic states in all cases.

As far as we are aware, none of the family of materials in Fig. 1b have been reported to have intrinsic localised multi-radical and quinoidal electronic states. However, for graphene, experimental and theoretical studies have shown that such localised states can be generated by: (i) nano-patterning[18–20], (ii) cutting it into nanoribbons[18, 21, 22], (iii) covalent grafting of molecules[23] or atoms[24, 25], (iv) inclusion of defects[26], or (v) applying external strains[27, 28]. Analogously, computational modelling has predicted similar states in α-graphyne (GY) upon application of strain[29] or by forming α-GY nanoribbons[30, 31]. These studies lend support to our chemically motivated proposal that extended resonance forms may lead to open-shell multi-radical and/or closed-shell solutions being stabilised in all the materials depicted in Fig. 1b.

In this work, we present a systematic computational modelling study employing accurate density functional theory (DFT) based calculations to assess the existence and stability of low lying localised electronic states in all the 2D PGOD materials shown in Fig. 1b. Inspired by the limiting resonance forms of Tschitschibabin's hydrocarbon, our results demonstrate the existence of stable open-shell multi-radical and/or closed-shell quinoidal semiconducting electronic solutions in the considered PGOD materials. These results thus establish a clear link between the world of bi-radical/quinoidal molecular systems[32–35] and that of PGOD materials. In all cases, these solutions are found to be energetically accessible and to significantly affect the electronic properties of the host materials, highlighting the potential of such systems for future organic electronics/spintronics applications.

Results

Choice of appropriate DFT functional. Largely due to their computational efficiency and relative accuracy, DFT based approaches have become the dominant method of choice when simulating the electronic structures of periodic materials. For numerous cases (e.g. metallic systems, mechanical properties) the standard generalised gradient approximation (GGA) produces reliable results. However, hybrid functionals (i.e. functionals which incorporate a fraction of Hartree–Fock-like exchange (HFE)) are now being widely adopted by material's modellers[36], especially for capturing the most subtle electronic features displayed by many systems (e.g. magnetism[37], mixed valence compounds[38], semiconductors[39]). The molecular computational chemistry community has a long tradition of using hybrid functionals where, especially for electronic structure, they are known to generally outperform GGA functionals[40, 41]. A particular case is that of bi-radical/quinoidal compounds (such as Tschitschibabin's hydrocarbon), which have attracted much attention in recent years for its use in organic electronics[33] and organic magnetism[34, 42]. When these compounds are reduced or doped by other elements (e.g., N), charge transfer phenomena between the two sp^2 centres takes place[43, 44]. The computational assessment of the electronic ground state of such molecular systems is thus quite challenging[38]. DFT calculations employing GGA functionals over-delocalise valence electrons, and cannot stabilise the localised states found in experimental observations. Calculations using hybrid functionals, on the other hand, are found to be able to capture the quite complex and sensitive electronic structure of such π-conjugated mixed valence compounds[38, 45].

Most of the periodic modelling studies assessing the electronic structure of Dirac materials are performed using pure GGA[9, 12, 46], or local density approximation (LDA)[10, 47] functionals, and seldom utilise hybrid functionals[8, 27]. A reason for this might be that the high tendency of GGA to delocalise electrons ensures the success in finding the known, and highly studied, semimetallic solutions. However, knowing how critical the proportion of HFE is for obtaining the correct localised solutions in π-conjugated molecular systems[38, 45], it is reasonable to think that possible localised solutions in Dirac cone materials might have remained

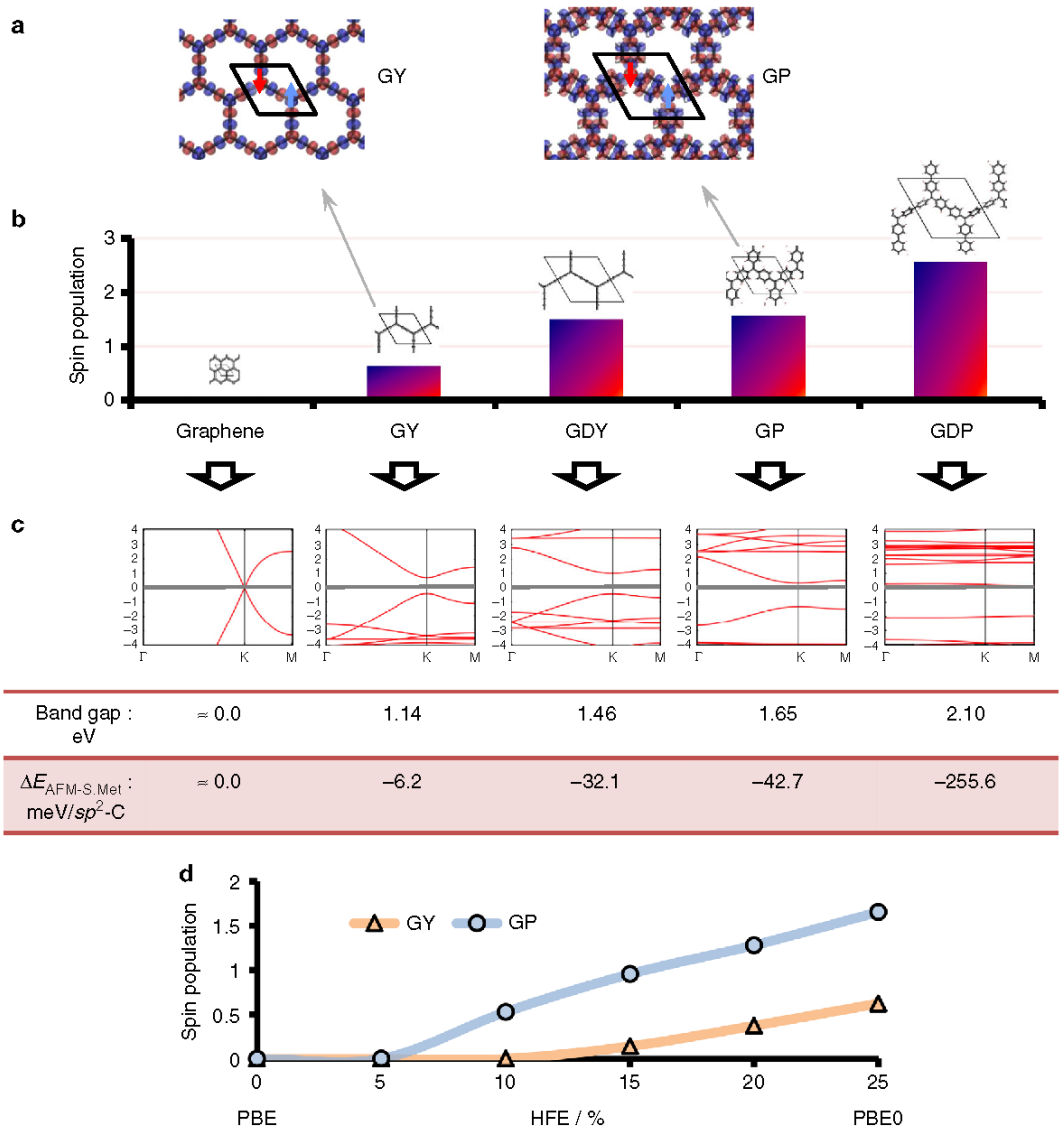

	Graphene	GY	GDY	GP	GDP
Band gap : eV	≈ 0.0	1.14	1.46	1.65	2.10
$\Delta E_{AFM\text{-}S.Met}$: meV/sp^2-C	≈ 0.0	−6.2	−32.1	−42.7	−255.6

Fig. 3 Multi-radical AFM state. The results from spin-unrestricted open-shell PBE0 optimizations initialised using an AFM spin configuration. **a** Spin density iso-surface on GY and GP structures (alpha = blue; beta = red), where the unit cell is highlighted. **b** Total absolute spin population (i.e., addition of all atom-partitioned spin-up and spin-down electronic populations) within the unit cell throughout the materials series. **c** Electronic band structures for each case. Below each band structure, we indicate the value of band gaps (eV) opening at the **K** point and the relative energy of the AFM solution with respect to the corresponding semimetallic solution per sp^2 triply bonded centre or node of the hexagonal net (each unit cell presents two nodes of the hexagonal net), $\Delta E_{AFM\text{-}S.Met}$ in meV. **d** Absolute spin population in number of electrons versus percentage of HFE used in the DFT calculations for GY (orange) and GP (blue)

elusive due to this bias. In this work, we find that PBE0[48] is a functional providing a good balance between localisation and delocalisation (see also Methodology section). Therefore, the main discussion is based on PBE0 results. For comparison with previous works, results obtained by the PBE GGA functional[49] are included in Supplementary Figs. 1–3.

Semimetallic state. In Fig. 2, we show the optimised unit cells of each considered material together with the corresponding band structures obtained from spin-unrestricted calculations. In all cases, we find a semimetallic state. Graphene, GY and GDY (Fig. 2a–c, respectively) are one atom thick planar materials and only differ by the distance between triply bonded sp^2 carbon atoms siting at the nodes of the hexagonal network, due to the inclusion of (-C≡C-)$_n$ linkers (where n = 0–2), between them. In these cases Dirac cones appear at the high-symmetry reciprocal space **K** point, as previously found[12, 14, 29]. Although the nodal sp^2 centres in GP and GDP lay in a plane, these networks cannot be regarded as one-atom planar materials, due to the fact their phenyl rings are partially twisted by ~35° due to inter-ring steric hindrance (see Fig. 2d and 2e, x views). These materials also present a zero band gap feature at **K**. This feature can be understood as resulting from the high symmetry of the hexagonal lattice, which is preserved in all cases.

Overall, it is possible to see a clear reduction in the energy scale of the band structures through the series from graphene to GDP, accompanied with a corresponding flattening of the bands. As reported in Supplementary Fig. 3, this gives rise to a lowering of

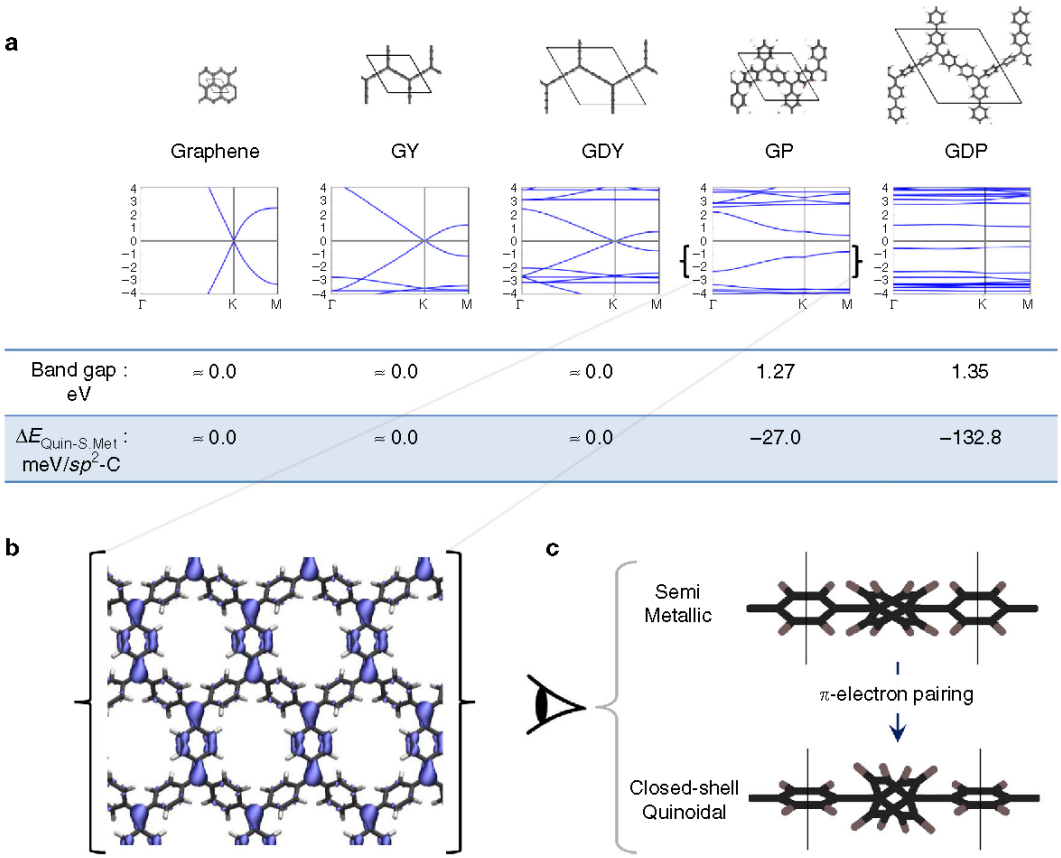

Fig. 4 Closed-shell quinoidal state. Results from restricted closed-shell PBE0 optimizations. **a** electronic band structures for each material. Below each band structure, we indicate the associated band gaps (eV) and the relative energies of each solution with respect to the semimetallic ones per sp^2 carbon centre ($\Delta E_{\text{Quin-S.Met}}$) in meV. **b** Iso-surface of the electron density corresponding to the highest occupied crystal orbital at the Γ point in GP. **c** *x*-view of the GP structure in the semimetallic and closed-shell quinoidal solutions, where the planarization of certain phenyl rings upon electron pairing can be observed

the Fermi velocities near the Dirac point going from $5.42 \cdot 10^6$ m/s for graphene to $3.04 \cdot 10^6$ m/s for GDP. These values are in line with those of previous studies[10, 50] and indicate that the increasingly separated π-conjugated sp^2 carbon centres when going from graphene to GDP has only a modest effect on the ballistic transport.

AFM state. After confirming the existence of a semimetallic state for each PGOD material, we further investigated possible localised solutions following the Lewis resonance forms depicted in Fig. 1c with an associated reduction of the hexagonal symmetry of each system. In order to examine possible multi-radical AFM states, all materials were optimised employing a spin-unrestricted calculation setup initialised with opposite spin moments on sp^2 triply bonded carbon atoms (purple positions in Fig. 1). After optimising the structures, all materials, except graphene, show considerable spin polarisation over the entire network with an anti-ferromagnetic spin alignment over the sp^2 triply bonded carbon centres. This spin-polarised solution exhibits a reduced trigonal symmetry. We note that plane wave based DFT calculations also confirm this result (see Supplementary Fig. 5). In Fig. 3a, we show the atom-projected spin density iso-surfaces for GY and GP (see up/down arrows for clarification) as example cases. This clearly demonstrates the partial open-shell multi-radical nature of this series of materials, where every sp^2 node bears an AFM coupled localised unpaired electron. In Fig. 3b, we plot the total absolute spin population per material (i.e. the sum of all atom-partitioned spin-up and spin-down populations in absolute value within each material's unit cell). With the notable exception of graphene, all other materials show a non-negligible spin population, which increases down through the series, towards the maximum value for GDP. The increasing spin population down through the series also suggests that, upon decreasing the π-overlap that connects neighbouring triply bonded carbon centres, there is a correspondingly higher tendency to stabilise this localised multi-radical state. This chemical rationalisation would also help explain why, in the highly planar and closely linked sp^2 network of graphene, such a solution cannot be stabilised. In Fig. 3d it can be seen how the spin density already emerges with low HFE percentages, demonstrating that the presented results are not a spurious singular effect of using PBE0 (25% HFE). Moreover, when no HFE is used, such multi-radical solutions are not found, even when initialising the calculations with an AFM alignment of spin moments. This may explain why such solutions have not been reported in previous works, mainly using pure LDA or GGA functionals.

In Fig. 3c, we show the band structures calculated for each material in the AFM solution using the PBE0 functional. In graphene, where the magnetisation is not exhibited, the Dirac cone is essentially unperturbed. However, for the remainder of the studied materials, with non-negligible spin polarisation, a sizeable band gap opens at the Dirac point, ranging from 1 eV (GY) to 2 eV (GDP). In line with these results, the correlation between radical centres with an AFM alignment of localised spins and the appearance of sizeable band gaps has been previously

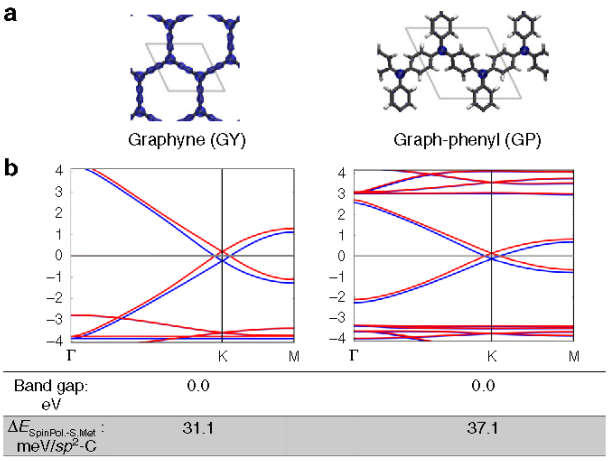

Fig. 5 Spin-polarised state. Results from spin-unrestricted open-shell static single point PBE0 calculations forcing a net spin polarisation of 0.15 unpaired electrons using the corresponding previously optimised structures in the semimetallic state. **a** Spin density iso-surface on GY (left) and GP (right) structures (alpha = blue; beta = red), where the unit cell is highlighted. **b** Corresponding electronic band structures for GY (left) and GP (right). Below the plots band gap values (eV) and the energy difference between the spin-polarised state and the corresponding purely semimetallic state ($\Delta E_{SpinPol.-S.Met}$) in meV is given for each material

reported for nanoribbons of graphene[21, 22, 51] and GY[30, 31], as well as for isotropically strained graphene[27]. In all cases the gap opening can be rationalised by the breaking of the hexagonal symmetry of the system. The relative energy per atom with respect to the corresponding semimetallic solutions (i.e., results of Fig. 2) show that such localised AFM multi-radical states (when obtained) are lower in energy as compared to the corresponding semimetallic state for all materials (see Fig. 3c and Supplementary Fig. 6). However, the energy differences in all cases are very small and, hence, both AFM multi-radical and semimetallic states may co-exist under normal conditions.

Closed-shell quinoidal state. To find the electronic state corresponding to the closed-shell quinoidal resonant form, following the analogy with Tschitschibabin's hydrocarbon, the structure of each material was optimised using a restricted closed-shell calculation to enforce electron pairing. As it can be seen in Fig. 4a, for graphene, GY and GDY, we were not able to stabilise such a closed-shell quinoidal state and the semimetallic solution prevailed. This indicates that these materials are not prone to have their sp^2 carbon π-electrons in localised pairs. We note that other closed-shell solutions based on localised pairing (e.g. Kekulé-like) may be possible for larger cells than used herein.[27] For graphene in particular the difficulty in obtaining gapped states (AFM and/or closed-shell) is highly problematic for its use in electronic applications where band gap control is essential. Consequently, highly invasive methods are needed to open such a band gap in this 2D material, ranging from nanopatterning[18, 19, 52, 53], covalently grafting of atoms and molecules[23, 24, 54] or the application of external strains[27, 28, 55]. Such approaches, however, tend to significantly affect other fundamental and technological interesting properties of graphene (e.g. ballistic charge transport). Conversely, GP and GDP display a sizeable band gap around the Fermi level (see Fig. 4a), which may be indicative of a transition from a delocalised to a localised electronic solution. Band gap values are around 1.3 eV for both GP and GDP, which is a typical value for semiconductor materials.

To better understand the appearance of band gaps in closed-shell GP and GDP, we can examine the iso-surface of the electronic density associated with the highest occupied crystal orbital (see Fig. 4b). Here one observes a quinoidal-like electron distribution, analogous to the closed-shell resonant form in Tschitschibabin's hydrocarbon (Fig. 1c). This demonstrates that the π-conjugated electrons of sp^2 centres, previously forming the Dirac cone in the semimetallic state (Fig. 2), or being antiferromagnetically coupled in the multi-radical solution (Fig. 3), now are being locally paired within the periodic 2D structure (Fig. 4b). As for the AFM state, the emergence of these gaps can be understood by the lowering of the hexagonal symmetry; in this case due to the trigonally symmetric charge-ordering resulting from bond formation. GDP exhibits a similar electron density for the highest occupied crystal orbital, as shown in the Supplementary Fig. 7. Examining the structure of GP from the in-plane x-axis view (as represented in Fig. 4c) one can see that, upon moving from the semimetallic solution to the closed-shell quinoidal solution, phenyl rings accomodating the electron pairing become significantly more planar. This twisting mechanism can be understood by the fact that double bonds are being formed between the two in-plane triply bonded carbon nodes, which strongly induce planarity in the bridging phenyl rings (see blue density in 4b). Hence, in GP and GDP, twisting of aryl rings represents an additional structural degree of freedom through which π-electron pairing can be reinforced. In other words GP and GDP have internal structural degrees of freedom which allow for relatively facile symmetry breaking and thus, the emergence of a quinoidal state.

In the perfectly planar GY and GDY, such a mechanism does not exist and, hence, the fully hexagonal symmetric delocalised solution prevails over the quinoidal state. This structure-electronic relationship between aryl ring twist angles and localisation/delocalisation of electrons, previously found for the analogous single-molecules[56], could represent a symmetry breaking tool with which to mechanically induce electron pairing by external strains[57] or, also, to spatially detect paired π-electrons by identifying particularly planarized aryl rings. The quinoidal solution is found to lay 27 meV and 133 meV below the semimetallic solution for GP and GDP, respectively (see Fig. 4a and Supplementary Fig. 6). Therefore, both localised solutions (i.e., AFM multi-radical and closed-shell quinoidal), when viable, are slightly lower in energy than the corresponding delocalised semimetallic state. Although the small energy differences between the three electronic states means that it is probable they would co-exist at finite temperatures, suitable low temperature experiments could potentially selectively stabilise a particular state. Additionally, due to the fact that AFM and closed-shell states have lower symmetries than the corresponding semimetallic state, suitable symmetry breaking influences (e.g. strain, magnetic fields, or lattice vibrations) could enhance the likelyhood of isolating them. Indeed, the fact that semimetallic states require high symmetry could make them difficult to stabilise.

Spin-polarised state. Finally, in bi-radical/quinoidal compounds it is known that a ferromagnetic (FM) alignment of unpaired electrons (a triplet state) can be induced by thermal excitations[32, 58]. To assess the feasibility of inducing such a state in our studied PGOD materials, we performed static single point calculations using the semimetallic structures of GY and GP while enforcing an increasing net spin polarisation in the alpha channel. The relative energies of these spin-polarised solutions with respect to the semimetallic solution are reported in Supplementary Fig. 8 for both materials. Figure 5 shows the results when forcing the system to have a net spin polarisation equal to 0.15 unpaired

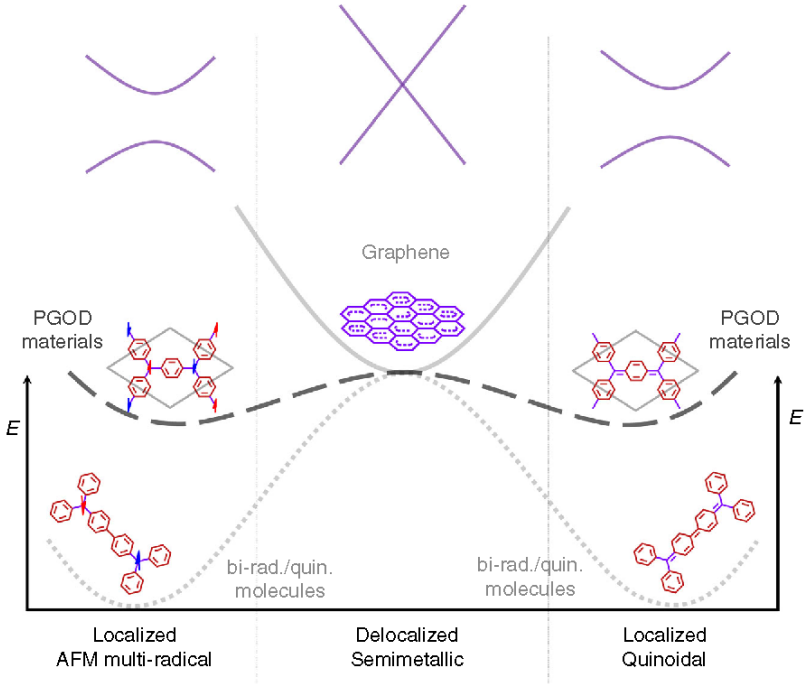

Fig. 6 PGODs as a bridge between graphene and molecular bi-radicals. PGOD materials (dashed black line) are systems with an electronic character that is intermediate between bi-radical/quinoidal molecules (dotted grey line) and graphene (continuous grey line). Schematic simplified electronic band structures of a generic PGOD material are represented by the solid purple lines above the corresponding electronic states. As such PGODs can exhibit both localised and delocalised solutions at very close energies, and thus possess an electronic tunability not easily obtainable from systems with dominant solutions (e.g., graphene and bi-radical/quinoidal molecules). Note: The relative positions of the different curves have been chosen for ease of illustration and should not be taken to indicate real energy differences between the three different systems

electrons (see Methods section). As it can be seen in Fig. 5a, upon doing so, π-electrons become alpha-spin polarised throughout the network. Examining the GP case, we can see that the spin polarisation (blue density) arises from sp^2 triply bonded carbon atoms, in full agreement with the open-shell character of such centres (see above).

As shown in Fig. 5b, these partially spin polarised solutions are similar in character to the semimetallic solutions, as confirmed by the conservation of a spin polarised Dirac cone in the corresponding band structures. Enforcing a spin polarisation excess in the alpha channel induces an occupation of the conduction band in this spin channel (doping with negative charges), emptying the valence band in the opposite one (doping with positive charges) with exactly the same amount. This spin polarisation can also be seen as a breaking of **K**-vector reversal symmetry (time reversal symmetry) resulting in a lifting of the degeneracy of spin-up and spin-down bands. One effect of this spin polarisation is to induce a small (~0.3 eV) energy gap at the previously spin degenerate crossing at **K** resulting in two crossings between bands of the same spin above and below the Fermi level. Additionally, two further crossings between bands of different spin appear at the Fermi level at $\mathbf{K}+\mathbf{k}_1$ and $\mathbf{K}-\mathbf{k}_2$. These two crossings close to **K** are reminiscent of Weyl points, however, as they are constituted by bands of different spin, they indicate the possibility of spin helical Dirac states as found on the edges of graphene nanoribbons (1D)[59] and within surfaces of toplogical insulators (2D)[60]. Applying spin-orbit coupling (SOC) in our calculations reveals that these crossings are maintained and not gapped out (see Supplementary Fig. 9). However, at **K**, the same-spin band crossings above and below the Fermi level are weakly split (0.025 eV) by SOC. The relative energies of these spin-polarised solutions with respect to the purely semimetallic solutions (see Fig. 5b) demonstrate such a doping process does not cost much energy (31 meV and 17 meV for GY and GP, respectively), suggesting it may be induced by application of moderate magnetic fields or, simply, by thermal excitations, as can occur in molecules exhibiting analogous states[32, 58].

Discussion

Our work represents a bridge between two important fields in materials science (graphene and PGOD materials) and chemistry (conjugated bi-radical/quinoidal molecules) which, until now, have not had significant overlap. Bi-radical/quinoidal molecules are finite systems and, consequently, their electronic character tends to vary between two localised electronic solutions: namely the bi-radical AFM and the closed-shell quinoidal, as represented by the bottom dotted line in Fig. 6. Because of this bi-stable nature, it is possible to favour one localised solution or the other by chemical design[33, 35], which has raised the interest in such systems for molecular magnetism[34] and molecular electronics[32]. Graphene presents the opposite extreme to bi-radical/quinoidal molecules in this respect. As depicted with the top grey line in Fig. 6, graphene is the perfect semimetal with a single-well energy minimum corresponding to a fully delocalised electronic configuration. This state is a direct consequence of its highly symmetric and planar arrangement of triply bonded sp^2 centres. The robustness of this feature has hindered the applicability of graphene for nano-electronics, where the existence of a band gap is a prerequisite[6, 61].

Electronically, the behaviour of PGOD materials lies between that of bi-radical/quinoidal molecules and graphene (see dashed black line in Fig. 6). As we have demonstrated by DFT based electronic structure computations, PGOD materials are a

fascinating system where the fully delocalised semimetallic solution can co-exist with localised multi-radical and closed-shell quinoidal solutions. These solutions can be understood as the result of different symmetry breakings (e.g. via charge-ordering, structural distortion and spin polarisation) from the perfect hexagonal symmetry. As expected from their molecular analogues, in the studied PGOD materials these broken symmetry states are found to be lower in energy than the corresponding symmetric semimetallic states. Moreover, these localised states give rise to band gaps between 1-2 eV, thus representing a clear transition from semimetallic to semiconducting behaviour. Because of the near energetic degeneracy of the semimetallic (and spin-polarised semimetallic) and semiconductor (multi-radical AFM and closed-shell quinoidal), it should be possible to induce particular solutions by external or internal means which deliberately induce symmetry breaking (e.g. strain, application of magnetic or electric fields, chemical design, etc). Hence, PGOD materials present a unique combination of electronic tunability and mechanical robustness, which, we believe, makes them particularly good candidates to become a prominent platform for future nano-electronics.

Methods

DFT calculations. Optimizations of the atomic and electronic structures were performed using different initial electronic guesses to induce different electronic solutions (i.e., semimetallic, closed-shell quinoidal and open-shell anti-ferromagnetic). This set of optimizations was separately performed using the GGA functional: PBE[49] and its hybrid functional extension: PBE0[37, 48]. After each optimisation, single point calculations were performed with the corresponding initial guesses to obtain band structures, Hirshfeld-partitioned atomic spin populations[52], and atom-projected electronic densities. GP and GDP results were obtained from fully symmetrised structures. Each optimisation employed increasingly sized k-meshes until convergence of properties was obtained (i.e., total energies and spin densities); here using $6\times6\times1$ and $18\times18\times1$ meshes for PBE and PBE0, respectively (see Supplementary Fig. 6). Denser k-meshes were required for particularly small unit cells (such as that of graphene) to obtain reasonable band structures. All DFT based calculations were performed employing the all-electron FHI-AIMS code[63], using a light/Tier1 numerical atom-centred orbital (NAO) basis set[64]. This basis set approximately provides results of a similar or higher quality to those obtained with valence triple-zeta plus polarisation Gaussian type orbitals[65]. For the periodic band structure calculations the energy zero (Fermi level) is set by the $G=0$ component of the long-range electrostatic potential. In addition, the entire set of PBE calculations was also performed using the Vienna ab initio simulation package (VASP)[66], using a plane-wave basis set with a 415 eV kinetic energy cut-off. Due to the very-high computational cost required for hybrid calculations using VASP, only single-point PBE0 calculations using the PBE0-optimised structures from FHI-AIMS were used in our comparisons. We find that in all cases the corresponding PBE and PBE0 results from VASP and FHI-AIMS are fully consistent, thus negating any significant influence of the DFT implementation (e.g. atom-centred numerical versus plane wave basis sets) in our results.

Use of hybrid functionals. For capturing the electronic states of mixed-valence organic molecules, some works recommend using hybrid functionals containing 35% HFE, or even higher[45]. For such systems, even widely used hybrid functionals such as PBE0[48] (25% HFE) or B3LYP[67] (20% HFE) still tend to over-delocalise electrons due to the inherent self-interaction error in GGA[68]. However, use of functionals having a relatively large percentage of HFE, although useful for stabilising localised states, can prevent one finding fully delocalised metallic solutions – essential for extended materials such as graphene[69]. As a consequence, we find that the PBE0 functional provides a good balance between electronic localisation and delocalisation for the 2D materials we consider. We note that the optimised structures obtained at using the PBE functional (see Supplementary Fig. 1) are almost indistinguishable to the ones obtained using PBE0 presented in Fig. 2.

Data availability. Atomic coordinates and lattice parameters for optimised structures of all considered materials in the semimetallic solution (calculated using the PBE0 functional and a light/Tier1 NAO basis set as implemented in the FHI-AIMS code) are made openly available in Supplementary Data 1.

Received: 7 July 2017 Accepted: 30 October 2017
Published online: 05 December 2017

References

1. Hirsch, A. The era of carbon allotropes. *Nat. Mater.* **9**, 868–871 (2010).
2. Iijima, S. Helical microtubules of graphitic carbon. *Nature* **354**, 56–58 (1991).
3. Iijima, S. Direct observation of the tetrahedral bonding in graphitized carbon black by high resolution electron microscopy. *J. Cryst. Growth* **50**, 675–683 (1980).
4. Novoselov, K. S. et al. Electric field effect in atomically thin carbon films. *Science* **306**, 666–669 (2004).
5. Geim, A. K. & Novoselov, K. S. The rise of graphene. *Nat. Mater.* **6**, 183–191 (2007).
6. Schwierz, F. Graphene transistors. *Nat. Nanotechnol.* **5**, 487–496 (2010).
7. Ding, Y. & Wang, Y. Unusual structural and electronic properties of porous silicene and germanene: insights from first-principles calculations. *Nanoscale Res. Lett.* **10**, 13 (2015).
8. Ni, Z. et al. Tunable bandgap in silicene and germanene. *Nano Lett.* **12**, 113–118 (2012).
9. Wang, J., Deng, S., Liu, Z. & Liu, Z. The rare two-dimensional materials with Dirac cones. *Natl. Sci. Rev.* **2**, 22–39 (2015).
10. Adjizian, J.-J. et al. Dirac Cones in two-dimensional conjugated polymer networks. *Nat. Commun.* **5**, 5842 (2014).
11. Malko, D., Neiss, C., Viñes, P. & Görling, A. Competition for graphene: graphynes with direction-dependent dirac cones. *Phys. Rev. Lett.* **108**, 86804 (2012).
12. Chen, J., Xi, J., Wang, D. & Shuai, Z. Carrier mobility in graphyne should be even larger than that in graphene: A theoretical prediction. *J. Phys. Chem. Lett.* **4**, 1443–1448 (2013).
13. Li, Y., Xu, L., Liu, H. & Li, Y. Graphdiyne and graphyne: from theoretical predictions to practical construction. *Chem. Soc. Rev.* **43**, 2572–2586 (2014).
14. Xi, J., Wang, D. & Shuai, Z. Electronic properties and charge carrier mobilities of graphynes and graphdiynes from first principles. *Wiley Interdiscip. Rev. Comput. Mol. Sci.* **5**, 215–227 (2015).
15. Li, G. et al. Architecture of graphdiyne nanoscale films. *Chem. Commun.* **46**, 3256–3258 (2010).
16. Tschitschibabin, A. E. Über einige phenylierte derivate des p, p-ditolyls. *Berichte der Dtsch. Chem. Gesellschaft* **40**, 1810–1819 (1907).
17. Montgomery, L. K., Huffman, J. C., Jurczak, E. A. & Grendze, M. P. The molecular structures of Thiele's and Chichibabin's hydrocarbons. *J. Am. Chem. Soc.* **108**, 6004–6011 (1986).
18. Wakabayashi, K., Fujita, M., Ajiki, H. & Sigrist, M. Electronic and magnetic properties of nanographite ribbons. *Phys. Rev. B* **59**, 8271–8282 (1999).
19. Bullard, Z., Girão, E. C., Owens, J. R., Shelton, W. A. & Meunier, V. Improved All-Carbon spintronic device design. *Sci. Rep.* **5**, 7634 (2015).
20. Morita, Y., Suzuki, S., Sato, K. & Takui, T. Synthetic organic spin chemistry for structurally well-defined open-shell graphene fragments. *Nat. Chem.* **3**, 197–204 (2011).
21. Magda, G. Z. et al. Room-temperature magnetic order on zigzag edges of narrow graphene nanoribbons. *Nature* **514**, 608–611 (2014).
22. Yu, Z. L., Wang, D., Zhu, Z. & Zhang, Z. H. Magneto-electronic properties of graphene nanoribbons with various edge structures passivated by phosphorus and hydrogen atoms. *Phys. Chem. Chem. Phys.* **17**, 24020–24028 (2015).
23. Lin, H., Fratesi, G. & Brivio, G. P. Graphene magnetism induced by covalent adsorption of aromatic radicals. *Phys. Chem. Chem. Phys.* **17**, 2210–2215 (2015).
24. Huang, H., Li, Z. & Wang, W. Electronic and magnetic properties of oxygen patterned graphene superlattice. *J. Appl. Phys.* **112**, 114332 (2012).
25. Manadé, M., Viñes, P. & Illas, P. Transition metal adatoms on graphene: A systematic density functional study. *Carbon* **95**, 525–534 (2015).
26. Dutta, S. & Wakabayashi, K. Magnetization due to localized states on graphene grain boundary. *Sci. Rep.* **5**, 11744 (2015).
27. Lee, S.-H., Kim, S. & Kim, K. Semimetal-antiferromagnetic insulator transition in graphene induced by biaxial strain. *Phys. Rev. B* **86**, 155436 (2012).
28. Zhu, S., Stroscio, J. A. & Li, T. Programmable extreme pseudomagnetic fields in graphene by a uniaxial stretch. *Phys. Rev. Lett.* **115**, 245501 (2015).
29. Wang, G., Si, M., Kumar, A. & Pandey, R. Strain engineering of Dirac cones in graphyne. *Appl. Phys. Lett.* **104**, 213107 (2014).
30. Yue, Q. et al. Magnetic and electronic properties of α-graphyne nanoribbons. *J. Chem. Phys.* **136**, 244702 (2012).
31. Ni, Y., Wang, X., Tao, W., Zhu, S.-C. & Yao, K.-L. The spin-dependent transport properties of zigzag α-graphyne nanoribbons and new device design. *Sci. Rep.* **6**, 25914 (2016).
32. Mayorga Burrezo, P., Zafra, J. L., López Navarrete, J. T. & Casado, J. Quinoidal/Aromatic Transformation in π-conjugated oligomers: Vibrational Raman studies on the limit of rupture for π-bonds. *Angew. Chem. Int. Ed.* **56**, 2250–2259 (2017).
33. Zeng, Z. et al. Pro-aromatic and anti-aromatic π-conjugated molecules: an irresistible wish to be diradicals. *Chem. Soc. Rev.* **44**, 6578–6596 (2015).

34. Trinquier, G. & Malrieu, J.-P. Kekulé versus Lewis: when aromaticity prevents electron pairing and imposes polyradical character. *Chem. - A Eur. J.* **21**, 814–828 (2015).
35. Zeng, Z. et al. Stable Tetrabenzo-Chichibabin's hydrocarbons: tunable ground state and unusual transition between their closed-shell and open-shell resonance forms. *J. Am. Chem. Soc.* **134**, 14513–14525 (2012).
36. Marsman, M., Paier, J., Stroppa, A. & Kresse, G. Hybrid functionals applied to extended systems. *J. Phys. Condens. Matter* **20**, 64201 (2008).
37. Improta, R. & Barone, V. Interplay of electronic, environmental, and vibrational effects in determining the hyperfine coupling constants of organic free radicals. *Chem. Rev.* **104**, 1231–1254 (2004).
38. Kaupp, M. et al. Computational and spectroscopic studies of organic mixed-valence compounds: where is the charge? *Phys. Chem. Chem. Phys.* **13**, 16973–16986 (2011).
39. Matsushita, Y., Nakamura, K. & Oshiyama, A. Comparative study of hybrid functionals applied to structural and electronic properties of semiconductors and insulators. *Phys. Rev. B* **84**, 75205 (2011).
40. Sai, N., Barbara, P. F. & Leung, K. Hole localization in molecular crystals from hybrid density functional theory. *Phys. Rev. Lett.* **106**, 226403 (2011).
41. Janesko, B. G. Comparing modern density functionals for conjugated polymer band structures: screened hybrid, Minnesota, and Rung 3.5 approximations. *J. Chem. Phys.* **134**, 184105 (2011).
42. Shishlov, N. M. From the Gomberg radical to organic magnets. *Russ. Chem. Rev.* **75**, 863–884 (2006).
43. Franco, C. et al. Operative mechanism of Hole-Assisted Negative charge motion in ground states of Radical-Anion molecular wires. *J. Am. Chem. Soc.* **139**, 686–692 (2017).
44. Heckmann, A. et al. Highly fluorescent open-shell NIR dyes: The time-dependence of back electron transfer in Triarylamine-Perchlorotriphenylmethyl radicals. *J. Phys. Chem. C* **113**, 20958–20966 (2009).
45. Renz, M., Theilacker, K., Lambert, C. & Kaupp, M. A reliable quantum-chemical protocol for the characterization of organic mixed-valence compounds. *J. Am. Chem. Soc.* **131**, 16292–16302 (2009).
46. Cao, X. et al. Band gap opening of graphene by forming heterojunctions with the 2D carbonitrides nitrogenated holey graphene, g-C3N4, and g-CN: Electric field effect. *J. Phys. Chem. C* **120**, 11299–11305 (2016).
47. Sławinska, J., Dabrowski, P. & Zasada, I. Doping of graphene by a Au(111) substrate: Calculation strategy within the local density approximation and a semiempirical van der Waals approach. *Phys. Rev. B* **83**, 245429 (2011).
48. Adamo, C. & Barone, V. Toward reliable density functional methods without adjustable parameters: The PBE0 model. *J. Chem. Phys.* **110**, 6158 (1999).
49. Perdew, J. P., Burke, K. & Ernzerhof, M. Generalized gradient approximation made simple. *Phys. Rev. Lett.* **77**, 3865–3868 (1996).
50. Puigdollers, A. R., Alonso, G. & Gamallo, P. First-principles study of structural, elastic and electronic properties of α-, β- and γ-graphyne. *Carbon* **96**, 879–887 (2016).
51. Son, Y.-W., Cohen, M. L. & Louie, S. G. Half-metallic graphene nanoribbons. *Nature* **444**, 347–349 (2006).
52. Grujić, M., Tadić, M. & Peeters, F. M. Antiferromagnetism in hexagonal graphene structures: Rings versus dots. *Phys. Rev. B* **87**, 85434 (2013).
53. Son, Y.-W., Cohen, M. L. & Louie, S. G. Energy gaps in graphene nanoribbons. *Phys. Rev. Lett.* **97**, 216803 (2006).
54. Hong, J. et al. Room-temperature magnetic ordering in functionalized graphene. *Sci. Rep.* **2**, 624 (2012).
55. Tang, H.-K. et al. Interaction-driven metal-insulator transition in strained graphene. *Phys. Rev. Lett.* **115**, 186602 (2015).
56. Alcón, I. & Bromley, S. T. Structural Control over Spin Localization in Triarylmethyls. *RSC Adv.* **5**, 98593–98599 (2015).
57. Alcón, I., Reta, D., Moreira, I., de, P. R. & Bromley, S. T. Design of multi-functional 2D open-shell organic networks with mechanically controllable properties. *Chem. Sci.* **8**, 1027–1039 (2017).
58. Rudebusch, G. E. et al. Diindeno-fusion of an anthracene as a design strategy for stable organic biradicals. *Nat. Chem.* **8**, 753–759 (2016).
59. Baringhaus, J. et al. Exceptional ballistic transport in epitaxial graphene nanoribbons. *Nature* **506**, 349–354 (2014).
60. Hsieh, D. et al. A tunable topological insulator in the spin helical Dirac transport regime. *Nature* **460**, 1101–1105 (2009).
61. Dash, G. N., Pattanaik, S. R. & Behera, S. Graphene for electron devices: The panorama of a decade. *IEEE J. Electron Devices Soc.* **2**, 77–104 (2014).
62. Hirshfeld, F. L. Bonded-atom fragments for describing molecular charge densities. *Theor. Chem. Acc.* **44**, 129–138 (1977).
63. Blum, V. et al. Ab initio molecular simulations with numeric atom-centered orbitals. *Comp. Phys. Comm.* **180**, 2175–2196 (2009).
64. Zhang, I. Y., Ren, X., Rinke, P., Blum, V. & Scheffler, M. Numeric atom-centered-orbital basis sets with valence-correlation consistency from H to Ar. *New J. Phys.* **15**, 123033 (2013).
65. Lamiel-Garcia, O., Ko, K. C., Lee, J. Y., Bromley, S. T. & Illas, F. When Anatase nanoparticles become bulklike: Properties of realistic TiO_2 nanoparticles in the 1–6 nm size range from all electron relativistic density functional theory based calculations. *J. Chem. Theory Comput.* **13**, 1785–1793 (2017).
66. Kresse, G. & Furthmüller, J. Efficiency of ab-initio total energy calculations for metals and semiconductors using a plane-wave basis set. *Comput. Mater. Sci.* **6**, 15–50 (1996).
67. Becke, A. D. Density-functional thermochemistry. III. The role of exact exchange. *J. Chem. Phys.* **98**, 5648 (1993).
68. Körzdörfer, T. & Brédas, J.-L. Organic electronic materials: Recent advances in the DFT description of the ground and excited states using tuned range-separated hybrid functionals. *Acc. Chem. Res.* **47**, 3284–3291 (2014).
69. Calado, V. E. et al. Ballistic transport in graphene grown by chemical vapor deposition. *Appl. Phys. Lett.* **104**, 23103 (2014).

Acknowledgements

This research was supported by the Spanish MINECO / AEI/FEDER grants CTQ2015-64618-R and CTQ2016-76423-P and, in part, by Generalitat de Catalunya grants 2014SGR97 and XRQTC. We acknowledge access to supercomputer resources as provided through grants from the Red Española de Supercomputación. I.A. acknowledges the Spanish Ministerio de Educación Cultura y Deporte for a FPU PhD scholarship. F.V. acknowledges MINECO for a postdoctoral Ramon y Cajal (RyC) research contract (RYC-2012-10129).

Author contributions

I.A. and S.T.B.: Came up with the original idea for the study and prepared the manuscript. I.A.: Carried out the FHI-AIMS DFT calculations. F.V.: Calculated the Fermi velocities and carried out the VASP DFT calculations. I.A., S.T.B. and I.P.R.M.: Contributed equally to the interpretation of results. All authors discussed the results and commented on the manuscript. S.T.B.: Supervised the project.

Additional information

Supplementary Information accompanies this paper at doi:10.1038/s41467-017-01977-4.

Competing interests: The authors declare no competing financial interests.

Reprints and permission information is available online at http://npg.nature.com/reprintsandpermissions/

Publisher's note: Springer Nature remains neutral with regard to jurisdictional claims in published maps and institutional affiliations.

Supporting Information of Publication #8

Existence of multi-radical and closed-shell semiconducting states in post-graphene organic Dirac materials.

Nat. Comm. 2017, *8*, 1957.

I. Alcón*, F. Viñes, I. de P.R. Moreira and S. T. Bromley*

Supporting Information

Existence of multi-radical and closed-shell semiconducting states in post-graphene organic Dirac materials

Isaac Alcón[a,*], Francesc Viñes[a], Iberio de P.R. Moreira[a] and Stefan T. Bromley[a,b,*]

[a)] *Departament de Ciència dels Materials i Química Física & Institut de Química Teòrica i Computacional (IQTCUB), Universitat de Barcelona, C/ Martí i Franquès 1, 08028 Barcelona, Spain.*

[b)] *Institució Catalana de Recerca i Estudis Avançats (ICREA), 08010 Barcelona, Spain.*

* Corresponding authors: ialcon@ub.edu, s.bromley@ub.edu

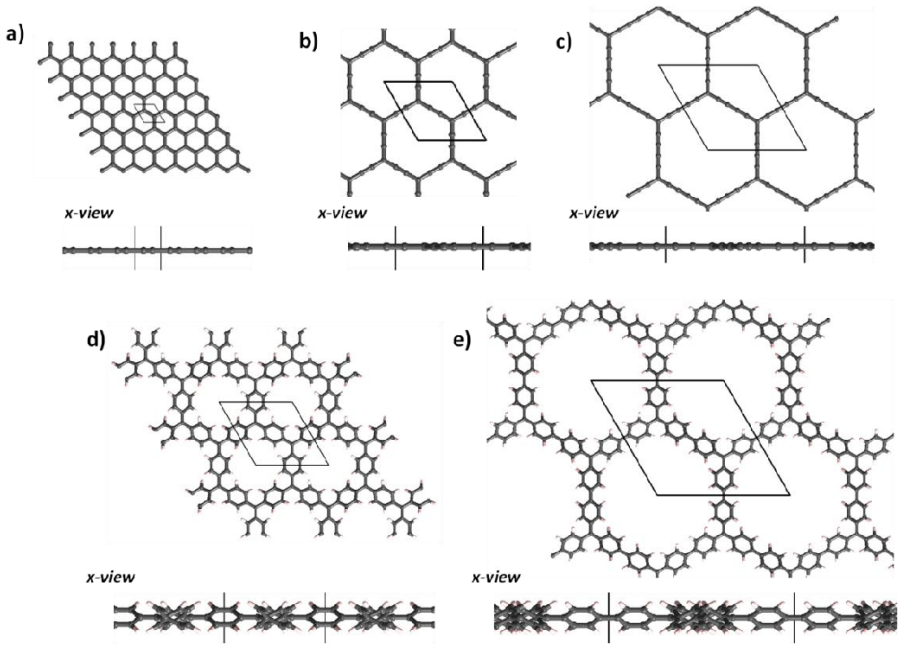

Fig. S1. Fully optimized structures of Graphene (a), GY (b), GDY (c), GP (d) and GDP (e), with the PBE functional within FHI-AIMS in an unrestricted open-shell calculation with no initial guess. The utilized unit cells are highlighted from both the *z* (top) and *x* view (bottom).

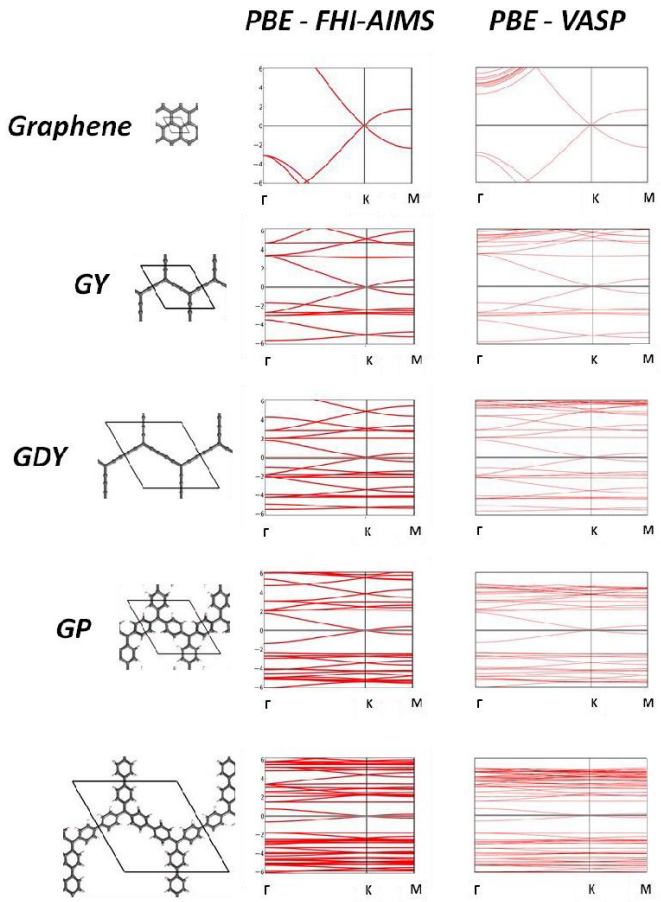

Fig. S2. Comparison of electronic band structures for the different materials from unrestricted open-shell optimizations with no initial guess using the PBE functional within FHI-AIMS (left column) and VASP (right column) and the corresponding atomical periodic structures. The Fermi level is placed at 0 energy (horizontal black line), separating the ocuppied and unocuppied bands.

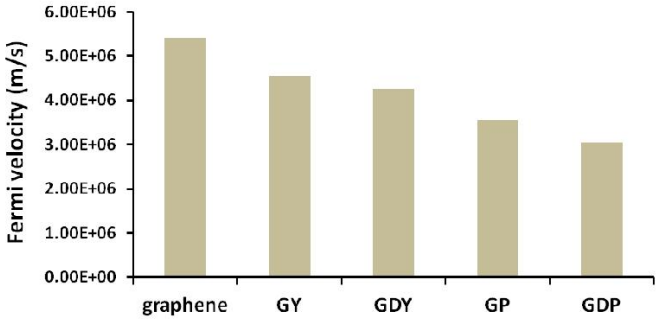

Fig. S3. Calculated Fermi velocites for each material based on unrestricted open-shell optimizations with no initial guess using the PBE funcitonal within VASP (i.e. results of Fig. S2 right). These values were extracted from the energy vs. length slopes in linear segments within the **Γ → K** path.

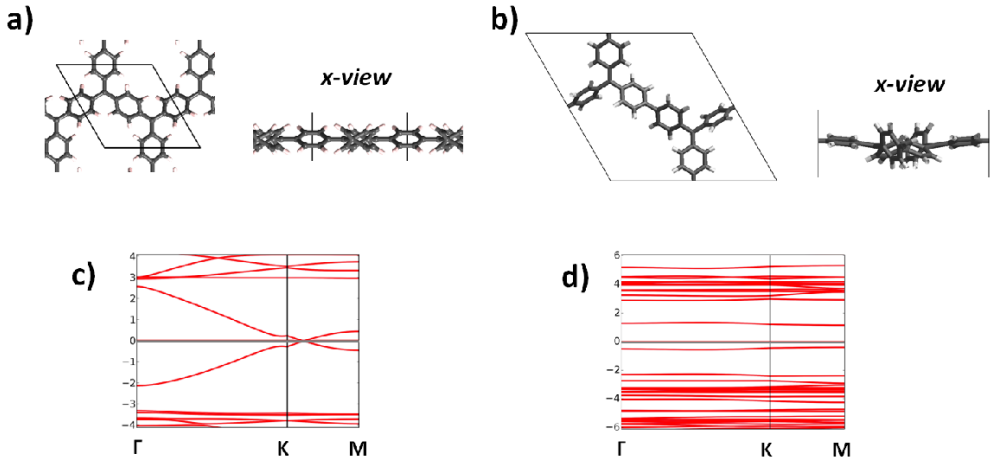

Fig. S4. Fully optimized structures of GP (a) and GDP (b) at the PBE0 level of theory within FHI-AIMS in an unrestricted open-shell calculation with no initial guess. The utilized unit cells are highlighted from both the *z* (top) and *x* views (bottom). In GP one of the three aryl rings within the unit cell gets slightly planarized (almost imperceptible), causing a higher tendency for π-electrons to delocalize in that particular direction, which is translated in a movement of the Dirac cone out of the highly symmetric **K** point (c). In GDP more important out-of-plane distortions take place (see *x*-view), which is translated in the opening of a sizeable band gap at the **K** point (d).

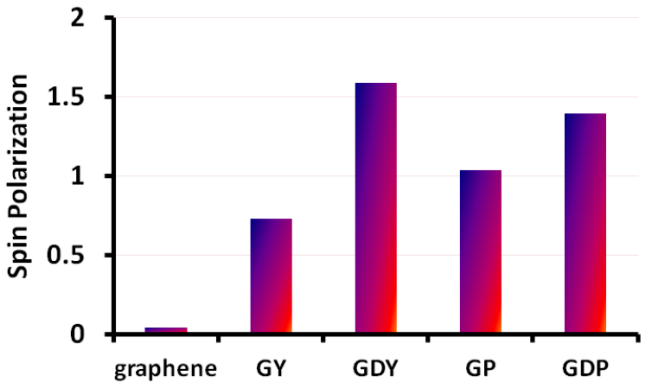

Fig. S5. Spin-unrestricted open-shell single point calculations at the PBE0 level of theory within VASP setting an AFM spin configuration as initial guess over the correspondingly fully optimized structures in FHI-AIMS. The graph shows the total absolute spin population (i.e. addition of all atom-partitioned spin up and spin down populations in absolute value) within the unit cell throughout the materials' series.

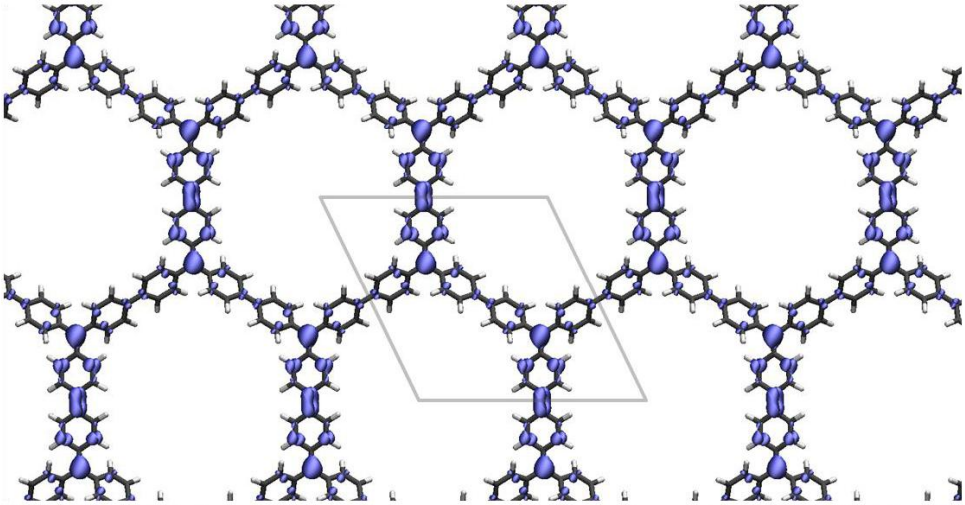

Fig. S6. Atom-projected electronic density isosurface of the highest occupied crystal orbital for GDP at the **Γ** point, as obtained from a restricted closed-shell optimization using the PBE0 functional within FHI-AIMS. The formation of a quinoidal-like pairing between adjacent triply-bonded sp^2 carbon nodes can be observed.

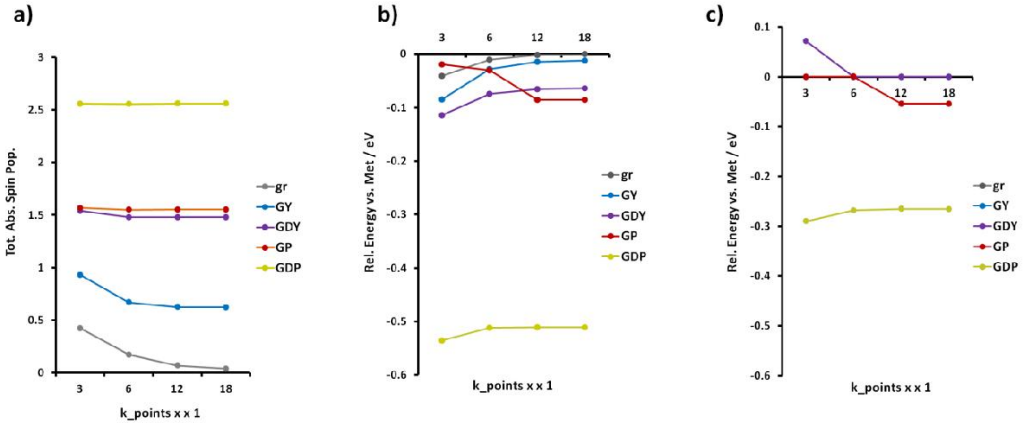

Fig. S7. Summary of results for the AFM open-shell and quinoidal closed-shell solutions at the PBE0 level of theory within FHI-AIMS per material (coloured lines) upon increasing number of **k**-points utilized in the calculations. a) Total absolute spin population (i.e. addition of all atom-partitioned spin up and spin down populations in absolute value) within the unit cell throughout the materials' series. b) Energy difference between the AFM solution and the semimetallic one per unit cell. c) Energy difference between the closed-shell solution and the semi-metallic one per unit cell. As it can be seen, all results are converged for the 18x18x1 **k**-mesh.

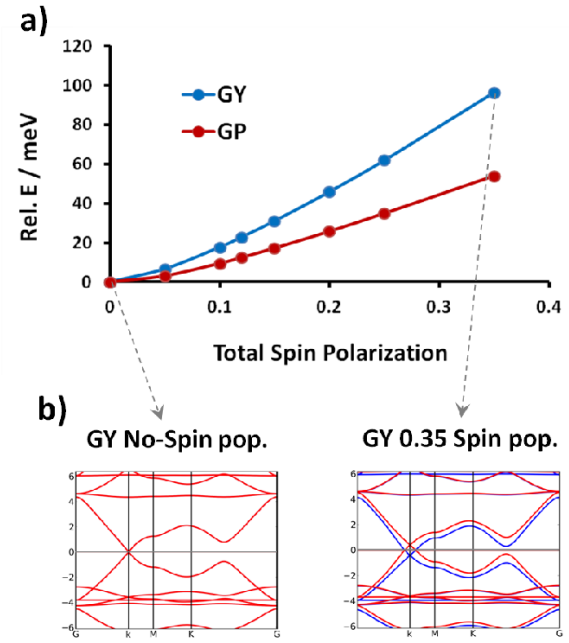

Fig. S8. Unrestricted open-shell single point calculations forcing an increasing spin polarization within the unit cell at the PBE0 level of theory within FHI-AIMS onto the semimetallic obtimized structures obtained at the same level of theory. a) Energy cost of spin polarizing the semi-metallic solution per sp^2 carbon node for GY (red) and GP (blue) and b) effect on the corresponding band-structures, as shown for GY. As it can be seen, the associated energies are easily accessible by thermal excitations which means that such spin-polarization could take place at normal conditions.

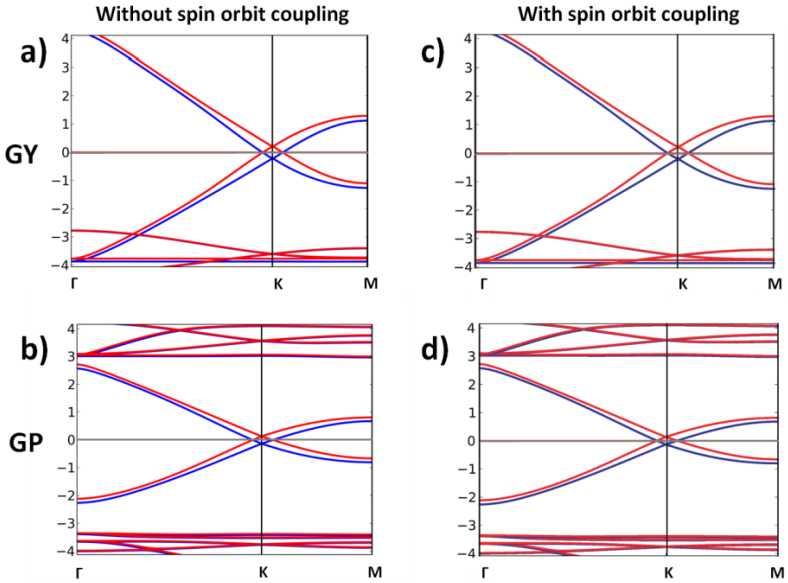

Fig. S9. Unrestricted open-shell single point calculations forcing a 0.15 spin polarization within the unit cell at the PBE0 level of theory onto the semimetallic obtimized structures for GY and GP without (a – b) and with spin-orbit coupling effects (c – d).

5.4 Overview

From basic chemical principles of π-conjugated organic systems we know that π-conjugated unpaired electrons of sp^2 carbons may be connected essentially in two ways, in *meta*- and in *para*-; they may also be connected in *ortho*-, but it is very difficult to extend 2D covalent networks through such positions due to significant steric hindrance effects and so we have not considered *ortho*-connected situations. As experimentally demonstrated in TAM dimers and trimers, when TAMs are connected in *meta*- the unpaired electrons remain localized in the corresponding TAM units and tend to be ferromagnetically coupled. Conversely, when radical centres are connected in *para*- respect to each other the ground state of the bi-radical presents a mixture between the solution with anti-ferromagnetically coupled unpaired electrons and the quinoidal configuration, where these unpaired electrons are paired in localized positions (i.e. a closed-shell solution). For mixed-valence compounds, where one of the TAM units is reduced to the anion, the *para*- (*meta*-) connectivity between TAM units gives rise to charge transfer (lack of charge transfer) of the negative charge between both extremes (see references 12 and 13 above). Charge transfer phenomena for *para*-bi-PTM mixed-valence compounds with different π-conjugated bridges has been experimentally demonstrated using different spectroscopic techniques such as UV-vis. and Raman as well as with variable-temperature EPR measurements. To explain such charge transfer phenomena different electronic mechanisms have been proposed, such as tunnelling or charge hopping, associated with bi-PTM mixed-valence compounds with short and long π-conjugated bridges, respectively (see ref. 14 above). In **Publication #7** we have collaborated with the experimental group of Prof. Veciana to elucidate the charge transfer mechanisms for a series of *para*-bi-PTM mixed-valence compounds with thiophene-vinylene (TV) bridges of increasing length. As shown in previous works (ref. 14), based on UV-vis. spectroscopy, variable temperature EPR and Raman, two different charge transfer regimes for short and long bridge compounds have been detected. For long TV chains, a hopping mechanism of positive charges has been determined as the main responsible mechanism explaining charge transfer of negative charges between both PTM units, which may be understood by the electro-donating nature of the TV bridge (i.e. by thiophene units). However, for the shorter compounds of the series, our first principles calculations pointed out to a different charge transfer mechanism as compared to the previously proposed quantum tunnelling in ref. 14: the so-called flickering resonance mechanism, or FR (see ref. 24 for details). In FR, the negative charge is supposed to be able to delocalize through the entire π-conjugated system composed by both PTM units and the π-conjugated bridge. Hence, through thermal fluctuations the negative charge tends to be localized in one PTM extreme but, for certain molecular conformations, it becomes completely delocalized between both PTM units through the π-conjugated TV wire. We observed this behaviour by studying a series of molecular conformations extracted form an AIMD simulation at 300K. Our computational results in **Publication #7** explain the different tendencies experimentally found for short and long bridged bi-PTM derivatives and also predict optical electronic

band gaps associated to the transition state of the charge transfer process with very similar values to those detected by UV-vis. spectroscopy.

As I highlighted in the introduction of this chapter, it turns out that theoretically designed 2D networks composed of TAM units connected in *para*- have been predicted to be semimetals (see refs 25 and 26 above), such as graphene. Interestingly, this exactly coincides with the experimental findings in *para*-connected bi-PTM mixed-valence compounds indicating charge transfer phenomena. However, we found out that for such predicted 2D materials the localized anti-ferromagnetic (AFM) and closed-shell quinoidal solutions existing in the corresponding bi-radicals had not been reported. In fact, the existence of such solutions had been missed for an entire series of post-graphene organic Dirac materials (PGODs) presenting a common hexagonal skeleton of radical sp^2 carbon centres connected through π-conjugated linkers. Being aware of such solutions, in **Publication #8** we performed an in-depth and systematic computational study where we report such localized open-shell AFM and closed-shell quinoidal solutions for a series of representative PGODs for the first time. Comparing different computational methods (i.e. plane waves vs. numerical basis set schemes) and DFT functional flavours (pure GGA vs. different degrees of HF-exchange DFT hybrids) our conclusive results show that such localized solutions open the Dirac cone in the band structures of each material with band gaps ranging from 1 to 2 eVs, hence indicating a clear transition from the semimetallic state to a semi-conductor one. Moreover, the different solutions (i.e. semimetallic and localized AFM and quinoidal) lay very close in energy, which indicates that at room temperature the studied PGOD materials should display an electronic equilibrium between the three solutions. Therefore, this study highlights the potential of the studied PGODs and, in particular, TAM-based PGODs, as highly tunable platforms for nano-electronics. Additionally, in **Publication #8** we make a clear link between the field of molecular electronics (i.e. bi-radicals and mixed-valence compounds) and that of graphene and PGODs, highlighting the potential of applying such chemical approach to this type of 2D organic materials mostly studied by physicists today.

Chapter 6
Conclusions

Here I will briefly summarize the main conclusions of each chapter. After that I will provide my personal future vision about the intellectual contribution that I consider most important of this PhD thesis: the TAM 2D-COFs.

6.1 Concluding Remarks

6.1.1 Chapter 3: Modelling TAMs as potential devices

As shown in Chapter 3, TAMs show great potential as components for molecular devices. This has been previously demonstrated in the literature.[1–5] With the works that this thesis has contributed I have added some extra valuable insight in this direction:

- In **Publication-draft #1** we have demonstrated that quinoidal closed-shell TTM-based derivatives may be used to form the corresponding radical SAMs. This is possible due to a unique electronic cascade mechanism through which, by chemically bonding the π-conjugated molecules on the surface, an unpaired electron is generated. Such a mechanism was predicted in 2012 theoretically,[6] and **Publication-draft #1** is the first experimental demonstration of such principle. In this contribution we also have shown that specially designed quinoidal TAM monomers and metal substrates with particular reactivity need to be used for such a goal.

- In **Publication #2** the synthesis of a similar radical SAM to those presented in **Publication-draft #1** was reported, using bi-radical compounds as starting building blocks. The generated radical SAMs bear the particular property that the radical core is in close proximity to the metallic substrate. As demonstrated by different on-surface techniques and our periodic DFT calculations, such close proximity does not perturb the unpaired electron which remains unpaired and localized on the central carbon atom of the perchlorated TAMs. As highlighted in **Publication #2**, such a radical SAMs may present potential for spintronics because the metallic electrons could feel the magnetic impurity of the radical SAM; this is, however, just a hypothesis at this point.

- **Publication #3** assesses the potential of hydrogenated PTMs (or H-PTMs) functionalized with an ethylene unit as photo-active switches. Typically, ethylene-based compounds may be switched from the E to the Z conformer through light irradiation.[7] Stilbene is a typical case study,[8] where the proportion between the E and Z conformers under light irradiation depends on the particular chemical functionalization of the stilbene derivative.[9] In the H-PTM-ethylene derivatives studied in **Publication #3** the photo-activated E ↔ Z equilibrium is completely displaced to the Z conformer and there is no way to isomerize back to the E conformer. This may not be understood by simple thermodynamical reasons, due to the fact the E isomer is the most stable conformer of the two. Based in AIMD DFT simulations at 300K we could show that bulky chlorine atoms of PTMs are the cause of a kinetic blocking effect occurring only on the Z isomer.

Such kinetic blockade prevents the twisting of the C=C ethylene unit even when the double-bond is opened by light or chemical treatment, thus preventing the isomerisation back to the E conformer. Such a hypothesis was entirely constructed based on our DFT simulations and could explain the previously difficult to interpret experimental findings.

Hence, with these three works I have not just contributed to show the continuous potential of TAMs for different types of molecular-based applications, but I have also shown my ability to use computational chemistry as a potential tool to obtain fundamental insight, providing original hypothesis and ideas not always available through experimental observations. I believe this is especially true for our computational contribution in **Publications #1** and **#3**, but also applies for our contribution in **Publication #7** within Chapter 5. Also, as highlighted in **Publication #1**, knowing the utilized level of theory and its associated errors is also very important to make reliable predictions. However, with such knowledge, computational modelling becomes an outstanding tool to complement experimental work in materials science.

6.1.2 Chapter 4: From aryl rings' twist to TAM 2D-COFs

Chapter 4 is entirely composed by purely computational works, representing the major contribution of this thesis in terms of predicting new systems with unique characteristics, in conjunction with **Publication #8** in Chapter 5. The basic initial goal of the works presented in this chapter was to find a way to control the localization/delocalization of the unpaired electron in TAMs, due to the fact this unpaired electron gives rise to most interesting properties of TAM-based systems for different applications within molecular magnetism and electronics.[4,5,10–12] Aryl ring twist angles are the structural parameter that provides such control over the unpaired electron, as computationally demonstrated in detail in **Publication #4**, where the correlation between this structural parameter and the electronic variable was tested for different chemical functionalities and temperatures. Hence, **Publication #4** highlights the potential of manipulating aryl ring twist angles in TAM-based systems to construct multi-functional materials with highly controllable properties. As shown in **Publication #5** a suitable platform to externally manipulate aryl ring twist angles is that of TAM 2D-covalent organic frameworks (or TAM 2D-COFs), where it is possible to externally twist aryl rings by application of an uniaxial strain. This twist, in turn, induces the localization of all unpaired electrons of the 2D networks and affects fundamental properties of these materials such as magnetic interactions between radical centres or the optical band gap. Therefore, the goal of designing TAM-based systems with externally highly tunable properties thanks to the structural-electronic correlation in TAMs was convincingly achieved in **Publication #5**, where TAM 2D-COFs are presented as a convenient system for such objective. An important point raised in **Publication #5** is the different structural response of both studied TAM networks: i.e. the triphenylmethyl based one (or TPM 2D-COF) and the perchloro-triarylmethyl based one (PTM 2D-COF). PTMs are the persistent version of TAMs[10,13] but, as we found in **Publication #5**,

the perchlorated functionalization prevents an efficient twisting of aryl rings by application of strains which, in turn, prevents any control of the 2D material's properties. The TPM 2D-COF, differently, is very flexible (low steric constrain associated to phenyl rings), but TPMs are not persistent radicals hence making the synthesis of the corresponding networks in the lab much less probable in the future, or even not possible at all. Solving such a complicated dilemma is the goal of **Publication #6** where we designed more than 50 different networks based on TAMs with different degrees of halogenations and systematically uniaxially stretched their structure following the variation of aryl ring twisting. We have thus found TAM 2D-COFs based on experimentally synthesized monomers which, at the same time, show significant structural flexibility. Hence, in **Publication #6** we show that it should be possible to experimentally synthesize persistent TAM 2D-COFs with externally controllable interesting properties such as spin localization and the band gap of the material by application of a uniaxial strain.

6.1.3 Chapter 5: para-connected TAMs: Towards 2D semimetals

In this last chapter I highlight the power of the different ways TAM units may be covalently connected within 2D-COFs to determine fundamentally interesting properties, with special emphasis on electrical characteristics. As experimentally demonstrated, charge transfer phenomena in bi-PTM mixed-valence compounds (MVC) entirely depends on how PTM units are covalently bonded with respect to each other through the π-conjugated bridge. *Meta*-connected bi-PTM MVCs do not show charge transfer phenomena[14,15] and the negative charge is localized on one of the PTM units. Contrary, *para*-connected bi-PTM MVCs do present charge transfer phenomena which may be detected by different techniques such as variable temperature EPR and UV-vis. and Raman spectroscopies.[15,16] In **Publication #7** a series of *para*-connected bi-PTM MVCs are studied experimentally by such spectroscopy techniques and our DFT calculations of the shortest compound of the series at room temperature (300K) by AIMD simulations. Our computational results point to the so-called flickering resonance mechanism[17] as the one explaining charge transfer in the studied compounds. This mechanism may be related to the so-called ballistic transport in graphene[17] and it is simply based on the delocalization ability of π-conjugated electrons as the principal mean for the negative charge to "travel" from one PTM extreme to the other in the ground state of the system. Moving to 2D, in **Publication #8** we study the behaviour of TAM 2D-COFs where TAM units are connected in *para*- one respect each other. As we show in this contribution, such 2D networks behave as semimetals with energetically close lying semiconducting electronic states: namely open-shell anti-ferromagnetic and the closed-shell quinoidal states. Both semiconducting solutions and the semimetallic one are so-close in energy that we could expect the three to co-exist at finite temperatures. As demonstrated in **Publication #8** this complex electronic structure, not previously reported, exists in a series of theoretically predicted post-graphene organic 2D materials and brings to such systems an electronic tunability not available in their experimental predecessor, graphene.

6.2 Future perspective

I personally believe the most important intellectual contribution of this PhD thesis is the proposition of TAM 2D-COFs as new promising materials for different future applications. Indeed, TAM 2D-COFs, if experimentally realized, would present a series of potential characteristics which make them unique platforms, specially, for future nano-electronics. Here I highlight a series of such characteristics that TAM 2D-COFs exhibit:

- Robustness: 2D-COFs are composed of the strongest type of bond: the covalent bond. Hence, our predicted TAM 2D-COFs should be robust networks bearing the structural stability required for any type of novel relevant technology.

- Ordered array of spins: TAM 2D-COFs are ordered arrays of spin moments (i.e. unpaired electrons) and, as demonstrated in **Publication #8**, their magnetic interactions, in turn, are coupled with the electrical behaviour of the network. This may be a particularly appealing property for quantum computing.

- Redox-active: TAMs are redox-active species, because of the fact they are easily reduced to the -1 state (i.e. anion). Moreover, the neutral and anion states present completely distinct magnetic and optical properties. Such redox-activity was exploited to construct PTM-based SAMs as robust memory devices.[4] TAM 2D-COFs, hence, inherit such redox-active nature from the TAM building blocks composing them.

- Electronic tunability at the molecular level: As demonstrated in this PhD thesis, in TAM 2D-COFs π-conjugated unpaired electrons may be controlled by different structural means. On one hand, aryl ring twist angles entirely control the localization/delocalization of unpaired electrons in TAMs (**Publication #4**). Aryl ring twist angles may be tuned, in turn, with the chemical functionality of the particular TAM derivative or, as demonstrated in **Publication #5**, by external means such as applied uniaxial strains (electric fields have also been proposed as a way to externally manipulate aryl ring twist angles in other 2D-COFs[18]). This could be used to construct TAM 2D-COFs-based sensors of different types. On the other hand, the way TAM units are covalently bonded determines the natural mobility of π-conjugated unpaired electrons through the network. As shown in **Publication #5**, *meta*-connected TAM 2D-COFs are electrical insulators with localized unpaired electrons. Conversely, as shown in **Publication #8**, *para*-connected TAM 2D-COFs are semimetals where π-conjugated unpaired electrons may be completely delocalized or localized unpaired (AFM) and paired (quinoidal). *Para*-connected TAM 2D-COFs are, intrinsically, highly tunable platforms due to the panoply of energetically close lying electronic

solutions. However, the *para-/meta-* paradigm offers an extra degree of electronic tunability at the nano-scale.

As far as I know, there is not another type of material (be it organic or inorganic, 2D or 3D) that exhibits such electronic tunability at the molecular level in conjunction with other technological important properties such as structural robustness and structural ordering. With such combination of appealing characteristics I believe TAM 2D-COFs possess a unique potential as a future platform for nano-electronics. Based on the list of properties presented above, it is easy to imagine QBit-arrays or redox data-storage devices based on a TAM 2D-COF (based on the spin and redox-switchability of TAM centres, respectively), different sorts of TAM-based nano-transistors or mechanical sensors (based on the conductive *para*-TAM 2D-COF) or, even, nano-covalent electrical circuits based on a TAM 2D-COF where *meta-* (insulator) and *para-* (conductor) paths could be combined in a rational way. Of course, each of these potential applications requires further computational and experimental confirmation. However, the basic results presented in this PhD thesis represent a robust fundamental theoretical basis upon which it should be relatively easy to design and investigate such devices and platforms. Moreover, today we have available computational tools that allow studying all the above presented ideas and hence it should be a matter of time, motivation and opportunity to demonstrate, or revoke, each of them. The experimental realization of the first TAM 2D-COF would, certainly, generate a huge interest in this type of unexplored 2D materials. Meanwhile, assessing their potential as future platforms for nano-electronics via state-of-the-art quantum chemical computations seems a very interesting path to explore.

6.3 Bibliography

1 N. Crivillers, M. Mas-Torrent, J. Vidal-Gancedo, J. Veciana and C. Rovira, *J. Am. Chem. Soc.*, 2008, **130**, 5499–506.

2 C. Simão, M. Mas-torrent, J. Veciana and C. Rovira, *Nano Lett.*, 2011, **11**, 4382–4385.

3 N. Crivillers, M. Paradinas, M. Mas-Torrent, S. T. Bromley, C. Rovira, C. Ocal and J. Veciana, *Chem. Commun.*, 2011, **47**, 4664–6.

4 C. Simão, M. Mas-Torrent, N. Crivillers, V. Lloveras, J. M. Artés, P. Gorostiza, J. Veciana and C. Rovira, *Nat. Chem.*, 2011, **3**, 359–64.

5 R. Frisenda, R. Gaudenzi, C. Franco, M. Mas-Torrent, C. Rovira, J. Veciana, I. Alcon, S. T. Bromley, E. Burzurí and H. S. J. van der Zant, *Nano Lett.*, 2015, **15**, 3109–3114.

6 F. Rissner, Z. Ma, O. T. Hofmann, C. Slugovc, Z. Shuai and E. Zojer, *J. Mater. Chem.*, 2012, **22**, 4269.

7 C. Dugave and L. Demange, *Chem. Rev.*, 2003, **103**, 2475–2532.

8 W.-G. Han, T. Lovell, T. Liu and L. Noodleman, *ChemPhysChem*, 2002, **3**, 167–178.

9 D. Gegiou, K. A. Muszjat and E. Fischer, *J. Am. Chem. Soc.*, 1968, **90**, 3907–3918.

10 J. Veciana and I. Ratera, in *Stable Radicals: Fundamentals and Applied Aspects of Odd-Electron Compounds (ed R. G. Hicks)*, ed. R. G. Hicks, John Wiley & Sons, Inc., 2010, pp. 33–80.

11 D. Maspoch, D. Ruiz-Molina, K. Wurst, N. Domingo, M. Cavallini, F. Biscarini, J. Tejada, C. Rovira and J. Veciana, *Nat. Mater.*, 2003, **2**, 190–5.

12 A. Rajca, J. Wongsriratanakul and S. Rajca, *Science*, 2001, **294**, 1503–1505.

13 M. Ballester, J. Riera, J. Castañer, C. Badía and J. M. Monsó, *J. Am. Chem. Soc.*, 1971, **93**, 2215–2225.

14 V. Lloveras, J. Vidal-Gancedo, D. Ruiz-Molina, T. M. Figueira-Duarte, J.-F. Nierengarten, J. Veciana and C. Rovira, *Faraday Discuss.*, 2006, **131**, 291.

15 C. Rovira, D. Ruiz-Molina, O. Elsner, J. Vidal-Gancedo, J. Bonvoisin, J.-P. Launay and J. Veciana, *Chemistry (Easton).*, 2001, **7**, 240–250.

16 V. Lloveras, J. Vidal-Gancedo, T. M. Figueira-Duarte, J. F. Nierengarten, J. J. Novoa, F. Mota, N. Ventosa, C. Rovira and J. Veciana, *J. Am. Chem. Soc.*, 2011, **133**, 5818–33.

17 J. Blumberger, *Chem. Rev.*, 2015.

18 D. Miguel, I. R. Márquez, L. Álvarez de Cienfuegos, N. Fuentes, S. Rodríguez-Bolivar, D. J. Cárdenas, A. J. Mota, F. Gómez-Campos and J. M. Cuerva, *Phys. Chem. Chem. Phys.*, 2015, **17**, 31902–31910.

Chapter 7
Contribution to publications

The results presented in this thesis have been organized as a compendium of publications, which are the final output of the work carried out by several authors beyond the author of this thesis. This chapter aims to clarify the contribution of the author of this thesis to each one of the publications.

"*" indicates full or shared correspondence for that particular paper. I have written first drafts of all papers where I appear as first author. My contribution is briefly explained after each article's details.

Publication-draft #1: M. R. Ajayakumar, C. Moreno, **I. Alcón**, S. T. Bromley,* F. Illas, J. Veciana, A. Mugarza* and M. Mas-Torrent*. *Realization of an open-shell self-assembled monolayer using closed-shell quinoidal molecular building blocks.* In preparation

Contribution: I performed the DFT structural optimizations in this collaborative paper and participated in all discussions regarding the interpretation of theoretical results in comparison with experimental measurements.

Publication #2: M. R. Ajayakumar, **I. Alcón**, S. T. Bromley, J. Veciana*, C. Rovira and M. Mas-Torrent*. *Direct covalent grafting of an organic radical core on gold and silver. RSC Adv.* 2017, *7*, 20076–20083.

Contribution: I performed the DFT calculations in this collaborative paper.

Publication #3: F. Bejarano, **I. Alcon**, N. Crivillers, M. Mas-Torrent*, S. T. Bromley, J. Veciana and C. Rovira*. *Study of the E–Z stilbene isomerisation in perchlorotriphenyl-methane (PTM) derivatives. RSC Adv.* 2017, *7*, 15278–15283. *Note: I share main authorship of this work with F. Bejarano*.

Contribution: I performed the DFT calculations in this collaborative paper and constructed the main hypothesis presented in the computational section to explain both theoretical and experimental results.

Publication #4: I. Alcon and S. T. Bromley*. *Structural Control over Spin Localization in Triarylmethyls. RSC Adv.* 2015, *5*, 98593–98599.

Contribution: I proposed the basic idea about the correlation between spin localization and aryl ring twist angles and its relevance for applications. I performed all DFT calculations.

Publication #5: I. Alcón, D. Reta, I. de P. R. Moreira, S. T. Bromley*. *Design of multi-functional 2D open-shell organic networks with mechanically controllable properties. Chem. Sci.* 2017, *8*, 1027–1039.

Contribution: I designed the presented materials and performed most DFT calculations of this work.

Publication #6: I. Alcón and S. T. Bromley*. *Triarylmethyl-based 2D covalent networks: virtual screening of chemical functionalisation for optimising strain-induced property control. PCCP*, 2018, doi: 10.1039/C7CP08076J

Contribution: I have done all DFT and FF calculations of this work.

Publication #7: C. Franco, P. M. Burrezo, V. Lloveras, R. Caballero, **I. Alcón**, S. T. Bromley*, M. Mas-Torrent, F. Langa, J. T. López Navarrete, C. Rovira*, J. Casado* and J. Veciana*. *Operative Mechanism of Hole-Assisted Negative Charge Motion in Ground States of Radical-Anion Molecular Wires. J. Am. Chem. Soc.* 2017, *139*, 686–692.

Contribution: I performed all DFT calculations of this collaborative work and proposed together with Prof. Stefan Bromley the mechanism explaining charge transfer phenomena for the shortest compounds of the studied series.

Publication #8: I. Alcón*, F. Viñes, I. de P.R. Moreira and S. T. Bromley*. *Existence of multi-radical and closed-shell semiconducting states in post-graphene organic Dirac materials. Nat. Commun.* 2017, 8, 1957.

Contribution: I have performed all calculations shown in the main article. I proposed the main idea presented in the work and its generality. I insisted on writing the paper in a chemical-biased approach and written the first draft of the manuscript. Because of the lead I have taken in this contribution, Stefan Bromley decided I deserved a shared correspondence with him.

In addition to the publications that constitute the present thesis, the following articles are also co-authored by the PhD candidate:

[i] J. Saiz-Poseu, **I. Alcón**, R. Alibés, F. Busqué, J. Faraudo*, D. Ruiz-Molina*. *Self-assembly of alkylcatechols on HOPG investigated by scanning tunneling microscopy and molecular dynamics simulations. CrystEngComm* 2012, *14*, 264–271.

Contribution: I synthesized one of the studied alkylcatechols.

[ii] V. Mugnaini, A. Calzolari, R. Ovsyannikov, A. Vollmer, M. Gonidec, **I. Alcon**, J. Veciana*, M. Pedio*. *Looking Inside the Perchlorinated Trityl Radical/Metal Spinterface through Spectroscopy. J. Phys. Chem. Lett.* 2015, *6*, 2101–2106.

Contribution: I participated in the spectroscopy measurements at synchrotron Bessy II (Berlin).

[iii] **I. Alcon**, M. Gonidec, M. R. Ajayakumar, M. Mas-Torrent*, J. Veciana*. *A Surface Confined Yttrium(III) bis-phthalocyaninato Complex: A Colourful Switch Controlled by Electrons. Chem. Sci.* 2016, *7*, DOI 10.1039/C6SC00443A.

Contribution: I carried out all the experimental work showed in the published article (i.e. compound's synthesis, CVs and UV-vis. spectroscopy and final spectro-electrochemistry experiments).

[iv] R. Frisenda, R. Gaudenzi, C. Franco, M. Mas-Torrent, C. Rovira, J. Veciana, **I. Alcon**, S. T. Bromley, E. Burzurí*, H. S. J. van der Zant. *Kondo Effect in a Neutral and Stable All Organic Radical Single Molecule Break Junction. Nano Lett.* 2015, *15*, 3109–3114.

Contribution: I performed all DFT calculations supporting the experimental observations in this work.

Chapter 8
Resum en Català

8.1 Introducció

Aquesta tesi està basada en l'estudi de sistemes moleculars basats en la família de compostos anomenats triarilmetils (d'ara endavant abreujats com a TAMs) mitjançant la química computacional. Aquest treball es presenta com a compendi de treballs publicats a diferents revistes científiques (o pendents de publicació). Aquests treballs es poden separar en dos grups: treballs en col·laboració amb els grups experimentals dels professors Jaume Veciana i Concepció Rovira i de la doctora Marta Mas-Torrent, d'una banda, o treballs purament computacionals d'altre. En els primers, en col·laboració amb els grups de l'Institut de Ciència de Materials de Barcelona (ICMAB), l'aportació d'aquesta tesi doctoral s'ha dut a terme en base a càlculs basats en principis fonamentals per complementar les mesures experimentals per tal d'entendre amb més profunditat els sistemes estudiats basats en TAMs. Als segons, purament computacionals, s'ha utilitzat la modelització basada en principis fonamentals de la mecànica quàntica per fer prediccions de materials basats en molècules TAM que encara no s'han sintetitzat experimentalment al laboratori. La contribució més important en aquesta segona part amb un caràcter més predictiu (i per tant creatiu), són les xarxes covalents 2D (o 2D covalent organic frameworks, 2D-COFs, de l'anglès) basades en molècules TAM. Aquests materials, d'ara endavant anomenats TAM 2D-COFs, representen l'aportació intel·lectual més important d'aquesta tesi.

Basat en això, en aquest capítol s'introduirà breument les molècules TAM i les aplicacions més importants d'aquestes i, més endavant, les xarxes covalents 2D, o 2D-COFs, mostrant alguns exemples d'aquests materials sintetitzats sobre diferents superfícies metàl·liques.

8.1.1 TAMs: Un mica d'història

La història dels TAM comença amb la síntesi del primer membre d'aquesta família de compostos, l'anomenat trifenilmetil, or TPM (Fig. 1b). El TPM el va sintetitzar el químic nord-americà Moses Gomberg (Fig. 8.1a) al 1900 en un intent de sintetitzar el tetra-fenilmetil.[1] Després de realitzar tota una sèrie de tests per entendre quin tipus de compost portava entre mans, Gomberg va concloure que havia sintetitzat el primer exemple de compost amb un carboni tri-valent; és a dir, un carboni amb només tres enllaços i, en conseqüència, un radical orgànic. Gomberg no va errar en la seva hipòtesi i, efectivament, el TPM és el primer radical orgànic sintetitzat i per tant, el descobriment de Moses Gomberg[1] no només va significar el naixement d'aquesta interessant família de compostos, sinó que també el començament del camp de la química orgànica dels radicals a principis del segle vint.

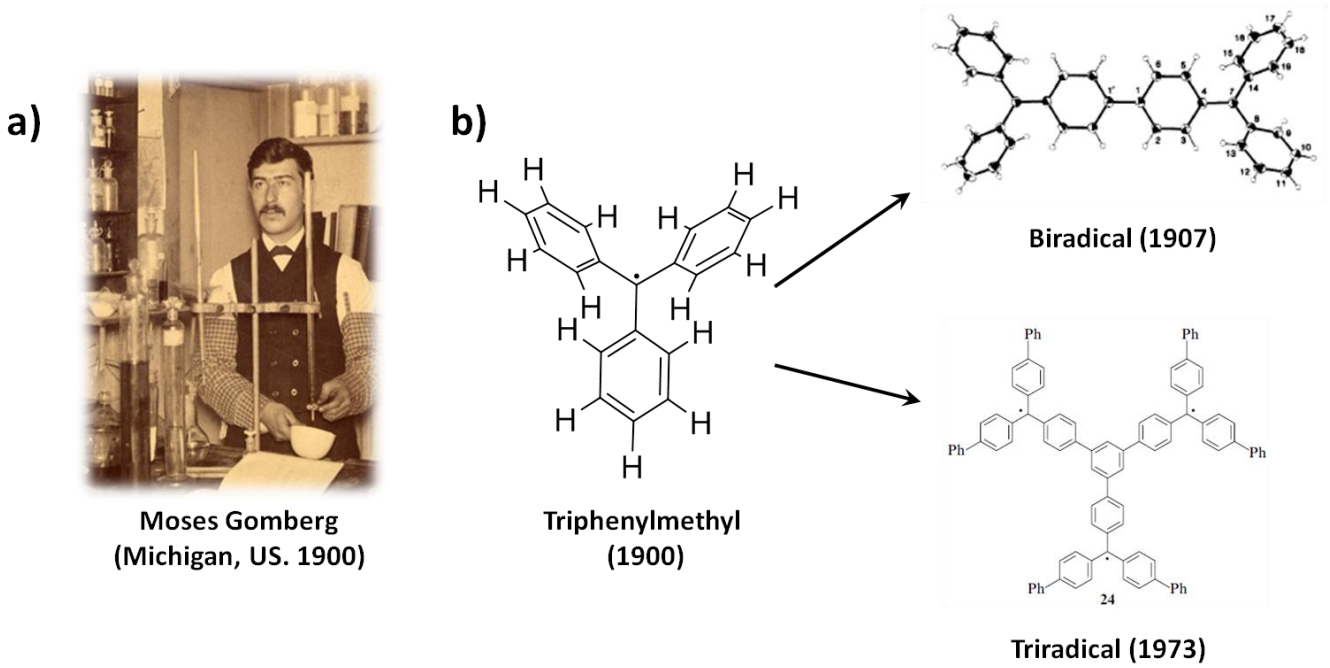

Fig. 8.1 a) Moses Gomberg treballant al seu laboratori a Michigan. **b)** Estructura química del TPM on l'electró desaparellat (punt) està situat al carboni central de la molècula.

Així doncs, a partir del descobriment de Gomberg, altres molècules amb dos, [3] tres[4] o múltiples[4] electrons desaparellats van començar a ser sintetitzades, totes basades en la unitat fonamental del TPM (Fig. 1b). Aquests van ser els primers treballs al camp dels poli-radicals. [5,6]

Tot i ser d'una gran rellevància a nivell fonamental, el descobriment del TPM no presentava cap importància a nivell tecnològic o per aplicacions químiques, donat que és estable en condicions normals durant uns pocs dies, reaccionant de manera contínua amb l'oxigen atmosfèric o amb altres espècies amb les que potser entrarà en contacte.[7] Això va canviar gràcies als experiments realitzats per un químic de la Universitat de Barcelona, Manuel Ballester, qui publicà al 1971 la síntesi d'un tipus de TAMs amb una estabilitat química extraordinària per a un radical orgànic: els percloro-triarilmetils o PTMs.[8] Com Ballester explicava en la seva contribució, els PTMs presentaven una resistència molt gran a espècies químiques altament reactives com l'àcid nítric o l'hidròxid de sodi. A més, els PTMs no es descomponien fins a 300 graus centígrads i tenien vides mitjanes en contacte amb l'aire de vàries dècades.[8] La raó que explica l'estabilitat química en els PTMs són els tres anells aril perclorats que contenen, cada un d'ells unit al carboni central de la molècula que conté l'electrò desaparellat (és a dir, el carboni tri-valent, o radical). A la Fig. 8.2a es mostra l'estructura del PTM on els clors de cada anell es representen com esferes amb el radi de Van der Waals corresponent.

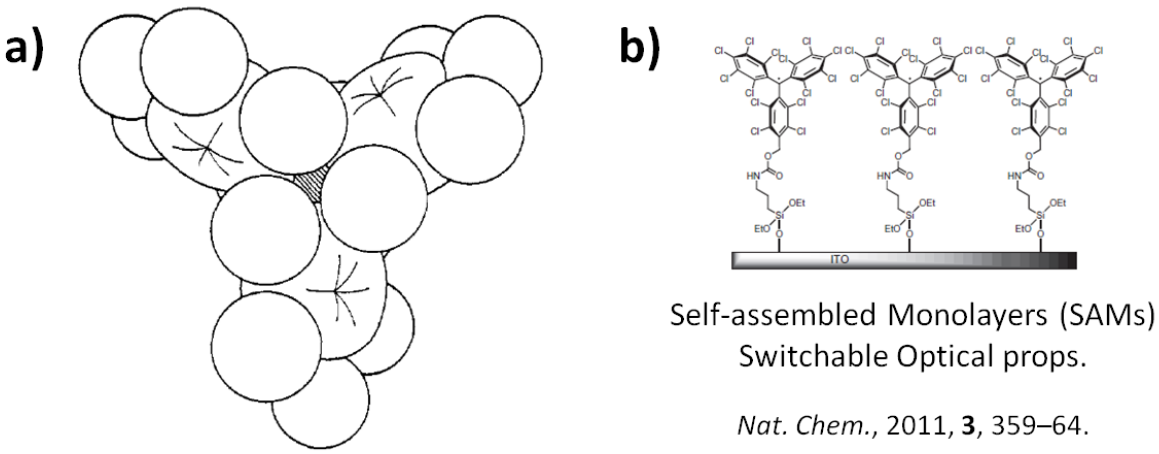

Fig. 8.2. a) Estructura del PTM utilitzant radis Van der Waals per il·lustrar l'important efecte estèric dels àtoms de clor sobre el carboni radical central (esfera ratllada). **b)** Mono-capa auto muntada de PTMs sobre una superfície d'or.

Com es pot veure en la Fig. 8.2a, l'estructura dels PTMs està molt impedida estèricament per l'important volum dels àtoms de clor. Aquest impediment estèric protegeix el carboni radicalari central (petita esfera ratllada en el centre de la molècula, Fig. 8.2a) de manera que és molt difícil que cap reactiu orgànic pugui accedir-hi i reaccionar-hi. Aquesta protecció estèrica és, per tant, la principal raó per la qual els PTMs són una de les famílies de compostos orgànics radicals més estables.

8.1.2 TAMs com a maons per materials i dispositius.

L'estabilitat química adquirida en els PTMs gràcies l'impediment estèric ofert pels anells perclorats, ha permès utilitzar aquest tipus de molècules radicals per a diferents aplicacions en el camp de la ciència de materials o el magnetisme i l'electrònica moleculars. Pel que fa a aplicacions, tot i que hi ha alguns exemples basats en el TPM,[5] la família dels PTMs són el tipus de TAMs més utilitzats,[9] per les raons ja esmentades.

La principal causa de l'atractiu d'aquests radicals orgànics per a aplicacions en magnetisme o electrònica és l'existència de l'electró desaparellat, localitzat en el carboni central de les molècules TAM. Aquest electró desaparellat és el que genera totes i cadascuna de les propietats d'interès per a diferents aplicacions en els camps esmentats. Per exemple, l'electró desaparellat en els TAMs els proporciona l'espín magnètic que posteriorment fa que certs materials basats en unitats TAM es comportin com a imants,[4,5,10–12] com per exemple els materials mostrats en la Fig. 8.3a, d. Altrament, els orbitals associats l'electró desaparellat, els anomenats orbitals moleculars individualment ocupats/desocupats (SOMO/SUMO respectivament, de l'anglès: singly occupied/unoccupied molecular orbitals) intervenen en l'absorció de llum en l'espectre visible, la qual proporciona a les molècules TAM color (absorció de llum) i fluorescència (emissió de llum) a certes longituds d'ona segons l'estructura de cada TAM particular. A més, aquestes propietats òptiques depenen de l'estat redox de la molècula TAM (és a dir, per l'estat neutre i l'anió corresponent), els quals es poden electro-generar per mitjà de potencials elèctrics.

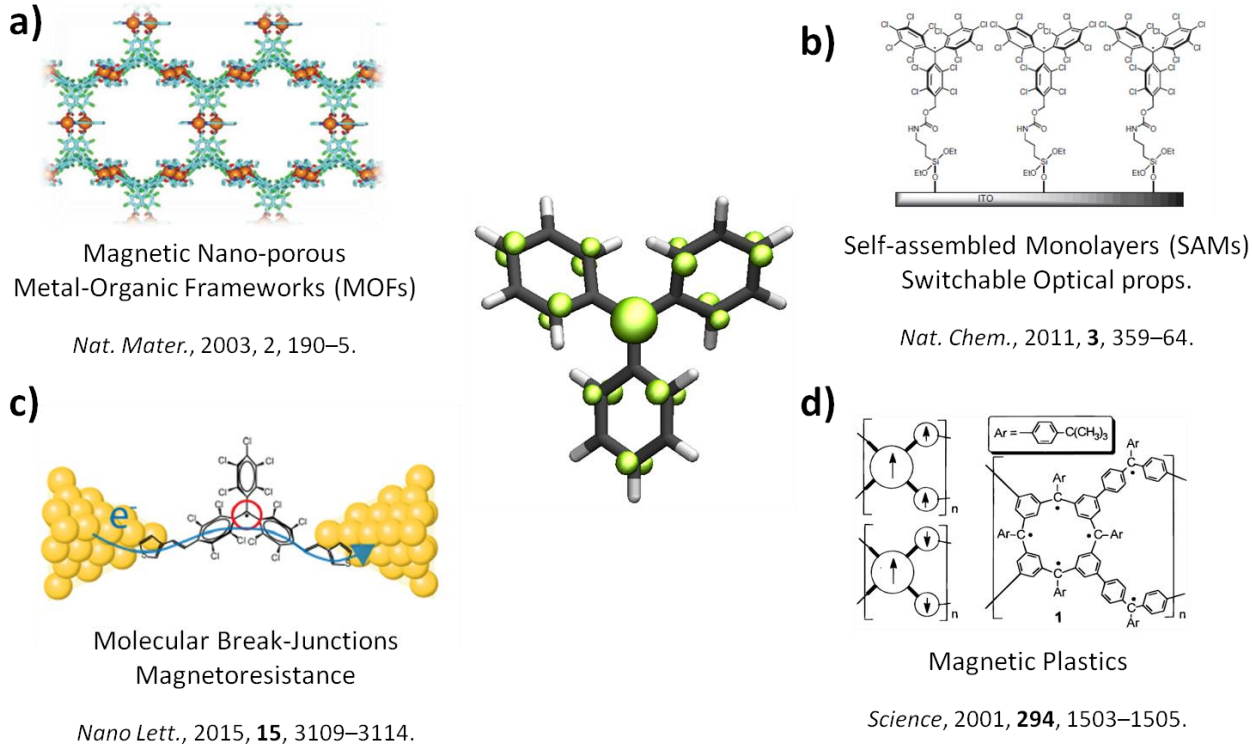

Fig. 8.3. Exemples de materials i dispositius basats en molècules TAM. **a)** Xarxa metall-orgànica amb comportament magnètic sensible al dissolvent absorbit, **b)** mono-capa auto muntada proposada com a dispositiu d'emmagatzematge d'informació, **c)** Unió uni-molecular mostrant interacció entre els electrons conductors i l'electró desaparellat de la unitat TAM i **d)** plàstic magnètic. Al centre de la figura es mostra l'estructura del TPM optimitzada dins de l'esquema del DFT, també mostrant la densitat d'espín en el canal α (en verd), associada a l'electró desaparellat.

Això va permetre preparar al laboratori una mono-capa auto muntada (SAM, de l'anglès) basada en PTMs químicament enllaçats a una superfície d'òxid d'indi-estany (indium-tin-oxide o ITO, de l'anglès) en la qual es va poder canviar entre els dos estats redox per mitjà d'un potencial elèctric (Fig. 8.3b).[13] Aleshores, a causa de les diferents propietats de cada estat (per exemple diferents colors absorbits, resposta magnètica diferent) es va poder llegir l'estat de la mono-capa amb diferents tècniques espectroscòpiques tal com la ressonància paramagnètica electrònica (EPR de l'anglès) o l'absorbància en el UV-visible. Per això, aquest dispositiu presentava molt potencial per aplicacions d'emmagatzematge d'informació.[13] Finalment, una altra de les propietats d'interès per a aplicacions, relacionada amb l'electró desaparellat en els TAMs, és l'alta conducció electrònica que es dóna a través d'aquestes molècules. Com es mostra en la Fig. 8.3c, s'ha demostrat que aquesta conducció té lloc a través de l'orbital SOMO associat l'electró desaparellat, donant lloc a propietats magneto-resistents.[14]

En resum, l'electró desaparellat en les molècules TAM és el que les fa molt interessants per a diferents aplicacions tant en el camp del magnetisme com l'electrònica i, recentment, espintrònica moleculars. Com s'explicarà més endavant, donada la gran rellevància de l'electró desaparellat en aquestes molècules,

un dels principals objectius d'aquesta tesi ha estat entendre la naturalesa i comportant d'aquest electró i buscar possibles maneres de controlar la seva distribució espacial i energia en sistemes basats en TAMs.

8.1.3 Xarxes covalents 2D, o 2D-COFs

Sense entrar molt en detall, les xarxes covalents 2D (o 2D-COFs de l'anglès) són materials estesos en dues dimensions que es preparen a sobre d'un substrat determinat. Els 2D-COF estan compostos per una unitat molecular que es diposita sobre un suport sòlid (normalment superfícies metàl·liques) i, a una certa temperatura, el conjunt de molècules s'auto ordenaran de manera periòdica en les dues dimensions. La Fig. 8.4a mostra aquest tipus d'ordenament 2D per a una molècula del tipus ftalocianina.[15]

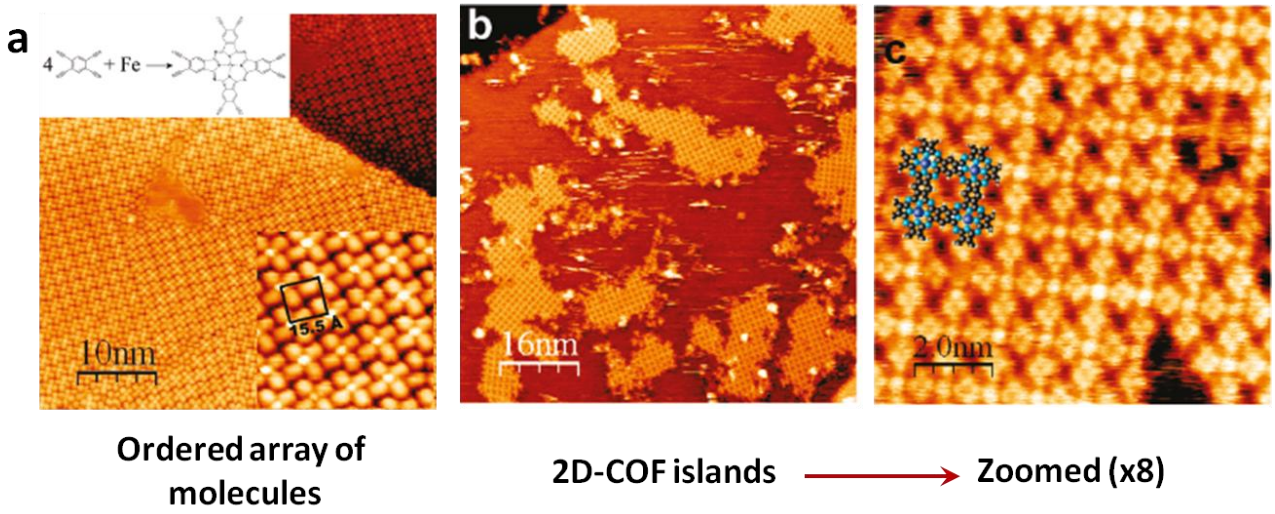

Fig. 8.4 Imatges STM de **a)** una capa ordenada d'unitats de ftalocianina-Fe(II) i **b-c)** xarxa covalent 2D quadrada.

Com es pot veure en la Fig. 8.4b-c, en augmentar la temperatura es dóna una reacció periòdica en les dues dimensions dins de les mono-capes moleculars, la qual cosa dóna lloc a les xarxes covalents 2D, les quals generen freqüentement en forma d'illes sobre la superfície metàl·lica (Fig. 8.4b). Com es pot apreciar a la Fig. 8.4c el 2D-COF hereta la topologia de les unitats moleculars corresponents. En aquest cas, la ftalocianina, d'estructura quadrada, dóna lloc a una xarxa quadricular. Així doncs, utilitzant unitats moleculars amb diferents topologies, es poden obtenir 2D-COFs amb topologies hexagonal,[16–19] quadrada,[15,20] rectangular,[21] lineal[22,23] i romboèdrica,[24,25] entre d'altres.[26]

Donada la gran versatilitat estructural i química dels 2D-COFs, i la possibilitat de generar xarxes 2D amb precisió atòmica, aquest tipus de xarxes es comença a estudiar per a aplicacions en nano-electrònica. El cas més evident és el de les nano-cintes de grafè[27] (GNRs de l'anglès), com es mostra a la Fig. 8.5: veiem com, depenent de la molècula utilitzada, s'obté un tipus de GNR o un altre. Així es pot generar GNR on els límits de la cinta presenten topologia zig-zag[28,29] (Fig. 8.5a) o GNR amb un dopatge amb precisió atòmica amb àtoms de B.[30]

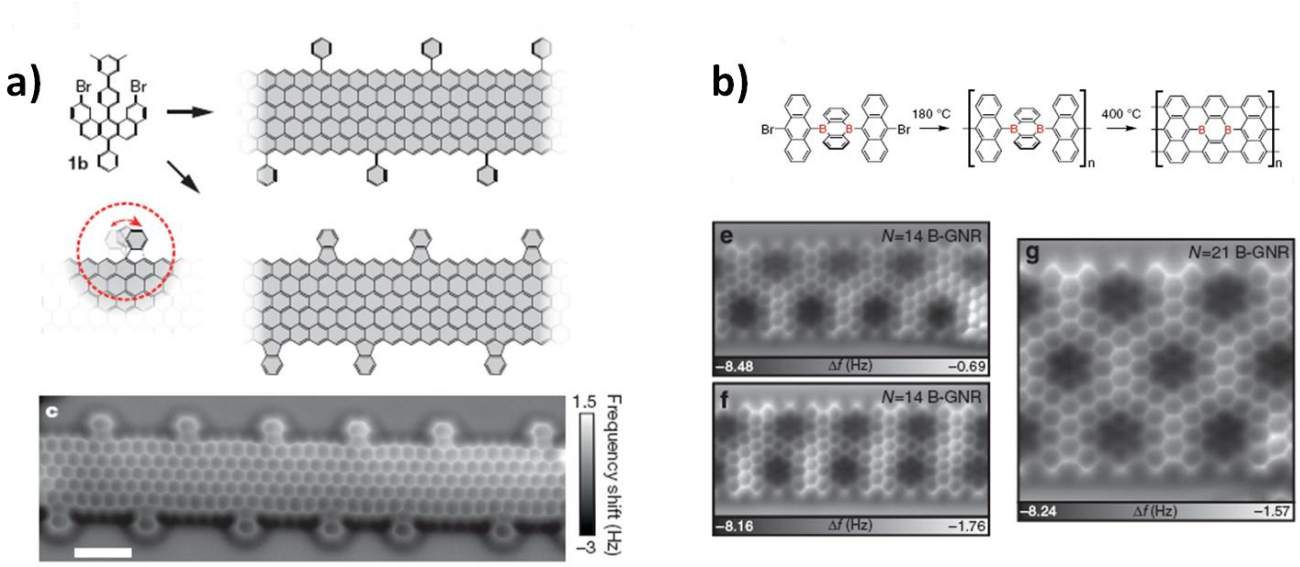

Fig. 8.5 Imatges de Microscopia de forces atòmiques (AFM de l'anglès) de GNRs preparades a partir de precursors moleculars amb **(a)** límits amb topologia zig-zag i **(b)** dopatge amb àtoms de B amb precisió atòmica.

És molt interessant veure que el STM (scanning tunnelling microscopy, de l'anglès) pot detectar la deficiència electrònica que els àtoms de B generen dins la xarxa covalent com esferes fosques en la imatge STM (Fig. 8.5b). Estudis preliminars indiquen el potencial d'aquestes GNRs com a portes lògiques[27] (és a dir, com a nano-transistors).

8.2 Metodología: La teoría del funcional de la densitat electrònica (DFT)

Aquesta tesi doctoral ha utilitzat principalment càlculs electrònics basats en la teoria del funcional de la densitat (o DFT, de l'anglès). El mètodes computacionals basats en l'esquema DFT són els més utilitzats dins de la comunitat de químics computacionals ja que genera resultats prou acurats en un temps relativament baix (és a dir, sense necessitar molt temps de càlcul en super-ordinadors). En aquesta secció introduiré breument l'enfocament DFT i les aproximacions corresponents utilitzades en aquesta tesi.

La idea fonamental del DFT és la utilització de la densitat de la probabilitat electrònica com a única variable per definir el Hamiltonià del nostre sistema d'electrons (dins d'un camp generat per una xarxa d'àtoms) i, per tant, la funció d'ona corresponent i qualsevol altra propietat mesurable d'aquesta (com l'espín total, per exemple). La densitat de probabilitat electrònica s'abreuja generalment com a densitat electrònica i té la següent forma matemàtica:

(1) $\rho(\vec{r}) = N \int \dots \int |\Psi(\vec{x}_1, \vec{x}_2, \dots, \vec{x}_N)|^2 \, d\vec{x}_1 d\vec{x}_2 \dots d\vec{x}_N$

on $\vec{x}_i$ són les posicions de cada electró i, i $\int \dots \int |\Psi(\vec{x}_1, \vec{x}_2, \dots, \vec{x}_N)|^2 \, d\vec{x}_1 d\vec{x}_2 \dots d\vec{x}_N$ es la funció de probabilitat de trobar cadascun d'aquests electrons a les posicions $d\vec{x}_i$, respectivament. La funció densitat $\rho(\vec{r})$ ha de complir unes condicions de contorn tal com que ha de valdre zero a una distància infinita del

sistema nuclear i que la seva integració a tot l'espai ha de ser igual al nombre total d'electrons del sistema, N.

Els primers intents per construir un funcional que connectés l'energia del nostre sistema amb la densitat electrònica, $\rho(\vec{r})$, data del 1927 i va ser proposada per Thomas i Fermi.[31,32] En la seva proposta, els autors proposaven tres termes energètics (tots ells en funció de la densitat electrònica) relacionats amb l'energia cinètica dels electrons del sistema, l'energia d'interacció atractiva d'aquests amb els nuclis del sistema, i l'energia d'interacció repulsiva entre electrons. Més tard, aquesta proposta es va complementar amb un altre terme, que relacionava la densitat electrònica amb el terme energètic degut a la interacció d'intercanvi entre electrons (anomenat exchange en anglès).[33,34]

Un pas molt important per l'èxit posterior de l'esquema DFT va ser l'estudi de Hohenberg i Kohn[35] on van demostrar per mitjà d'un raonament força senzill *ad absurdum* que la densitat electrònica de l'estat fonamental d'un sistema d'electrons determina de manera exclusiva el Hamiltonià del sistema i, en conseqüència, la funció d'ona corresponent, l'energia fonamental i totes les altres propietats. Això ho van poder demostrar provant que la densitat electrònica determina el potencial extern (és a dir, el potencial creat pels nuclis) el qual, al seu torn, determina el Hamiltonià. Matemàticament:

(2) $\rho_0 \Rightarrow V_{ext}\{N, Z_A, R_A\} \Rightarrow \widehat{H} \Rightarrow \Psi_0 \Rightarrow E_0$.

on ρ_0 és la densitat de l'estat fonamental del sistema, V_{ext} el potencial extern creat pels nuclis atòmics, $\widehat{H}$ és el Hamiltonià del sistema i Ψ_0 i E_0 son la funció d'ona i energia de l'estat fonamental, respectivament. En el mateix treball publicat per Hohenberg i Kohn[35] els autors també van proposar una manera de trobar la densitat electrònica de l'estat fonamental del sistema, ρ_0. La seva proposta estava basada en el mètode variacional, mètode matemàtic fonamental de la mecànica quàntica que diu que qualsevol funció d'ona que no sigui la funció d'ona exacta de l'estat fonamental del nostre sistema, en aplicar-li el Hamiltonià mitjançant l'equació de Schrödinger resultarà en una energia per sobre de l'energia fonamental exacta, E_0. Hohenberg i Kohn van demostrar que el principi variacional també s'aplica al funcional de la densitat electrònica: és a dir, l'energia que obtindrem del funcional només serà l'energia fonamental exacta, E_0, si la densitat utilitzada és la densitat fonamental exacta, ρ_0, altrament l'energia resultant serà per sobre de E_0. Matemàticament,

(3) $E_0 \leq E[\tilde{\rho}] = T[\tilde{\rho}] + E_{ee}[\tilde{\rho}] + E_{Ne}[\tilde{\rho}]$

on $E[\tilde{\rho}]$ és el funcional de densitat electrònica compost del terme cinètic, $T[\tilde{\rho}]$, el terme d'interacció electrònica, $E_{ee}[\tilde{\rho}]$, i el terme d'interacció entre electrons i nuclis, $E_{Ne}[\tilde{\rho}]$. D'aquesta manera, el que hauríem de fer seria minimitzar el funcional de densitat electrònica en funció de la densitat electrònica per trobar ρ_0 i E_0.

Tot i que pot semblar que l'estudi de Hohenberg i Kohn ofereix una ruta completa per poder utilitzar la densitat electrònica de manera exclusiva per trobar la funció d'ona de l'estat fonamental i totes les propietats associades, a la pràctica no és el cas. Això és així perquè el seu estudi no donava cap pista, o manera de trobar, la forma dels funcionals $T[\tilde{\rho}]$ i $E_{ee}[\tilde{\rho}]$ en l'equació 3. Sense saber la forma d'aquests funcionals respecte la densitat electrònica no es pot utilitzar el principi variacional per trobar ρ_0 i E_0. Això va canviar amb la contribució de Kohn i Sham[36] al 1965 on, sense entrar molt en detall, van demostrat que el funcional de l'energia cinètica $T[\tilde{\rho}]$ es podia calcular de manera exacta per un sistema d'electrons no interactius (és a dir, un sistema on els electrons no interaccionen entre ells com, per exemple, dins de l'esquema de Hartree-Fock) i la part romanent de l'energia cinètica exacta del nostre sistema d'electrons interactius es podria aproximar. D'aquesta manera, Kohn i Sham van definir el funcional universal, $E_{XC}[\rho]$, on contenia tots aquells paràmetres energètics dels quals no es coneix la seva dependència vers la densitat electrònica, ρ_0, tal com la part que no hem considerat de l'energia cinètica real del nostre sistema, el terme d'interacció d'intercanvi entre electrons i l'anomenada energia de correlació electrònica.

Sense entrar molt en detalls, s'ha d'esmentar que un dels objectius principals del DFT modern ha estat trobar millors i millors aproximacions del terme $E_{XC}[\rho]$. Per a tal empresa diferents enfocaments han estat aplicats al llarg del temps. Els més importants han estat l'aproximació de la densitat local (LDA de l'anglès),[33,34] l'aproximació general del gradient[37,38] (o GGA, de l'anglès) o els anomenats funcionals híbrids, on una part del terme energètic degut a l'intercanvi electrònic, E_X, es calcula de manera exacta dins de l'esquema Hartree-Fock.[39] Aquest últim tipus de funcionals (els híbrids), han estat força utilitzats en aquesta tesi doctoral. És el cas, per exemple, de l'anomenat PBE0,[40] el qual conté un 25% d' intercanvi exacte i com s'ha vist, és força apropiat per estudiar radicals orgànics amb sistemes π-conjugats.[41]

8.3 Simulació de dispositius basats en TAMs

Aquest capítol està relacionat amb els primers tres treballs d'aquesta tesi doctoral, els tres en col·laboració amb els grups experimentals dels Profs. Jaume Veciana i Concepció Rovira i de la Dr. Marta Mas-Torrent, de l'Institut de Ciència dels Materials de Barcelona (ICMAB). En els tres treballs s'estudia sistemes basats en molècules TAM amb propietats potencials per diferents tipus de dispositius electrònics. Els dos primer treballs, molt relacionats entre ells, estan centrats en la preparació de mono-capes auto-muntades sobre diferents superfícies metàl·liques on el centre radicalari dins dels TAMs es troba particularment a prop de la superfície metàl·lica, el qual podria donar lloc a propietats magnetoresistents (és a dir, interacció entre els electrons conductors del metall i el centre radicalari). El tercer treball es centra en l'estudi d'uns compostos de capa tancada (és a dir, no radicals) basats en TAMs hidrogenats units a una unitat d'etilè (és a dir: C=C) on s'observa un bloqueig de l'isòmer cis- no vist anteriorment. En aquest capítol introduiré de manera breu els tres treballs, explicant la rellevància de cadascun i,

posteriorment, resumiré els principals resultats. Informació detallada de cada treball es pot trobar al Capítol 3 d'aquesta tesi doctoral on els tres treballs són inclosos (dos publicats i un en format esborrany).

8.3.1 Síntesi de mono-capes auto-muntades radicals mitjançant molècules TAM de capa tancada.

Aquest primer treball es basa en un treball computacional publicat al 2012[42] on es va proposar el mecanisme electrònic representat en la Fig. 8.6. Com es pot veure, de manera computacional, mitjançant càlculs DFT, es va demostrar que enllaçant molècules de capa tancada quinoides amb una superfície metàl·lica, com or, genera una mono-capa radical[42] (r-SAM, de l'anglès) i, per tant, amb spín magnètic, com es mostra a la Fig. 8.6b.

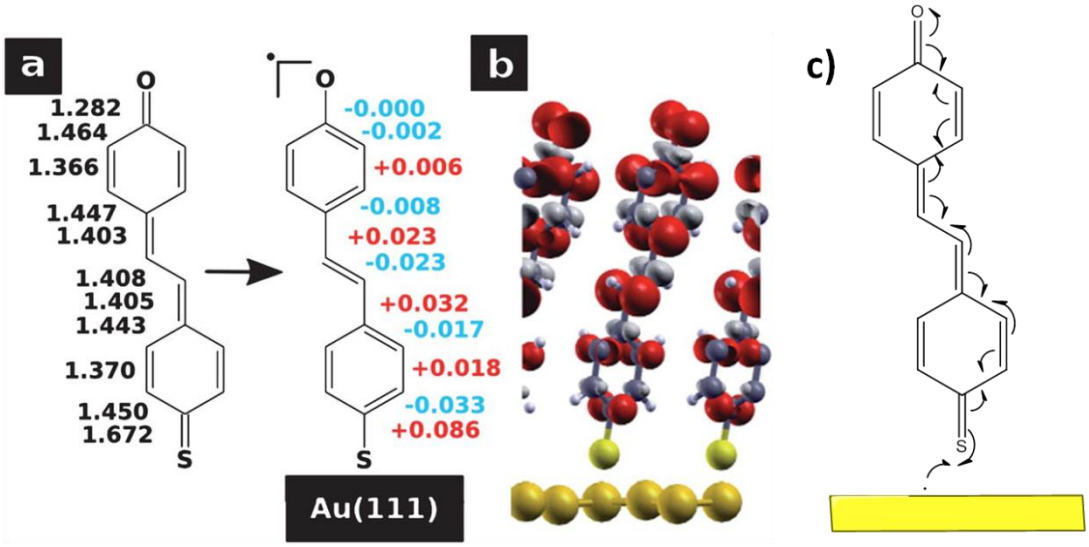

Fig. 8.6 a) Esquema general on, per mitjà d'una molècula de capa tancada quinoide es genera una mono-capa radical. **b)** Densitat d'espín electrònic de la mono-capa resultant en una superfície d'or, calculada dins de l'esquema DFT. **c)** Mecanisme electrònic que explica la generació de l'electró desaparellat en formar un enllaç covalent amb la superfície metàl·lica.

El mecanisme que explica la generació de l'electró desaparellat en formar l'enllaç covalent entre les molècules i la superfície es mostra en la Fig. 8.6c. Aquest mecanisme és molt interessant perquè, si es demostrés experimentalment, ofereix una manera de generar SAMs radicals, de força interès per aplicacions en electrònica i espintrònica,[43,44] utilitzant molècules de capa tancada (és a dir, no radicals) i per tant, a priori, menys reactives que les espècies radicals.

Tot i que la predicció de Rissner et al.[42] és de gran interès a nivell fonamental, manca potencial a nivell pràctic, donat que la mono-capa proposada en el seu treball no seria estable i, per tant, rarament aplicable en cap tipus de dispositiu. La principal raó és l'alta exposició de l'electró desaparellat generat en el mecanisme proposat en la Fig. 8.6, el qual podria reaccionar fàcilment amb espècies reactives del medi (com l'oxigen) o, fins i tot, amb la pròpia superfície metàl·lica.

En aquest treball hem testejat la utilització de les molècules TAM de capa tancada que es mostren en la Fig. 8.7 com a candidates per formar una SAM radical mitjançant el mecanisme mostrat en la Fig. 8.6.

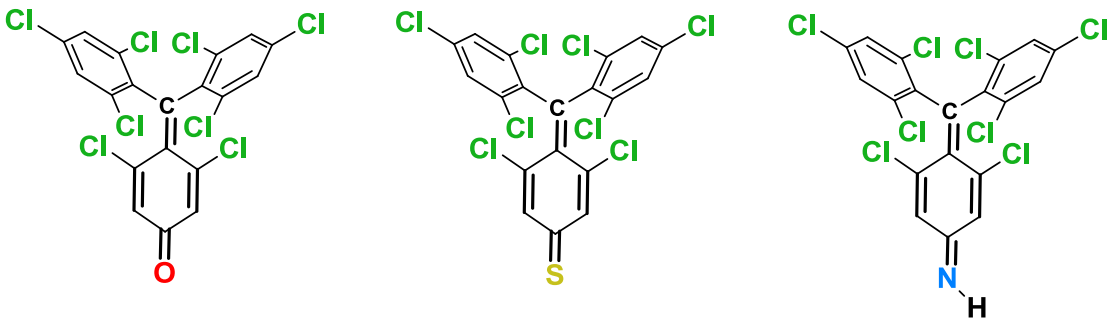

Fig. 8.7. Candidats moleculars proposats en aquest treball.

Com es veu en la figura, aquests candidats moleculars són TAMs modificats de manera que en l'anell aril inferior hi ha una configuració quinoide que, en cas de reaccionar el grup inferior amb una superfície metàl·lica, donaria lloc a la generació d'una SAM radical formada per molècules molt semblants a la família de compostos PTMs[45] (o perclorotriarilmetils). Els PTMs, com s'explicarà més endavant són radicals TAM persistents a causa de la protecció estèrica que els clors ofereixen al carboni central, on es troba l'electró desaparellat. En el cas dels compostos radicals que es generarien a partir de la utilització dels candidats moleculars mostrats a la Fig. 8.7, aquests també serien estables perquè els àtoms de clor de la molècula (en verd en la Fig. 8.7) protegirien de manera estèrica l'electró desaparellat.

Al treball **Publication-draft #1** presentat en aquesta tesi es mostra els resultats d'aquesta investigació fruit d'una col·laboració estreta entre els grups experimentals del ICMAB i del ICN2 (Institut Català de Nano-ciència i Nano-tecnologia) i la nostra contribució computacional. Aquest treball es troba en el format d'un esborrany on es mostren les conclusions de les diferents contribucions teòriques i experimentals. Inicialment es va veure que dels tres candidats moleculars mostrats a la Fig. 8.7 només el candidat basat en el grup oxo-carbonil (anomenat TTM-O) era suficientment estable com per ser aïllat. Els altres dos compostos dimeritzaven o es descomponien en condicions normals. Així doncs el TTM-O es va sublimar en condicions d'ultra-buit sobre una superfície d'Au, de Ag i de Cu. Abans i després de cada sublimació les superfícies es van determinar amb diferents tècniques de caracterització superficial tal com X-ray photo-electron spectroscopy (XPS) i angle-resolved ultraviolet photoemission spectroscopy (ARUPS). En paral·lel, càlculs periòdics basats en DFT (utilitzant el funcional PBE[38]) es van portar a terme per cada sistema molècula-superfície. Les mesures experimentals en superfície demostraven la formació d'electrons desaparellats en la SAM construïda sobre la superfície de Ag, i no en les superfícies d'Au i de Cu. Els nostres càlculs periòdics mostraven l'aparició de densitat d'espín per les SAMs sobre Ag i Cu on les molècules presenten una conformació vertical respecte el pla superficial. Pel cas del Cu, però, els càlculs també mostren una forta interacció amb les molècules adsorbides quan aquestes mostren una conformació plana respecte la superfície. Això està en acord amb les mesures experimentals de la SAM sobre Cu, que indicaven la pèrdua d'àtoms de clor sobre aquesta superfície i la posterior polimerització de molècules TTM, però no la formació d'una SAM radical (és a dir, amb electrons

desaparellats). Per tant, la conclusió general del treball **Publication-draft #1** és la demostració experimental de la predicció teòrica proposada per Rissner et al. al 2012: és a dir, es pot utilitzar molècules de capa tancada basades en TAM quinoides per formar la corresponent SAM radical. Tot i això, el nostre estudi també demostra que no totes les molècules TAM quinoides són viables, ja que no totes són estables experimentalment. A més, també demostrem que no totes les superfícies metàl·liques poden ser utilitzades per donar lloc al mecanisme electrònic mostrat a la Fig. 8.6 a partir del qual es genera l'electró desaparellat. Un cert grau de reactivitat per part de la superfície és necessari i, en el nostre cas particular, sembla que la superfície de Ag és la més adequada.

8.3.2 Enllaç directe entre un radical orgànic sobre or i plata

El compost thio-carbonil mostrat a la Fig. 8.7 (compost central en la figura, TTM-S) es va trobar que dimeritza en solució donant lloc al corresponent compost bi-radical com es mostra en la Fig. 8.8.

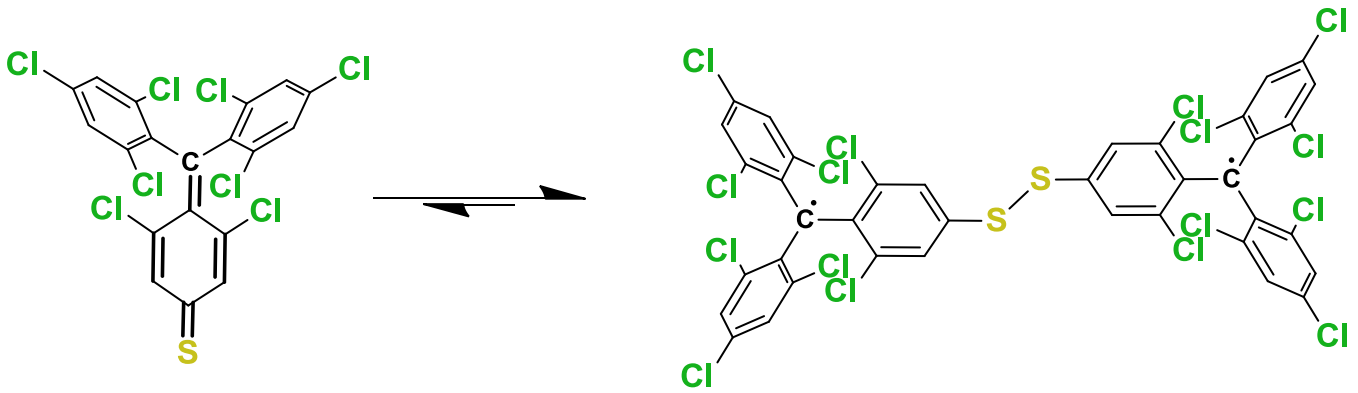

Fig. 8.8 Procés de dimerització del compost quinoide TTM-S en solució generant el corresponent bi-radical.

Aquest tipus de compostos amb enllaços di-thiol es poden utilitzar per formar les SAMs corresponents sobre superfícies d'or, ja que l'enllaç S-S es trenca per formar dos enllaços S-Au. Mitjançant aquesta ruta, prèviament es va sintetitzar SAMs basades en radicals PTMs utilitzats com a interruptors electro-actius.[46] Per tant, el bi-radical mostrat a la Fig. 8.8 es podria utilitzar per formar la SAM dels monòmers corresponents. Aquestes SAMs però, tindrien la particularitat que la unitat TTM estaria directament enllaçada amb la superfície metàl·lica. Normalment, com es representa en la Fig. 8.9 (part esquerra), les SAMs basades en PTMs tenen una cadena alquílica o aromàtica que separa el cor radical del grup que reacciona amb la superfície, aconseguint així separar físicament el cor radical dels electrons metàl·lics (evitant així possibles reaccions amb l'electró desaparellat). En el cas d'utilitzar el bi-radical representat en la Fig. 8.8, com es pot entendre, la unitat radical TTM serà directament enllaçada amb la superfície metàl·lica, com es representa a la part dreta de la Fig. 8.9. En aquest cas es podria esperar una reacció entre l'electró desaparellat de la unitat TTM i els electrons metàl·lics, per la gran proximitat entre ells. Malgrat això, en el cas que tal reacció no tingués lloc i la SAM radical fos estable, es podrien esperar fenòmens interessants com, per exemple, la interacció magnètica entre l'electró desaparellat de la monocapa TTM i els electrons conductors metàl·lics.[43] Tal interacció ja s'ha demostrat per corrents

elèctrics a través de molècules TAM situades entre dos elèctrodes d'or, donant lloc al conegut efecte de Kondo.[14]

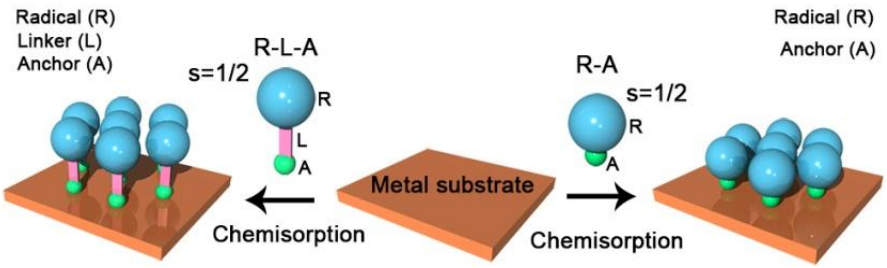

Fig. 8.9 Diferents possibles SAMs en superfícies metàl·liques. En l'esquema de l' esquerra es mostra la formació de SAMs on el radical (esfera blava) es troba separat físicament de la superfície per mitjà d'un grup linker (rosa). En el nostre cas, el cap radical està directament enllaçat a la superfície metàl·lica (esquema de la dreta).

En el treball **Publication #2**, la molècula bi-radical TTM-S-S-TTM (veure estructura a la Fig. 8.8) va ser utilitzada per funcionalitzar una superfície d' Au i d' Ag mitjançant processos de formació de SAMs en solució (veure **Publication #2** per detalls). Les superfícies es van caracteritzar mitjançant XPS, UPS i EPR. Les tres tècniques van corroborar la formació de la SAM i de la presència d'electrons desaparellats en la mono-capa orgànica. Mesures de voltametria cíclica (CV de l'anglès) també van corroborar la naturalesa electro-activa de la SAM, típica dels TAMs radicals.[13] Els nostres càlculs periòdics DFT també van corroborar la persistència de densitat d'espín a la SAM de TTM-S. La densitat d'espín es trobava localitzada a la unitat TTM, però vam observar una certa polarització d'espín a la superfície metàl·lica, que podria ser indicatiu d'efectes magnetoresistents. Concloent, al treball **Publication #2** hem demostrat la possibilitat de formar SAMs radicals on el cor radical es troba directament enllaçat a la superfície metàl·lica. Això, com els nostres resultats indiquen, no comporta la reacció entre l'electró desaparellat i els electrons conductors del metall. Aquests sistemes, com s'ha explicat anteriorment, mostren un cert potencial per aplicacions en espintrònica molecular.[43]

8.3.3 Estudi de la isomerització E-Z en compostos de H-PTM amb unitats d'etilè

Els compostos basats en la unitat molecular etilè (C=C) poden mostrar la coneguda isomerització E-Z, com es mostra a la Fig. 8.10 per l'estilbè. Aquest tipus d'isomerització s'ha d'activar amb llum o amb productes químics,[47] com el iode, ja que no té lloc de manera espontània, fins i tot a temperatures elevades. Això és així perquè per tenir lloc la isomerització la molècula ha de passar a través d'un estat de transició on el doble-enllaç C=C es trenca donant lloc a l'estat bi-radical, com es mostra a la Fig. 8.10b. Aquest mecanisme que involucra el gir sobre l'eix de l'enllaç C=C ha estat proposat teòricament com el mecanisme més probable connectant ambdós confòrmers.[48]

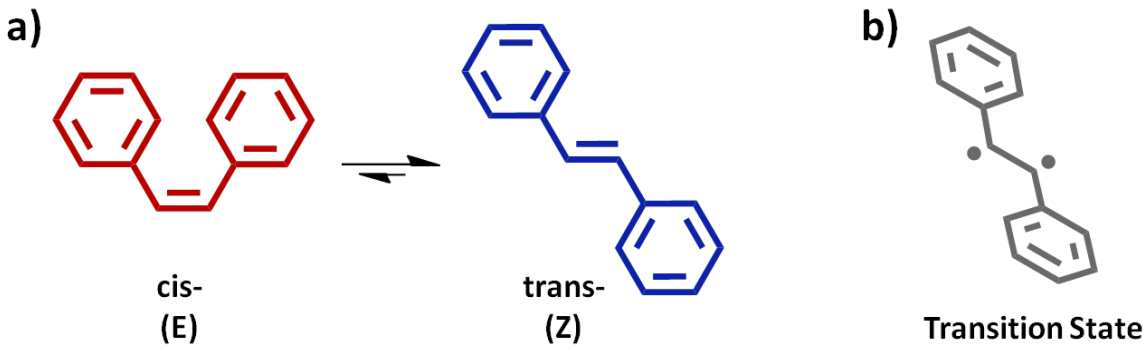

Fig. 8.10 a) Equilibri de foto-isomerització entre el confòrmer E (trans-) i Z (cis-) en l'estilbè. **b)** Estat de transició bi-radical connectant ambdós isòmers en el punt quan l'enllaç C=C és rotat 90 graus.

Aquest estat bi-radical, a més, es troba aproximadament 2 eV[48] per sobre de l'energia de cada isòmer, el qual explica perquè la isomerització ha de ser catalitzada amb llum o reactius químics. Per tant, en condicions fosques, cada isòmer es mantindrà estable sense inter-convertir a l'altre. En condicions lumíniques, l'equilibri entre els dos, com s'ha representat a la Fig. 8.10a, tindrà lloc. En aquest últim cas les energies de cada confòrmer respecte de l'altre determinaran la proporció de cada isòmer. Això s'ha demostrat depèn moltíssim de la funcionalització química particular del compost.[49]

Els sistemes basats en la versió hidrogenada dels PTMs (i per tant de capa tancada) funcionalitzats amb una unitat d'etilè-fenil estudiats en el treball **Publication #3** estan representats a la Fig. 8.11.

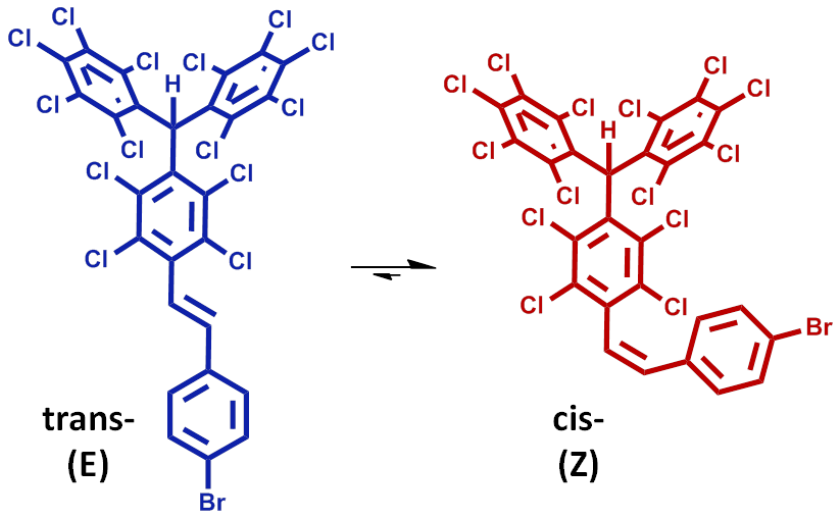

Fig. 8.11 Procés de la foto-isomerització E↔Z en el compostos H-PTM-etilè sintetitzats en el grup del Prof Jaume Veciana, on l'equilibri es troba completament desplaçat l'isòmer Z (cis-; estructura en vermell a mà dreta).

Ambdós compostos (el funcionalitzat amb un àtom de Br- l'anell fenil, a la Fig. 8.11, i el corresponent anàleg amb un grup thio-acetat a la mateixa posició) es van sintetitzar donant lloc al confòrmer E (trans-) en un percentatge al voltant del 90%. El confòrmer E es va separar del restant confòrmer Z i, un cop aïllat, es va estudiar la corresponent foto-isomerització al confòrmer Z. Irradiant amb llum, el confòrmer

E de cada compost es va observar una foto-isomerització completa al confòrmer Z. Un cop purificat el confòrmer resultant (Z), es va tornar a irradiar amb llum per tornar a isomeritzar i regenerar l'isòmer E (més estable termodinàmicament). Es va trobar, però, que el confòrmer Z no es veia afectat per la llum i la isomerització Z → E no tenia lloc. Es va intentar realitzar la isomerització a diferents temperatures sense èxit. Finalment, es van tractar els compostos Z amb iode, procés estàndard per realitzar aquest tipus d'isomeritzacions. De nou, no es va detectar cap transició de l'isòmer Z al E.

La nostra contribució al treball **Publication #3** va ser l'aportació d'una hipòtesi basada en els nostres càlculs computacionals per explicar els resultats experimentals no esperats. Es van realitzar dinàmiques moleculars per ambdós compostos de PTM hidrogenat i per l'estilbè, utilitzat com a compost de referència. En aquestes dinàmiques moleculars dins de l'esquema DFT vam observar que ambdós compostos estudiats mostraven una conformació més bloquejada en el confòrmer Z. Aquest bloqueig es donava pel contacte entre la unitat de PTM i l'anell fenil connectats a través del grup etilè C=C i causava que ambdós grups no tinguessin la llibertat de rotació que en canvi mostraven en el confòrmer E. Per mitjà de càlculs a 0K on vam rotar l'enllaç C=C "a mà", vam observar que certes conformacions dels grups PTM i fenil no permetien el gir de l'enllaç C=C, necessari per realitzar la isomerització, ja que els dos grups es trobaven físicament durant el procés de gir. Per tant, certes conformacions dels grups PTM i fenil eren necessàries per permetre la isomerització. Així doncs, la hipòtesi aportada a partir dels resultats computacionals obtinguts és que en el confòrmer Z la falta de rotació dels grups PTM i fenil no permet que s'accedeixi a les conformacions d'aquests grups que permeten el gir de l'enllaç C=C. En conseqüència, tot i activant l'enllaç C=C per mitjà de llum o reactius químics, el gir no pot tenir lloc ja que en el procés el grup PTM i fenil es troben i causen un bloqueig del confòrmer Z de tipus estèric.

Aquesta hipòtesi, tot i la seva complexitat, explica de manera adequada els resultats experimentals obtinguts en aquest treball (**Publication #3**).

8.4 Del gir dels anells aril als TAM 2D-COFs

8.4.1 Què controla l'electró desaparellat en els TAMs?

Com ja s'ha explicat a la introducció d'aquest capítol, pràcticament totes les propietats dels TAMs interessants per diverses aplicacions dins dels camps del magnetisme i electrònica molecular estan directament relacionats amb l'electró desaparellat existent en aquestes molècules. Així doncs, el magnetisme[12] que s'ha vist en certs materials basats en TAM, com xarxes metall-orgàniques o plàstics magnètics (Fig. 8.12a,d), emergeix a causa de l'espín magnètic de l'electró desaparellat. També, el color dels TAMs (és a dir, absorció de llum visible) i la seva fluorescència (emissió de llum visible) es donen per transicions electròniques que involucren els orbitals semi-ocupats/desocupats (SOMO i SUMO, respectivament, de l'anglès) associats a l'electró desaparellat. A més, aquestes propietats òptiques

depenen de l'estat redox de la molècula, la qual cosa va permetre construir un interruptor basat en una SAM de PTMs[13] (Fig. 8.12b) sobre una superfície conductora i transparent d'òxid d'indi i estany (ITO de l'anglès). Finalment també s'ha demostrat en un dispositiu mono-molecular[14] que la conducció d'electrons a través d'una molècula TAM té lloc per mitjà de l'orbital SUMO, associat a l'electró desaparellat (Fig. 8.12c).

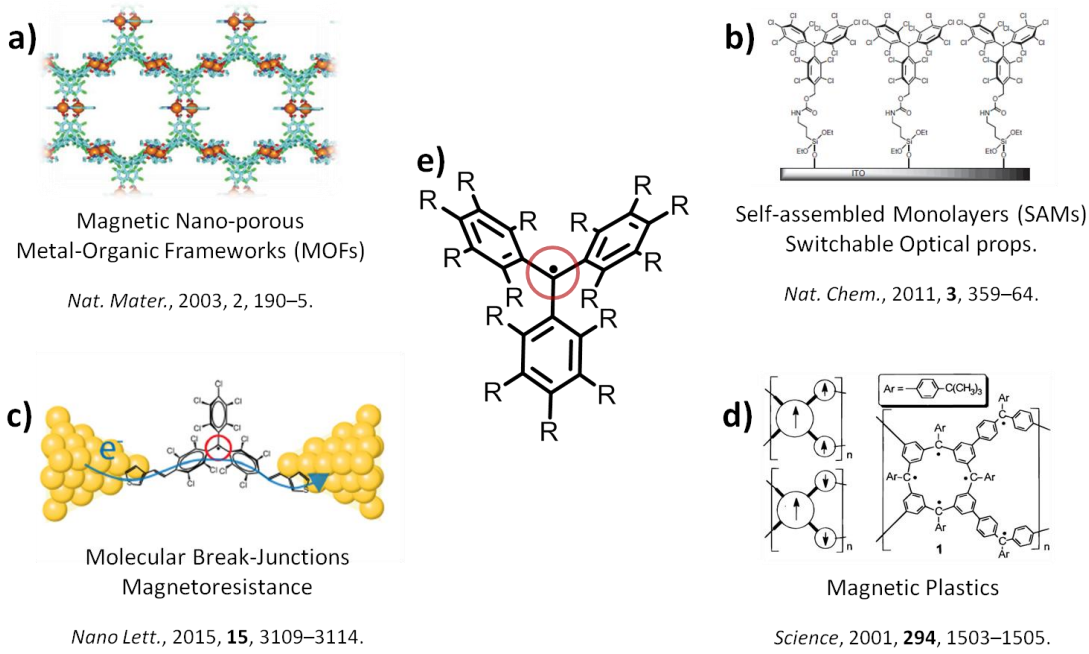

Fig. 8.12 Utilització dels TAMs en diferents tipus de materials i dispositius.

Optimitzant l'estructura del trifenilmetil (o TPM, de l'anglès), el més simple de tots els TAMs, dins de l'esquema DFT (utilitzant el funcional PBE[38] dins del Gaussian09[50]) la distribució de l'espín en el canal α ens permet tenir una idea de la distribució electrònica de l'electró desaparellat. Com es pot veure en la Fig. 8.13a la densitat d'espín- α (en verd) no està totalment localitzada en el carboni central sinó que es troba parcialment deslocalitzada en els tres anells aril.

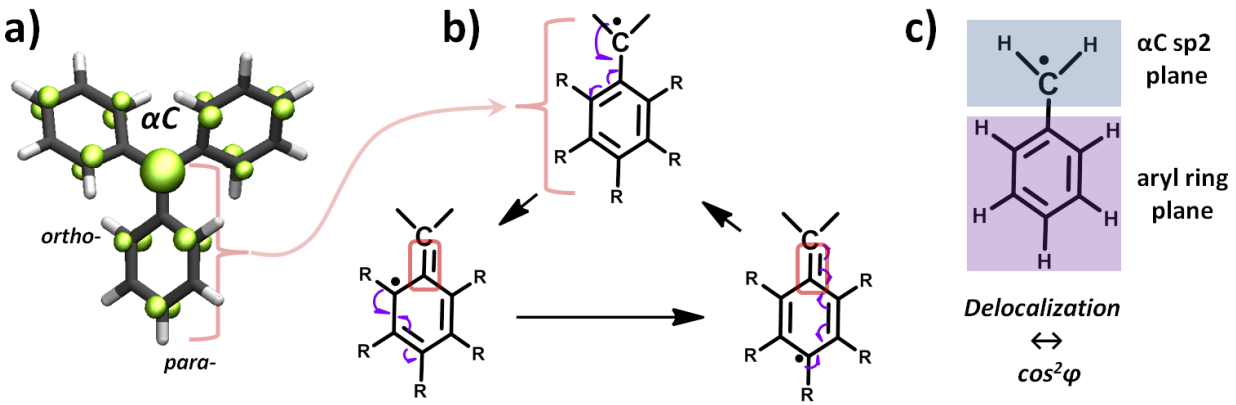

Fig. 8.13 a) Estructura del TPM amb la densitat d'espín-α associada a l'electró desaparellat en verd. **b)** Formes ressonants de Lewis que ajuden a entendre el mecanisme de deslocalització de l'electró desaparellat. **c)** Plans moleculars que defineixen l'angle de gir que determina la localització/deslocalització de l'electró desaparellat en el radical fenil-metil (també conegut com radical benzil).

Escriure les formes ressonants de l'electró desaparellat per un anell aril particular (Fig. 8.13b) ajuda a entendre el mecanisme de deslocalització d'aquest electró. Així podem veure com l'electró desaparellat es pot trobar a les posicions ortho- i para- de cada anell, el qual és confirmat amb la densitat d'espín mostrada a la Fig. 8.13a (en verd). Per tant, les formes ressonants de Lewis expliquen de manera adequada el mecanisme de deslocalització de l'electró desaparellat en les molècules TAM. Mirant amb més detall cada forma ressonant, es pot veure que quan l'electró desaparellat es troba en un anell determinat, la formació d'un doble enllaç entre l'anell particular i el carboni central (anomenat αC) és necessari (rectangles vermells en la Fig. 8.13b). Això, al seu torn, fa que l'angle de gir entre el pla del carboni central, αC, i el pla de l'anell aril, suposadament, hauria de poder controlar la localització/deslocalització de l'electró desaparellat. Això és així perquè en girar els dos plans cap a conformacions perpendiculars entre ells, evita la formació del doble enllaç i, en conseqüència segons el mecanisme de deslocalització mostrat a la Fig. 8.13b, també la deslocalització de l'electró desaparellat. Aquesta correlació electrònica-estructural ja es va demostrar entre els anys 50 i 60 pel radical fenil-metil[51–54], on es va trobar una correlació entre ambdues variables proporcional a $cos^2\varphi$ on φ és l'angle de gir entre els dos plans.

Si tal correlació entre el gir dels anells aril i la localització/deslocalització de l'electró desaparellat existís en els TAMs, podria representar una eina molt útil per controlar totes les propietats relacionades amb potencial tecnològic tal com el color, l'spin magnètic o la conducció. L'objectiu del treball **Publication #4** ha estat avaluar aquesta relació electrònica-estructural en les molècules TAM. Així doncs, en aquest treball hem demostrat que la localització d'espín (i per tant de l'electró desaparellat) en les molècules TAM segueix una correlació lineal amb el $\langle cos^2\varphi_i \rangle$, on φ_i és l'angle de gir de cada anell aril respecte del pla sp^2 del carboni central, αC. Estudiant un conjunt de TAMs amb diverses funcionalitzacions químiques vam comprovar que la correlació electrònica-estructural és independent de la naturalesa electro-donant o electro-atraient dels grups funcionals en els anells aril. Per tant, la funcionalització química determinada només afecta la localització de l'electró desaparellat en tant que determina el gir dels tres anells aril per mitjà d'efectes estèrics. Finalment, en el **Publication #4**, per mitjà de dinàmiques moleculars dins l'esquema DFT (AIMD de l'anglès) també demostrem que la correlació entre la localització de l'espín i $\langle cos^2\varphi_i \rangle$ és robusta a temperatures finites (e.g. 300K). Això significa que aquesta correlació en les molècules TAM es pot utilitzar a temperatura ambient per aplicacions.

8.4.2 Hi ha alguna manera de manipular externament el gir dels anells aril?

El gir dels anells aril ve determinat principalment per la seva funcionalització química. Això es mostra en el nostre treball anteriorment esmentat (**Publication** #4), però ja s'havia proposat a principis del segle XX per a les molècules TAM.[55] Aquesta correlació entre la funcionalització química i el gir entre anells aril també va ser utilitzada al 2006 per demostrar la correlació entre l'angle de gir entre dos anells aril i la

conducció a través de la molècula fent mesures de conductivitat en una sèrie de molècules bi-aril (veure Fig. 8.14).

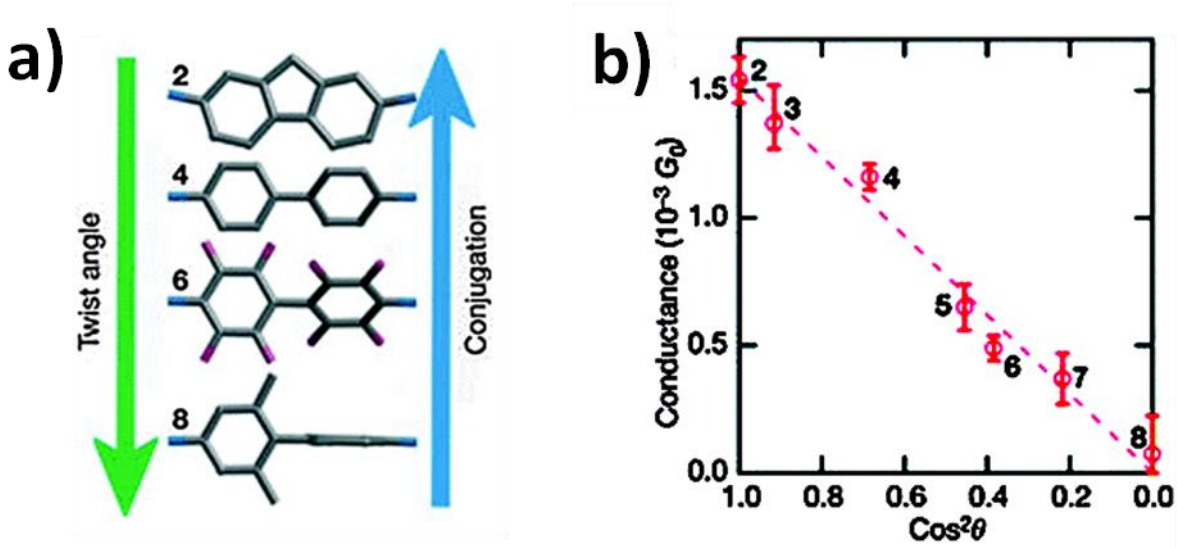

Fig. 8.14 a) Sèrie de compostos bi-aril estudiats al 2006 com cables conductors mono-moleculars. **b)** Conductivitat elèctrica front el cosinus al quadrat de l'angle de gir entre els dos anells aril dins de cada molècula.

Aquesta correlació entre la funcionalització química i els anells aril és important perquè implica que, en sistemes basats en TAMs, les propietats corresponents es poden determinar per mitjà d'un disseny químic específic. Malgrat això, la funcionalització química no ens permet controlar de manera externa el gir de l'angle, ja que, donat un disseny químic del nostre sistema, aquest no es pot modificar de manera externa, ràpida i reproduïble.

En el treball **Publication #5** hem buscat la manera de dissenyar un sistema basats en TAMs on es pugui manipular de manera externa l'angle de gir dels anells aril. Amb aquest objectiu, hem trobat que l'única plataforma on aquesta manipulació externa seria possible és en xarxes covalents 2D (o 2D-COFs de l'anglès) basades en unitats TAM. Com es mostra en el treball **Publication #5** els TAM 2D-COFs dissenyats són materials plans on cada electró desaparellat es troba localitzat en la unitat TAM corresponent. Aquests materials són aïllants elèctrics amb una tendència feble a tenir els electrons desaparellats ferro-magnèticament acoblats. Com demostrem en aquest treball, estirant en una direcció el material 2D s'aconsegueix girar tots els anells aril de la xarxa de manera ordenada i controlada. Aquest gir, en total acord amb els resultats mostrats l'anterior **Publication #4**, produeix una localització de tots els electrons desaparellats de la xarxa. Això, al seu torn, produeix uns canvis molt importants tant en les interaccions magnètiques dins del material com al forat de bandes d'aquest (d'ara endavant anomenat band gap, de l'anglès), característiques que mostren una correlació lineal amb el $\langle cos^2\varphi_i \rangle$, on φ_i és l'angle de gir de cadascun dels anells aril dins de la cel·la periòdica del TAM 2D-COF. Per tant, en aquest treball, hem pogut demostrar que la correlació electrònica-estructural existent en les molècules TAM es pot utilitzar per dissenyar materials basats en TAMs amb propietats fonamentals molt controlables per

mitjans externs, com l'estirament mono-direccional.

8.4.3 Es pot tenir estabilitat dels monòmers radicals i flexibilitat en el gir dels anells aril?

Com ja s'ha explicat a la introducció d'aquest capítol, els anells perclorats en els TAMs són necessaris per garantir l'estabilitat del centre radicalari, a causa d'una protecció estèrica que no permet la penetració de cap agent químic reactiu (com l'oxigen) que pugui reaccionar amb l'electró desaparellat. Com vam també explicar en el treball anterior, **Publication #5**, vam dissenyar dos TAM 2D-COFs, un basat en el TPM (on els anells estan hidrogenats) i un basat en els PTM (amb els anells clorats), com es mostra a la Fig. 8.15. El que vam observar és que, en estirar el material, només en el TPM 2D-COF és generava un gir dels anells aril important. Així doncs, per mitjà de dinàmiques moleculars a 300K, vam comprovar que l'efecte estructural en la xarxa PTM 2D-COF no era suficient (és a dir, el gir dels anells aril) com per generar un canvi en les propietats estudiades detectable a temperatura ambient.

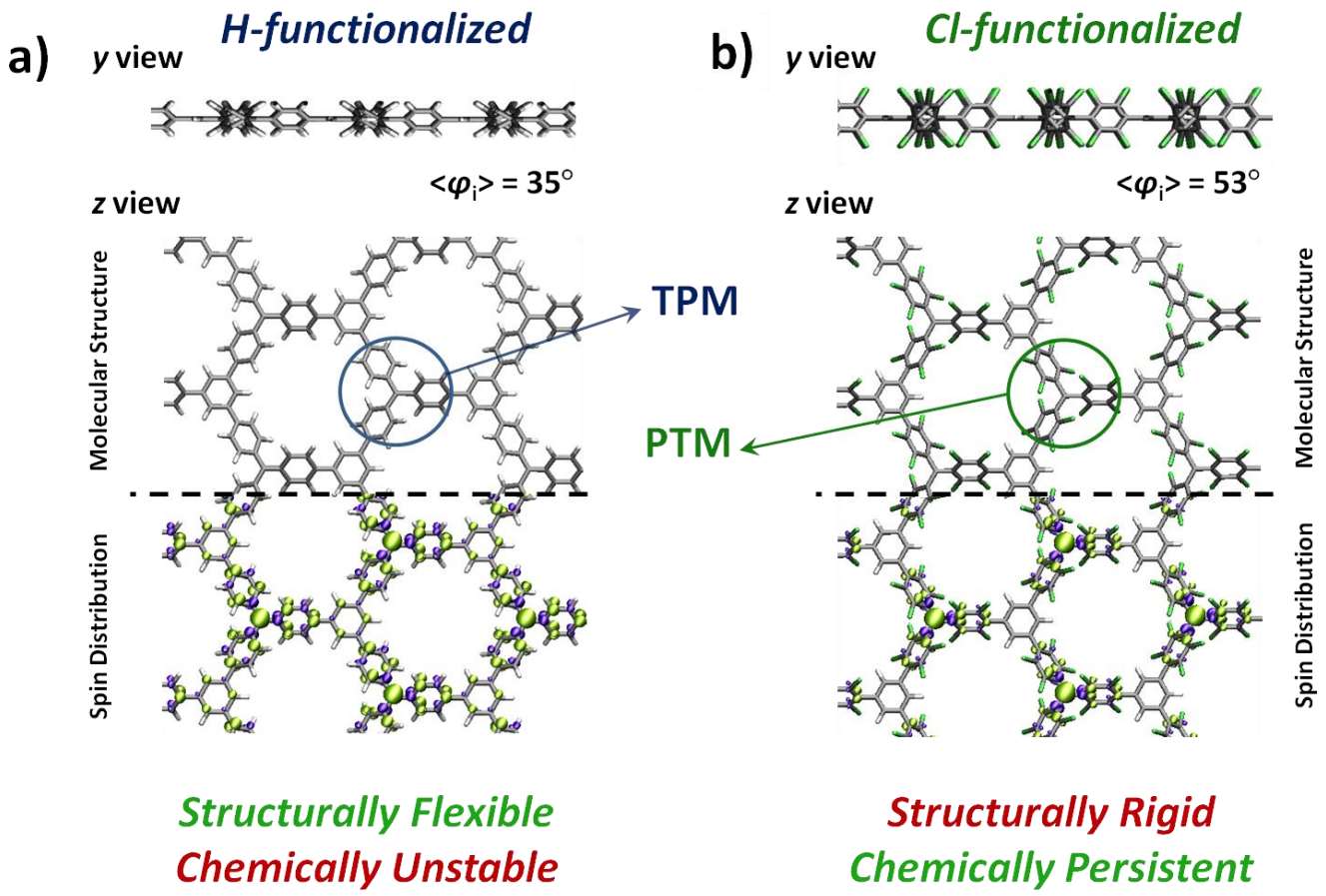

Fig. 8.15 TPM **(a)** i PTM **(b)** 2D-COFs vistos desde l'eix *y* i *z*, mostrant també la densitat d'espín associada en els panells inferiors (verd: α; púrpura: β).

Així doncs en el treball **Publication #6** hem intentat resoldre aquesta qüestió testejant tota una sèrie de funcionalitzacions dels monòmers TAM utilitzats per construir les xarxes covalents i estirant aquestes xarxes per avaluar la capacitat de gir de cada cas. Ens hem centrat en funcionalitzacions basades en la sèrie d'àtoms halogenats, incloent l'hidrogen com a referència (és a dir, H-, Cl-, Br- i I-), ja que els TAMs

funcionalitzats amb aquesta sèrie d'àtoms són els més estables químicament.[45,56] En l'estudi **Publication** #6 hem considerat tant funcionalitzacions completes dels tres anells aril amb un únic tipus d'àtom, com funcionalitzacions parcials combinant dos tipus d'elements (H- i Cl- or Cl- i F-, per exemple). Així, dissenyant 50 TAM 2D-COFs diferents i estirant cada estructura mono-direccionalment en 35 punts diferents d'estirament, hem hagut de realitzar un total de 1750 càlculs periòdics en aquest estudi. Òbviament aquest nombre de càlculs no es podia realitzar dins de l'esquema DFT i llavors hem utilitzat camps de forces (o FFs, de l'anglés) que, per estudiar la estructura atòmica d'aquests materials aporten una bona relació entre exactitud i cost computacional. D'aquesta manera hem pogut trobar tota una sèrie de xarxes formades per TAMs que han estat sintetitzats al laboratori mostrant una certa persistència química on es pot causar un gir dels anells aril important en estirar el material en una direcció. A més, amb càlculs DFT realitzats en les xarxes més prometedores, hem comprovat que aquest gir dóna lloc a canvis electrònics detectables. Per tant, la conclusió general del **Publication #6** és que hi ha molècules TAM informades a la literatura que es podrien utilitzar per construir xarxes covalents 2D amb propietats molt controlables per mitjans externs (com un estirant mono-direccional).

8.5 TAMs connectats en para-: Cap a semimetalls 2D

8.5.1 Connectant radicals orgànics π-conjugats: meta- vs. para-

Com sabem gràcies a la química bàsica de sistemes orgànics π-conjugats, múltiples centres radicals π-conjugats es poden connectar essencialment de dues maneres: en meta- o en para-. Aquestes dues opcions estan representades a la Fig. 8.16.

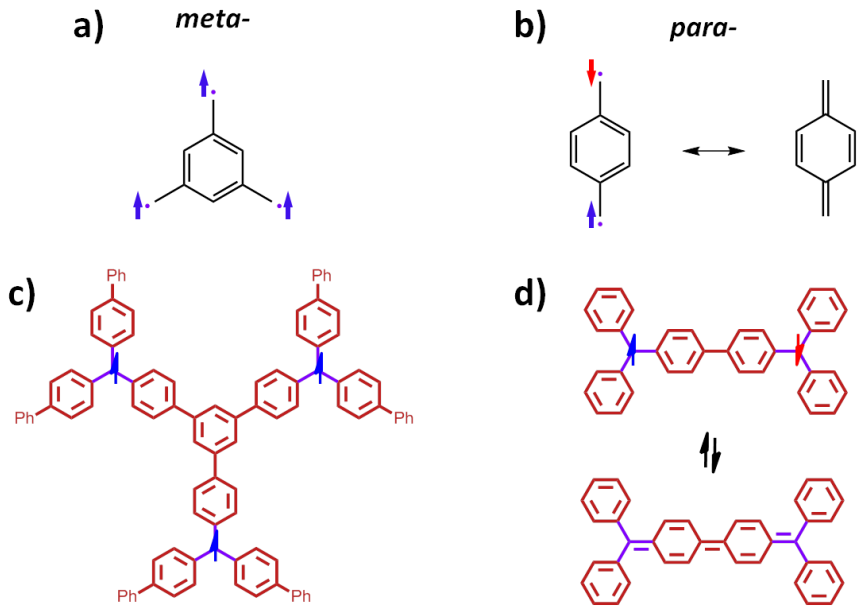

Fig. 8.16 Connectivitats *meta-* **(a)** i *para-* **(b)** entre carbonis radicals (en color púrpura) en sistemes orgànics π-conjugats. **c)** i **d)** mostren l'estructura de tri-/bi-radicals experimentalment sintetitzats basats en unitats TAM amb connexions *meta-* i *para-* entre els centres radicalaris, respectivament. Per als casos para- (columna dreta) dues formes ressonants de Lewis són possibles.

Com es representa en la Fig. 8.16, s'ha comprovat experimentalment que connectant centre radicalaris a través d'un sistema π-conjugats en meta- un respecte de l'altre, els electrons desaparellats corresponents es mantenen localitzats i mostren una interacció lleugerament ferro-magnètica,[3,57] com és representat a la Fig. 8.16a,c. En canvi, quan els centres radicalaris es connecten en para- un respecte l'altre, com en el cas del bi-radical anomenat hidrocarbur de Chichibabin[58] (Fig. 8.16d), els electrons desaparellats es troben anti-ferromagnèticament acoblats però, a més, també es poden aparellar donant lloc a una configuració de capa tancada quinoidal[59] (Fig. 8.16b,d).

8.5.2 Compostos de valència mixta: cap a l'electrònica orgànica.

Què passa amb cadascun dels exemples mostrats anteriorment quan es redueix un dels centres radicals a l'estat redox -1 (és a dir, l'anió). En tal situació, el bi-radical esdevé un compost mono-radical on cada extrem de la molècula conté un nombre diferent d'electrons de valència. Per aquesta raó, aquest tipus de sistemes s'anomenen compostos de valència mixta (o MVC, de l'anglès). MVC s'han preparat basats en dos unitats PTM unides per diferents ponts π-conjugats[60–62] on s'ha detectat la transferència de la càrrega negativa entre les dues unitats PTM (veure Fig. 8.17). És a dir, la càrrega negativa no està localitzada en una unitat PTM, sinó que pot "saltar" entre les dues unitats.

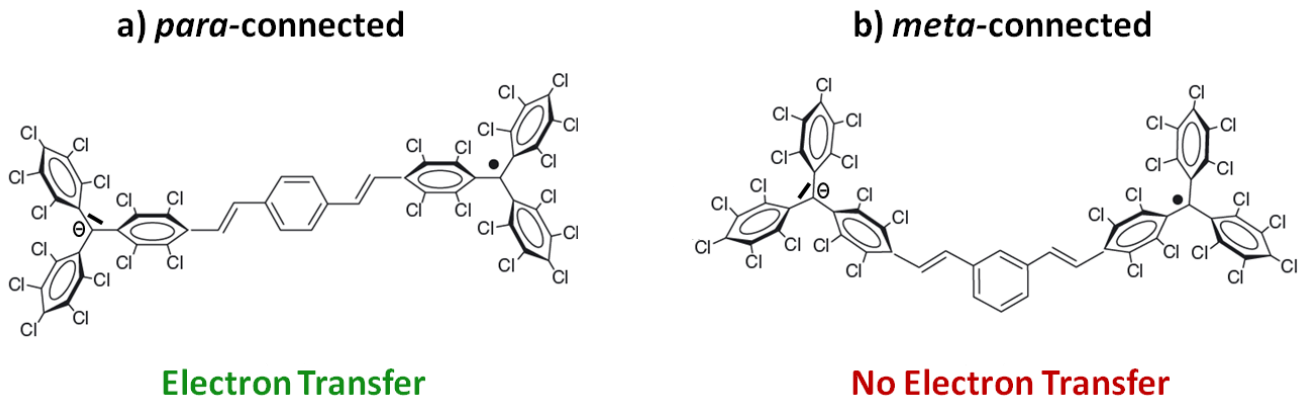

Fig. 8.17 MVC basats en unitats PTM connectats en **a)** *para*- i **b)** *meta*- on una de les unitats PTM conté un electró desaparellat i l'altre un parell d'electrons associats a la càrrega negativa del compost.

És força interessant el fet que depenent de com les dues unitats de PTM estiguin connectades, la càrrega negativa tindrà, o no, la capacitat de "saltar" entre les dues unitats, el que s'anomena transferència de càrrega dins del compost MVC. Així doncs, s'ha vist experimentalment que MVC-PTM connectats en meta- (Fig. 8.17b) mostren la càrrega negativa localitzada en un dels PTMs i, en canvi, MVC-PTM connectats en para- (Fig. 8.17a) mostren la transferència de càrrega, demostrat amb diferents tècniques espectroscòpiques tal com absorció en el UV-visible o ressonància electrònica paramagnètica (EPR, de l'anglès).[60,61]

8.5.3 Quin és el mecanisme de transferència de càrrega en compostos para-MVC-PTM?

Gràcies a la gran estabilitat dels PTMs i la facilitat per reduir-los a l'estat negatiu, s'ha pogut estudiar amb detall el comportament de MVC basats en aquests radicals orgànics.[63–66] En els estudis més recents s'ha proposat principalment dos mecanismes electrònics diferents per explicar el procés de transferència de càrrega: els anomenats túnel electrònic i salts de càrrega (o tunneling i charge hopping, en anglès). La Fig. 8.18 representa cadascun d'aquests mecanismes.

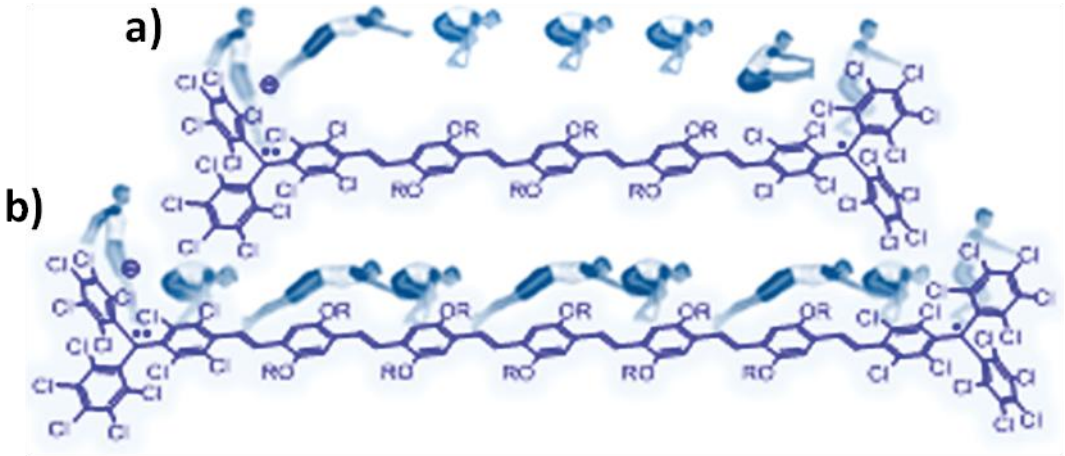

Fig. 8.18 a) En el mecanisme de túnel els electrons no interaccionen amb el pont π-conjugat, saltant directament d'una unitat de PTM a l'altra. **b)** En el mecanisme de salts de càrrega, la càrrega negativa viatja d'una unitat de PTM a l'altra, passant abans per cadascuna de les unitats del pont i, per tant, es pot arribar a detectar la càrrega localitzada al pont (el que s'anomena polaró).

Com es veu a la Fig. 8.18a, el mecanisme túnel explica la transferència de càrrega com salts de la càrrega negativa directament d'un PTM l'altre, sense interaccionar amb el pont π-conjugat. Aquest mecanisme està directament relacionat amb l'efecte túnel explicat dins del camp de la mecànica quàntica. El mecanisme de salts de càrrega (Fig. 8.18b) explica la transferència de càrrega mitjançant salts de càrrega puntuals a través de cadascuna de les unitats moleculars que componen el pont π-conjugat. Així doncs, en aquest segon mecanisme, la càrrega negativa dins del MVC-PTM es pot trobar localitzada en el pont π-conjugat en un moment determinat, el que s'anomena polaró.[62] El mecanisme túnel s'ha assignat als MVC-PTM on el pont és de curta longitud, i el mecanisme de salts de càrrega als de pont de llarga longitud.[62]

Durant aquesta tesi doctoral he participat en l'estudi d'una sèrie de compostos MVC-PTM on les unitats PTM estan connectades per mitjà d'un pont de tiofè-vinil (TV), com es representa en la Fig. 8.19. Com es demostra en aquest treball, **Publication** #7, mitjançant diferents tècniques espectrocòpiques (com les esmentades anteriorment), afegint en aquest cas l'espectroscòpia Raman, per als MVC-PTM amb ponts llargs el mecanisme de transferència de càrrega entre els dos PTMs es basa en l'anteriorment explicat salts de càrrega. Per als compostos curts, però, els nostres càlculs basats en l'esquema DFT apuntaven a

un mecanisme diferent al mecanisme túnel proposat en treballs anteriors.[62]

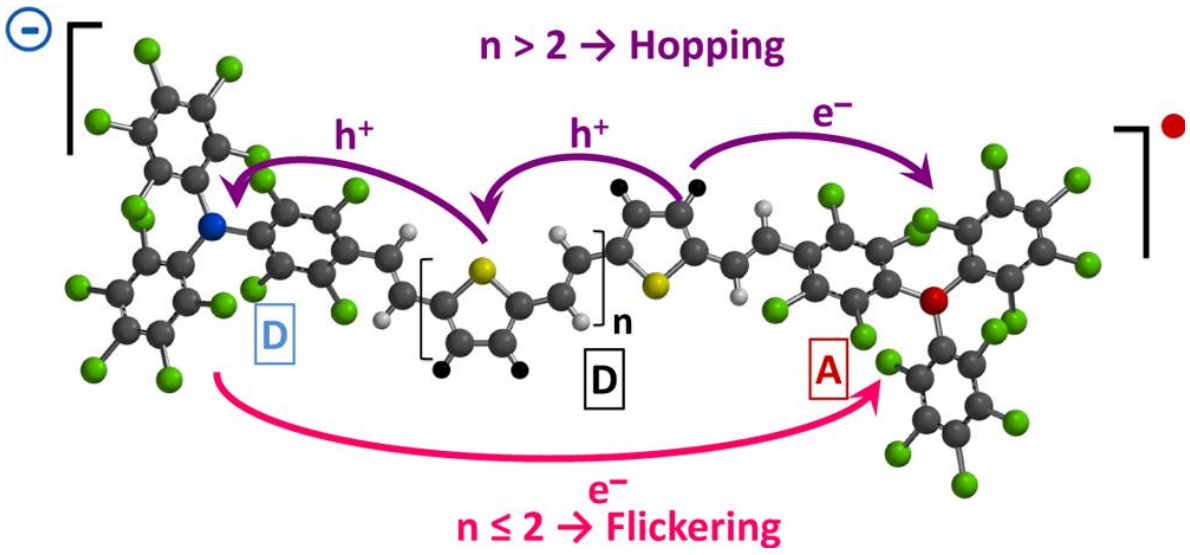

Fig. 8.19 MVC-PTM estudiats amb ponts de TV de mida creixent.

En el **Publication** #7 vam realitzar una dinàmica molecular a 300K i vam estudiar la localització o deslocalització de la densitat d'espín associada l'electró desaparellat. Vam trobar que per una meitat de les conformacions tèrmicament activades a 300K l'espín es trobava localitzat en una de les unitats PTM i, per tant, la càrrega negativa localitzada en l'altra unitat. L'altra meitat de les conformacions però, la densitat d'espín estava totalment deslocalitzada entre les dues unitats PTM, la qual cosa també implicava una deslocalització de la càrrega negativa en ambdues unitats PTM i sobre el pont π-conjugat. Aquests resultats, com expliquem en aquesta contribució, apunta a un mecanisme anomenat ressonància parpelleig (o flickering resonance, FR, de l'anglès). Així doncs, el mecanisme FR entén que la carrega negativa té la capacitat de deslocalitzar-se a través del pont π-conjugat entre les dues unitats PTM en l'estat fonamental però que no totes les conformacions ho permeten. Així doncs a temperatura ambient, algunes conformacions localitzaran la càrrega en una unitat PTM i, unes altres, la deslocalitzaran en tota la molècula, així permeten que la càrrega vagi localitzant-se en una unitat PTM o a l'altra. Val la pena esmentar que aquest mecanisme està relacionat amb la conducció balística demostrada en el grafè.[67]

8.5.4 De MVC-PTM a materials orgànics de Dirac post-grafè

Aquest efecte tan important de les connectivitats meta- i para- provades per compostos multi-radicals (Fig. 8.16) i en els corresponents MVC (Fig. 8.17) haurien de tenir un efecte anàleg en les xarxes covalents basades en TAM (TAM 2D-COFs). En el treball **Publication** #5 el TAM 2D-COF estudiats presentaven una estructura on les unitats TAM estan connectades en meta- una respecte l'altra (Fig. 8.20a). Com s'explica en aquell treball, aquestes xarxes presenten una estructura electrònica d'aïllant elèctric, on cada electró desaparellat es troba localitzat en la unitat TAM corresponent.

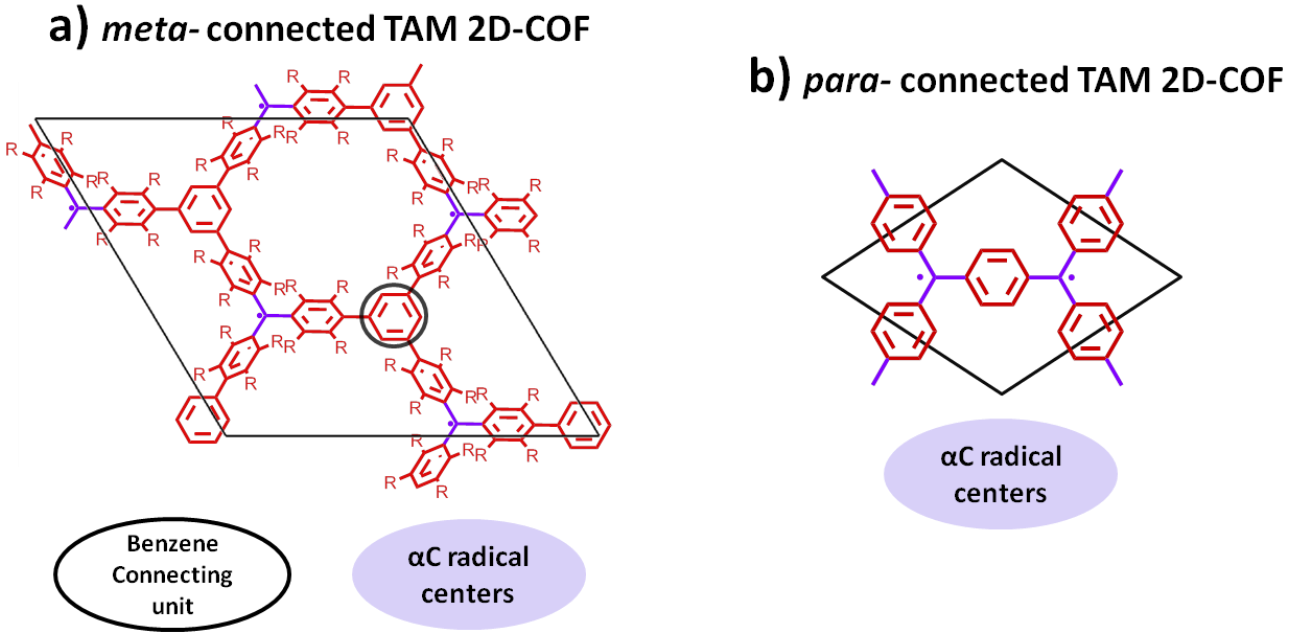

Fig. 8.20 a) Estructura química del TAM 2D-COF connectat en meta- estudiat en el treball **Publication #5 b)** del connectat en *para*- estudiat en el treball **Publication #8**.

Quines propietats electròniques mostraria un TAM 2D-COF on les unitats TAM estiguin connectades en para- una respecte de l'altra? Resulta que, com va publicar Adjizian et al.[68,69] aquest tipus de xarxes 2D es comporten com a semimetalls, tal com el grafè, mostrant un con de Dirac en l'estructura de bandes corresponent (veure Fig. 8.21). Aquesta interessant característica electrònica està associada a la conducció balística ja demostrada experimentalment en grafè.[70,71]

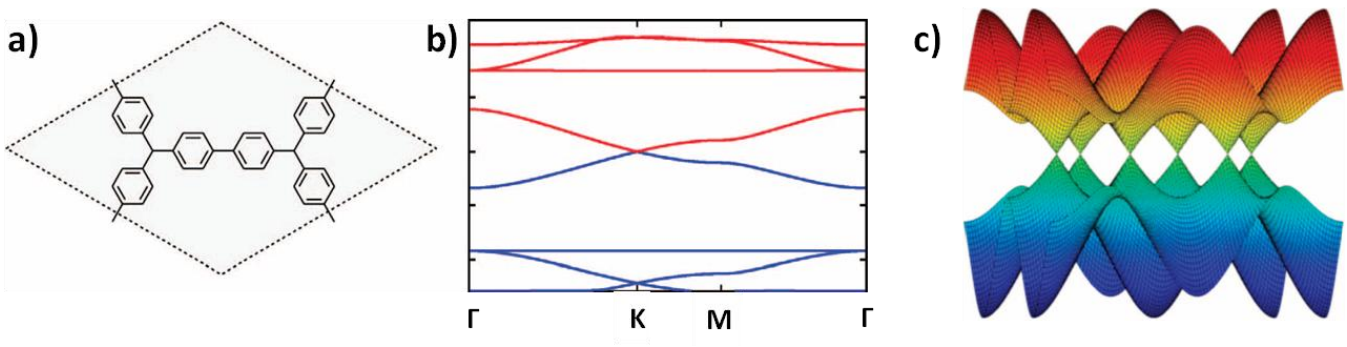

Fig. 8.21 a) Estructura periòdica del TAM 2D-COF connectat en *para*- proposat per Adjizian et al. **b)** Estructura de bandes de tal xarxa covalent mostrant la presència d'un encreuament lineal de bandes al nivell de Fermi (anomenat con de Dirac) **c)** Representació 3D del con de Dirac en aquest tipus de xarxes.

En el treball **Publication #8** hem fet una connexió entre una sèrie de materials orgànics de Dirac post-grafè (PGODs, de l'anglès) i els bi-radicals basats en TAM connectats en para-. Com s'ha mostrat anteriorment aquests bi-radicals mostren dues formes ressonants, sent aquestes l'anti-ferromagnètica de capa oberta (és a dir, bi-radical) i la quinoide de capa tancada (veure Fig. 8.16). Aquestes formes ressonants però, també haurien d'existir en els PGODs, ja que en aquests materials els centres radicalaris

també estan connectats en para- un respecte de l'altre.

Tot i així, per a la sèrie de PGODs mostrats en la Fig. 8.22 aquestes solucions electròniques localitzades no s'han informat.

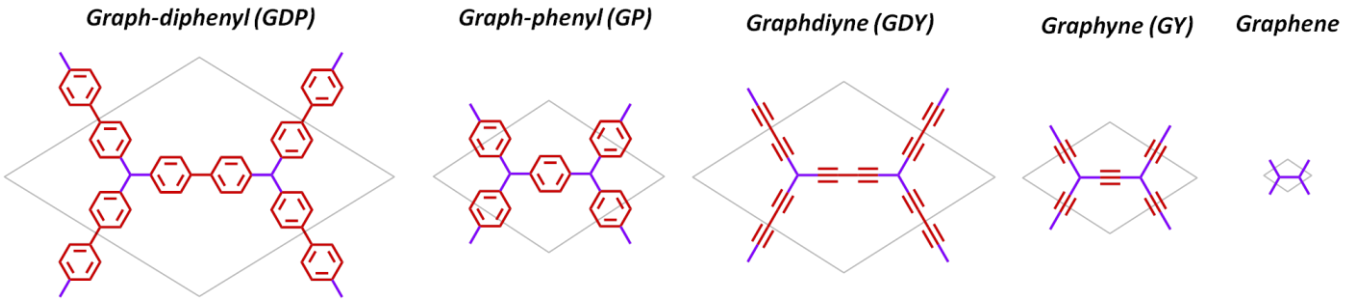

Fig. 8.22 Sèrie de materials PGODs estudiats en el treball **Publication #8**. Tots aquests materials presenten un con de Dirac en l'estructura de bandes corresponent, la qual cosa indica la seva naturalesa com a semimetalls, com el grafè.

Per tant, en el treball **Publication #8**, hem realitzat un estudi sistemàtic on demostrem en detall l'existència d'aquestes solucions localitzades (la AFM i quinoide) per primera vegada. Aquest estudi s'ha basat en càlculs DFT utilitzant el funcional híbrid PBE0 i comparant els resultats en dos programes que utilitzen un tipus diferent de representacions electròniques. Els resultats obtinguts coincideixen per ambdós enfocaments. Així doncs, els nostres resultats demostren que els materials PGODs presenten una estructura altament tunejable a la nano-escala i que, per tant, tenen un potencial per a futures aplicacions en nano-electrònica molt important.

8.6 Conclusions

En la meva opinió la contribució intel·lectual més important d'aquesta tesi és el disseny dels materials 2D TAM 2D-COFs. Aquests materials, no sintetitzats encara al laboratori, presenten tota una sèrie de propietats que els fan molt interessants per a aplicacions futures en nano-electrònica. Com s'ha vist amb els resultats presentats en els treballs **Publications** #4 – 6, el gir dels anells aril determinen la localització/deslocalització de l'electró desaparellat en els TAMs. Aquesta característica es pot utilitzar per dissenyar TAM 2D-COFs on, per mitjà d'un estirament mono-direccional l'angle de gir dels anells aril es pot manipular externament. Aquesta manipulació estructural dóna lloc, al seu torn, a un control extern de propietats electròniques fonamentals del material tal com la localització d'espín, les interaccions magnètiques i el band gap del material, totes elles variant linealment amb la mitjana del cosinus al quadrat de l' angle de gir de tots els anells aril del material. Així doncs, els TAM 2D-COFs es podrien utilitzar com a sensors mecànics. D'altra banda, en canviar la connectivitat entre els TAMs dins del material, fa que aquest es comporti com a un semi-metall amb solucions semiconductores properes en energia. Per tant, simplement canviant la manera en la qual els TAMs estan covalentment units permet dissenyar aïllants elèctrics o conductors 2D, la qual cosa torna a ressaltar la gran versatilitat electrònica

d'aquests materials.

En general, aquest treball de tesi m'ha permès experimentar dos modes del químic computacional: el mode on es col·labora amb grups experimentals estudiant sistemes ja sintetitzats per aprofundir en la seva comprensió i, d'altra banda, el mode on s'utilitza la simulació com a eina per predir materials i sistemes no sintetitzats al laboratori. Poder aprofitar ambdós enfocaments per nodrir-los l'un de l'altre (com es pot veure entre els últims treballs **Publications** #7 i #8) és per a mi un dels millors aprenentatges que trec d'aquesta tesi doctoral.

8.7 Referències

1 M. Gomberg, *J. Am. Chem. Soc.*, 1900, **22**, 757–771.

2 A. E. Tschitschibabin, *Berichte der Dtsch. Chem. Gesellschaft*, 1907, **40**, 1810–1819.

3 G. Kothe and H. Zimmermann, *Tetrahedron*, 1973, **29**, 2305–2313.

4 A. Rajca, K. Lu and S. Rajca, *J. Am. Chem. Soc.*, 1997, **119**, 10335–10345.

5 A. Rajca, J. Wongsriratanakul and S. Rajca, *Science*, 2001, **294**, 1503–1505.

6 N. M. Shishlov, *Russ. Chem. Rev.*, 2006, **75**, 863–884.

7 M. Gomberg, *J. Am. Chem. Soc.*, 1903, **25**, 1274–1277.

8 M. Ballester and J. Riera-Figueras, *J. Am. Chem. Soc.*, 1971, **4254**, 2215–2225.

9 J. Veciana and I. Ratera, in *Stable Radicals: Fundamentals and Applied Aspects of Odd-Electron Compounds*, ed. R. G. Hicks, John Wiley & Sons, Inc., 2010, pp. 33–80.

10 A. Rajca, S. Rajca and J. Wongsriratanakul, *J. Am. Chem. Soc.*, 1999, **121**, 6308–6309.

11 S. Rajca, A. Rajca, J. Wongsriratanakul, P. Butler and S. M. Choi, *J. Am. Chem. Soc.*, 2004, **126**, 6972–86.

12 D. Maspoch, D. Ruiz-Molina, K. Wurst, N. Domingo, M. Cavallini, F. Biscarini, J. Tejada, C. Rovira and J. Veciana, *Nat. Mater.*, 2003, **2**, 190–5.

13 C. Simão, M. Mas-Torrent, N. Crivillers, V. Lloveras, J. M. Artés, P. Gorostiza, J. Veciana and C. Rovira, *Nat. Chem.*, 2011, **3**, 359–64.

14 R. Frisenda, R. Gaudenzi, C. Franco, M. Mas-Torrent, C. Rovira, J. Veciana, I. Alcon, S. T. Bromley, E. Burzurí and H. S. J. van der Zant, *Nano Lett.*, 2015, **15**, 3109–3114.

15 M. Abel, S. Clair, O. Ourdjini, M. Mossoyan and L. Porte, *J. Am. Chem. Soc.*, 2011, **133**, 1203–1205.

16 M. Bieri, M. Treier, J. Cai, K. Aït-Mansour, P. Ruffieux, O. Gröning, P. Gröning, M. Kastler, R. Rieger, X. Feng, K. Müllen and R. Fasel, *Chem. Commun. (Camb).*, 2009, 6919–21.

17 X.-H. Liu, Y.-P. Mo, J.-Y. Yue, Q.-N. Zheng, H.-J. Yan, D. Wang and L.-J. Wan, *Small*, 2014, **10**, 4934–9.

18 X.-H. Liu, C.-Z. Guan, S.-Y. Ding, W. Wang, H.-J. Yan, D. Wang and L.-J. Wan, *J. Am. Chem. Soc.*, 2013, **135**, 10470–4.

19 C. Steiner, J. Gebhardt, M. Ammon, Z. Yang, A. Heidenreich, N. Hammer, A. Görling, M. Kivala and S. Maier, *Nat. Commun.*, 2017, **8**, 14765.

20 Q. Fan, J. M. Gottfried and J. Zhu, *Acc. Chem. Res.*, 2015, **48**, 2484–2494.

21 W. Liu, X. Luo, Y. Bao, Y. P. Liu, G.-H. Ning, I. Abdelwahab, L. Li, C. T. Nai, Z. G. Hu, D. Zhao, B. Liu, S. Y. Quek and K. P. Loh, *Nat. Chem.*, 2017, **9**, 563–570.

22 A. Basagni, F. Sedona, C. A. Pignedoli, M. Cattelan, L. Nicolas, M. Casarin and M. Sambi, *J. Am. Chem. Soc.*, 2015.

23 A. Basagni, G. Vasseur, C. A. Pignedoli, M. Vilas-Varela, D. Peña, L. Nicolas, L. Vitali, J. Lobo-Checa, D. G. de Oteyza, F. Sedona, M. Casarin, J. E. Ortega and M. Sambi, *ACS Nano*, 2016, **10**, 2644–2651.

24 W. Dong, L. Wang, H. Ding, L. Zhao, D. Wang, C. Wang and L.-J. Wan, *Langmuir*, 2015, **31**, 11755–11759.

25 Q. Sun, C. Zhang, L. Cai, L. Xie, Q. Tan and W. Xu, *Chem. Commun.*, 2015, **51**, 2836–2839.

26 G. Gu, N. Li, L. Liu, X. Zhang, Q. Wu, D. Nieckarz, P. Szabelski, L. Peng, B. K. Teo, S. Hou, Y. Wang, R. Bhosale, A. Mateo-Alonso, J. V. Barth, K. Wu and Y. F. Wang, *RSC Adv.*, 2016, **6**, 66548–66552.

27 J. P. Llinas, A. Fairbrother, G. Borin Barin, W. Shi, K. Lee, S. Wu, B. Yong Choi, R. Braganza, J. Lear, N. Kau, W. Choi, C. Chen, Z. Pedramrazi, T. Dumslaff, A. Narita, X. Feng, K. Müllen, F. Fischer, A. Zettl, P. Ruffieux, E. Yablonovitch, M. Crommie, R. Fasel and J. Bokor, *Nat. Commun.*, 2017, **8**, 633.

28 P. Ruffieux, S. Wang, B. Yang, C. Sanchez, J. Liu, T. Dienel, L. Talirz, P. Shinde, C. A. Pignedoli, D. Passerone, T. Dumslaff, X. Feng, K. Muellen and R. Fasel, *Nature*, 2015, **531**, 15.

29 A. Narita, X.-Y. Wang, X. Feng and K. Müllen, *Chem. Soc. Rev.*, 2015, **44**, 6616–6643.

30 S. Kawai, S. Saito, S. Osumi, S. Yamaguchi, A. S. Foster, P. Spijker and E. Meyer, *Nat. Commun.*, 2015, **6**, 8098.

31 L. H. Thomas, *Proc. Camb. Phil. Soc.*, 1927, **23**, 542.

32 E. Fermi, *Rend. Accad. Lincei*, 1927, **6**, 602.

33 P. A. M. Dirac, *Proc. Camb. Phil. Soc.*, 1930, **26**, 376.

34 F. Bloch, *Z. Phys.*, 1929, **57**, 545.

35 P. Hohenberg and W. Kohn, *Phys. Rev.*, 1964, **136**, B864.

36 W. Kohn and L. J. Sham, *Phys. Rev.*, 1965, **140**, A1133.

37 A. D. Becke, *Phys. Rev. A*, 1988, **38**, 3098.

38 J. P. Perdew, K. Burke and M. Ernzerhof, *Phys. Rev. Lett.*, 1996, **77**, 3865–3868.

39 A. D. Becke, *J. Chem. Phys.*, 1993, **98**, 1372.

40 C. Adamo and V. Barone, *J. Chem. Phys.*, 1999, **110**, 6158.

41 R. Improta and V. Barone, *Chem. Rev.*, 2004, **104**, 1231–54.

42 F. Rissner, Z. Ma, O. T. Hofmann, C. Slugovc, Z. Shuai and E. Zojer, *J. Mater. Chem.*, 2012, **22**, 4269.

43 M. Mas-Torrent, N. Crivillers, V. Mugnaini, I. Ratera, C. Rovira and J. Veciana, *J. Mater. Chem.*, 2009, **19**, 1691.

44 M. Mas-Torrent, N. Crivillers, C. Rovira and J. Veciana, *Chem. Rev.*, 2012, **112**, 2506–27.

45 J. Guasch, X. Fontrodona, I. Ratera, C. Rovira and J. Veciana, *Acta Crystallogr.*, 2013, **C69**, 255–7.

46 N. Crivillers, M. Mas-Torrent, J. Vidal-Gancedo, J. Veciana and C. Rovira, *J. Am. Chem. Soc.*, 2008, **130**, 5499–5506.

47 C. Dugave and L. Demange, *Chem. Rev.*, 2003, **103**, 2475–2532.

48 W.-G. Han, T. Lovell, T. Liu and L. Noodleman, *ChemPhysChem*, 2002, **3**, 167–178.

49 D. Gegiou, K. A. Muszjat and E. Fischer, *J. Am. Chem. Soc.*, 1968, **90**, 3907–3918.

50 M. J. Frisch, G. W. Trucks, H. B. Schlegel, G. E. Scuseria, M. A. Robb, J. R. Cheeseman, G. Scalmani, V. Barone, B. Mennucci, G. A. Petersson, H. Nakatsuji, M. Caricato, X. Li, H. P. Hratchian, A. F. Izmaylov, J. Bloino, G. Zheng, J. L. Sonnenberg, M. Had and D. J. Fox, 2009.

51 F. C. Adam and S. I. Weissman, *J. Am. Chem. Soc.*, 1958, **80**, 2057–2059.

52 M. Karplus and G. K. Fraenkel, *J. Chem. Phys.*, 1961, **35**, 1312–1323.

53 J. A. Pople and D. L. Beveridge, *J.Chem.Phys.*, 1968, **49**, 4725–4726.

54 M. J. S. Dewar, *J. Am. Chem. Soc.*, 1952, **74**, 3345–3350.

55 G. N. Lewis, D. Lipkin and T. T. Magel, *J. Am. Chem. Soc.*, 1944, **66**, 1579–1583.

56 M. Ballester, J. Riera, J. Castañer, C. Badía and J. M. Monsó, *J. Am. Chem. Soc.*, 1971, **93**, 2215–2225.

57 N. M. Gallagher, A. Olankitwanit and A. Rajca, *J. Org. Chem.*, 2015, **80**, 1291–8.

58 L. K. Montgomery, J. C. Huffman, E. A. Jurczak and M. P. Grendze, *J. Am. Chem. Soc.*, 1986, **108**, 6004–6011.

59 P. Ravat and M. Baumgarten, *Phys. Chem. Chem. Phys.*, 2015, **17**, 983–991.

60 C. Rovira, D. Ruiz-Molina, O. Elsner, J. Vidal-Gancedo, J. Bonvoisin, J.-P. Launay and J. Veciana, *Chemistry (Easton).*, 2001, **7**, 240–250.

61 V. Lloveras, J. Vidal-Gancedo, D. Ruiz-Molina, T. M. Figueira-Duarte, J.-F. Nierengarten, J. Veciana and C. Rovira, *Faraday Discuss.*, 2006, **131**, 291.

62 V. Lloveras, J. Vidal-Gancedo, T. M. Figueira-Duarte, J. F. Nierengarten, J. J. Novoa, F. Mota, N. Ventosa, C. Rovira and J. Veciana, *J. Am. Chem. Soc.*, 2011, **133**, 5818–33.

63 J. Sedo, D. Ruiz, J. Vidal-Gancedo, C. Rovira, J. Bonvoisin, J.-P. Launay and J. Veciana, *Adv. Mater.*, 1996, **8**, 748–752.

64 A. Heckmann and C. Lambert, *J. Am. Chem. Soc.*, 2007, **129**, 5515–5527.

65 A. Heckmann, S. Dümmler, J. Pauli, M. Margraf, J. Köhler, D. Stich, C. Lambert, I. Fischer and U. Resch-Genger, *J. Phys. Chem. C*, 2009, **113**, 20958–20966.

66 J. Wu, X. Wu, J. O. Kim, S. Medina, F. J. Ramírez, P. M. Burrezo, S. Wu, Z. L. Lim, C. Lambert, J. Casado and D. Kim, *Chem. - A Eur. J.*, 2017.

67 J. Blumberger, *Chem. Rev.*, 2015, **115**, 11191–11238.

68 J.-J. Adjizian, P. Briddon, B. Humbert, J.-L. Duvail, P. Wagner, C. Adda and C. Ewels, *Nat. Commun.*, 2014, **5**, 5842.

69 J.-J. Adjizian, A. Lherbier, S. M.-M. Dubois, A. R. Botello-Méndez and J.-C. Charlier, *Nanoscale*, 2016, **8**, 1642–1651.

70 V. E. Calado, S.-E. Zhu, S. Goswami, Q. Xu, K. Watanabe, T. Taniguchi, G. C. A. M. Janssen and L. M. K. Vandersypen, *Appl. Phys. Lett.*, 2014, **104**, 23103.

71 J. Baringhaus, M. Ruan, F. Edler, A. Tejeda, M. Sicot, A. Taleb-Ibrahimi, A.-P. Li, Z. Jiang, E. H. Conrad, C. Berger, C. Tegenkamp and W. A. de Heer, *Nature*, 2014, **506**, 349–354.